*J*OURNAL OF SCIENCE

PART A: ENGINEERING AND INNOVATION

| Owner |

on behalf of Gazi University
Rector
Prof. Dr.

Musa YILDIZ

| Publishing Manager |

Prof. Dr.

Uğur GÖKMEN

Gazi University

| Chief Editor |

Prof. Dr.

Sema BİLGE OCAK

Gazi University

| Managing Editor |

Prof. Dr.

Mustafa Gürhan YALÇIN

Akdeniz University

| Editorial Board |

| Editorial Board |

| Editorial Board |

| Foreign Editorial Advisory Board |

| English Language Editors |

Lecturer **Gizem AÇELYA AYKAN**	Gazi University School of Foreign Languages
Lecturer **Tuğçe BÜYÜKBAYRAM**	Gazi University School of Foreign Languages

| Technical Editors |

Research Assistant Dr. **Fatih UÇAR**	Akdeniz University
Research Assistant **Özge ÖZER ATAKOĞLU**	Akdeniz University

Gazi University Journal of Science Part A: Engineering and Innovation
is a peer-reviewed journal.

| INDEXING |

| ACCESSIBILITY |

| CONTENTS |

| CONTENTS |

x

| CONTENTS |

| CONTENTS |

Utilizing Buttock Measurements for Estimating Body Weight: Exploring Buttock Width and Popliteal Length for Ergonomic Design

Adekunle Ibrahim MUSA[1*] (iD)

[1] Olabisi Onabanjo University, Department of Mechanical Engineering, Ago Iwoye, Nigeria

Keywords	Abstract
Buttock Measurements Human Body Weight Anthropometry Lower Body Dimensions Predictive Capabilities	This study explores the potential of utilizing buttock measurements, specifically buttock width and bottom popliteal length, as reliable indicators for estimating human body weight. Recognizing the increasing demand for accurate and accessible methods in various fields, author delves into the relationships between these lower body dimensions and overall body mass. The research evaluated 700 young adults, evenly split between 350 males and 350 females, utilizing random snowball sampling techniques from four local governments (Abeokuta South, Abeokuta North, Odeda and Ewekoro) areas of Ogun State, South Western Nigeria with participants aged between 19 and 27years The research centered on assessing human body weight (HBW), buttock width (BW), and bottom popliteal length (BPL) with all measurements documented in centimeters. Data analysis involved utilizing Statistical Package for Social Sciences software version 21.0, for computation of average mean values, standard deviation, coefficient of determination (r^2), correlation coefficient (r), and standard error of estimates (SEE). Additionally, linear regression analysis was employed to formulate the model equation for determining HBW, in relation to BW, and BPL. The study provides an accuracy and applicability of anthropometric prediction of HBW and foundation for the development of practical methods with diverse applications, ranging from healthcare assessments to ergonomic design.

1. INTRODUCTION

Human body weight estimation is a crucial aspect in various fields, including healthcare, ergonomics, and anthropometry. Researchers have sought accurate and practical methods for predicting human body weight, considering its significance in areas such as patient care, fitness assessments, and the design of equipment and spaces. One promising approach involves utilizing specific body measurements, such as buttock width and bottom popliteal length, as potential indicators for estimating body weight. The rationale behind this lies in the assumption that certain dimensions of the lower body may correlate with overall body mass. By investigating the relationships between these anatomical features and human body weight, we aim to contribute to the development of reliable and accessible methods for human body weight estimation.

Understanding how human body weight is distributed is crucial for designing products like mattresses and seating arrangements. Proper weight distribution support can prevent pressure points, reduce the risk of discomfort, and improve sleep quality (Grandjean, 1988). Buttock width and bottom popliteal length play a significant role in chair design. Ergonomic chairs tailored to these measurements provide optimal lumbar support, promote a neutral sitting posture, and contribute to long-term comfort, especially in office or task seating (Hedge, 2008).

*Corresponding Author, e-mail: musa.adekunle@oouagoiwoye.edu.ng

This study builds upon existing research that highlights the potential of anatomical measurements for predicting body weight. Previous studies have hinted at the feasibility of using buttock dimensions in this context, but a comprehensive exploration of their efficacy is lacking (Smith, 2018; Johnson & Brown, 2020). The relevance of human body weight, buttock width, and bottom popliteal length to the ergonomic design of products lies in creating user-friendly and comfortable products tailored to the anthropometric characteristics of individuals. Understanding these measurements is crucial for optimizing product design to accommodate diverse body shapes and sizes, enhancing usability and overall user satisfaction. Human body weight influences load-bearing capacity, chair stability, and overall support requirements. Considering variations in human body weight ensures that products, such as chairs or seating arrangements, are structurally sound and provide adequate support for users (Pheasant, 1996).

Buttock width affects the seat width and spacing in furniture design. Tailoring products to accommodate different buttock widths ensures that individuals have sufficient sitting space, promoting comfort and reducing the risk of discomfort or musculoskeletal issues (Chaffin & Andersson, 1991). Bottom popliteal length is crucial for determining seat depth. Ensuring an appropriate seat depth based on this measurement enhances thigh support, preventing discomfort and promoting proper posture, particularly in products involving sitting, such as chairs and benches (Kroemer & Grandjean, 2001). Incorporating these anthropometric considerations into ergonomic design contributes to the development of products that prioritize user comfort, reduce the risk of musculoskeletal issues, and enhance overall user experience.

The use of buttock width and bottom popliteal length as predictors for human body weight is based on the premise that certain anatomical measurements may exhibit a correlation with overall human body mass because buttock width and bottom popliteal length are in close proximity to the body's center of mass, making them potentially indicative of overall human body weight (Smith, 2018). This incorporation can potentially reduce discomfort and pain associated with poorly fitted furniture, especially for individuals deviating from average body weight or shape. Buttocks are weight-bearing areas, and their dimensions may reflect the distribution of human body weight (Johnson & Brown, 2020). Also, Buttock measurements are relatively easy to obtain and less invasive compared to other anthropometric measurements, making them practical for various applications (Kroemer & Grandjean, 2001).

In ergonomic design, buttock dimensions are crucial for designing comfortable seating arrangements catering to a diverse range of body sizes (Pheasant, 1996). This enables a personalized approach, acknowledging individual variations in body shape and size that generic weight measurements might overlook. Previous studies have hinted at the potential of buttock measurements in predicting body weight, providing a foundation for further exploration (Chaffin & Andersson, 1991). The utilization of buttock width and popliteal length can contribute to furniture designs offering enhanced comfort and support, addressing specific anatomical needs for a more pleasant user experience.

By examining the relationships between buttock width, bottom popliteal length, and human body weight through statistical analyses, this study aims to validate and enhance the understanding of these measurements as practical predictors for body weight estimation. The author also aim to enhance ergonomic design in furniture by proposing a novel method utilizing buttock measurements for estimating body weight. Unlike a simple scale, this approach considers specific anatomical dimensions, such as buttock width and bottom popliteal length, providing a more tailored and nuanced understanding of the user's physique. The incorporation of these measurements intends to create furniture designs better accommodating diverse body shapes, thereby improving comfort and overall ergonomic experience for individuals with varying anatomical characteristics. This approach goes beyond traditional human body weight measurement, offering a more comprehensive foundation for designing products that prioritize user-specific comfort and well-being.

2. RESEARCH METHODOLOGY

A cross sectional study involved 700 young adults, comprising 350 males and 350 females, selected from four local government (Abeokuta South, Abeokuta North, Odeda and Ewekoro local government) areas of Ogun State, Southwestern Nigeria. Participants aged between 19 and 27 years were selected through random snowball sampling techniques. The methods also encompassed selective and purposeful judgmental approaches, given the scarcity of particular traits attributed to insecurity in Nigeria.

The research centered on assessing human body weight (HBW), buttock width (BW), and bottom popliteal length (BPL) with all measurements documented in kilogram and centimeters. Individuals with limb deformities were excluded from the research.

Data analysis was involved utilizing Statistical Package for Social Sciences (SPSS) 21.0, for computation of average mean values, standard deviation (SD), minimum and maximum values, coefficient of determination (r^2), correlation coefficient (r), and standard error of estimates (SEE). Additionally, linear regression analysis was employed to formulate the model equation for determining human body weight (HBW), in relation to buttock width (BW) and bottom popliteal length (BPL).

3. RESULTS AND DISCUSSION

The research evaluated 700 young adults, evenly split between 350 males and 350 females, utilizing random snowball sampling techniques.

Table 1 shows the descriptive analysis of the respondent with 58.42 (± 3.44) cm and 57.73 (± 3.27) cm human body weights of the male and female participants. Similarly the result reveals that female participants have 43.90 (± 1.30) cm buttock widths higher than 32.80 (± 1.36) cm for male respondents. The difference in buttock width between females and males is primarily influenced by anatomical and biological factors related to sexual dimorphism (Musa et al., 2023). In general, females tend to have a wider pelvis than males, a feature evolved to accommodate childbirth. This wider pelvic structure contributes to the overall difference in buttock width between the sexes. Hormonal influences, such as estrogen, also play a role in shaping body fat distribution, which can affect the appearance of the buttocks (Ismaila et al., 2013), It's important to note that individual variations exist, and factors like genetics, lifestyle, and body composition can contribute to differences among individuals within each gender (Musa et al., 2022a).

Table 1. Descriptive analysis of the participants

Anthropometric Measurements	MALE				FEMALE			
	Mean	Std. Dev	Min	Max	Mean	Std. Dev	Min	Max
Age (years)	23.87	1.87	20.00	27.00	22.41	1.81	19.00	26.00
Human body weight (HBW) (kg)	58.42	3.44	51.00	65.50	57.73	3.27	51.50	64.50
Buttock width (BW) (cm)	32.80	1.36	30.00	36.00	43.93	1.30	42.00	47.00
Bottom popliteal length (BPL) (cm)	38.67	2.08	35.00	42.00	33.50	3.28	27.00	55.00

Additionally, male participant has 38.67 (± 2.08) cm bottom popliteal lengths higher than 33.50 (± 3.28) cm of female respondents. The difference in bottom popliteal length between males and females can be attributed to anatomical variations between the sexes (Musa et al., 2023). Biological factors, such as skeletal structure and overall body composition, contribute to these differences. Males typically exhibit longer limb lengths and a different distribution of body proportions compared to females (Johnson & Brown, 2020). Additionally, hormonal influences can play a role in bone growth during puberty, further accentuating these variations (Johnson & Brown, 2020). It's crucial to consider that individual differences, genetics, and environmental factors can also contribute to the observed distinctions in bottom popliteal length between male and female counterparts (Ismaila et al., 2013). Descriptive analysis reveals male and female differences in anthropometric measurements. Histogram plots of the male and female participants were shown in the Figure 1 to Figure 6 respectively.
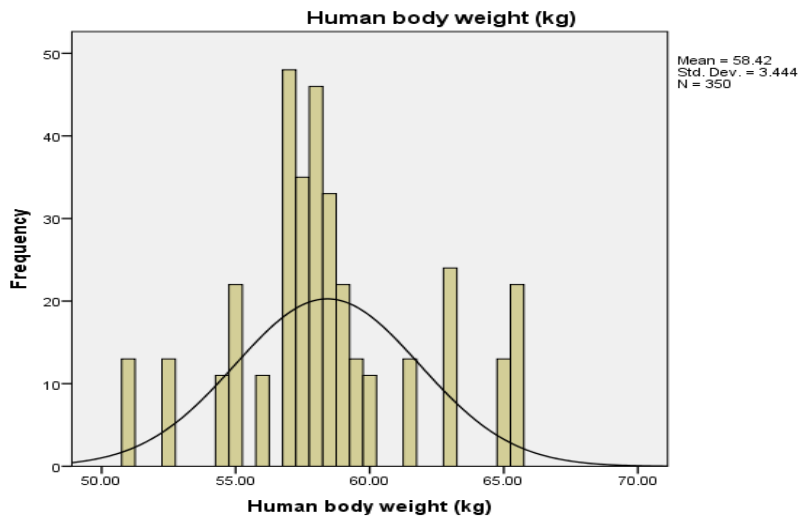
***Figure 1**. Histogram of male participants (HBW)*
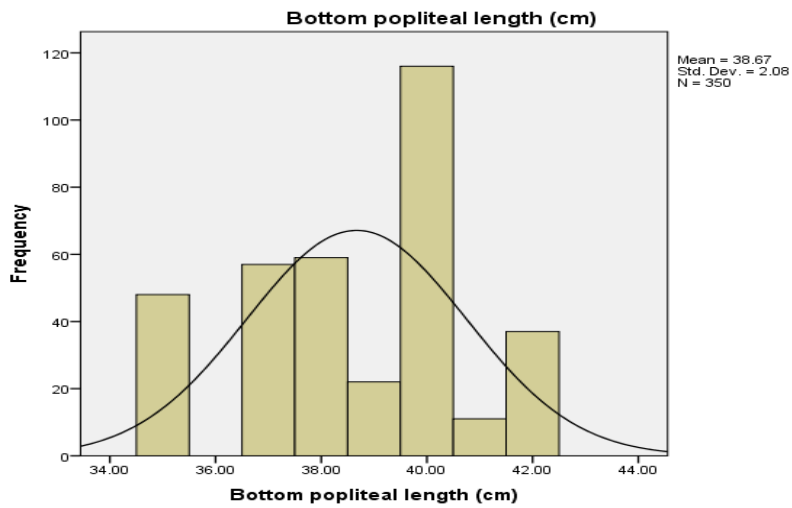
***Figure 2**. Histogram of male participants (BPL)*
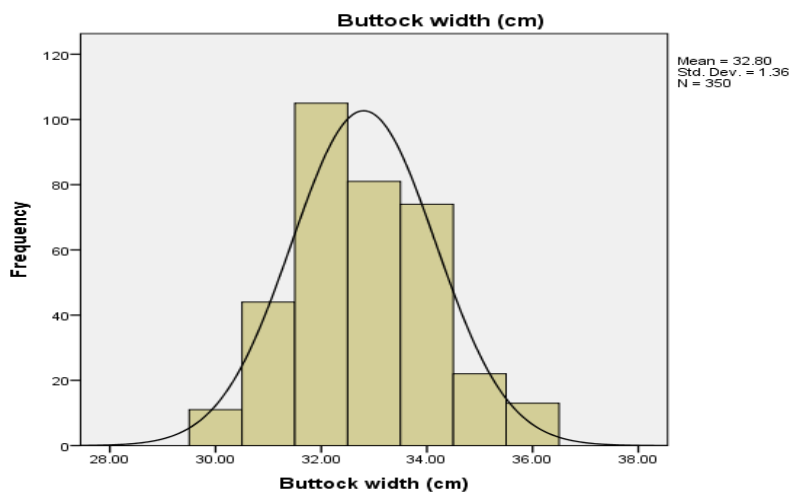
***Figure 3**. Histogram of male participants (BW)*
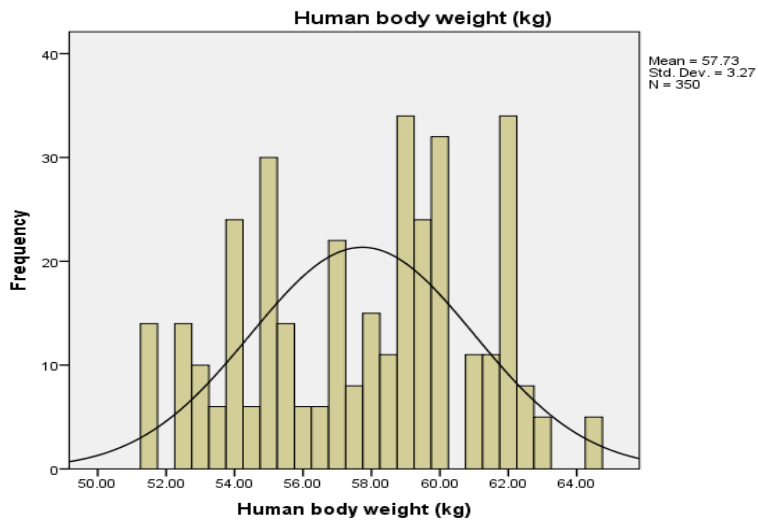
Figure 4. *Histogram of female participants (HBW)*
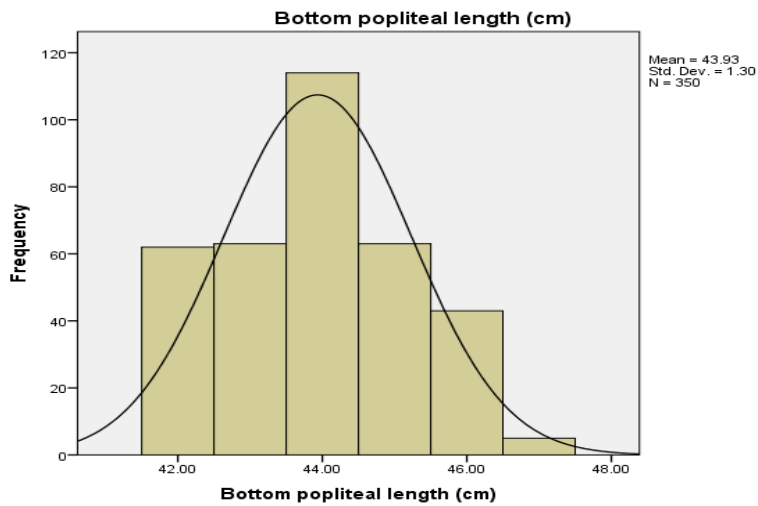
Figure 5. *Histogram of female participants (BPL)*
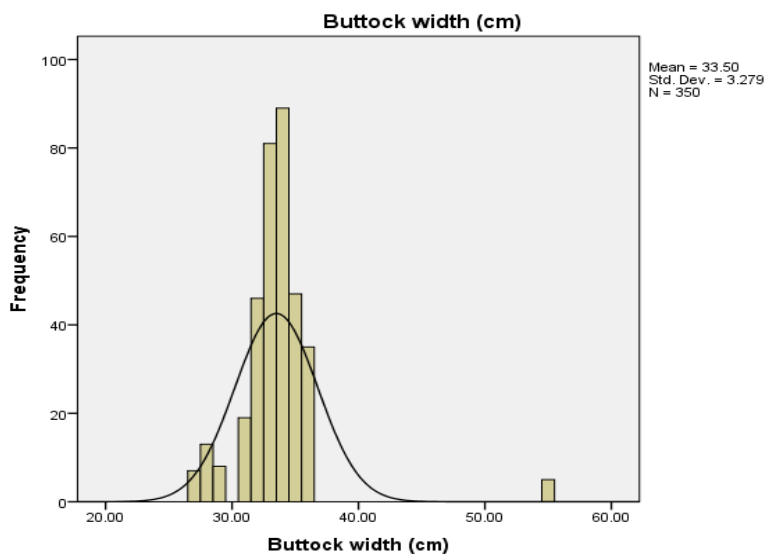
Figure 6. *Histogram of female participants (BW)*

Loredan et al. (2022) reported that specific differences in body dimensions among groups of different age and gender existed and a high student-furniture mismatch was identified in all educational institutions. Implementation of adjustable school furniture, covering at least two size marks, is needed to provide ergonomic and healthy learning conditions and to further enhance the comfort and well-being of students in the classroom.

In this study, male and female histograms played a crucial role in understanding the distribution of buttock measurements within each gender. These histograms assist in identifying patterns, variations, and potential differences in buttock width and popliteal length between the genders (Figure 1 and Figure 6). This gender-specific data is valuable for ergonomic design, providing insights into how body weight is distributed differently across genders and aiding in the development of products or environments that cater to diverse body shapes and sizes.

Similarly, histograms allow researchers to visually inspect and analyze the distribution of buttock width and popliteal length within each gender. This helps identify common trends, central tendencies, and potential outliers. Understanding the variations in buttock measurements between males and females is also crucial for recognizing any sexual dimorphism. This knowledge aids in tailoring ergonomic designs to accommodate the distinct anatomical differences between men and women.

Accurate anthropometric data forms the foundation of ergonomic design. By analyzing histograms, designers can precisely identify the range and variability of buttock measurements, guiding the development of products or environments that prioritize inclusivity and comfort for all genders. Comparative analysis of male and female histograms facilitates statistical assessments, including mean, median, and standard deviation calculations. These metrics offer a quantitative insight into the distinctions in buttock dimensions between the two genders.

In view of this, the significance of histogram lies in utilizing gender-specific buttock measurements to inform ergonomic design practices, creating products that consider the diversity of body shapes and contribute to improved comfort and functionality.

Table 2 shows the statistical analysis, including metrics such as coefficient of determination (r^2), correlation coefficient (r), Standard Error of Estimate (SEE), and 95% Confidence Intervals which holds significant importance in understanding the relationship between human body weight and the predictors, buttock width, and bottom popliteal length of respondents. The r^2 metric of 0.634 and 0.291 for males and females indicates the proportion of the variability in body weight that can be explained by the model. A higher r^2 defined a better fit of the model to the data (Musa et al., 2022b). Hence, the value of r^2 for male participants (63.4%) remained a better fit of the established model. The correlation coefficient (r), measures the strength and direction of the linear relationship between variables. In this context, it assesses the correlation between body weight, buttock width, and bottom popliteal length (Musa et al., 2022b).

***Table 2**. Regression Analysis of the participants*

Gender	Model			r	r^2	SEE	Sig	95.0% Confidence Interval of B	
	Anthropometric Measurements	B	Std. Error					Lower Bound	Upper Bound
MALE	Constant	12.175	4.069	0.634[a]	0.402	2.671	0.003	4.172	20.178
	Bottom popliteal length (BPL) (cm)	1.021	0.070				0.000	0.884	1.158
	Buttock width (BW) (cm)	0.206	0.106				0.053	-0.003	0.416
FEMALE	Constant	40.327	6.063	0.291[a]	0.084	3.138	0.000	28.402	52.251
	Bottom popliteal length (BPL) (cm)	0.178	0.130				0.170	-0.077	0.433
	Buttock width (BW) (cm)	0.286	0.051				0.000	0.185	0.387
Predictors: Constant, Buttock width (cm), Bottom popliteal length (cm) Dependent Variable: Human Body weight (kg)									

The Standard Error of Estimate, (SEE) quantifies the accuracy of predictions made by the model. A lower SEE indicates a better precision in estimating body weight based on buttock width and bottom popliteal length (Musa et al., 2022a). Table 2 shows a lower SEE of 2.671 and 3.138 for males and females participants respectively. The 95% Confidence Intervals provide a range within which we can be 95% confident that the true value of the parameters, such as coefficients in the model equation, lies. Table 2 offer insights into the precision of our estimates (Musa et al., 2022a; Yeasmin et al., 2022). The male and female regression scatter plots generated from the study were shown in Figure 7 to Figure 10.
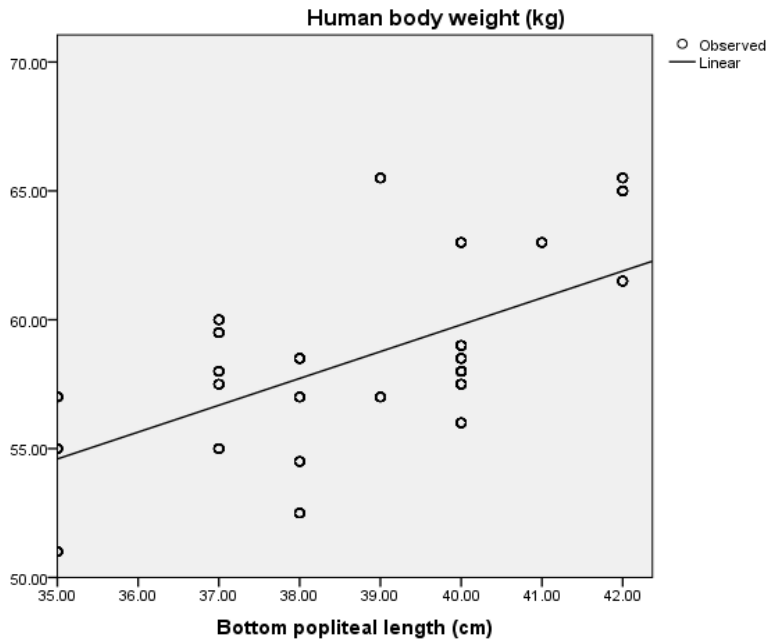
Figure 7. Female scatter plot for HBW-BPL
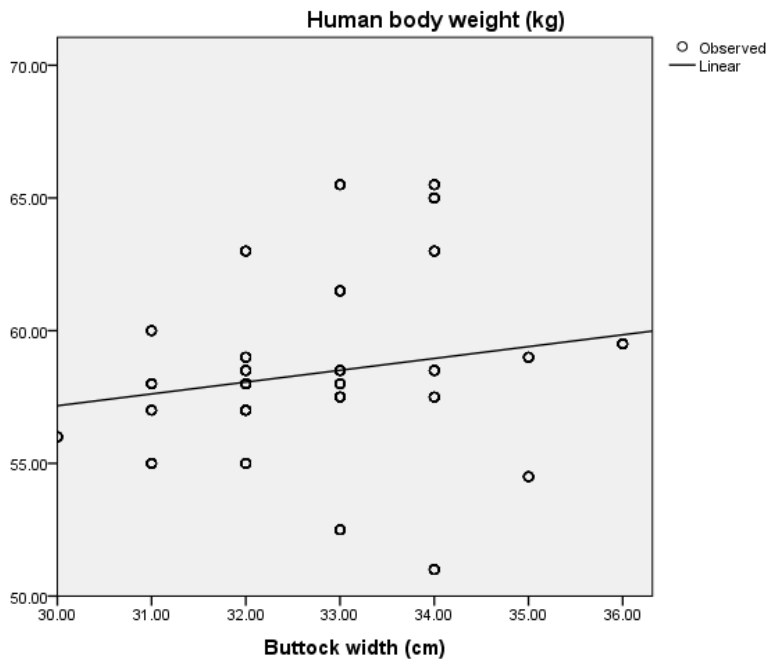
Figure 8. Male scatter plot for HBW-BW
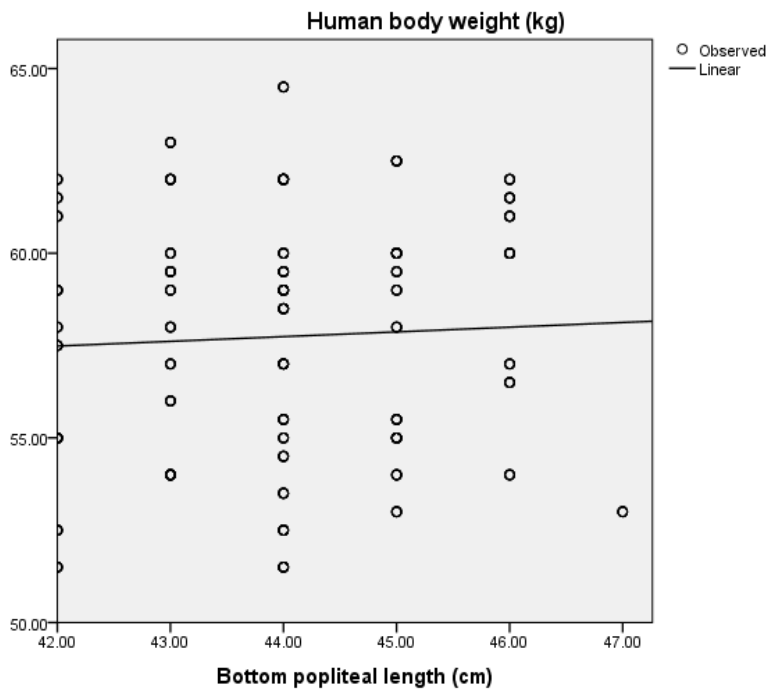
Figure 9. *Female scatter plot for HBW-BPL*
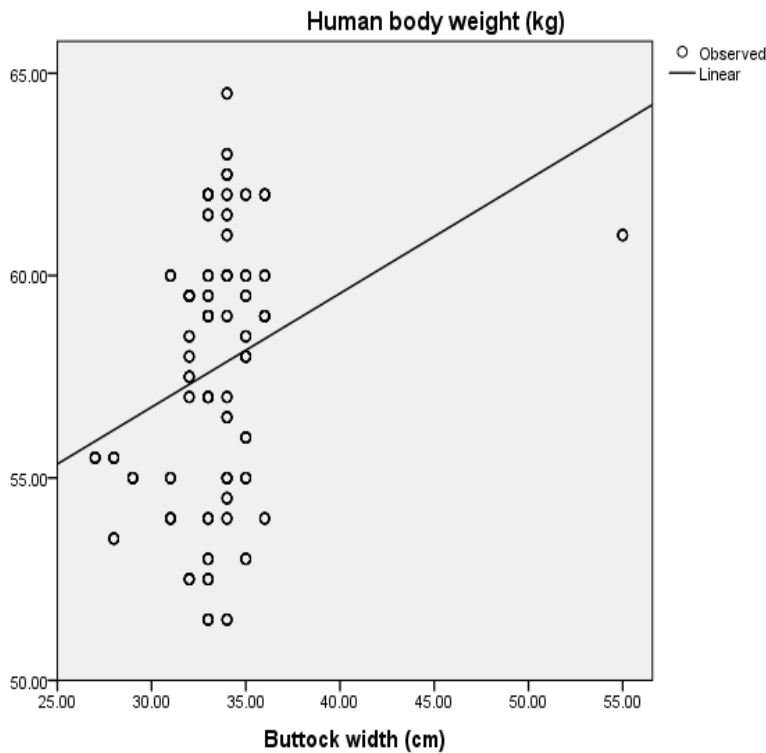
Figure 10. *Female scatter plot for HBW-BW*

This scatter plots serves as crucial tools for understanding the relationship between buttock measurements (width and popliteal length) and human body weight within each gender. This scatter plots assist the author to visually assess the correlation between buttock measurements and human body weight (Figure 3 and Figure 4). Analyzing the regression lines allows for a quantifiable understanding of how changes in buttock dimensions correspond to changes in human body weight.

The regression scatter plots contributes to the precision of ergonomic design by providing designers with specific data points and statistical measures. This information aids in creating products that are not only inclusive but also accurate in estimating human body weight based on buttock dimensions. The scatter plots also serve as a visual representation of the data, helping to validate or refine assumptions made in the study.

Regression scatter plots also help identify any outliers or unusual data points within each gender group. Detecting outliers is crucial for understanding cases where the relationship between buttock measurements and body weight may deviate from the general trend. The regression scatter plots are essential for validating the accuracy of the regression models developed in the study. Researchers can compare the predicted body weight values from the regression equations with the actual body weights, ensuring the reliability and validity of the estimation models.

Human body weight estimation based on buttock measurements have inherent variability. The scatter plots allow the author to observe the spread of data points around the regression line, providing insights into the degree of variability in the relationship and helping designers account for this variability in their ergonomic solutions. Regression scatter plots also highlight potential variations in the relationship between buttock measurements and body weight across different demographics within each gender, such as age groups or ethnicities. This information contributes to designing products that consider diverse demographic characteristics.

In view this submission, male and female regression scatter plots play a pivotal role in quantifying and visualizing the relationship between buttock measurements and human body weight. These tools enhance the precision of ergonomic design and contribute to the development of more accurate estimation models tailored to specific gender differences. In essence, male and female regression scatter plots offer a comprehensive and dynamic view of the relationship between buttock measurements and body weight. They not only aid in immediate design considerations but also provide a foundation for ongoing refinement and adaptation in the field of ergonomic design. Table 3 shows the established model equations.

Table 3. Model equations

Gender	Anthropometric Measurement	Model Equations
Male	Human Body weight (HBW)	= 12.175 + 1.021(BPL) + 0.206 (BW)
Female	Human Body weight (HBW)	= 40.327 + 0.178 (BPL) + 0.286 (BW)
Dependent Variable: Human Body weight (kg)		

The established model equations are crucial for predicting body weight based on buttock width and bottom popliteal length (Table 3). They provide a mathematical representation of the relationship uncovered through the analysis (Musa et al., 2023). These statistical measures collectively enhance our understanding of the reliability and validity of the model in estimating body weight from the specified predictors, contributing to the overall robustness of the study findings. Yuan et al. (2020) reported that Buttock-popliteal length, weight, body mass index, body shape and weight distribution, all have important effects on the distribution of body pressure at the human-chair interface.

4. CONCLUSION

This study provides valuable insights into the use of buttock measurements, specifically buttock width and bottom popliteal length, as predictors for estimating body weight. Through thorough statistical analysis and exploration of these anthropometric dimensions, the author has established meaningful correlations with overall body weight. The findings emphasize the practicality of incorporating buttock measurements in diverse fields, including healthcare, ergonomics, and product design. Building upon previous studies hinting at the feasibility of using buttock dimensions for body weight estimation, this research delves into the intricacies of these measurements, offering a comprehensive understanding of their relationships with body weight and enhancing the foundation for accurate and accessible methods of body weight prediction.

The findings suggest integrating buttock width and popliteal length measurements in ergonomic product design, especially for seating arrangements and weight-bearing products. Healthcare practitioners can consider incorporating buttock measurements into health assessments, aiding in more accurate estimations of body weight without the need for direct weight measurements. Manufacturers and designers are encouraged to customize products such as chairs, mattresses, and vehicle seats based on buttock dimensions, ensuring optimal comfort and support for a diverse range of individuals.

The study's significance lies in the innovative link it establishes between furniture design and body weight estimation, a connection not previously explored. Unlike conventional approaches solely focused on furniture design, this research uniquely integrates anthropometric measurements like buttock width and bottom popliteal length. By examining the relationships between these measurements and the distribution of human body weight, as well as body mass index, the study pioneers a comprehensive understanding that extends beyond existing research. This novel approach contributes to ergonomic design by providing a nuanced perspective, ensuring that furniture is tailored not only to anatomical dimensions but also aligned with individual body weight variations. Consequently, this study bridges a crucial gap in the existing literature, offering an original and holistic exploration of the interplay between furniture design and body weight estimation.

The author recommends further research to explore the predictive capabilities of buttock measurements across different demographics and populations. Additionally, longitudinal studies could provide insights into the stability of these correlations over time. Validation of the findings in clinical settings is recommended to ascertain the reliability of buttock measurements for body weight estimation in practical applications, especially in healthcare and rehabilitation contexts.

In conclusion, the study advocates for the integration of buttock measurements as a viable and accessible method for estimating body weight, offering potential benefits in various domains. The recommendations provide practical implementation avenues and suggest future research to enhance the robustness of these predictive relationships.

CONFLICT OF INTEREST

The author declares no conflict of interest.

REFERENCES

Chaffin, D. B., & Andersson, G. B. (1991). *Occupational biomechanics*. Wiley.

Grandjean, E. (1988). *Fitting the Task to the Man: An Ergonomic Approach*. Taylor & Francis.

Hedge, A. (2008). *Human Factors and Ergonomics in Consumer Product Design: Methods and Techniques.* CRC Press.

Ismaila, S. O., Musa, A. I., Adejuyigbe, S. B., & Akinyemi, O. D. (2013). Anthropometric Design of Furniture for Use in Tertiary Institutions in Abeokuta South-western Nigeria. *Engineering Review*, 33(3), 179-192.

Johnson, C., & Brown, L. (2020). Exploring the relationship between lower body dimensions and body weight. *International Journal of Anthropometry*, 45(2), 123-137.

Kroemer, K. H., & Grandjean, E. (2001). *Fitting the Task to the Human. A Textbook of Occupational Ergonomics.* CRC Press.

Loredan, N. P., Kastelic, K., Burnard, M. D., & Sarabon, N. (2022). Ergonomic evaluation of school furniture in Slovenia: From primary school to university. *Work,* 73, 229–245). https://www.doi.org/110.3233/WOR-210487

Musa, A. I., Ogedengbe, T. S., Amusan, G. M., & Giwa, S. O. (2022a). Anthropometric Determination of Body height from Foot length of Adults in Abeokuta Southwest Nigeria. *Daffodil International University Journal of Science and Technology*, 17(2), 11-15.

Musa, A. I., Ogedengbe, T. S., Adeleke, A. E., Ajayeoba, A. O., Qutubuddin, S. M., & Okokpujie, I. P. (2022b). Forensic Appraisal of leg length as a predictor for Determination of Nigeria Students' Body height. *Ethiopian Journal of Science and Technology*, 15(3), 329-338. https://www.doi.org/10.4314/ejst.v15i3.8

Musa, A. I., Musa A. I., & Ogedengbe, T. S. (2023). Ergonomics modeling of human height from stride length for adult population in South Western Nigeria. *Engineering and Applied Science Research,* 50(3), 220-225. https://www.doi.org/10.14456/easr.2023.24

Smith, A. (2018). Anthropometric predictors of body weight in adults: A comprehensive review. *Journal of Human Kinetics*, 62, 85-96.

Pheasant, S. (1996). *Bodyspace: Anthropometry, ergonomics and the design of work*. CRC Press.

Yeasmin, N., Asadujjaman, Md., Rakibul Islam, Md., & Robiul Hasan, Md. (2022). Stature and sex estimation from shoulder breadth, shoulder height, popliteal height, and knee height measurements in a Bangladeshi population. *Forensic Science International: Reports,* 5, 100258. https://www.doi.org/10.1016/j.fsir.2022.100258

Yuan, F., Guo, Y., Shi, Y., Zhang, K., Zhu, Z., & Chen, Y. (2020). A novel bamboo sheet chair and its influence on sitting comfort. *Peer Journal,* 8, e9476. https://www.doi.org/10.7717/peerj.9476

Impedance Response and Phase Angle Determination of Metal-Semiconductor Structure with N-Doped Diamond Like Carbon Interlayer

Nuray URGUN[1*] [iD]   Aylar FEIZOLLAHI VAHID[2] [iD]   Jaafar Abdulkareem Mustafa ALSMAEL[3] [iD]   Barış AVAR[4] [iD]
Serhat Orkun TAN[5] [iD]

[1] Karabük University, Faculty of Engineering, Department of Mechatronics Engineering, Karabük, Türkiye
[2] Zonguldak Bülent Ecevit University, Department of Nanotechnology Engineering, Zonguldak, Türkiye
[3] Basrah University, Oil and Gas Engineering, Faculty of Oil and Gas, Basrah, Iraq
[4] Zonguldak Bülent Ecevit University, Department of Metallurgy and Material Engineering Faculty of Science, Zonguldak, Türkiye
[5] Karabük University, Faculty of Technology, Department of Electrical Engineering, Karabük, Türkiye

Keywords	Abstract
DLC Interlayer Schottky Barrier Diode Tunable Material/Device Selective Frequency Response Impedance Spectroscopy	With their superior properties over p-n barriers, Schottky Barrier Diodes have a wide usage area, especially as a test tool to produce better-performance devices. The main performance parameter of these devices is measured by their conduction, which can develop with an interlayer addition through the sandwich design. Regarding the DLC, which also has outstanding specifications under thermal, chemical, and physical conditions, is a good candidate for interlayer tailoring, specifically when used with doping atoms. Thus, this study investigates the impedance response of the fabricated device with an N-doped DLC interlayer by employing the electrochemical technique as a combination of electrolysis, RF magnetron sputtering, and thermal evaporation. The measurements were conducted for broad scales of voltage and frequency corresponding between (-3V) and (+4V) and 1kHz and 1MHz, respectively. According to the impedance analysis, complex impedance decreases by rising bias and frequency, from 1.8 MΩ to 2 kΩ at 1MHZ due to the additional insulating layer. At the same time, the phase angle indicates the quality of the dielectric layer with an average of 81.36 ° for the sample logarithmic frequency values with an almost constant-like trend in the inversion stage. In comparison, it reduces to an average of 30.25 ° after the depletion stage by showing the rising conductivity. Moreover, it has some unexpected rising values at the strong accumulation stage, possibly due to the deposited thin film's unique structure. The supported results by phase angle changes, showing frequency-adjustable working conditions, may offer that selective electrical conduction can be tuned.

Author ID (ORCID Number)		Article Process	
0000-0001-6574-4287	Nuray URGUN	**Submission Date**	21.11.2023
0000-0003-3157-2725	Aylar FEIZOLLAHI VAHID	**Revision Date**	25.12.2023
0000-0002-2426-9421	Jaafar Abdulkareem Mustafa ALSMAEL	**Accepted Date**	19.01.2024
0000-0002-6234-5448	Barış AVAR	**Published Date**	30.01.2024
0000-0001-6184-5099	Serhat Orkun TAN		

1. INTRODUCTION

In electronics technology, Schottky barrier diodes (SBDs) or metal-semiconductor (MS) structures, which are distinguished from other diodes by their fast-switching ability, due to the being unipolar devices, at high frequencies and low-level forward biasing, still have an important place in the scientific community with many different applications (Northrop & Rhoderick, 1978; Sharma, 1984; Soylu & Yakuphanoglu, 2011; Hwang et al., 2013; Tan, 2017). SBDs also have speed adjustments among themselves besides being better performance devices over P-N junctions. In one related work, researchers compared the tri-anode and planar SBDs and found that the tri-anode SBD's switching mechanism was faster than the planar one (Nela et al., 2019). Moreover, SBD applications can be extended from the Schottky structures in scanning electronic microscopes (SEM) to the high-power frequency multiplier designs (Ersöz et al., 2018; Konstantinou et al., 2021).

These applications usually arise by choosing different interfacial layers between metal and semiconductors. Metal-insulator-semiconductor (MIS), metal-ferroelectric-semiconductor (MFS), and metal-polymer-semiconductor (MPS) structures are fabricated by using insulating, ferroelectric, and organic in the interfacial layer, respectively. The characterization of these structures under many external factors such as temperature, irradiation, and illumination intensity has been investigated in many studies (Singh et al., 1990; Sharma et al., 2007; Tataroğlu & Altındal, 2009; Tecimer et al., 2013; Lee et al., 2016; Tan et al., 2016). As a result of these investigations, it was emphasized that the use of the mid-layer has a positive efficacy on the characteristics of the structure by regulating the charge transitions at the interface and improving the device's performance (Card & Rhoderick, 1971; Goetzberger et al., 1976; Lin et al., 2014; Maril et al., 2018). Diamond-like carbon (DLC) films, which have the necessary interlayer properties such as thermal stability, adhesion on the substrate and wear resistance, can be preferred as the interlayer material that can be used to obtain MIS structures with higher barrier heights (Basman et al., 2015; Bootkul et al., 2014).

DLC films can be used in MIS structures in electronic technology as well as in solar cells, microelectronic-mechanical systems and various heterostructures. While factors such as H content, sp^2 and sp^3 bond content and lattice disorder reveal the properties of these films, it is known that sp^2 bonds are effective on electronic act and optical properties, while sp^3 bonds control mechanical and tribological properties (Evtukh et al., 2003; Hajimazdarani et al., 2021; Cetinkaya et al., 2023). To effectively increase the graphitization of carbon films, doping DLC films with dopants such as Si, N, Cu, Ti, and S is beneficial for conduction states (Evtukh et al., 2003; Basman & Varol, 2019; Feizollahi Vahid et al., 2023). DLC films, which are also delineated as amorphous forms of carbon materials, take place in many applications such as magnetic storage disks, wear-resistant films, biomedical coatings, and optical coatings (Basman et al., 2015; Zeng et al., 2014; Zhang et al., 2020). In a study in which DLC layer was electrochemically grown and used as an interlayer in Al/(DLC)/p-Si/Au MIS type structure, the electrical parameters of the structure were calculated, and it was concluded that the electrodeposited DLC interlayer can be used to reduce surface states or dislocations instead of the commonly used oxide/insulator interlayer (Şafak Asar et al., 2023). In another study, the electrical parameters of the MS structure using Ti doped DLC interlayer were investigated in the 1kHz-4kHz range by impedance-spectroscopy method. SEM, EDX and XPS methods were used for the structural characterization of the interlayer grown by electrochemical deposition method and the important effect of interfacial states and their relaxation times in the depletion region at low frequencies and series resistance in the accumulation region at high frequencies was emphasized (Berkün et al., 2023).

In the present study, the impedance and phase angle of a metal-semiconductor structure (Al/N: DLC/p-Si/Au) with an N-doped DLC interfacial layer are calculated for a wide frequency range. The impedance response under varying electric field ($\vec{E}$) was studied between 1MHz and 1kHz to detail the structure's operating characteristics. The impedance data obtained were used to observe the relative impedance variation depending on the conduction states of the structure. It is also important to determine the phase angle to follow the evolution and trend of the conduction mechanisms in terms of low capacitive or inductive effects. From this point of view, the Al/N: DLC/p-Si/Au structure, the frequency dependent impedance and phase angle data are analyzed in detail. The reducing trend for the impedance was observed by rising bias and frequency, which is a proof for rising conduction performance. Besides, the high values of the impedance parameter at the reverse polarization region, which should be directly related to the contribution of the N-doped DLC layer's dielectric behavior, showed that the studied structure has the capability to store more charge in it when it is not in the conductive phase.

2. MATERIAL AND METHOD

Al/N:DLC/p-Si/Au MIS structure, 100 mL of methanol (CH3OH Sigma Aldrich) (N 99.5%) and 200 mg of urea were stirred with a magnetic stirrer for 15 minutes. A boron-doped p-type Si substrate with <100> surface alignment and ≈300 μm thickness was used as the negative electrode and a graphite plate was placed at 4 mm intervals as the counter electrode. N: DLC thin film layer was deposited on the p-Si substrate by electrolysis. Then, Au back contact was formed by RF magnetron sputtering at 550 V and annealed at 550 °C for achieving better ohmic connection for the device. As the last step, high purity Al rectifier contacts were formed by thermal evaporation to obtain Al/N:DLC/p-Si/Au MIS structure. So, the fabrication process was completed by electrochemical deposition technique by combination of several methods. The measurements were conducted

for a voltage range of (-3V) to (+4V) and a frequency range of 1kHz to 1MHz via impedance spectroscopy method by HP 4192A LF impedance analyzer. The impedance and phase angle calculations were made from the computer processed analyzer outputs of C(ω)-V; G(ω)-V, and C(ω)-f(Hz) ; G(ω)- f(Hz) measurements.

Figure 1, illustrates the variable device capacitance behavior according to the different phases of DLC film as an interlayer specifically in depletion region.
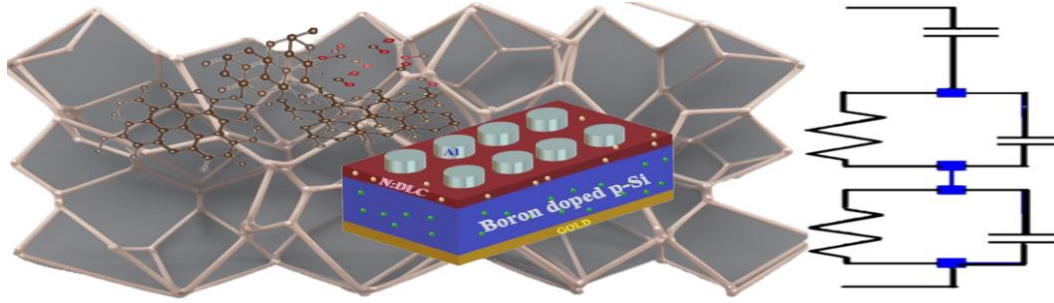
Figure 1. *Illustration of fabricated structure with the DLC dependency effects on capacitance shaping*

3. RESULTS AND DISCUSSION

3.1. Impedance Response

Impedance response of a device gives the detailed working characteristics of the structure under an altering electric field. In this section, we provide a large scale of impedance response of our structure by both (*Z', Z'', Z)-V* and *Z''-Z* plots in a wide frequency scale to investigate the behavior change by varying parameters. *Z''-Z'* plots are quite a useful tool to observe the relative impedance change in a structure due to conduction changes. The impedance calculations were done with Equation 1 as follows where *Z** is the complex impedance, and *Z', Z''* are real and imaginary components of it, respectively. All other relations and constants used for this study are given in Table 1.

$$Z^*(\omega) = Z'(\omega) - jZ''(\omega) = \frac{1}{j\omega C_0 \varepsilon^*} = \frac{\varepsilon''}{2\pi f C_0 (\varepsilon'^2 + \varepsilon''^2)} - j\frac{\varepsilon'}{2\pi f C_0 (\varepsilon'^2 + \varepsilon''^2)} \tag{1}$$

Table 1. *The table gives the employed relations and constants*

Parameter	Symbol	Formula & Value
Complex Dielectric	$\varepsilon^*(\omega)$	$\varepsilon^*(\omega) = \varepsilon'(\omega) - j \cdot \varepsilon''(\omega)$
Dielectric constant	$\varepsilon'(\omega)$	$\varepsilon'(\omega) = \left(\frac{C_m}{C_o}\right)$
Dielectric loss	$\varepsilon''(\omega)$	$\varepsilon''(\omega) = \left(\frac{G_m}{\omega \cdot C_o}\right)$
Permittivity of Free Space	ε_o	Constant 8.854×10^{-12} F/m
Vacuum Capacitance	C_o	$C_o = \frac{\varepsilon_o \cdot A}{d_i} = 6{,}95$ pF
Measured Capacitance	C_m	Measured value, Variable for 0.55V between 3.77nF for 1khz, and 0.18nF for 1MHz
Measured Conductance	G_m	Measured value
angular frequency	ω	$\omega = 2\pi f$
Interfacial Layer Width	d_i	Constant, $d_i = 10^{-6}$ m
Schottky Contact Area	A	$A = \pi r^2 = 0.00785$ cm²

The given plots in Figure 2 show the impedance variations due to the real and imaginary components of complex impedance (*Z**) value and the magnitude of it │*Z*│ in A, B, and C, respectively. In Figure 2c, impedance decreases with increasing bias voltage, and it changes from 2 MΩ to few kΩ, and then to few hundred Ω and

Nuray URGUN, Aylar FEIZOLLAHI VAHID, Jaafar Abdulkareem Mustafa ALSMAEL, Barış AVAR, Serhat Orkun TAN

after that it gets closer to zero at the highest bias voltage. The transition between conduction regions in terms of impedance is also clear in the inset of the plot. The random peaks of real impedance at negative polarization stage are easily seen in Figure 2a, and they are mostly effective at the lowest frequencies. It also exhibits the depletion peaks at around 0 V, followed by smaller secondary peaks around 1 V. The similarity between Z''-V and Z-V plots implies that Z'' is more effective in impedance behavior until the conduction. To analyze the physics behind the behavior of the complex impedance response of the interlayered device, the entire conduction path, from the strong inversion to the strong accumulation phases, is offered in Figure 3, and focused on accumulation region in Figure 3g, h, i.
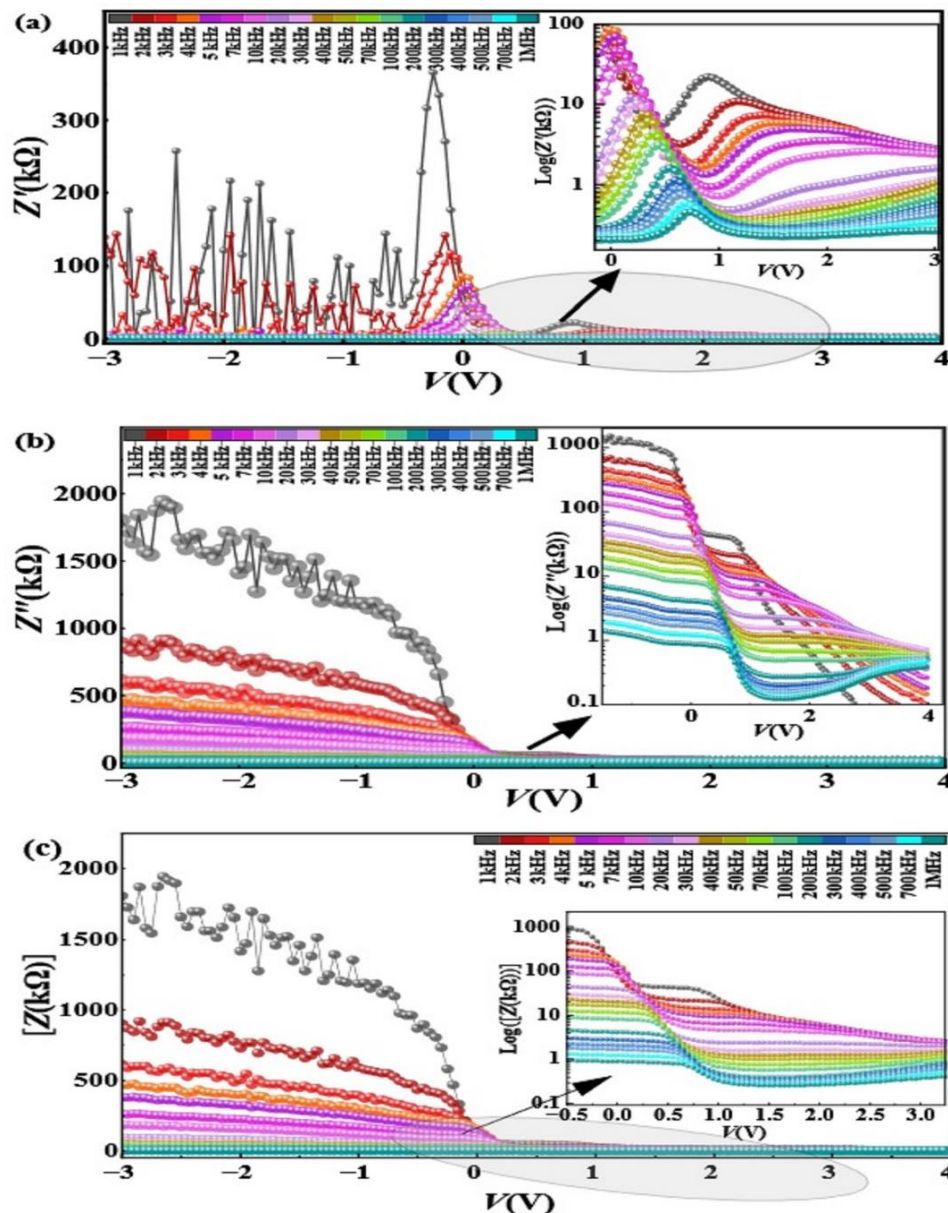
Figure 2. *For (-3) to (+4) V between 1 kHz-1 MHz : a) Z'-V, b) Z''-V, c) Z-V*

One can see that in Figure 3a, there is almost a steep trend in Z'' vs Z' plot for each of the low frequencies. Thus, in Figure 3a, the structure shows strongly capacitive behavior at low frequencies at a few MΩ scale; while the frequency rises from low to medium, it becomes a mix-up of predominantly capacitive and slightly parasitic behavior in Figure 3b at several tens of kΩs.

Nuray URGUN, Aylar FEIZOLLAHI VAHID, Jaafar Abdulkareem Mustafa ALSMAEL, Barış AVAR, Serhat Orkun TAN
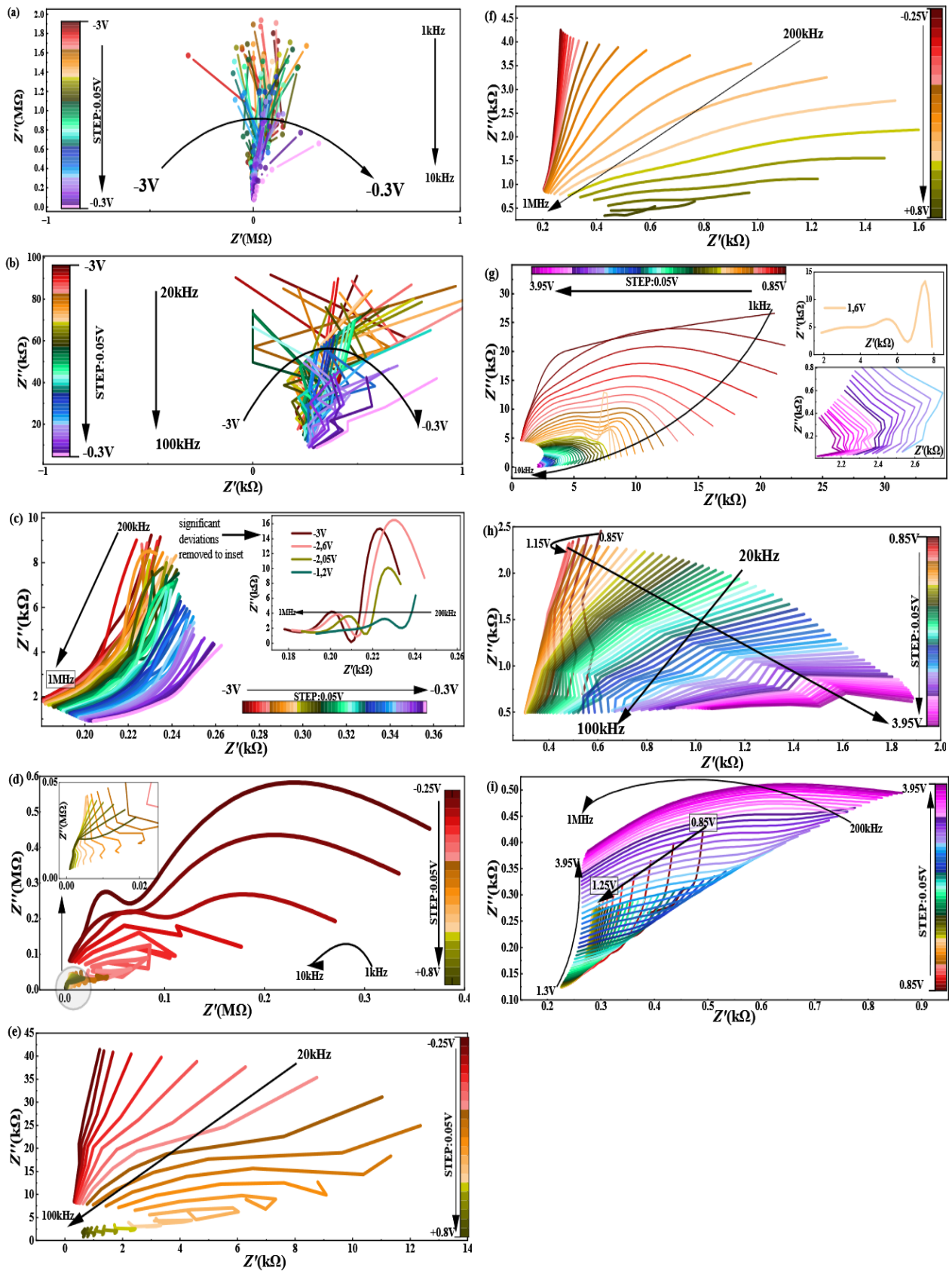
Figure 3. *Z″ vs Z′ at:* ***a-c)*** *Inversion (-3V to -0.3V);* ***d-f)*** *Depletion (-0.25 to 0.8V);* ***g-i)*** *Accumulation (0.8 to 3.95V). Frequency Ranges:* ***a, d, g)*** *1-10 kHz; b, e, h) 20-100 kHz;* ***c, f, i)*** *200 kHz-1 MHz*

Lastly, in Figure 3c, Z shows negligibly resistive-like and parasitic-like behavior besides highly capacitive behavior by rising bias for a high-frequency scale at a few kΩ. So, it is a 3-step process at the inversion stage as strong, medium, and weak levels. Overall, Z'' is found to be always greater than Z' in all those inversion stages. These step transitions in the inversion stage are also observable in depletion and accumulation stages in the following plots. When Figure 3d, e and f are compared, the Z'' values decrease almost by 5 orders of its previous value each time, while corresponding Z' values lessen faster. In accumulation stage, impedance has to show small values for device performance, which is observed in studied structure as in Figure 3g, h, i. The first plot is demonstrating right after the depletion region completely loses its effectiveness, so the capacitive impedance still has a value of kΩ around 30 to 2 at low frequencies in Figure 3g. One can see the flattening curves of plots become more apparent since the capacitive effects are lessening and diminishing, instead the total conduction is rising so the real part of impedance is relatively rising compared to imaginer one's change with an overall decreasing in plots from around 2.5 kΩ to 0,5 kΩ in Figure 3h, and from around 0.5 kΩ to around 50 Ω in Figure 3i.

In the low frequency range both Z'' and Z' values are decreasing with increasing frequency and bias. Moreover, at medium frequency range Z" remains decreasing while Z' increases with rising bias and frequency which is a proof for the Rs effect. And at high frequencies, both Z'' and Z' decrease with rising frequency while Z'' increases when Z' stays almost constant with rising bias. These behaviors of conduction can be explained as *Rs* is effective at medium frequencies and medium to high voltages as in Figure 3h while at high frequencies it almost disappears as in Figure 3i. And employing impedance response in plots, it is possible to define a basic equivalent circuit corresponding to these behaviors of fabricated MIS device.

In Figure 4a, and 4b both Z' and Z'' are rising with lessening frequency and voltage. And after the obvious peak, the impedance plot exhibits opposite behavior. And these kinds of interchanges in the plot mean equivalent circuit should have capacitive reactance and inductive or resistive components. Moreover, the linear like trend at the very first region of this plot where Z'' gets high values when Z' gets ten orders lower values than Z'', meaning that the structure is strongly capacitive at this scale and does not allow any current to flow except metal plates' surface leakage currents. As a basic MOS capacitor equivalent, according to the change at the C-V and G/ω-V values, a study group used an example circuit in their work which is generally appropriate for our structure, as well (Tan et al., 2022). In the structure studied, there is a very unique interface with aligned and randomly located clusters, which has the potential to significantly affect electrical conduction by changing the impedance of the structure through its components. Thus, in addition to operating conditions in different conduction regimes, this situation can also change the impedance by contributing to changes in effective capacitance and conductance values, resulting in deviations from the general trend of the plots. Especially when looking at Figures 2a, 3c, 3g and 4a, these deviations can easily be seen as markedly low voltage and frequency responses, respectively. Therefore, in comparison to a simple MOS capacitor, our structure should be slightly different. In several studies, researchers have mentioned how the structure responds differently to the input signal at high and low frequencies (Rodrigues, 2008; Das et al., 2018). In another work, Kadri et al. (2017) related the low frequency response with grain boundaries while relating the high frequency response with grains, employing by a parameter in their Nyquist plots of Z. Besides the results of these studies, counting on the depletion layer effect on effective capacitance at high and low frequency scales is quite reasonable for our structure, too (Rodrigues, 2008).

Thus, considering the structural changes as a matrix, the deviations from well-known laws like Ohm's law can be explained when changes are counted on both between different dielectric layers as vertical and between more than one phase compounds as horizontal. Since the distribution of clusters, surface and deeper state traps are dramatically important parameters on conduction, they can be used as input variables to adjust the output impedance/capacitance or conductance in a simple equivalent circuit estimation corresponding to our structure. There is one major semicircle after a linear-like region and before a medium-sized semi-circle followed by a third and smallest semicircle. So, the 3 points of tangency at these 3 semicircles show that at the same frequency there are 2 different responses due to the 2 same directional semicircles possibly due to the existence of 2 different structural components in Figure 4a. In other saying the reason for the existence of the materials' relaxation behavior under the $(E^{\rightarrow})$, which shows up in different scales of the impedance when frequency stays still is a result of the different material composition existence besides the voltage dependent response of N_{SS}. Upon careful observation of all the plots, it is evident that this structure exhibits an asymmetrical charge

distribution behavior reminiscent of the matrix as illustrated in Figure 5a. According to these descriptions for our model it should be a little leaky capacitor at the beginning when also considering the phase angle in Figure 4c, and then it should be a combination of capacitor and resistance or inductor since there is an interchange in charge storage and release this energy as current flow. And the following semi-circle should have the same components with lower values. So, our probable structure is as in Figure 5b (Rodrigues, 2008; Das et al., 2018).
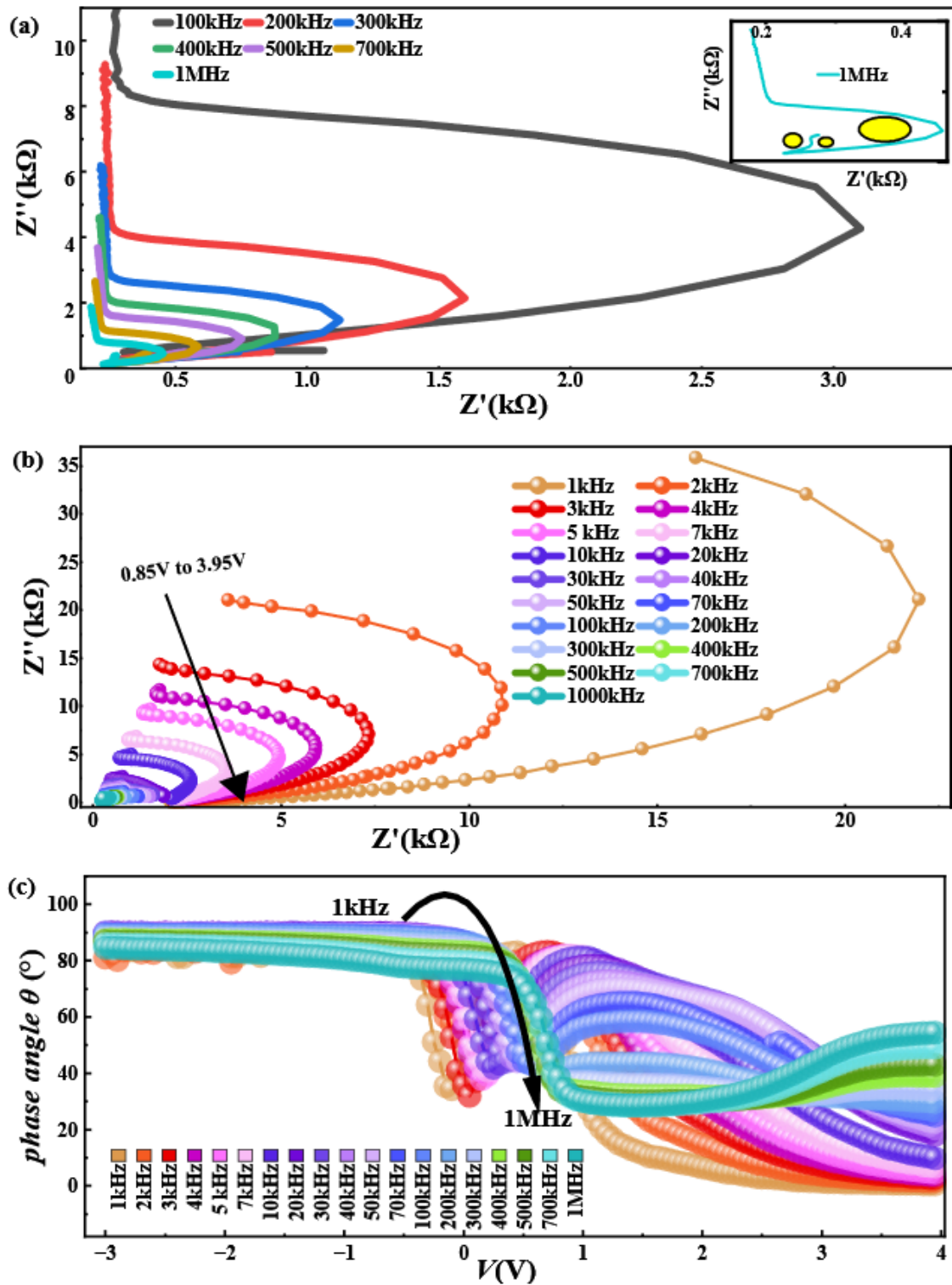
Figure 4. a) *Z″ vs Z′ for -3 to 3.95 V at several frequencies, **b)** Z″ vs Z′ for 1 kHz -1 MHz for several biases,*
c) *Voltage dependency of Phase Angle for 1 kHz -1 MHz*

3.2. Phase Angle

Phase angel is another tool to observe conduction mechanisms change and trend in terms of under capacitive or inductive effects. It is calculated as follows in Equation 2.

$$\theta = tan^{-1}\left(\frac{Z''}{Z'}\right) \tag{2}$$

Phase angle ($\theta°$) in Figure 4c, has values around almost 90 degrees in reverse polarization which shows the combination of N: DLC and p-Si is dramatically capacitive in this region since the capacitive current follows the resistive current almost 90 degrees lagging. Thus, it is evidence for the added interlayer is serving as a good dielectric barrier in inversion region which is desired to be. After inversion region, phase angle's values exhibit mixed behaviors by decreasing halfway, and increasing again in depletion region, and then flattening in accumulation region. The trend in depletion stage shows that effective current type changes in time by mostly applied biases, besides frequency which also approves Figure 2a. As it can be seen after around 1 V, the current losses its charge storage function gradually and the distinguishing features of conduction mechanisms components lessen by decreasing phase difference.
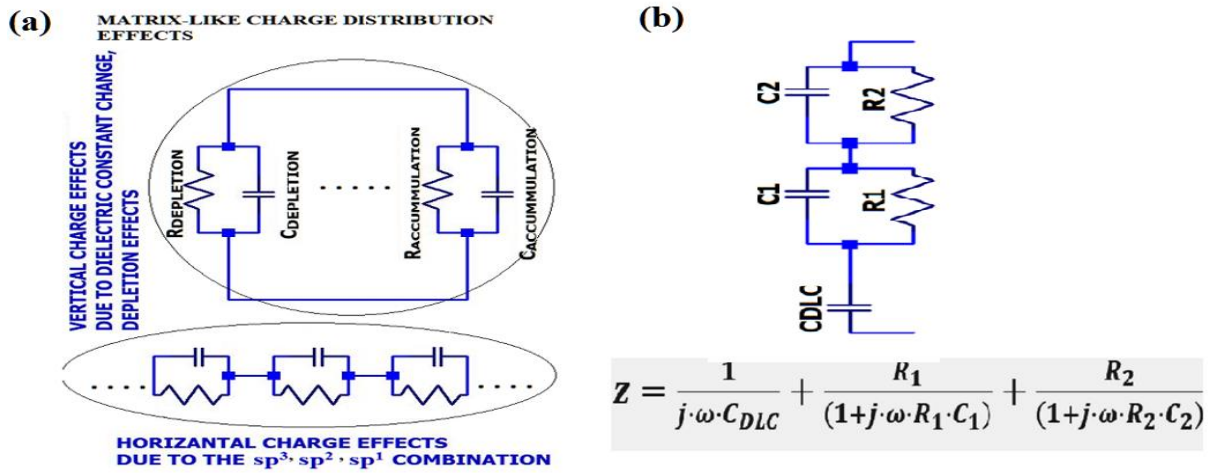
Figure 5. a) Matrix approach of interfacial states between more than one structural component, b) Equivalent circuit of fabricated structure according to altering N-DLC, depletion effects and surface parameters with MOS capacitor approach

To show how the device parameters change altogether over frequency and voltage, Table 2 is given below for logarithmic steps of frequency at few voltage points from the expected non-conductive stage to the conductive stage. When comparing any value of the samples with the corresponding value at the same, previous, and next voltages and frequencies, if the general behavior of the structure, as aforementioned in the plots' explanations above, stays still but shows only slight deviations, they can be categorized as ignorable changes. For example, phase angle has a regular trend as high constant-like values at first in the inversion stage, then falls for the depletion stage, and after that follows another rise into transition to the accumulation stage and falls again due to the Rs and complete discharging process of capacitive charges. So, a rise from 86.89 ° (at -3 V and 1 kHz) to 89.89 ° (at -3 V and 10 kHz) shows the components of Z* become 3° distant from each other, and this can be a slight deviation from the regular trend due to the surface charges' ignorable capacitive effects at low frequency. However, the change from 30.38°at (2 V and 1 MHz) to 44.98° (at 3 V and 1 MHz) shows a notable deviation. Since the real and imaginary parts of the impedance at 3V and 1 MHz are identical as 0.27kΩ and their phase angle is almost 45°, they can be interpreted as somehow in resonance, but when considered the real part of Z*, which contributes as RS effect and should be responsible for the maximum power transfer, there are lower values for Z' than 0.27 k Ω as 0.23 k Ω for the same frequency at 2V. This change seems ignorable, but when counting on the regular falling trend for Z*, this rise can be sourced from rising bias-sensitive material composition, which can be helpful for tunable parameters. Similarly, at 3.95V, the phase angle has another unexpected rise.

Table 2. *Device parameter changes comparation according to applied bias and frequency*

BIAS (V)	Frequency f (kHz)	REAL IMPEDANCE Z' (kΩ)	IMAGINARY IMPEDANCE Z'' (kΩ)	COMPLEX IMPEDANCE Z^* (kΩ)	PHASE ANGLE θ (°)
- 3V	1	97.86	1803.60	1806.25	86.89
	10	-0.33	181.51	181.51	89.89
	100	0.23	18.23	18.23	89.27
	1000	0.18	1.88	1.88	84.58
-2V	1	120.31	1411.03	1416.15	85.13
	10	1.43	154.53	154.54	89.47
	100	0.26	15.41	15.41	89.03
	1000	0.19	1.58	1.59	83.31
-1V	1	28.20	1187.27	1187.61	88.64
	10	0.94	116.02	116.02	89.53
	100	0.26	11.68	11.68	88.73
	1000	0.19	1.19	1.20	80.66
0V	1	62.93	71.30	95.10	48.57
	10	20.79	72.03	74.97	73.90
	100	0.45	8.10	8.11	86.79
	1000	0.20	0.88	0.90	76.88
1V	1	19.71	12.01	23.08	31.37
	10	0.71	4.56	4.61	81.09
	100	0.38	0.57	0.69	56.23
	1000	0.29	0.17	0.33	30.12
2V	1	5.63	0.65	5.66	6.56
	10	2.38	3.27	4.04	53.92
	100	0.35	0.50	0.61	54.47
	1000	0.23	0.14	0.27	30.38
3V	1	2.58	0.07	2.58	1.51
	10	2.37	1.07	2.60	24.22
	100	0.73	0.52	0.89	35.38
	1000	0.27	0.27	0.38	44.98
3.95V	1	2.08	0.02	2.08	0.65
	10	2.08	0.36	2.11	9.87
	100	1.06	0.54	1.19	26.76
	1000	0.28	0.38	0.47	54.33

4. CONCLUSION

In the present study, the impedance and phase angle of a metal-interlayer-semiconductor structure (Al/(N: DLC)/p-Si/Au) have been analyzed both in the wide frequency range of 1kHz-1MHz and voltage range of -3V – (+4V) at room temperature to get more information on the relaxation phoneme depend on frequency and voltage. The (N: DLC) thin interfacial layer was grown between Al and p-Si by using electrochemical deposition technique. The analysis of impedance and phase angle of the Al/(N: DLC)/p-Si/Au (MIS) structure shows that the used (N: DLC) interfacial layer leads to an important increase in device performance when compared to metal-semiconductor (MS) structure with an oxide/insulator layer. The phase angle change from 86.89° to 0.65° even at the lowest frequency by rising bias effect, is one of the samples among these significant behavior changes. Also, the device showed similar decreasing behavior for higher frequency scales, too. For instance, (N: DLC) thin interfacial layer served as a high-quality dielectric interlayer in cut-off region with a sharp phase angle below the breaking voltage to prevent any possible conduction. Moreover, after this specific voltage, it showed good electrical conductivity, with some intersections related to capacitance change outcomes through the structure, which allows for a future study to adjust the device working scale for desired band-enhancing filter component designs. The frequency-dispersion of the complex impedance was analyzed using modified Cole-Cole model, and the diameter of the semi-circles in the plot decreased with increasing frequency. A plain resistance-capacitance parallel circuit diagram is enough to explain the N-doped DLC film's inner-grain and grain-boundary effect. The observed an important decrease in the impedance's imaginary part and real part with increasing well agreed with Debye's type relaxation.

AUTHOR CONTRIBUTIONS

Conceptualization and manuscript-original draft, N.U; measurements and laboratory, A.F.V; visualization, N.U.; manuscript-review and editing, N.U., J.A.M.A, and S.O.T; supervision, B.A., and S.O.T. All authors have read and legally accepted the final version of the article published in the journal.

CONFLICT OF INTEREST

The authors declare no conflict of interest.

REFERENCES

Basman, N., Aslan, N., Uzun, O., Cankaya, G., & Kolemen, U. (2015). Electrical characterization of metal/diamond-like carbon/inorganic semiconductor MIS Schottky barrier diodes. *Microelectronic Engineering*, 140, 18–22. https://doi.org/10.1016/j.mee.2015.05.001

Basman, N., & Varol, S. F. (2019). High Temperature Characterization of a MIS Schottky Diode Based on Diamond-Like Carbon Nanocomposite Film. *Journal of Electronic Materials*, *48*(12), 7874–7881. https://doi.org/10.1007/s11664-019-07621-9

Berkün, Ö., Ulusoy, M., Altındal, Ş., & Avar,B (2023). On frequency and voltage dependent physical characteristics and interface states characterization of the metal semiconductor (MS) structures with (Ti:DLC) interlayer, *Physica B: Condensed Matter*, 666, 415099. https://doi.org/10.1016/j.physb.2023.415099

Bootkul, D., Saenphinit, N., Supsermpol, B., Aramwit, C., & Intarasiri, S. (2014). Synthesis of Ti-doped DLC film on SS304 steels by Filtered Cathodic Vacuum Arc (FCVA) technique for tribological improvement. *Applied Surface Science*, 310, 293–299. https://doi.org/10.1016/j.apsusc.2014.04.053

Card, H. C., & Rhoderick, E. H. (1971). Studies of tunnel MOS diodes I. Interface effects in silicon Schottky diodes. *Journal of Physics D: Applied Physics*, *4*(10), 1589–1601. https://doi.org/10.1088/0022-3727/4/10/319

Cetinkaya, H. G., Feizollahi Vahid, A., Basman, N., Demirezen, S., Şafak Asar, Y., & Altındal, S. (2023). On the wide range frequency and voltage dependence of electrical features and density of surface states of the Al/(Cu:DLC)/p-Si/Au Schottky diodes (SDs). *Journal of Materials Science*: *Materials in Electronics*, *34*(9). https://doi.org/10.1007/s10854-023-10247-7

Das, A., Hatada, R., Ensinger, W., Flege, S., Baba, K., & Meikap, A. (2018). Dielectric constant, AC conductivity and impedance spectroscopy of zinc-containing diamond-like carbon film UV photodetector. *Journal of Alloys and Compounds*, 758, 194–205. https://doi.org/10.1016/j.jallcom.2018.05.121

Ersöz, M., Sulak, M., Bersani, M., Işıtan, A., Balaban, M., Yakar, Z., Ünlü, C. G., & Onar, V. (2018). *Nanoteknoloji 2: karakterizasyon ve uygulamalar*. https://hdl.handle.net/11499/3118

Evtukh, A. A., Litovchenko, V. G., Litvin, Y. M., Fedin, D. V., Dzyan, O. S., Pedchenko, Y. N., Chakhovskoi, A. G., & Felter, T. E. (2003). Silicon doped diamond-like carbon films as a coating for improvement of electron field emission. *Journal of Vacuum Science & Technology B: Microelectronics and Nanometer Structures Processing, Measurement, and Phenomena*, *21*(1), 627–630. https://doi.org/10.1116/1.1528918

Feizollahi Vahid, A., Alptekin, S., Basman, N., Ulusoy, M., Şafak Asar, Y., & Altındal. (2023). The investigation of frequency dependent dielectric properties and ac conductivity by impedance spectroscopy in the Al/(Cu-doped Diamond Like Carbon)/Au structures. *Journal of Materials Science: Materials in Electronics, 34*(13). https://doi.org/10.1007/s10854-023-10546-z

Goetzberger, A., Klausmann, E., & Schulz, M. J. (1976). Interface states on semiconductor/insulator surfaces. *C R C Critical Reviews in Solid State Sciences*, 6(1), 1–43. https://doi.org/10.1080/10408437608243548

Hajimazdarani, M., Derakhshandeh, M. R., Eshraghi, M. J., & Massoudi, A. (2021). Investigation of optoelectrical and Schottky behavior of diamond-like carbon coating deposited by hollow cathode PACVD method. *Optical Materials*, 119, 111385. https://doi.org/10.1016/j.optmat.2021.111385

Hwang, J. D., Kung, C. Y., & Lin, Y. L. (2013). Non-Surface-Treated Au/ZnO Schottky Diodes Using Pre-Annealed Hydrothermal or Sol-Gel Seed Layer. *IEEE Transactions on Nanotechnology*, *12*(1), 35–39. https://doi.org/10.1109/tnano.2012.2226188

Kadri, E., Dhahri, K., Zaafouri, A., Krichen, M., Rasheed, M., Khirouni, K., & Barillé, R. (2017). Ac conductivity and dielectric behavior of a−Si:H/c−Si$_{1-y}$ Ge$_y$/p−Si thin films synthesized by molecular beam epitaxial method. *Journal of Alloys and Compounds*, 705, 708–713. https://doi.org/10.1016/j.jallcom.2017.02.117

Konstantinou, X., Herrera-Rodriguez, C. J., Lai, J., Hardy, A., Albrecht, J. D., Seo, J. H., Muehle, M., Grotjohn, T., & Papapolymerou, J. (2021). Towards high-power multipliers using diamond Schottky barrier diodes. In 2021 *IEEE International Conference on Microwaves, Antennas, Communications and Electronic Systems (COMCAS)* (pp. 111-115). IEEE. https://doi.org/10.1109/comcas52219.2021.9629034

Lee, H. K., Jyothi, I., Janardhanam, V., Shim, K. H., Yun, H. J., Lee, S. N., Hong, H., Jeong, J. C., & Choi, C. J. (2016). Effects of Ta-oxide interlayer on the Schottky barrier parameters of Ni/n-type Ge Schottky barrier diode. *Microelectronic Engineering*, 163, 26–31. https://doi.org/10.1016/j.mee.2016.06.006

Lin, C. C., Wu, Y. H., Hung, T. H., & Chang, Y. T. (2014). Impact of Interfacial Layer Position on Resistive Switching Behaviors for ZrTiO$_x$-Based Metal–Insulator–Metal Devices. *IEEE Transactions on Nanotechnology*, *13*(4), 634–638. https://doi.org/10.1109/tnano.2014.2323198

Maril, E., Tan, S. O., Altındal, S., & Uslu, I. (2018). Evaluation of Electric and Dielectric Properties of Metal–Semiconductor Structures With 2% GC-Doped-(Ca$_3$Co$_4$Ga$_{0.001}$O$_x$) Interlayer. *IEEE Transactions on Electron Devices*, *65*(9), 3901–3908. https://doi.org/10.1109/ted.2018.2859907

Nela, L., Kampitsis, G., Ma, J., & Matioli, E. (2019). Fast-switching tri-anode Schottky barrier diodes for monolithically integrated GaN-on-Si power circuits. *IEEE Electron Device Letters*, *41*(1), 99-102. https://doi.org/10.1109/led.2019.2957700

Northrop, D. C., & Rhoderick, E. H. (1978). The Physics of Shottky barriers, in Impedance Devices, *Solid State Electron*, *4*, 37-73

Rodrigues, A. (2008). Effect of non-homogeneity of Al/CVD diamond interfaces on AC properties. *Diamond and Related Materials*, *17*(7–10), 1264–1268. https://doi.org/10.1016/j.diamond.2008.02.004

Sharma, A., Shahnawaz, Kumar, S., Katharria, Y., & Kanjilal, D. (2007). Barrier modification of Au/n-GaAs Schottky diode by swift heavy ion irradiation. *Nuclear Instruments and Methods in Physics Research Section B: Beam Interactions With Materials and Atoms*, 263(2), 424–428. https://doi.org/10.1016/j.nimb.2007.05.031

Sharma, B. (1984). Metal-Semiconductor Schottky Barrier Junctions and Their Applications. Springer.

Singh, A., Reinhardt, K. C., & Anderson, W. A. (1990). Temperature dependence of the electrical characteristics of Yb/*p*-InP tunnel metal-insulator-semiconductor junctions. *Journal of Applied Physics*, *68*(7), 3475–3483. https://doi.org/10.1063/1.346358

Soylu, M., & Yakuphanoglu, F. (2011). Photovoltaic and interface state density properties of the Au/n-GaAs Schottky barrier solar cell. *Thin Solid Films*, *519*(6), 1950–1954. https://doi.org/10.1016/j.tsf.2010.10.030

Şafak Asar, Y., Feizollahi Vahid, A., Basman, N., Çetinkaya, H. G., & Altındal. (2023). Frequency-dependent electrical parameters and extracted voltage-dependent surface states in Al/DLC/p-Si structure using the conductance method. *Applied Physics A*, *129*(5). https://doi.org/10.1007/s00339-023-06639-5

Tan, S. O. (2017). Comparison of Graphene and Zinc Dopant Materials for Organic Polymer Interfacial Layer Between Metal Semiconductor Structure. *IEEE Transactions on Electron Devices*, *64*(12), 5121–5127. https://doi.org/10.1109/ted.2017.2766289

Tan, S. O., Çiçek, O., Türk, A. G., & Altındal, E. (2022). Dielectric properties, electric modulus and conductivity profiles of Al/Al$_2$O$_3$/p-Si type MOS capacitor in large frequency and bias interval. *Engineering Science and Technology, an International Journal*, 27, 101017. https://doi.org/10.1016/j.jestch.2021.05.021

Tan, S. O., Uslu Tecimer, H., Çiçek, O., Tecimer, H., Orak, & Altındal. (2016). Electrical characterizations of Au/ZnO/n-GaAs Schottky diodes under distinct illumination intensities. J*ournal of Materials Science: Materials in Electronics*, *27*(8), 8340–8347. https://doi.org/10.1007/s10854-016-4843-4

Tataroğlu, A., & Altındal. (2009). Gamma-ray irradiation effects on the interface states of MIS structures. *Sensors and Actuators A: Physical*, *151*(2), 168–172. https://doi.org/10.1016/j.sna.2009.02.035

Tecimer, H., Türüt, A., Uslu, H., Altındal, & Uslu. (2013). Temperature dependent current-transport mechanism in Au/(Zn-doped)PVA/n-GaAs Schottky barrier diodes (SBDs). *Sensors and Actuators A: Physical*, 199, 194–201. https://doi.org/10.1016/j.sna.2013.05.027

Zeng, A., Neto, V. F., Gracio, J. J., & Fan, Q. H. (2014). Diamond-like carbon (DLC) films as electrochemical electrodes. *Diamond and Related Materials*, 43, 12–22. https://doi.org/10.1016/j.diamond.2014.01.003

Zhang, M., Xie, T., Qian, X., Zhu, Y., & Liu, X. (2020). Mechanical Properties and Biocompatibility of Ti-doped Diamond-like Carbon Films. *ACS Omega*, *5*(36), 22772–22777. https://doi.org/10.1021/acsomega.0c01715

A New and Efficient Pan Sharpening Method Based on Optimized Pixel Coefficients

Tuba ÇAĞLIKANTAR[1] (iD) Melih Can KILIÇ[1*] (iD)

[1] Gazi Üniversitesi, Fen Bilimleri Enstitüsü, Bilgisayar Mühendisliği Ana Bilim Dalı, Ankara, Türkiye

Keywords	Abstract
Pan Sharpening Image Fusion Remote Sensing Optimization	Pan sharpening aims to create a multispectral, high spatial resolution image by combining the multispectral image (MSI) with a high spatial resolution panchromatic image (PAN). Pan sharpening methods are performed between the MS image, which is the MSI image brought to PAN dimensions with the help of interpolation, and the PAN image. In this study, PAN sharpening is approached as an optimization problem. It is assumed that the optimal solution consists of multiplying the pixels of the MS image by optimized coefficients. It would be costly to optimize all the coefficients in this coefficient matrix one by one. For this reason, these coefficients were tried to be found with 5 different optimization-based methods. It was also compared with 19 different methods commonly used in the literature. 6 different evaluation criteria were used for this comparison. These comparisons were made on 3 different datasets. It has been observed that the proposed methods are superior to other methods.

1. INTRODUCTION

An image from remote sensing has four basic resolutions. These four types of resolution are: temporal, radiometric, spectral, and spatial. The time difference between taking a remote sensing image of a location and taking another one after a predetermined amount of time is known as temporal resolution. The amount of bits used to indicate the electromagnetic energy acquired by remote sensing on a digital image is known as radiometric resolution. Pixel values in an image expressed with 8 bits take values between 0 and 255, whereas values in an image stated with 7 bits take values between 0 and 127. The wavelength range of the electromagnetic spectrum from which the image generated by remote sensing is obtained and the number of bands are related to spectral resolution. Narrower wavelength ranges correspond to higher spectral resolution for a given band. In other words, a band's sensitivity to, or the wavelength range it is received in, decreases with increasing spectral resolution. Spatial resolution can simply be defined as the area occupied by an image (pixel) on the surface. There is an inverse proportion between the amount of area a pixel represents on the ground and the spatial resolution.

Images are captured in various resolutions and across various electromagnetic spectrum bands by remote sensing systems. The MSI image has red, green, and blue bands from these sensors, which have a low spatial resolution yet provide a viewable image. Furthermore, PAN image with great spatial resolution is also acquired. When it comes to spatial resolution, the MSI which has color information is less precise than the PAN image. Fused high-resolution images with complementary data from multispectral bands are necessary for remote sensing applications such as feature extraction, classification, change detection, and clustering (Kurban, 2022). Pan sharpening is the term specifically used to describe image fusion techniques used to

produce an image with both color information and high spatial resolution. Interpolation is used to bring the MSI image to PAN image dimensions and the MS image is obtained.

The pan sharpening procedure is regarded as an optimization problem in this study. Every pixel in the MS image is multiplied by a coefficient to determine the ideal pan-sharpened image. Consequently, several approaches have been attempted to arrive at this optimal solution due to the large number of variables that require optimization. Low-pass PAN images were created by various methods to obtain an acceptable ratio between the PAN image and the low-pass PAN image. To our knowledge, this work is the third application of the Weighted Differential Evolution Algorithm (WDE) for pan sharpening in the literature (Civicioglu et al., 2020) WDE is applicable to several optimization-based pan sharpening techniques as a global minimizer. In addition, the study employed an objective function based on a Laplacian filter. The spatial information similarity between the low-pass PAN image and the MS image was compared using the Laplacian filter. The Laplacian filter regulates the transition between pixels by concentrating on the differences between image pixels and their spatial neighbors. This provides us with information on derivative, or border information, which is a crucial component of spatial information. The outcomes were contrasted with techniques from the literature that employed various evaluation standards. The amount of spatial features transferred from the PAN image and the amount of spectral features transferred from the MS image to the pan-sharpened image are measured using different metrics. The lack of a reference image to compare the final image to is one of the difficulties with pan sharpening. Some methods, like the Wald protocol (Wald et al., 1997), rely on the MSI image rather than the reference image to get over this problem.

Other than Component Substitution (CS) and Multiresolution Analysis (MRA) techniques, pan sharpening techniques have been studied and classified differently in the literature; however, more recent research has shown that these classifications are comparable. Amro et al. (2011) categorized pan sharpening techniques into five categories in their study: the CS family, the MRA family, the high frequency injection family, the relative spectral contribution family, and approaches based on image statistics. Vivone et al. (2020) looked at it in a more recent study and divided it into four categories: CS, MRA, VO, and machine learning (ML) techniques in 2021. Similar to Vivone, Meng et al. (2020) investigated it in 2021 within the following four headings: CS, MRA, VO, and deep learning (DL) techniques. Yilmaz et al. (2022) examined it under 6 headings: MRA, CS, Colour-Based (CB), DL, VO and hybrid methods. The basis of traditional CS approaches is to decompose the MS into components and replace the spatial context with PAN. Then, the PI image is obtained by inverse transformation. Matching the histogram of PAN and MS before component replacement will increase the correlation and create lower distortion (Ghassemian, 2016). Tu et al. (2001) expanded the traditional approach (Meng et al., 2019).

$$PI_i = MS_i - G_i * (PAN - I_L) \qquad (1)$$

PI is the fused image, G is the injection coefficient, I_L is the component that needs to be changed to PAN, and i is the representation of the bands. In general, CS approaches are simple to use and are successful in transferring spatial information. Many methods have been proposed in this regard. The focus of these methods is on accurate modeling of the relationship between MS and PAN (Vivone et al., 2020). However, they struggle to transfer the color information from the MS image. As examples of the most popular CS techniques, consider Brovey, Intensity Hue Saturation (IHS), Gram Schmidt (GS), Principal Component Analysis (PCA), Band Dependent Spatial Detail (BDSD).

In traditional MRA approaches, MS and PAN are moved to a different space with transformation functions. Spatial features from PAN are injected into the MS. Then the PI image is created by inverse transformation. The approach of traditional MRA techniques has been extended (Meng et al., 2019)

$$PI_i = MS_i - G_i * (PAN - PAN_L) \qquad (2)$$

PI is the fused image, G is the injection coefficient, PAN_L is the low-pass PAN, and i is the representation of the bands. Different MRA techniques have been tried to obtain G injection weight and PAN_L image (Meng et

al., 2019). Among the most well-known MRA methods, there are methods using wavelet transform like Discrete Wavelet Transform (DWT), à Trous Wavelet Transformation (ATWT). Numerous examples of generalized Laplacian pyramid (GLP) techniques have been given in the literature. These approaches rely on filters that utilize the Modulation Transfer Function (MTF) of the MS sensor by altering the injection coefficient estimate (Vivone et al., 2020). One such system that makes advantage of High Pass Modulation (HPM) is MTF-GLP-HPM (Vivone et al., 2020). While MRA-based techniques outperform CS-based techniques in terms of spectral feature preservation, they perform worse in terms of spatial feature preservation. However, according to Aiazzi et al. (2006), if the MTF approach is used, the performance will improve significantly. The paper is organized as follows: In the Introduction section, information about the pan sharpening process and the literature is given. In the second part, the method used in the paper is explained. In the third part, results and discussion are given. The fourth section contains the conclusion.

2. MATERIAL AND METHOD

Assuming that there is 1 most suitable pan sharpened image in the solution space for the pan sharpening process, this image is k times larger, with a separate coefficient for each pixel of the MS image.

$$PI_i = MS_i * MSK_i \tag{3}$$

PI is the optimum solution in the solution space, MS is the multispectral image, and MSK is a coefficient matrix of MS dimensions. i represents the bands of the image. Finding the optimum value of each coefficient in this MSK matrix is an optimization problem. If we consider a 1024x1024 image, there will be a total of 3145728 coefficients that need to be optimized for 3 bands. Calculating the optimum value of these coefficients would be very costly. Therefore, calculating the coefficient matrix MSK in another way will reduce the computational cost.

$$\frac{PI}{MS} = \frac{PANHM}{PANHM_{LP}} \tag{4}$$

$$PI = MS * \frac{PANHM}{PANHM_{LP}} \tag{5}$$

PANHM is the histogram matching image of the PAN image with the MS, and $PANHM_{LP}$ is the low pass version of the PANHM. The equality here shows that the ratio of the PI image to the MS image is also between PANHM and $PANHM_{LP}$. Therefore, to ensure this equality and reach the PI solution, a suitable $PANHM_{LP}$ must be created. For the purpose of pan sharpening, the PI is spatially similar to PANHM. Therefore, the $PANHM_{LP}$ should likewise resemble the MS image spatially. The $PANHM_{LP}$ picture was created in this study using five distinct techniques, or PL Methods.

2.1. PL Methods

PL Method-1 (PL1)

The $PANHM_{LP}$ is created by multiplying each band with an appropriate coefficient after applying a Gaussian filter to the PANHM. Separate k coefficients for each band are calculated with the optimization algorithm. Bands are represented by i.

$$PANHM_{LP_i} = Gauss(PANHM_i, 2) * k_i \tag{6}$$

PL Method-2 (PL2)

The $PANHM_{LP}$ is created by extracting the information that constitutes the spatial details from the PANHM. The MS is multiplied with the required coefficients after being subtracted from MS_{LP}, the Gauss-filtered MS. Separate k coefficients for each band are calculated with the optimization algorithm. Bands are represented by i.

$$PANHM_{LP_i} = PANHM_i - (MS_i - MS_{LP_i}) * k_i \qquad (7)$$

PL Method-3 (PL3)

In this method, it is assumed that the MS is a multiple of the PI image first reduced to X, Y dimensions and then re-extracted to its previous dimensions. Therefore, the same assumption is applied to the PANHM and tried to be verified. X, Y dimensions and k coefficients for each band are calculated with the optimization algorithm. H is height, W is width. These are the dimensions of PAN. Bands are represented by i.

$$PD_i = Interpolation(PANHM_i, size(X, Y)) \qquad (8)$$

$$PANHM_{LP_i} = Interpolation(PD_i, size(H, W)) * k_i \qquad (9)$$

PL Method-4 (PL4)

Discrete wavelet transform is applied to the PANHM (I_1) and MS (I_2) smoothed with a Gaussian filter. For the first component LL, an adaptive combination is performed with optimized k coefficients for all 3 bands, while the max method is used for the other components. Bands are represented by i. You can see the flow in Figure 1.

$$PANHM_{LP_i} = DWT(Gauss(PANHM_i, 2), MS_{LP_i}, k_i) \qquad (10)$$

$$LL_i = (LL_{I_1} * k_i + LL_{I_2} * (1 - k_i)) \qquad (11)$$

$$HH_i = max(HH_{I_1}, HH_{I_2}) \qquad (12)$$
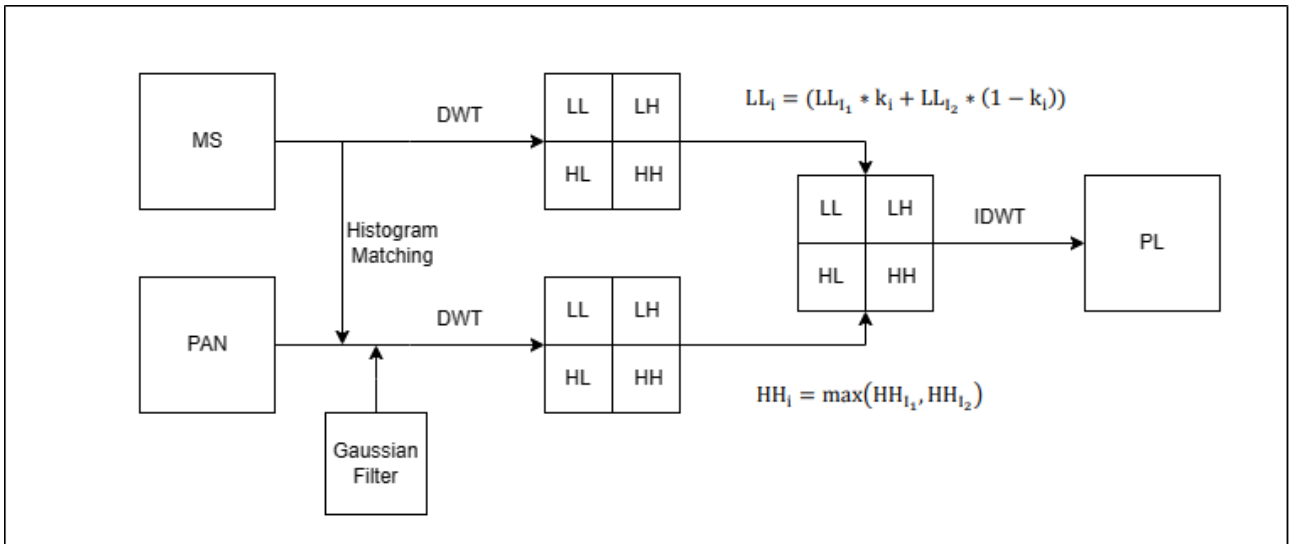
Figure 1. *Flow diagram of PL Method-4*

PL Method-5 (PL5)

PL is a modified version of PL Method-4. In this method, discrete wavelet transform is applied to the PANHM (I_1) softened with the Gaussian filter and the PL3 (I_2) created as in PL Method-3. H is height, W is width. These are the dimensions of PAN.

$$PANHMG_i = Gauss(PANHM_i, 2) \tag{13}$$

$$PD_i = Interpolation(PANHMG_i, size(\frac{H}{5}, \frac{W}{5})) \tag{14}$$

$$PL3_i = Interpolation(PD_i, size(PANHM_i)) \tag{15}$$

$$PANHM_{LP_i} = DWT(Gauss(PANHM_i, 2), PL3_i, k_i) \tag{16}$$

2.2. Optimization

WDE used as the optimization algorithm was developed by Civicioglu et al. (2020). WDE is a pattern matrix based Evolutionary Search algorithm (Civicioglu & Besdok, 2022) and also a stochastic, iterative and bi-population based algorithm. (Günen, 2021). Objective function (OF) consists of 2 parts. The first part is the SAM value calculated for MS and PI images. The second part uses the Laplacian filter to measure spatial information. This measurement is applied to MS (I_1) and $PANHM_{LP}$ (I_2) images, between which we want to have a high level of spatial similarity. After the Laplacian filter is applied to both images, the difference is calculated, and a 3-dimensional DIFF matrix enclosed in absolute value is obtained. With the help of Otsu thresholding, values below the limit in the DIFF matrix are eliminated. Finally, the average of all values is taken. H, W, C are the length, width, and number of bands of the MS image, respectively. (i = 1,2)

$$h = Laplacian\ Filter = \begin{bmatrix} 0 & 1 & 0 \\ 1 & -4 & 1 \\ 0 & 1 & 0 \end{bmatrix} \tag{17}$$

$$LAP_{I_i} = I_i \otimes h \tag{18}$$

$$DIFF_{ABS} = |LAP_{I_1} - LAP_{I_2}| \tag{19}$$

$$DIFF = DIFF_{ABS} * Otsu(DIFF_{ABS}) \tag{20}$$

$$OF_2 = \frac{1}{H * W * C} \sum_{h=1}^{H} \sum_{w=1}^{W} \sum_{c=1}^{C} DIFF_{h,w,c} \tag{21}$$

$$OF_1 = SAM(MS, PI) \tag{22}$$

$$OF = \frac{1}{2}(OF_1 + OF_2) \tag{23}$$

2.3. Evaluation Criteria

There are 2 approaches to evaluate pan-sharpened images, methods that need a reference image and methods that do not. The lack of a reference image needed in the first approach is a fundamental problem. Various approaches have been developed to overcome this problem. Wald et al. (1997) basically has two approaches. The first approach is based on the principle of reducing PI to MSI dimensions and making the two images similar to each other. The second approach is based on the similarity between the reference image obtained by the sensor in PAN dimensions and the PI. Since the mentioned image does not exist, the approach is implemented by reducing the dimension. After applying size reduction to the ratio between PAN and MSI, the original MSI is used as a reference. The QNR protocol was proposed by Alparone et al. (2008) in contrast to

techniques that call for references. As per Kallel (2014), high quality MS is not required for the QNR protocol to function. In this study, the first method in the Wald protocol was preferred in evaluation criteria requiring reference. This is because in the second method the quality of the reconstructed MSI image after down sampling is highly degraded. Since the dimensions of the images in the datasets are 1024x1024, the size of the reconstructed MSI image after subsampling is 64x64, which causes a large loss of information.

2.3.1. Evaluation criteria that require reference image

Spectral Angle Mapper (SAM)

SAM measures the angle between two spectral vectors. The operation is calculated for each pixel. The final value is calculated by averaging the values calculated for all pixels. If the value is close to zero, it means that the images are similar.

$$SAM(x,y) = \arccos\left(\frac{\sum_{i=1}^{N} x_i y_i}{\sum_{i=1}^{N} x_i^2 \ \sum_{i=1}^{N} y_i^2}\right) \tag{24}$$

N indicates the number of bands. The pixels of the compared images are represented by x and y.

Root Mean Squared Error (RMSE)

RMSE calculates pixel level differences between images.

$$RMSE = \sqrt{\frac{\sum_{x=1}^{H*W} \sum_{i=1}^{N} (X_i(x) - Y_i(x))^2}{H*W*N}} \tag{25}$$

The compared images are represented by X and Y. The pixels of the images are expressed as x, the length is H, the width is W, and the number of bands is N.

Erreur Relative Globale Adimensionnelle de Synthése (ERGAS)

ERGAS measures the quality of the resulting image by taking into account the normalized average error of each band. Increasing the value indicates distortion in the image, while decreasing indicates similarity to the reference image.

$$ERGAS = 100 \frac{h}{l} \sqrt{\frac{1}{N} \sum_{i=1}^{N} \left(\frac{RMSE(i)}{\mu(i)}\right)^2} \tag{26}$$

N refers to the number of bands. The average of the pixels of band i is denoted by $\mu(i)$. RMSE(i) means calculating RMSE only for band i. The dimensions of PAN and MS images are represented by h and l, with the ratio taken as 1/4 for Ikonos and QuickBird.

Universal Image Quality Index (UIQI - Q)

Q makes a measurement by taking into account the correlation, brightness and contrast between images. This measurement is divided into BxB parts of the image, calculated separately in each part, and averaged.

$$Q = \frac{4\sigma_{xy} \bar{x} \, \bar{y}}{(\sigma_x^2 + \sigma_y^2) + [(\bar{x})^2 + (\bar{y})^2]} \tag{27}$$

$$\bar{x} = \frac{1}{N} \sum_{i=1}^{N} x_i \tag{28}$$

$$\overline{y} = \frac{1}{N} \sum_{i=1}^{N} y_i \tag{29}$$

$$\sigma_x^2 = \frac{1}{N-1} \sum_{i=1}^{N} (x_i - \overline{x})^2 \tag{30}$$

$$\sigma_y^2 = \frac{1}{N-1} \sum_{i=1}^{N} (y_i - \overline{y})^2 \tag{31}$$

$$\sigma_{xy} = \frac{1}{N-1} \sum_{i=1}^{N} (x_i - \overline{x})(y_i - \overline{y}) \tag{32}$$

N is the total number of pixels in the image, while x and y denote individual image pixels. The Q value that was computed for each band was averaged for this study.

2.3.2. Evaluation criteria that do not require reference image

Quality With No Reference (QNR)

QNR consists of 2 separate metrics that examine images from a spectral (D_λ) and spatial (D_S) perspective.

$$QNR = (1 - D_\lambda)^\alpha (1 - D_S)^\beta \tag{33}$$

$$D_\lambda = \sqrt[p]{\frac{1}{N(N-1)} \sum_{i=1}^{N} \sum_{j=1, j\neq1}^{N} |d_{i,j}(MS, PI)|^p} \tag{34}$$

$$D_S = \sqrt[q]{\frac{1}{N} \sum_{i=1}^{N} |Q(PI_i, PAN) - Q(MS_i, PAN_{LP})|^q} \tag{35}$$

$$d_{i,j}(MS, PI) = Q(MS_i, MS_j) - Q(PI_i, PI_j) \tag{36}$$

PAN_{LP} is the low pass version of the PAN image. N is the number of bands. In this study, $\alpha = \beta = p = q = 1$ was used.

2.4. Datasets and Compared Methods

The methods have been tested on 3 types of datasets: Pléiades (Vivone et al., 2014a; Open Remote Sensing, 2015), Ikonos (Shahdoosti & Ghassemian, 2014) and Rasat (Gezgin, 2013). In all datasets, the size of PAN images is 1024x1024 and the ratio between PAN and MSI is 4. The images are shown in Figure 2.
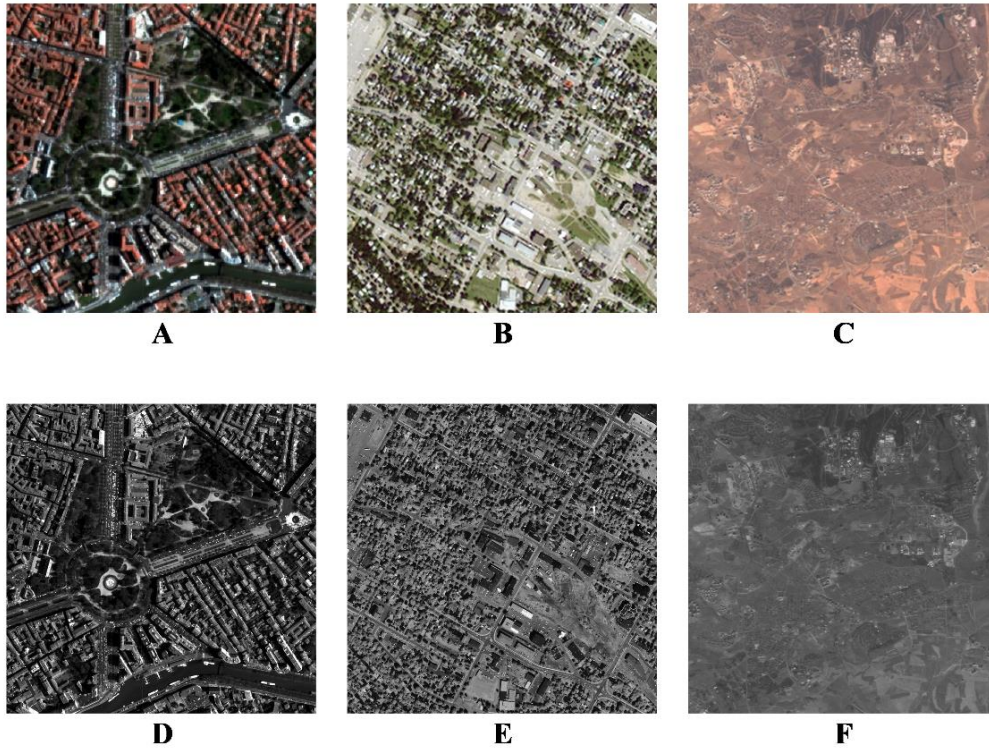
Figure 2. *Pléiades, Ikonos, Rasat dataset MS images A,B,C respectively, Pléiades, Ikonos, Rasat dataset PAN images D,E,F respectively*

The following methods, frequently used in the literature, were used for comparison:

CS methods: BT-H (Lolli et al., 2017), BDSD, C-BDSD (Garzelli, 2014), BDSD-PC (Vivone, 2019), GS, GSA.

MRA methods: AWLP (Otazu et al., 2005), MTF-GLP (MTF1) (Aiazzi et al., 2002; Aiazzi et al., 2006), MTF-GLP-FS (MTF2) (Vivone et al., 2018), MTF-GLP-HPM (MTF3) (Vivone et al., 2013), MTF-GLP-HPM-R (MTF4) (Vivone et al., 2017), MF (Restaino et al., 2016).

VO methods: FE-HPM (Vivone et al., 2014b), TV (Palsson et al., 2013), CSP (Civicioglu & Besdok, 2022).

DL methods: PNN (Masi et al., 2016), PNN-IDX (Masi et al., 2016), A-PNN (Scarpa et al., 2018), L-PNN (Ciotola et al., 2023).

3. RESULTS AND DISCUSSION

The evaluation results of the Pleiades, Ikonos, and Rasat data sets are shown in Tables 1, 2, and 3 of this section, respectively. Figures 3, 4, and 5 present the visual results in the same sequence. The results of evaluation criteria that require reference and those that do not require reference are located side by side. In the tables, CS, MRA, VO, DL and PL methods are listed one under the other and the winning values are marked in bold.

Table 1 shows that, except for some values for the Pleiades dataset, many methods produce similar results and the difference between them is small. In general, it seems that MRA, VO and PL methods produce results close to each other. CS methods are slightly behind them. It is seen that the PL3 method is superior to other methods in evaluation criteria that do not require reference. However, in those requiring reference, PL2 prevails in Q and ERGAS, and PL1 prevails in SAM. PL1 and PL2, although not spatially perfect, are more similar to the MSI image when subsampled according to the Wald protocol. This makes them stand out in evaluation criteria. Especially in PL2, directly benefiting from the MS image and using SAM in the objective function puts it

ahead in the SAM criterion. DWT-based PL4 and PL5 produced results close to other PL methods. There was not much difference for this dataset.

Table 1. *Pléiades dataset results*

Pléiades	D-λ	D-S	QNR	Q	SAM	ERGAS
BT-H	0.015086	0.10512	0.88138	0.8874	2.0684	8.9245
BDSD	0.015509	0.065875	0.91964	0.94454	2.2965	5.5375
C-BDSD	0.058699	0.029445	0.91358	0.91924	3.1281	6.4711
BDSD-PC	0.0068153	0.10579	0.88812	0.92477	2.7586	6.6378
GS	0.02214	0.1314	0.84937	0.85585	3.124	8.6249
GSA	0.035588	0.08787	0.87967	0.8931	8.6561	8.4995
AWLP	0.010393	0.046233	0.94385	0.97179	2.3634	4.0648
MTF1	0.030636	0.051806	0.91915	0.97058	2.1593	4.1855
MTF2	0.026306	0.051181	0.92386	0.97183	2.0306	4.0739
MTF3	0.13318	0.059385	0.81534	0.84878	5.982	994.5831
MTF4	0.013105	0.040637	0.94679	0.96619	2.0906	8.3344
MF	0.017977	0.067615	0.91562	0.95007	2.0175	5.4872
FE-HPM	0.022031	0.03094	0.94771	0.96249	2.0584	4.9903
TV	0.011811	0.059647	0.92925	0.9688	2.2762	4.2825
CSP	0.026358	0.063147	0.91216	0.91799	5.7096	6.5927
PNN	0.093615	0.083307	0.83088	0.85184	6.5904	8.5347
PNN-IDX	0.1213	0.1334	0.76148	0.62703	8.7662	14.878
A-PNN	0.064581	0.11914	0.82398	0.95796	4.4282	4.8877
L-PNN	0.031406	0.093676	0.87786	0.8971	3.9991	8.0688
PL1	0.012639	0.040972	0.94691	0.80247	1.9318	11.4409
PL2	0.027111	0.22301	0.75592	0.9764	2.0628	3.7289
PL3	0.0059155	0.008558	0.98558	0.95968	1.9445	4.7549
PL4	0.018083	0.062969	0.92009	0.95693	2.1216	4.9929
PL5	0.014618	0.045644	0.94041	0.96185	1.9566	4.7159

In the visual results of the Pleiades dataset, in Figure 3, it is seen that DWT-based PL methods can carry both spectral and spatial information in a balanced manner. In this dataset, MTF-based methods injected spatial information well. VO methods appear to convey spectral information well. CS methods could not transfer spatial and spectral information in a balanced manner.

In Table 2, the average of all QNR values is 0.7695 and the variance is 0.0177. The mean of the Pleiades dataset is 0.8824 and the variance is 0.0064. These values tell us that the Ikonos dataset is more discriminative in comparing the methods. D-λ values in the Ikonos dataset are similar to those in the Pleiades dataset. Although the variance is almost the same between D-S values, there is a difference of 0.11 on average. This shows us that this dataset is more difficult in terms of carrying spatial information.
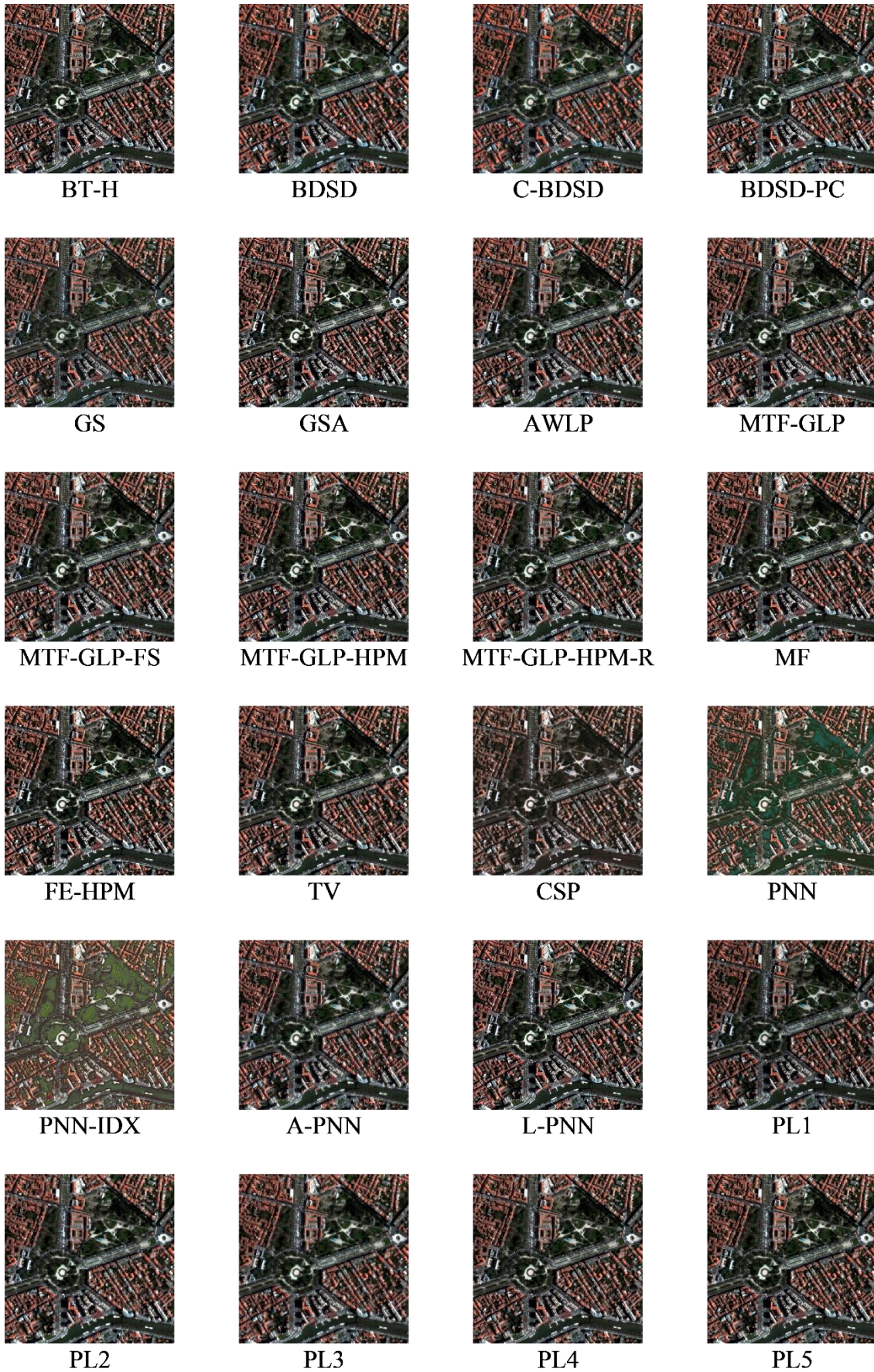
Figure 3. *Pléiades dataset results*

Table 2. Ikonos dataset results

Ikonos	D-λ	D-S	QNR	Q	SAM	ERGAS
BT-H	0.050228	0.14701	0.81015	0.29874	8.8132	49.3399
BDSD	0.022886	0.11062	0.86903	0.98079	0.86477	1.8819
C-BDSD	0.041303	0.080003	0.882	0.97971	1.5667	1.9298
BDSD-PC	0.012479	0.12237	0.86667	0.98381	0.70801	1.7972
GS	0.027725	0.45209	0.53272	0.44585	2.6587	10.2561
GSA	0.017065	0.24919	0.73799	0.87853	1.6225	5.1437
AWLP	0.018906	0.202	0.78291	0.98106	0.55645	1.9158
MTF1	0.032489	0.20205	0.77202	0.97438	1.0674	2.2848
MTF2	0.011005	0.17164	0.81924	0.99332	0.39928	1.1147
MTF3	0.2051	0.088696	0.72439	0.73453	5.2431	61.2218
MTF4	0.0097461	0.14872	0.84299	0.99312	0.24207	1.1311
MF	0.023117	0.18625	0.79494	0.96684	0.81553	2.6188
FE-HPM	0.021544	0.16457	0.81743	0.98384	0.56367	1.8028
TV	0.029596	0.19318	0.78295	0.9607	2.7201	3.0736
CSP	0.016969	0.29922	0.68889	0.89976	2.1917	4.3224
PNN	0.04607	0.18722	0.77533	0.95502	4.589	3.0803
PNN-IDX	0.056905	0.21731	0.73815	0.88718	4.3976	4.7213
A-PNN	0.067098	0.085699	0.85295	0.98693	2.5538	1.5769
L-PNN	0.021057	0.16792	0.81456	0.99061	12.944	13.335
PL1	0.014623	0.15275	0.83486	0.8674	1.2313	11.0606
PL2	0.012346	0.071896	0.91665	0.99657	0.39531	0.81308
PL3	0.018227	0.17256	0.81236	0.94033	1.064	3.4762
PL4	0.023405	0.36667	0.61851	0.83664	1.8075	5.5437
PL5	0.017267	0.18205	0.80382	0.97969	0.58728	2.0151

When we examine Figure 4, it can be seen that CS methods are not very successful in transferring spectral information in this data set. In the measurements, it is seen that PL2 is superior in 4 out of 6 measurements. There is also a big difference in results between other PL methods. When we examine the image, it can be seen that it conveys the spectral information in the MS image very well. MTF4 was successful in conveying spectral quality by obtaining the best values in two criteria that were successful in measuring spectral features.

When the Rasat dataset in Table 3 results are examined, the results of many methods are very close to each other, especially in methods that require reference. We can attribute this to the fact that the spatial resolution of Rasat data is not as high as other datasets. It is seen that CS methods are generally superior to MRA methods. However, there are no major differences.

When we examine the images in Figure 5, it is seen that the brightness value of the PL1 image cannot be adjusted well. The PL1 method fell far behind other PL methods in D-S, QNR and ERGAS criteria. The reason for this may be that the image is created with the help of only 3 optimized coefficients in total, 1 per band.

It has been observed that PL methods are superior to other methods frequently used in the literature in many evaluation criteria. Although there is no superior visual spatial performance, especially in evaluation criteria that require reference, it is seen that spectral information is conveyed well. However, it has been observed that visual evaluation and objective evaluation criteria do not always yield the same results. Civicioglu and Besdok (2024) mentioned, color distortion was observed in CS methods, especially in the Ikonos data results. Aiazzi et al. (2006) mentioned, it was also seen in this study that MRA methods using the MTF approach are successful in transferring spatial information. Feng et al. (2024) also mentioned, it has been observed that MRA-based approaches generally provide superior spectral preservation results than CS-based methods.
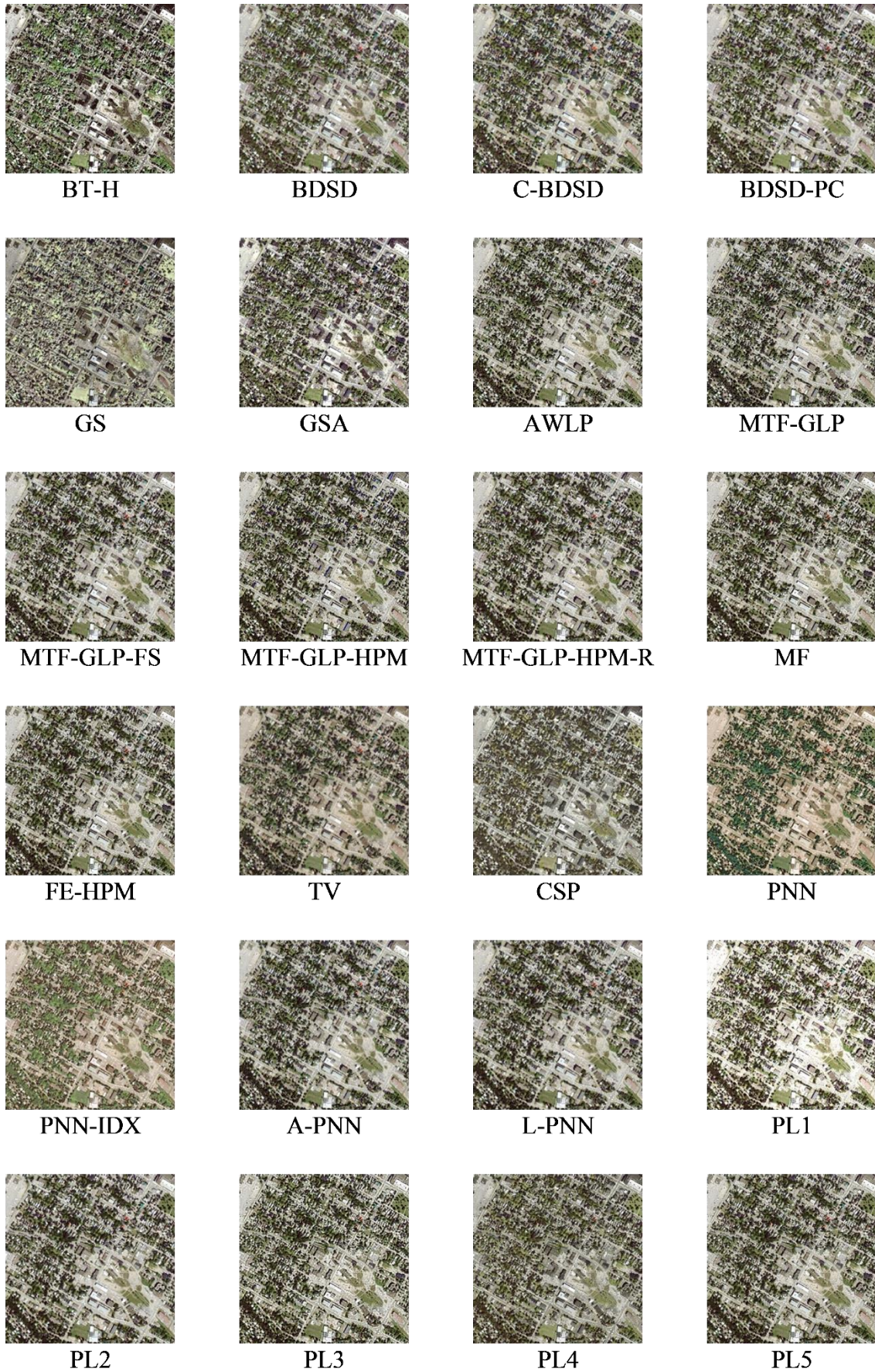
Figure 4. *Ikonos dataset results*

Table 3. *Rasat dataset results*

Rasat	D-λ	D-S	QNR	Q	SAM	ERGAS
BT-H	0.037075	0.071621	0.89396	0.91528	0.68672	1.1669
BDSD	0.0034129	0.061771	0.93503	0.91312	0.5211	1.0995
C-BDSD	0.0082902	0.058071	0.93412	0.91348	0.53358	1.0705
BDSD-PC	0.0062483	0.074998	0.91922	0.91039	0.52178	1.0977
GS	0.0059761	0.099265	0.89535	0.9022	0.51035	1.11
GSA	0.011029	0.068409	0.92132	0.91389	0.52601	1.1432
AWLP	0.0066989	0.042147	0.95144	0.89771	0.53709	1.2053
MTF1	0.021725	0.037048	0.94203	0.89747	0.52678	1.2141
MTF2	0.019214	0.040237	0.94132	0.89738	0.52917	1.216
MTF3	0.022773	0.037616	0.94047	0.89754	0.52396	1.2194
MTF4	0.017167	0.036352	0.94711	0.89797	0.52621	1.2135
MF	0.026001	0.040301	0.93475	0.87225	0.55609	1.3807
FE-HPM	0.018626	0.025861	0.95599	0.88207	0.53672	1.2749
TV	0.022874	0.045822	0.93235	0.96262	1.5805	1.6298
CSP	0.022217	0.092562	0.88728	0.89324	0.78026	1.1809
PNN	0.052711	0.053492	0.89662	0.90627	1.7789	1.4354
PNN-IDX	0.10696	0.052078	0.84653	0.89197	2.9251	1.8026
A-PNN	0.047995	0.15749	0.80207	0.89221	0.99395	1.2328
L-PNN	0.055579	0.065375	0.88268	0.9131	0.64214	11.063
PL1	0.0065028	0.15521	0.8393	0.75687	0.52235	8.4083
PL2	0.0073171	0.010126	0.98263	0.89479	0.52277	1.1925
PL3	0.0066768	0.045148	0.94848	0.89463	0.5203	1.184
PL4	0.029312	0.05911	0.91331	0.90036	0.54958	1.1657
PL5	0.012472	0.024136	0.96369	0.89831	0.52181	1.1904

4. CONCLUSION

In this study, pan sharpening is approached as an optimization problem. The optimum solution was tried to be achieved by optimizing the pixels of the MS image. 5 different optimization-based methods have been tried. The purpose of these methods is to create a low-pass PAN image. The ratio between low-pass PAN and PAN was used to obtain the PI image. WDE algorithm was used as the optimization algorithm. Laplacian filter and SAM were used as objective functions. The proposed methods have been proven to be superior to other methods in many criteria. When we compared the proposed methods among themselves, it was seen that DWT-based PL methods were left behind compared to other PL methods. This may be due to not providing the correct combination. It was observed that the band-based coefficient method used in the methods was insufficient. Creating a compositing factor of 1 for the entire band sometimes caused the image not to be produced at the desired quality. To overcome this shortcoming, the MS image can be divided into segments and a coefficient can be optimized for each segment in each band. Thus, region-based merging can produce a higher quality image. Additionally, in the PL1 method, there appears to be a brightness issue. To solve this problem, the PL1 method can be transformed into an optimization-based contrast stretching method. It has been observed that the ratio between PAN and low-pass PAN will bring us closer to the optimum solution. Optimization-based solutions used to create the low-pass PAN have been shown to be useful.
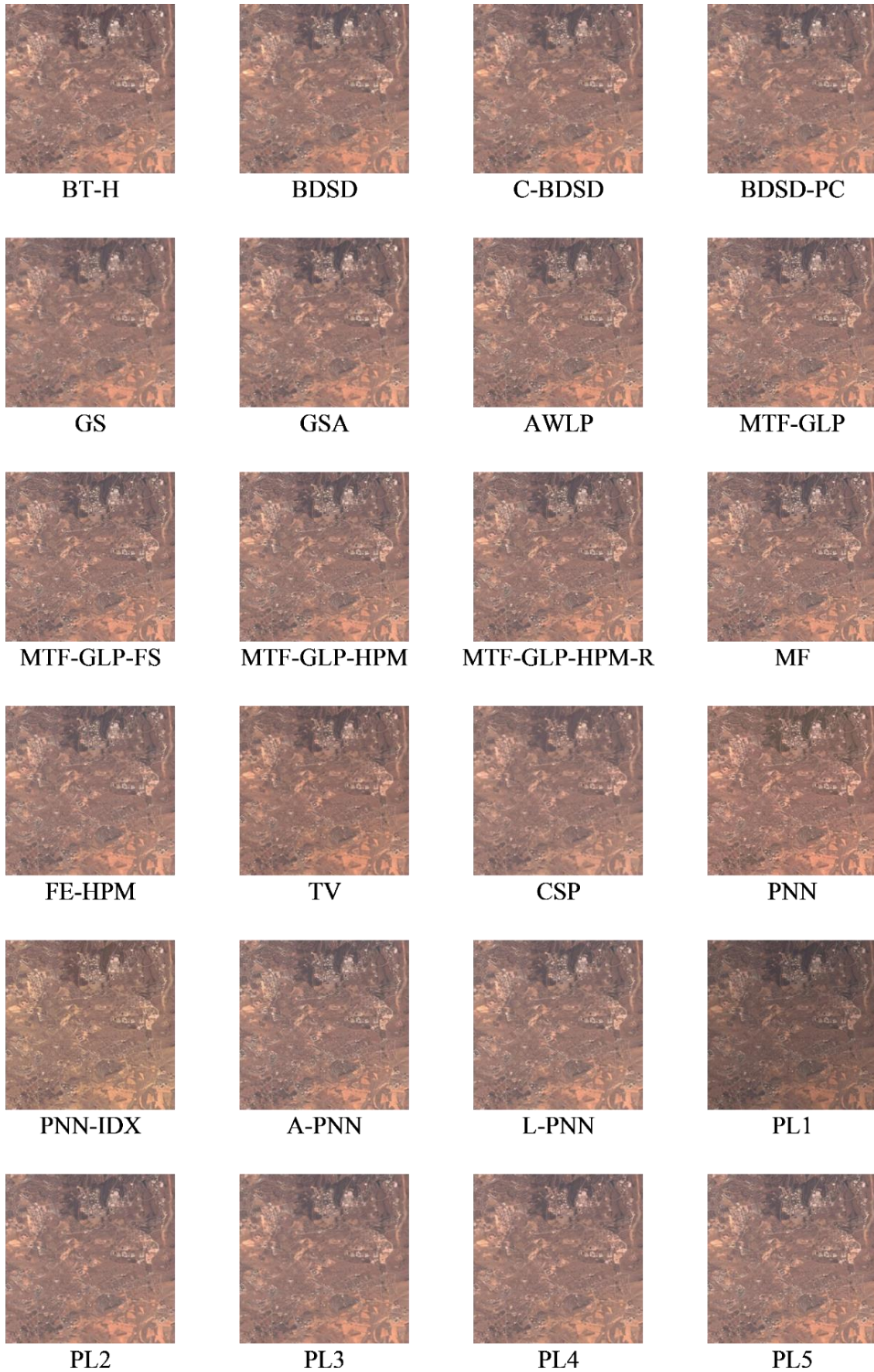
Figure 5. Rasat dataset results

ACKNOWLEDGEMENT

AUTHOR CONTRIBUTIONS

Methodology and writing-reviewing, T.Ç, and M.C.K; editing, T.Ç; conceptualization and software, M.C.K. All authors have read and legally accepted the final version of the article published in the journal.

CONFLICT OF INTEREST

The authors declare no conflict of interest.

REFERENCES

Aiazzi, B., Alparone, L., Baronti, S., & Garzelli, A. (2002). Context-driven fusion of high spatial and spectral resolution images based on oversampled multiresolution analysis. *IEEE Transactions on geoscience and remote sensing*, *40*(10), 2300-2312. https://doi.org/10.1109/TGRS.2002.803623

Aiazzi, B., Alparone, L., Baronti, S., Garzelli, A., & Selva, M. (2006). MTF-tailored multiscale fusion of high-resolution MS and Pan imagery. *Photogrammetric Engineering & Remote Sensing*, *72*(5), 591-596. https://doi.org/10.14358/PERS.72.5.591

Alparone, L., Aiazzi, B., Baronti, S., Garzelli, A., Nencini, F., & Selva, M. (2008). Multispectral and panchromatic data fusion assessment without reference. *Photogrammetric Engineering & Remote Sensing*, *74*(2), 193-200. https://doi.org/10.14358/PERS.74.2.193

Amro, I., Mateos, J., Vega, M., Molina, R., & Katsaggelos, A. K. (2011). A survey of classical methods and new trends in pansharpening of multispectral images. *EURASIP Journal on Advances in Signal Processing*, *2011*(1), 1-22. https://doi.org/10.1186/1687-6180-2011-79

Ciotola, M., Poggi, G., & Scarpa, G. (2023). Unsupervised Deep Learning-based Pansharpening with Jointly-Enhanced Spectral and Spatial Fidelity. *IEEE Transactions on geoscience and remote sensing*. https://doi.org/10.48550/arXiv.2307.14403

Civicioglu, P., & Besdok, E. (2022). Contrast stretching based pansharpening by using weighted differential evolution algorithm. *Expert Systems with Applications*, *208*, 118144. https://doi.org/10.1016/j.eswa.2022.118144

Civicioglu, P., & Besdok, E. (2024). Pansharpening of remote sensing images using dominant pixels. *Expert Systems with Applications*, *242*, 122783. https://doi.org/10.1016/j.eswa.2023.122783

Civicioglu, P., Besdok, E., Gunen, M. A., & Atasever, U. H. (2020). Weighted differential evolution algorithm for numerical function optimization: a comparative study with cuckoo search, artificial bee colony, adaptive differential evolution, and backtracking search optimization algorithms. *Neural Computing and Applications*, *32*, 3923-3937. https://doi.org/10.1007/s00521-018-3822-5

Feng, Y., Yan, B., Jeon, S., & Yang, X. (2024). A hyperspectral pansharpening method using retrain transformer network for remote sensing images in UAV communications system. *Wireless Networks*, 1-14. https://doi.org/10.1007/s11276-023-03611-2

Garzelli, A. (2014). Pansharpening of multispectral images based on nonlocal parameter optimization. *IEEE Transactions on geoscience and remote sensing*, *53*(4), 2096-2107. https://doi.org/10.1109/TGRS.2014.2354471

Gezgin. (2013). (Accessed:01/11/2023) https://gezgin.gov.tr/geoportal/app/main?execution=e3s1

Ghassemian, H. (2016). A review of remote sensing image fusion methods. *Information Fusion*, *32*, 75-89. https://doi.org/10.1016/j.inffus.2016.03.003

Günen, M. A. (2021). Weighted differential evolution algorithm based pansharpening. *International Journal of Remote Sensing*, *42*(22), 8468-8491. https://doi.org/10.1080/01431161.2021.1976874

Kallel, A. (2014). MTF-adjusted pansharpening approach based on coupled multiresolution decompositions. *IEEE Transactions on geoscience and remote sensing*, *53*(6), 3124-3145. https://doi.org/10.1109/TGRS.2014.2369056

Kurban, T. (2022). Region based multi-spectral fusion method for remote sensing images using differential search algorithm and IHS transform. *Expert Systems with Applications*, *189*, 116135. https://doi.org/10.1016/j.eswa.2021.116135

Lolli, S., Alparone, L., Garzelli, A., & Vivone, G. (2017). Haze correction for contrast-based multispectral pansharpening. *IEEE Geoscience and Remote Sensing Letters*, *14*(12), 2255-2259. https://doi.org/10.1109/LGRS.2017.2761021

Masi, G., Cozzolino, D., Verdoliva, L., & Scarpa, G. (2016). Pansharpening by convolutional neural networks. *Remote Sensing*, *8*(7), 594. https://doi.org/10.3390/rs8070594

Meng, X., Shen, H., Li, H., Zhang, L., & Fu, R. (2019). Review of the pansharpening methods for remote sensing images based on the idea of meta-analysis: Practical discussion and challenges. *Information Fusion*, *46*, 102-113. https://doi.org/10.1016/j.inffus.2018.05.006

Meng, X., Xiong, Y., Shao, F., Shen, H., Sun, W., Yang, G., Yuan, Q., Fu, R., & Zhang, H. (2020). A large-scale benchmark data set for evaluating pansharpening performance: Overview and implementation. *IEEE Geoscience and Remote Sensing Magazine*, *9*(1), 18-52. https://doi.org/10.1109/MGRS.2020.2976696

Open Remote Sensing. (2015). (Accessed:01/11/2023) https://openremotesensing.net/knowledgebase/a-critical-comparison-among-pansharpening-algorithms/

Otazu, X., González-Audícana, M., Fors, O., & Núñez, J. (2005). Introduction of sensor spectral response into image fusion methods. Application to wavelet-based methods. *IEEE Transactions on geoscience and remote sensing*, *43*(10), 2376-2385. https://doi.org/10.1109/TGRS.2005.856106

Palsson, F., Sveinsson, J. R., & Ulfarsson, M. O. (2013). A new pansharpening algorithm based on total variation. *IEEE Geoscience and Remote Sensing Letters*, *11*(1), 318-322. https://doi.org/10.1109/LGRS.2013.2257669

Restaino, R., Vivone, G., Dalla Mura, M., & Chanussot, J. (2016). Fusion of multispectral and panchromatic images based on morphological operators. *IEEE Transactions on Image Processing*, *25*(6), 2882-2895. https://doi.org/10.1109/tip.2016.2556944

Scarpa, G., Vitale, S., & Cozzolino, D. (2018). Target-adaptive CNN-based pansharpening. *IEEE Transactions on geoscience and remote sensing*, *56*(9), 5443-5457. https://doi.org/10.1109/TGRS.2018.2817393

Shahdoosti, H. R., & Ghassemian, H. (2014). Fusion of MS and PAN images preserving spectral quality. *IEEE Geoscience and Remote Sensing Letters*, *12*(3), 611-615. https://doi.org/10.1109/LGRS.2014.2353135

Tu, T., Su, S., Shyn, H., & Huang, P. (2001). A new look at IHS-like image fusion methods. *Information Fusion*. https://doi.org/10.1016/S1566-2535(01)00036-7

Vivone, G. (2019). Robust band-dependent spatial-detail approaches for panchromatic sharpening. *IEEE Transactions on geoscience and remote sensing*, *57*(9), 6421-6433. https://doi.org/10.1109/TGRS.2019.2906073

Vivone, G., Alparone, L., Chanussot, J., Dalla Mura, M., Garzelli, A., Licciardi, G. A., Restaino, R., & Wald, L. (2014a). A critical comparison among pansharpening algorithms. *IEEE Transactions on geoscience and remote sensing*, *53*(5), 2565-2586. https://doi.org/10.1109/TGRS.2014.2361734

Vivone, G., Dalla Mura, M., Garzelli, A., Restaino, R., Scarpa, G., Ulfarsson, M. O., Alparone, L., & Chanussot, J. (2020). A new benchmark based on recent advances in multispectral pansharpening: Revisiting pansharpening with classical and emerging pansharpening methods. *IEEE Geoscience and Remote Sensing Magazine*, *9*(1), 53-81. https://doi.org/10.1109/MGRS.2020.3019315

Vivone, G., Restaino, R., & Chanussot, J. (2017). A regression-based high-pass modulation pansharpening approach. *IEEE Transactions on geoscience and remote sensing*, *56*(2), 984-996. https://doi.org/10.1109/TGRS.2017.2757508

Vivone, G., Restaino, R., & Chanussot, J. (2018). Full scale regression-based injection coefficients for panchromatic sharpening. *IEEE Transactions on Image Processing*, *27*(7), 3418-3431. https://doi.org/10.1109/TIP.2018.2819501

Vivone, G., Restaino, R., Dalla Mura, M., Licciardi, G., & Chanussot, J. (2013). Contrast and error-based fusion schemes for multispectral image pansharpening. *IEEE Geoscience and Remote Sensing Letters*, *11*(5), 930-934. https://doi.org/10.1109/LGRS.2013.2281996

Vivone, G., Simões, M., Dalla Mura, M., Restaino, R., Bioucas-Dias, J. M., Licciardi, G. A., & Chanussot, J. (2014b). Pansharpening based on semiblind deconvolution. *IEEE Transactions on geoscience and remote sensing*, *53*(4), 1997-2010. https://doi.org/10.1109/TGRS.2014.2351754

Wald, L., Ranchin, T., & Mangolini, M. (1997). Fusion of satellite images of different spatial resolutions: Assessing the quality of resulting images. *Photogrammetric engineering and remote sensing*, *63*(6), 691-699.

Yilmaz, C. S., Yilmaz, V., & Gungor, O. (2022). A theoretical and practical survey of image fusion methods for multispectral pansharpening. *Information Fusion*, *79*, 1-43. https://doi.org/10.1016/j.inffus.2021.10.001

Numerical Analysis of the Effects of Fuel Injection Duration and Spray Angle on the Combustion Process in a Compression Ignition Engine

Fethi BALABAN[1]   Serdar HALİS[2*]   H. Serdar YÜCESU[3]

[1] National Defense University, Army NCO Vocational HE School, Balıkesir, Türkiye
[2] Pamukkale University, Department of Automotive Engineering, Faculty of Technology, Denizli, Türkiye
[3] Gazi University, Department of Automotive Engineering, Faculty of Technology, Ankara, Türkiye

Keywords	Abstract
Diesel Engine CFD Spray Angle Injection Duration	The changes in injection strategies for diesel engines have a major impact on the performance and pollutant emission characteristics of diesel engines. If injection strategies like injection duration, injection timing, injection pressure and spray angle are properly adjusted, combustion can be improved. The engine performance will increase and emissions will decrease with the combustion improvement. In this work, the influences of injection duration and spray angle on the combustion characteristics of single cylinder, natural aspirated, electronically controlled injection, compression ignition engine were investigated. In the first stage of the work, experiments were executed on a single cylinder CI engine using a Cussons P8160 DC dynamometer. After the experiments, the piston bowl geometry of the engine was modeled and numerical simulation studies were achieved at 7 different injection durations and 7 different spray angles using Converge CFD software. As a result of this study, it was observed that there is a good match between experimental and simulation data of heat release rate (HRR) and in-cylinder pressure. In-cylinder pressure decreased with longer injection duration. The highest max. in-cylinder pressure was roughly 101.0 bar at 4°CA injection duration and the lowest max. in-cylinder pressure was roughly 82.0 bar at 10°CA injection duration. When the HRR data were analyzed, it was seen that as the injection duration increased, the amount of heat released by combustion decreased. When examining the results of the spray angle analysis, it was concluded that there were not very large differences in-cylinder pressure and HRR data, and there was a difference of 1.4 bar between the highest and lowest max. in-cylinder pressure values. In addition, the highest in-cylinder pressure of approximately 86.7 bar was obtained at a spray angle of 77°. It was observed that the CA50 value was obtained at angles closer to the top dead center by increasing the spray angle and decreasing the injection duration. Moreover, the longest combustion durations were realized at 60° spray angle and 10°CA injection duration.

1. INTRODUCTION

Nowadays, increasing global warming is a significant threat to life on Earth. High energy intensive processes that generate significant carbon dioxide (CO), carbon monoxide (CO_2), hydrocarbon (HC) and carbon black emissions on the earth's surface greatly increase global warming. The internal combustion engine is the main source of these emissions. These emissions consist of the combustion of petroleum-derived fuels such as diesel and petroleum used in internal combustion engines.

In the diesel engine, combustion characteristics are improved to reduce exhaust pollutants and also increase the performance of engine and reduce fuel consumption. Many modification processes have been carried out to improve combustion characteristics. Modifications to the combustion chamber and injection system are the

most important changes. The combustion efficiency of the engine has been increased by improving the movement of air into the combustion chamber through changes in the piston bowl geometry. By using various piston bowl geometries, the turbulent motion of the air entering the combustion chamber can be increased so that the air and fuel mixture in the cylinder is evenly distributed throughout the cylinder (Basshuysen & Schafe, 2004). At the same time, modifications to the injection system in CI engines aim to provide higher atomization of fuel injected inside the cylinder. Through this higher atomization, combustion efficiency is increased by providing a homogenous blend of air and fuel into the piston bowl. Injection system modifications such as injection timing, injection pressure, injection characteristics and spray angle greatly affect combustion in diesel engines. In the literature, many studies have been conducted considering these parameters. Jha et al. (2022) investigated the combustion of diesel-methane fuel pairs at different injection timing in their simulation study. Consequently in this work, they found that the combustion process of diesel was delayed with methane and after the combustion was completed, methane could not participate in the combustion reaction by accumulating in the piston ring gaps, piston crown and near the cylinder liner. Sener (2022) analyzed the influences of the grooved injection method on CI engine pollutant emission and combustion characteristics in a numerical study. Consequently in this work, they concluded that emissions were significantly reduced by using the grooved injection method. Jurić et al. (2019), in their analysis study with different injection methods, concluded that the common rail pressure has less effect on the combustion processes by shifting the injection timing to after TDC and that both single and multiple injection timings are consistent with experimental data. Mohan et al. (2014) researched the influence of injector spray characteristics on pollutant exhaust gases and combustion characteristics in the system using biodiesel. Consequently, they found that a balance between NO_x-soot emission values can be achieved by using a spark plug head injection profile under medium load and medium speed conditions. Huang et al. (2019) researched the effect of pre-injection method on combustion and pollutant exhaust gases of a CI engine using 100% diesel fuel and 30% butane + 70% diesel blend fuel. Consequently in this work, it was found that the in-cylinder pressure enhanced and brake specific fuel consumption (BSFC) reduced with a range of decreasing pre-injection timing and enhancing pre-injection rate. In case of using 100% diesel, the highest maximum in-cylinder pressure was approximately 9.0 MPa at 15% pre-injection rate and 15°CA pre-injection range, and the highest BSFC was roughly 260 g/kWh at 20% injection rate and 45°CA pre-injection interval. They also concluded that soot and NOx emissions increased with decreasing pre-injection range and enhancing pre-injection rate. Yousefi et al. (2018) examined the influences of conventional single injection timing on emissions and combustion in natural gas-diesel double fuel combustion. In this work, they concluded that advancing the single injection timing of diesel engines increased thermal efficiency by approximately 6%, reduced unburnt methane and carbon monoxide emissions by 62% and 61% respectively, and increased NO_x emissions by 74%. Halis et al. (2022) analyzed the influences of lambda and injection timing on RCCI engine combustion. They concluded that the max. cylinder pressure enhanced by bringing forward the timing of the injection. They also concluded that the max. in-cylinder pressure increased and combustion improved by the reduction of the lambda. They obtained the highest in-cylinder pressure and HRR of roughly 45 bar and 213 J/°CA at the start of injection at -50° CA aTDC and at a lambda value of 1.2. Khan et al. (2018) analyzed the influences of different spray angles and piston bowl geometries on pollutant exhaust gases and combustion. They concluded the pressure in the cylinder, the HRR, nitrogen oxide and carbon black emissions increase as the spray angle increases. They also obtained the highest max. pressure in the cylinder and HRR of roughly 70 bar and 80 J/°CA in a toroidal re-entry piston bowl and 165° spray angle. Wei et al. (2014) investigated the effects of different nozzle angles and a new vortex chamber combustion system on combustion and emissions. Consequently, they stated that as the nozzle angle increased, the equivalence ratio and soot emission rose, the amount of NO decreased. Jaichandar et al. (2012) focused on the piston bowl geometry and optimization of injection timing to improve engine performance and pollutant exhaust gases in a CI engine using bio-diesel as fuel. In this work, they finalized that the specific fuel consumption (SFC) and HC, CO and carbon black emissions decreased, but nitrogen oxide emissions increased with the use of toroidal reentrant combustion chamber geometry. It was also found that when a toroidal reentrant piston bowl was used, a decrease in in-cylinder pressure occurred by the retardation of the injection timing due to the ignition delay of about 2°CA. Ranganatha Swamy et al. (2014) analyzed the influences of injection timing, piston bowl geometry and injector nozzle holes on CI engine performance. Consequently in this work, It has been shown that delaying the injection timing increases soot emissions by 20%, while the use of a toroidal piston cup geometry increases brake thermal efficiency and nitrogen oxide emissions and reduces carbon black, carbon monoxide and HC emissions. The injector with 5 nozzle hole numbers provides a more homogeneous air and fuel mixture and reduces soot emissions. In addition, It was found that the use of a 0.2

mm orifice injector increased cylinder pressure and HRR. Mehta and Tamma (1998) investigated the influences of air vortex and injection pressure on combustion characteristics in a CI engine. It is observed that as the swirl ratio increased, the in-cylinder pressure and HRR decreased. They obtained the highest in-cylinder pressure of approximately 70 bar at an air vortex ratio of 2.0 and an injection pressure of 300 bar. They also concluded that the increased injection pressure improved combustion characteristics and allowed combustion to occur in less time. Sener et al. (2020) examined the influences of parameters such as spray angle of fuel, the new version of the swirl combustion chamber, re-entrant piston bowl geometry and injection pressure on engine performance. When the results were analyzed, it was seen that reduced thermal efficiency and increased exhaust emissions by the increase in the spray angle in both the re-entry and basic piston bowl geometry of the engine. They also indicated that pressure inside the cylinder increased and soot emission decreased with increasing injection pressure and the highest in-cylinder pressure was obtained at approximately 11.0 MPa with the use of 150° spray angle and 1000 bar injection pressure in dual swirl piston bowl geometry. Mishra et al. (2023) investigated the influence of hemispherical and toroidal piston bowl geometries on engine performance in a CI engine with HCCI combustion mode. In addition, they used variable spray angles to provide a good mixture of air and fuel in the piston bowl and to reduce fuel density in certain areas of the combustion chamber. Consequently, they concluded that the thermal efficiency increased by 3-5% with the use of toroidal combustion chamber and the combustion processes were improved with modified piston geometry and multi-stage injection strategy. They also defined that the max. in-cylinder pressure increases up to 45° spray angle and decreases up to 70° spray angle. Cengiz and Unverdi (2023) researched the influences of injection timing and injection angle on combustion and exhaust pollutants of a diesel engine using PCCI combustion mode. As a result, they stated that combustion efficiency and average effective pressure increased with decreasing spray inclusion angle; while improvement in NO_x emissions was observed, soot and carbon monoxide emissions decreased. They obtained the highest combustion efficiency of 97.8%, average effective pressure of 3.37 bar, the lowest carbon black emission of 33.5 ppm and the lowest CO emission of 2.2 ppm with staggered spraying into the combustion chamber, 100° spray inclusion angle and -50°CA start of injection. Kumar et al. (2022) investigated the effects of fuel injection pressure and injection timing of Jatropha biodiesel as a pilot fuel on the operation and pollutant exhaust gases of an engine using hydrogen as fuel. Consequently, they found that BSFC increased to 32.15% and nitrogen oxide emissions enhanced by 20.61% at 1500 bar injection pressure and 17°CA bTDC with the use of a biodiesel-hydrogen fuel pair. At 1500 bar injection pressure and 11°CA bTDC, they concluded that unburned HC emissions decreased by 59.12% and soot emissions decreased by 46.18%. They also concluded that the max. in-cylinder pressure and heat dispersion increased with enhancing injection pressure and injection timing. Ge et al. (2022) analyzed the influences of variable multiple injection strategies on the performance and exhaust pollutants of a diesel-biodiesel-ethanol triple mix fuel engine at low idle conditions in their experimental study. They concluded that the diesel-biodiesel-ethanol blend and different main pilot injection timings have a major influence on the CI engine performance and pollutant exhaust gas characteristics. Hao et al. (2022) optimized the injection timing and piston bowl geometry to increase the mixing process of air and fuel in a CI engine and to optimize full load combustion process in their study. They concluded that spray angle has a major effect on the combustion process and mixture of air and fuel, engine power is increased by optimizing the piston bowl geometry. Also, they obtained maximum power as 80 kW at a spray angle of 153°. Using a premixed charge compression ignition (PCCI) combustion mode, Lu et al. (2023) researched the influence of a multiple injection strategy on heavy-duty engine operation and pollutant exhaust gases characteristics. They obtained a very small rise in thermal efficiency of 8.66% with the injection strategy at low speed of the engine and 0.33% at medium engine speeds for single injection with 15° CA bTDC. Pham et al. (2022) researched the effect of spray angle on combustion and polluted exhaust gases in a four-stroke CI engine using natural gas combined with diesel. Consequently, they found that soot emissions were reduced by 17% in dual fuel use and 56% in single diesel use with a spray angle of 150° and the optimal NO_x emission was observed at a spray angle of 145°. They also concluded that the spray angle alone is not sufficient to determine the engine combustion quality.

In this study, a four-stroke diesel engine was operated at a compression rate of 17.5:1, intake air temperature of 300 K and a constant engine speed of 2000 rpm. The effects of fuel injection duration and spray angle on combustion characteristics in a CI engine were analyzed numerically using Converge CFD computer program along with validation of experimental results. Numerical studies investigating the effects of injection parameters such as injection duration and spray angle in a compression ignition engine using diesel fuel are not found in the literature. It is aimed to obtain the best combustion conditions by determining the appropriate

injection duration and spray angle in a CI engine using diesel fuel and to overcome this gap in the literature with this numerical research.

2. MATERIAL AND METHOD

2.1. Experimental Set-up

Experiments were achieved by connecting the water-cooled, four-stroke, electronically controlled, direct injection, single cylinder LD510 model Lombardini-Antor CI engine to a Cussons P8160 electric DC dynamometer capable of absorbing 10 kW power at a maximum of 4000 rpm. Technique specifications of the experiment engine obtained from the manufacturer are shown in Table 1.

Table 1. Characteristics of the experiment engine

Cylinder number	1
Fuel type	Diesel
Compression rate	17,5:1
Stroke (mm) × cylinder diameter (mm)	90 × 85
Max. torque (Nm)	32,8@1800 rpm
Cylinder volume (cm³)	510
Max. engine speed (rpm)	3000
Engine power (HP)	12
Crankcase oil volume (lt)	1,75
Fuel tank capacity	5,3
Oil consumption (g/h)	8

The injection system of experiment engine was modified and converted into an electronically controlled common-rail system. Thanks to this system, parameters affecting combustion such as injection pressure, timing, duration and amount can be easily adjusted via electronic controls shown in Figure 1.
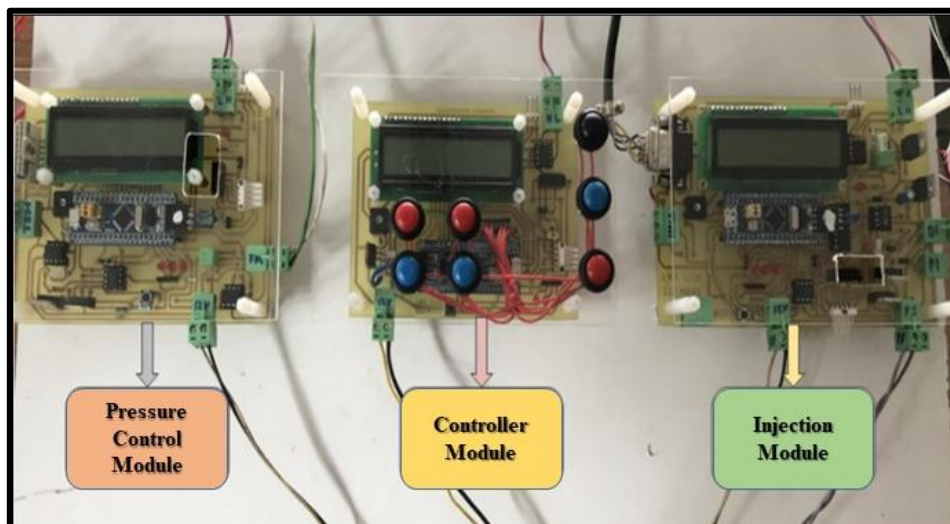
Figure 1. Fuel injection system

KISTLER 6056A model cylinder pressure sensor, whose technical specifications are given in Table 2, was used to read the in-cylinder pressure inputs instantaneously during the experiments on the L9Motor. To obtain the most accurate cylinder pressure data, the position of the sensor is very important. For this reason, the in-cylinder pressure sensor was positioned on the cylinder cover near the center of the engine, taking into account the position of the valves and injectors.

Table 2. *KISTLER 6056A sensor technical specifications*

Measurement interval	0 – 250 (bar)
Sensivity	-20 (pC/bar)
Operating temperature	(-20°C) – (+350°C)
Linearity	≤±0.3
Frequency of natural	160 (kHz)

At the same time, the position of the crankshaft is very important for accurate pressure data acquisition. For this reason, OPKON brand 1000 pulse optical incremental encoder was used to determine the position of the crankshaft. Then, National Instruments 6259 USB data transfer card was used to read the data received from the in-cylinder pressure sensor and encoder. In addition, Merriam brand Z50MC2-4F model laminar flow measurement device was used to measure the air consumption of the experiment engine. In general, the schematic of the test rig is shown in Figure 2. In-cylinder pressure, temperature, HRR, SFC, cumulative heat release rate (IHRR) and variable engine efficiency values obtained as a result of the experiments were calculated with a MATLAB code. An average of 50 cycles was obtained with this code for removing cyclic differences and offering a precise method for data collection. The amount of HRR depending on the crank angle is obtained from Eq. 1 by the energy conservation law of thermodynamics (Heywood, 2018).

$$\frac{dQ}{d\theta} = \frac{n_c}{n_c - 1} P \frac{dV}{d\theta} + \frac{1}{n_c - 1} V \frac{dP}{d\theta} + \frac{dQ_{heat}}{d\theta} \tag{1}$$

The heat transfer between the cylinder and the jackets was computed using Eq. 2. In the equation, the heat transfer coefficient was computed using Woshcnie's revised heat transfer model (Heywood, 2018).

$$\frac{dQ_{heat}}{d\theta} = \frac{1}{6n} h_g A \left(T_g - T_w \right) \tag{2}$$
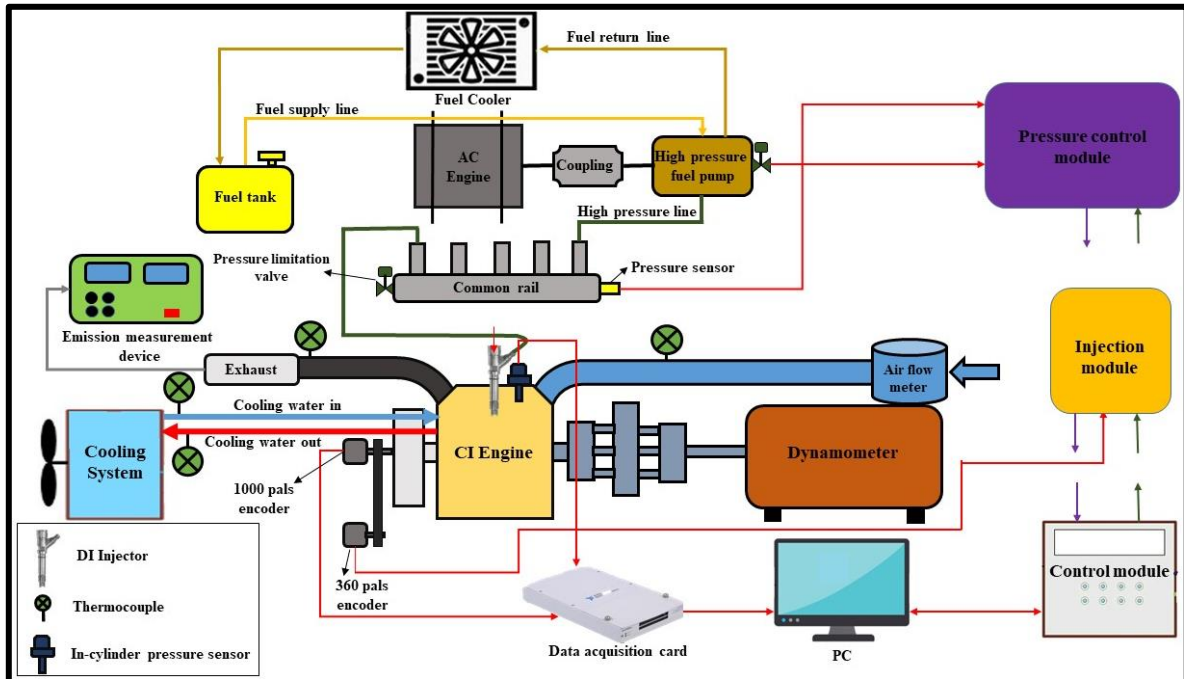
Figure 2. *Schematic of experimental set-up*

2.2. Numerical Model and Validation Study

Converge CFD simulation program was used to analyze the data obtained after the experimental work on a single cylinder CI engine. The piston bowl geometry of the experiment engine was modeled in Solidworks design program. The mesh structure was then applied to the combustion chamber geometry using the auto-mesh determination module. In the simulation, an adaptive mesh refinement (AMR) was applied to sensitive and dense areas of combustion and mobile flow zones. The combustion chamber geometry model and mesh structure of a single cylinder engine are shown in Figure 3.
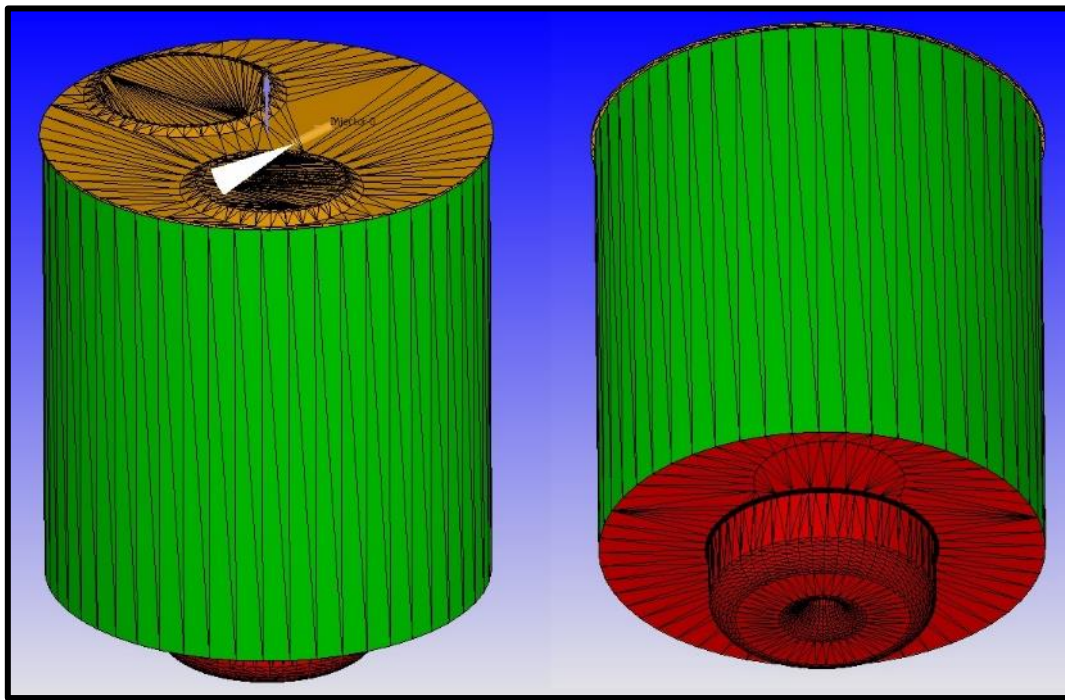
Figure 3. Piston bowl geometry used in the simulation study

In the numerical simulation model, the pressure of the injection system was set to 750 bar, injection duration to 8.25°CA, injection timing to 6.5°CA and injection amount to 24 mg/cycle. In addition, the simulation was performed using closed loop assumptions from closing the inlet valve to opening the exhaust valve.

In the simulation study, the Reynolds Averaged Navier-Stokes based Renormalised Group (RNG) k-epsilon turbulence model improved by Yakhot and Orszag (1986) has been used to model the turbulent motion of fuel drops in the combustion chamber. The Kelvin-Helmholtz (KH)/Rayleigh-Taylor (RT) fragmentation model improved by Beale and Reitz (1999) was used to model the fragmentation of fuel spray droplets. In this model, the primary fragmentation of the droplet is predicted using the KH model and the RT model is used to predict the secondary fragmentation. To model the combustion phenomena inside the cylinder, SAGE chemical kinetic solvents as described by Turns (1996) were used. The Naber and Reitz wall impact model developed by Gonzalez et al. (1991) has been used to model the interaction of fuel droplets between the cylinder or cylinder walls. For DSMC computations, the NTC model, on the basis of techniques from gas dynamics, was used to model the collision of fuel droplets (Schmidt & Rutland, 2000). The O'Rourke&Amsden heat transfer model has been used to model the heat transfer to the combustion chamber or cylinder walls (Amsden & Findley, 1997; Converge, 2016).

A validation study was carried out using experimental data and a simulation model. To select the appropriate base grid size, which is one of the most important steps of the validation study, analyses were performed at different base grid sizes. Figure 4 demonstrates the crank angle dependent in-cylinder pressure results obtained from different base grid size analyses. As a result of the numerical simulation study, the optimum base grid size for the simulation model was determined as 5.8 mm. After determining the appropriate base grid size, the numerical simulation model was successfully validated using the initial conditions shown in Table 3. Figure 5 shows the variation of in-cylinder pressure and HRR as a function of crank angle. When the experimental and

numerical simulation data of the combustion processes of the experiment engine are analyzed, there is a difference of 3°CA in-cylinder pressure, while there is a small difference of 0.5 J/°CA in the HRR.
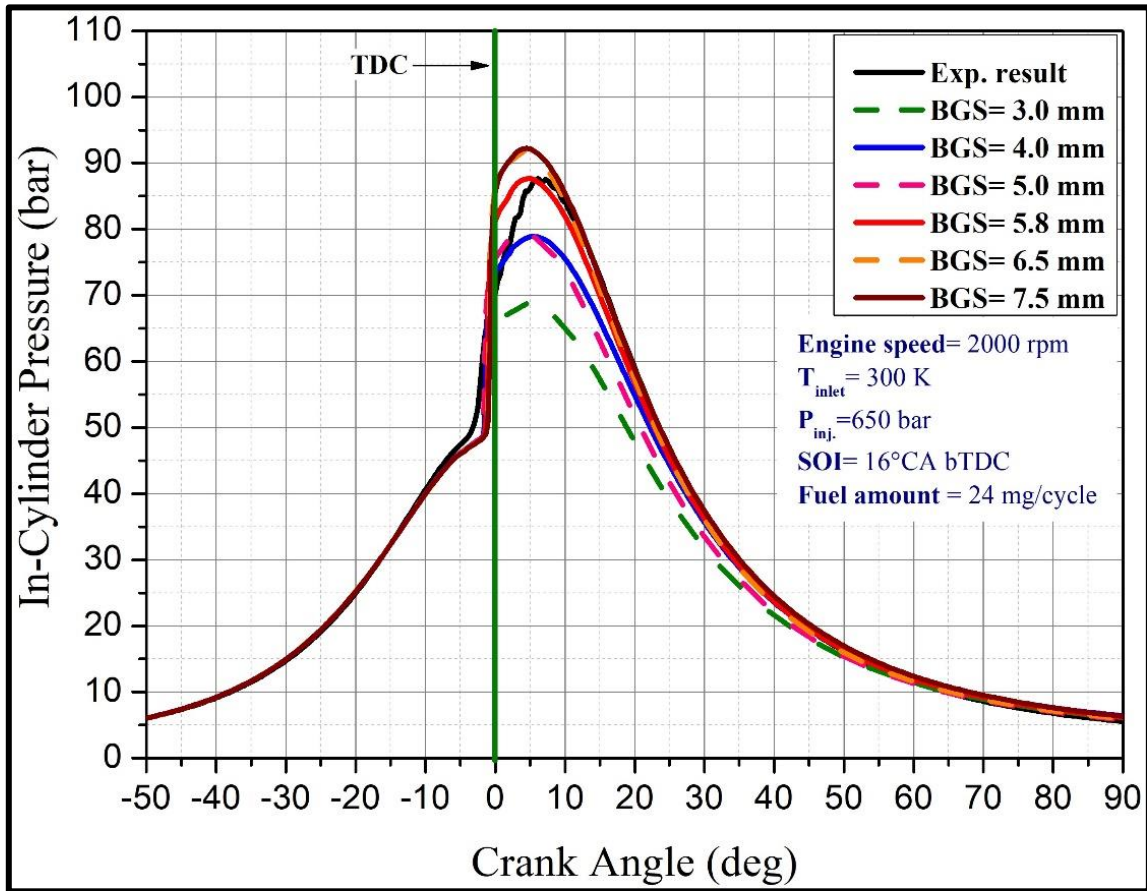
Figure 4. *In-cylinder pressure graphs for variable partition sizes*

Table 3. *Numerical simulation model conditions*

Fuel type	Diesel
Inlet air temp.	300 K
Cylinder Wall temp.	450 K
Engine speed	2000 rpm
Lambda	1.35
Inj. pressure	650 bar
Start of injection (SOI)	-16°CA
Amount of fuel injected	24 mg/cycle
Embedded AMR level	2
Base grid size	5.8 mm
Cell size with AMR	1.45 mm × 1.45 mm × 1.45 mm
Min. time increment	1e-08 s
Max. time increment	1e-04 s
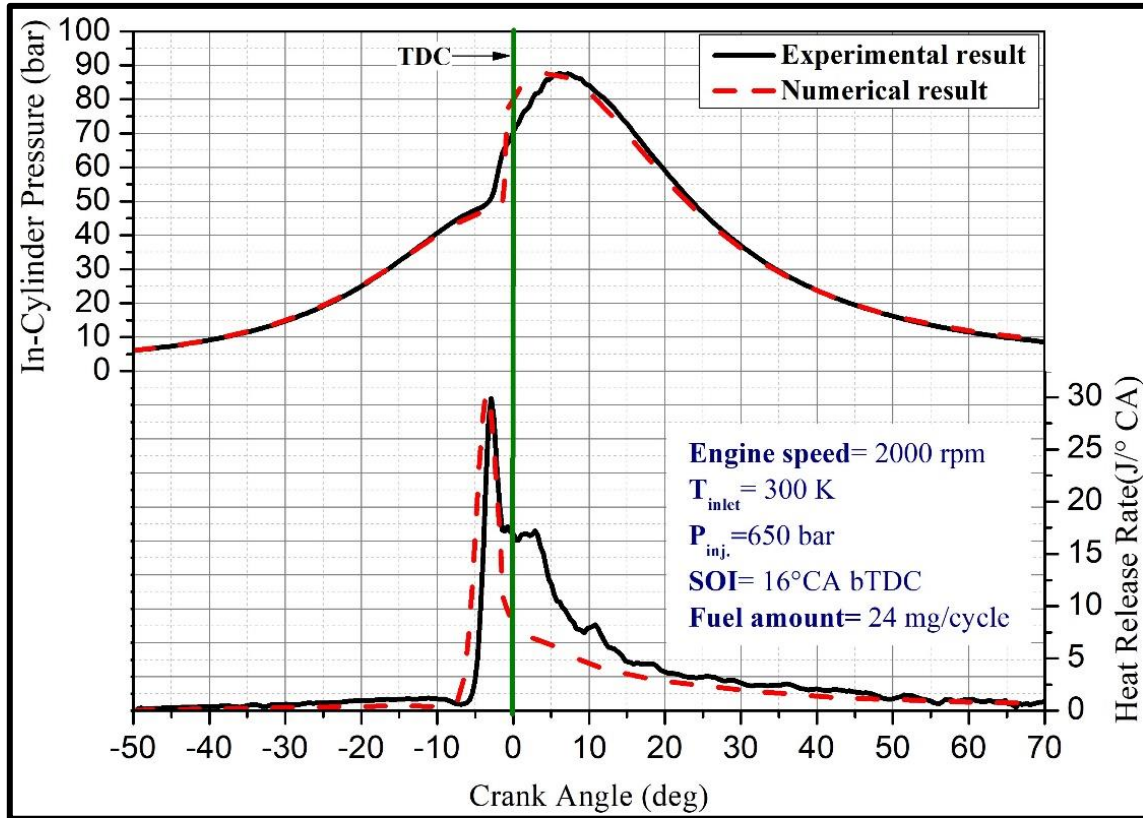
Figure 5. *Results of experimental and numerical simulations*

3. RESULTS AND DISCUSSION

After the validation of the numerical model was successfully performed, the influences of injection duration and spray angle on the process of diesel combustion were investigated through this numerical simulation study.

3.1. Effect of Injection Duration

Analyses were achieved at variable injection durations and the influences on the in-cylinder pressure and HRR of the diesel engine are shown in Figures 6 and 7, separately. To investigate the effect of this parameter, analyses were performed under the conditions of 2000 rpm engine speed, 300 K inlet temperature, 650 bar injection pressure, 24 mg/cycle fuel amount and 16°CA bTDC. Consequently in the analyses, it was observed that the max. in-cylinder pressure increased with decreasing injection pressure. The highest max. in-cylinder pressure was obtained at 4°CA injection duration and the lowest maximum pressure was attained at 10°CA injection duration. The reason for this situation is thought to be that the ignition delay time will also shorten at low injection duration and the pressure and temperature in the cylinder increases due to the abbreviated ignition delay. In an article, Du et al. (2018) stated that with enhancing injection pressure, the injection duration is abbreviated, finer fuel spray droplets are formed and thus efficient combustion is achieved. As with the in-cylinder pressure results, the highest maximum HRR was approximately 42.22 J/°CA at 4°CA injection duration and the lowest maximum HRR was approximately 24.12 J/°CA at 10°CA injection duration.

CA50, defined as the crank angle position at which half of the mixture in the cylinder is completely combusted, is an important parameter that provides information about the combustion characteristics. The CA50 value should be reached just after the top dead center (TDC) to achieve higher thermal efficiency (Gunaydin, 2022; Gupta & Subramanian, 2022; Sanli et al., 2023). Another parameter that provides information about combustion characteristics is the duration of combustion. The crank angle position at which 10% of the mixture combusts (also known as the flame propagation angle) is referred to as CA10 and the crank angle position at which 90% of the mixture combusts is referred to as CA90. Combustion continues for the period between these two crank angle positions. The combustion duration also referred to as the rapid combustion angle, is denoted as CA10-90 (Gurbuz et al., 2013).
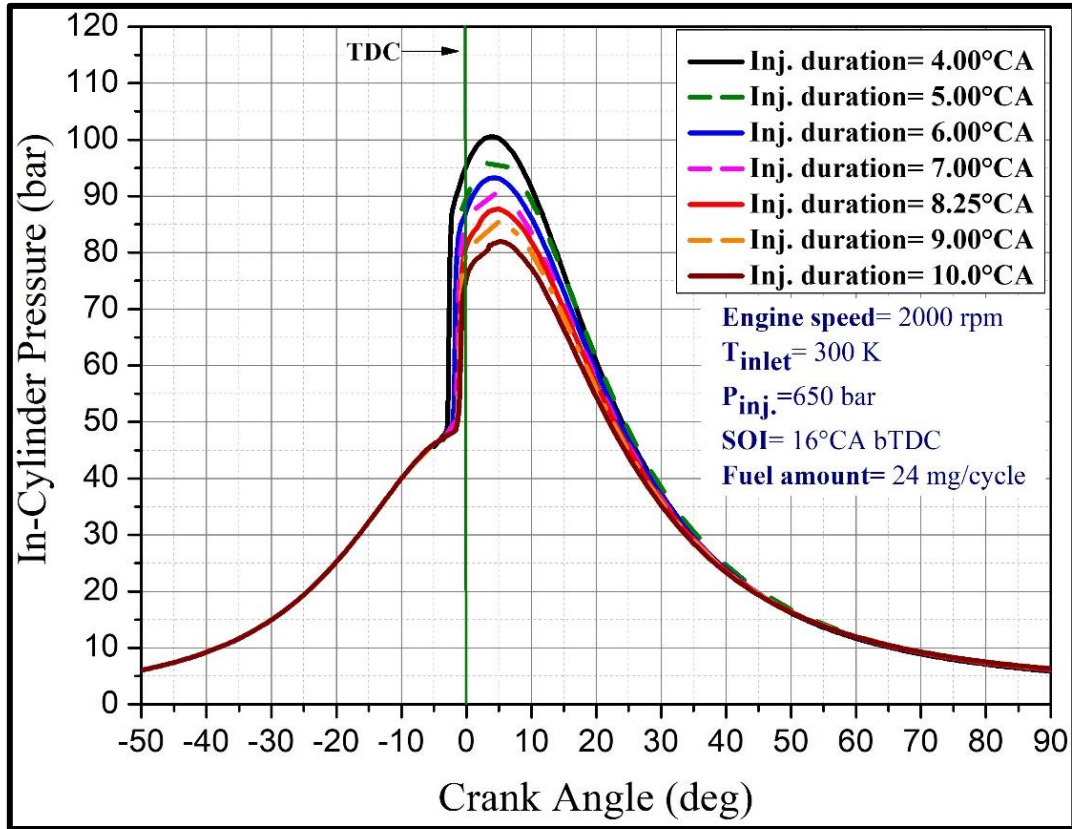
Figure 6. *Variation graph of in-cylinder pressure at variable injection durations*
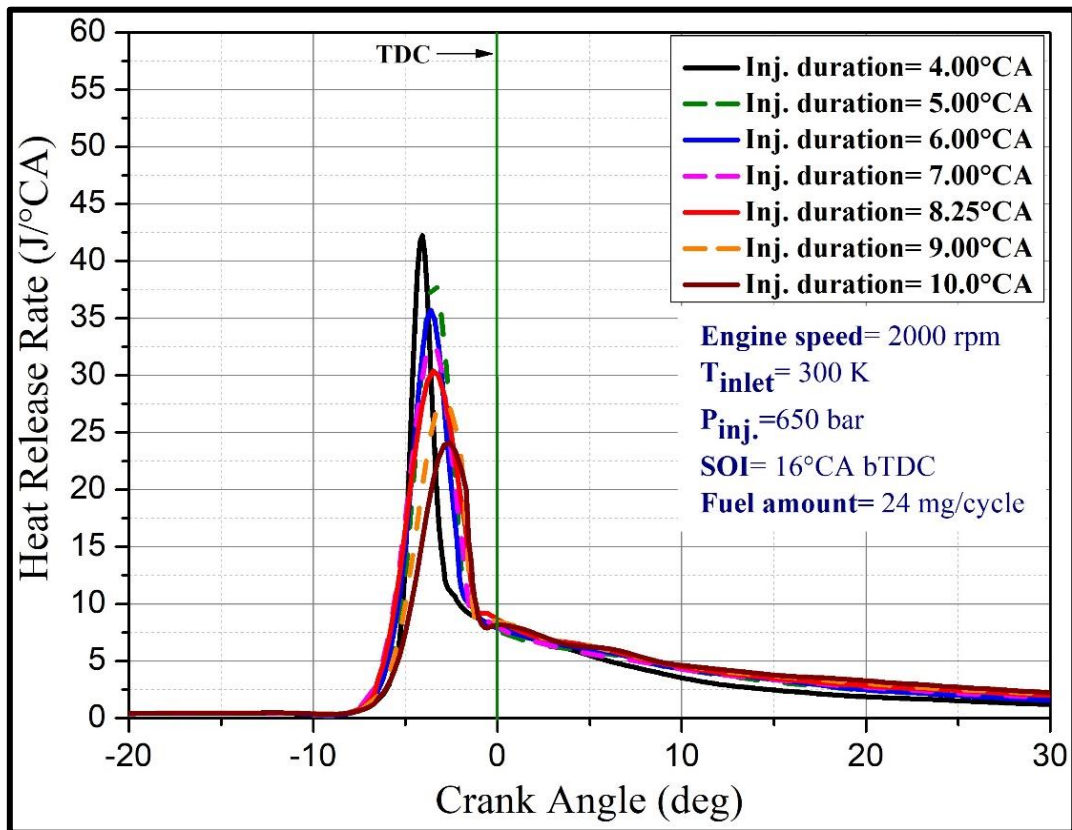
Figure 7. *Variation graph of HRR at variable injection durations*

Figure 8 presents the changes in CA50 and combustion duration depending on the lambda values for different injection durations. It is seen that the CA50 value tends to decline with the rise in lambda value due to the decreasing amount of diesel fuel in the mixture. Similarly, it can be stated that combustion takes place in a shorter time with increasing lambda value. Because more time is required to complete the combustion of the overall mixture at lower lambda values. The longest combustion of the fuel mixture occurred at 10°CA injection duration. As the injection duration increases, it is seen that the crank angle at which the CA50 value is obtained moves away from the top dead center and the combustion continues longer. This is thought to be due to the better atomization behavior of the fuel at lower injection durations.
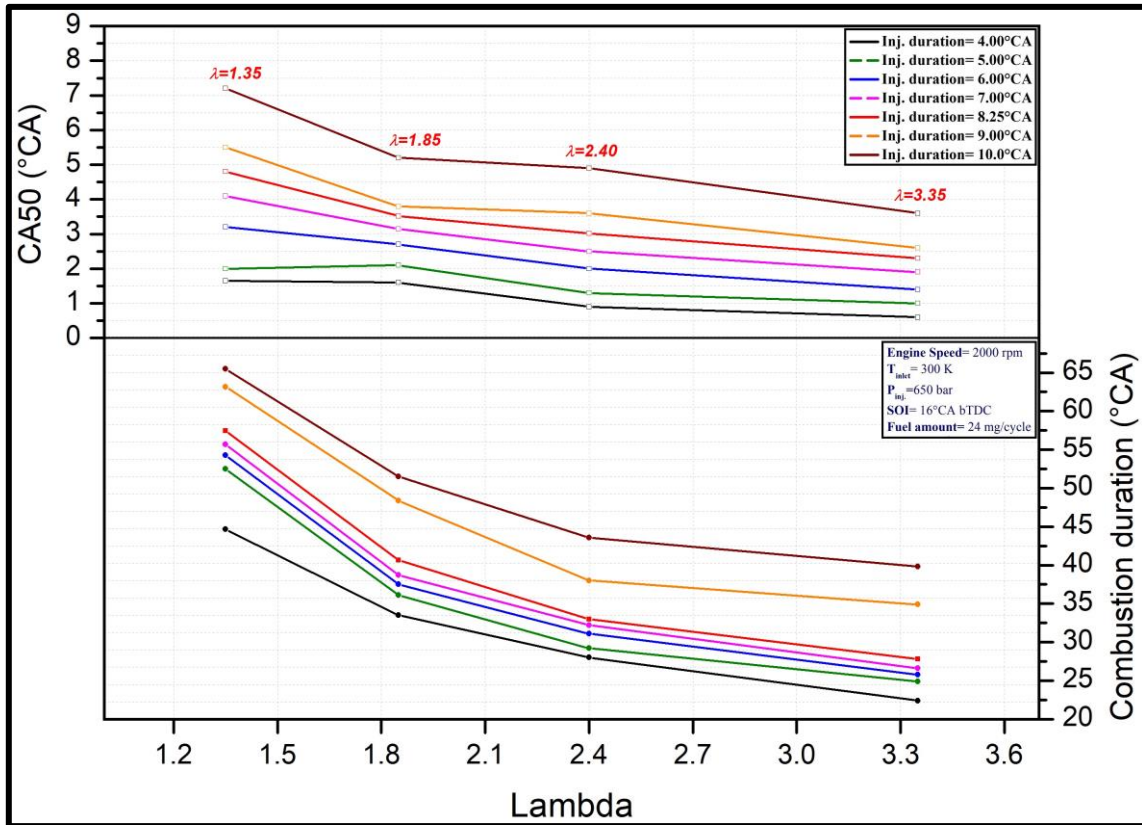
Figure 8. Variation of CA50 and combustion duration for different injection durations

3.2. Effect of Spray Angle

In this passage of the work, the influence of fuel spray angle (injector position) on combustion characteristics was investigated. The analysis was carried out by considering the change in-cylinder pressure and HRR according to the crankshaft angle.

The results attained as a result of the examination are shown in Figure 9 and Figure 10. The study made use of the same simulated initial conditions as were used in the injection duration analysis. Consequently, in the numerical simulation study, it is observed that the changes in the spray angle do not cause excessive changes in the in-cylinder pressure. The reason for this is thought to be that the spray angle alone cannot be effective. In a study, Shu et al. (2019) stated that spray angle alone cannot be effective on diesel combustion and that the combustion chamber geometry should be optimized together with the spray angle. When the pressure values inside the cylinder were also analyzed, a difference of approximately 1.2 bar was observed between the 77° spray angle with the highest max. in-cylinder pressure and the 60° spray angle with the lowest max. end of in-cylinder pressure. Regarding the HRR, the highest maximum HRR was approximately 30.3 J/°CA at 70° spray angle and the lowest maximum HRR was approximately 27.5 J/°CA at 60° and 62° spray angles.
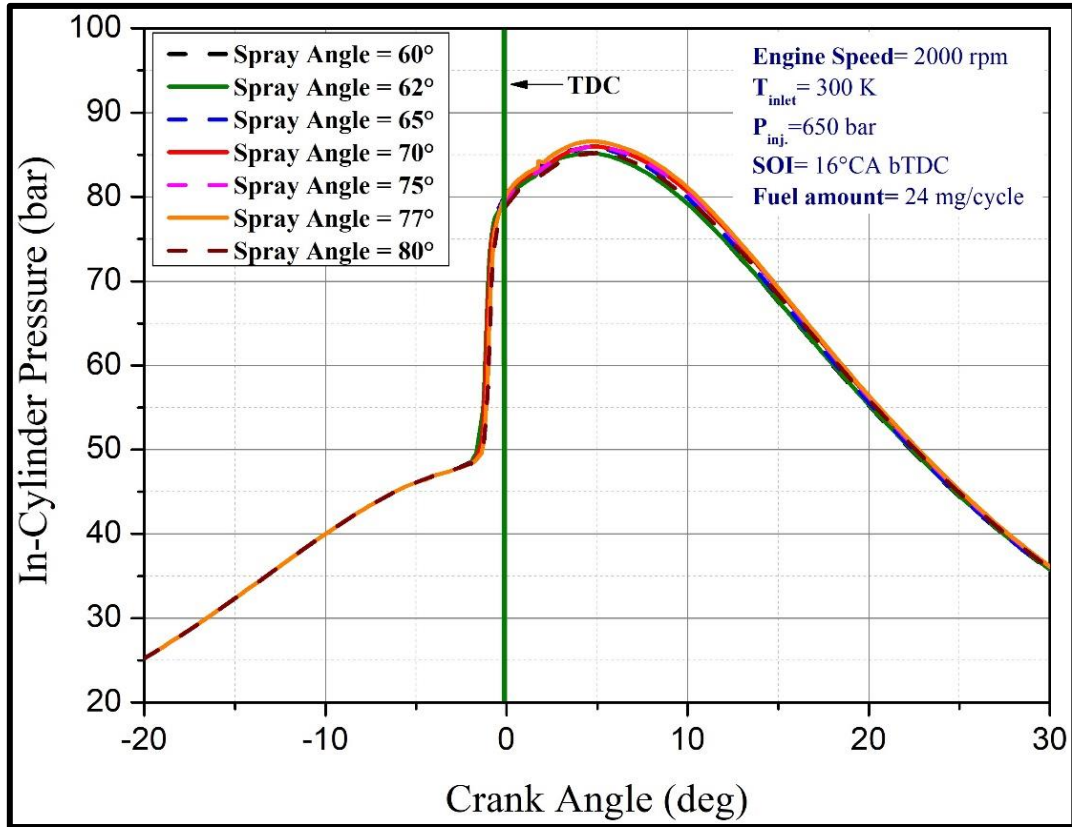
Figure 9. *Variation graph of in-cylinder pressure at variable spray angles*
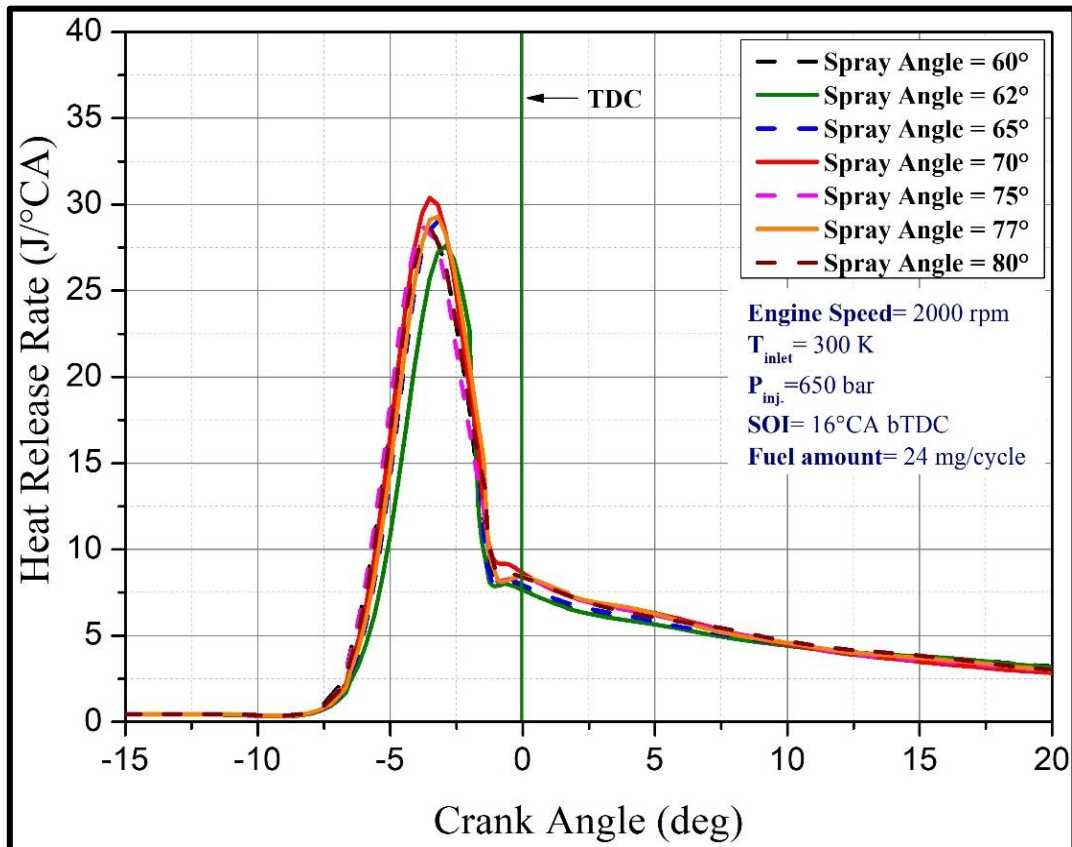
Figure 10. *Variation graph of HRR at variable spray angles*

Figure 11 illustrates how the lambda values for various spray angles affect the CA50 and combustion duration. Although changing the spray angle concerning the injector position did not have much effect on the in-cylinder pressure, it considerably affected the CA50 and combustion duration. It can be said that the CA50 value trends downward with the increase in lambda value. As a result of the mixture's decreased diesel fuel content, it can be observed that the combustion duration shortens as the lambda value increases. The lower the lambda value, the more time is required to complete the combustion of the total mixture. It is thought that by increasing the spray angle except for the 80° spray angle, a more homogeneous mixture is formed in the cylinder and the combustion process is completed in shorter periods. The longest combustion of the fuel mixture occurred at 60° spray angle. It is seen that as the spray angle increases, the crank angle at which the CA50 value is obtained gets closer to TDC. It is thought that this may be due to the better atomization behavior of the fuel as the spray angle is increased.
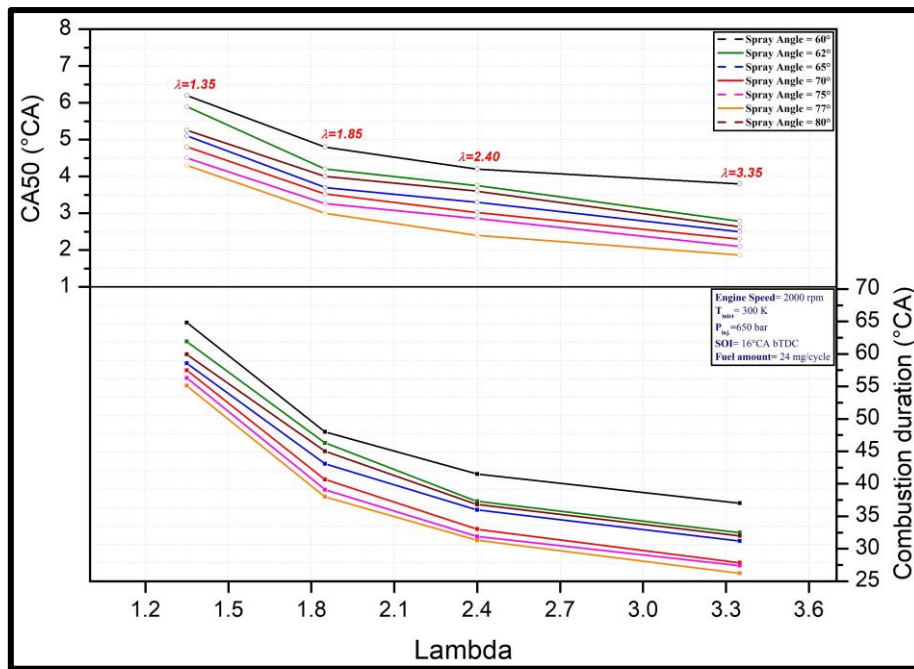
Figure 11. *Variation of CA50 and combustion duration for different spray angles*

4. CONCLUSION

In this work, the influences of injection duration and spray angle on diesel combustion were researched using experimental values validated using Converge CFD program in a single cylinder CI engine. When the data attained from the numerical simulation and the experimental data are compared, it can be said that the validation of study has been achieved successfully. The following results were obtained from the numerical study:

✓ The in-cylinder pressure and HRR values decreased with the raise in injection duration and the highest max. in-cylinder pressure was obtained at 4°CA injection duration. The lowest in-cylinder pressure was attained at 10°CA injection duration. Likewise, when the change in HRR is analyzed, the highest maximum HRR of 42.22 J/°CA at 4°CA injection duration and the lowest maximum HRR value of 24.12 J/°CA at 10°CA injection duration were obtained.

✓ It was also found that the change in spray angle did not affect the in-cylinder pressure much. A pressure difference of 1.2 bar was observed between the 77° spray angle, where the highest max. in-cylinder pressure was obtained, and the 60° and 62° spray angles, where the lowest max. in-cylinder pressure was obtained. In the study, it was attained that the max. HRR was approximately 30.3 J/°CA at the highest spray angle of 70°.

✓ It was observed that the CA50 value was obtained at angles closer to the top dead center by increasing the spray angle and decreasing the injection duration. In addition, the longest combustion durations were realized at 60° spray angle and 10°CA injection duration.

How other different injection parameters affect the combustion process can also be investigated. Considering this numerical study, comparative studies can be carried out using methods such as Response Surface Method.

ACKNOWLEDGEMENT

AUTHOR CONTRIBUTIONS

CONFLICT OF INTEREST

The authors declare no conflict of interest.

Abbreviations

A	Area
AMR	Adaptive mesh refinement
BGS	Base grid size
BSFC	Fren özgül yakıt tüketimi
CA	Crank angle
CI	Compression ignition
CFD	Computitional fluid dynamics
CO	Carbonmonoxide
CO_2	Carbondioxide
DSMC	Direct simulation monte carlo
HC	Hydrocarbon
HCCI	Homogenous charged compression ignition
HRR	Heat release rate
h_g	Gas heat transfer coefficient
IHRR	Cumulative heat release
KH	Kelvin Helmholtz
NO_x	Nitrogen oxide
NTC	Negative temperature coefficient
P	Pressure
PCCI	Premixed controlled compression ignition
Q	Heat
RCCI	Reactivity controlled CIcombustion
RNG	Renormalization group
RT	Rayleigh-Taylor
SI	Spark ignition
SFC	Specific fuel consumption
SOI	Start of injection
TDC	Top dead center
T_g	Gas temperature
T_w	Cylinder wall temperature
V	Volume
θ	Crank angle

REFERENCES

Amsden, A. A., & Findley, M. (1997). *KIVA-3V: A block-structured KIVA program for engines with vertical or canted valves* (First edition). Livermore: Lawrence Livermore National Lab.(LLNL), 1-95.

Basshuysen, V. R., & Schafer, F. (2004). *Internal Combustion Engine Handbook Basics, Components, Systems and Prespectives* (First edition). Warrendale, Pa.: SAE International, 390-412, 446-470.

Beale, J. C., & Reitz, R. D. (1999). Modeling spray atomization with the Kelvin-Helmholtz/Rayleigh-Taylor hybrid model. *Atomization and Sprays*, *9*(6), 623-650. https://doi.org/10.1615/AtomizSpr.v9.i6.40

Cengiz, C., & Unverdi, S. O. (2023). A CFD Study on the Effects of Injection Timing and Spray Inclusion Angle on Performance and Emission Characteristics of a DI Diesel Engine Operating in Diffusion-Controlled and PCCI Modes of Combustion. *Energies*, *16*(6), 2861. https://doi.org/10.3390/en16062861

Converge CFD Software. (2016). CONVERGE (v2.4) Theory Manual. Wisconsin: Convergent Science Inc., 298-316, 319-325, 335-337, 386-390, 479-520.

Du, W., Zhang, Q., Zhang, Z., Lou, J., & Bao, W. (2018). Effects of injection pressure on ignition and combustion characteristics of impinging diesel spray. *Applied Energy*, *226*, 1163-1168. https://doi.org/10.1016/j.apenergy.2018.06.032

Ge, J. C., Wu, G., Yoo, B.-O., & Choi, N. J. (2022). Effect of injection timing on combustion, emission and particle morphology of an old diesel engine fueled with ternary blends at low idling operations. *Energy*, *253*, 124150. https://doi.org/10.1016/j.energy.2022.124150

Gonzalez, D, M. A., Borman, G. L., & Reitz, R. D. (1991). A study of diesel cold starting using both cycle analysis and multidimensional calculations. *SAE International Journal of Engines*, *100*(3), 189-208.

Gunaydin, S. (2022). *The effect of dibutyl maleate addition to diesel fuel on engine performance and emissions*. MSc Thesis, Afyon Kocatepe University.

Gupta, S. K., & Subramanian, K. A. (2022). Analysis of combustion and cycle to cycle variations of an ethanol (E100) fueled spark-ignition engine. *International Journal of Automotive Science And Technology*, *6*(1), 68-74. https://doi.org/10.30939/ijastech..999559

Gurbuz, H., Buran, D., & Akcay, I. H. (2013). An experimental study on performance and cyclic variations in a spark ignition engine fuelled with hydrogen and gasoline. *Journal of Thermal Science and Technology*, *33*(1), 33-41.

Halis, S., Solmaz, H., Polat, S., & Yücesu, H. S. (2022). Numerical Study of the Effects of Lambda and Injection Timing on RCCI Combustion Mode. *International Journal of Automotive Science and Technology*, *6*(2), 120-126. https://doi.org/10.30939/ijastech..1105470

Hao, C., Zhang, Z., Wang, Z., Bai, H., Li, Y., Li, Y., & Lu, Z. (2022). Investigation of spray angle and combustion chamber geometry to improve combustion performance at full load on a heavy-duty diesel engine using genetic algorithm. *Energy Conversion and Management*, *267*, 115862. https://doi.org/10.1016/j.enconman.2022.115862

Heywood, J. B. (2018). *Internal combustion engine fundamentals*. McGraw-Hill Education.

Huang, H., Zhu, Z., Zhu, J., Lv, D., Pan, Y., Wei, H., & Teng, W. (2019). Experimental and numerical study of pre-injection effects on diesel-n-butanol blends combustion. *Applied Energy*, *249*, 377-391. https://doi.org/10.1016/j.apenergy.2019.04.163

Jaichandar, S., Kumar, P. S., & Annamalai, K. (2012). Combined effect of injection timing and combustion chamber geometry on the performance of a biodiesel fueled diesel engine. *Energy*, *47*(1), 388-394. https://doi.org/10.1016/j.energy.2012.09.059

Jha, P. R., Wijeyakulasuriya, S., Krishnan, S. R., & Srinivasan, K. K. (2022). Numerical investigations of low load diesel-methane dual fuel combustion at early diesel injection timings. *Fuel*, *315*, 123077. https://doi.org/10.1016/j.fuel.2021.123077

Jurić, F., Petranović, Z., Vujanović, M., Katrašnik, T., Vihar, R., Wang, X., & Duić, N. (2019). Experimental and numerical investigation of injection timing and rail pressure impact on combustion characteristics of a diesel engine. *Energy Conversion and Management*, *185*, 730-739. https://doi.org/10.1016/j.enconman.2019.02.039

Khan, S., Panua, R., & Bose, P. K. (2018). Combined effects of piston bowl geometry and spray pattern on mixing, combustion and emissions of a diesel engine: A numerical approach. *Fuel*, *225*, 203-217. https://doi.org/10.1016/j.fuel.2018.03.139

Kumar, M., Bhowmik, S., & Paul, A. (2022). Effect of pilot fuel injection pressure and injection timing on combustion, performance and emission of hydrogen-biodiesel dual fuel engine. *International Journal of Hydrogen Energy*, *47*(68), 29554-29567. https://doi.org/10.1016/j.ijhydene.2022.06.260

Lu, Y., Fan, C., Chen, Y., Liu, Y., & Pei, Y. (2023). Effect of injection strategy optimization on PCCI combustion and emissions under engine speed extension in a heavy-duty diesel engine. *Fuel*, *332*, 126053. https://doi.org/10.1016/j.fuel.2022.126053

Mehta, P. S., & Tamma, B. (1998). Effect of swirl and fuel injection characteristics on premixed phase of diesel combustion. International Congress and Exposition, Detroit Michigan, SAE Technical Paper 980534. https://doi.org/10.4271/980534

Mishra, A., Kulshrestha, S., Patel, F. M., Tiwari, N., & Sharma, A. (2023). Effect of piston bowl geometry and spray angle on engine performance and emissions in HCCI engine using multi-stage injection strategy. *Environmental Progress & Sustainable Energy*, e14203. https://doi.org/10.1002/ep.14203

Mohan, B., Yang, W., Tay, K. L., & Yu, W. (2014). Experimental study of spray characteristics of biodiesel derived from waste cooking oil. *Energy Conversion and Management*, *88*, 622-632. https://doi.org/10.1016/j.enconman.2014.09.013

Pham, V. C., Le, V. V., Yeo, S., Choi, J.-H., & Lee, W.-J. (2022). Effects of the Injector Spray Angle on Combustion and Emissions of a 4-Stroke Natural Gas-Diesel DF Marine Engine. *Applied Sciences*, *12*(23), 11886. https://doi.org/10.3390/app122311886

Ranganatha Swamy, L., Chandrashekar, T. K., Banapurmath, N. R., & Nashipudi, P. (2014). Effect of injection timing, combustion chamber shapes and nozzle geometry on the diesel engine performance. *Universal Journal of Petroleum Sciences*, *2*, 74-95.

Schmidt, D. P., & Rutland, C. J. (2000). A new droplet collision algorithm. *Journal of Computational Physics*, *164*(1), 62-80. https://doi.org/10.1006/jcph.2000.6568

Sener, R., Yangaz, M. U., & Gul, M. Z. (2020). Effects of injection strategy and combustion chamber modification on a single-cylinder diesel engine. *Fuel*, *266*, 117122. https://doi.org/10.1016/j.fuel.2020.117122

Sener, R. (2022). Numerical Investigation of Ducted Fuel Injection Strategy for Soot Reduction in Compression Ignition Engine. *Journal of Applied Fluid Mechanics*, *15*(2), 475-489. https://doi.org/10.47176/jafm.15.02.33088

Shu, J., Fu, J., Liu, J., Ma, Y., Wang, S., Deng, B., & Zeng, D. (2019). Effects of injector spray angle on combustion and emissions characteristics of a natural gas (NG)-diesel dual fuel engine based on CFD coupled with reduced chemical kinetic model. *Applied Energy*, *233-234*, 182-195. https://doi.org/10.1016/j.apenergy.2018.10.040

Sanli, A., Yilmaz, I. T., & Gumus, M. (2023). Effects of Thermal Barrier Coated Piston on Performance and Combustion Characteristics in Dual-Fuel Common-Rail Diesel Engine. *International Journal of Automotive Science and Technology*, *7*(2), 141-153. https://doi.org/10.30939/ijastech..1268355

Turns, S. R. (1996). *Introduction to combustion*. New York, NY, USA: McGraw-Hill Companies, 568-569.

Wei, S., Ji, K., Leng, X., Wang, F., & Liu, X. (2014). Numerical simulation on effects of spray angle in a swirl chamber combustion system of DI (direct injection) diesel engines. *Energy*, *75*, 289-294. https://doi.org/10.1016/j.energy.2014.07.076

Yakhot, V., & Orszag, S. A. (1986). Renormalization group analysis of turbulence. I. Basic theory. *Journal of Scientific Computing*, 1(1), 3-51. https://doi.org/10.1007/BF01061452

Yousefi, A., Guo, H., & Birouk, M. (2018). An experimental and numerical study on diesel injection split of a natural gas/diesel dual-fuel engine at a low engine load. *Fuel*, *212*, 332-346. https://doi.org/10.1016/j.fuel.2017.10.053

Boron-Doped Thin Films Fabricated by the Spin Coating Method: The Effect of Doping Concentrations

Abdullah ATILGAN[1,2*] (iD)   Kenan OZEL[3] (iD)

[1] Department of Energy Systems Engineering, Faculty of Engineering and Natural Sciences, Ankara Yıldırım Beyazıt University, Ankara, Türkiye
[2] Central Research Laboratory Application and Research Center, Ankara Yıldırım Beyazıt University, Ankara, Türkiye
[3] Department of Electrical and Energy, GAMA Vocational School, Ankara University, Ankara, Türkiye

Keywords	Abstract
Boron Doped ZnO B Doping Spin Coating Method Thin Film	This work examined the impact of different levels of B-doping on the structural, morphological, optical, and electrical characteristics of ZnO thin films. Boron-doped zinc oxide thin films were deposited on glass substrates using the spin-coating technique. The B concentrations employed were 1, 2, 3, 4, and 5 at. %. The systematic characterizations manifest that the properties of the deposited films were heavily influenced by changing concentrations of B doping. It was found that as the concentration of B-doping increases, the values of grain size decrease. In addition, it was observed that ZnO thin films containing a lower concentration of B dopant exhibited higher transparency. Finally, it was figured out that the resistivity of the films declines dramatically with a higher content of B-doping. The results of our research may initiate further inquiries into the creation of superior thin films.

1. INTRODUCTION

Zinc oxide (ZO) thin films (TFs) have garnered significant attention in recent decades due to their ability to high infrared reflectance, high visible transmittance, a lower price, and a non-toxic nature (Hu & Gordon, 1992). ZO is classified as an n-type semiconductor due to its electronic properties. It owns a band gap (E_g) of around 3.2 eV. ZO-TFs in their pure form exhibit a notable degree of visible light transmittance and possess a high level of resistance. Non-stoichiometric ZO-TFs show the desirable characteristics of high transparency and high conductivity. However, their stability is compromised when exposed to high temperatures. In contrast, doped ZO-TFs exhibit exceptional stability in terms of their electrical and optical characteristics. ZO-TFs that have been doped with different IIIA elements, like indium, aluminum, gallium, and boron (B), have low electrical resistance and let a lot of light through (Hu & Gordon, 1992; Kara et al., 2017; Kayani et al., 2020, Atilgan et al., 2023).

Previous study has indicated that the E_g of ZO-TFs, even with high B concentrations of up to 1.4 at. %, did not undergo major changes (Tahar & Tahar, 2005). The observed impact on the optical E_g property and conductivities of TFs was significant, even at a minimal B concentration of 0.2 at.%. The reported range of conductivities spanned from 250 to 2500 Ω^{-1} cm^{-1} (Hu & Gordon, 1992). Lokhande et al. (2001) utilized the spray pyrolysis method to coat TFs with B dopant ranging from 0 to 1 at.%. They observed a decrease in resistance and an increase in E_g. The researchers documented that the ideal doping concentration for achieving good optical transmittance and low resistance was determined to be 0.8 at.%. In contrast, the introduction of B doping has been seen to enhance the density and mobility of carriers within ZO-TFs, as a result of which

their electrical conductivity has increased. The introduction of B doping into ZO results in an enhancement of its magnetic moment, a characteristic that distinguishes it from the magnetic properties observed in ZO doped with other elements. Nevertheless, the existing body of literature reveals a limited number of studies pertaining to the synthesis of B-doped zinc oxide (B-ZO) TFs. These TFs have predominantly been created using various methods such as electrochemical deposition, atomic layer deposition, chemical vapor deposition, spray pyrolysis, and RF magnetron sputtering (Hu & Gordon, 1992). Conversely, their systems exhibit a high degree of complexity, substantial cost implications, and pose challenges in terms of manageability. Hence, owing to its user-friendly nature and enhanced film quality, sol-gel synthesis, namely sol-gel, spin-coating, and dip-coating, has emerged as a prominent method for the fabrication of B-ZO-TFs. The primary benefits of sol-gel synthesis encompass its simplicity and cost-effectiveness, its facilitation of ZO doping with diverse elements, its independence from complex equipment or hazardous source materials, and its efficacy in efficiently coating ZO-TFs (Lee et al., 2013). The sol-gel technique has numerous benefits, including enhanced homogeneity, purity, cost-effectiveness, the ability to be deposited on vast substrate surfaces, precise compositional control, and simplicity of handling (Kayani et al., 2020). Ozel and Atilgan were investigated the synergistic effect of gallium and boron co-doping on the optical and electrical features of ZO-TFs using spin coating technique. The sample with a B/Ga ratio of 0.5/2.5, while keeping a constant total doping rate of 3 at. %, exhibited superior properties compared to the sample with a B/Ga ratio of 0/3. This improvement can be attributed to the synergistic effect of enhanced conductivity and transparency. (Ozel & Atilgan, 2023a).

As for the comparison of widely utilized deposition techniques, spin-coating and spray-pyrolysis offer cost-effective and uncomplicated alternatives to more expensive equipment and high-energy processes associated with other approaches (Zhussupbekova et al. 2020). Utilizing the spray pyrolysis process in a single container with continuous output is its significant advantage. As spray pyrolysis is performed in the micrometer volume and seconds of all the operations described, deviations are possible in the planned experiments, and nanoparticles synthesized based on this method are often metastable (Majerič & Rudolf, 2020). Nevertheless, the spin-coating technique provides excellent consistency in both macroscopic and nanoscale, and it also frequently eliminates the need for subsequent thermal processing. The spin-coating method possesses qualities that render it very suitable for both research purposes and rapid prototype creation. In addition, it is noteworthy to say that spin coating is the mostly preferred method for depositing the ZO-TF on the various substrates thanks to its simplicity, capacity to produce uniform coating, and ease of setup (Farrag & Balboul, 2017; Kamaruddin et al., 2011; Smirnov et al. 2010). Moreover, the spin coating technique not only provides fast and high-quality film production, but also allows the reproducible preparation of TF coatings over large areas with excellent structural homogeneity (Faisal et al., 2015).

The present study investigates the deposition of B-ZO-TFs by utilizing the spin-coating approach. The study focuses on analyzing the electrical, optical, and structural characteristics of the TFs and subsequently presents a comprehensive discussion of the obtained results. Systematically, the impact of B doping concentration on the characteristics of ZO-TFs has been examined. The findings of the characterization indicate that various concentrations of B doping have a substantial effect on the characteristics of the deposited TFs.

2. MATERIAL AND METHOD

B-ZO-TFs with a range of dopant concentrations were spin-coated onto glass substrates (GSs) using a sol-gel process. The transparent solution, made by employing ZADH (zinc acetate dihydrate, $ZnC_4H_6O_4.2H_2O$; Emsur) as a precursor, trimethyl borate ($C_3H_9BO_3$; Merck) as a dopant, and MAE (monoethanolamine, C_2H_7NO; Emsur) as a stabilizer, was dissolved in ethanol (CH_3OH; Merck). The concentration of ZADH in the ethanol solvent was 0.5 M, and the molar ratio of MEA to ZADH was consistently maintained at a 1:1 molar ratio. The concentration of B dopant ($[n_B/[n_B+n_{Zn}]]$) was determined to be 1%, 2%, 3%, 4%, and 5% atomic percent, respectively. The resultant solution was agitated at a speed of 500 revolutions per minute (rpm) at a temperature of 25 °C for a duration of 2 hours, resulting in the formation of transparent and uniform solutions. The solutions were allowed to mature for 48 hours at room temperature (RT) prior to being utilized as coating solutions. As for the deposition procedure, the prepared solutions were placed on the surface of GSs, and then the substrates were brought up to a spinning speed of 2000 rpm with an acceleration time of 5 s for a spinning duration of 30 s. The coated GSs were preheated at 500 °C for 5 minutes to remove organic compounds. Ten

cycles of this coating and preheating procedure were performed. Finally, the obtained TFs were annealed at 500 °C for 1 hour to get the polycrystalline oxide TFs.

An X-ray diffractometer (XRD; Rigaku Miniflex 600) was performed to investigate the crystal structure of the deposited TFs. Atomic force microscope (AFM; Ambios-Quesant) measurements were used to analyze the surface morphology and roughness. A UV-vis spectrophotometer (Shimadzu 1700) was utilized to characterize the optical transmittance and absorbance properties of the samples. The electrical sheet resistance values of the TFs were found at RT using the four-point probe method and a Keithley 2400 source meter along with a Lucas Labs 302.

3. RESULTS AND DISCUSSION

Figure 1 (a) illustrates the XRD spectra of ZO-TFs with various B concentrations. The observed diffraction peaks are consistent with the specifications for ZO crystal (JCPDS Card No. 36-1451) (Kayani et al., 2020). The spectra indicate that the TFs exhibit a polycrystalline structure, and no impurity peak is detected. In order to investigate the variation of the grain size with varying doping concentrations, the size of the grains along the (002) plane is determined by using the Debye-Scherer equation (1) (Kayani et al., 2020);

$$D = \frac{K\lambda}{\beta cos\theta} \tag{1}$$

where β, λ, and θ stand for the full width of half-maximum (FWHM), the wavelength of X-rays (0.15406 nm), and the Bragg angle, respectively. As the concentration of B doping increases, both the intensity and the FWHM of the (002) peaks exhibit simultaneous changes. Specifically, the intensity of the peaks drops as the FWHM expands. The findings indicate a noticeable drop in both the degree of crystallinity and the diameters of crystalline as the concentration of B doping increases. (Figure 1(b-f) and Table 1). The average crystallite size decreased from 18.8 nm to 14.1 nm due to the increase in B concentration. The decrease seen can be ascribed to the distortion of the ZO lattice subsequent to the injection of B dopants into the ZO material. The observed distortion can be related to the mismatch in ionic radii between B^{3+} (0.23 Å) and Zn^{2+} (0.74 Å). Since the very small ionic radius of additive B in comparison to the Zn ion, it can easily settle in the crystal lattice (Hu & Gordon, 1992). Incorporating B doping into ZO-TFs caused both lattice deformation and the formation of lattice defects and nucleation sites, hence impeding the growth of grains. Heavy doping of B resulted in a reduction in the level of crystallinity and disruption of the crystal symmetry. The findings presented herein exhibit a high level of concordance with the previously reported results. (Jana et al., 2011; Kim et al., 2013).

While the concentration of B in the TFs increases, lattice constants change, and the position of the (002) peaks shift towards the higher angles of the 2θ scale. This suggests that the B-ZO-TFs have higher levels of residual stress than strain-free ZO. Besides, the amount of residual stress in the B-ZO-TFs appears to increase with higher concentrations of B in the TFs. There are therefore interstitial Zn^{2+} ions present along with the B^{3+} ions, which move the (002) peak to a greater angle. This phenomenon can be attributed to the reduction in the distance between adjacent crystal planes. Sun et al. (2020) and Kim et al. (2013) tested lower B concentrations of 0-0.5 at.% and 0-2.5 at.%, respectively. They subsequently argued that the shift in the position of the (002) peaks at a higher angle as the concentration of dopant in the ZO-TFs increases. Contrary to this, in a study that set out to determine dopant concentrations 1, 3, 5, 7, and 9 wt.%, Kayani et al. (2020) found that the presence of a higher concentration of B dopant leads to the position of the (002) peaks shifting towards the lower angles of the 2θ scale. As an overarching finding in this study, which does not contradict the previous reports, the 002 peaks shift to larger angles up to a critical dopant concentration of 3 % and then shift to lower angle values.

Lattice constants are determined using equations (2, 3):

$$a = \frac{\lambda}{\sqrt{3}\sin\theta_{100}} \tag{2}$$

$$c = \frac{\lambda}{\sin \theta_{002}} \qquad (3)$$

where a and c are lattice constants (Kayani et al., 2020). Lattice spacing d is found by applying Bragg's law equation (4):

$$d = \frac{n\lambda}{2\sin \theta} \qquad (4)$$

Table 1. Structural properties of B-ZO-TFs

B Content (at. %)	Lattice constants		Lattice spacing, d_{002} (nm)	D (nm)	Strain ε ($\times 10^3$)	Stress σ (GPa)	δ ($\times 10^3$)
	a (nm)	c (nm)					
1	0.3248	0.5208	0.2604	18.8	-2.11	0.49	2.83
2	0.3246	0.5207	0.2603	17.4	-2.39	0.56	3.30
3	0.3242	0.5205	0.2603	16.1	-2.67	0.62	3.88
4	0.3244	0.5208	0.2604	15.6	-2.11	0.49	4.13
5	0.3244	0.5211	0.2606	14.1	-1.54	0.36	5.06

here n is the order of diffraction and is taken as 1. The presence of dislocation density (δ) signifies the existence of imperfections inside the crystal lattice. The presence of defects and distortions inside a crystalline structure result in an increase in dislocation density, which exhibits an inverse relationship (equation 5) with the size of the crystallite:

$$\delta = D^{-2} \qquad (5)$$

where δ represents the dislocation density (Kayani et al., 2020). Dislocation density refers to the concentration of dislocations inside a specific volume of crystalline materials, and it is observed to grow proportionally with the rise in the concentration of B. This is due to an improvement in defects. Strain (ε) in the TFs along the c-axis can be determined by applying equation (6):

$$\varepsilon = \left[\frac{c_{film} - c_{bulk}}{c_{bulk}} \right] \qquad (6)$$

The unstrained lattice parameter, denoted as c_{bulk}, was figured out for bulk ZO and found to be 0.521939 nm (Kaur et al., 2015). The observed strain in the thin films is a result of the combined influence of thickness and B doping in ZO. The biaxial strain model can be utilized to determine the stress in TFs. The stress present in the film is determined by the utilization of a biaxial strain model (Kaur et al., 2015).

$$\sigma = -232.8 \times \varepsilon \qquad (7)$$

Biaxial stress shows tensile characteristics when the stress sign is positive, whereas it demonstrates compressive properties in the opposite case. The residual stress levels in the ZO-TFs, which were doped with B concentrations of 1, 2, 3, 4, and 5%, were measured to be 0.49, 0.56, 0.62, 0.49, and 0.36 GPa, respectively. To better understand the relationship between temperature and stress, Kumar et al. (2012) conducted a series of experiments. The annealing temperatures employed in this study spanned from 350 to 550 °C, while the doping ratio of B maintained at a constant level of 0.6 at. % for all the TFs. It is worth noting that the stress in B-ZO-TFs has a first compressive character, transitioning to a tensile state when subjected to annealing temperatures over 450 °C. The results align with the stress levels seen in our research. The presence of both intrinsic and extrinsic stresses is an inherent characteristic of ZO. Intrinsic stress is typically attributed to the

presence of defects and impurities within a material, while extrinsic stress mostly arises from factors such as lattice mismatch, doping, thermal mismatch, and growth conditions (Kumar et al., 2012).
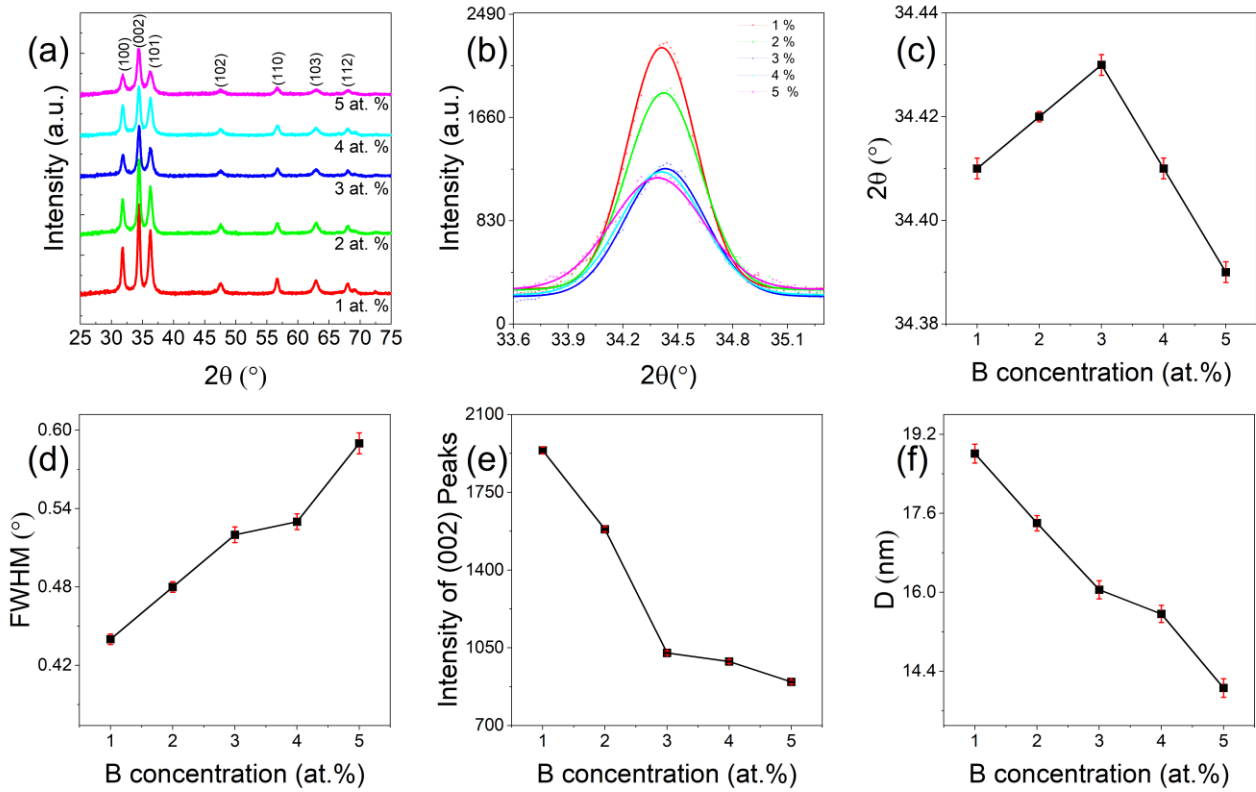
Figure 1. *(a)X-ray diffraction patterns for the ZO-TFs with various B contents, (b) 002 diffraction peak fitted with a Lorentz function, (c) position of 002 peaks (2θ), (d) FWHMs, (e) intensity of 002 peaks (f) crystallite sizes of B-ZO-TFs with 1–5% with error bars representing the standard error*

Figure 2 (a-f) shows how AFM images are used to look at the surface morphology and roughness of the B-ZO-TFs. The surface parameters, i.e., root mean square RMS, surface area, and volume of B-ZO-TFs, have been calculated using Gwyddion software (Nečas & Klapetek, 2012). The values of skewness and kurtosis for 1, 2, 3, 4, and 5% are 0.47 and 0.24, 0.35 and 0.20, 0.37 and 0.13, 0.49 and 0.27, 0.69 and 0.79, respectively, and point out that the surfaces have more high peaks and fewer valleys and surfaces. As evaluated from AFM results, RMS values are examined to be 80.9, 67.4, 99.7, 72.3, and 33.9 nm for the B-ZO-TFs having a B content of 1%, 2%, 3%, 4%, and 5%, respectively. Values of RMS and volume of TFs showed a similar trend. TF with 1% doping had the highest surface area improvement, and the highest roughness was observed in TF with 3% doping. The complete set of obtained results is presented in Table 2.

The absorbance, absorption coefficient, and transmittance characteristics of B-ZO-TFs are illustrated in Fig. 3 (a–c). As seen in Figure 3 (a), the absorbance profiles of the samples exhibit a sharp absorption edge at around 380 nm, indicating that these TFs might be used in UV photodetector applications (Ozel & Yildiz, 2021). Note that the absorbance profiles of the TFs are substantially affected by the doping process. Specifically, the B-ZO film with a B doping concentration of 3% shows enhanced absorption characteristics through the solar spectrum. Based on this result, one can expect that the photovoltaic cells fabricated with B-ZO TFs with a B content of 3% have better power conversion efficiency than others due to their high absorption ability of incoming light. As for the transmittance spectra of the TFs, the average transmittance values of the TFs are estimated between 400 and 800 nm wavelength and listed in Table 2. Moreover, the transmittance values at 550 nm, which correspond to the maximum intensity value of the solar spectrum at sea level (Ozel et al., 2023), are determined and given in Table 2. The highest transmittance values among the films are obtained 85.3%, 83.6% for 2% and 1%, respectively. The values of the optical E_g for the deposited TFs are evaluated by

calculating the absorption coefficient (α), which is obtained from transmittance data. It can be determined by the equation (8);

$$\alpha = \frac{\ln T^{-1}}{t} \qquad (8)$$

where t and T denote the thickness and transmittance of the TFs, respectively (Tahar & Tahar, 2005). In the direct band gap semiconductor, the relationship between α and E_g can be estimated by using the relation (9) (Hu & Gordon, 1992);

$$(\alpha h\nu)^2 = A(h\nu - E_g) \qquad (9)$$

where hν and A refer to the photon energy and the band edge constant, respectively. Figure 3(d) presents the plots of $(\alpha h\nu)^2$ versus hν for the obtained B-ZO-TFs. The linear nature of the plots suggests the presence of a direct transition. The E_g values of the TFs can be acquired from extrapolation of the linear portions to αhν=0 in the plots $(\alpha h\nu)^2$ versus hν. Thin-film band-gap values are 3.27 eV, 3.26 eV, 3.23 eV, 3.24 eV, and 3.26 eV, which correspond to 1, 2, 3, 4, and 5%, respectively. From the estimated values, it can be deduced that the E_g values of the B-ZO-TFs are lower than the pristine ZO-TFs (Tan et al., 2005). The obtained values are summarized in Table 2. According to the acquired values of E_g, one can notice that the values of E_g get reduced to some extent with the increase of B content from 1 to 3%. On the other hand, the values of E_g get widen by further B dopants. These slight changes might be related to the formation of localized states and carrier concentration (Kara et al., 2017; Sbeta et al., 2018). Kumar et al. (2012) reported that the Eg of B-ZO-TFs decreased with an increase in annealing temperature and had a strong dependence on the stress of TFs. Our results are in agreement with the E_g and stress values obtained from similar annealing temperatures (Kumar et al., 2012). With increasing stress, E_g narrows, and when stress begins to decrease, E_g begins to expand, although it is still in the positive region. The Swanepoel method was used to determine the thicknesses of the B-ZO-TFs thin film. The approach showed B-ZO-TFs have thicknesses of 881±5.2 nm. The results of Swanepoel, an optical method, were confirmed by Hacini et al. by comparing them with measured values for cross sectional SEM results. The results of both are quite similar, proving the validity of the optical method (Hacini et al., 2021).

Four-point probe I-V curves and the plot of the values of resistivity (ρ) of B-ZO-TFs as a function of B content are depicted in Figure 4(a, b). To calculate the ρ values of the TFs, the sheet resistance (R_{sh}) values are first determined using the following formula (10) (Atilgan et al., 2021);

$$R_{sh} = \frac{\pi}{ln(2)}\left(\frac{V}{I}\right) \qquad (10)$$

where $\pi/ln2$ is the geometric correction factor. V and I refer to the values of measured voltage and current, respectively. By calculating R_{sh}, the ρ values of the TFs are determined by $\rho = R_{sh}t$. Note that the obtained values of ρ are consistent with the literature (Senol et al., 2015). According to our findings, one can figure out that the values of ρ decrease to moderate levels with increasing B content. B is a dopant of the n-type that can either replace zinc atoms or occupy interstitial positions within the crystal lattice. This substitution or interstitial incorporation of boron atoms leads to an increase in the density of free electrons inside the TFs. Consequently, this phenomenon leads to an elevation in the concentration of free carriers, resulting in a reduction in resistivity (Lokhande et al., 2021). At doping concentrations from 1 to 3%, the resistance decreased sharply, but at doping concentrations above 3%, the resistance value remained almost constant. There are two possible explanations for this phenomenon. Firstly, at high-levels of doping, the impact of grain boundary scattering is rather insignificant compared to the scattering mechanisms that occur within the grains themselves. Alternatively, this behavior might be attributed to the limitations imposed by the solubility of B dopant elements in the lattice of ZO as a host material (Steinhauser et al., 2007; Kim et al., 2013; Pawar et al., 2005).
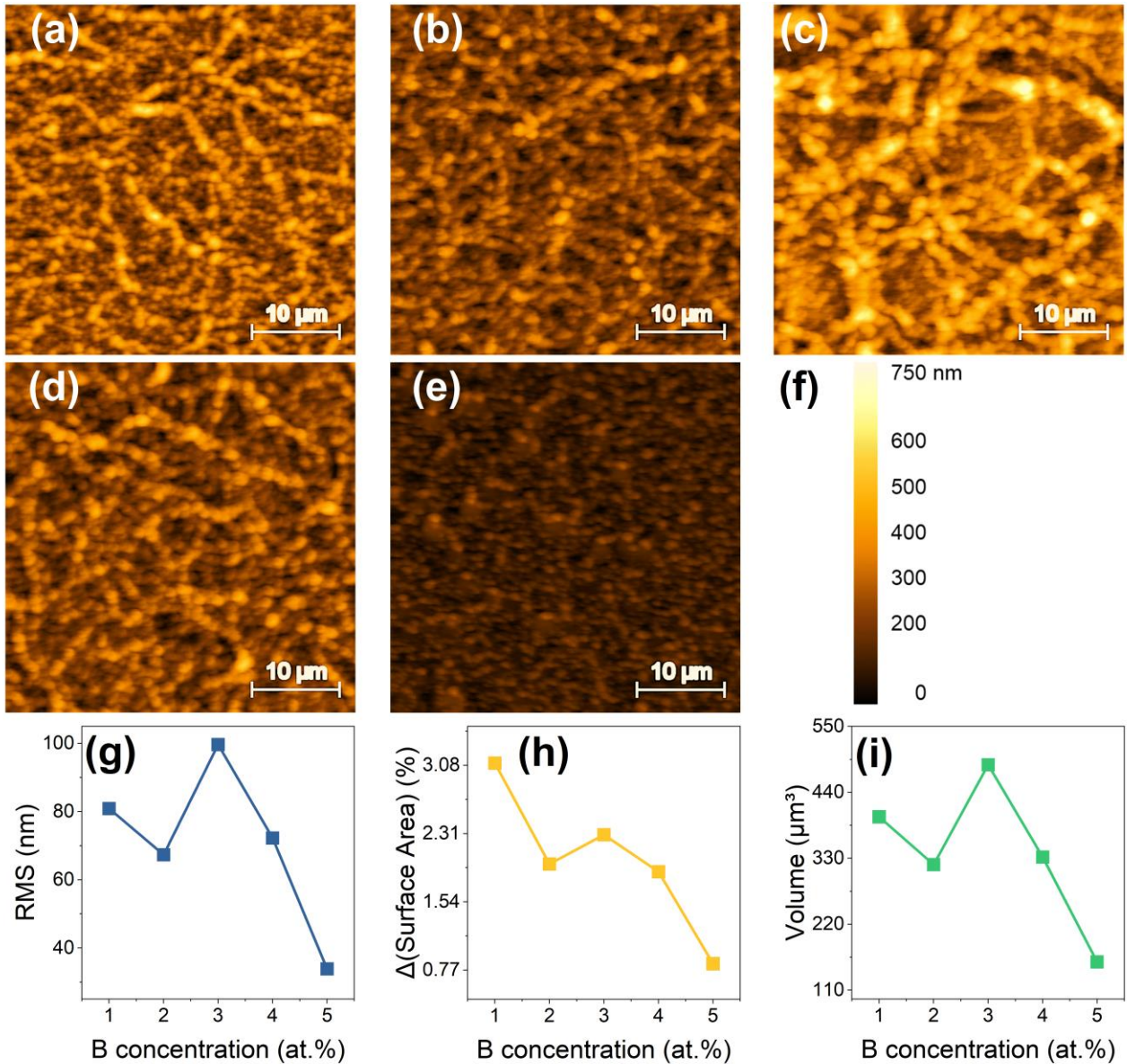
Figure 2. *2D AFM images of the B-ZO-TFs with different various concentration of B (a) 1, (b) 2, (c) 3, (d) 4, (e) 5, (f) The color code shows the scale bar for the height in the image, (g) RMS values, (h) surface areas improvement (i) volume of B-ZO-TFs*

Ultimately, our findings reveal that the characteristics of the sol-gel-derived ZO-TFs can be altered by varying the levels of B doping. Based on the acquired findings, it can be posited that optical characteristics exhibit favorable attributes at lower levels of doping, while electrical qualities demonstrate enhanced performance at higher levels of doping.

Table 2. *Structural and optical characteristics of the B-ZO-TFs for various B contents*

B Content (at. %)	RMS (nm)	T_{av} (%) (400-800nm)	T (%) @550nm	E_g (eV)
1 %	80.9	83.9 ±7.08	83.6	3.27±0.001
2 %	67.4	83.4±5.69	85.3	3.26±0.001
3 %	99.7	62.0±9.94	61.5	3.23±0.006
4 %	72.3	69.3±8.84	70.4	3.24±0.003
5 %	33.9	72.7±9.69	75.0	3.26±0.002
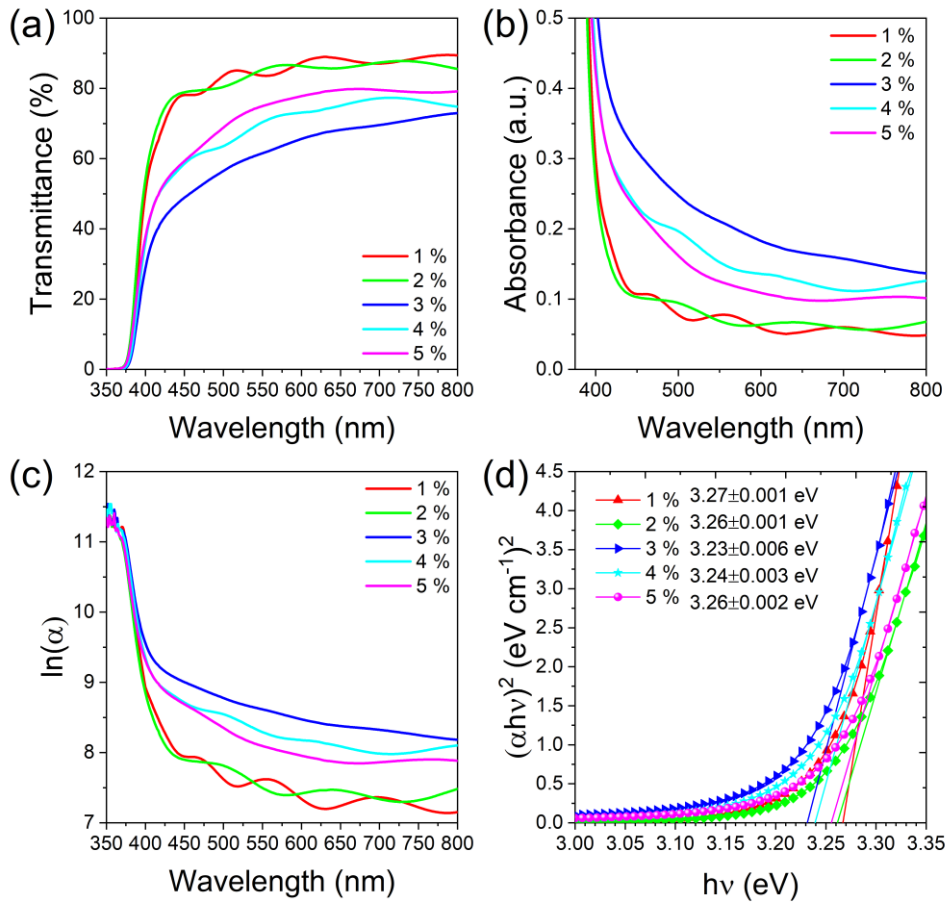
Figure 3. *(a) transmittance and (b) absorbance characteristics of B-ZO-TFs fabricated with different doping concentrations. (c) ln(α) versus wavelength for various B content (d) The plots of (αhν)² versus photon energy (hν) for TFs doped with 1-5% B content. Band gap values were calculated using linear regression, which aims to find a linear relationship to describe the correlation between a dependent variable. The E_g values are given as the average of the intercept constant ± standard error of the intercept*
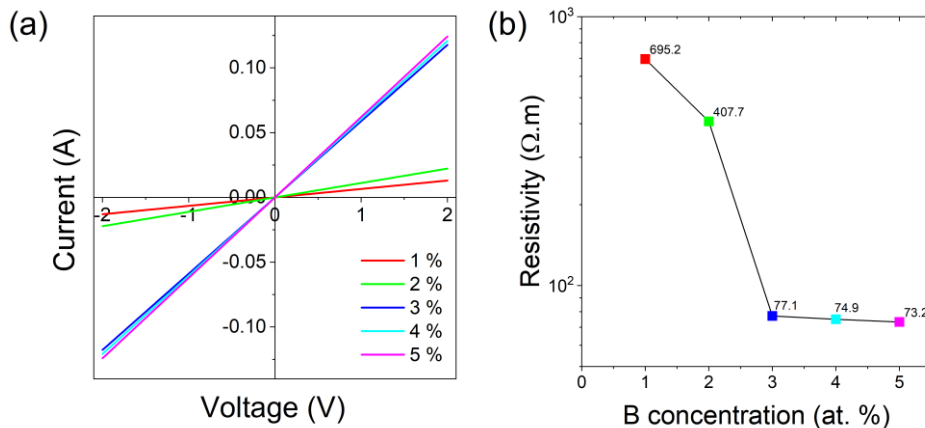
Figure 4. *(a) Four-point probe I-V curves showing sheet resistance and (b) plots of the values of resistivity of B-ZO-TFs as a function of B content*

4. CONCLUSION

In summary, B-doped ZO-TFs were successfully deposited on GSs by using the spin coating method. We investigated the structural, morphological, optical, and electrical properties of B-doped ZO films, focusing on

the effect of varying the B content. The findings revealed that various B-doping concentrations significantly affected the characteristics of deposited films:

- The values of grain size decrease with an increase in B-doping concentration.
- The surface roughness of the TFs has a trend of fluctuation with the increase in doping concentration of B. While the highest surface roughness was observed in the film with 3% doping, the highest surface area was observed in the film with 1% doping.
- The ZO-TFs containing a lower concentration of B dopant exhibit high transparency above 80%. In addition to this, the best absorption capability was obtained at 3% B-ZO-TFs.
- The 3% B doping rate is the saddle point for E_g, σ, T%, and resistivity values. Up to 3%: While R, E_g, and T tend to decrease, after the saddle point, R remains almost constant and E_g and T tend to increase, respectively. Stress values increase up to the saddle point and then suddenly decrease.

Eventually, it was figured out that the resistivity of the films exhibits a substantial decrease as the B-doping concentration raises. The results of our study have the potential to stimulate further research in the field of thin film development for the purpose of creating advanced optoelectronic devices. The saddle point of doping concentration to gain the best optical and electrical properties is changing depending on the crystalline sizes and stress values of TFs. In other words, the optimal B doping concentration for ZO-TFs may depend on the annealing temperature. Future studies should explore the effects of various annealing temperatures versus doping concentrations with narrow steps.

ACKNOWLEDGEMENT

AUTHOR CONTRIBUTIONS

A.A. and K.O. contributed to the design and implementation of the research, to the analysis of the results and to the writing of the manuscript. All authors have read and legally accepted the final version of the article published in the journal.

CONFLICT OF INTEREST

The authors declare no conflict of interest.

REFERENCES

Atilgan, A., Ozel, K., Sbeta, M., & Yildiz, A. (2023). Engineering the visible light absorption of one-dimensional photonic crystals based on multilayers of Al-doped ZnO (AZO) thin films. Materials Science in Semiconductor Processing, 166, 107747. https://doi.org/10.1016/j.mssp.2023.107747

Atilgan, A., Kurtulus, A. Y., Oktem, M. F., & Yildiz, A. (2021). W-doped ZnO transparent conducting nanostructures synthesized by hydrothermal method. *Journal of Materials Science: Materials in Electronics*, *32*(14), 19126-19135. https://doi.org/10.1007/s10854-021-06432-1

Faisal, M., Bouzid, H., Harraz, F. A., Ismail, A. A., Al-Sayari, S. A., & Al-Assiri, M. S. (2015). Mesoporous Ag/ZnO multilayer films prepared by repeated spin-coating for enhancing its photonic efficiencies. *Surface and Coatings Technology*, 263, 44-53. https://doi.org/10.1016/j.surfcoat.2014.12.063

Farrag, A. A. G., & Balboul, M. R. (2017). Nano ZnO thin films synthesis by sol–gel spin coating method as a transparent layer for solar cell applications. *Journal of Sol-Gel Science and Technology*, 82, 269-279. https://doi.org/10.1007/s10971-016-4277-8

Hacini, A., Ali, A. H., & Adnan, N. N. (2021). Optimization of ITO thin film properties as a function of deposition time using the swanepoel method. Optical Materials, 120, 111411. https://doi.org/10.1016/j.optmat.2021.111411

Hu, J., & Gordon, R. G. (1992). Deposition of boron doped zinc oxide films and their electrical and optical properties. Journal of The Electrochemical Society, 139(7), 2014. https://doi.org/10.1149/1.2221166

Jana, S., Vuk, A. S., Mallick, A., Orel, B., & Biswas, P. K. (2011). Effect of boron doping on optical properties of sol–gel based nanostructured zinc oxide films on glass. Materials Research Bulletin, 46(12), 2392-2397. https://doi.org/10.1016/j.materresbull.2011.08.038

Kamaruddin, S. A., Chan, K. Y., Yow, H. K., Zainizan Sahdan, M., Saim, H., & Knipp, D. (2011). Zinc oxide films prepared by sol–gel spin coating technique. *Applied Physics A*, 104, 263-268. https://doi.org/10.1007/s00339-010-6121-2

Kara, I., Atilgan, A., Serin, T., & Yildiz, A. (2017). Effects of Co and Cu dopants on the structural, optical, and electrical properties of ZnO nanocrystals. Journal of Materials Science: Materials in Electronics, 28, 6088-6092. https://doi.org/10.1007/s10854-016-6285-4

Kaur, G., Mitra, A., & Yadav, K. L. (2015). Pulsed laser deposited Al-doped ZnO thin films for optical applications. Progress in Natural Science: Materials International, 25(1), 12-21. https://doi.org/10.1016/j.pnsc.2015.01.012

Kayani, Z. N., Bashir, Z., Riaz, S., Naseem, S., & Saddiqe, Z. (2020). Transparent boron-doped zinc oxide films for antibacterial and magnetic applications. Journal of Materials Science: Materials in Electronics, 31, 11911-11926. https://doi.org/10.1007/s10854-020-03745-5

Kim, S., Park, H., Nam, G., Yoon, H., & Leem, J. Y. (2013). Improved optical and electrical properties of sol–gel-derived boron-doped zinc oxide thin films. Journal of sol-gel science and technology, 67, 580-591. https://doi.org/10.1007/s10971-013-3117-3

Kumar, V., Singh, R. G., Singh, F., & Purohit, L. P. (2012). Highly transparent and conducting boron doped zinc oxide films for window of Dye Sensitized Solar Cell applications. Journal of alloys and compounds, 544, 120-124. https://doi.org/10.1016/j.jallcom.2012.07.124

Lee, S. H., Kim, M., Jung, Y., Jung, J. H., Kim, S., Leem, J. Y., & Kim, H. (2013). Enhanced optical and electrical properties of boron-doped zinc-oxide thin films prepared by using the sol-gel dip-coating method. *Journal of the Korean Physical Society*, *63*, 1804-1808. https://doi.org/10.3938/jkps.63.1804

Lokhande, B. J., Patil, P. S., & Uplane, M. D. (2001). Studies on structural, optical and electrical properties of boron doped zinc oxide films prepared by spray pyrolysis technique. Physica B: Condensed Matter, 302, 59-63. https://doi.org/10.1016/S0921-4526(01)00405-7

Majerič, P., & Rudolf, R. (2020). Advances in ultrasonic spray pyrolysis processing of noble metal nanoparticles. Materials, 13(16), 3485. https://doi.org/10.3390/ma13163485

Nečas, D., & Klapetek, P. (2012). Gwyddion: an open-source software for SPM data analysis. Open Physics, 10(1), 181-188. https://doi.org/10.2478/s11534-011-0096-2

Ozel, K., & Atilgan, A. (2023a). Systematic Investigation on the Synergistic Impact of Gallium (Ga)-Boron (B) Co-Doping on the Features of ZnO Films. Gazi University Journal of Science Part A: Engineering and Innovation, 10(4), 442-451. https://doi.org/10.54287/gujsa.1358177

Ozel, K., Atilgan, A., & Yildiz, A. (2023b). Multi-layered blocking layers for dye sensitized solar cells. Journal of Photochemistry and Photobiology A: Chemistry, 115297. https://doi.org/10.1016/j.jphotochem.2023.115297

Ozel, K., & Yildiz, A. (2021). High-detectivity ultraviolet-B photodetector based on SnO2 thin film/Si 30 heterojunction. *Semiconductor Science and Technology*, 36(9), 095001. https://doi.org/10.1088/1361-6641/ac1051

Pawar, B. N., Jadkar, S. R., & Takwale, M. G. (2005). Deposition and characterization of transparent and conductive sprayed ZnO: B thin films. Journal of Physics and Chemistry of Solids, 66(10), 1779-1782. https://doi.org/10.1016/j.jpcs.2005.08.086

Sbeta, M., Atilgan, A., Atli, A., & Yildiz, A. (2018). Influence of the spin acceleration time on the properties of ZnO: Ga thin films deposited by sol–gel method. Journal of Sol-Gel Science and Technology, 86, 513-520. https://doi.org/10.1007/s10971-018-4652-8

Senol, S. D., Ozturk, O., & Terzioğlu, C. (2015). Effect of boron doping on the structural, optical and electrical properties of ZnO nanoparticles produced by the hydrothermal method. Ceramics International, 41(9), 11194-11201. https://doi.org/10.1016/j.ceramint.2015.05.069

Smirnov, M., Baban, C., & Rusu, G. I. (2010). Structural and optical characteristics of spin-coated ZnO thin films. *Applied Surface Science*, 256(8), 2405-2408. https://doi.org/10.1016/j.apsusc.2009.10.075

Steinhauser, J., Fay, S., Oliveira, N., Vallat-Sauvain, E., & Ballif, C. (2007). Transition between grain boundary and intragrain scattering transport mechanisms in boron-doped zinc oxide thin films. Applied Physics Letters, 90(14). https://doi.org/10.1063/1.2719158

Sun, Y. T. A., Pan, P. C., Koo, H. S., & Lin, N. Y. (2020). Growth of low resistivity and high transparency boron-doped zinc oxide film by pulse laser deposition. Precision Engineering, 66, 605-610. https://doi.org/10.1016/j.precisioneng.2020.08.001

Tahar, R. B. H., & Tahar, N. B. H. (2005). Boron-doped zinc oxide thin films prepared by sol-gel technique. Journal of materials science, 40, 5285-5289. doi:10.1007/s10853-005-0522-1

Tan, S. T., Chen, B. J., Sun, X. W., Fan, W. J., Kwok, H. S., Zhang, X. H., & Chua, S. J. (2005). Blueshift of optical band gap in ZnO thin films grown by metal-organic chemical-vapor deposition. Journal of Applied Physics, 98(1). https://doi.org/10.1063/1.1940137

Zhussupbekova, A., Caffrey, D., Zhussupbekov, K., Smith, C. M., Shvets, I. V., & Fleischer, K. (2020). Low-cost, high-performance spray pyrolysis-grown amorphous zinc tin oxide: the challenge of a complex growth process. *ACS Applied Materials & Interfaces*, 12(41), 46892-46899. 3. https://doi.org/10.1021/acsami.0c12148

A Comparative Study for Privacy-Aware Recommendation Systems

Yavuz CANBAY[1*]   Anıl UTKU[2]

[1] Department of Computer Engineering, Faculty of Engineering and Architecture, Sutcu Imam University, Kahramanmaraş, Türkiye
[2] Department of Computer Engineering, Faculty of Engineering, Munzur University, Tunceli, Türkiye

Keywords	Abstract
Recommender System Privacy Protection Differential Privacy	Recommendation systems are sophisticated processes for information filtering designed to offer users tailored recommendations based on their preferences and interests. Users need help to choose between options as the amount of information on the web grows. As a result, it is critical to deliver personalized recommendations to consumers to promote user loyalty and satisfaction. Because recommender systems use sensitive user information such as ratings, comments, likes, and dislikes, this information can be leaked if no privacy measures are taken. As a result, we presented a comparison of privacy-aware recommendation systems in this paper. Two experiments are carried out. In the first experiment, we examined collaborative filtering algorithms on perturbed ratings and then compared hybrid, collaborative, and content-based algorithms on perturbed ratings in the second experiment. According to the results, the Singular Value Decomposition++ (SVDpp) algorithm presented the lowest Root Mean Square Error (RMSE) and Mean Absolute Error (MAE) values for epsilon 100, with 0.8889 and 0.6822, respectively. Furthermore, for epsilon 100, the hybrid filtering technique had the lowest RMSE and MAE rates of 0.90664 and 0.69813, respectively.

1. INTRODUCTION

The amount of online data generated nowadays is rising as a result of technical advancements and increased internet usage. Feedback from users, including ratings, comments, likes, and dislikes, generates many data. (Yu et al., 2019). By analyzing data gathered from various users and sources, recommender systems seek to provide users with recommendations for relevant and engaging content (Kunaver & Požrl, 2017). By selecting items that may be helpful for users from vast volumes of data, the algorithms used in these systems seek to offer the most beneficial items to the user. Recommender systems identify patterns in the dataset based on the user's choices and interests after learning about the user's interests (Cai et al., 2018).

The utilization of recommendation systems by e-commerce platforms and social media applications has become increasingly prevalent, resulting in the provision of diverse recommendations to their customers. These recommendations facilitate consumers to obtain valuable recommendations from the information stack, hence providing benefits to companies in terms of sales strategies. One further advantage of recommendation systems is that they enhance customer satisfaction and promote client loyalty (Mehrotra et al., 2018). Recommendation systems also facilitate the presentation of products that may not be prominently shown but are potentially of interest to users.

Besides the advantages of recommender systems, user privacy is an important issue to be considered. Recommender systems utilize digital data, which commonly include personal information such as search

queries, purchase records, preferences, ratings, comments, etc. Nevertheless, the divulgence of this type of information may result in negative consequences for the individuals who own the data. In 2016, the European Parliament and Council established the General Data Protection Regulation (GDPR) to regulate data privacy. GDPR establishes criteria pertaining to the acquisition and processing of private user information, resulting in a fundamental transformation of data processing practices across several sectors. Therefore, ensuring compliance with the GDPR is a significant concern for those responsible for managing data. In the realm of recommender systems, it is crucial to employ privacy protection mechanisms to protect users' privacy (Hu et al., 2021).

Therefore, this study applies a privacy-aware methodology and proposes a recommender system that prioritizes privacy. Furthermore, it does a comparative analysis of the performance of recommender systems using data that has been perturbed. The present paper has been organized in the following manner. The introduction of recommender systems is given in Section II. Section III provides a comprehensive literature review. Differential privacy is presented in Section IV. Experimental studies are conducted in Section V, and the paper is concluded in Section VI.

2. RECOMMENDER SYSTEMS

Recommender system can be characterized as an application that endeavors to forecast consumer preferences. The field of recommender systems has witnessed significant growth in research due to its advantages to content creators and users (Milano et al., 2020). These systems facilitate the expeditious acquisition of desired products by providing personalized recommendations to consumers (Guo et al., 2017). For professionals engaged in content production, it is of the most significant importance as it enhances user engagement, raises user traffic and facilitates the development of sales tactics.

Recommender systems mostly employ collaborative, content-based and hybrid filtering techniques. Collaborative filtering approach operates under the assumption that individuals who exhibit similar behavioral patterns would possess comparable preferences in subsequent instances (Cunha et al., 2018). The process primarily involves collecting data pertaining to users' behaviors and preferences, followed by analyzing this data to ascertain the degree of similarity amongst users. This type of filtering mainly utilizes user similarities as a basis for generating recommendations without relying on product content. This filtering approach can be implemented using two distinct approaches, namely user-based and item-based methodologies. User-based collaborative filtering is a system that creates recommendations by identifying similarities between users (Kawasaki & Hasuike, 2017). The process of item-based collaborative filtering involves generating recommendations by identifying and analyzing similarities between items. Given the resemblance between the things with which the user engages, the objective is to provide the other item as a recommendation to other users in the event that one of the two adjacent items is engaged (Garanayak et al., 2019). The process of collaborative filtering involves the calculation of similarities between user profiles to generate recommendations. Utilizing cosine similarity and pearson correlation coefficient is prevalent in determining similarities among users. Content-based filtering relies on analyzing the descriptions of items and the content of items that consumers engage with them. Keywords are employed in content-based filtering to describe the items (Javed et al., 2021). Finally, hybrid recommendation systems combine the utilization of collaborative filtering and content-based filtering techniques. Hybrid approaches are utilized to optimize performance while mitigating the drawbacks associated with their constituent methods (Geetha et al., 2018).

SVD is a matrix factorization method commonly used in collaborative filtering. It aims to reduce the dimensionality of a dataset by transforming a space of size N into a lower-dimensional space of size K. Within the context of recommender systems, a matrix is commonly employed to describe the relationship between users and items. In this matrix, users and items are represented by rows and columns, respectively. Each element of this matrix corresponds to the ratings that users provide to the respective items (Zhao et al., 2019). SVD++ incorporates an additional factor vector into the SVD method for each item. These item-specific factor vectors are utilized to characterize the features of items, irrespective of whether they have been assessed by users (Xian et al., 2017). The kNNwithZScore algorithm is a collaborative filtering approach incorporating z-score normalization for each user (Sütçü et al., 2021). In the co-clustering algorithm, clusters and co-clusters

are assigned to users and items, respectively. The assignment of clusters is accomplished by the utilization of an optimization technique, specifically the k-means algorithm.

3. LITERATURE REVIEW

This section provides a summary of previous researches considering privacy-aware recommender systems.

In their study, Xiong et al. (2020) introduced a framework for a private recommender system that operates on a client-server architecture. This study operates under the assumption that the server side is untrusted and each client uses a differential privacy technique to generate randomized ratings. A novel methodology was devised to represent user ratings using symbolic representations. The server-side algorithm utilizes these symbols to implement a collaborative filtering technique in order to make predictions about user ratings. The researchers utilized the Netflix and MovieLens datasets in conjunction with the exponential mechanism to ensure differential privacy. The algorithm proposed by the researchers offers a suitable methodology for both user-based and item-based approaches. Ultimately, they achieved low error rates, as measured by MAE.

The authors Neera et al. (2021) emphasized the utilization of a local perturbation model with differential privacy, wherein user ratings are randomized at the user's side before being transmitted to the service provider. However, a decrease in accuracy is observed when perturbation is employed. To address this issue, the researchers put out a Matrix Factorization approach based on Local Differential Privacy and incorporated a Gaussian Mixture Model. The researchers employed MovieLens, Jester, and Libimseti datasets in their experimental analysis, thereafter conducting a comparative evaluation of their algorithm against two previously established algorithms documented in the literature. Finally, they achieved superior outcomes compared to their counterparts.

Zhang et al. (2019) proposed a novel probabilistic matrix factorization approach with privacy considerations for recommender systems. To fulfill the consumers' privacy needs, a modified sampling process incorporating differential privacy was used. The researchers conducted a comparative analysis of matrix factorization schemes, examining their performance under both personalized differential privacy and traditional differential privacy frameworks. The researchers employed three distinct datasets, namely MovieLens 100k, MovieLens 1M, and the Netflix datasets. The authors conducted a comparative analysis between the proposed method and current approaches. In the end, the experimental results demonstrated that the proposed method presented superior performance compared to the current approaches.

The paper presented by Selvaraj & Gangadharan (2021) proposed a novel hybrid recommender system that incorporates deep learning techniques while ensuring privacy preservation. Differential privacy was utilized to ensure users' privacy, and a deep neural network was utilized for recommendation. The MovieLens 100k, Film trust, and Book-crossing datasets were utilized in the study, and experiments were undertaken for various epsilon values. Based on the experimental results, their approach demonstrated superior performance in terms of RMSE and MAE metrics compared to alternative approaches.

Liu et al. (2019) utilized autoencoders and differential privacy techniques to develop a recommender system that ensures user privacy. The technique of gradient perturbation is employed to obscure the underlying method, while the performance of the declared approach is evaluated using the MovieLens 100k and MovieLens 1M datasets. The measurement of error rates in this study was conducted using the RMSE metric. The experimental findings consistently demonstrated that the proposed method yielded superior outcomes compared to alternative approaches.

In their study Badsha et al. (2017), introduced a novel recommender system that incorporates collaborative filtering techniques while also ensuring privacy preservation. The utilization of homomorphic encryption was implemented to encrypt the ratings of users, hence enabling the provision of recommendations within an encrypted domain. The GroupLens dataset is utilized for conducting experiments, wherein the performance comparison is made according to computational and communication costs.

Yin et al. (2020) have proposed a novel privacy-preserving collaborative filtering approach for recommender systems. The MovieLens dataset is utilized for conducting experiments, and the RMSE metric is employed for

evaluating performance. To ensure data privacy, the original dataset is subjected to the DiffGen algorithm, which is based on differential privacy principles. The researchers enhanced the traditional collaborative filtering algorithm and conducted a comparative analysis with the traditional approach. As a result, experimental results have demonstrated that the enhanced algorithm yields better outcomes than traditional methods.

The improved collaborative filtering recommendation system that takes into account differential privacy was introduced by Wang & Wang (2020). Differential privacy was employed as a means to ensure privacy in the process of matrix factorization. The suggested method is tested using the MovieLens 100k and Netflix datasets, and the performance evaluation is conducted using the RMSE metric. The researchers conducted a comparative analysis of the proposed approach and other established methods, including user-based k-nearest neighbor (kNN), item-based kNN, SVD++, and alternating least squares. Based on the study results, their approach showed better results than other methods.

The current literature presents clear evidence that matrix factorization, autoencoders, deep neural networks, kNN, and SVD++ are among the techniques commonly employed for recommendation systems. The datasets commonly employed in experimental studies are MovieLens, Netflix, GroupLens, and Libimseti. The error metrics utilized for performance evaluations include RMSE and MAE. In contrast to the existing works, this study is the first use of differential privacy in both hybrid and collaborative recommendation systems and presenting a comprehensive comparison.

4. DIFFERENTIAL PRIVACY

The concept of privacy can be described as "the right to be let alone" according to Warren and Brendis (1890), and as "the selective control of access to the self" as proposed by Altman (1976). In time, privacy has been classified into various categories (Banisar & Davies, 1999);

- Information privacy; refers to the set of regulations and guidelines that govern collecting, processing, and managing individuals' personal data,

- Bodily privacy; refers to the regulations of protecting individuals' physical well-being from harmful or unwelcome actions,

- Communication privacy; describes the act of ensuring the privacy of many forms of communication, including but not limited to email and telephone conversations,

- Territorial privacy; means the regulations that establish the boundaries of permissible intrusion into the household and other physical spaces.

The protection of information privacy or data privacy is of utmost importance in an individual's life, as personal data has the ability to directly or indirectly identify a person. Furthermore, it is worth noting that data, particularly raw data, serves as the fundamental source for digital world. Therefore, researchers are currently placing significant emphasis on the topic of information privacy or data privacy.

Within the existing body of literature, other privacy protection methods have been established, including k-anonymity (Sweeney, 2002), l-diversity (Machanavajjhala et al., 2006), t-closeness (Li et al., 2007) and δ-presence (Nergiz et al., 2007). In addition, Dwork (2006) suggested the concept of differential privacy as a potential solution to the issue of background attacks, which all aforementioned protection models suffer. This technique facilitates the execution of privacy-preserving procedures on raw datasets. The assurance is that the outcome of any query performed on a dataset will remain consistent, regardless of whether a record is included in the dataset or not. This implies that the addition or removal of any record will have no impact on the result of any query. Therefore, this scenario allows for the mitigation of background information attacks.

Definition: a mechanism M is said to satisfy ε-differential privacy if, for any neighboring databases D and D', and for any subset S of all potential outputs;

$$Pr[M(D) \in S] \leq \exp(\varepsilon) * Pr[M(D') \in S] \tag{1}$$

The sensitivity of a query on a dataset is an essential property. Sensitivity refers to the extent to which the outcome of a query is influenced by the presence or absence of a particular record.

Definition: the sensitivity of a query can be described as in Equation 2;

$$\Delta f = \max_{DD\prime} \|f(D) - f(D')\| \tag{2}$$

Definition: the given mechanism *M* satisfies e-differential privacy for a function *f*;

$$M(D) = f(D) + Laplace(\frac{\Delta f}{e}) \tag{3}$$

Within the existing body of literature, there are five distinct techniques that encompass the provision of a guarantee of differential privacy (Mirshghallah et al., 2020);

- Input perturbation; involves the addition of noise to the raw dataset.

- Gradient perturbation; refers the addition of noise to gradients as a means of perturbation.

- Objective perturbation; involves the injection of noise into the results of the objective function of an optimization problem.

- Label perturbation; the integration of noise into the voting mechanism that decides the assignment of labels

- Output perturbation; the outputs of a function running on a database are made noisy.

In this research, the method of input perturbation was selected as the preferred technique. The main reasons are outlined below:

- Among these perturbation techniques, only the input perturbation recognizes the presence of untrusted third parties,

- Additionally, it facilitates the sharing of sensitive data while maintaining privacy.

Differential privacy can be classified into two categories, namely global and local, as stated in reference (Arachchige et al., 2019). In the context of global differential privacy, a curator deemed trustworthy is responsible for data collection. Subsequently, this curator generates noisy responses to queries posed by untrusted third parties. In the context of local differential privacy, data perturbation occurs at the data owner's side, after which the perturbed data is shared with untrusted third parties or servers. Figure 1 illustrates the operational mechanisms of global and local differential privacy.

The proliferation of digital platforms and smart televisions has facilitated the consumption of movies and films by viewers, who can then express their preferences through voting mechanisms. Therefore, this scenario enables platform businesses to gather data through the utilization of local perturbation, similar to the approach employed by Apple in reference (Differential Privacy). The utilization of local differential privacy was motivated by the observation made in (Fukuchi et al. 2017) that input perturbation adheres to the principles of local differential privacy. Consequently, local differential privacy was also employed in this study.

Definition; Let *D* represent an input database, *x* denote a d-dimensional vector representing any data instance in *D*, *i* and *j* symbolize row number and attribute number, respectively. Input perturbation can be defined as the following transformation:

$$x_i^j\_private = x_i^j + Laplace(\frac{\Delta f}{\epsilon}) \tag{4}$$

where;

$$\Delta f = \|\max(x^j) - \min(x^j)\| \tag{5}$$

Δf is calculated for each attribute and then a differentially private version of D can be obtained by using Equation 4.
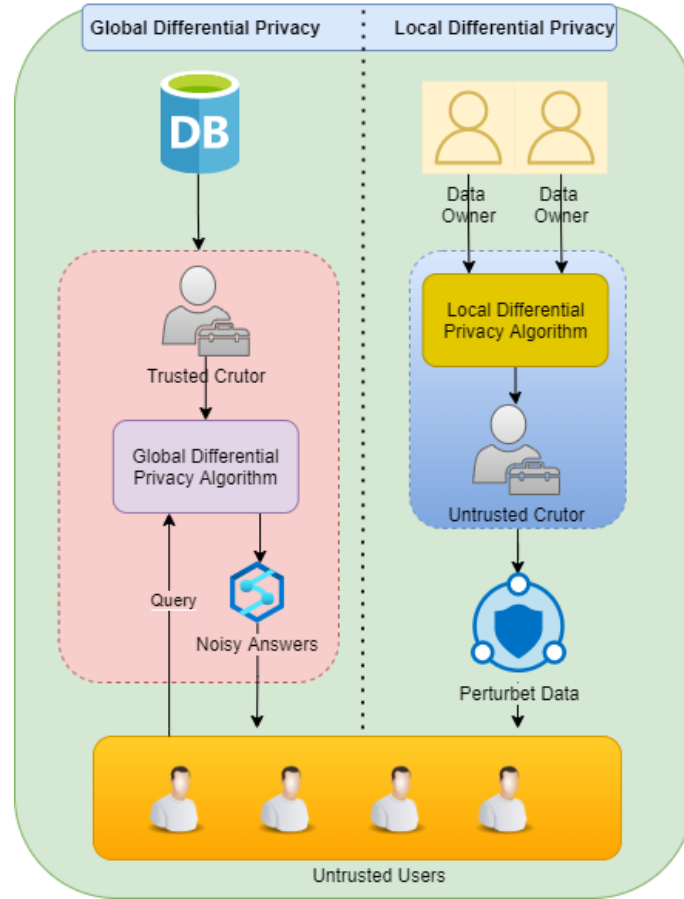
Figure 1. Global and local differential privacy

5. EXPERIMENTS

Recommender systems utilize behavioral and preference data, regarded as personal data. Given the potential lack of trustworthiness associated with such systems, it is imperative to provide privacy measures. Firstly, this work presents an analysis of the outcomes of a recommendation system that utilizes collaborative filtering, specifically focusing on the effects of perturbed input data. Secondly, this study aims to examine the outcomes of hybrid, collaborative, and content-based filtering algorithms when applied to input data that has been perturbed by noise.

5.1 Performance evaluation metrics

Let, t_x be the actual value, t'_x be the predicted value, and *n* is the number of samples.

RMSE is calculated by using Equation 6;

$$RMSE = \sqrt{\frac{1}{n}\sum_{x=1}^{n}(t_x - t'_x)^2} \tag{6}$$

MAE is calculated using Equation 7 by averaging the absolute values of the differences between the predicted values and the actual values.

$$MAE = \frac{1}{n} \sum_{x=1}^{n} |t_x - t'_x| \tag{7}$$

5.2 Experiment-1

In conducting the first experiment, the Movies Dataset is utilized (The Movies Dataset). The dataset consists of 100,000 evaluation points for 9,066 movies made by 671 users.

Figure 2 illustrates the whole process of the system as applied in Experiment-1. In the traditional recommendation system, denoted in path 1, the original dataset is provided to the collaborative filtering algorithm. Subsequently, the resulting outputs are assessed using specific metrics, leading to the final outcomes. In the context of the differentially private recommender system, as depicted in path 2, the process involves the application of input perturbation to the original data, resulting in the acquisition of perturbed data. The perturbed data is subjected to collaborative filtering, and the resulting outputs are assessed using several metrics to achieve the final results.
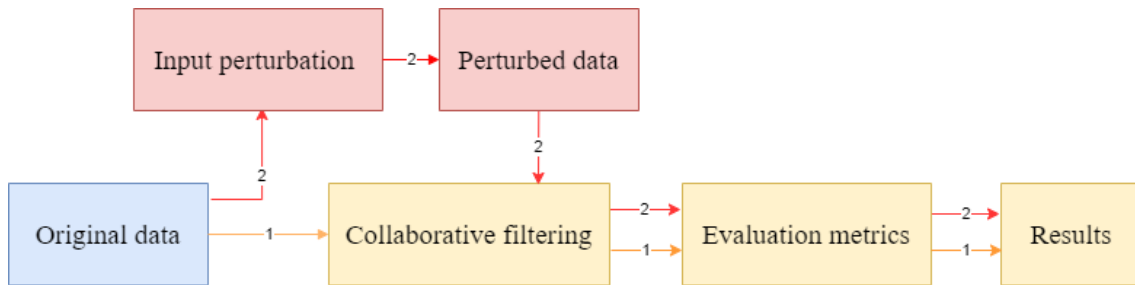
Figure 2. *The general workflow in Experiment-1*

The first experiment yielded the performance outcomes of a recommender system that respects privacy. The most often used collaborative filtering algorithms include SVD, kNNBasic, SVDpp, kNNwithZscore, and CoClustering. This experiment utilized the aforementioned techniques to assess the performances on perturbed data. As previously stated, input perturbation was employed on the raw data, and the outcomes were assessed across several epsilon values, specifically 5, 10, 50 and 100. The performance criteria are selected as RMSE and MAE (Canbay & Taş, 2022). The results that were acquired were presented Table 1. Furthermore, Figure 3 presents a visual representation that allows for a comparative analysis of the outcomes.

Table 1. *The results of Experiment-1*

Epsilon	SVD	kNNBasic	SVDpp	kNNwithZscore	CoClustering	Metrics
100	0.8983	0.9702	0.8889	0.9199	1.0705	RMSE
	0.6923	0.7466	0.6822	0.7012	0.8611	MAE
50	0.9066	0.9771	0.8959	0.9271	1.0754	RMSE
	0.6986	0.7530	0.6876	0.7069	0.8642	MAE
10	1.1184	1.1775	1.1212	1.1372	1.2567	RMSE
	0.8696	0.9142	0.8702	0.8788	1.0010	MAE
5	1.6292	1.6469	1.6702	1.6156	1.6983	RMSE
	1.2458	1.2585	1.2807	1.2294	1.3144	MAE
no privacy	0.8969	0.9675	0.8863	0.9174	0.9618	RMSE
	0.6907	0.7439	0.6794	0.6984	0.7452	MAE
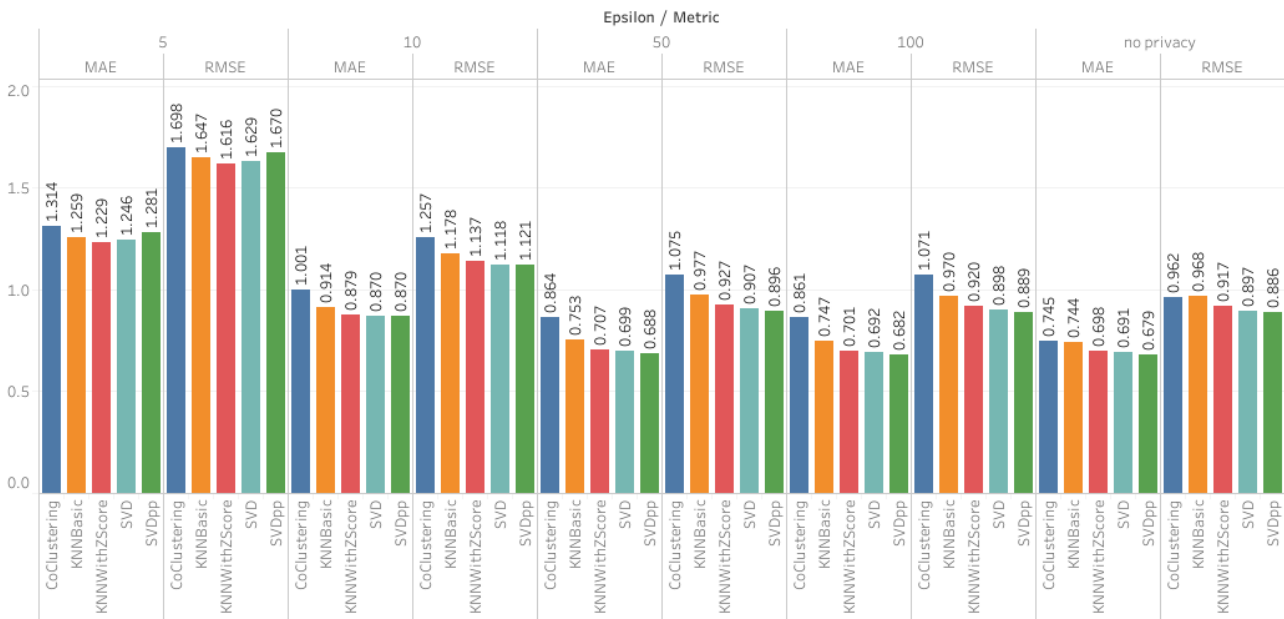
Figure 3. Graphical comparison of the results of Experiment-1

As depicted in Figure 3, RMSE and MAE values present a decreasing trend, whereas the epsilon values increase. Furthermore, RMSE and MAE show optimal performance for epsilon 100. The results indicate that our technique demonstrates successful applicability in privacy-preserving recommender systems.

5.3 Experiment-2

In this experiment, Goodbooks dataset is employed (Goodbooks Dataset). The dataset encompasses the ratings provided by 53,424 individuals for a collection of 10,000 widely-read novels.

The workflow for Experiment-2 is illustrated in Figure 4. Traditional recommendation system, denoted by path 1, processes the original raw data. Following this, the generated outputs are assessed using specific metrics, and ultimately, the results are acquired. Nevertheless, the perturbed data is provided as input for algorithms that perform collaborative filtering, content-based filtering, and hybrid filtering. The assessments are conducted utilizing a variety of evaluation metrics, and a comparison is made of the results.
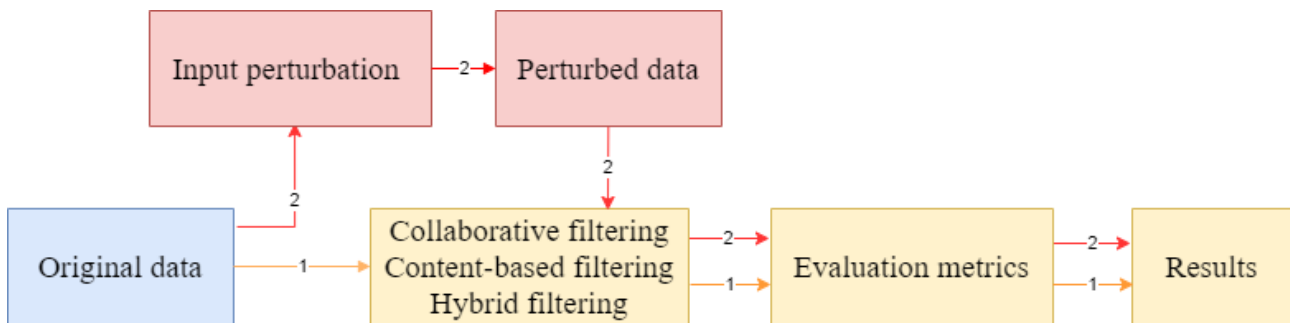
Figure 4. The general workflow in Experiment-2

In this experiment, we conducted a comparison of hybrid, collaborative filtering, and content-based filtering methodologies. Experiments are undertaken for various epsilon values. Based on the findings depicted in Table 2 and Figure 5, it can be observed that the optimal performance in terms of RMSE and MAE is achieved for epsilon 100. Therefore, it is evident that hybrid recommendation systems yield the lowest error rates.

Table 2. *The results of Experiment-2*

Epsilon	Hybrid filtering	Collaborative filtering	Content-based filtering	Metrics
100	0.90664	1.08282	0.95007	RMSE
	0.69813	0.86515	0.72732	MAE
50	0.91604	1.0905	0.96019	RMSE
	0.70704	0.87385	0.73434	MAE
10	1.10979	1.26876	1.15695	RMSE
	0.85954	1.00469	0.89377	MAE
5	1.57873	1.72447	1.6389	RMSE
	1.19621	1.32805	1.25	MAE
no privacy	0.90327	0.97872	0.93991	RMSE
	0.69786	0.75621	0.71738	MAE
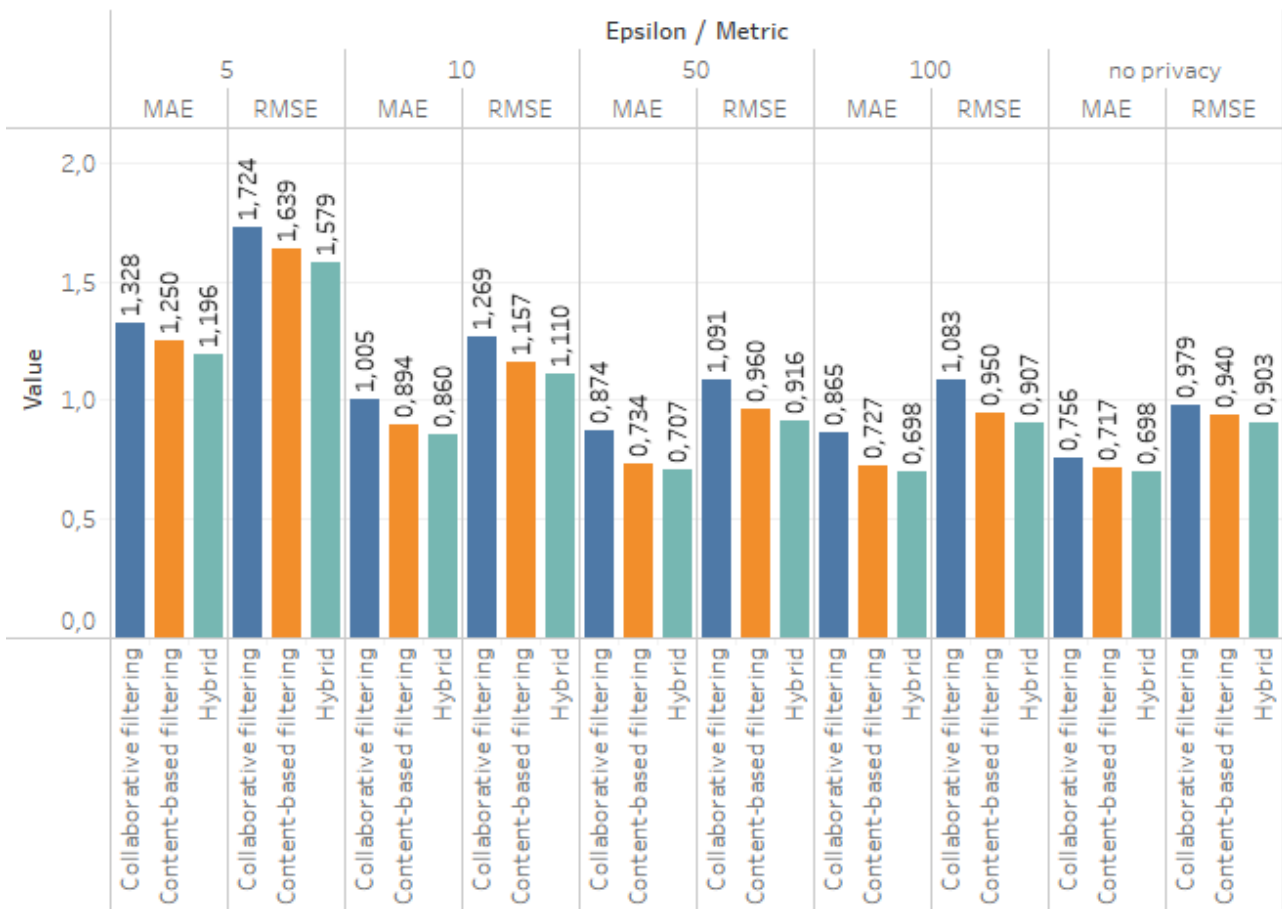
Figure 5. *Graphical comparison of the results of Experiment-2*

6. CONCLUSION

The widespread adoption of smartphones has significantly contributed to the increased utilization of online shopping platforms. As the shift towards online retail continues to gain momentum, consumers are increasingly experiencing a sense of inundation due to the abundance of choices available to them. Consequently, they encounter difficulties in locating a product or service that aligns with their specific requirements and desired outcomes. Most online shopping platforms employ recommendation systems to assist customers in discovering things that may be of interest to them.

Recommendation systems heavily depend on users' behavioral and preference data, such as ratings, likes and dislikes, to generate precise recommendations. Nevertheless, customers often encounter privacy concerns as a result of unethical data gathering and analytical practices conducted by service providers. This study presents a comparative study for a recommender system that prioritizes privacy considerations. Input perturbation is utilized to perturb the raw data.

The experiments were conducted on two distinct cases. The first experiment is the comparison of collaborative filtering approaches on perturbed data. It has been observed that an increase in epsilon leads to a decrease in error. Among the algorithms, SVD++ gave the minimum error rates for all metrics. The second experiment investigates the efficacy of hybrid, collaborative, and content-based filtering techniques. The results showed that the hybrid filtering strategy demonstrated the most favorable outcomes in terms of error rates, regardless of the epsilon values. Both experiments have shown that the implementation of differential privacy effectively protects the privacy of users in recommender systems while providing higher utility.

AUTHOR CONTRIBUTIONS

Methodology and writing-reviewing, Y.C and A.U; editing, Y.C and A.U; conceptualization and software, Y.C and A.U. All authors have read and legally accepted the final version of the article published in the journal.

CONFLICT OF INTEREST

The authors declare no conflict of interest.

REFERENCES

Altman, I. (1976). A conceptual analysis. *Environment and behavior, 8*(1), 7-29. https://doi.org/10.1177/001391657600800102

Arachchige, P. C. M., Bertok, P., Khalil, I., Liu, D., Camtepe, S., & Atiquzzaman, M. (2019). Local Differential Privacy for Deep Learning. *IEEE Internet of Things Journal*. https://doi.org/10.1109/JIOT.2019.2952146

Badsha, S., Yi, X., Khalil, I., & Bertino, E. (2017). *Privacy preserving user-based recommender system.* IEEE 37th International Conference on Distributed Computing Systems (ICDCS). https://doi.org/10.1109/ICDCS.2017.248

Banisar, D., & Davies, S. (1999). Privacy and human rights: An international survey of privacy laws and practice. *Global Internet Liberty Campaign*. (Accessed:17/04/2023) https://gilc.org/privacy/survey/intro.html

Cai, G., Lee, K., & Lee, I. (2018). Itinerary recommender system with semantic trajectory pattern mining from geo-tagged photos. *Expert Systems with Applications, 94*, 32-40. https://doi.org/10.1016/j.eswa.2017.10.049

Canbay, P., & Hüseyin, T. (2022). Yapıların Isıtma ve Soğutma Yükünün Yapay Zeka ile Tahmini. *International Journal of Pure and Applied Sciences, 8*(2), 478-489. https://doi.org/10.29132/ijpas.1166227

Cunha, T., Soares, C., & de Carvalho, A. C. (2018). Metalearning and Recommender Systems: A literature review and empirical study on the algorithm selection problem for Collaborative Filtering. *Information Sciences, 423*, 128-144. https://doi.org/10.1016/j.ins.2017.09.050

Differential Privacy. (Accessed:23/05/2023) https://www.apple.com/privacy/docs/Differential_Privacy_Overview.pdf

Dwork, C. (2006). *Differential Privacy.* International Colloquium on Automata, Languages and Programming, Berlin, Heidelberg. https://doi.org/10.1007/11786986

Fukuchi, K., Tran, Q. K., & Sakuma, J. (2017). *Differentially private empirical risk minimization with input perturbation.* International Conference on Discovery Science. https://doi.org/10.1007/978-3-319-67786-6_6

Garanayak, M., Mohanty, S. N., Jagadev, A. K., & Sahoo, S. (2019). Recommender system using item based collaborative filtering (CF) and K-means. *International Journal of Knowledge-based and Intelligent Engineering Systems, 23*(2), 93-101. https://doi.org/10.3233/KES-190402

Geetha, G., Safa, M., Fancy, C., & Saranya, D. (2018). *A hybrid approach using collaborative filtering and content based filtering for recommender system.* Journal of Physics: Conference Series. https://doi.org/10.1088/1742-6596/1000/1/012101

Goodbooks Dataset. (Accessed:02/06/2023) https://www.kaggle.com/datasets/zygmunt/goodbooks-10k

Guo, Y., Wang, M., & Li, X. (2017). Application of an improved Apriori algorithm in a mobile e-commerce recommendation system. *Industrial Management & Data Systems, 117*(2), 287-303. https://doi.org/10.1108/IMDS-03-2016-0094

Hu, M., Wu, D., Wu, R., Shi, Z., Chen, M., & Zhou, Y. (2021). RAP: A Light-Weight Privacy-Preserving Framework for Recommender Systems. *IEEE Transactions on Services Computing, 15*(5), 2969-2981. https://doi.org/10.1109/TSC.2021.3065035

Javed, U., Shaukat, K., Hameed, I. A., Iqbal, F., Alam, T. M., & Luo, S. (2021). A review of content-based and context-based recommendation systems. *International Journal of Emerging Technologies in Learning (iJET), 16*(3), 274-306. https://doi.org/10.3991/ijet.v16i03.18851

Kawasaki, M., & Hasuike, T. (2017). *A recommendation system by collaborative filtering including information and characteristics on users and items.* 2017 ieee symposium series on computational intelligence. https://doi.org/10.1109/SSCI.2017.8280983

Kunaver, M., & Požrl, T. (2017). Diversity in recommender systems–A survey. *Knowledge-based systems, 123*, 154-162. https://doi.org/10.1016/j.knosys.2017.02.009

Li, N., Li, T., & Venkatasubramanian, S. (2007). *t-Closeness: Privacy Beyond k-Anonymity and l-Diversity.* IEEE International Conference on Data Engineering, Istanbul, Turkey. https://doi.org/10.1109/ICDE.2007.367856

Liu, X., Li, Q., Ni, Z., & Hou, J. (2019). *Differentially private recommender system with autoencoders.* 2019 International Conference on Internet of Things and IEEE Green Computing and Communications (GreenCom) and IEEE Cyber, Physical and Social Computing (CPSCom) and IEEE Smart Data (SmartData). https://doi.org/10.1109/iThings/GreenCom/CPSCom/SmartData.2019.00094

Machanavajjhala, A., Gehrke, J., Kifer, D., & Venkitasubramaniam, M. (2006). *l-Diversity: Privacy Beyond k-Anonymity.* International Conference on Data Engineering, Atlanta, USA. https://doi.org/10.1109/ICDE.2006.1

Mehrotra, R., McInerney, J., Bouchard, H., Lalmas, M., & Diaz, F. (2018). *Towards a fair marketplace: Counterfactual evaluation of the trade-off between relevance, fairness & satisfaction in recommendation systems.* Acm international conference on information and knowledge management. https://doi.org/10.1145/3269206.3272027

Milano, S., Taddeo, M., & Floridi, L. (2020). Recommender systems and their ethical challenges. *AI & society, 35*, 957-967. https://doi.org/10.1007/s00146-020-00950-y

Mirshghallah, F., Taram, M., Vepakomma, P., Singh, A., Raskar, R., & Esmaeilzadeh, H. (2020). Privacy in Deep Learning: A Survey. *arXiv preprint arXiv:2004.12254.* https://doi.org/10.48550/arXiv.2004.12254

The Movies Dataset. (Accessed:13/05/2023) https://www.kaggle.com/datasets/rounakbanik/the-movies-dataset

Neera, J., Chen, X., Aslam, N., Wang, K., & Shu, Z. (2021). Private and Utility Enhanced Recommendations with Local Differential Privacy and Gaussian Mixture Model. *IEEE Transactions on Knowledge and Data Engineering*. https://doi.org/10.1109/TKDE.2021.3126577

Nergiz, M. E., Atzori, M., & Clifton, C. (2007). *Hiding the Presence of Individuals from Shared Databases*. ACM SIGMOD International Conference on Management of Data, Beijing, China. https://doi.org/10.1145/1247480.1247554

Selvaraj, S., & Gangadharan, S. S. (2021). Privacy preserving hybrid recommender system based on deep learning. *Turkish Journal of Electrical Engineering and Computer Sciences, 29*(5), 2385-2402. https://doi.org/10.3906/elk-2010-40

Sütçü, M., Ecem, K., & Erdem, O. (2021). Movie Recommendation Systems Based on Collaborative Filtering: A Case Study on Netflix. *Erciyes Üniversitesi Fen Bilimleri Enstitüsü Fen Bilimleri Dergisi, 37*(3), 367-376.

Sweeney, L. (2002). k-Anonymity: A Model for Protecting Privacy. *International Journal of Uncertainty, Fuzziness and Knowledge-Based Systems, 10*(5), 557-570. https://doi.org/10.1142/S0218488502001648

Wang, J., & Wang, A. (2020). *An improved collaborative filtering recommendation algorithm based on differential privacy.* 2020 IEEE 11th International Conference on Software Engineering and Service Science (ICSESS). https://doi.org/10.1109/ICSESS49938.2020.9237702

Warren, S. D., & Brandeis, L. D. (1890). The Right to Privacy. *Harvard law review*, 193-220. https://doi.org/10.2307/1321160

Xian, Z., Li, Q., Li, G., & Li, L. (2017). New collaborative filtering algorithms based on SVD++ and differential privacy. *Mathematical Problems in Engineering, 2017*. https://doi.org/10.1155/2017/1975719

Xiong, P., Zhang, L., Zhu, T., Li, G., & Zhou, W. (2020). Private collaborative filtering under untrusted recommender server. *Future Generation Computer Systems, 109*, 511-520. https://doi.org/10.1016/j.future.2018.05.077

Yin, C., Shi, L., Sun, R., & Wang, J. (2020). Improved collaborative filtering recommendation algorithm based on differential privacy protection. *The Journal of Supercomputing, 76*, 5161-5174. https://doi.org/10.1007/s11227-019-02751-7

Yu, T., Shen, Y., & Jin, H. (2019). *A visual dialog augmented interactive recommender system.* ACM SIGKDD international conference on knowledge discovery & data mining. https://doi.org/10.1145/3292500.3330991

Zhang, S., Liu, L., Chen, Z., & Zhong, H. (2019). Probabilistic matrix factorization with personalized differential privacy. *Knowledge-based systems, 183*, 104864. https://doi.org/10.1016/j.knosys.2019.07.035

Zhao, J., Geng, X., Zhou, J., Sun, Q., Xiao, Y., Zhang, Z., & Fu, Z. (2019). Attribute mapping and autoencoder neural network based matrix factorization initialization for recommendation systems. *Knowledge-based systems, 166*, 132-139. https://doi.org/10.1016/j.knosys.2018.12.022

General Purpose and Focused Invention, Market Value, and Productivity

Burak DİNDAROĞLU[1*] 🆔

[1] Izmir Institute of Technology, Engineering Management Department, İzmir, Türkiye

Keywords	Abstract
General Purpose Technologies Market Value Total Factor Productivity Patents Intellectual Property	We study returns to general purpose and focused invention at the firm level for a panel of manufacturing firms in the U.S. for the period 1976-1995, by studying their relationships with market value and Total Factor Productivity. We construct stocks of patents that lie at the two relevant tails of the distribution of the generality index (Trajtenberg et al., 1997; Henderson et al, 1998) to measure general purpose and focused invention at the firm level. In line with expectations, there is a market value premium to focused invention, and a productivity premium to general purpose invention. Estimates for the value of focus indicate that moving a single patent from the upper tail of the generality distribution to the lower tail would increase market value by $.24 \times q$ million 1992 dollars on average, where q is Tobin's q. The firm with the average general patent stock would gain $6.7 \times q$ million in market value if all its patents at the highest quartile of the generality distribution were moved to the lowest. In terms of the value of general purposeness, moving all its focused patents to the general category increases Total Factor Productivity by 2.3% to 2.8%, and five-year productivity growth by 3.9% to 5.2%, for the average firm. A potential implication is that corporate basic research is associated with significant long-term benefits in terms of productivity growth.

Author ID (ORCID Number)		Article Process	
0000-0003-2889-3704	Burak DİNDAROĞLU	Submission Date	10.09.2023
		Revision Date	20.11.2023
		Accepted Date	19.12.2023
		Published Date	06.02.2024

1. INTRODUCTION

This paper examines returns to *general purpose* and *focused* invention at the firm level. We use valuation and productivity analysis to examine the relationship of each type of invention to the traded market value and Total Factor Productivity (TFP) at the firm level. No previous study, to our knowledge, has considered the valuation of patents across this important dimension of heterogeneity in the nature of invention.

For the purpose of identifying inventions that are more general purpose or focused than others, we use the measure of patent generality proposed by Trajtenberg et al. (1997) and Henderson et al. (1998). The generality index is originally proposed as a measure of the "basicness" of invention, i.e., the closeness of the knowledge embedded in the patent to basic science. A patent with a larger generality score is one that finds future applications and antecedents in a larger variety of technological classes. In this sense, the generality index is a proxy for the general purpose nature of the technology embedded in the patent. A patent with a small index value is one whose technological antecedents belong in a more concentrated set of technological classifications. These latter patents are deemed more "focused" in their inventive content and the opportunities they generate. Generality has been extensively used to identify and study General Purpose Technologies (GPTs) in patent data (Hall & Trajtenberg, 2004; Moser & Nicholas, 2004; Youtie et al., 2008; Raiteri, 2018; Martinelli et al., 2021; among others.).

*Corresponding Author, e-mail: burakdindaroglu@iyte.edu.tr

We identify the general purpose (*resp.* focused) inventions of a given firm using its patents that have generality scores above (*resp.* below) a given threshold. Hence, we study the association with market value and productivity of a firm's patents that are located at the two tails of the distribution of the generality index. Market value and productivity approaches are not substitutes with one another, nor they are alternative measures of firm performance: market value of a firm quantifies the valuation of the firm by investors, while factor productivity is a measure of the firm's productive efficiency. It is then interesting to see whether different portions of a firm's patent portfolio are associated more or less strongly with these two measures, whether some patents are highly valued by investors, while others contribute more to productivity.

A large literature in Economics deals with the valuation of R&D expenditures and patents at the firm level (Griliches, 1981; Hall et al., 2005; Hall & Oriani, 2005; among others). The approach holds that the excess market value of the firm relative to the value of its physical assets (a quantity known as Tobin's q) can be explained by the intangible assets of the firm, including its "knowledge assets." Hence, the market's valuation of the various knowledge assets of the firm can be estimated, which are proxied by the stock of its R&D expenditures, its patent stock, and related and derivative properties of its knowledge base (Cockburn & Griliches, 1987; Blundell et al., 1999). However, the literature has overlooked the heterogeneity of patents in various dimensions. The main premise of the current study is that the heterogeneity of patented inventions with respect to generality matters in interesting and important ways.

Another key interest in Economics has been the productivity effects of R&D, invention and innovation at various levels of aggregation (Hall, 2011). This literature uses a production function framework that can incorporate knowledge assets, to study the association between total factor productivity and the said knowledge assets. The approach attempts to estimate the private (and also social) rate of return to R&D and patent holdings of a company (and also, industry, region, ...etc.). Authors mostly focused on R&D stocks ("R&D capital"), but the relationship between productivity and patenting, and various other properties of the firm's knowledge base have also been studied (Crépon et al., 1998; Harhoff, 1998; Greenhalgh & Longland, 2005; Griffith et al., 2006; Crass & Peters, 2014).

We begin with the simple idea that patents that are highly general and those that are focused are indicators of different kinds of research activities. One therefore expects the generality distribution of a firm's patent stock to be reflected in observable economic outcomes in predictable ways. Main hypotheses of the paper are that (*i*) more focused patents are primarily associated with the market value of the firm, but (*ii*) highly general patents are primarily associated with firm-level productivity. We test these hypotheses by estimating hedonic Tobin's q equations on the one hand, and production function estimates on the other, in conjunction with measurements of general purpose and focused patent stocks described above.

Results of the paper indeed show that different tails of the generality distribution are associated with different measures in predicted ways. The market places a larger premium on focused invention than general purpose invention. This is in line with the interpretation of generality, in that more general invention may not find immediate applicability, hence short-term returns for the firm, leading to relatively small increases in market value. Productivity analyses show that this delimitation matters for productivity estimates as well: productivity at the firm level is associated more strongly with general purpose invention rather than focused invention. [1] According to estimates, moving a single patent from the upper tail of the generality distribution to the lower tail results in a $.24 \times q$ million dollars increase in market value, where q denotes Tobin's q.[2] The firm with mean general patent stock would gain an additional $6.7 \times q$ million dollars in market value if all its general patents were moved to the lower tail of the generality distribution On the other hand, the firm would gain approximately 0.23% to 0.28% increase in productivity, and 0.39% to 0.52% in five-year productivity growth if 10% of its patents at the lower tail of the generality scale were instead at the upper tail, indicating that the

---

[1] To be more specific, both general and focused invention are positively associated with market value and productivity. However, the effect of general patents is greatly diminished, and loses significance in some specifications, when we control its stock of highly focused patents. Productivity results mirror this, in that the effect of focused patents is reduced or loses significance when the firm's general patent stock is controlled for.

[2] Tobin's q is a measure of the traded value of the firm above the value of its physical assets. For specific calculations, note that Tobin's q takes values between .08 and 14.77 with mean value 1.76 across all firms in the sample.

productivity effect of moving all focused patents to the general category would amount to 2.3% to 2.8%, with the associated gain in five-year productivity growth ranging from 3.9% to 5.3%. Such valuations are relevant for Technology Management and Engineering Management in helping strategic planning and capital budgeting decisions within the firm, and for Economics in their potential guidance for policy making.

Overall, our results confirm that there is a large productivity premium to general purpose invention. We also show that this premium is associated with an opportunity cost in terms of foregone market value, which would have been realized with a more focused strategy. These results, along with recent results that study the strategic choice of basic and applied research (Guo et al., 2022; Arora et al., 2021), send to the idea of balancing focused and general purpose inventive activity at the firm level. Our results provide valuations in terms of market values and productivity that can guide formalizations and decision making in this context.

2. RELATED LITERATURE

The current study relies on Trajtenberg et al. (1997) and Henderson et al. (1998) by attempting a direct application of their measure of generality. Trajtenberg et al. (1997) find that university patents in their sample have higher generality scores than non-academic patents, from which they discern that generality is associated with basic science. Henderson et al. (1998) and Schmid and Fajebe (2019) report similar results. Generality is also positively related to usual indicators of patent value, such as forward citations, the likelihood of renewal, and the likelihood to be traded (Serrano, 2010).

The generality measure has been used in empirical studies of invention for a variety of purposes. Hall and Trajtenberg (2004) identified and studied General Purpose Technologies (GPTs) using various formulations of generality. Mowery and Ziedonis (2002) reported a decline in the importance and generality of academic patents in the US during 1980s, in the wake of the Bayh-Dole act. This finding is disputed by Sampat et al. (2003). Moser and Nicholas (2004) used the measure to show that electricity inventions in the 1920s, as a group, did not accord with the commonly used definitions of a GPT. Gómez-Baquero (2009) and Youtie et al. (2008) used generality to argue that nanotechnologies were becoming GPTs. The former also identified transitions from focused to general technologies. Raiteri (2018) uses the generality index to show that government procurement encouraged and led developments in GPTs. Filippova (2019) shows that the generality of blockchain technology rose consistently between 2013 and 2017 and was of comparable magnitude to that of ICT technologies by 2017. Martinelli et al. (2021) study generality (and originality) to argue that Big Data and AI showed characteristics of distinct GPTs, while other enablers of Industry 4.0 (IoT, cloud, robotics, additive manufacturing) did not. Industry 4.0 fields in general exhibited less general (more focused) character than the average invention. Barirani et al. (2015) study the relationship between a measure of recombination depth (including more distinct domains in its knowledge sources) and generality for a sample of Canadian nanotechnology patents, showing that corporate invention generality is more sensitive to recombination depth than public invention.[3]

A large literature in Economics studies the valuation of various knowledge-related assets at the firm level by using the variation in the market values of firms in relation to R&D, invention and innovation. The premise of the literature is that the excess market value of a firm relative to the value of its physical assets (a quantity known as Tobin's q) is due to its intangible holdings, which must include its knowledge assets. The literature has shown that both the amount and various attributes of a firm's R&D inputs and invention activity are indeed valued by market actors, allowing a market-based valuation strategy for corporate knowledge assets. Griliches (1981) reported a positive association between market value, R&D and patent stocks. Cockburn and Griliches (1987) include survey-based measures of appropriability at the firm level in the market value equation, showing the latter are not valued by the market. Megna and Klock (1993) provide industry-specific estimates from the semiconductor industry, also including rival firms' patents. Blundell et al. (1999) and Hall and Vopel

---

[3] A critique to the measure has been posed by Petralia (2020), who criticizes the index by demonstrating its inability to differentiate fields at the highest level of generalization (Chemical, Mechanical, Electrical) in terms of generality. However, each of these aggregate technologies have their own citation habits and patterns, and it is known that unnormalized citation-based metrics should not be used to make comparisons *between* and *across* different disciplines. For this reason, we use a classification method that makes comparisons only *within*, and not *between*, the six large technology classes (Section 3.1.3).

(1997) report that the market's valuation of knowledge assets is higher if the firm has higher market share. Hall and Oriani (2007) provide estimates for European firms, while Toivanen et al. (2002) restrict attention to the value of knowledge assets in the UK. Hall et al. (2005) use the market value framework to study the valuation of the company's citation stock, finding that the market values citations of the firm over and above its R&D expenditures and patents. Belenzon (2012) finds that not all citations have a uniform effect on market value: citations on which the firm can capitalize in later periods affect market value positively, while those the firm does not build on in later invention are associated negatively with market value. Bessen (2009) extends the theoretical framework in order to obtain direct measures of patent rents. Sandner and Block (2011) extended the analysis to the valuation of trademarks. Hsu et al. (2021) show that academic publications by Chinese firms are associated with higher market value. A related literature extends the analysis to the valuation (hence measurement) of spillover effects (Jaffe, 1986; Bloom et al., 2013; Lychagin et al., 2016; Dindaroglu, 2014; among others).

Another key line of inquiry in Economics has been the measurement of the productivity effects of patenting and R&D, usually in a production function framework.[4] The interest was initially on finding explanations for the productivity increase during the 1960s (Griliches, 1963) and fall during the 1970s (Griliches, 1979, 1986, 1998) with the premise that changes in the rate of technological progress may be an underlying factor (Griliches, 1988). Crépon et al. (1998) show that productivity is positively associated with the share of sales due to new products, a common measure of innovation. They introduce a structural model that corrects for selection and simultaneity biases specific to patent and R&D data. Griffith et al. (2006) extend the same framework to four European countries and provide interesting differences with respect to product and process invention. Variants of the production function framework have been estimated for the Netherlands (Bartelsman et al., 1996), Germany (Harhoff, 1998), Spain (Dorazelski & Jaumandreu, 2008), China (Jefferson et al., 2006), among many others. A survey of the earlier literature is provided by Mairesse and Sassenou (1991). Hall et al. (2009) offer a survey with an econometric focus, while Hall (2011) surveys the general findings and accumulated evidence till then.

The current study contributes to these two lines of research traditions by directly studying the significance of heterogeneity in an important technological characteristic. Studies that have looked at patenting and other innovation indicators in their relationship to productivity have found little relation between patents and productivity (Crass and Peters, 2014), or found that positive effects are short-lived (Greenhalgh and Longland, 2005). This supports one of the main insights of the current paper: market value is most immediately linked to aspects of innovation and other intangibles that are of quick or immediate commercial use, but such activity exhibits a weaker relationship with productivity. The current paper shows that patent generality may be an important confounder in these previous studies, since it is able to demonstrate a large productivity premium to general invention.

The generality index is proposed as a measure of the "basicness" of the underlying invention. The evidence that links patent generality to the "basic" character for underlying research (Trajtenberg et al., 1997; Henderson et al., 1998; Schmid and Fajebe, 2019) also relates the current work to the literature examining the productivity effects of basic and applied research activity at the firm level. Lichtenberg and Siegel (1991) found that the productivity effect of R&D comes mostly from basic research, and many others reported a productivity premium to corporate basic research activity (Lichtenberg, 1992; Link, 1981; Griliches, 1986; Czarnitzki & Thorwarth, 2012; among others). Ernst (1998) finds that firms that spend a larger share of their overall R&D expenditures on research hold higher quality patents. Bolívar-Ramos (2023) show that corporate science expenditures lead to innovation in Environmental Technologies, while Zhao et al. (2023a, 2023b) show that scientific publishing and corporate scientific labs are associated with higher invention counts and impact in China. Krieger et al. (2022) show that patents that build on a scientific publication are, on average, 26% more valuable than otherwise. Hsu et al. (2021) show that academic publications by Chinese firms are associated

---

[4] The literature on the estimation of links between R&D, invention and productivity is vast. We focus here on firm-level analysis using micro data, rather than industry and country-level analysis, and only discuss a representative set of papers that are most relevant for the current study.

with higher market value and exhibit synergetic effects with firm-level patenting. Chen et al. (2024) report that corporations that produce and cite scientific literature produce more inventions overall.

Trends in basic research in relation to applied research has been the focus of Arora et al. (2021), who show that returns to corporate basic research depend on the balance between in-house potential and spillovers to rivals and report a trend towards less "R" and more "D" in corporate R&D in recent decades. In previous work, Arora et al. (2018) document a shift away from basic science in most industries -except, and notably, biotechnology- between 1980 and 2006. Coad et al. (2020) and Leten et al. (2022) note the same trend, the former in Spanish manufacturing and the latter in global pharmaceuticals. Camerani and Rotolo (2023) argue that the fall is in proportional terms while corporate basic research expenditures had been on the rise, studying the first half of 2010s. Krieger et al. (2021) show that the number and share of publishing firms have declined and publications became more concentrated in Germany between 2008 and 2016, while Yang et al. (2023) report fewer management science publications and fewer citations to existing publications over time between 2000-2019.

More recent research has also demonstrated and measured the social and private value of corporate basic research. Leten et al. (2022) propose and demonstrate an absorptive capacity motive to corporate basic science that is stronger than a direct innovation sourcing effect. Rotolo et al. (2020) review the literature on the scientific publications of corporations and argue that corporations publish to increase absorptive capacity, to attract and retain better researchers, to support their IP strategies, to build reputation, and to support commercialization. Shvadron (2023) adds and empirically studies a leadership motive to corporate basic research, i.e., that basic research influences the direction of external research in ways that benefit the focal firm. In line with these observations, Wen (2023) discusses policy measures to boost basic research at corporations. Choi et al. (2022) and Ceccagnoli et al. (2024) both show that the relationship between basic research and productivity is positively mediated by technological diversity. Arora et al. (2023) show that innovation that is science-based tend to be socially and privately more valuable, where the latter also exhibits a strong first-mover advantage. Dean et al. (2023) discuss and demonstrate the effect of organizational and product complexity on a firm's ability to translate basic research into market success. Guo et al. (2022) examine the strategic balance between basic research and applied development, finding that corporate basic research increases the productivity of the firm up to a saturation point (about 65% research intensity of R&D) and plateaus afterwards. They also report an inverted-U type relationship between applied development intensity and productivity, peaking at 28% intensity. These recent results, as well as of the current paper, point towards benefits of balancing focused and general purpose inventive activity at the firm level.

3. MATERIAL AND METHOD

3.1 Measurement of General Purpose and Focused Invention Stocks

3.1.1. Generality

Trajtenberg et al. (1997) construct an index of patent generality based on information on citations made to the original patent by its antecedents, i.e., its forward citations. The measure is based on the spread of citing patents among existing technological classes. If patent i receives N_i citations, N_{ik} coming from patents classified in technology class $k \in \{1, \dots, \overline{k}\}$, then its generality is defined as

$$G_i = 1 - \sum_{k=1}^{\overline{k}} \left(\frac{N_{ik}}{N_i}\right)^2 \tag{1}$$

Notice that G_i will be relatively low if i's citations are from few distinct technological classes, and will be larger, the larger the spread of citations across different technological fields. The idea is that patent i is more general if it spawns antecedents in a larger number of different technology fields, which coincides with the definition of general purpose technologies, as well as the definition of fundamental (basic) science.

3.1.2. Classification of Patents and Construction of Stock Variables

A firm's general and focused invention stocks for a given year are constructed as follows. For two thresholds f and g such that $0 < f \leq g < 1$, let $\{p_{it}^g\}_{t=0}^{T_i}$ denote the sequence of the number of it (firm i, year t) patents that have a generality score above g, and $\{p_{it}^f\}_{t=0}^{T_i}$ the sequence of the number of it patents that have a generality score below f (g is chosen as shorthand for general, and f as shorthand for focused). Also let P_{it}^g be the depreciated stock of $\{p_{it}^g\}_{t=0}^{T_i}$, P_{it}^f the depreciated stock of $\{p_{it}^f\}_{t=0}^{T_i}$, and P_{it}^{fg} the depreciated stock of remaining patents, all calculated as perpetual inventories. That is,

$$P_{it}^g = \sum_{\tau=0}^{T_i-1} (1-d)^\tau p_{it-\tau}^g + (1-d)^{T_i} P_{i0}^g, \text{ and } P_{it}^f = \sum_{\tau=0}^{T_i-1} (1-d)^\tau p_{it-\tau}^f + (1-d)^{T_i} P_{i0}^f \qquad (2)$$

where T_i is the number of years firm i is observed in the panel, and d is the depreciation rate for patent stocks. Following convention, a depreciation rate of 15% is assumed.[5] The (unobserved) initial values P_{i0}^g and P_{i0}^f are approximated by extrapolating the relevant series to minus infinity using the aggregate growth rate of respective sequences, i.e., $P_{i0}^l = P_{i1}^l/(d + r^l), l \in \{f, g\}$ where r^l represents the aggregate growth rate of p_{it}^l in the sample.

The classification into general and focused categories is made only for patents that have at least three overall citations. An additional stock variable (P_{it}^{lc}) is computed for the remaining low-cite (cites < 3) patents. This variable is included in most regressions, except where its inclusion leads to multicollinearity (see Section 3.3.1). Finally, we use P_{it} to represent the firm's total patent stock, i.e., $P_{it} = P_{it}^f + P_{it}^{fg} + P_{it}^g + P_{it}^{lc}$.

3.1.3. Thresholds

We use a different pair of thresholds for each of the six aggregate technology categories (Chemicals, Computers and Communication, Drugs and Medical, Electric and Electronics, Mechanical, and Others). For each of the six aggregate technologies, we first choose thresholds such that a patent is deemed as general (resp. focused) if its generality score lies in the lowest (resp. highest) quartile of the generality distribution in its aggregate technological category. That is, we set the thresholds for category $k \in \{1, \dots, 6\}$ to be $f_k = F_{G_k}^{-1}(0.25)$ and $g(k) = F_{G_k}^{-1}(0.75)$, where F_{G_k} is the cumulative distribution of generality in category k. General inventions (P_{it}^g), then, are those who have generality scores at the highest quartile of the respective generality distribution, while patents at the lowest quartile of the distribution in their aggregate categories are deemed as focused (P_{it}^f). Remaining patents (P_{it}^{fg}) are those that are in the interquartile range. As a robustness check, we also construct patent stocks by decomposing the overall distribution of generality into its *thirds*, i.e., by choosing $f_k = F_{G_k}^{-1}(1/3)$ and $g_k = F_{G_k}^{-1}(2/3)$. Main results are robust to the choice between the two sets of thresholds.

3.2. Econometric Specification

3.2.1. Market Value

We begin with the standard market value specification, which expresses firm i's stock market value at the end of year t (V_{it}) as

$$V_{it} = q_{it}(A_{it} + \gamma K_{it})^\sigma \qquad (3)$$

---

[5] It is reasonable to expect more general patents to depreciate more slowly than specific ones. Incorporating these differences is outside the scope of the study.

where A_{it} represents ordinary physical assets, K_{it} denotes intangible knowledge capital, γ is the shadow value of knowledge capital with respect to physical assets, and q_{it} is a constant that is parametrized with firm and year effects, and other variables. Some algebraic manipulation, imposing constant returns to scale ($\sigma = 1$), and the approximation $\log(1 + x) \approx x$ yields the equation,

$$\log\left(\frac{V_{it}}{A_{it}}\right) = \tilde{q}_{it} + \gamma \frac{K_{it}}{A_{it}} \tag{4}$$

where $V_{it}/A_{it} \equiv Q_{it}$ is called Tobin's q, which is defined as the market value of the firm relative to its total asset value. Equation (4) naturally leads to a linear multivariate regression specification for Tobin's q, regressed on measures of normalized knowledge capital. Knowledge capital (K_{it}) is usually proxied with stocks of R&D expenditures, patents, and/or citation-weighted patents of the firm. Using R&D and various patent stocks as proxies for intangible knowledge capital, distinguishing general purpose and focused invention capital, and following Hall et al. (2005), the market value equation to be estimated becomes,

$$\log Q_{it} = \gamma_F \tilde{P}_{it}^f + \gamma_{FG} \tilde{P}_{it}^{fg} + \gamma_G \tilde{P}_{it}^g + \gamma_R \tilde{R}_{it} + \gamma_{FG} \tilde{P}_{it}^{fg} + \lambda_t + \eta_i + v_{it} \tag{5}$$

where $\tilde{P}_{it}^j = P_{it}^j/A_{it}$ for $j \in \{f, fg, g\}$ represent general (g) and focused (f) patent stocks and the patent stock in the interquartile range (fg), all divided by the value of physical assets. $\tilde{R}_{it} = R_{it}/A_{it}$ is R&D stock of the firm divided by physical assets and $\tilde{C}_{it} = C_{it}/P_{it}$ is citation stock divided by patent stock. λ_t, η_i and v_{it} represent year effects, permanent firm effects, and the usual error term, respectively. All stock variables in equation (5) are calculated as perpetual inventories with 15% yearly depreciation as described by equation (2). We estimate the coefficients in equation (5) using Least Squares (henceforth LS) and panel data regression methods that control for fixed effects, i.e., account for unobserved permanent heterogeneity among firms.

3.2.2. Total Factor Productivity

In order to obtain an estimate for Total Factor Productivity (TFP) and study its determinants, we begin with the standard Cobb-Douglas production function in logs,

$$y_{it} = \alpha_0 + \alpha_K \cdot a_{it} + \alpha_L \cdot l_{it} + \xi_t + \mu_i + u_{it} \tag{6}$$

where y_{it} is the logarithm of firm i's output level (measured by total sales) at year t, a_{it} denotes the logarithm of physical capital, l_{it} denotes the logarithm of labor inputs (employment). We use the usual two-way error component specification, where ξ_t, μ_i and u_{it} are year effects, permanent firm effects and the usual error term, respectively.

Consistent estimation of the parameters in equation (6) is not straightforward since productivity shocks in the current period (which are part of u_{it}) are at least partially observed by the firm prior to making its input decisions. Hence, all variable inputs in the production function are endogenous, and usual least squares or panel data methods will yield biased and inconsistent estimates. Additionally, standard estimates of the production function suffer from selection bias since productivity shocks observed by the firm are correlated with subsequent exit decisions. Since labor inputs can be adjusted in the short-run, endogeneity will result in a positive bias in the coefficient of labor. Selection bias, on the other hand, is likely to cause a negative bias in the coefficient of capital.

Due to these empirical issues, we rely on an estimation procedure developed by Olley and Pakes (1996) to obtain consistent estimates of production function coefficients. This method relies on the three assumptions that (i) productivity evolves as a first order Markov process, (ii) firms decide whether to stay in the market or exit in the current period based on realizations of productivity and other relevant state variables (usually assumed to be the capital stock, but a richer set of state variables can be used as well) at the beginning of the period, and (iii) if the firm decides to keep it operations, it determines current investments based on observed productivity and state variables. The procedure estimates equation (6) in three steps. Assuming that the firm's

investment function is an increasing function of productivity, current productivity level can be inverted and expressed as a function of investment and state variables. In the first step, this function is approximated by a polynomial function and replaces the part of u_{it} in equation (6) that is observed by the firm. Least squares estimation of this transformed equation identifies the labor coefficient, $\hat{\alpha}_L$. The second step estimates exit probabilities for each firm by using a regression model for observed exit decisions. Fitted probabilities from this specification are then used to control for selection bias in a third stage regression that identifies the capital coefficient, $\hat{\alpha}_K$. The procedure requires that current investments, as well as exit decisions to be observed by the econometrician. In the current case, we use capital as the sole relevant state variable and define firm exit as the occurrence of bankruptcy or liquidation. Parameter estimates are robust to conditioning productivity (stage 1) on additional state variables, such as firm age.[6]

Productivity is calculated as Total Factor Productivity, which is given by

$$TFP_{it} = \exp(y_{it} - \hat{\alpha}_K \cdot a_{it} - \hat{\alpha}_L \cdot l_{it}) \tag{7}$$

where $\hat{\alpha}_K$ and $\hat{\alpha}_L$ are estimates of production function coefficients obtained using the Olley and Pakes procedure. The estimate for the constant term is excluded from (7) since it cannot be consistently estimated, and it is just a multiplier common for all observations. The logarithm of expression (7) and its 5-year compounded growth rate ($\log TFP_{it} - \log TFP_{it-5}$) are used as dependent variables in second stage regressions, which are estimated using Fixed-Effects LS (for TFP) and LS (for TFP growth) methods. Sample statistics for all variables are given in Table 1.

3.3. Data Sources and Variables

Data from patent records are taken from the NBER US Patent Citations Data File initiated by Hall et al. (2001) and the following literature. The latest update used for this paper contained information on all patents granted in the U.S. between 1976 and 2006, and all citations made to these patents till 2006. Generality for each patent in the sample is computed using all citations made to the patent till 2006. Data on market value, physical capital, employment, current investments, and firm status are from the Compustat database. We matched the NBER assignee codes to Compustat GVKEY and CUSIP identifiers using the NBER PDP Project match file constructed by Bessen (2009). We focus on a 20 year window between 1976 and 1995 (inclusive). Year 1995 is chosen as the final year to minimize the bias in citations and the generality measure due to the truncation in the citation distribution (Hall et al., 2001). Removing observations outside the sample period, firms with a single year of observations between 1975 and 1990, cleaning key variables and deleting large outliers ($|\ln(x_{it}/x_{it-1})| \geq 1.5$), result in an unbalanced panel of 10469 total observations for the estimation of the market value equation, and 8472 observations for the estimation of the production function and the productivity equations. The two samples differ due to missing variables and cleaning procedures for different variables used. All values in current U.S. dollars are deflated using the GNP deflator with base year 1992. Table 2 includes correlations among variables for both specifications as well as Variance Inflation Factors (VIFs) for addressing potential collinearity among key variables.

3.3.1. Multicollinearity

A potential problem with this set of variables is the presence of multicollinearity among key variables. Table 2 reports simple correlations between key variables, as well as variance inflation factors (VIF) for a number of specifications. In Table 2, correlations and VIF calculations for the two specifications are reported separately in Panel A (market value) and Panel B (productivity). In Panel A, it is observed that the correlation between the interquartile-range patent stock (divided by assets) and remaining patent stock variables are quite high (between .79 and .88). The column VIF/UR contains variance inflation factors for each variable in the *unrestricted* specification in which the interquartile-range patent stock is included as a regressor. The VIF corresponding to this variable (6.93) is above commonly used thresholds (usually, 5) to detect problematic regressors. VIF/R reports variance inflation factors for each variable in the *restricted* case that excludes this

---

[6] Olley & Pakes method is implemented using the Stata command opreg provided by Yasar et al (2008).

variable. When the patent stock in the interquartile-range of the generality distribution is excluded, VIF levels for all variables fall to acceptable ranges. Hence, the market value equation is estimated after excluding this variable. Note that including this variable in the market value specification remains key conclusions of the study unchanged. Panel B in Table 2 performs a similar exercise for variables in the productivity equation, where two controls were excluded to obtain low VIF values for all specifications. Finally, note that citation stock is not included productivity regressions due to its high correlation with patent stock(s). This is not the case in market value regressions where citation stock is used after being divided by patent stock.

Table 1. *Sample Statistics*

		Mean	Median	Standard Deviation	Minimum	Maximum
Market Value*		2031.92	330.18	5889.40	0.10	120756.5
Tobin's q*		1.76	1.20	1.78	0.08	14.77
Sales		2532.12	671.15	5691.08	0.04	84231
Employment		17.33	5.36	33.26	0.02	480
Capital		1882.07	380.42	4647.53	0.72	51652.4
R&D Stock		428.90	65.81	1474.95	0.00	30245.1
Patent Stock		141.40	27.90	369.49	1.65	8353.1
Citation Stock		2084.18	375.25	7305.35	9.36	233246.6
R&D Stock/Assets*		0.38	0.19	0.68	0.00	14.46
Patent Stock/Assets*		0.24	0.09	0.91	0.00	20.58
Citation Stock/Patent Stock*		14.71	11.44	12.51	0.00	154.97
Low-Cite Patent Stock/Assets*		0.03	0.01	0.16	0.00	4.41
General Patent Stock	*Upper quartile*	27.92	5.46	86.65	0.05	2477.84
Interquartile P. Stock		47.54	9.54	133.72	0.09	3340.99
Focused Patent Stock	*Lower quartile*	37.49	7.62	99.78	0.12	2007.16
General Patent Stock	*Upper third*	34.95	6.88	107.47	0.10	3057.38
Middle Third P. Stock		31.78	6.51	92.77	0.00	2446.80
Focused Patent Stock	*Lower third*	46.21	9.23	120.89	0.20	2321.81
Low-Cite Patent Stock		26.04	3.91	73.52	0.00	1371.41

Notes: Sample size: 10755 (max) for starred variables (market value sample) and 8472 (max) for remaining variables (production function sample). The two samples differ due to missing variables and cleaning procedures for different variables involved. All monetary values are in millions of 1992 U.S. dollars. Sample statistics for general, focused, and intermediate patent stock variables per physical asset are avoided to preserve space. Sample period: 1976-1995.

Table 2. *Correlations and Variance Inflation Factors*

Panel A: Variables in Market Value Regressions										
Variable Name	Abbr.	GPA	FPA	IPA	LCPA	RA	CP		VIF/UR	VIF/R
General Patent Stock/Assets	GPA	1							2,99	2,55
Focused Patent Stock/Assets	FPA	.618	1						3,18	2,53
Interquartile P. Stock/Assets	IPA	.790	.817	1					6,93	-
Low-Cite Patent Stock/Assets	LCPA	.745	.763	.877	1				5,03	3,61
R&D Stock/Assets	RA	.398	.300	.339	.255	1			1,62	1,30
Citation Stock/Patent Stock	CP	.121	.100	.094	-.032	.299	1		1,17	1,15
Panel B: Variables in Productivity Regressions										
Variable Name	Abbr.	GPS	FPS	IPS	LCPS	RS		VIF/UR	VIF/R1	VIF/R2
log (General Patent Stock)	GPS	1						5,59	3,79	3,79
log (Focused Patent Stock)	FPS	.810	1					6,67	4,90	3,22
log (Interquartile P. Stock)	IPS	.894	.903	1				11,24	-	-
log (Low-Cite Patent Stock)	LCPS	.808	.863	.873	1			4,81	4,52	-
log (R&D Stock)	RS	.733	. 716	.747	.697	1		2,50	2,89	2,79

Notes: Patents are classified according to quartiles of the generality distribution. Correlations and VIFs for the classification with respect to lower and upper thirds of the generality distribution are similar and are not reported. VIF is calculated as $1/(1-R^2_{Aux})$, where R^2_{Aux} is the R^2 from an OLS regression where the row variable is regressed on a constant and all remaining independent variables. VIF/UR (Unrestricted) is the variance inflation factor when patent stock in the interquartile range of the generality distribution (IPA) is included and VIF/R (Restricted) is the VIF from the specification that excludes this variable. In Panel B, VIF/R1 excludes the interquartile range patent stock (IPS), and VIF/R2 excludes the low-cite patent stock (LCPS) as well. Based on correlations and variance inflation factors, including IPA in the market value equation significantly increases collinearity among independent variables. A similar situation is observed in the productivity equation (Panel B) for IPS and LCPS. These variables are excluded from their respective baseline specifications to avoid multicollinearity.

4. RESULTS AND DISCUSSION

4.1. Market Value

Estimates of the market value specification in equation (5) are reported in Table 3[7]. Panel A reports coefficient estimates for the case in which general and focused invention stocks are computed using the upper and lower quartiles of generality. We begin by reporting least squares estimates (columns 1 and 2), and then move on to a fixed effects panel specification (column 3). For comparison, the specification in column 1 includes the overall patent stock, while remaining columns introduce general and focused invention stocks separately. All specifications include year and industry dummies[8] except column 3, where industry dummies are differenced out in the fixed effects specification.

Coefficients in column 1 indicate that market value is positively associated with the firm's R&D stock, total patent stock and citation stock. All of these invention indicators have positive associations with market value above and beyond each other. Column 2 replaces the aggregate patent stock with general and focused patent

---

[7] Likelihood Ratio (LR) tests for the presence of time and individual effects all reject the null hypothesis with p < 0.0001.

[8] Industry classification used is due to Hall and Vopel (1997) and it follows the 2-digit SIC classification with some modification.

stocks, as well as the firm's low-cite patent stock. It is observed that both general and focused patents are associated positively with market value with effects that are statistically significant, while the coefficient of focused patent stock (.249) is much larger than that of the general patent stock (.154).

Low-cite patent stock of the firm has a large and negative coefficient (-.320) that is statistically significant, indicating the cost of technological efforts that end up being unimpactful. R&D and citation stock coefficients have comparable magnitudes to their counterparts in column 1. An interesting finding is that the magnitudes of general, focused, and low-cite patent stocks, while in different directions, are of much greater magnitude than the coefficient of the aggregate patent stock term in column 1. This has been common in the literature, i.e., the additional explanatory power of patents above and beyond R&D has been found to be low, which is often interpreted to mean that patenting choices do not contribute to value over and above R&D inputs. However, current analysis show that these studies may be suffering from aggregation bias. Patent heterogeneity matters greatly, and different portions of a firm's patent stock have different roles in creating value for the firm. These distinct effects are lost when one does not pay attention to patent heterogeneity (column 1).

In column 3, we estimate the market value equation (Eq. 5) using fixed-effects least squares. A Hausman test rejects the null hypothesis that individual effects are random ($\chi^2_{26} = 225.7$, $p < 0.0001$). Most importantly, after controlling for permanent firm effects, the coefficient of the firm's focused patent stock remains high and statistically significant, while the sign of the firm's general patent stock becomes negative and insignificant. This indicate that investors reward inventions with more focused and narrow content that will bear short-term gains. Reported estimates in Table 4 allow measuring the value of a focus strategy, by hypothetically changing the nature of an existing patent or a group of patents. According to the difference between the coefficients of focused and general invention stocks (reported as Δ(Focused-General), moving a single patent from the upper tail of the generality distribution to the lower tail results in a $.24 \times q$ million dollars increase in market value (note that q takes values between .08 and 14.77 in the sampke with a mean value of 1.76). The firm with mean general patent stock, then, would gain an additional $6.7 \times q$ million dollars in market value if all its general patents were instead focused in nature, while this number is $27.5 \times q$ million dollars for a firm with a general patent stock that is one standard deviation above the sample average. As expected, accounting for permanent firm effects reduces the coefficient of knowledge assets, and especially that of the R&D stock variable, which is also common in the larger literature.

Column 4 reports between-firm estimates of the market value specification. While these coefficients are inconsistent estimates of the true coefficients in (5), it is useful to see what we can learn by examining the variation *between* firms in addition to the variation *within* firms. Between-firm estimates suggest that the relationship between focused invention stock and market value remains positive and is much stronger in the between dimension. R&D stock has a coefficient comparable to its counterpart from LS regressions (columns 1 and 2), which is expected since most of the variation in R&D is observed between (rather than within) firms.

Panel B in Table 3 estimates the market value equation with general and focused stock variables that are classified using the upper and lower thirds of the relevant generality distribution. Each column in Panel B replicates the results in the column directly above it using this new set of variables. Due to the new partition, the magnitudes of coefficients change, but the basic result remains unaltered. Focused invention stock is positively and strongly associated with market value, with coefficients somewhat smaller than their counterparts in Panel A.[9]

---

[9] Recall that patents that are at the intermediate range of the generality distribution are excluded from all regressions in Table 2 due to a concern for multicollinearity. Results in Table 3 are robust to including a stock variable for these intermediate range patents. These additional estimates are available from the author upon request.

Table 3. *Market Value Regressions. Dependent variable is the logarithm of Tobin's q*

	(1)	(2)	(3)	(4)
	LS	**LS**	**Fixed Effects LS (Within)**	**Fixed Effects LS (Between)**
Panel A: Patents are classified according to the upper and lower quartiles of the generality distribution				
Patent Stock/Assets	0.0128**			
	(2.03)			
General Patent Stock/Assets *Upper quartile*		0.154***	-0.072	0.105
		(3.99)	(-1.46)	(1.05)
Focused Patent Stock/Assets *Lower quartile*		0.249***	0.167***	0.562***
		(5.42)	(3.31)	(4.43)
Low-Cite Patent Stock/Assets		-0.320***	-0.022	-0.334*
		(-4.90)	(-0.25)	(-1.79)
R&D Stock/Assets	0.118***	0.102***	0.038***	0.116***
	(12.01)	(10.07)	(2.76)	(4.86)
Citation Stock/Patent Stock	0.012***	0.012***	0.002***	0.001***
	(23.65)	(22.51)	(3.23)	(7.17)
Δ (Focused - General)		0.104	0.239	0.457
R-squared	0.406	0.409	0.192	0.655
N	10469	10469	10469	10469

		(5)	(6)	(7)
		LS	**Fixed Effects LS (Within)**	**Fixed Effects LS (Between)**
Panel B: Patents are classified according to the upper and lower thirds of the generality distribution				
General Patent Stock/Assets *Upper third*		0.058*	-0.116***	-0.088
		(1.73)	(-2.83)	(-0.97)
Focused Patent Stock/Assets *Lower third*		0.175***	0.121**	0.478***
		(4.24)	(2.55)	(4.31)
Low-Cite Patent Stock/Assets		-0.237***	0.067	-0.168
		(-3.28)	(0.71)	(-0.81)
R&D Stock/Assets		0.110***	0.043***	0.219***
		(10.92)	(3.19)	(9.70)
Citation Stock/Patent Stock		0.012***	0.003***	0.013***
		(22.62)	(3.40)	(9.48)
Δ (Focused - General)		0.117	0.237	0.566
R-squared		0.408	0.191	0.585
N		10469	10469	10469

Notes: Constant terms are not reported. Δ (Focused - General) is the difference in the coefficients of focused and general patent stock terms. LS and between-firm Fixed Effects LS specifications include year and industry dummies (three-digit SIC), and within-firm specifications include year dummies. All logarithms are natural logs. t-statistics are reported in parentheses. Significance indicators: *** p < 0.01, ** p < 0.05, * p < 0.10.

Table 4. Production Function Estimates. Dependent variable is the natural logarithm of sales

	(1)	(2)	(3)	(4)
	Olley and Pakes	LS	Fixed Effects LS (Within)	Blundell and Bond System GMM
log (Employment)	0.524***	0.549***	0.558***	0.567***
	(20.92)	(51.75)	(20.62)	(15.85)
log (Capital)	0.451***	0.437***	0.367***	0.234***
	(16.99)	(48.17)	(16.44)	(7.68)
R-squared		0.967	0.827	
N	8472	8472	8472	7696
Sargan				452.5 (186) [p = 0.00]
Arellano and Bond m1				-9.403 [p=0.000]
Arellano and Bond m2				.0047 [p=0.996]

Notes: Columns 1, 2 and 4 include year and industry dummies (three-digit SIC), and column 3 includes year dummies. All logarithms are natural logs. *t*-statistics are reported in parentheses. Constant terms are not reported.

Column 1: The proxy for unobserved productivity shock is the natural logarithm of current investments. Firm exit is defined as bankruptcy or liquidation.

Column 4: Lags 3 through 5 are used as instruments for both the level and first-differenced equations. Standard errors are from a two-step GMM procedure. Sargan is a test of overidentifying restrictions, i.e., tests the hypothesis that the instrument set is valid conditional on the validity of at least one instrument in the set. Sargan degree of freedom is given in parentheses and p-values are reported in brackets. Arellano and Bond (1991) m1 and m2 are tests for the lack (null hypothesis) of first-order and second-order serial correlation in first-differenced residuals, respectively. These jointly indicate that residuals are not serially correlated after accounting for permanent firm effects. The coefficients and standard errors for lagged sales, employment and capital are not reported in the table. These are 0.647 (28.55) for lagged sales, -0.348 (-9.32) for lagged employment and -0.099 (-3.45) for lagged capital.

Significance indicators: *** $p < 0.01$, ** $p < 0.05$, * $p < 0.10$.

4.2. Total Factor Productivity

We now turn to studying the association between invention indicators of interest and firm-level productivity. To repeat, the effects of general and focused invention on productivity are estimated in two steps. First, we obtain consistent estimates of a standard firm-level Cobb-Douglas production function using the Olley and Pakes (1996) methodology. We then calculate Total Factor Productivity (TFP) for each firm-year as the natural logarithm of (7), and the compounded TFP growth rate in 5-year intervals. We then study the determinants of TFP and its growth rate using standard panel data (for TFP) and least squares (for TFP growth) regressions.

We begin by reporting and discussing estimates of the production function model (6), which are reported in Table 4. Column 1 of the table reports estimates obtained by the preferred Olley and Pakes (1996) methodology. For comparison, we also report coefficient estimates using methods that are commonly employed in production function estimation. Column 2 reports LS estimates of production function coefficients, column 3 uses fixed-effects LS, and column 4 uses the system-GMM methodology due to Arellano and Bond (1991) and Blundell and Bond (2000).

The estimated coefficients of capital and labor in Table 4 are in line with expectations. Endogeneity and selection biases that remain unchecked are expected to create a downward bias in the coefficient of capital,

and an upward bias in the coefficient of labor. Compared to column 1, columns 2, 3 and 4 exhibit lower coefficients for capital and higher coefficients for labor. Assuming that estimates reported in column 1 are consistent, the difference between an estimate and the coefficient estimate in this column is a measure of bias in estimated effects. We can thus see that the bias in both coefficients increase as one moves (i) from LS to fixed-effects, and (ii) from fixed-effects to system-GMM. The former point (i) suggests that productivity shocks are not time-invariant and cannot be accounted for by employing differencing. The latter (ii) is expected if lagged levels and differences of endogenous variables are not valid instruments. In the current exercise, finding instruments that are irrefutably valid in system-GMM estimation proves to be infeasible according to the Sargan test of overidentifying restrictions ($\chi^2_{(186)} = 452.2$ with $p = 0.00$ for the set of instruments reported in column 4). The coefficient of capital is particularly low in column 4, which indicates that lagged capital adjustments are not valid instruments for the current level of capital. This is usual for persistent variables such as capital or R&D stocks, and the system-GMM methodology does not resolve the problem in the current case.

Total Factor Productivity is calculated according to equation (7) using the preferred Olley and Pakes (1996) estimates reported in column 1 of Table 4. Figure 1 gives the histogram of estimated Total Factor Productivity and its logarithm for the sample used in productivity analysis. The logarithm of TFP gives a distribution that is slightly asymmetric and clearly non-normal, as indicated by the Jacque-Bera test for normality ($p < 0.0001$). Note that normality of (log) TFP is not required for the following analysis. We expect this variable to be skew, due to survival bias, i.e., that we are less likely to see firms with bad realizations for productivity in the sample.
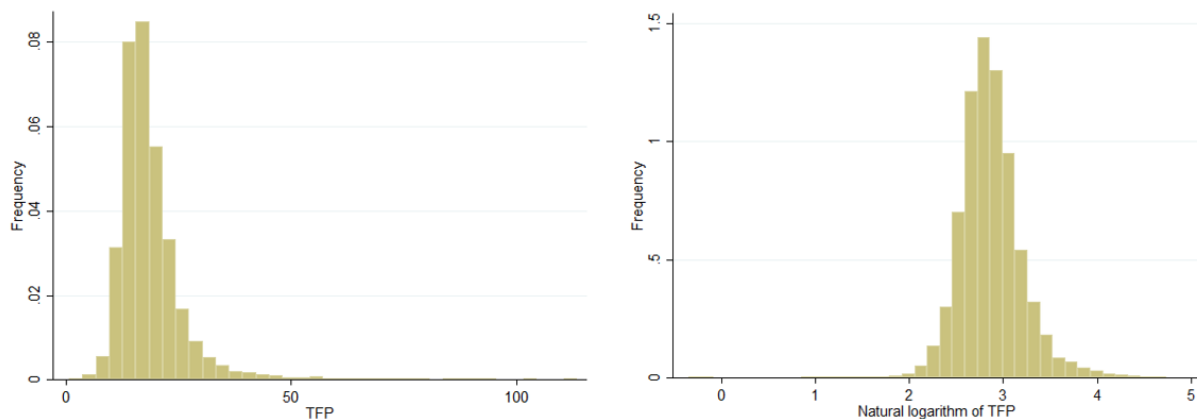
Figure 1. *The distribution of estimated Total Factor Productivity (left panel) and its logarithm (right panel)*

Table 5 turns to the analysis of the determinants of firm-level productivity. The distinction between results in Panel A and Panel B is similar to that in Table 3, and each column in Panel B is comparable the one directly above it. Before estimation, observations with *annual* log TFP growth outside $[-1,1]$ are deleted, as these may represent outliers. The sample used in Table 5 is also smaller than previously used samples due to missing variables for R&D and patent stock variables.[10]

When one is dealing with the *level* of Total Factor Productivity (columns 1,2 and 6), a fixed effects specification that removes the permanent component of TFP is preferred, since the productivity level can easily be linked to unobserved and permanent differences among firms which need to be accounted for. The Hausman test also strongly rejects the null hypothesis that individual effects are random ($\chi^2_{19} = 490.71$, $p < 0.0001$). The fixed-effects estimation links the deviation of productivity from its average to the deviation of knowledge assets from their own averages. This is also preferred to studying a first-differenced specification (i.e., examining the annual compounded growth rate of TFP) since it is difficult to link annual changes in productivity to its correlates, i.e., one year is likely too short to large productivity effects. Simple LS regression

---

[10] Similar to Market Value regressions, Likelihood Ratio (LR) tests for the nested models indicate that both individual fixed effects and time effects are present in the *level* of TFP, with $p < 0.0001$.

is preferred for the analysis of TFP growth, since the fixed effects specification is too demanding, as well as unnecessary, for a variable that is already constructed as a growth rate, i.e., is already in differenced form.

We begin with estimating a specification that takes the logarithm of TFP as the dependent variable, and invention indicators as independent variables. These estimates are reported in columns 1 and 2 of Table 5. Column 1 includes the firm's total R&D and patent stocks, as well as year dummies as independent variables, while column 2 replaces the total patent stock with its general and focused components. Not surprisingly, both the R&D and aggregate patent stock of the firm are positively associated with productivity. Column 2 replaces the patent stock variable with its general and focused components. According to these estimates, the firm's general patent stock has a positive effect on productivity that is statistically significant. On the other hand, focused patent stock does not have a statistically significant coefficient. It is also interesting to note that almost all of the explanatory power provided by the patent stock variable (column 1) is in fact explained by patents at the upper tail of generality (column 2).

It is useful to compare these findings with those from market value regressions (Table 3). It is seen that different portions of a firm's patent stock have different effects on market value and productivity. The market mechanism places value on the focused portion of the firm's patent portfolio more strongly, while the general patent stock is more strongly associated with productivity. The difference in coefficient estimates of general and focused patent stocks (Δ(General - Focused)) in column 2 indicates that the average firm would gain an approximately 0.23% increase in productivity if 10% of its patents at the lower tail of the generality scale were moved to the upper tail. The same figure implied by estimates in Panel A (column 6) is a bit higher, at 0.28%. These estimates imply that the productivity effect of moving all focused patents of the average firm to the general category would have a productivity effect that ranges between 2.3% and 2.8%.

Columns 3 through 5 in Table 5 use the five-year compounded TFP growth rate as dependent variable. The sample consists of the four non-overlapping five-year intervals between 1976 and 1995. Figure 2 gives the distribution of five-year TFP growth. Mean productivity growth in the sample over five-year intervals is 0.0874 (8.74%). This variable is expected, and indeed observed to be skewed as well, due to the same survival bias with respect to productivity. To analyze the correlates of this variable, and avoid endogeneity issues, all independent variables are measured at the beginning of the relevant five-year window. In column 3, it is observed that R&D stock is positively related to TFP growth. However, patent stock has no additional effect above and beyond that of R&D. Similar to the market value estimates in Table 3, a low productivity estimate for the overall patent stock term (column 3) is observed to hide the separate and significant effects of its components (columns 4 and 5). In column 4 we replace the aggregate patent stock with general and focused patent stocks and find that the two types of patents have different relationships with productivity. General patent stock at the beginning of a period has a positive effect on productivity growth during the ensuing five years (coefficient is .197 and statistically significant). On the other hand, focused patent stock at the beginning of the period obtains a negative coefficient. When the R&D term is excluded and only patent-related measures are included (column 5), the negative effect of the focus patent stock disappears, and the coefficient of general patent stock increases. These set of results support and complement those found in TFP regressions reported in column 2.

Finally, we replicate the analyses in Panel A with the classification that uses thirds (instead of quartiles) of the relevant generality distribution. All columns in Panel B replicate the model directly above using these new set of invention indicators. Coefficient estimates are larger in magnitude to their counterparts in Panel A, but main results remain unchanged. Estimates reported in Table 5 indicate that moving 10% of a firm's focused patents to the upper tail of the generality distribution would lead to 0.39% (column 4) to 0.52% (column 8) increase in productivity growth during the following five years, on average. In terms of the productivity effect of the average firm's entire patent cohort, moving all of the average firm's focused patents to the general category would increase five-year productivity growth by 3.9% to 5.2%.

Table 5. *Total Factor Productivity Regressions*

	Natural logarithm of TFP (From Table 4, Column 1)		5-year compounded TFP growth (Independent variables are lagged 5 years)		
Panel A: Patents are classified according to the upper and lower quartiles of the generality distribution					
	(1)	(2)	(3)	(4)	(5)
	Fixed Effects LS	Fixed Effects LS	LS	LS	LS
log (Patent Stock)	0.0191***		-0.0080		
	(3.49)		(-1.03)		
log (General Patent Stock) *Upper quartile*		0.0181***		0.0197**	0.0243***
		(4.12)		(2.29)	(3.11)
log (Focused Patent Stock) *Lower quartile*		-0.0051		-0.0191**	-0.0153
		(-1.08)		(-2.26)	(-1.92)
log (R&D Stock)	0.0350***	0.0367***	0.0138**	0.0080	
	(6.70)	(7.17)	(2.25)	(1.29)	
Δ (General - Focused)		0.0232		0.0388	0.0396
R-squared	0.312	0.313	0.007	0.0122	0.0106
N	7258	7258	972	972	1027
Panel B: Patents are classified according to the upper and lower thirds of the generality distribution					
		(6)		(7)	(8)
		Fixed Effects LS		LS	LS
log (General Patent Stock) *Upper third*		0.0208***		0.0251***	0.0307***
		(4.24)		(2.66)	(3.60)
log (Focused Patent Stock) *Lower third*		-0.0075		-0.0239***	-0.0214**
		(-1.49)		(-2.68)	(-2.50)
log (R&D Stock)		0.0366***		0.0075	
		(7.11)		(1.21)	
Δ (General - Focused)		0.0283		0.0490	.0521
R-squared		0.313		0.0143	0.0136
N		7258		972	1027

Notes: Constant terms are not reported. Total Factor Productivity is calculated using production function coefficients given in Table 4, column 1 (Olley and Pakes methodology). Δ (General - Focused) is the difference in the coefficients of general and focused patent stock terms. All Fixed Effects LS specifications (1, 2 and 6) include year dummies. 5-year TFP growth regressions (3, 4, 5, 7 and 8) use 5-year lagged values of all independent variables, and the sample consists of the years 1995, 1990, 1985 and 1980. All logarithms are natural logs. *t*-statistics are reported in parentheses. Significance indicators: *** $p < 0.01$, ** $p < 0.05$, * $p < 0.10$.
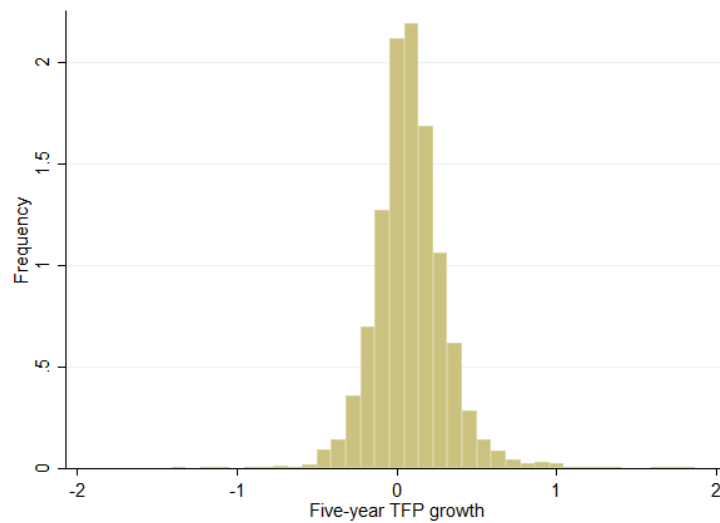
Figure 2. The distribution of five-year Total Factor Productivity growth

5. CONCLUSION

This paper has studied the association of general purpose and focused invention at the firm level, with firm market value, productivity, and productivity growth. Valuation and productivity estimation frameworks have been employed at the firm level in relation to the traded market value and the Total Factor Productivity of the firm, by also distinguishing the two types of invention among the firm's patents. Examining corporate patenting with respect to its heterogeneity in generality is shown to be empirically valuable and informative. In line with expectations, there is a market value premium to a firm's focused, and a productivity premium to its general purpose invention activity. That is, market value is most immediately linked to aspects of innovation that signal short-term commercial potential, but such activity exhibits a weaker relationship with productivity. On the other hand, invention in general purpose technologies as part of corporate R&D is associated with longer-term benefits in terms of productivity growth. This is intuitive since general-purpose technologies offer wider varieties of commercialization opportunities, which are reflected in firm-level productivity, even though such benefits are expected to come later and are not priced by the market quickly. The valuations and estimates produced by the analysis are important for decision making as they shed light on the nature of the trade-off between research efforts that are geared towards general vs. more specific and focused areas.

While we do not directly observe basic research expenditures at the firm level, there is extensive evidence showing that patent generality is correlated with the closeness of the embedded knowledge to basic science (Trajtenberg et al., 1997; Henderson et al., 1998; Schmid & Fajebe, 2019). In this sense, results of the paper speak indirectly of corporate basic science and point to the existence of large long-term benefits to corporate basic science in terms of productivity growth, potentially compensating for deferring immediate gains of a more focused strategy.

Recall that all estimates that are presented in the paper are of *private*, and not *social* returns to inventive activity. Estimates of social returns would require measurements of the relevant spillover effects, which differ for general purpose and focused technologies (Akcigit et al., 2021). Further studies of such differences in the spillover potential, as well as in the social returns to different types of inventive activity are promising areas for future work.

While the study period is a bit dated, it is a period that has witnessed significant technological change as well as the creation of new technological fields and industries. Estimates and valuations produced for this period, while calling for more recent analysis, are useful for understanding returns to inventive activity, which can further guide management decisions at the firm level as well as the policy choices of governing bodies.

CONFLICT OF INTEREST

The author declares no conflict of interest.

REFERENCES

Akcigit, U., Hanley, D., & Serrano-Velarde, D. (2021). Back to Basics: Basic Research Spillovers, Innovation Policy, and Growth. *The Review of Economic Studies*, 88(1), 1–43. https://doi.org/10.1093/restud/rdaa061

Arellano, M., & Bond, D. (1991) Some Tests of Specification for Panel Data: Monte Carlo Evidence and an Application to Employment Equations. Review of Economic Studies, 58(2), 277-297. https://doi.org/10.2307/2297968

Arora, A., Belenzon, S., Patacconi, A. (2018). The decline of science in corporate R&D. Strategic Management Journal, 39(1), 1-266. https://doi.org/10.1002/smj.2693

Arora, A., Belenzon, S., & Sheer. L. (2021). Knowledge spillovers and corporate investment in scientic research. American Economic Review, 111(3), 871-898. https://doi.org/10.1257/aer.20171742

Arora, A., Belenzon, S., Dionisi, B. (2023). First-mover advantage and the private value of public science. Research Policy, 52, 104867. https://doi.org/10.1016/j.respol.2023.104867

Barirani, A., Beaudry, C., & Agard, N. (2015). Distant recombination and the creation of basic inventions: An analysis of the diffusion of public and private sector nanotechnology patents in Canada. Technovation, 36-37, 39-52. https://doi.org/10.1016/j.technovation.2014.10.002

Bartelsman, E., Haltiwanger, J., & Scarpetta, S. (2013). Cross-Country Differences in Productivity: The Role of Allocation and Selection. American Economic Review, 103(1), 305-334. https://doi.org/10.1257/aer.103.1.305

Belenzon, S. (2012). Cumulative Innovation and Market Value: Evidence from Patent Citations. Economic Journal, 122, 265-285. https://doi.org/10.1111/j.1468-0297.2011.02470.x

Bessen, J. (2009). NBER PDP Project User Documentation: Matching Patent Data to Compustat Firms. Unpublished manuscript.

Bloom, N., Schankerman, M., & Reenen, J.V. (2013). Identifying Technology Spillovers and Product Market Rivalry. Econometrica, 81(4), 1347-1393. https://doi.org/10.3982/ecta9466

Blundell, R., Griffith, R., & Reenen, J.V. (1999). Market Share, Market Value and Innovation in a Panel of British Manufacturing Firms. Review of Economic Studies, 66(3), 529-554. https://doi.org/10.1111/1467-937x.00097

Blundell R., & Bond, S. (2000). GMM Estimation with Persistent Panel Data: An Application to Production Functions. Econometric Reviews, 19(3), 321-340. https://doi.org/10.1080/07474930008800475

Bolívar-Ramos, M.T. (2023). The impact of corporate science on environmental innovations: the role of universities and research institutions. R&D Management, 53(3), 503-523. https://doi.org/10.1111/radm.12574

Camerani, R., Rotolo, E. (2023). Is corporate basic science growing or declining? In: 27th International Conference on Science, Technology and Innovation Indicators (STI 2023). https://doi.org/10.55835/6442bcd51194fc7a73b429f5

Ceccagnoli, M., Lee, Y-N., Walsh, J.P. (2024). Reaching beyond low-hanging fruit: Basic research and innovativeness. Research Policy, 53, 104912. https://doi.org/10.1016/j.respol.2023.104912

Chen, X., Mao, J., Ma, Y., Li, G. (2024). The knowledge linkage between science and technology influences corporate technological innovation: Evidence from scientific publications and patents. Technological Forecasting and Social Change, 198, 122985. https://doi.org/10.1016/j.techfore.2023.122985

Choi, J-U., Lee, C-Y. (2022). The differential effects of basic research on firm R&D productivity: The conditioning role of technological diversification. Technovation, 118, 102559. https://doi.org/10.1016/j.technovation.2022.102559

Coad, A., Segarra-Blasco, A., & Teruel, M. (2021), A bit of basic, a bit of applied? R&D strategies and firm performance. Journal of Technology Transfer, 46, 1758-1783. https://doi.org/10.1007/s10961-020-09826-1

Cockburn, I., & Griliches, Z. (1987). Industry Effects and Appropriability Measures in Stock Market's Valuation of R&D and Patents. NBER Working Paper No. 2465. https://doi.org/10.3386/w2465

Crass, D., & Peters, B. (2014). Intangible Assets and Firm-Level Productivity. ZEW Discussion Paper No.14-120. https://doi.org/10.2139/ssrn.2562302

Crépon, B., Duguet, E., & Mairesse, J. (1998). Research, Innovation, and Productivity: An Econometric Analysis at the Firm Level. Economics of Innovation and New Technology, 7(2), 115-158. https://doi.org/10.1080/10438599800000031

Czarnitzki, D., & Thorwarth, S. (2012). Productivity effects of basic research in low-tech and high-tech industries. Research Policy, 41, 1555-1564. https://doi.org/10.1016/j.respol.2012.04.009

Dean, T., Zhang, H., Xiao, Y. (2022). The role of complexity in the Valley of Death and radical innovation performance. Technovation, 109, 102160. https://doi.org/10.1016/j.technovation.2020.102160

Dindaroglu, B. (2014). Scientific Labor Mobility, Market Value, and Knowledge Flows. MPRA Working Paper No. 88043.

Doraszelski, U., & Jaumandreu, J. (2013). R&D and Productivity: Estimating Endogenous Productivity. Review of Economic Studies, 80, 1338-1383. https://doi.org/10.1093/restud/rdt011

Ernst, H. (1998). Industrial research as a source of important patents. Research Policy, 27, 1-15. https://doi.org/10.1016/s0048-7333(97)00029-2

Filippova, E. (2019). Empirical Evidence and Economic Implications of Blockchain as a General Purpose Technology. In: 2019 IEEE Technology & Engineering Management Conference (TEMSCON), Atlanta, GA (pp. 1-8). https://doi.org/10.1109/TEMSCON.2019.8813748

Gómez-Baquero, F. (2009). Measuring the generality of nanotechnologies and its potential implications. In: 2009 Atlanta Conference on Science and Innovation Policy, Atlanta, GA (pp. 1-9). https://doi.org/10.1109/acsip.2009.5367858

Greenhalgh, C., & Longland, M. (2005). Running to Stand Still? - The Value of R&D, Patents and Trade Marks in Innovating Manufacturing Firms. International Journal of the Economics of Business, 12(3), 307-328. https://doi.org/10.1080/13571510500299326

Griffith, R., Huergo, E., Mairesse, & J., Peters, B. (2006). Innovation and Productivity Across Four European Countries. Oxford Review of Economic Policy, 22, 483-498. https://doi.org/10.1093/oxrep/grj028

Griliches, Z. (1963). The Sources of Measured Productivity Growth: United States Agriculture, 1940-60. Journal of Political Economy, 71(4), 331-346. https://doi.org/10.1086/258782

Griliches, Z. (1979). Issues in Assessing the Contribution of R&D to Productivity Growth. Bell Journal of Economics, 10(1), 92-116. https://doi.org/10.2307/3003321

Griliches, Z. (1981). Market Value, R&D, and Patents. Economics Letters, 7, 181-187. https://doi.org/10.1016/0165-1765(87)90114-5

Griliches, Z. (1986). Productivity, R and D, and Basic Research at the Firm Level in the 1970's. NBER Working Paper No: 1547. https://doi.org/10.3386/w1547

Griliches, Z. (1988). Productivity Puzzles and R & D: Another Nonexplanation. Journal of Economic Perspectives, 2(4), 9-21. https://doi.org/10.1257/jep.2.4.9

Griliches, Z. (1998). Patent Statistics as Economic Indicators: A Surveyç In: Z. Griliches (Ed.), R&D, patents, and productivity. University of Chicago Press, Chicago, IL. 287-343. https://doi.org/10.7208/chicago/9780226308920.001.0001

Guo, Y., Gao, P., & Cheng, D. (2022). The Effects of R&D and its Different Types on Firm Productivity: Evidence from China. International Journal of Innovation Management, 26(08), 2250065. https://doi.org/10.1142/s1363919622500657

Jefferson, G.H., Huamao, B., Xiaojing, G. & Xiaoyun, Y. (2006). R&D Performance in Chinese industry. Economics of Innovation and New Technology, 15, 345-366. https://doi.org/10.1080/10438590500512851

Hall, B.H. (2011). Innovation and Productivity. NBER Working Paper No. 17178. https://doi.org/10.3386/w17178

Hall, B.H., & Oriani, R. (2006). Does the Market Value R&D Investments by European Firms? Evidence From a Panel of Manufacturing Firms in France, Germany, and Italy. International Journal of Industrial Organization, 24, 971-993. https://doi.org/10.1016/j.ijindorg.2005.12.001

Hall, B.H., & Trajtenberg, M. (2004). Uncovering GPTS with Patent Data. NBER Working Paper No. 10901. https://doi.org/10.3386/w10901

Hall, B.H., & Vopel, K. (1997). Innovation, Market Share, and Market Value. Unpublished manuscript.

Hall, B.H., Jaffe, A., & Trajtenberg, M. (2001). The NBER Patent Citations Data File: Lessons, Insights and Methodological Tools. NBER Working Paper No.8498. https://doi.org/10.3386/w8498

Hall, B.H., Jaffe, A., & Trajtenberg, M. (2005). Market value and patent citations. RAND Journal of Economics, 36(1), 16-38.

Hall, B.H., Mairesse, J., & Mohnen, P. (2010). Measuring the Returns to R&D. In: Hall, B.H., & Rosenberg, N. (Eds.), Handbook of the Economics of Innovation, Vol. 2 (pp. 1033-1082). https://doi.org/10.1016/s0169-7218(10)02008-3

Harhoff, D. (1998). R&D and productivity in German manufacturing firms. Economics of Innovation and New Technology, 6(1), 29-49. https://doi.org/10.1080/10438599800000012

Henderson, R., Jaffe, A.B., & Trajtenberg, M. (1998). Universities as a Source of Commercial Technology: A Detailed Analysis of University Patenting. The Review of Economics and Statistics, 80(1),119-127. https://doi.org/10.1162/003465398557221

Jaffe, A.B. (1986). Technological Opportunity and Spillovers of R&D: Evidence From Firms' Patents, Profits, and Market Value. The American Economic Review, 76, 984-1001.

Krieger, J.L., Pellens, M., Blind, K., Gruber, S., Schubert, T. (2021). Are firms withdrawing from basic research? An analysis of firm-level publication behaviour in Germany. Scientometrics, 126, 9677-9698. https://doi.org/10.1007/s11192-021-04147-y

Krieger, J.L., Schnitzer, M., Watzinger, M. (2022). Standing on the shoulders of science. Harvard Business School Working Paper 21-128.

Leten, B., Kelchtermans, S., & Belderbos, R. (2022). How does basic research improve innovation performance in the world's major pharmaceutical firms? Industry and Innovation, 29(3), 396-424. https://doi.org/10.1080/13662716.2021.1997723

Lichtenberg, F.R., & Siegel, D.S. (1991). The Impact of R&D Investment on Productivity-New Evidence Using Linked R&D-LRD Data. Economic Inquiry, 29, 203-228. https://doi.org/10.1111/j.1465-7295.1991.tb01267.x

Link, A.N. (1981). Basic research and productivity increase in manufacturing: some additional evidence. American Economic Review, 71(5) 1111-1112.

Lychagin, S., Pinske, J., Slade, M.E., & Reenen, J.V. (2016). Spillovers in Space: Does Geography Matter? The Journal of Industrial Economics, 64/2: 295-335. https://doi.org/10.1111/joie.12103

Mairesse, J., & Sassenou, M. (1991). R&D and productivity: a survey of econometric studies at the firm level. NBER Working Paper No. 3666. https://doi.org/10.3386/w3666

Martinelli, A., Mina, A., & Moggi, M. (2021). The enabling technologies of industry 4.0: examining the seeds of the fourth industrial revolution. Industrial and Corporate Change, 30(1), 161-188. https://doi.org/10.1093/icc/dtaa060

Megna, P., & Klock, M. (1993). The Impact of Intangible Capital on Tobin's q in the Semiconductor Industry. American Economic Review Papers and Proceedings, 83(2), 265-269.

Moser, P., & Nicholas, T. (2004). Was Electricity a General Purpose Technology? Evidence from Historical Patent Citations. American Economic Review Papers and Proceedings, 94(2), 388-394. https://doi.org/10.1257/0002828041301407

Mowery, D.C., & Ziedonis, A.A. (2002). Academic patent quality and quantity before and after the Bayh–Dole act in the United States. Research Policy, 31, 399-418. https://doi.org/10.1016/s0048-7333(01)00116-0

Olley, G.S., & Pakes, A. (1996). The Dynamics of Productivity in the Telecommunications Industry. Econometrica, 64(6), 1263-1297. https://doi.org/10.2307/2171831

Petralia, S. (2020). Mapping general purpose technologies with patent data. Research Policy, 49, 104013. https://doi.org/10.1016/j.respol.2020.104013

Raiteri, E. (2018). A time to nourish? Evaluating the impact of public procurement on technological generality through patent data. Research Policy, 47, 936-952. https://doi.org/10.1016/j.respol.2018.02.017

Rotolo, D., Camerani, R., Grassano, N., & Martin, B.R., (2020). Why do firms publish? A systematic literature review and a conceptual framework. Research Policy, 51, 104606. https://doi.org/10.1016/j.respol.2022.104606

Sampat, B.N., Mowery, D.C., & Ziedonis, A.A. (2003). Changes in university patent quality after the Bayh–Dole act: a re-examination. International Journal of Industrial Organization, 21, 1371-1390. https://doi.org/10.1016/s0167-7187(03)00087-0

Sandner, P.G., & Block, J. (2011). The market value of R&D, patents and trademarks. Research Policy, 40, 969-985. https://doi.org/10.1016/j.respol.2011.04.004

Shvadron, D. (2023). Bread Upon the Waters: Corporate Science and the Benefits from Follow-On Public Research. Unpublished manuscript.

Serrano, C.J. (2010). The dynamics of the transfer and the renewal of patents. RAND Journal of Economics, 41(4), 686-708. https://doi.org/10.1111/j.1756-2171.2010.00117.x

Schmid, J., & Fajebe, A. (2019). Variation in patent impact by organization type: An investigation of government, university, and corporate patents. Science and Public Policy, 46(4), 589–598. https://doi.org/10.1093/scipol/scz010

Trajtenberg, M., & Henderson, R. (1997). University versus Corporate Patents: A Window on the Basicness of Invention. Economics of Innovation and New Technology, 5(1), 19-50. https://doi.org/10.1080/10438599700000006

Wen, K. (2023) Accelerating Efforts to Improve Policy System to Support Basic Research in Enterprises. Bulletin of Chinese Academy of Sciences. 38(4), Article 9. https://doi.org/10.16418/j.issn.1000-3045.20230220003

Yang, R., Wu, Q., Xie, Y. (2023). Are scientific articles involving corporations associated with higher citations and views? an analysis of the top journals in business research? Scientometrics, 128, 5659-5685. https://doi.org/10.1007/s11192-023-04808-0

Yasar, M., Raciborski, R., & Poi, B. (2008). Production function estimation in Stata using the Olley and Pakes method. The Stata Journal, 8(2), 221-231. https://doi.org/10.1177/1536867x0800800204

Youtie, J., Iacopetta, M., & Graham, S. (2008). Assessing the Nature of Nanotechnology: Can We Uncover an Emerging General Purpose Technology. Journal of Technology Transfer, 33, 315-329. https://doi.org/10.1007/s10961-007-9030-6

Zhao, Q., Luo, Q., Tao, Y. (2023a). The power of paper: Scientific disclosure and firm innovation. Finance Research Letters, 56, 104147. https://doi.org/10.1016/j.frl.2023.104147

Zhao, Q., Luo, Q., Zhao, X., Yu, Y. (2023b). Corporate key labs: Breakthrough or White elephant? China Economic Review, 79, 101954. https://doi.org/10.1016/j.chieco.2023.101954

Kinetics of Nonenzymatic Browning Reactions in Pumpkin Puree During Storage

Feryal KARADENİZ[1]*   Betül IŞIK[1]   Soner KAYA[1]   Osman ASLANALİ[1]   Fatma MİDİLLİ[1]

[1] Göknur Gıda R&D Center, Yeni Mahalle, Kayseri Caddesi No:32, Merkez-Niğde, Türkiye

Keywords	Abstract
Pumpkin Puree Kinetics HMF Browning Color Storage	Pumpkins (*Cucurbita moschata*) are a great source of essential nutrients counting vitamins, minerals, carotenoids, and dietary fiber. Due to their healthy composition, it draws consumer attention. Pumpkin puree is used for preparation of baby foods, soups, flour, jam, jellies, and desserts. To assess the main quality parameters of the foods such as color and hydroxymethylfurfural (HMF) formation, CIE-L*a*b* color changes and HMF formation which is also an indicator of Maillard browning reactions were evaluated storing the pumpkin puree at 27°, 37° and 47°C for 17 weeks. Kinetic parameters for HMF formation and color changes were calculated. The findings showed that HMF quantity linearly increased with the temperature and storage duration following the reaction model of zero order. The values of b* coordinate, Lightness, Chroma, and hue lessened linearly as a* coordinate values increased linearly fitting zero order reaction kinetic. By means of Arrhenius equation, the temperature dependency of the rate constant of color variation was demonstrated and the values of the activation energy (kj mol^{-1}) were calculated as 76.15, 30.60, 46.08, 28.44, 27.61 and 38.32 for HMF formation, Lightness, a* coordinate, b* coordinate, Chroma, and hue, respectively.

1. INTRODUCTION

Pumpkin, a member of the Cucurbitaceae family covering different species e.g. *Cucurbita moschata, Cucurbita maxima* and *Cucurbita pepo,* is widely grown plant particularly in China, India, Russia, Ukraine, United States of America, Egypt, Mexico, Italy, Spain, and Türkiye. Pumpkin, squash, and gourds production in the world was 23.783.936,41 tons, and harvested area was 1.501.696 ha, while Türkiye's production was 771.651,00 tons, and harvested area was 100.853 ha in the year of 2021 (Kulczynski et al., 2020; FAOSTAT, 2023).

Carotenoids, including lutein and β-carotene, as well as minerals, and vitamins C, B6, thiamine, K, and riboflavin are abundant in this orange-colored and fibrous vegetable. Pumpkin also contains a lot of dietary polyphenols, which have been exemplified to have neuroprotective, chemo preventive, antioxidant, and anti-inflammatory features. Thus, it is considered as a healthy nutrient for adults and children and may be consumed directly or used in a variety of meal preparations. Several types of phytochemicals, involving phenolics, carotenoids, tocopherols, phytosterols, cucurbitacin etc. were detected in the examination of pumpkin fractions. The seeds, peel, and flesh comprise of different ingredients which play an active role as antioxidant and antimicrobial agents in a therapeutic way (Hussain et al., 2022). There are many different countries that benefit from pumpkin as medicine in China, Argentina, Yugoslavia, Mexico, India, America, and Brazil given that its high nutritional value and easing capability of hypertension, diabetes, and liver diseases' symptoms (Kulczynski et al., 2020). Adams et al. (2011) stated that pumpkins also have hypoglycemic impacts.

Furthermore, some related studies have demonstrated that *Cucurbita moschata* is potentially able to encourage the effects of anti-obesity, anti-diabetic, anti-cancer, and antibacterial (Men et al**.,** 2021).

For the last years, there has been much research conducted on pumpkins and pumpkin based products, such as oil content and composition of pumpkin seeds (Fedko et al., 2020), pumpkin based probiotic beverage (Koh et al., 2018), air drying and kinetic behavior of pumpkins (Guine et al., 2012). Effects of butternut fibres acquired from *C. moschata* on bread production was studied and reported that adding fiber ranging from 5 to 15 grams to 1 kilogram wheat flour can be promising to enhance the structure of the bread following baking process and through storage (de Escalada Pla et al**.,** 2013). Aziz et al. (2023) stated that pumpkin flour might also promote the way of gluten working in the dough such as assisting the rise of the bread and stabilization of the gas cell texture.

On the other hand, browning is among the greatest quality issues observed throughout food processing and its storage. The formation of browning in processed foods is primarily based on the nonenzymatic browning reactions which includes Maillard reaction, caramelization, and the degradations of pigment and ascorbic acid (Cornwell & Wrolstad, 1981). Reducing sugars and α-amino groups are responsible for the first stage of the Maillard reaction (Buedo et al., 2000), which is unfavorable for concentrated or dried foods (Burdurlu & Karadeniz, 2003; Koca et al., 2007), respectively. HMF, a sign of the intensity of applied heat treatment, is also known to take place through the Maillard reaction (Lee & Nagy, 1988).

As consumers' preferences are shaped with the quality and appearance of the foods, process and storage circumstances of a food product should be necessarily controlled. Many researchers have investigated the kinetics mechanism of chemical browning reactions (Toribio & Lozano, 1984; Beveridge & Harrison, 1984; Burdurlu & Karadeniz, 2003; Özhan et al., 2010). Peroxidases and polyphenol oxidases leading to browning, become inactivated enzymes during heat application, otherwise there are various other nonenzymatic paths that cause to color changes in the food along storage, for example, phenolic compounds and carotenoids degradation. The primary carotenoids obtained from pumpkin e.g. lutein, β-carotene, and α-carotene oversee the pumpkin-based products' color. Therefore, all aspects regarding the color loss of pumpkin based products should be examined because color retention is a significant attributor of product quality during storage and carotenoids are not stable at high temperatures. There are few research available reviewing the manufacture of pumpkin puree and the stability of quality parameters throughout its storage (Provesi et al., 2012).

For this reason, kinetic models of the reactions are required to optimize processing and storage conditions and to estimate optimum shelf life of the pumpkin puree. The kinetic parameters like rate constant, reaction order, and activation energy ensure beneficial data both on the quality changes arising from heat treatment applied (Dutta et al., 2006) and on the shelf-life determination of foods through different storage conditions. This investigation aims to specify the kinetics of nonenzymatic browning occurred in pumpkin puree by measuring both HMF content and the values of CIE L*, a*, b*, Chroma (C), and hue (h) during storage at 27°, 37°, and 47°C and to define the correlation among the data obtained from each parameters analyzed.

2. MATERIAL AND METHOD

2.1. Materials

Pumpkins *(C. moschata)* were supplied by local farmers at Niğde and processed into pumpkin puree at Göknur Gıda A.Ş. fruit and vegetable concentrate production factory. According to the process flow diagram, pumpkins were washed, sliced, deseeded, steamed, crushed, heat treated at 95°C for 3 minutes, passed through 2 consecutive screens that are 1.2 mm and 0.8 mm, respectively.

Citric acid was added to prevent enzymatic browning reactions. Pumpkin puree was filled into pouches and capped hermetically before pasteurization applied at 96°C for 15 minutes. Then, it was cooled until reaching to room temperature by applying cold water with ice. This process is repeated for the preparation of replicate samples. Prepared samples were put into incubators as replicated sets at 27°, 37° and 47°C.

Randomly selected replicate samples were taken on weekly basis from 47°C incubator, on two weeks basis from 37°C incubator, for 3 weeks basis from 27°C incubator and analyzed in respect of HMF amount and CIE L*a*b* color indices for the evaluation of nonenzymatic browning reaction in pumpkin puree. Pumpkin

purees were also analyzed for titratable acidity (%, citric acid), total soluble solids, and pH to determine the physicochemical properties of the samples.

2.2. Methods

2.2.1. Chemicals

Merck (Germany) was the supplier for all analytical-grade chemicals utilized in this investigation.

2.2.2. Physical and Chemical Analysis

2.2.2.1. Titratable Acidity, Total Soluble Solids (TSS, Bx), and pH

TSS was analyzed at 20°C using ATAGO refractometer (RX-5000α, Atago Co., Ltd., Japan). The distilled water diluted pumpkin puree samples (1:1, v/v) were subjected to pH analysis at 20°C by a pH meter (Mettler-Toledo GmbH, Switzerland). Titratable acidities were analyzed by potentiometric method using the same pH meter by water dilution of the puree samples as (1:1, v/v) and reported as % anhydrous citric acid. Each sample was measured in triplicate.

2.2.2.2. Color Measurement

Color changes in pumpkin puree were determined with the help of Minolta CR-300 reflectance colorimeter (Osaka, Japan). The calibration of the device was performed on a white colored ceramic reference plate before starting the analysis. A glass cell was used in the filling of pumpkin puree samples, and the samples were directly measured without any other treatment. Lightness (L*), a* and b* coordinates, Chroma (C) and hue (h) values were noted. Three evaluations were conducted for each sample.

2.2.2.3. Hydroxymethylfurfural (HMF) Analysis

The amount of HMF in stored pumpkin purees was quantitatively defined by reference to the procedure expressed by Anonymous (1984), which is associated with the colorimetric reaction occurred among barbituric acid, p-toluidine, and HMF generating a red complex. Since red intensity depends on the HMF quantity, the analysis of HMF was implemented by reading the red color at 550 nm with a Spectrophotometer (UV mini-1240 UV-VIS Spectrophotometer, Schimadzu Corp. Kyoto-Japan).

2.2.2.4. Calculation of Kinetic Parameters

The alterations in HMF and CIE-L*a*b* color parameters of pumpkin puree were analyzed through the standard equation for a reaction model of zero-order that means HMF and product's brown color linearly rises with time, described below:

$$C = kt + C_0$$

where C, the concentration at time t; C_0, the concentration at time zero; k, the zero-order rate constant; t, the storage time (week).

Temperature dependence of HMF occurrence and CIE color indexes (L*, a*, b*, C, h) was defined by Arrhenius equation given below:

$$k = k_0 \times e^{-Ea/RT}$$

where Ea, the activation energy (kJ mol^{-1}); k, the rate constant (week^{-1}); k_0, the frequency factor (week^{-1}); R; the universal gas constant (8.314 x 10^{-3} kJ mol^{-1} K^{-1}); T, the absolute temperature (°K). Additionally, Q_{10} values were calculated with the below equation:

$$Q_{10} = (k_2/k_1)^{(10/T_2 - T_1)}$$

where k_2, the rate constant of the browning reaction at the temperature of T_2 (mg HMF week^{-1} and Lightness, Chroma value, hue value, a* and b* color coordinates); k_1 the rate constant of the browning reaction at the temperature of T_1 (mg HMF week^{-1} and Lightness, Chroma value, hue value, a* and b* color coordinates) (Labuza, 1984).

2.2.3. Statistical Analysis

IBM SPSS Statistics programme (Version 29.0.1.0) has been used to conduct statistical analysis. Correlation test at significance level of 0.01 and 0.05 has been performed by determining the correlations between HMF and CIE color parameters.

3. RESULTS AND DISCUSSION

For nonenzymatic browning of pumpkin puree, changes in color parameters and HMF generation compared to storage time were defined as a function of temperatures (27°, 37°, 47°C). The optimum model was opted considering the determination coefficients (R^2) defined using regression analysis. Rate constants were calculated from best-fit regression equations. Alterations in HMF content, CIE L*, a*, b*, C, h values during storage at the temperature conditions of 27°, 37° and 47°C are demonstrated in Figure 1-6, respectively.

HMF amount present in pumpkin puree showed a rise from the formal value of 3.06 mg L^{-1} to 6.3, 8.9, and 14.76 mg L^{-1} at the termination of the storage period at 27°, 37° and 47°C, respectively. Zhang et al. (2019) and Lee and Nagy (1988) found that HMF amount elevated by time and heating temperature in apple puree and canned grapefruit juices, respectively. The highest HMF increase in pumpkin puree was found as 383% at the storage temperature of 47°C. It was followed by the storage temperature of 37°C with 193% increase. Linearly increased HMF content indicating that HMF occurrence in pumpkin puree is in good agreement with zero-order kinetics which is analogous to the outcomes of the two studies (Burdurlu et al., 2006) and (Lozano, 1991) found in citrus juice concentrates and apple juice model systems, respectively.
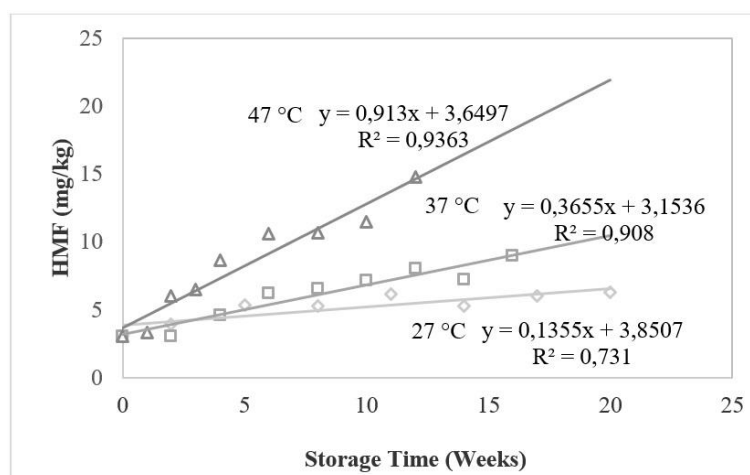
Figure 1. *HMF occurrence in pumpkin puree during storage*

The CIE color indices were considered in the evaluation of browning in pumpkin puree, and it was monitored that while a* coordinate was increasing, L*, b* coordinate, chroma and hue value decreased with time at all storage temperatures (Figure 2-6). Redness increased 32% while yellowness and lightness decreased 24% and 11% at 47°C stored pumpkin puree, respectively. Increases in redness (Figure 3) and decreases in yellowness (Figure 4) and lightness (Figure 2), are the indicators of browning reactions. Hue angle represents the relative amounts of redness and yellowness was also decreased by 8%, 7%, and 5% at 47°, 37° and 27°C, respectively. Özhan et al. (2010) expressed that there was a slight but significant difference in L* value ($p < 0.05$) for carob pekmez samples that were stored at all temperatures throughout the storage period.

Piepiórka -Stepuk et al. (2023) evaluated one of the pumpkin cultivars, namely *Cucurbita moschata,* reviewing the variation in the color indexes such as CIE Lab, C and h values after thermally treating such as blanching,

boiling, steaming. According to the results they have, only steaming process have similarities with L* and h values of this research since it was applied same thermal treatment in this study. Provesi et al. (2012) studied on pumpkin purees by keeping the sample at relative humidity and ambient temperature for 6 months. They found that the L*, a*, b* values for *C. moschata* were 41.50 ± 1.06, 7.61 ± 1.09, 27.23 ± 1.74 after storing 120 days, respectively. The results of this study are within similar ranges, but small distinction is likely associated with the preparation of pumpkin puree that is at pilot-plant scale versus industrial scale. Chikpah et al. (2022) reviewed the impacts of varying slice thicknesses, convective air-drying temperatures, and bioactive substances on the kinetics of drying and color change in dried pumpkin slices. Pumpkin's L* and b* indices reduced from the value of 74.61 ± 1.18 to 56.50–70.15 and 61.95 ± 2.03 to 51.90–56.10 kj mol^{-1} respectively while a* value increased from 8.47 ± 0.09 to 9.98-11.07 after drying. During the drying process, the values of L* and b* showed a decline as a* rose. Similar results related with color indices of pumpkin puree were also found in this research.

Dutta et al. (2006) indicated that pumpkin puree darkened as time and temperature rose from 60°C to 100°C through 2 hours and resulted decline in L* value.

Analysis of kinetic data from CIE-L*a*b* color parameters in pumpkin puree revealed that a reaction model of zero order for nonenzymatic browning. Karabacak (2023) produced pumpkin pestils by several drying techniques like microwave, vacuum, and hot air for examining the formation of HMF and color degradation kinetics. L*, a*, b*, C and h values all fitted to zero order reaction model, similar to the kinetic models of this research.
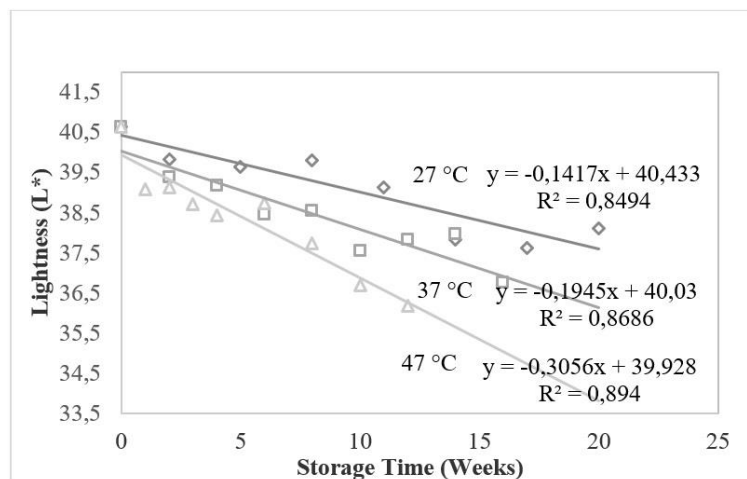
Figure 2. Lightness changes in pumpkin puree during storage
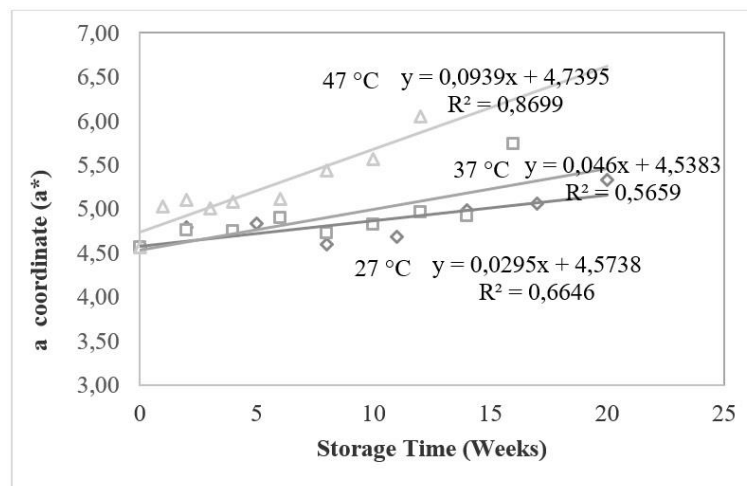
Figure 3. a coordinate changes in pumpkin puree during storage*
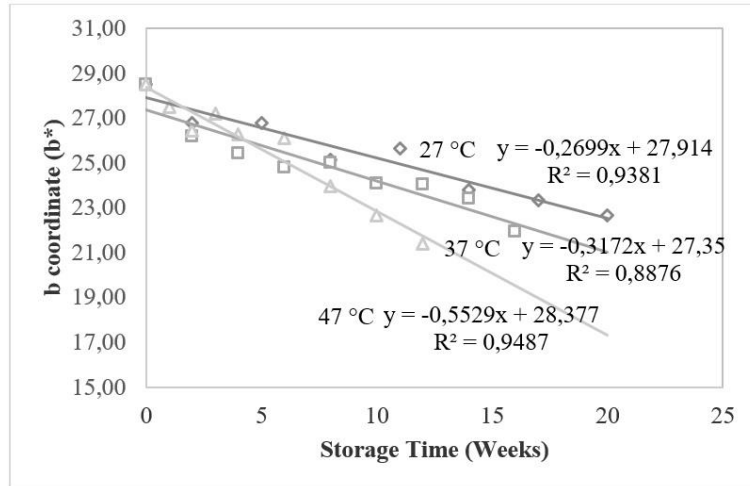
Figure 4. *b* coordinate changes in pumpkin puree during storage*
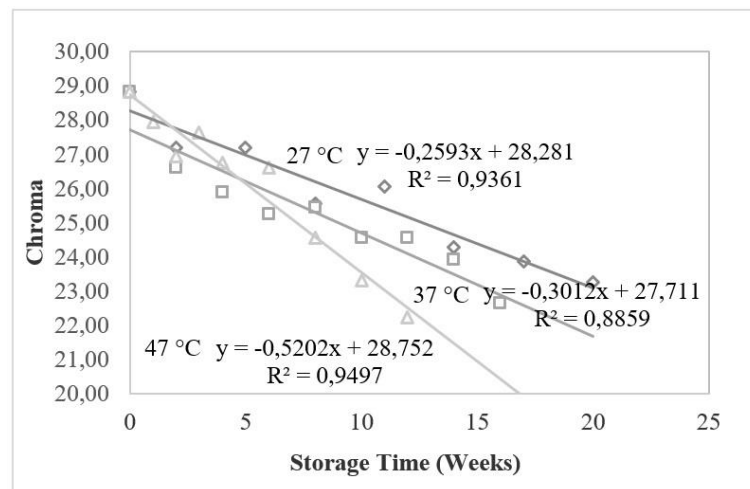
Figure 5. *Chroma changes in pumpkin puree during storage*
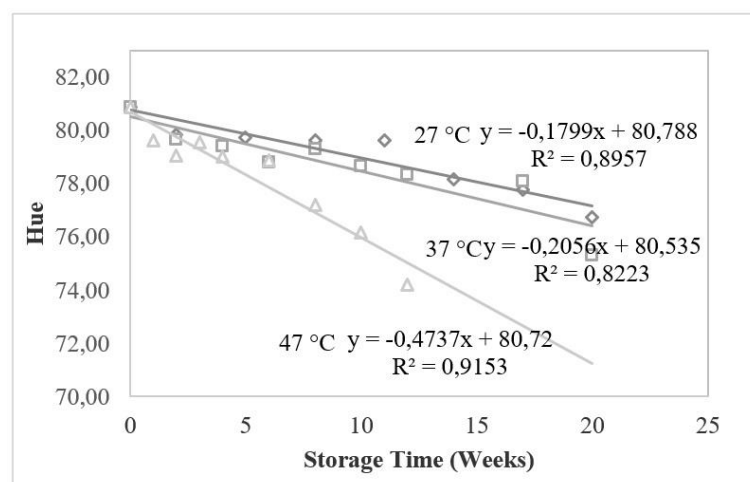
Figure 6. *Hue changes in pumpkin puree during storage*

The heat dependency of the rate constants of HMF generation and L*, a*, b*, C, h values were described by Arrhenius equation (Figure 7). Activation energies for HMF, Lightness, a* coordinate, b* coordinate, chroma and hue values in pumpkin puree in the range of 27° and 47°C were calculated as 76.15, 30.60, 46.08, 28.44, 27.61 and 38.32 kj mol^{-1}, respectively (Table 1).

The value of activation energy present in pineapple juice for the formation of HMF was reported as 29.401 kj mol^{-1} during heat treatment whose temperatures vary from 55°C to 95°C (Rattanathalanerk et al., 2005). The difference in activation energy values might be due to the lower temperature studied in this research and the chemical composition differences between studied food items. In pumpkin puree, higher activation energy needed to initiate the browning reaction. They also explained that HMF and L* value fitted zero order reaction model that coincide with the result of this study.
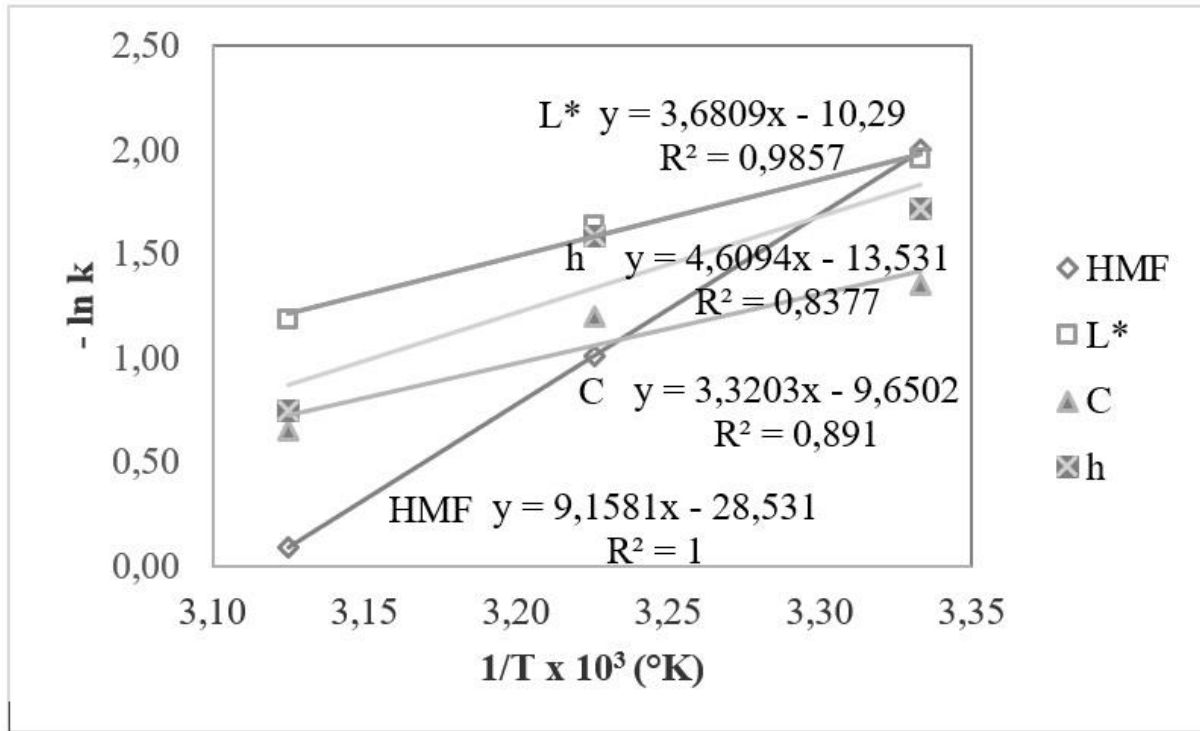
***Figure 7.** Arrhenius plots of HMF, L*, C and hue values in pumpkin puree*

The values of Q_{10} obtained for HMF was acquired in the temperature ranges of 27°-37°, 37°-47°C and 27°-47°C were 2.7, 2.5 and 2.6, respectively. The highest Q_{10} value of HMF occurrence detected at the range of 27°-37°C, showing the generation rate of HMF rose about 2.7 times once the temperature increased from 27° to 37°C (Table 1). Burdurlu et al. (2006) clarified that Q_{10} values of citrus juice concentrates for HMF accumulation between 28°-37°C, 28°-45°C and 37°-45°C were much higher than this study's results since citrus products are more susceptible to the storage temperature and time. Additionally, Q_{10} values of color indices (CIE Lab, C, h) were reported between 0.68 and 1.53 for drying process of pumpkin slices, which have similarities with the results of this investigation (Chikpah et al., 2022).

Since both HMF and CIE color parameters all shows browning reactions in pumpkin puree the correlations were evaluated between these parameters and the results were given in Table 2. Except a* coordinate value of pumpkin puree stored at 27°C, a negative high correlation was encountered between Lightness, Chroma, hue, b* coordinate, HMF and C values (r = 0.73-0.94, $p<0.05$), whereas positive correlation was noticed between HMF and a* coordinate (r = 0.72-0.89, $p<0.05$).

At the beginning of the storage TSS, pH, and titratable acidity (%, citric acid), of pumpkin puree were found as 4.98, 4.21 and 0.36, respectively. pH values were found between 4.18-4.21, titratable acidities were found between 0.37-0.41 and TSS were found between 4.60-4.63 in all samples analyzed at the end of storage. This indicates that there are no significant changes in the physicochemical parameters of pumpkin puree stored at varied temperatures and storage periods.

Table 1. *Kinetic parameters for HMF and Color Changes (CIE-L*a*b*, chroma, hue) in pumpkin puree[a]*

Parameters	Storage Temperature (°C)	Zero order reaction equation	Activation Energy (kJ mol^{-1})	Q_{10}		
				27-37°C	37-47°C	27-47°C
HMF	27	y = 0.1355x + 3.8507 (0.731)	76.15 (1)	2.70	2.50	2.60
	37	y = 0.3655x + 3.1536 (0.9089)				
	47	y = 0.913x + 3.6497 (0.9363)				
Lightness	27	y = -0.1417x + 40.433 (0.8494)	30.60 (0.9857)	1.37	1.57	1.47
	37	y = -0.1945x + 40.03 (0.8686)				
	47	y = -0.3056x + 39.928 (0.8945)				
a* coordinate	27	y = 0.0295x + 4.5738 (0.6646)	46.08 (0.977)	1.56	2.04	1.78
	37	y = 0.046x + 4.5383 (0.5659)				
	47	y = 0.0939x + 4.7395 (0.8699)				
b* coordinate	27	y = -0.2699x + 27.914 (0.9381)	28.44 (0.8975)	1.18	1.74	1.43
	37	y = -0.3172x + 27.35 (0.8876)				
	47	y = -0.5529x + 28.377 (0.9487)				
Chroma	27	y = -0.2593x + 28.281 (0,9361)	27.61 (0.891)	1.16	1.73	1.42
	37	y = -0.3012x + 27.711 (0.8859)				
	47	y = -0.5202x + 28.752 (0.9497)				
Hue	27	y = -0.1799x + 80.788 (0.8957)	38.32 (0.8377)	1.14	2.30	1.62
	37	y = -0.2056x + 80.535 (0.8223)				
	47	y = -0.4737x + 80.72 (0.9153)				

[a] Numbers in brackets describe the determination coefficients (R^2)

Table 2. *Results of the correlation analysis among HMF and CIE-L*a*b* color parameters[a]*

Parameters	HMF		
	27°C	37°C	47°C
Lightness	-0.74*	-0.94**	-0.89**
Chroma	-0.81*	-0.91**	-0.92**
Hue	-0.73*	-0.87**	-0.9**
a* value	0.59	0.72*	0.89**
b* value	-0.81*	-0.91**	-0.92**

[a]Values of the correlation coefficients for different level of significance *P <0.05 ** P <0.01

4. CONCLUSION

Hydroxymethylfurfural occurrence and changes in CIE Lab color indexes were quantified to assess nonenzymatic browning reactions observed in stored pumpkin puree at 27°, 37° and 47°C. When the storage period terminated, there was no difference distinguished in pH, titratable acidity, and soluble solids (°Bx) values. HMF formation and all the CIE color parameters followed zero order reaction kinetic. HMF content and L*, b*, C, hue values showed negative correlations (r= -0.74-0.94) for all the storage temperatures studied, while at 37° and 47°C storage temperatures a* coordinate and HMF content showed positive correlations (r=0.72 and 0.89, respectively). The values calculated for the activation energy (kj mol^{-1}) were 76.15; 30.60; 46.08; 28.44; 27.61 and 38.32 for HMF formation, Lightness, a* coordinate, b* coordinate, Chroma, and hue, respectively.

Consequently, CIE Lab values are useful parameters for determination of the degree of nonenzymatic browning reactions occurred in purees without conducting repeated laboratory analysis of HMF content. Thanks to this situation, since it does not only eliminate the labor for analyzing the amount of HMF but also can contribute to the nature by reducing the use of analysis chemicals.

AUTHOR CONTRIBUTIONS

Methodology and writing-reviewing, F.K., B.I., and S.K.; editing, F.M.; conceptualization and software, O.A., F.M. All authors have read and legally accepted the final version of the article published in the journal.

CONFLICT OF INTEREST

The authors declare no conflict of interest.

REFERENCES

Adams, G. G., Imran, S., Wang, S. Mohammad, A., Kok, S., Gray, D. A., Channell, G. A., Morris, G. A. & Harding S. E. (2011). The hypoglycaemic effect of pumpkins as anti-diabetic and functional medicines. *Food Research International, 44(4),* 862-867, https://doi.org/10.1016/j.foodres.2011.03.016

Anonymous. International Federation of Fruit Juice Producers (IFFJP) Methods. (1984). *Analysen-Analyses. Zug*, *12,* (pp. 1-2).

Aziz, A., Noreen, S., Khalid, W., Ejaz, A., Faiz ul Rasool, I., Munir, A., Javed, M. Ercisli, S., Okcu, Z., Marc, R. A., Nayik, G. A., Ramniwas, S. and Uddin, J. (2023). Pumpkin and Pumpkin Byproducts: Phytochemical Constitutes, Food Application and Health Benefits. *ACS Omega, 8(26),* 23346-23357. https://doi.org/10.1021/acsomega.3c02176

Beveridge T. & Harrison, J. E. (1984). Nonenzymatic Browning in Pear Juice Concentrate at Elevated Temperatures. *Journal of Food Science, 49(5),* 1335-1336. https://doi.org/10.1111/j.1365-2621.1984.tb14984.x

Buedo, A. P., Elustondo, M. P. & Urbicain, M. J. (2000). Non-enzymatic browning of peach juice concentrate during storage. *Innovative Food Science & Emerging Technologies, 1(4),* 255-260, https://doi.org/10.1016/S1466-8564(00)00031-X

Burdurlu, H. S. & Karadeniz, F. (2003). Effect of storage on nonenzymatic browning of apple juice concentrates. *Food Chemistry, 80,* 91-97. https://doi.org/10.1016/S0308-8146(02)00245-5

Burdurlu, H., Koca, N. & Karadeniz, F. (2006). Degradation of vitamin C in citrus juice concentrates during storage. *Journal of Food Engineering, 74(2),* 211-216. https://doi.org/10.1016/j.jfoodeng.2005.03.026

Chikpah, S. K., Korese, J. K., Sturm, B. & Hensel, O. (2022). Colour change kinetics of pumpkin (Cucurbita moschata) slices during convective air drying and bioactive compounds of the dried products. *Journal of Agriculture and Food Research, 10,* 100409, https://doi.org/10.1016/j.jafr.2022.100409

Cornwell, C. J. & Wrolstad, R. E. (1981). Causes of browning in pear juice concentrate during storage. *Journal of Food Science, 46(2),* 515-518. https://doi.org/10.1111/j.1365-2621.1981.tb04899.x

De Escalada Pla, M. E., Rojas, A. M. & Gerschenson, C. N. (2013). Effect of Butternut (*Cucurbita moschata* Duchesne ex Poiret) Fibres on Bread Making, Quality and Staling. *Food Bioprocess Technol*, 6, 828–838. https://doi.org/10.1007/s11947-011-0744-y

Dutta, D., Dutta, A., Raychaudhuri, U. & Chakraborty, R. (2006). *Journal of Food Engineering, 76(4),* 538–546. https://doi.org/10.1016/j.jfoodeng.2005.05.056

FAOSTAT. (2023). Production quantities of Pumpkins, squash, and gourds by country, Average 1994 – 2021 (Accessed: 30/10/2023). https://www.fao.org/faostat/en/#data/QCL/visualize

Fedko, M., Kmiecik, D., Siger, A., Kulczyński, B., Przeor, M. & Kobus Cisowska, J. (2020). Comparative characteristics of oil composition in seeds of 31 Cucurbita varieties. *Journal of Food Measurement and Characterization*, 14, 894–904. https://doi.org/10.1007/s11694-019-00339-6

Guine, R. P. F., Henrriques, F. & Barroca, M. J. (2012). Mass Transfer Coefficients for the Drying of Pumpkin (*Cucurbita moschata*) and Dried Product Quality. *Food Bioprocess Technol, 5,* 176–183. https://doi.org/10.1007/s11947-009-0275-y

Hussain, A., Kausar, T., Sehar, S., Sarwar, A., Ashraf, A. H., Jamil, M. A., Noreena, S., Rafique, A., Iftikhar, K., Quddoos, M. Y., Aslama, J. & Majeed, M. A. (2022). A Comprehensive review of functional ingredients, especially bioactive compounds present in pumpkin peel, flesh and seeds, and their health benefits. *Food Chemistry Advances, 1,* 100067. https://doi.org/10.1016/j.focha.2022.100067

Karabacak, A, Ö. (2023). Assessment of Total Phenolic Compounds, Antioxidant Capacity, β-Carotene Bioaccessibility, HMF Formation, and Color Degradation Kinetics in Pumpkin Pestils. JOTCSA, *10(3),* 729-44. https://doi.org/10.18596/jotcsa.1302567

Koca, N., Burdurlu, H. S. and Karadeniz, F. (2007). Kinetics of Colour Changes in Dehydrated Carrots. *Journal of Food Engineering, 78(2),* 449-455. http://dx.doi.org/10.1016/j.jfoodeng.2005.10.014

Koh, W. Y., Uthumporn, U., Rosma, A., Irfan, A. R. & Park, Y. H. (2018). Optimization of a fermented pumpkin-based beverage to improve *Lactobacillus mali* survival and α-glucosidase inhibitory activity: A response surface methodology approach. *Food Science and Human Wellness, 7(1),* 57–70. https://doi.org/10.1016/j.fshw.2017.11.001

Kulczynski, B., Sidor, A., & Gramza-Michałowska, A. (2020). Antioxidant potential of phytochemicals in pumpkin varieties belonging to *Cucurbita moschata* and *Cucurbita pepo* species. *CyTA - Journal of Food, 18(1),* 472-484. https://doi.org/10.1080/19476337.2020.1778092

Labuza, T. (1984). Application of chemical kinetics to deterioration of foods. *Journal of Chemical Education, 61(4),* 348-358. https://doi.org/10.1021/ed061p348

Lee, H. S. & Nagy, S. (1988). Quality changes and nonenzymic browning intermediates in grapefruit juice during storage. *Journal of Food Science, 53(1),* 168–172. https://doi.org/10.1111/j.1365-2621.1988.tb10201.x

Lozano, J. E. (1991). Kinetics of non-enzymatic browning in model systems simulating clarified apple juice. *Food Science and Technology, 24,* 355–360.

Men, X., Choi, S., Han, X., Kwon, H. Y., Jang, G. W., Choi, Y. E., Park, S. M. & Lee, O. H. (2021). Physicochemical, nutritional, and functional properties of *Cucurbita moschata*. *Food Sci Biotechnol, 30*, 171–183. https://doi.org/10.1007/s10068-020-00835-2

Özhan, B., Karadeniz, F., Erge, H. S. (2010). Effect of storage on nonenzymatic browning reactions in carob pekmez. *International Journal of Food Science and Technology. 45(4),* 751-757. https://doi.org/10.1111/j.1365-2621.2010.02190.x

Piepiórka-Stepuk, J., Wojtasik-Kalinowska, I., Sterczyńska, M., Mierzejewska, S., Stachnik, M. & Jakubowski, M. (2023). The effect of heat treatment on bioactive compounds and color of selected pumpkin cultivars. *LWT, 175, 114469,* https://doi.org/10.1016/j.lwt.2023.114469

Provesi, J. G., Dias, C. O., de Mello Castanho Amboni, R. D. & Amante, E. R. (2012). Characterisation and stability of quality indices on storage of pumpkin (*Cucurbita moschata and Cucurbita maxima)* purees. *International Journal of Food Science and Technology, 47(1),* 67–74. https://doi.org/10.1111/j.1365-2621.2011.02808.x

Rattanathalanerk, M., Chiewchan, E. & Srichumpoung, W. (2005). Effect of thermal processing on the quality loss of pineapple juice. *Journal of Food Engineering, 66(2),* 259–265. https://doi.org/10.1016/j.jfoodeng.2004.03.016

Toribio, J. L. & Lozano, J. E. (1984). Nonenzymatic Browning in Apple Juice Concentrate during Storage. *Journal of Food Science, 49(3),* https://doi.org/10.1111/j.1365-2621.1984.tb13234.x

Zhang L. L., Kong Y., Yang, X., Zhang, Y. Y., Sun, B. G., Chen, H. T. & Sun, Y. (2019). Kinetics of 5-hydroxymethylfurfural formation in the sugar-amino acid model of Maillard reaction. *J Sci Food Agric., 99(5),* 2340-2347. https://doi.org/10.1002/jsfa.9432

Zeolite A Thin Film Growth on Silica Optical Fibers

Sezin GALİOĞLU ÖZALTUĞ[1]* 🆔

[1] *National Nanotechnology Research Center (UNAM), Bilkent University, Ankara, Türkiye*

Keywords	Abstract
Zeolite A Thin Films Nanoporous Secondary Growth	Thin films of zeolite A (Linde type A, LTA) were fabricated on silica optical fibers using dip coating method, followed by a secondary growth process. Zeolite A seed crystals with an average crystal size of 247.3 nm were synthesized through hydrothermal method. Then, the dip coating technique was applied to coat silica optical fibers. The one and two-time dip coating resulted in island-like growth, while three-time dip coating process led to the intergrowth of seed crystals, resulting in nearly continuous films on the optical fiber. The seed crystals, initially deposited as a monolayer, were grown by secondary growth method, leading to film thicknesses of 255.3 nm ± 10.1 nm (average ± standard deviation). Upon extending the secondary growth reaction time from 2 hours to 4 hours, the film thickness increased from 255.3 nm ± 10.1 nm to 649.6 nm ± 28.1 nm. Epitaxial growth was identified as the mechanism through which the seed crystals grow. The nanoporous zeolite A films formed on the optical fiber exhibit potential applications as gas sensors. These sensors function by detecting changes in optical reflection caused by the differential adsorption of gases.

1. INTRODUCTION

Zeolites are preferred adsorbents, ion-exchangers, and catalysts for many reactions of industrial importance (Bennett et al., 2021). They have acidity with both Bronsted and Lewis acid sites, ion-exchange properties, and high specific surface area (Gumidyala et al., 2016; Sousa-Aguiar et al., 2019). Up to now, around 245 types of zeolites have been approved by the International Zeolite Association (Structural database of zeolites, 2023). Among other nanoporous materials, zeolites are the most important commercialized porous materials (Bennett et al., 2021). They are a crucial part of the heterogeneous catalysis industry, primarily due to their molecular size micropores (< 2 nm), and high thermal stability (650 - 900 °C) (Sousa-Aguiar et al., 2019).

Synthesized zeolites are obtained in powder form. They are typically processed into specific forms such as pellets or thin films to make use of them in advanced application areas. Having continuous thin films with preferred crystallographic orientation is an important task in the field of zeolites (Pham et al., 2011) to use them in advanced application areas such as sensing (Wales et al., 2015), catalysis (Hedlund et al., 2004; Kumar et al., 2020), nanofiltration (Kong et al., 2021) pervaporation (Cao et al., 2019; Shao et al., 2014) etc. Zeolite thin films are usually formed on porous substrates such as α-alumina (Al₂O₃). However, zeolite film growth is not thoroughly investigated for optical fibers because it is challenging to prepare zeolite thin films on cylindrical and non-porous substrates (Ji et al., 2007). Partial coverage of the seed layer and separation of the films from the fibers are the most encountered problems during the growth. Thin film formation of zeolite X and zeolite Y (FAU framework type) (Deng & Balkus, n.d.; Pradhan et al., 2000), silicalite-1 and ZSM-5 (MFI frame type) (Nazari et al., 2014; Zhang et al., 2005) and zeotype titanosilicate ETS-10 (Ji et al., 2007) on optical fibers was investigated in the literature. Among them, the potential of using silicalite-1 thin film

prepared on optical fibers as optical chemical sensors for the detection of dissolved organics in water (Zhang et al., 2005) and selective sensing of alcohols in water (Nazari et al., 2014) was examined. It was shown that the formed films can be used as sensors by monitoring the optical reflection changes. The efficacy of a sensor based on Silicalite-1 zeolite thin film coated long-period fiber grating was examined for direct measurement of trace amount of organic vapors (Zhang et al., 2008). Optical fibers coated with Silicalite-1 zeolite thin film were employed as sensors for volatile organic compounds (VOCs) optical fiber sensors (Wu et al., 2017). In another approach, a chemical sensor for acetone vapors was developed using a tantalum pentoxide waveguide coated with hydrophobic MFI-type Silicalite-1 zeolite films with a thickness of 330 nm (Babeva et al., 2017).

Thin film formation of zeolite A (LTA framework type) on optical fibers has not yet been investigated. Zeolite A, which has both scientific and commercial importance, is frequently used both as a catalyst in petrochemistry and in detergent production technologies due to its ion exchange feature, and is considered one of the most commercially used zeolites (Mintova et al., 1999). The production of commercial zeolite A covers 73% of the total synthetic zeolite production (Antúnez-García et al., 2021). Zeolite A is also used extensively in sensor technologies (Vilaseca et al., 2007), membranes (Cao et al., 2019; Shao et al., 2014), thermal energy storage (Li et al., 2017), and water purification (Li et al., 2017).

Here we investigate the feasibility of forming zeolite A thin films on silica optical fibers. Mono-layer or double layer zeolite A thin films were formed on silica fibers to use them in potential gas sensors. These sensors function by detecting changes in optical reflection caused by the differential adsorption of gases. First, hydrothermal synthesis of nano-sized zeolite A crystals (average crystal size: 247.3 nm) was performed. Then, zeolite A seed layer coating on silica fibers was optimized. One-time, two-, three-, four- and five-time dip coating steps were examined to obtain mono- or double-layer seed layer formation. Then, seed layers deposited on silica optical fibers (diameter of 250 µm) were grown by the secondary growth method. Thin film thicknesses were altered and controlled by applying different secondary growth reaction times of 2 h, 3 h, 4 h, 6 h, and 7 h. Nearly continuous zeolite A thin films with different thicknesses were obtained via the intergrowth of seed crystals by applying the secondary growth method.

2. MATERIAL AND METHOD

2.1. Materials

Aluminium isopropoxide (Al(iPro)$_3$, > 98%, 220418, Aldrich), tetrapropylammonium hydroxide tetramethylammonium hydroxide (TMAOH, 25 wt. %, Aldrich), Silica sol (Ludox-HS 30, 30 wt. % SiO$_2$, pH=9.8, Aldrich), tetraethyl orthosilicate (TEOS, 98%, 131903, Aldrich), sodium hydroxide (NaOH, 99%, Merck), ethanol (EtOH, 99.99%, IsoLab), acetone (99.99 % Isolab). Corning specialty silica fibers were purchased from Fujikura Ltd., Japan. Deionized water (DI H$_2$O, resistivity = 18.2 MΩ) is used in synthesis and centrifugation.

2.2. Synthesis of Zeolite A (LTA Framework Type) Seed Crystals

$Al(iPro)_3 : 3\ TEOS : 7.36\ TMAOH : 0.33\ NaOH : 192.41\ H_2O$ molar formula was used for the synthesis of nano-sized zeolite A seed crystals (average crystal size: 247.3 nm). 0.95 g of DI water was added to 2.17 g of TMAOH and stirred for 20 min. Next, 0.17 g of Al(iPro)$_3$ was added gradually to the mixture and stirred for 1 h. Later, 0.53 g of TEOS was added to the mixture and stirred for 2 more hours. Simultaneously, 0.01 g NaOH and 0.23 g DI water were mixed in a different beaker and added to the final mixture dropwise. Lastly, the final mixture was stirred for 15 h at RT for aging. The hydrothermal reaction was carried out at 100 °C oven (Binder FD 115) for 8 h. The crystals were collected after centrifugation (14000 rpm, Eppendorf Centrifuge 5420), washed with DI water until the pH reached 7, and dried overnight under ambient air at 45 °C in an oven.

2.3. Treatment of Optical Silica Fibers

Silica fibers with a cutoff wavelength of 870 - 950 nm and a diameter of 250 µm were used. Silica fibers were cut into 3 cm sections. Then, they are immersed in pure acetone for 20 minutes to remove the protective polymer coating on the silica fiber. After acetone treatment, the coatings were gently wiped off using lint-free Kimwipe tissues. The fibers were further rinsed with fresh acetone to ensure no polymer pieces were left and dried at room temperature.

2.4. Seed Layer Coating

The zeolite A thin film preparation on silica fibers consists of two steps: seed layer coating and secondary growth. In the first step, previously synthesized powder zeolite A was prepared in ethanol (5 wt. %) and sonicated for 1h. Clean polymer-free silica fibers were immersed in zeolite A ethanol solution for 30 s and dried for 20 s in each dip coating step. Depending on the experiment, each dip coating step was repeated two, three, four, and five times. The seed layer coated silica fibers were dried at 70 °C oven for 30 minutes. The seeded silica fibers were calcined at 450 °C rapid thermal annealing oven (ATV Technology Rapid thermal Processor, heating from 20 °C to 450 °C at 5 °C/min, isothermal heating at 450 °C for 1h and convective cooling to 20 °C).

2.5. Secondary Growth of Zeolite A Crystals

The seed crystals on silica fibers were formed by using a molar composition of $0.72\ Al_2O_3 : 5\ SiO_2 : 5.8\ (TMA)_2O : 0.12\ NaO_2 : 250\ H_2O$ (Mintova et al., 2001; Pradhan et al., 2000) in the following step of thin film preparation. In the formulation of the growth mixture, aluminum isopropoxide were mixed with TMAOH. Vigorous stirring was applied for 1h until clear suspension was obtained. NaOH and silica sol were added and 24 h RT aging was applied. The seeded silica fibers were diagonally placed in chromatography glass vials (Isolab), where they were completely immersed in the growth mixture. Depending on the experiments, after 2h, 3h, 4h, 6h, and 7h static hydrothermal treatment at 100 °C, the glass vials were cooled down to room temperature. The resulting zeolite A thin films on silica fibers were extracted from the growth mixture, rinsed several times with deionized water, and allowed to air-dry overnight at 45 °C.

2.6. Characterizations

The crystallographic structure of the zeolite powder samples was analyzed using an X-ray diffraction (XRD) spectrometer (Malvern Panalytical X'Pert Pro Multi-purpose Diffractometer), with a Cu K_α X-ray source (K_α = 1.54187 Å) operating at 45 kV and 40 mA, scanning between the 2θ angle range of 5° - 50°. The micrographs were taken using a Scanning Electron Microscopy (SEM) FEI Quanta 200F microscope operating at 30 kV after coating the samples with a 10 nm Au/Pd conductive layer using a Gatan 682 Precision Etching Coating system. SEM analyses were used to examine the morphology of zeolite seed crystals, particle size distribution, the coverage ratio of seed crystals on silica fibers, the growth behavior of thin films, and the thickness of the thin film.

3. RESULTS AND DISCUSSION

Being one of the important classes of nanoporous materials, zeolites have substantial scientific, technological, and commercial application areas. (Gumidyala et al., 2016; Wales et al., 2015). These materials are inorganic materials with pore size below 2 nm, a uniform and ordered pore structure throughout the crystal, and a large surface area. It is regarded as the integration of two systems. One of them is a negatively charged and covalently bonded aluminosilicate framework (Si, Al) and the other one is the ionically bonded extra framework cations (Na$^+$, K$^+$). They have extraordinary properties such as molecular pore size, high crystallinity, high surface area, gas adsorption sites, exchangeable ions, and selective gas penetration, which make zeolites good tools for gas sensor applications (Sasaki et al., 2002; Vilaseca et al., 2007; Wales et al., 2015; Zampieri et al., 2008). Among them, zeolite A, which has both scientific and commercial importance, is frequently used both as a catalyst in petrochemistry and in detergent production technologies due to its ion exchange feature, and is considered one of the most commercially used zeolites (Mintova et al., 1999). Zeolite A with an extra-framework cation of Na$^+$ has a nominal pore opening of 0.4 nm and different forms of zeolite A can be obtained by ion-exchange of extra-framework cations. K$^+$, Na$^+$, and Ca^{2+} form is considered as 3A, 4A, and 5A zeolites which have pore apertures of 0.3 nm, 0.4 nm, and 0.5 nm, respectively (Structural database of zeolites, 2023). The surface area of it provides available active sites for gas adsorption/desorption (Khoramzadeh et al., 2019; Valencia & Rey, 2020). It has high thermal stability and reversible gas adsorption/desorption behavior upon heating (Khoramzadeh et al., 2019; Valencia & Rey, 2020). The advantages above make zeolite A good candidate for gas sensor application which has been explored in our previous studies as well.

As synthesized zeolite powders are typically processed into specific forms, such as pellets or thin films, to be used in advanced application areas such as sensing (Wales et al., 2015). Having continuous thin films with preferred crystallographic orientation is an important task in the field of zeolites Pham et al., 2011). The preparation of thin zeolite films on the optical fibers is challenging due to the difficulties of preparing thin films on cylindrical and non-porous supports andremains to be elucidated. To the best of our knowledge, the thin film formation of zeolite A (LTA framework type) on optical fibers has not been investigated up to now. In the scope of this study, the feasibility of forming zeolite A thin films on silica fibers was examined. The films were produced using a two-step method. First, zeolite A seed layer coating was prepared via the dip coating procedure. Then, the growth of the seed layer deposited film was conducted via the secondary growth method (Figure 1a). Mono- or double-layer zeolite A thin films were formed on silica fibers to use them in potential gas sensors that function by monitoring the optical reflection changes caused by the selective adsorption of gas molecules (Figure 1b). To obtain a high response from the gas sensor, reflection changes due to the adsorption of gas molecules should be significant because the response increases as the thickness of the thin film decreases.
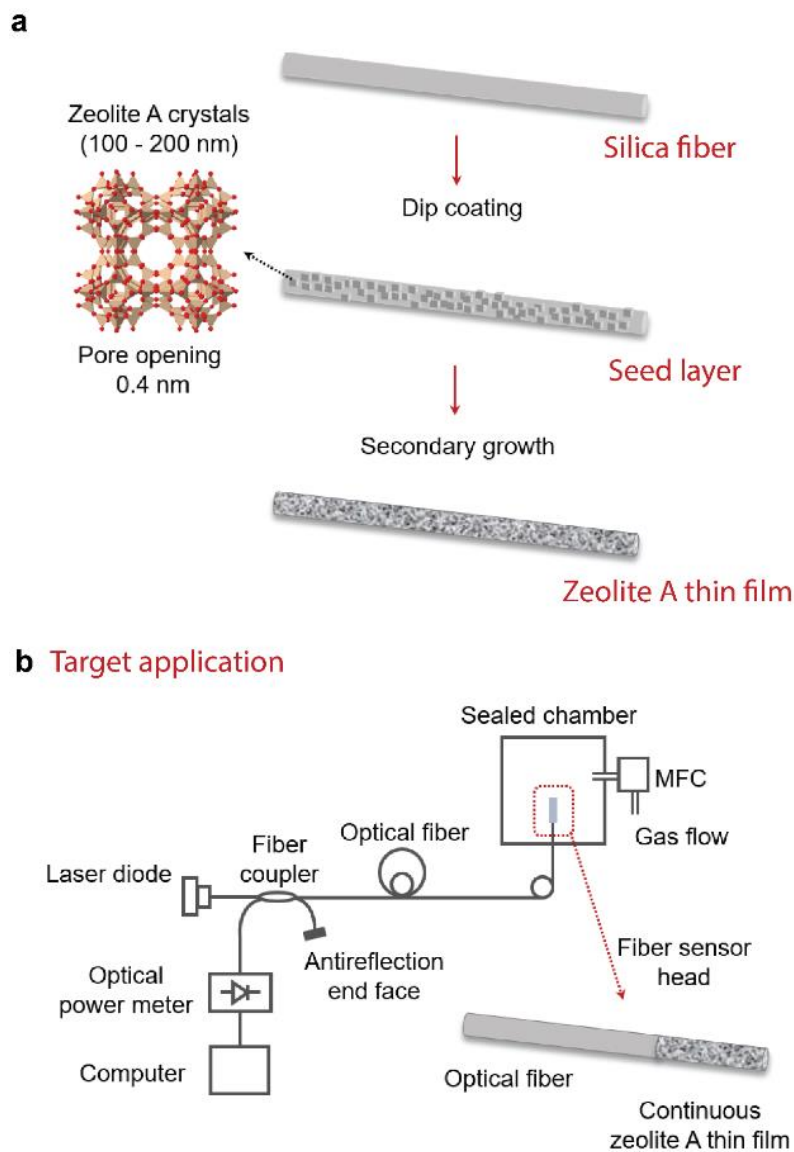
Figure 1. a) *Schematic figure shows the growth of zeolite A (LTA framework type) thin films on silica optical fibers. Zeolite A seed layer coating was performed via dip coating procedure and growth of seed layer deposited film was conducted via secondary growth method,* ***b)*** *The nanoporous zeolite A thin films formed on the optical fiber exhibit potential applications as gas sensors. These sensors function by detecting changes in optical reflection caused by the differential adsorption of gases*

Accordingly, the growth of a multi-layer seed layer is not desired for the potential gas sensor application. The proposed principle can be explained detecting changes in optical reflection caused by the differential adsorption of gases. The light from the laser diode can be sent into optical silica fiber. Then, a fiber coupler can be used to divide to two paths. A splicer can be used to splice zeolite-coated 3 cm long fiber to the main fiber. A sealed chamber and mass flow controller (MFC) can be used to load the chamber with a single gas or gas mixture at the specified rate. An optical power meter and a computer can be used to detect changes in optical reflection caused by the differential adsorption of gases on zeolite A thin film coated fiber part.

First of all, hydrothermal synthesis of zeolite A crystals was performed to obtain seed crystals. SEM analysis revealed that the morphology of the seed crystals with an average crystal size of 247.3 nm was cubic (Figure 2a). The biggest crystals within the population did not surpass a size of ~ 250 nm. The nano size of the seed crystals ensures uniform coating of the crystals on optical silica fibers. The crystalline nature of zeolite A is confirmed by XRD compared with reference XRD data of zeolite A data taken from the IZA web page (Figure 2b) (Structural database of zeolites, 2023).
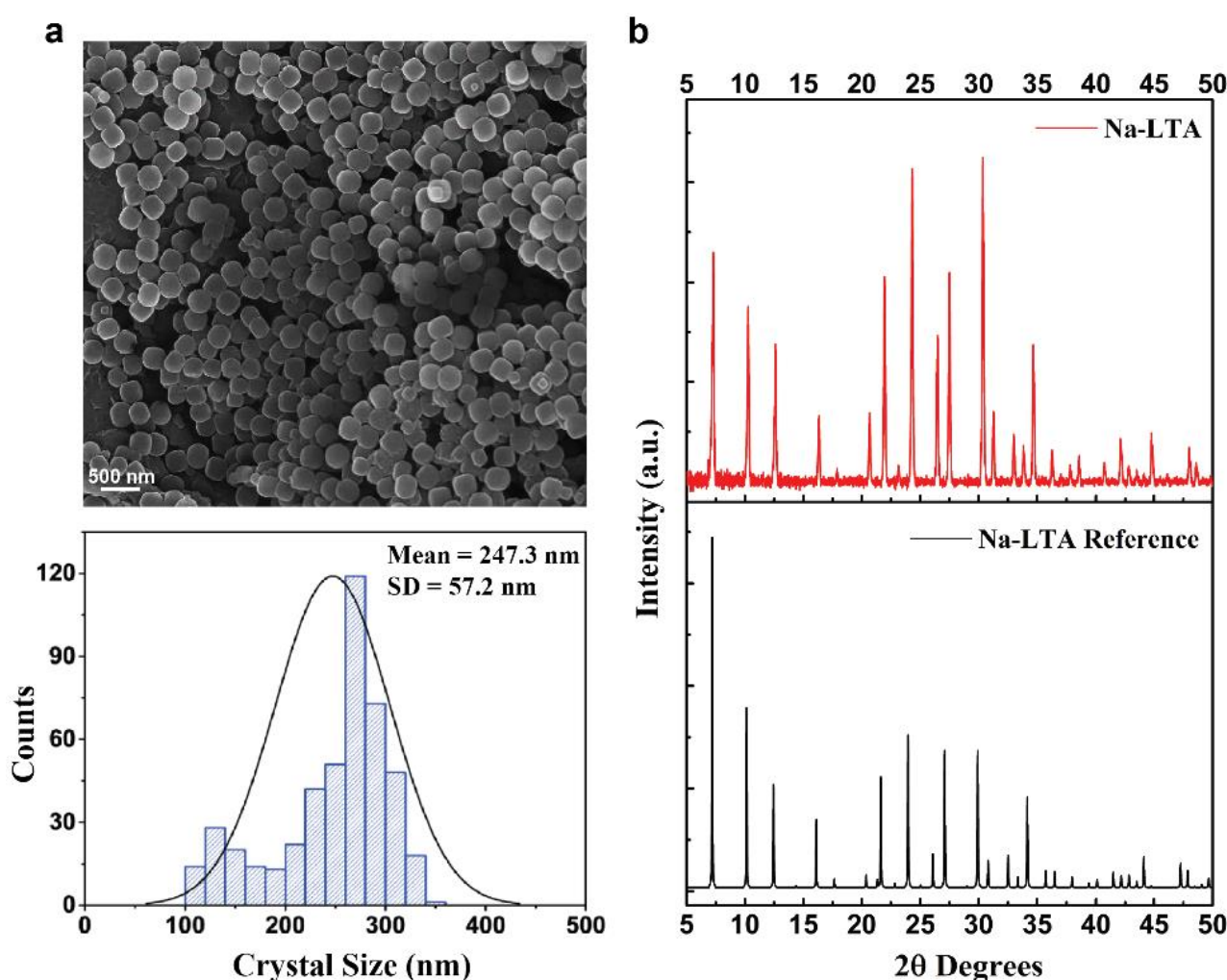
Figure 2. a) SEM image of zeolite A seed crystals synthesized via hydrothermal method. The morphology of the seed crystals with an average crystal size of 247.3 nm was cubic (SD: standard deviation), b) XRD data of synthesized zeolite A compared with reference XRD data taken from IZA web page (Structural database of zeolites, 2023)

3.1. Effect of the Seed Layers

To obtain thin film of zeolite A, first of all, zeolite A seed layer coating on silica fibers was optimized. 5 wt. % nano-sized zeolite A, synthesized previously, in ethanol suspension was used to dip coat silica optical fibers.

One-time, two-, three-, four- and five-time dip coating steps were examined to obtain mono- or double-layer seed layer formation. Figure 3a shows bare optical silica fiber surface and Figure 3b indicates one-time dip coating step was not adequate to coat the surface of silica fibers. As can be seen from the SEM images, island-like coverages were formed with spacing > 15 μm and the uncovered silica fiber surface was clearly observed. A similar trend was observed for two-time dip coating (not shown). One-time or two-time dip coating steps were not sufficient to obtain full coverage of silica fibers. Although island-like coverages were observed, mono-layer seed formation was seen when one-time and two-time dip coating steps were applied. Three-time dip coating of the seed layer was found to be optimum to obtain mono- or double-layer zeolite A crystals on silica fibers (thicknesses of the mono-layer seed layers ~ 200 nm) (Figure 3c) while four-time (Figure 3d) or five times dip coatings (not shown) were resulted in multi-layer seed formation not desired for potential gas sensor applications.
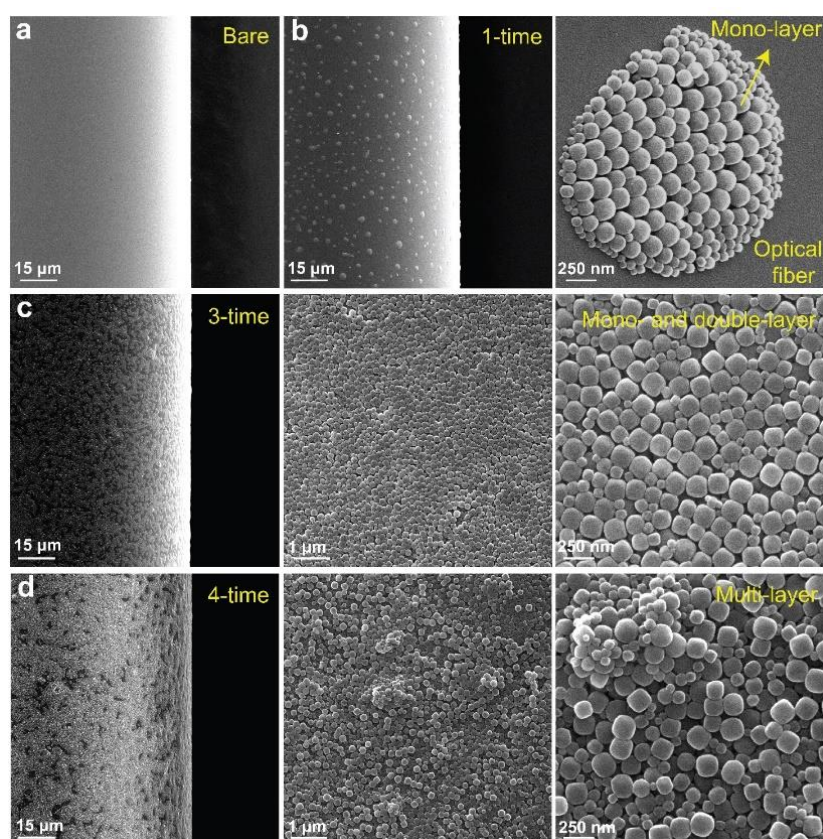
Figure 3. *Nano-sized zeolite A seed layer coatings on silica optical fibers. SEM images of a) bare silica optical fibers, b) one-time dip coated, c) three-time dip coated, d) four-time dip-coated samples with different magnifications*

3.2 Zeolite A Thin Film Formation Through Secondary Growth

The seed layers deposited on silica optical fibers (diameter of 250 μm) were grown by the secondary growth method (Figure 4) in freshly prepared growth suspension using the molar composition of $0.72\ Al_2O_3$: $5\ SiO_2$: $5.8\ (TMA)_2O$: $0.12\ NaO_2$: $250\ H_2O$ (Mintova et al., 2001; Pradhan et al., 2000). The seeded silica fibers were diagonally placed in chromatography glass vials (Isolab), where they were completely immersed in the growth mixture. Then, hydrothermal treatments were carried out at 100 °C oven. Figures 4a and 4b show that when nearly continuous coverage of seed layers was not achieved (i.e., one-time and two-time seed layers), intergrowth of seed crystals could not be possible even though the reaction time increased to 7 hours (Figure 4a and 4b). Continuous growth of seed crystals prepared by one-time and two-time dip coating steps cannot be obtained due to the presence of ~ 15 μm spacing between island-like seed crystals. It was observed that as the reaction time increased to 7 hours to achieve epitaxial growth of island-like seed crystals, the thickness of the islands increased and separate phases appeared over the growth zone (Figure 4a and 4b, highlighted with red circles).
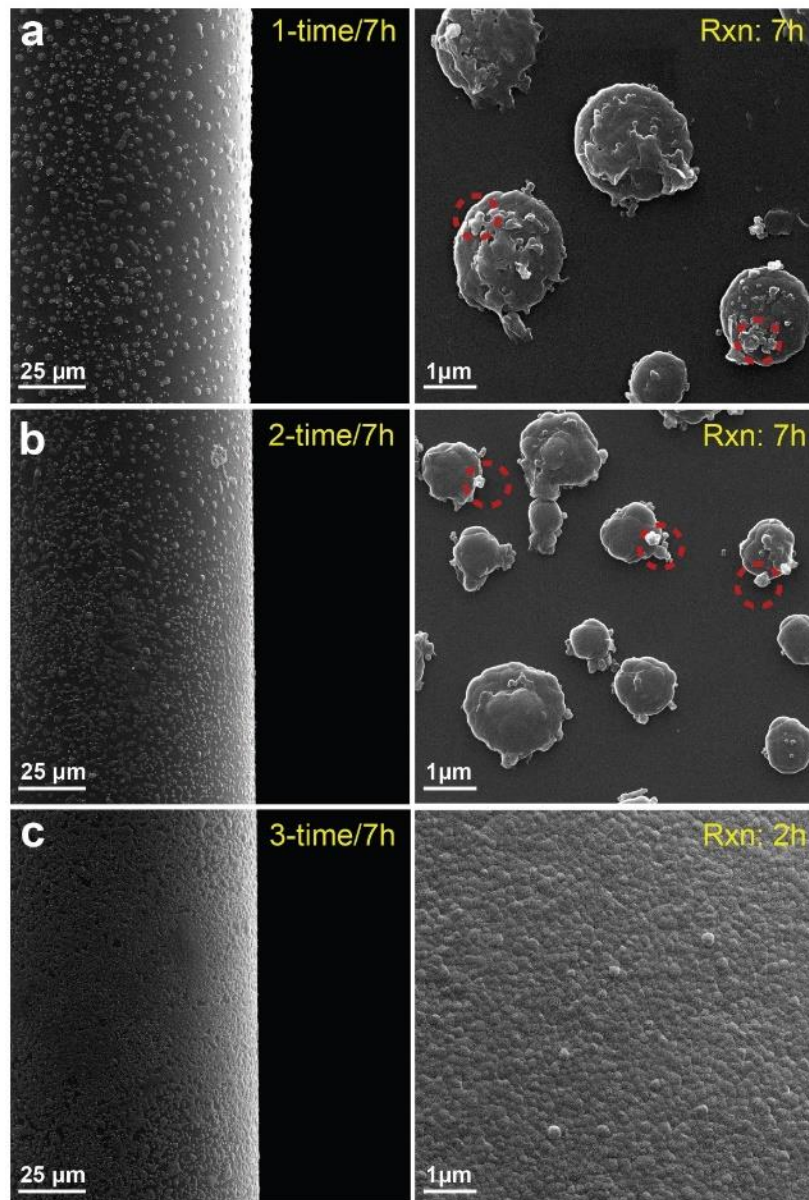
***Figure 4.** SEM images of zeolite A thin films formed on silica optical fibers through secondary growth of seed crystals dip-coated **a**) one-time, **b**) two-time, and **c**) three-time. The separate zeolite A phase that appeared over the growth zone is highlighted with red circles*

To obtain nearly continuous zeolite A thin films, the spacing between seed crystals must be in the range where intergrowth of the crystals can occur. As shown above, three-time dip coating of the seed layer was found to be optimum to obtain mono- or double-layer zeolite A crystals on silica fibers. Besides, the spacing between the seed crystals was in the range where intergrowth of seed crystals can occur (Figure 4c).

To alter and control zeolite A thin film thicknesses, different hydrothermal reaction times of 2 h, 3 h, 4 h, 6 h, and 7 h were carried out for optical fibers seeded with a three-time dip coating step (Figure 5). For the optical fibers seeded with three-time dip coating step, intergrowth of the homogenous mono-layer seed crystals can be achieved even after 2 h secondary growth reaction time (Figure 4c). However, it was found that 2 h reaction time was insufficient to achieve continuous growth when there was spacing between the seed crystals (spacing > ~ 1 μm) (Figure 5a). Nearly continuous zeolite A thin films were obtained via intergrowth of seed crystals by applying 3 h secondary growth reaction time (Figure 5b). When the reaction time increased to 4 h, a separate zeolite A phase appeared as can be seen in Figure 5c (highlighted with red circles). Further increase of the reaction time to 6 h resulted in thicker growth with a substantial amount of unattached cubic zeolite A crystals on the surface of the film (Figure 5d, highlighted with red circles).

Figure 5. *Top view SEM images of zeolite A thin films grown on optical fibers via the secondary growth method with **a**) 2 h, **b**) 3 h, **c**) 4 h, and **d**) 6 h secondary growth reaction times. The silica optical fibers were seeded with three-time dip coating step*

The initial transparent color of the secondary growth suspension in the glass vial was still transparent after 2 h secondary growth reaction time and light milky after 3 h reaction time. However, the white precipitation of the crystals started after 4 h reaction time with milky suspension at the top. Distinct segregation was observed after 5 h reaction time, that is, a significant amount of white precipitation (i.e., crystalline zeolite A) was observed at the bottom of the glass vial and a clear suspension appeared at the top. This phenomenon can be clearly observed from the presence of a considerable amount of unattached cubic zeolite A crystals on the surface of the film after 6 h of reaction time (Figure 5d, highlighted with red circles).

To further analyze thin film thicknesses altered upon increasing the secondary growth reaction time, optical fibers were cut with a razor blade after growth. The fibers with thin film were placed on cross-section SEM stub and analyses were carried out. The film thicknesses averaged out from at least six different spots. The film thicknesses of 255.3 nm ± 10.1 nm, 283.2 nm ± 18.6 nm, 649.6 ± 28.1 nm, and 632.1 nm ± 72.5 nm (average ± standard deviation) were obtained for 2 h, 3 h, 4 h, and 6 h secondary growth reaction times, respectively (Figure 6).

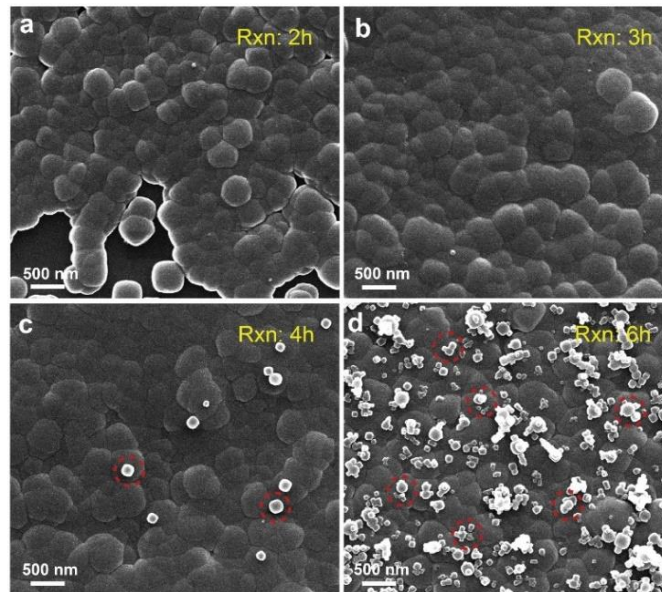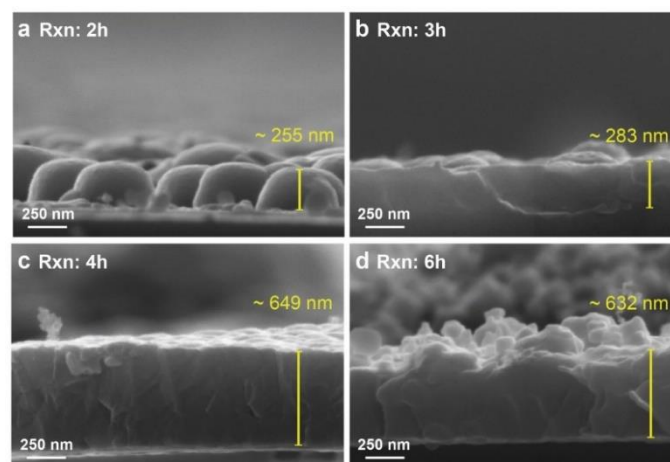***Figure 6.*** *Cross-sectional SEM images of zeolite A thin films formed on optical fibers via secondary growth method with **a**) 2 h, **b**) 3 h, **c**) 4 h, and **d**) 6 h secondary growth reaction times. The silica optical fibers were seeded with three-time dip coating step*

As can be seen from cross-section images, the boundaries of the cubic seed crystals were still observable for 2 h reaction time (Figure 6a) while complete intergrowth of the seed crystals. Besides, the thin films were attached to optical fibers with reaction times of 3 hours and 4 hours, ensuring a strong adhesion (Figures 6b and 6c). Besides, the surfaces of the films grown by 3 h and 4 h secondary growth reaction times were smoother compared to those grown by 6 h reaction time as observed in top view SEM images as well (Figure 5). The average film thicknesses indicate that film growth is saturated after 4h reaction time. As the reaction time increased, growth was achieved not only in the lateral direction (i.e., intergrowth) but also in the vertical direction, thus increasing the thickness of the films and the roughness of the thin film surface as well.

4. CONCLUSION

The feasibility of forming zeolite A thin films on silica fibers was investigated. Mono-layer or double-layer zeolite A thin films were formed on silica fibers to use them in potential gas sensor applications. First, hydrothermal synthesis of nano-sized zeolite A crystals (average crystal size: 247.3 nm) was performed. Then, seed layer coating on silica fibers was optimized. One-time or two-time dip coating steps were not sufficient to obtain full coverage of silica fibers while four-time or five-time dip coatings resulted in multi-layer seed formation neither of which are desired for potential gas sensor applications. Accordingly, three-time dip coating of the seed layer was found to be optimum to obtain mono- or double-layer zeolite A crystals on silica fibers (thicknesses of the mono-layer seed layers ~ 200 nm). Then, seed layers deposited on silica fibers (diameter of 250 μm) were grown by the secondary growth method. To obtain nearly continuous zeolite A thin films, the spacing between seed crystals must be in the range where intergrowth of the crystals can occur (i.e., less than 1 μm). When nearly continuous coverage of seed layers was not achieved (i.e., one-time and two-time seed layers), intergrowth of seed crystals cannot be achieved even though the reaction time increased to 7 h due to the presence of ~ 15 μm spacing between island-like seed crystals. It was observed that as the reaction time increased to 7 h to achieve epitaxial growth of island-like seed crystals, the thickness of the islands increased and separate crystal phases appeared on the growth zone. To alter and control zeolite A thin film thicknesses, different secondary growth reaction times of 2 h, 3 h, 4 h, 6 h, and 7 h were carried out for optical fibers seeded with three-time dip coating step. Intergrowth of mono-layer seed crystals can be achieved even after 2 h secondary growth reaction time. As the reaction time increased to 4 h, a separate zeolite A phase appeared on the surface of the film. When the reaction time was increased to 6 h, a substantial amount of unattached cubic zeolite A crystals were observed on the surface of the films. The film thicknesses of 255.3 nm ± 10.1 nm, 283.2 nm ± 18.6 nm, 649.6 ± 28.1 nm, and 632.1 nm ± 72.5 nm (average ± standard deviation) were obtained for 2 h, 3 h, 4 h, and 6 h secondary growth reaction times, respectively. Smoother surfaces were obtained for the films grown by 3 h and 4 h secondary growth reaction times compared to those grown by 6 h reaction time. Nearly continuous and firmly attached zeolite A thin films were obtained via intergrowth of seed crystals by applying 3 h secondary growth reaction time for the optical fibers seeded with three-time dip coating step. The nanoporous zeolite A films formed on optical fiber can be used as potential gas sensors. These sensors function by detecting changes in optical reflection caused by the differential adsorption of gases.

ACKNOWLEDGEMENT

CONFLICT OF INTEREST

The author declares no conflict of interest.

REFERENCES

Antúnez-García, J., Galván, D. H., Petranovskii, V., Murrieta-Rico, F. N., Yocupicio-Gaxiola, R. I., Shelyapina, M. G., & Fuentes-Moyado, S. (2021). The effect of chemical composition on the properties of LTA zeolite: A theoretical study. *Computational Materials Science*, *196*. https://doi.org/10.1016/j.commatsci.2021.110557

Babeva, T., Andreev, A., Grand, J., Vasileva, M., Karakoleva, E., Zafirova, B. S., Georgieva, B., Koprinarova, J., & Mintova, S. (2017). Optical fiber–Ta2O5 waveguide coupler covered with hydrophobic zeolite film for vapor sensing. *Sensors and Actuators, B: Chemical*, *248*, 359–366. https://doi.org/10.1016/j.snb.2017.03.157

Bennett, T. D., Coudert, F. X., James, S. L., & Cooper, A. I. (2021). The changing state of porous materials. In *Nature Materials* (Vol. 20, Issue 9, pp. 1179–1187). Nature Research. https://doi.org/10.1038/s41563-021-00957-w

Cao, Y., Li, Y. X., Wang, M., Xu, Z. L., Wei, Y. M., Shen, B. J., & Zhu, K. K. (2019). High-flux NaA zeolite pervaporation membranes dynamically synthesized on the alumina hollow fiber inner-surface in a continuous flow system. *Journal of Membrane Science*, *570–571*, 445–454. https://doi.org/10.1016/j.memsci.2018.10.043

Deng, Z., & Balkus, K. J. (n.d.). *Pulsed laser deposition of zeolite NaX thin films on silica fibers*. www.elsevier.com/locate/micromeso

Gumidyala, A., Wang, B., & Crossley, S. (2016). Direct carbon-carbon coupling of furanics with acetic acid over Brønsted zeolites. *Science Advances*, *2*(9). https://doi.org/10.1126/sciadv.1601072

Hedlund, J., Öhrman, O., Msimang, V., van Steen, E., Böhringer, W., Sibya, S., & Möller, K. (2004). The synthesis and testing of thin film ZSM-5 catalysts. *Chemical Engineering Science*, *59*(13), 2647–2657. https://doi.org/10.1016/j.ces.2004.03.012

Structural database of zeolites (2023). *International Zeolite Association, IZA*. Retrieved 22 November 2023, from https://europe.iza-structure.org/IZA-SC/ftc_table.php

Ji, Z., Warzywoda, J., & Sacco, A. (2007). Titanosilicate ETS-10 thin film preparation on fused silica optical fibers. *Microporous and Mesoporous Materials*, *101*(1-2 SPEC. ISS.), 279–287. https://doi.org/10.1016/j.micromeso.2006.10.003

Khoramzadeh, E., Mofarahi, M., & Lee, C. H. (2019). Equilibrium Adsorption Study of CO2 and N2 on Synthesized Zeolites 13X, 4A, 5A, and Beta. *Journal of Chemical and Engineering Data*, *64*(12), 5648–5664. https://doi.org/10.1021/acs.jced.9b00690

Kong, G., Fan, L., Zhao, L., Feng, Y., Cui, X., Pang, J., Guo, H., Sun, H., Kang, Z., Sun, D., & Mintova, S. (2021). Spray-dispersion of ultra-small EMT zeolite crystals in thin-film composite membrane for high-permeability nanofiltration process. *Journal of Membrane Science*, *622*. https://doi.org/10.1016/j.memsci.2020.119045

Kumar, P., Kim, D. W., Rangnekar, N., Xu, H., Fetisov, E. O., Ghosh, S., Zhang, H., Xiao, Q., Shete, M., Siepmann, J. I., Dumitrica, T., McCool, B., Tsapatsis, M., & Mkhoyan, K. A. (2020). One-dimensional intergrowths in two-dimensional zeolite nanosheets and their effect on ultra-selective transport. *Nature Materials*, *19*(4), 443–449. https://doi.org/10.1038/s41563-019-0581-3

Li, Y., Li, L., & Yu, J. (2017). Applications of Zeolites in Sustainable Chemistry. In *Chem* (Vol. 3, Issue 6, pp. 928–949). Elsevier Inc. https://doi.org/10.1016/j.chempr.2017.10.009

Mintova, S., Mo, S., & Bein, T. (2001). Humidity sensing with ultrathin LTA-type molecular sieve films grown on piezoelectric devices. *Chemistry of Materials*, *13*(3), 901–905. https://doi.org/10.1021/cm000671w

Mintova, S., Olson, N. H., Valtchev, V., & Bein, T. (1999). Mechanism of zeolite a nanocrystal growth from colloids at room temperature. *Science*, *283*(5404), 958–960. https://doi.org/10.1126/science.283.5404.958

Nazari, M., Hill, M. R., Duke, M., Sidiroglou, F., & Collins, S. F. (2014). Selective sensing of alcohols in water influenced by chemically Zeolite coatings on optical fiber sensors. *23rd International Conference on Optical Fibre Sensors*, *9157*, 915752. https://doi.org/10.1117/12.2059516

Pham, T. C. T., Kim, H. S., & Yoon, K. B. (2011). Growth of Uniformly Oriented Silica MFI and BEA Zeolite Films on Substrates. *Science*, *334*, 1533–1538.

Pradhan, A. R., Macnaughtan, M. A., & Raftery, D. (2000). Zeolite-coated optical microfibers for intrazeolite photocatalysis studied by in situ solid-state NMR. *Journal of the American Chemical Society*, *122*(2), 404–405. https://doi.org/10.1021/ja992683s

Sasaki, I., Tsuchiya, H., Nishioka, M., Sadakata, M., & Okubo, T. (2002). Gas sensing with zeolite-coated quartz crystal microbalances—principal component analysis approach. *Sensors and Actuators B: Chemical*, *86*(1), 26–33. https://doi.org/10.1016/S0925-4005(02)00132-6

Shao, J., Zhan, Z., Li, J., Wang, Z., Li, K., & Yan, Y. (2014). Zeolite NaA membranes supported on alumina hollow fibers: Effect of support resistances on pervaporation performance. *Journal of Membrane Science*, *451*, 10–17. https://doi.org/10.1016/j.memsci.2013.09.049

Sousa-Aguiar, E. F., Arroyo, P. A., de Barros, M. A. S. D., & de Miranda, J. L. (2019). The Future of Zeolite and MOF Materials. In *Zeolites and Metal-Organic Frameworks* (pp. 307–342). Amsterdam University Press. https://doi.org/10.2307/j.ctvcmxprm.15

Valencia, S., & Rey, F. (2020). *New Developments in Adsorption/ Separation of Small Molecules by Zeolites*. http://www.springer.com/series/430

Vilaseca, M., Coronas, J., Cirera, A., Cornet, A., Morante, J. R., & Santamaria, J. (2007). Gas detection with SnO_2 sensors modified by zeolite films. *Sensors and Actuators, B: Chemical*, *124*(1), 99–110. https://doi.org/10.1016/j.snb.2006.12.009

Wales, D. J., Grand, J., Ting, V. P., Burke, R. D., Edler, K. J., Bowen, C. R., Mintova, S., & Burrows, A. D. (2015). Gas sensing using porous materials for automotive applications. *Chemical Society Reviews*, *44*(13), 4290–4321. https://doi.org/10.1039/c5cs00040h

Wu, B., Zhao, C., Kang, J., & Wang, D. (2017). Characteristic study on volatile organic compounds optical fiber sensor with zeolite thin film-coated spherical end. *Optical Fiber Technology*, *34*, 91–97. https://doi.org/10.1016/j.yofte.2017.01.010

Zampieri, A., Dubbe, A., Schwieger, W., Avhale, A., & Moos, R. (2008). ZSM-5 zeolite films on Si substrates grown by in situ seeding and secondary crystal growth and application in an electrochemical hydrocarbon gas sensor. *Microporous and Mesoporous Materials*, *111*, 530–535.

Zhang, J., Dong, J., Luo, M., Xiao, H., Murad, S., & Normann, R. A. (2005). Zeolite-fiber integrated optical chemical sensors for detection of dissolved organics in water. *Langmuir*, *21*(19), 8609–8612. https://doi.org/10.1021/la0514967

Zhang, J., Tang, X., Dong, J., Wei, T., & Xiao, H. (2008). Zeolite thin film-coated long period fiber grating sensor for measuring trace chemical. *Optics Express*, *16*(11), 8317. https://doi.org/10.1364/OE.16.008317

Genres Classification of Popular Songs Listening by Using Keras

İlhan TARIMER[1*] 🆔 Buse Cennet KARADAĞ[1] 🆔

[1] *Muğla Sıtkı Koçman University Faculty of Technology, Muğla, Türkiye*

Keywords	Abstract
Musical Genre MFCC Keras Classification	Listening to the music affects the brain in ways which might help to promote the human health and arrange various diseases symptoms. Music is a phenomenon that is intertwined at every stage of human life. In the modern era music is shaped by the combination of an incredible number of genres, some of which are contemporary, and some come from the previous times. The music genre represents a collection of musical works that develop according to a certain shape, expression and technique. The music genre of interest varies from person to person in society. Most listeners today do not know what kind of music they listen to. In this study, sound features were extracted from music data and the Keras model was trained using these attributes. The correct classification rate of a music genre of the trained model was determined as 71.66%. Mel Frequency Cepstral Coefficients (MFCC), Mel Spectrogram, Chroma Vector and Tonnetz methods in the Librosa library were used to extract sound properties from music data. Using the features probed by means of the library, the most listened songs with Shazam in Türkiye were categorized in with TensorFlow/Keras. Many methods can be used in classification. It is uncertain which method the researchers should opt. It has been emphasized that classification of the genres of newly released songs by using Keras in this study. At result, it is said that the study has presented a sound processing are Keras classification of musical parts.

1. INTRODUCTION

Music is one kind of therapy that boosts our mood and happiness and might help the patients during treatments for some health disorders. Music is one of the indispensable elements of life, which is thought to exist with the existence of people in the world (İmik & Haşhaş, 2020). It is usually defined as the art of expressing certain feelings and thoughts with harmonious sounds within the framework of certain regulations. Music can also be defined as the art of bringing together measured and regulated sounds within artistic thoughts with or without rhythm to express feelings, thoughts or events.

It is known that music has an inevitable locus in human life. It is possible to come across music on television, in cinema films, in advertorials, in cafeterias, and in shopping malls. Some of these musical artifacts can be ones that we listen to and some that we have never heard. In the era in which we live, different types of digital platforms offering musical arranged or covered songs have been developed for people to listen to music and discover new music. The most well-known of these digital platforms are given as Spotify, Youtube Music and iTunes & Apple. By means of these platforms, people can easily access to their sideburn genres of music, and songs.

Shazam application was developed in 1999 by Chris Barton, and his team members, it was only released to use in the UK. It is Shazam which can listen to music currently playing in the environment within 5-10 seconds

and that find out who is the singer and which song has now been playing through the database, providing access to the lyrics of the song in the Lyrics section. The application makes these as to be listing of the searched songs in My Shazams section. The application which provides the opportunity to monitor the clip of the song on the video side, also permits to share the song on many platforms by using sharing button (Hussain et al., 2019).

Shazam finds music frequencies in fingerprint logic and executes them in the database. Then, the determined frequencies are searched and matched. The sound frequencies are firstly converted into a recognizable format by an algorithm. This process done is called as hashing. The data that they are received through a series of mathematical operations, produce complex outputs by using hash algorithms. This is considered as the most matched song frequencies among the frequencies coded via the hash system and its information is shared.

Acoustic fingerprint, as the name suggests, is a kind of identity that belongs solely to that sound. Each sound type contains sound and bandwidth values together in a frequency band. While the sounds we hear sometimes sound alike, on the other hand, the formulae reveal differences. In order to detect songs, acoustic fingerprint is constituted when identifying a sound, providing voice searching operations by searching among all sounds, and then, Shazam can detect songs searched (Web Source 1). Figure 1 displays operation of a Shazam application.
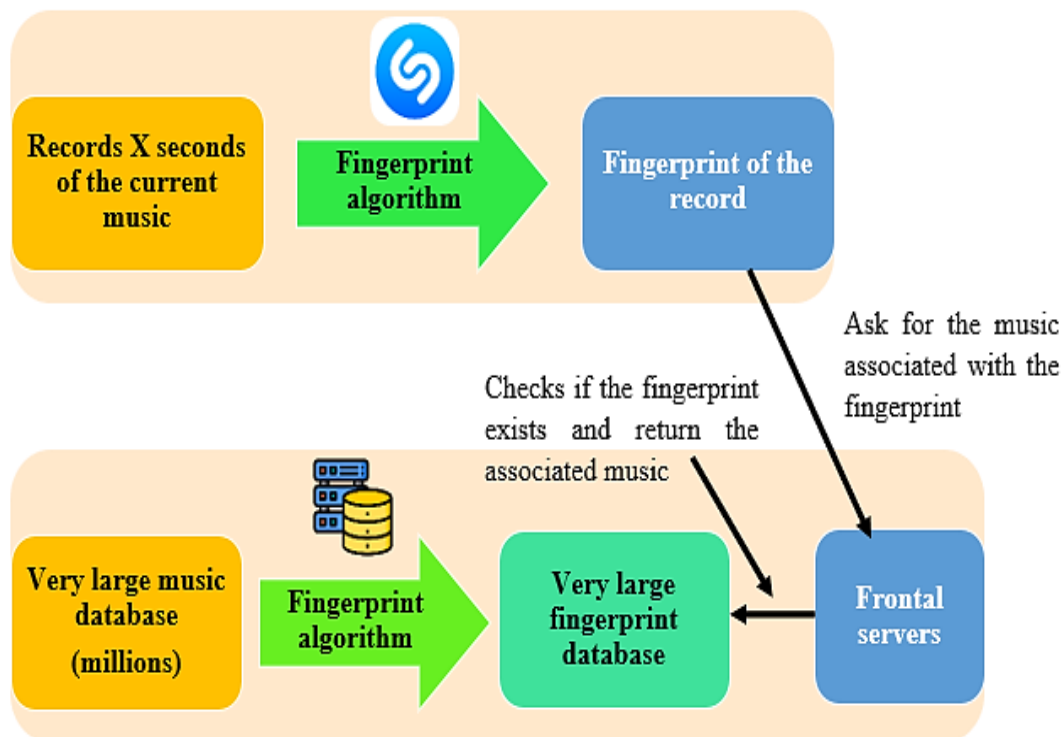
Figure 1. Working Diagram of Shazam Application

1.1. Related Works

The recently published papers point out that researches on the sound processing have increased and it indicates that this is an active research field that emerges new music genres. The authors in Tzanetakis & Cook (2020), pioneered the works on music genre classification using a machine learning algorithm. These two researchers created the GTZAN dataset and to date it has been considered that it is a standard for species classification. According to Bahuleyan (2018), an approach to automatic music classification was presented by providing tags to songs in the user's library. In the study, it is understood that two separate approaches were used. The first is Convolutional Neural Network, the second is various Machine Learning algorithms. Both two approaches have been compared separately, and it has resulted to a conclusion that the VGG-16 CNN model gave the highest accuracy with an accuracy of 0.894. Pelchat & Gelowitz (2020), have studied the classification of musical genres. They have used neural networks to classify songs based upon their musical genres in the

research. The images of the created spectrograms were used as input in the neural network from the time intervals of the songs. Vishnupriya & Meenakshi (2018) have conducted a study on the classification of musical genres. In their study, CNN was used training and classifying the genres; feature extraction and sound analysis were performed on the dataset. The proposed system separates the music into various genres by extracting the feature vector. The results show that the accuracy level of the system is around 76% and will widely thrive and facilitate automatically classification of music genres.

Nirmal & Mohan (2020), have proposed a method for classifying music by using spectrograms. In their papers, they approved that the music signals were first converted to their corresponding spectrograms. These spectrograms are then given as input to the classifier. It is seen that a CNN was used as the classifier. They evaluated performance of the classifier via performance measuring such as confusion matrix and classification accuracy. To do this, the GTZAN dataset was used as the dataset. Chillara et al. (2019), put forward multiple classification models. These models were trained using the Free Music Archive (FMA) dataset. A few of the classification models were trained on mel-spectrograms with the sound features of songs, while a few were trained solely on spectrograms of songs. It was found that the Convolutional Neural Network, which is one of the models in which only spectrograms are given as the dataset, gives the highest accuracy with 88.5% among all other models. Ghildiyal et al. (2020) have studied several classification models which have been established for the classification of musical genres. Most of the patterns were trained using the GTZAN dataset, and a few of the models were trained on the spectrogram. CNN model produced the best performance.

Zhang et al. (2019) have compared various classification algorithms and proposed a new near real-time classification model using RNN with a low accuracy of 64%. The authors used the mean and common variance of the MFCC to train their patterns. Yang & Zhang (2019), have extracted the mel-spectrogram of the fragments in the GTZAN dataset and used it as an input. The authors used the double convolution layer, where the output is passed through different pooling layers and a statistical analysis is done. Another paper determined MFCC and compared the CNN model with the Long ShortTerm Memory model (Gessle & Åkesson, 2019). The results showed that CNN had 56.0% prediction accuracy in GTZAN dataset and 50.5% prediction accuracy in FMA dataset, while LSTM model had 42.0% prediction accuracy in GTZAN dataset and 33.5% prediction accuracy in FMA dataset. From this paper, it is known that the CNN pattern has given better accuracy. Chen et al. (2019), have aimed to classify environmental sounds using the UrbanSound8K dataset. The researchers proposed a CNN-based model to classify environmental sounds in the dataset. Moreover, the researchers stated that they also examined the effect of the number of layers on the performance in this study. In this proposed model, an accuracy value of 78% was obtained.

Demir et al. (2020). have converted audio files to images by using the Short Time Fourier Transform to classify the environmental sounds in the UrbanSound8K dataset in their study. The researchers used pre-trained Convolutional Neural Networks architectures in the model proposed, and VGG16, VGG19 and Densenet201 architectures were used for feature extraction. The obtained feature maps were classified in the Support Vector Machines classifier; this pattern gave an accuracy value of 78.14%. Davish & Suresh (2018), have proposed a CNN-based model to classify environmental sounds in the UrbanSound8K dataset in the study. In their research, data augmentation techniques have been used to increase the model's performance. In addition, different augmentation methods were used in the study for determining the best augmentation technique for making environmental sound analysis. Researchers stated that LPCC is the most successful method among data augmentation methods, and an accuracy rate of 67.8% was seemed from the original dataset. Salamon et. al (2017), have used the UrbanSound8K dataset for classification of environmental sounds. In their study, they have stated that they made data augmentation due to the low environmental sounds. In the proposed CNN-based model, an accuracy value of 73% was obtained in the classification of environmental sounds.

1.2. Datasets

In our study, the most popular dataset in music genre classification, GTZAN was presented to utilize. The GTZAN dataset collection is used to classify music into different types. It has been used by Tzanetakis and Cook contained a series of records reflecting different situations, and they were 10 classes, each containing 100 different 30-second audio files with .wav extension (Tzanetakis & Cook, 2020). These classes consist of blues, classical, country, disco, hip-hop, jazz, metal, pop, reggae, and rock. Some of the sample audio files are seen in Figure 2.
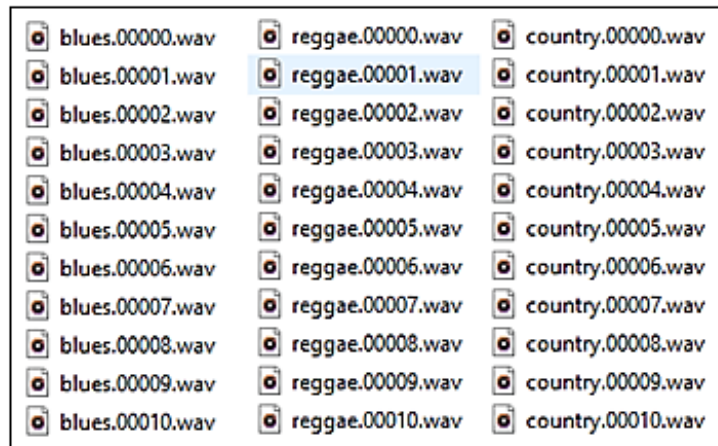
***Figure 2.** Audio Files in the Dataset*

The remaining of the paper is organized as follows: Section 2 presents audio analysis methods used to extract new features from existing audio files. Section 3 presents and discusses the extraction of new features from various audio files in the existing dataset, the creation of a new dataset, and the experimental results of the proposed classification method. Chapter 4 concludes the findings, summarizes the paper and makes some prepositions and directions for possible researches in the future.

2. MATERIAL AND METHOD

The method used for classifying music genres in this chapter. Figure 3 displays the generalized block diagram of the proposed method.
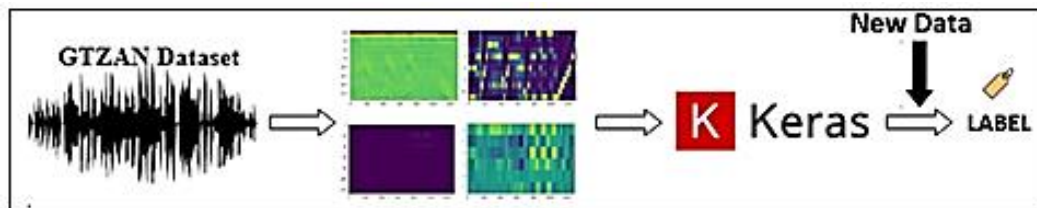
***Figure 3.** Block Diagram of the Method*

Each type of music is described by own characteristics, pitch, melody, chord sequences and type of instrumentation. In order to have a reliable classification, a set of features ought to be used to capture essence of these elements. To divulge the features, the Librosa Package of Phyton has been used for analyzing the music and its sound. The library evaluates audio signal recordings. Mel frequency cepstral coefficients, mel spectogram, chroma vector and tonal centroid features are the features that will use to create a single feature vector for each file on which the model will be trained. These are explained in the below lines.

2.1. Audiotic Features

Mel Frequency Cepstrum Coefficients that is the most well-known, robust, accurate and established methods for feature extraction from audio signals are Cepstral coefficients are calculated by a discrete cosine transform applied to the power spectrum of a signal. The frequency bands of this spectrum are logarithmically spaced according to the Mel scale (Web Source 2). The procedures of the MFCC method are given in Figure 4. The training data set includes GTZAN music data. The MFCC algorithm splits an audio stream into frames by reforming it into smaller windows using the Hamming window. The Fourier transforms stage is used to transform the limited area of the audio signal into a frequency spectrum. The spectrum is generated for each frame using the fast fourier transform and each spectrum is weighted using a filter bank. At the last step, the MFCC vector is calculated by using the Logarithm and the Discrete Cosine Transform. In the cepstrum stage, the mel spectrum is converted to the time domain using DCT and produces the result called MFCC (Yıldırım, 2022).
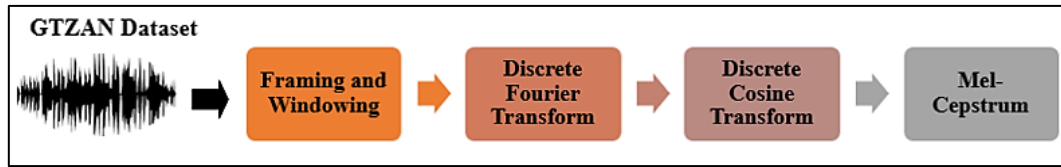
Figure 4. Steps Involved in the MFCC Extraction

The MFCC image of the 25th hip-hop audio file in the GTZAN dataset used is shown in Figure 5.
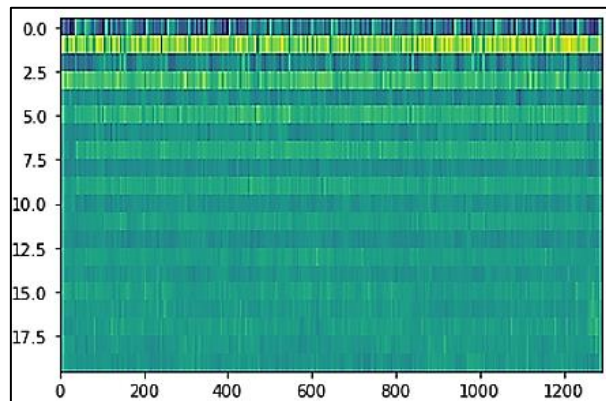
Figure 5. MFCC of the File hiphop.00025.wav

As human ear cannot perceive frequencies linearly, a perceptual scaling created according to the hearing feature of human ear, like Mel Spectogram is used for this purpose (Eray, 2008). MFCC is the expression of the short-time power spectrum of the audio signal on the Mel scale. While the unit of true frequency is Hertz, on the other hand Mel scale frequency is stated by the unit of Mel. Equation 1 defines the converting to Mel scaling from frequency (Karhan et al., 2016). 1 KHz is chosen as the reference and is accepted that it corresponds to 1000 mel (Eray, 2008).

$$\text{mel(f)} = 2595 * \log_{10}(1 + \left(\frac{f}{700}\right))$$

(1)

The view of Mel spectrogram of the 25th hip-hop sound file in the GTZAN dataset used is given in Figure 6.
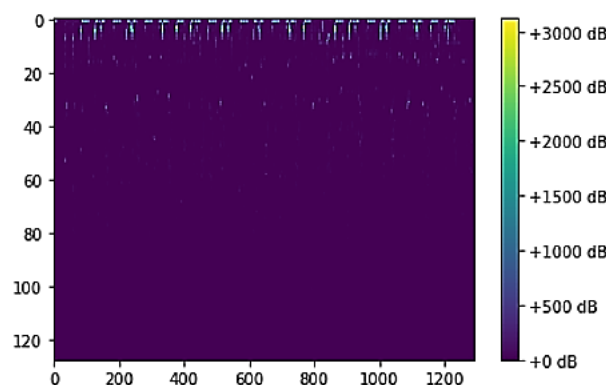
Figure 6. Mel Spectrogram of the Audio File hiphop.00025.wav

Chroma Vector (Chromagram) is a qualitative value that it determines a pitch grade quality referring to "colour" of a musical pitch. It can be dissociated into an octave-invariant value called chroma and pitch height presenting the octave the pitch is in the references (Kattel et al., 2019; Patil et al., 2017). It is a strong representation for sound in which 12 parts representing the 12 different halftones (chroma) of the spectrum musical octave are specified (Web source 3). These parts are C, C#, D, D#, E, F, F#, G, G#, A, A#, B. The chroma vector is a perceptually motivated feature vector, and uses the concept of chroma in the cyclic spiral

representation of the musical pitch perception. Thus, the Chroma vector represents magnitudes in twelve pitch classes on a standard chromatic scale (Kattel et al., 2019). Chroma vector for the same sound sample is given in Figure 7.
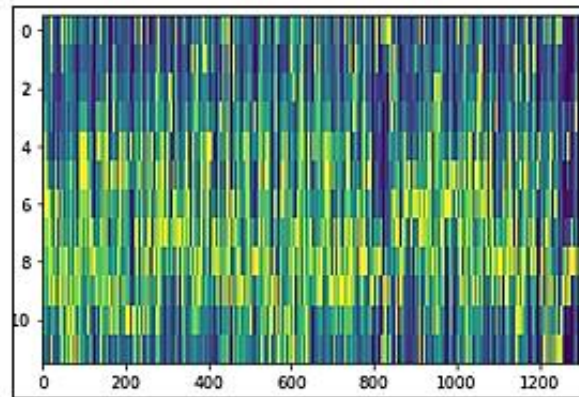
Figure 7. *Chroma Vector of the Audio File hiphop.00015.wav*

Tonal Centroid Features computes the tonal centroid features (tonnetz). This representation uses the method of 1 to project chroma features onto a 6-dimensional basis representing the perfect 5rd, minor 3rd, and major 3rd each as two-dimensional coordinates (Web Source 4) (Harte et al., 2006). Figure 8 displays the tonnetz network.
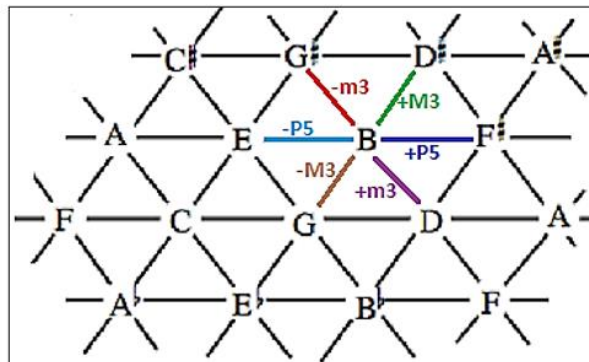
Figure 8. *The Harmonic Vector or the Tonnetz*

In the provided Tonnetz network, the connection shown in green and +M3 indicates minor 3rd, the connection labeled with dark blue and +P5 indicates perfect 5th, purple and the connection labeled with +m3 indicates major 3rd. The created Tonnetz network for Chroma vector of the same sound file is given in Figure 9.
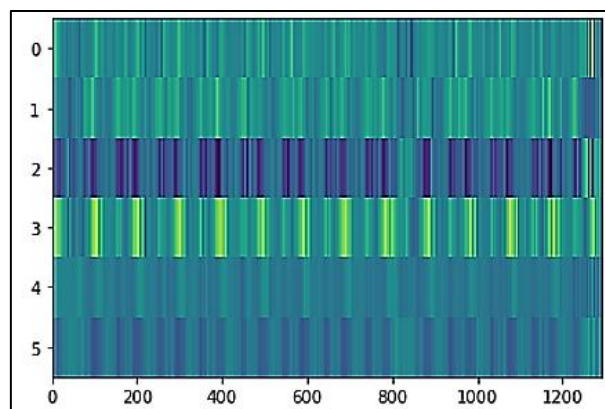
Figure 9. *Tonnetz Feature of the Audio File hiphop.00025.wav*

2.2. Keras

As TensorFlow is an open-source math library for Deep Learning tasks, Deep Learning, which is a subset of the Machine Learning cluster, processes new data from the existed ones. Keras is a Deep Learning library and runs on TensorFlow. While it is written library in Phyton, it does not define almost any Deep Learning model. It is a high-level neural networks API that can work not only on TensorFlow but also on other Theano and CNTK. Creating a deep learning model with Keras is done quietly easy. The procedural steps can be summarized: Defining the trained data, defining layers–model, hyper parameters such as epoch, loss function and optimizer.

3. RESULTS AND DISCUSSION

In this chapter, the sounds in the current dataset are analyzed with the functions provided by the Librosa library. A new dataset is created from the data obtained as a result of the analysis. The new dataset created is used for the training Keras. After training the algorithm, the most searched songs in Türkiye are given as input to the algorithm by using Shazam and it is provided to estimate the type of music.

3.1. Creating a New Dataset with Audiotic Analysis

To extract MFCC, Mel Spectrogram, Chroma Vector and Tonnetz features from the audio files withdrawn from the GTZAN dataset, four functions are created as same name as the above. These functions hold the extracted features of each audio files in separate sequences, are combined using the *concatenate()* function available in the Numpy library. In the last generated dataset array, each element represents an audio file. The dataset includes the features of 1000 audio files in total. The feature set of the extracted and combined features from the audio file is given in Figure 10, and the labeled version of each audio file is given in Figure 11.
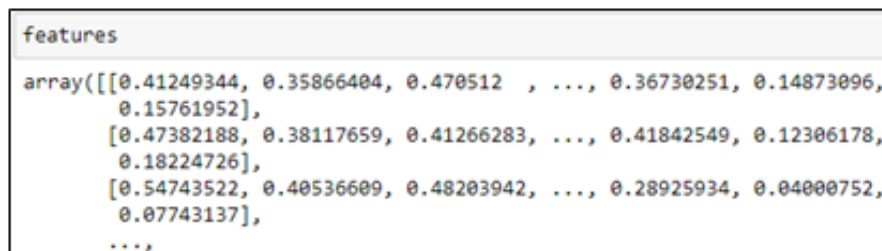
Figure 10. View of Analyzed Audio Files in Dataset
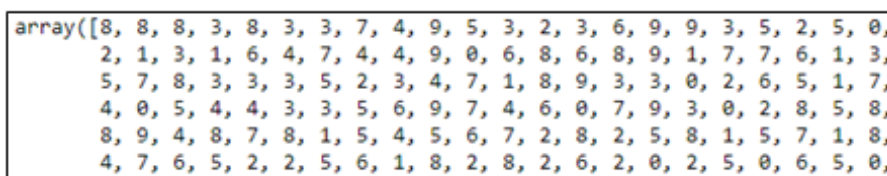
Figure 11. View of Labeled Audio Files in Dataset

The numbers in the sequence given in Figure 11 represent the music genres included in the GTZAN dataset. 0 blues, 1 classical, 2 country, 3 disco, 4 hip-hop, 5 jazz, 6 metal, 7 pop, 8 reggae and 9 rock.

3.2. Splitting the Dataset

Data splitting is to divide data into two or more subsets. In a two-part partition, one part is used to evaluate or test the data and the other to train the model. The random.permutation function of the Numpy library is used to mix the recordings after the property set of the audio files is created so that the model had information about each music genre. This function is used to randomly change an array. During training the model, the dataset is splatted as 60% for training, 20% for validation and 20% for testing. As the result, 600 audio files for training, 200 for validation and 200 for testing are used.

3.3. Training and Evaluation of the Model

The steps how to train and evaluate Keras data are given in Figure 12. First, the model is created While creating the model, some metrics ought to determine. These metrics are a function used to evaluate performance of the model, and are given as arguments to the *compile()* function. They are optimizer, accuracy metrics, probability metrics, regression metrics, based on positive and negative classification metrics. The mentioned above metrics configure training data. The trained model obtains the test data by making inferences.
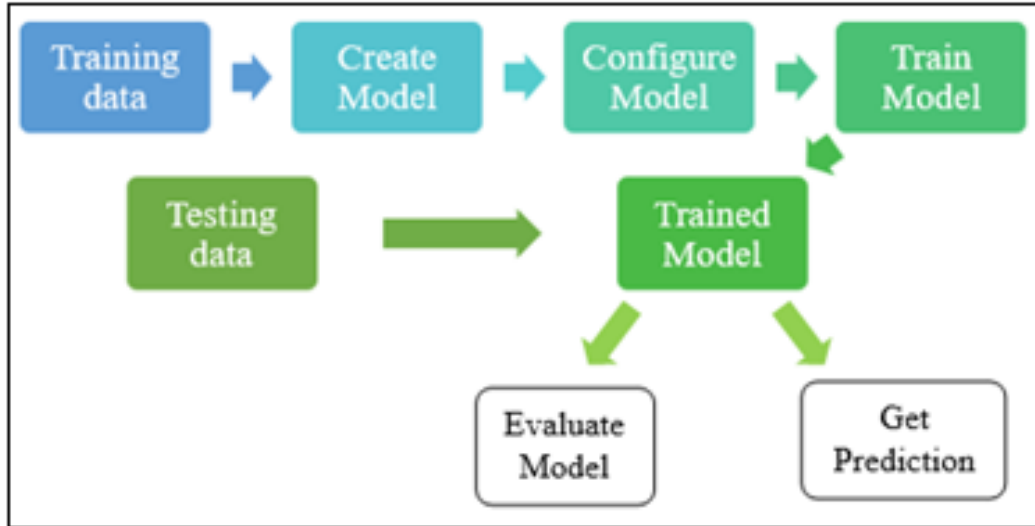
Figure 12. *Keras Algorithm Training Steps*

Two regular densely connected neural network layers which are with a rectified linear unit activation function "relu", and 300 hidden units (the first layer) and 200 (the second layer) are implemented by using Keras for this model. Then, heavily correlated layer with the probability distribution activation function "softmax" is also applied for the output layer. Why Nadam is chosen as the optimizer is chosen is that this give the highest accuracy value in the trials. Next, the model is trained using 64 epochs. The trained Keras is evaluated after the values are obtained. The resulted set of features achieves around 71,66% classification rate.

3.4. Finding the Genre of a New Audio File

The new audio file is withdrawn from the most wanted songs in Türkiye list offering by Shazam, and given in Table 1.

Table 1. *Top 10 shazamed songs in Türkiye*

Rank	Artist	Title	Genre
1	Lvbel C5	Dacia	Reggae
2	DEHA INC. & Reckol	Talibana	Hip-hop
3	Heijan & Muti	İmparator	Hip-hop
4	BLOK3	Affetmem	Hip-hop
5	Metro Boomin, The Weeknd & 21 Savage	Creepin'	Hip-hop
6	Güneş	NKBİ	Hip-hop
7	Alok & Alan Walker	Headlights (feat. KIDDO)	Pop
8	Lady Gaga	Bloody Mary	Pop
9	Mert Demir & Mabel Matiz	Antidepresan	Pop
10	Dj Belite	All Eyez On Me	Hip-hop

The audio file of the songs given in Table 1 ought to be created for determining the type of songs. The Youtube link of this song can be used for this aim. The library is used to generate the audio file over the youtube link by determining the metrics required to use. The metrics consist of information of audio file's name in which will be recorded with and what its extension will be. By means of these metrics, the model is established and the audio file is downloaded using the YouTube link of the song. It ought to be noticed that not all the size of the downloaded audio file is used in estimating the genre of the song. Therefore, the pydub library is used to trim the file size. A 30-second portion of the new audio files from 01:00:00 to 01:30:00 is taken since the audio files in the GTZAN dataset are 30 seconds long. The resulting audio files are recorded with a different name. The created sound files are given as input to the Keras model. Genres predicted are given in Table 2.

***Table 2.** Top 10 shazamed songs in Türkiye*

Rank	Artist	Title	Genre	Estimated
1	Lvbel C5	Dacia	Reggae	Pop
2	DEHA INC. & Reckol	Talibana	Hip-hop	Hip-hop
3	Heijan & Muti	İmparator	Hip-hop	Hip-hop
4	BLOK3	Affetmem	Hip-hop	Hip-hop
5	Metro Boomin, The Weeknd & 21 Savage	Creepin'	Hip-hop	Pop
6	Güneş	NKBİ	Hip-hop	Hip-hop
7	Alok & Alan Walker	Headlights (feat. KIDDO)	Pop	Pop
8	Lady Gaga	Bloody Mary	Pop	Hip-hop
9	Mert Demir & Mabel Matiz	Antidepresan	Pop	Reggae
10	Dj Belite	All Eyez On Me	Hip-hop	Hip-hop

The graphics of the Talibana song estimated correctly in hip-hop by the established model, and the graphics of 50th sample sound file in the hip-hop genre in the GTZAN dataset are given below. The signal graph of the song named "Taliban", which the model predicts correctly, and the signal graph of the 50th sound file in the hip-hop genre in the sample dataset are shown in Figure 13.
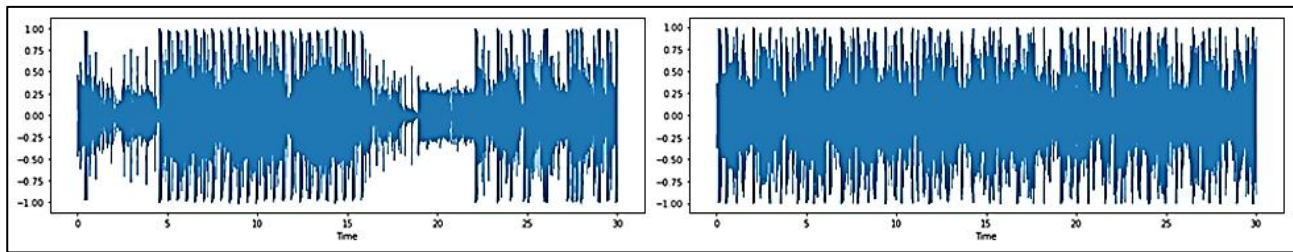
a. Talibana Song   *b. Hip-hop 50. example*

***Figure 13.** Signal Graph, **a)** Talibana Song, **b)** Hip-hop 50. example*

The MFCC graph of the song called Talibana, which the model predicts correctly, and the MFCC graph of the 50th sound file in the hip-hop genre in the sample dataset are seen in Figure 14. The Chromagram graph of the song called Talibana, which the model predicts correctly, and the Chromagram graph of the 50th sound file in the hip-hop genre in the sample dataset are seen in Figure 15. The signal frequencies of the song titled Headlights, which the established model estimated correctly in the pop genre, and the signal frequencies of the 35th sample sound file in the pop genre in the GTZAN dataset are seen in Figure 16. The MFCC signal frequencies of the song titled Headlights, and the MFCC graph of the 35th pop sound file are seen in Figure 17.
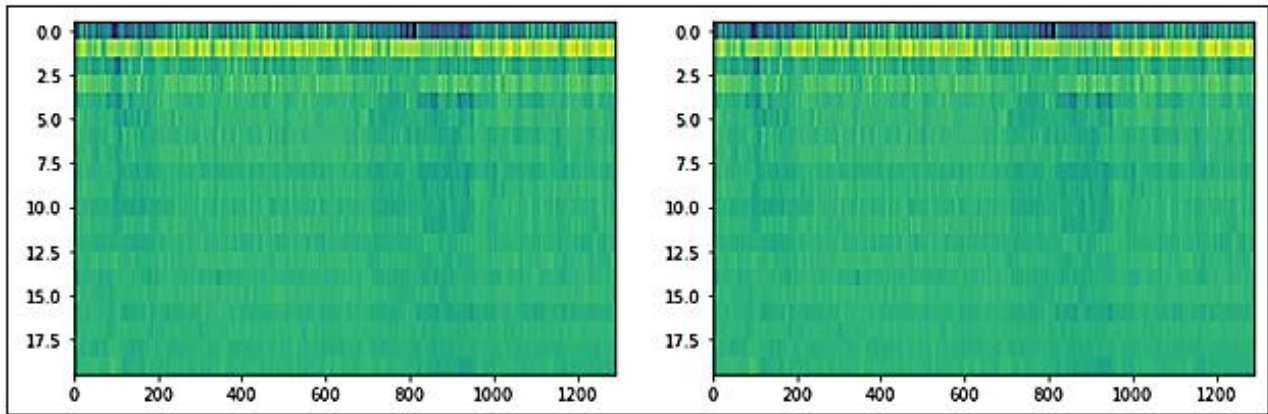
a. *Talibana Song*   **b.** *Hip-hop 50. example*

***Figure 14.** MFCC Graph, **a)** Talibana Song, **b)** Hip-hop 50. example*

In Figure 15, the Chromagram graph of the song called Talibana, which the model predicts correctly, and the Chromagram graph of the 50th sound file in the hip-hop genre in the sample dataset are given. Figure 16 and Figure 17 show signal graphics and MFCC graphics.
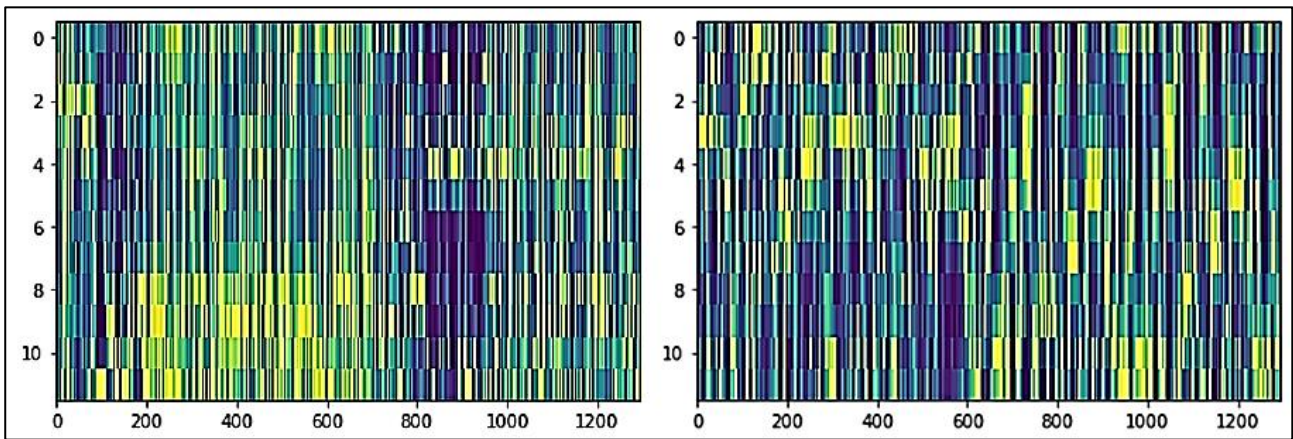
a. *Talibana Song*   **b.** *Hip-hop 50. example*

***Figure 15.** Chromagram Graph, **a)** Talibana Song, **b)** Hip-hop 50. example*
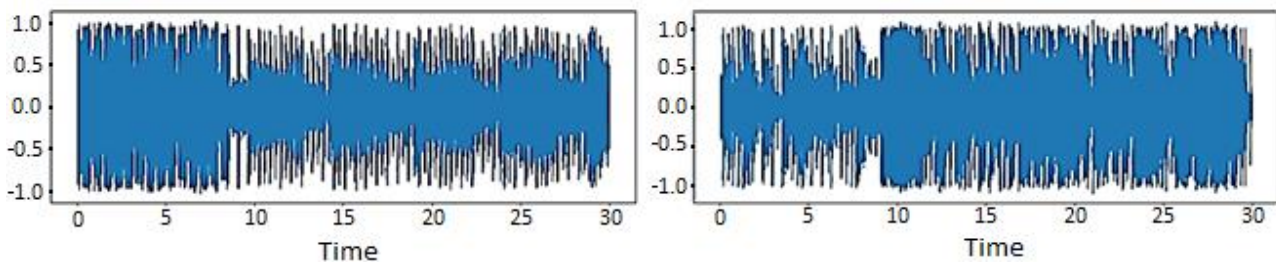
a. *Headlights Song*   **b.** *Pop 35. example*

***Figure 16.** Signal Graph, **a)** Headlights Song, **b)** Pop 35. example*

a. Headlights Song   *b. Pop 35. example*
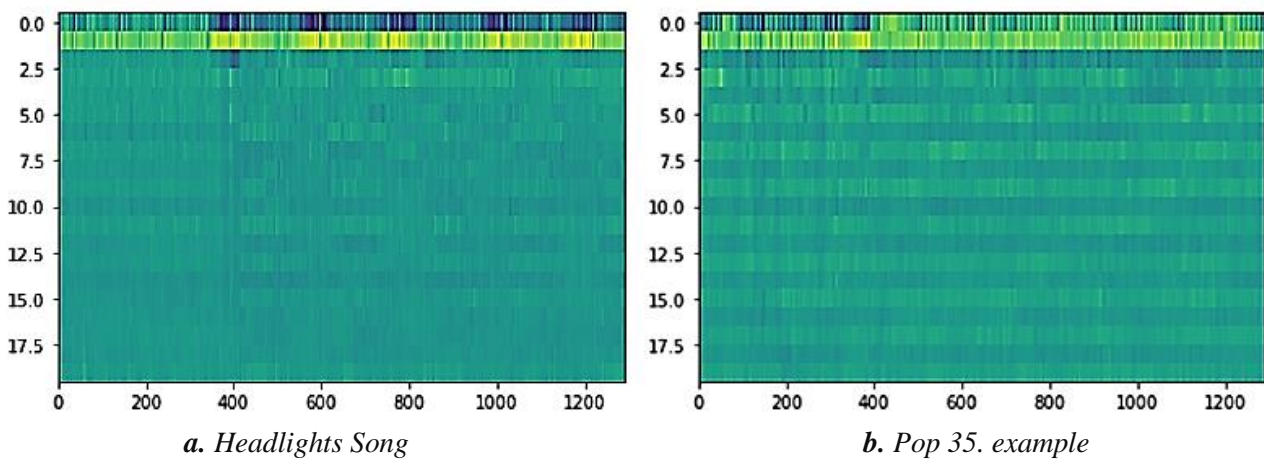
***Figure 17.** MFCC Graph, **a)** Headlights Song, **b)** Pop 35. example*

In this step, we benchmark our proposed system with other existing systems. Comparison amid previous studies and our proposed system is presented in Table 3.

Table 3 indicates that all studies which divide the existing dataset into two parts as training and testing data. A comparison related to the accuracy values among the established models is made. New sound files are not given as input to the established models and no genre prediction is made. The study deals with the established model that it is trained with the existing dataset, and is calculated how accurately it could predict new audio files with the data reserved for validation in the dataset. It has been calculated that the estimated model can predict a new audio file with an accuracy rate of 71.66%.

4. CONCLUSION

The paper examines several scientific modelling techniques presenting music genre classification. In order to extract new attributes of the audio files in the used dataset, the Librosa library has been used. A new dataset has been created by combining the new features. This model was created and trained with Tensorflow / Keras to find the music genre that audio files are entered externally. The dataset is being mixed for training the model. Hence, it is assured that the model had information about music genres. The 60% of the dataset is used for training the model, 20% for testing and 20% for validation.

For realizing this model, the corrected linear unit activation function called as relu is used. two normative connected neural network layers are obtained with 300 hidden units for the first and 200 hidden units for the second layer. followed by, a layer closely related to the probability dispersion activation function softmax is also applied for the output layer. As Nadam gives the highest accuracy in try-outs, it has been chosen for optimizing element. Next, the model is trained by using 64 epochs. The success rate of the trained model in predicting a new audio file is determined as 71,66%. In order to find out whether the trained model correctly predicted the music genre, the top 10 most searched songs in Türkiye by shazam are used. On the other hand, to estimate the genre of the popular song, the audio file of the song is created first by youtube-dl library is used. The resulting sound file is transmitted to the Keras model for the prediction of the music genre. The Keras model correctly estimates 60% of the new audio files given.

To realize this study, machine learning algorithms are used. Nevertheless, different machine learning algorithms can be using to classify musical genres in future studies. We propose that both the dataset is increased and the research is furthered by adding sample audio files values in the current one.

Table 3. Comparison of the Proposed System with Similar Studies

Research, Year	Datasets	Algorithms Used	Results
(Vishnupriy et al., 2018)	GTZAN dataset. Spectrogram images of musics.	Convolutional Neural Network	The system separates the music into various genres by extracting the feature vector. The results show that the accuracy level of the system is around 76%.
(Chillara et al., 2019)	Free Music Archive dataset. Spectrogram images of musics.	CNN–RNN Logistic Regression Simple Artificial Neural Network	The classification accuracies of the CNN model and CRNN are 88.54% and 53.5% respectively. The classification accuracies of the feature-based models LR and ANN are 60.89% and 64.06% respectively.
(Zhang et al., 2019)	GTZAN dataset MFCC features	Support Vector Classification Recurrent Neural Network	They concluded that the short-term MFCC features of the RNN can achieve sufficient classification accuracy. By listening to a piece of music for 0.5 seconds, they determined its genre with 64% accuracy.
(Yang et al., 2019)	GTZAN dataset Mel-Spectrogram features	Convolutional Neural Network	Two different networks, net1 and net2, were created. net1 network achieved 90.7% accuracy, net2 88.3% accuracy.
(Gessle et al., 2019)	GTZAN dataset FMA dataset MFCC features	(CNN) LSTM-Keras	CNN achieved 56% accuracy, and in the FMA dataset, 50.5% accuracy. LSTM achieved 42% accuracy, and in the FMA dataset, 33.5% accuracy.
(Nirmal et al., 2020)	GTZAN dataset. Spectrogram images of musics.	Convolutional Neural Network Pre-trained convnet	Two CNN models are discussed: A user-defined CNN model and a pre-trained convnet. Three music genres (blues, classical and rock) from the GTZAN dataset are selected for testing. The classification accuracies of user-defined CNN model and MobileNet are 40% and 67% respectively.
(Nirmal et al., 2020)	Two music libraries. 1880 songs categorized into 10 genres.	Convolutional Neural Network	Each of these spectrograms was labeled by music genre and then used as inputs in a CNN. The results were obtained 85% accurately during testing data.
(Ghildiyal et al., 2020)	GTZAN dataset	Simple Artificial Neural Network Support Vector Machines Multilayer Perceptron Desicion Tree CNN	The proposed research work has compared few classification models. Among the models created, CNN showed the highest accuracy. The classification accuracy of the model is 91%.
(Proposed Research, 2024)	GTZAN dataset Spectrogram images of musics.	Keras	Keras model is trained by using GTZAN dataset. Therefore, the genres of 10 popular songs in Türkiye are estimated by Shazam application. The Keras model estimates types of the songs with 71.66% accuracy.

REFERENCES

Bahuleyan, H. (2018). Music Genre Classification Using Machine Learning Techniques, *ArXiv:1804.01149v1*, *1*(1). https://doi.org/10.48550/arXiv.1804.01149

Chen, Y., Guo, Q., Liang, X., Wang, J., Qian, Y. (2019). Environmental Sound Classification with Dilated Convolutions, *Elsevier Applied Acoustics*, *148*(1). 123-132, https://dig.sxu.edu.cn/docs/2019-03/2d147cee7cfb4f3eb25ee73f6e6dd3de.pdf

Chillara, S., Kavitha, A. S., Neginhal, S. A., Haldia, S., Vidyullatha, K. S. (2019). Music Genre Classification Using Machine Learning Algorithms: A Comparison. *International Research Journal of Engineering and Technology*, *6*(5), 851-858, https://www.irjet.net/archives/V6/i5/IRJET-V6I5174.pdf

Davis, N., Suresh, K. (2018). Environmental sound classification using deep convolutional neural networks and data augmentation, *IEEE Recent Advances in Intelligent Computational Systems (RAICS)*, (pp. 41-45). https://ieeexplore.ieee.org/stamp/stamp.jsp?tp=&arnumber=8635051&tag=1

Demir, F., Türkoğlu, M., Aslan, M., Sengur, A. (2020). A New Pyramidal Concatenated CNN Approach For Environmental Sound Classification, *Elsevier*, *170*(2020), 7. https://www.sciencedirect.com/science/article/pii/S0003682X20306241

Eray, O. (2008). The speech recognition application with support vector machines, *Pamukkale University*, (pp. 1-90). https://gcris.pau.edu.tr/handle/11499/1501

Gessle, G., & Åkesson, S. (2019). A comparative analysis of CNN and LSTM for music genre classification, Degree Project In Technology 2022 https://www.diva-ortal.org/smash/get/diva2:1354738/FULLTEXT01.pdf

Ghildiyal, A., Singh, K., Sharma, S. (2020). Music genre classification using machine learning, *International Conference on Electronics, Communication and Aerospace Technology (ICECA)*, (pp. 1368-1372). https://ieeexplore.ieee.org/stamp/stamp.jsp?tp=&arnumber=9297444

Harte, C., Sandler, M., Gasser, M. (2006). Detecting harmonic change in musical audio, *1st ACM Workshop on Audio and Music Computing Multimedia (AMCMM)*, (pp. 21-26). https://dl.acm.org/doi/10.1145/1178723.1178727

Hussain, A., Mkpojiogu, E., Almazini, H., Almazini, H. (2019). Assessing the usability of Shazam mobile app, *The 2nd İnternatİonal Conference on Applied Science and Technology (ICAST'17)*, (pp. 0200571– 0200575). https://pubs.aip.org/aip/acp/article/1891/1/020057/886329/Assessing-the-usability-of-Shazam-mobile-app

İmik, U., Haşhaş, S. (2020). What is Music and Where Is It In Our Lives?, *İnönü University Journal of Culture and Art*, *6*(2), 196-202, https://dergipark.org.tr/en/download/article-file/1491772

Karhan, M., Çakır, M., Uğur, M. (2016). Analysis of Electrical Discharge Sound Data Using MEL Frequency Cepstral Coefficients (MFCC), *In Proceeding of the 2016 cigrė Türkiye*, (pp. 4). http://gsk.cigreturkiye.org.tr/bildiriler2016/5.2.pdf

Kattel, M., Nepal, A., Shah, A. K., & Shrestha, D. (2019). Chroma feature extraction, *Conference: Chroma Feature Extraction Using Fourier Transform*, (pp 1-4). https://www.researchgate.net/publication/330796993_Chroma_Feature_Extraction

Nirmal M. R., & Shajee Mohan B. S. (2020). Music Genre Classification using spectrograms*, International Conference on Power, Instrumentation, Control and Computing (PICC)*, (pp. 1-5). https://ieeexplore.ieee.org/document/9362364

Pelchat, N., & Gelowitz, C. M. (2020). Neural Network Music Genre Classification, *Canadian Journal of Electrical and Computer Engineering*, *43*(3), 170-173. https://ieeexplore.ieee.org/stamp/stamp.jsp?tp=&arnumber=9165253

Patil, N. M., Nemade, & M. U. (2017). Music Genre Classification Using MFCC, K-NN and SVM Classifier, *International Journal of Computer Engineering In Research Trends*, *4*(2), 43-47. https://www.ijcert.org/index.php/ijcert/article/view/371/313

Salamon, J., & Bello, J. P. (2017). Deep convolutional neural networks and data augmentation for environmental sound classification, *IEEE Signal Processing Letters*, (pp. 279-283). https://ieeexplore.ieee.org/stamp/stamp.jsp?tp=&arnumber=7829341

Yang, H., & Zhang, W. Q. (2019). Music genre classification using duplicated convolutional layers in neural networks, *INTERSPEECH*, (pp. 3382-3386). https://www.isca-archive.org/interspeech_2019/yang19f_interspeech.html

Yıldırım, M. (2022). Automatic Classification of Environmental Sounds with the MFCC Method and the Proposed Deep Model, *Fırat University Journal of Engineering Sciences*, *34*(1), 449-457. https://dergipark.org.tr/en/download/article-file/2186156

Tzanetakis, G., Cook, P. (2020). Musical Genre Classification of Audio Signals, *IEEE Transactions on Speech and Audio Processing*, *10*(5), 293-302. https://ieeexplore.ieee.org/stamp/stamp.jsp?tp=&arnumber=1021072

Vishnupriya, S., & Meenakshi, K. (2018). Automatic music genre classification using convolution neural network, *International Conference on Computer Communication and Informatics (ICCCI)*, (pp. 1-4.). https://ieeexplore.ieee.org/stamp/stamp.jsp?tp=&arnumber=8441340

Web Source 1: (Shazam Nasıl Çalışıyor?). (2024). (Accessesd: 12.02.2024) https://musiconline.co/tr/blog/shazam-nasil-calisiyor

Web Source 2: (Music genre classification using Librosa and Tensorflow/Keras). (2024). (Accessesd: 12.02.2024) https://musiconline.co/tr/blog/shazam-nasil-calisiyor

Web Source 3: (Librosa). (2024). (Accessesd: 12.02.2024) https://medium.com/datarunner/librosa-9729c09ecf7a

Web Source 4: (librosa.feature.tonnetz). (2024). (Accessesd: 12.02.2024) https://librosa.org/doc/main/generated/librosa.feature.tonnetz.html

Zhang, S., Gu, H., & Li, R. (2019). Music Genre Classification: Near-Realtime vs Sequential Approach, *PrePrint*. (pp. 6). https://cs229.stanford.edu/proj2019spr/report/3.pdf

Analysis of Current-Voltage Properties of Al/p-si Schottky Diode with Aluminium Oxide Layer

Elanur DİKİCİOĞLU[1*] [ID] Barış POLAT[2] [ID]

[1] Yüksek İhtisas University, Vocational School of Health Services, Ankara, Türkiye
[2] Ankara Medipol University, Faculty of Engineering and Natural Science, Department of Industrial Engineering, Ankara, Türkiye

Keywords	Abstract
Schottky Diode Current-Voltage Ideality Factor Barrier Height Atomic Layer Deposition	In our study, the effects of the metal oxide (aluminum oxide, Al_2O_3) thin film placed between the metal and the semiconductor on the diode's characteristics were investigated. The Al_2O_3 thin film was suitable for its growth on a p-type silicon substrate by the atomic layer deposition (ALD) technique. In this study, a diode structure with an oxide interlayer was fabricated. To investigate the electrical parameters of the fabricated Schottky diode, measurements of current-voltage (I-V) were carried out at room temperature and in the 5 V voltage range. Using the I-V measurements, diode parameters such as the barrier height (Φb), the ideality factor (n), and the current density (I0) were evaluated using the theory of thermionic emission (TE) and Cheung's method. Using the TE method and Cheung's method, the approximate values of Φb, n parameters were calculated as 0.77 eV, 5.43, and 0.77 Ev, 5.97, respectively. According to calculations, the developed Schottky diode is a rectifier diode and has been determined to have photodiode properties. This research offers an understanding of the production and electrical characteristics of Schottky devices based on Al_2O_3.

1. INTRODUCTION

Schottky diodes (SDs) are one of the important topics for research based on both theoretical and experimental findings in the fields of physics and electronics. While these types of structures have an important place in revealing the measurable electrical magnitude of semiconductor technology, their usage areas are gradually increasing due to the knowledge of their distinctive features and ease of production. Metal-semiconductor (MS) contacts, also known as Schottky diodes, are also called structures that can respond to sudden transitions between the voltage drop parameters applied at high frequencies, rapid direction change, and conductivity as well as insulation properties. In other words, important features that distinguish these diodes from other structures are that they have a very fast switching ability, low series resistance, and a minimum forward voltage drop. Considering these advantages, MS contacts maintain their place as the most used contacts in the field of semiconductor technology (Buyukbas et al., 2023; Sze, 1981). Schottky diodes are used in many electronic devices today, with the development of technology. Schottky diodes have minimal forward voltage drop, low series resistance, and fast switching (Sze, 1981). Metal insulator semiconductor (MIS) structures and Metal-Oxide Semiconductor (MOS) structures are formed by placing an insulating layer between the metal and semiconductor layers using an artificial or natural oxidation method (Nicollian & Brews, 1982). The schematic view of the metal-semiconductor Schottky diode is given in Figure 1.

*Corresponding Author, e-mail: elanurdikicioglu@yiu.edu.tr

MIS and MOS structures are quite similar in terms of layer structure and formation techniques. The thickness of the insulating layer at the interface separates these two similar structures. The insulating layer in MOS structures is thicker than in MIS structures (Nicollian & Brews, 1982). An insulating intermediate layer is created between the semiconductor and metal layers using a natural or artificial oxidation method. Thus, the MIS structure is obtained. The insulator in the intermediate layer between the metal and the semiconductor regulates the charge transitions between these layers over time by insulating the layers from each other (Kong et al., 2019).

Metal-oxide-semiconductor Field Effect Transistors (MOSFETs), a crucial component of integrated circuits in the contemporary electronics industry, are largely composed of MOS structures. MOSFET structures are basic electronic circuit elements that have a great impact on the development of chip and transistor technologies. Therefore, all studies on any MOS device first require an understanding of the basic operating principles of MOS structures.
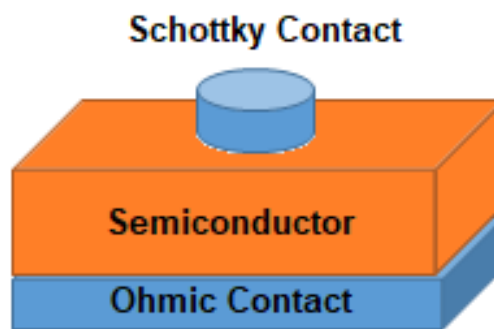
Figure 1. Schematic view of the contacts of a metal-semiconductor Schottky diode

Metals with work functions selected depending on the semiconductor type (p-type/n-type) are used in the preparation of MIS and MOS structures as rectifier contacts. Metals such as gold (Au), aluminum (Al), and silver (Ag) with high purity values are preferred to change the purity of the metal and make it higher. As a semiconductor, silicon (Si) material is generally preferred as it has a stable structure at high temperatures and is cheaper to manufacture. The quality of the insulating layer and the semiconductor surface placed between the M/S in MIS structures significantly affect and greatly increase the performance, reliability, and accuracy of the Schottky diode. Increasing leakage current in MIS structures may negatively affect the performance of the device. Therefore, to minimize the leakage current in these structures, the insulating interface layer is selected from materials with a high dielectric constant. MIS structures with low leakage current enable the construction of integrated electronic devices that have a fast response time, reduce power losses, and operate more stably. To reduce the amount of leakage current in MIS structures, materials with high dielectric constants such as Al_2O_3, HfO_2, and $SrTiO_3$, which have a dielectric constant higher than the dielectric constant of the SiO_2 layer, are preferred (Choi et al., 2023; Tongpeng et al., 2023; Seven et al.,2024). Since Al_2O_3 has a dielectric constant that is significantly greater than SiO_2, it has been recommended as a material that can be used as an insulating material in electronic applications as well as MOS and MIS structures. The dielectric constant of Al_2O_3 is 9.0, and the dielectric constant of SiO_2 is 3.9.

Aluminum oxide (Al_2O_3) is a compound whose chemical formula consists of Al and O atoms. Aluminum oxide is a white powder in its pure form and is a component of many minerals found in nature. The crystal structure of aluminum oxide can be found in both amorphous and crystalline forms. Its crystal structure exists in two main forms, alpha-Al_2O_3 (α) and gamma-Al_2O_3. In the α form, Al^{3+} ions are arranged in a hexagonal coating arrangement and O^{2-} ions are arranged according to this arrangement. In gamma form, they occur in cubic structures. Figure 2 shows the schematic representation of the α-Al_2O_3 hexagonal close-packed lattice structure (Troncy, 2021). Aluminum oxide has high-temperature resistance, high hardness, and chemical resistance, and thanks to these properties, it is preferred in applications such as ceramics, metallurgy, chemical industry, glass industry, catalyst, fiber composite, and electronics. Al_2O_3 has a high dielectric constant (high-k ~9), large bandgap (~7 eV), high thermal conductivity, mechanical strength, and high-temperature resistance. This means that aluminum oxide can store electric charges better. Because of these superior properties, it is a

technologically important material and one of the most studied among all oxides. Aluminum oxides are used as a suitable insulation material for MIS structures thanks to their physical and chemical properties (Troncy, 2021). For this reason, Al_2O_3 was preferred as the oxide layer in this study.
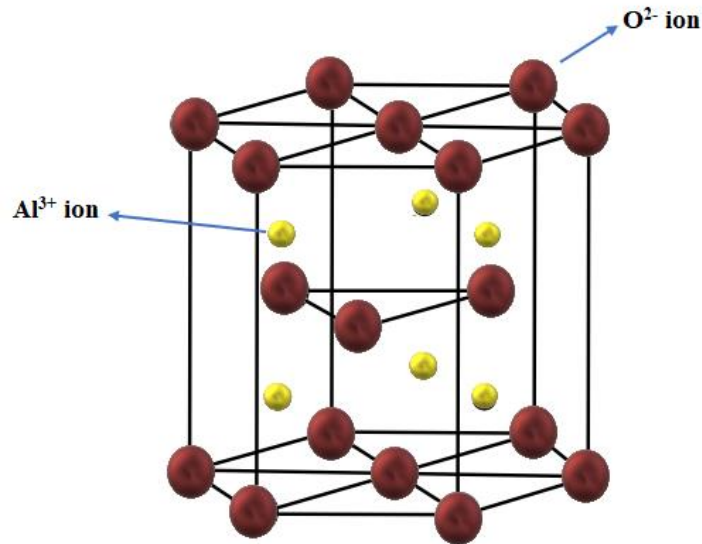
Figure 2. α-Al₂O₃ Hexagonal Close-Packed Lattice Structure

There are many methods to grow the Al_2O_3 insulating interfacial layer. Atomic layer deposition (ALD) is one of the most preferred methods due to the control over film homogeneity and great chemical versatility. The ALD method has been widely used recently because it is more advantageous than other growth techniques and can be controlled while growing the layer (Schilirò et al., 2023). ALD method; It is a chemical vapor coating method that provides thickness control at values below nanometers, where the chemical reactions occurring periodically on the surface are self-limiting and allow the production of films with high homogeneity at low temperatures by preventing reactions in the gas phase by separating the precursor gases (Suntola, 1992). By holding the gas phase precursors to the surface at low temperatures without reaching extremely high temperatures, the ALD process creates high-quality thin coatings. This method aims to obtain a smoother, homogeneous surface, thus minimizing the interfacial effect and obtaining an ideal structure (Ji et al., 2023). With this method, a better-quality layer can be grown and the thickness of the grown layer can be easily determined. Due to such advantages, the ALD method was preferred when growing the Al_2O_3 insulating interfacial layer.

In this study, we have produced the Al/Al_2O_3/p-type Si diode using the ALD technique. We used I-V measurements to determine the electrical parameters of this structure. In the I-V measurements, we then calculated the diode parameters such as the barrier height (Φ_b), current density (I_0), and ideality factor (n) using the TE method and the Cheung method.

2. MATERIAL AND METHOD

In this study, a p-type silicon crystal with a thickness of 380 μm, (100) surface orientation, and a resistivity of 1-10 Ω-cm, shiny on one side and matte on the other, was used. Firstly, the p-type Si substrate was purified by applying chemical purifying procedures. Then, an Al ohmic contact with a 124 nm thick high-purity was formed on the matte surface of the p-type silicon substrate to create an ohmic contact.

In the second step, a 17 nm thick Al_2O_3 as an interfacial layer was grown and deposited on the entire shiny surface of the crystal using the ALD technique. With the utilization of ALD at 170 ^{0}C which is a low substrate temperature, Al_2O_3 was deposited on the bright surface of the wafer. Al_2O_3 thin film was deposited at 170 ^{0}C using aluminum (trimethylaluminum-TMA) and oxygen (water-H_2O) precursors. Thus, a 17 nm thick Al_2O_3 thin film was obtained. Nitrogen (99.999%) was used as cleaning and carrier gas to separate the precursor cycles. Table 1 gives the recipe for the Al_2O_3 film grown on a Si substrate with ALD.

Table 1. Al_2O_3 coating recipe on Si substrate with ALD

Precursor	Trimethylaluminum (TMA)
H_2O pulse time (ms)	15
Purge time (ms)	10
Precursor pulse time (ms)	100
Purge time (ms)	20
Operating temperature (°C)	170
Cycles	125

After growing a 17 nm Al_2O_3 film on the p-type Silicon substrate, it was time to create Schottky contacts. In this last stage, approximately 128 nm Al metal was coated on Al_2O_3 using the Physical Vapor Deposition (PVD) technique to create a Schottky contact. The metal contacts are circular and 1.5 mm in diameter.

A depiction of the produced Al_2O_3/p-Si Schottky diode is given in Figure 3. After the calculations, it was seen that the Al_2O_3/p-Si Schottky diode has a rectifying feature. Electrical measurements were carried out to obtain the I-V characteristics of the Al/Al_2O_3/p-Si Schottky diode. The energy band diagram of the Al/Al_2O_3/p-Si Schottky diode is given in Figure 4.
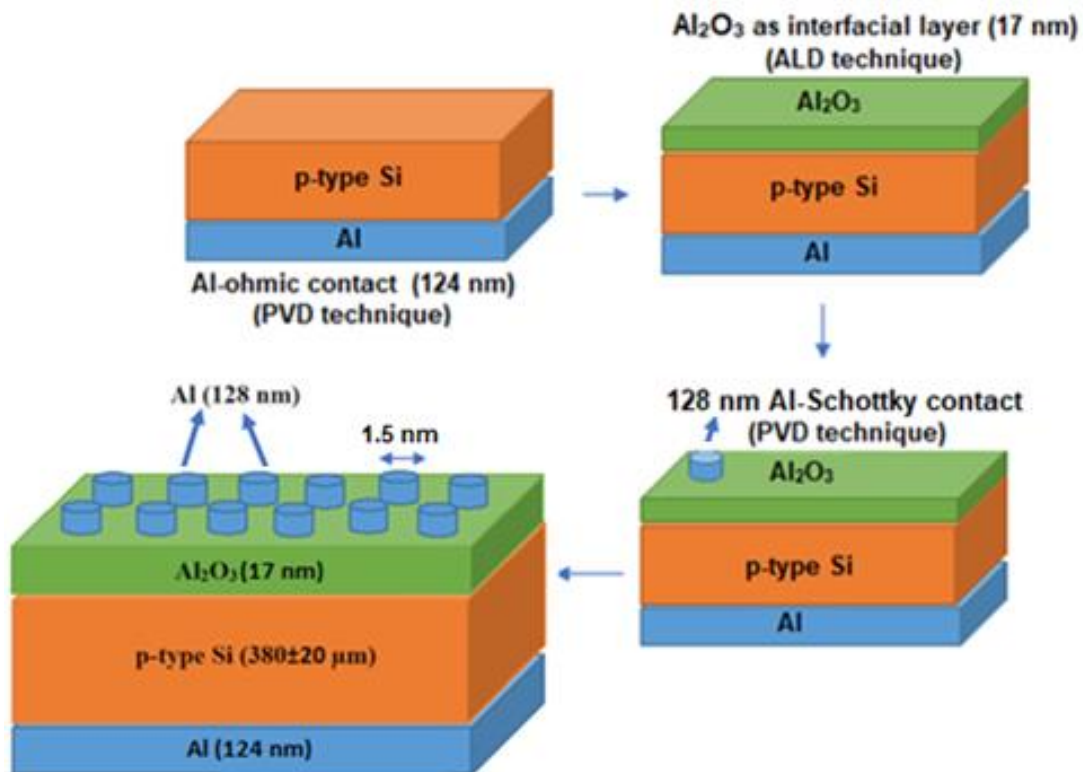
Figure 3. Layer-by-layer view of Al/Al_2O_3/p-type Silicon diode
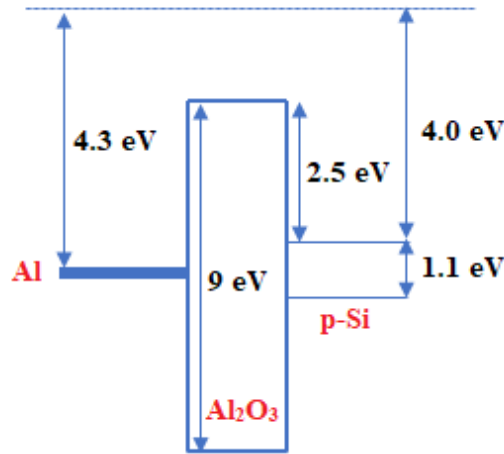
Figure 4. Energy band diagram of Al/Al₂O₃/p-type Silicon MIS schottky diode

3. RESULTS AND DISCUSSION

To investigate the electrical characteristics of the Al/Al$_2$O$_3$(17 nm) /p-type Si design, electrical data was gathered through I-V measurements. All measurements were carried out in a dark environment at room temperature (300 K). The current-voltage graph is presented in Figure 5.

As can be seen in Figure 5, the graph of the ln (I)-V drawn using the I-V characteristic of the Al/Al$_2$O$_3$/p-Si diode measured in the dark environment is given. When the I-V characteristics of the Al/Al$_2$O$_3$/p-Si diode in the dark are examined, it is seen that this structure has good rectification properties and exhibits a rectifying diode behavior. The rectification ratio (RR) of the diode was obtained as 1.08×10^5. The ln(I)-V graph's upward curving at high currents is caused by series resistance's dominant effect on the current curve in the forward polarization area, which can originate from either the contact wires or the mass resistance of the MOS structures. The R_s effect and the existence of interfacial states cause the I-V curves to bend downward at sufficiently high supply voltages.

The insulating layer created naturally or artificially between the metal and semiconductor transforms this structure into a MIS structure. This insulating layer significantly affects the parameters of the I-V characteristics. A single current conduction mechanism may be effective at a certain temperature and over the entire voltage range, or two or more current conduction mechanisms may be effective at the same time (Kong et al., 2019).

TE method was used to study the electrical properties of its structure. Due to the presence of the interface layer in MOS structures, the relationship between forwarding bias voltage and current for V>3kT/q is given (Sze, 1981; Rhoderick & Williams, 1988):

$$I = I_0 \, exp\left(\frac{qV}{nkT}\right)\left[1 - exp\left(-\frac{qV}{kT}\right)\right] \tag{1}$$

In ideal Schottky diodes, unless the applied voltage is high, current conduction follows the TE model. The current expression is written as;

$$I = I_0 \, exp\left(\frac{qV}{nkT}\right) \tag{2}$$

The semi-logarithmic ln(I)-V graph's straight-line intersection at V=0 yields I$_0$ (the saturation current) value;

$$I_0 = AA^* T^2 \, exp\left(-\frac{q\varphi_b}{kT}\right) \tag{3}$$
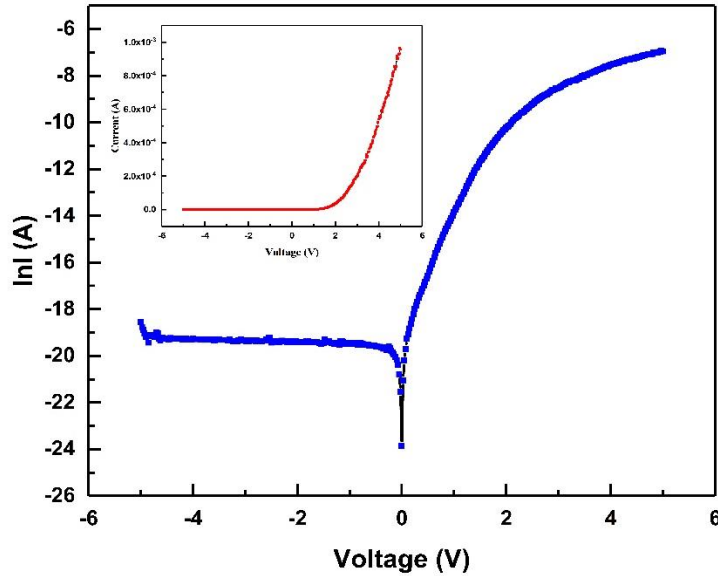
Figure 5. *Investigation of the ln(I)–V characteristics of the produced Al/Al$_2$O$_3$(17 nm) /p-type Si Schottky diodes*

Here *n* represents the ideality factor, q signifies the electronic charge, k symbolizes the Boltzmann constant, T denotes the temperature in Kelvin, I$_0$ represents the reverse saturation current, A* is determined as the Richardson constant (32 A/cm^{2}K^2 for p-type Si), A is known as the diode area, V represents the applied voltage and Φ_b denotes the effective barrier height.

In the graph of the ln(I)-V, it is expected to be a line. If the graph is nonlinear, the ideality factor is large, and the diode has moved away from ideality. In practice, many Schottky diodes deviate from the TE method. This non-ideal diode behavior is described by using a dimensionless parameter *n*, called the ideality factor, in the current expression. Equation (2) and the slope of the linear zone in the ln(I)-V plot can be used to calculate the ideality factor. The ideality factor is a metric frequently used to evaluate how much practical diodes deviate from the ideal TE characteristic (Sze, 1981).

$$n = \frac{q}{kT} \frac{dV}{d(\ln I)} \tag{4}$$

Φ_b can be derived from Eq. (5) as are given by

$$\varphi_b = \frac{kT}{q} \ln\left(\frac{AA^*T^2}{I_0}\right) \tag{5}$$

The Φ_b value was calculated from the intersection points of the forward trend ln(I)-V graph at room temperature. The ideality factor, as per the TE method, ought to be 1. The ideality factor depends on the presence of an insulating layer between the metal-semiconductor, the series resistance, and the distribution of the interfacial density of states (N$_{ss}$) in the forbidden energy band gap (Kong et al., 2019). The ideal situation where *n* = 1 has not been encountered. Because the applied voltage affects the obstacle height to some extent. The reason for this effect is the natural formation of an insulating oxide layer approximately 5–20 Å thick at the metal-semiconductor interface, even in near-ideal Schottky diodes (Kong et al., 2019).

The method developed by N.W Cheung and S.K. Cheung was used to calculate the values of *n*, Φ_b, and *Rs* (Wang, 2004). Cheung's model is applied to the non-linear high-voltage area of the forward bias of the I-V graphs (Cheung & Cheung, 1986). Based on this approach, *n*, Φ_b. R_s, and H(I) can be expressed as

$$\frac{dV}{d(\ln I)} = n\frac{kT}{q} + IR_s \tag{6}$$

$$H(I) = V - \frac{nkT}{q}\ln\left(\frac{I}{AA^*T^2}\right) \tag{7}$$

$$H(I) = n\varphi_b + IR_s \tag{8}$$

The Φ_b was determined from the linear section of the forward bias I-V curve. Figure 6 displays the H(I) vs I and dV/dlnI vs I graphs for an Al/Al_2O_3/p-type Si diode at 300 K.
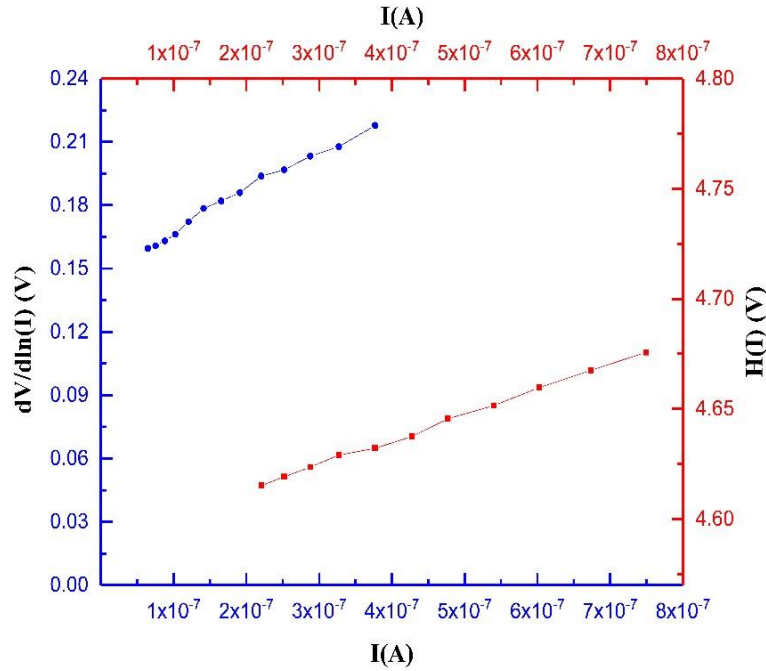
Figure 6. *H(I) vs I and dV/d(ln I) vs. I characteristics of produced Al/Al_2O_3 /p-type Si Schottky diode*

The graph of dV/d(ln I) versus I is a straight line with a slope of R_s and an intercept of nkT/q on the y-axis. This is because Eq. (6) results in a linear relationship in the lower left curvature region of the forward bias I-V characteristics. The R_s value is calculated from the gradient of the dV/d(ln I) vs. I curve, while *n* is determined from the intersection point of the curve. In Eq. (8), the value of R_s is determined from the gradient of the H(I) vs I curve, and the value of Φ_b is obtained from the point where the curve is cut off, using the *n* value calculated in Eq. (6).

As seen in this figure, the semi-logarithmic ln(I)-V slope can be obtained by extrapolating the straight line and this can be used to extract the ideality factor of the diode design. Φ_b, I_0, and *n* values gained from current-voltage measurements over the Al/Al_2O_3/p type Si Schottky diode are shown in Table 2.

Table 2. *Diode parameters of Al/Al_2O_3/p-Si Schottky structure*

Methods		n	Φ_b (eV)	R_s (kΩ)	I_0 (A)	RR
Standard (TE) Method		5.43	0.77	-	2.43E-09	
Cheung	dV/dlnI vs I	5.97	-	186.11		1.08×10^5
	H(I) vs I	-	0.77	114.20		

In this study, *n* and Φ_b were determined from forward I–V features using the TE method and Cheung method. From the flat supply I-V graphs of the produced diode structure, *n* values were calculated as 5.43 and 5.97,

and Φ_b values were calculated as 0.77 eV and 0.77 eV, respectively, using the TE method and Cheung methods. Regarding the Al/Al$_2$O$_3$/p-Si Schottky diode structure, we can say that although its rectification feature is good, it exhibits a non-ideal diode behavior due to its high ideality factor. The n value of the TE theory is close to the n value of the Cheung method, as shown in Table 1. The diode's non-ideal behavior (n>1) indicated the existence of interfacial states. The reason why the values of the ideality factor are greater than unity is due to series resistance, interface impurities, barrier inhomogeneity, and interface states. Because of the dispersion of the interface states at the interface and the existence of an insulating interface layer between the metal and semiconductor, the computed n value is greater than 1 (Singh, 1985; Szatkowski & Sierański, 1988). The Φ_b values for both methods are consistent with each other for the diode. We have presented in Table 3 the diode properties of different Schottky diodes with Al$_2$O$_3$ interlayers created by other researchers at 300 K, coated with different coating methods and with different thicknesses, to compare them with our current work.

Table 3. Comparison of diode parameters for various types of Schottky diodes with Al$_2$O$_3$ interlayer

Diodes	Interlayer Coating Methods	n	Φ_b (eV)	RR	References
Al/Al$_2$O$_3$ (17 nm)/*p-Si*	ALD	5.43 (TE) 5.97 (Cheung)	0.77 0.77	1.08×10^5	Present work
Al/Gr/Al$_2$O$_3$ (17 nm)/p-Si	RF magnetron sputtering	3.89 (TE) 5.54 (Cheung)	0.69 0.68	10^3	(Efil et al., 2020)
Au/ Al$_2$O$_3$ (30 nm)/*p-Si*/Al	Spin coating	1.59	0.91	3.58×10^4	(Deniz et al., 2022)
Al/ Al$_2$O$_3$ (2.5 nm)/p-Si	ALD	3.014 (TE) 3.44 (Cheung)	0.75 0.97	-	(Yıldız & Cavuş, 2016)
Al/ Al$_2$O$_3$ (4 nm)/p-Si	ALD	1.82	0.50	4.74×10^4	(Kosal et al., 2019)
Au/Al$_2$O$_3$(50 nm)/n-Si	RF magnetron sputtering	1.23	0.77	-	(Eymur &Tuğluoğlu, 2021)

As indicated in Table 3, variations in the technique and thickness employed to form the interface layer in the measurements impacted the *n* and Φ_b values. When the study of Efil et al. (17 nm Al$_2$O$_3$) and our study (17 nm Al$_2$O$_3$) are compared, it is seen that graphene improves the n value. It is thought that the coating method (RF magnetron sputtering) also affects this change. The reasons for the high ideality factor values in our study are interface impurities, series resistance, interface states, and barrier inhomogeneity. When Φ_b values are compared with all coating methods, it can be seen that they are almost compatible with each other. The RR value is higher than structures coated with RF magnetron sputtering and spin coating.

4. CONCLUSION

At room temperature and in the dark, we examined the I-V characteristics of the Al /Al$_2$O$_3$ (17 nm) /p-type Si structure. The standard TE method and Cheung's method were used to measure and assess the electrical characteristics of this semiconductor, including the ideality factor and barrier height. The electrical properties that belong to the Al/Al$_2$O$_3$/p-Si diode are very sensitive to voltage. The electrical characteristics of the structure are crucial for accurately and consistently evaluating the interface states. Using the TE method and Cheung's method, the approximate values of Φ_b, *n* parameters were calculated as 0.77 eV, 5.43, and 0.77 Ev, 5.97 respectively. The deviation of the ideality factor value from the ideal was attributed to the Al$_2$O$_3$ insulating layer between the semiconductor/metal and the special distribution of interfacial states. In practice, for an ideal situation, *n* =1. However, since the applied voltage affects the obstacle height to some extent, this situation has rarely been encountered in the literature. The reason for this effect is the natural formation of a thin oxide layer with a thickness of at least 5-20 Å at the metal-semiconductor interface, even in Schottky diodes that are closest to ideal. The deviation of the obstacle height from the ideal situation resulting from its dependence on the applied voltage is expressed as $1/n=1-(\delta\Phi_b/\delta V)$. Since some of the applied voltage falls on the diode and some on the oxide layer, the barrier height becomes a function of the applied voltage. Another reason why the ideal factor is greater than 1 is that the series resistance value is large. Due to the voltage drop across the insulating

layer, the voltage across the diode decreases. This decrease in voltage causes the current-voltage characteristics to deviate from the ideal situation. In summary, the reasons for the high ideality factor values in our study are interface impurities, series resistance, interface states, and barrier inhomogeneity. This research offers an understanding of the production and electrical characteristics of Schottky devices based on Al_2O_3.

As a result, many studies have been carried out by preparing various insulation layers for the metal-semiconductor interface, and various models have been developed. Al_2O_3 shows advantages over SiO_2 and SnO_2, which have been widely used in micro-electronics to date, and thus allows the production of higher quality, longer lasting, and faster Schottky structures, transistors, and integrated circuits. Therefore, it is expected that studies on the production of various dielectric and oxide films with high dielectric coefficients using the atomic layer deposition technique will remain current and important in the coming years. In future studies, the thickness of Al_2O_3 can be changed in a way that will positively affect the electrical properties of Al_2O_3 and coating can be done with different methods as alternatives to the ALD method. Additionally, the effects can be examined by applying different types and ratios of coating on the Al_2O_3 layer. According to the findings, it was observed that the thickness of the Al_2O_3 structure and the coating method significantly affected the ideality factor, series resistance, and barrier height properties.

AUTHOR CONTRIBUTIONS

Methodology and writing-reviewing, E.D., B.P.; editing, E.D.; conceptualization and software, E.D., B.P. All authors have read and legally accepted the final version of the article published in the journal.

CONFLICT OF INTEREST

The authors declare no conflict of interest.

REFERENCES

Buyukbas-Ulusan, A., Tataroglu, A., & Altındal-Yerişkin, Seçkin (2023). Analysis of the Current Transport Characteristics (CTCs) in the Au/n-Si Schottky Diodes (SDs) with Al_2O_3 Interfacial Layer over Wide Temperature Range. *ECS Journal of Solid State Science and Technology*, *12*(8), 083010. http://doi.org/10.1149/2162-8777/acf06e

Cheung, S. K., & Cheung, N. W. (1986). Extraction of Schottky diode parameters from forward current-voltage characteristics. *Applied physics letters*, *49*(2), 85-87. http://doi.org/10.1063/1.97359

Choi, H. Y., Jeon, J. D., Kim, S. E., Jang, S. Y., Sung, J. Y., & Lee, S. W. (2023). Strained $BaTiO_3$ thin films via in-situ crystallization using atomic layer deposition on $SrTiO_3$ substrate. *Materials Science in Semiconductor Processing*, *160*, 107442. https://doi.org/10.1016/j.mssp.2023.107442

Deniz, A. R., Caldıran, Z., & Taşyürek, L. B., (2022). Electrical characteristics of Al_2O_3/p-Si heterojunction diode and effects of radiation on the electrical properties of this diode. *Journal of Materials Science: Materials in Electronics*, *33*(36), 26954-26965. https://doi.org/10.2139/ssrn.4136068

Efil, E., Kaymak, N., Seven, E., Orhan, E. O., Bayram, O., Ocak, S. B., & Tataroglu, A. (2020). Current–voltage analyses of Graphene-based structure onto Al_2O_3/p-Si using various methods. *Vacuum*, *181*, 109654. https://doi.org/10.1016/j.vacuum.2020.109654

Eymur, S., & Tuğluoğlu, N. (2021). Fabrication and characterization of Au/MO/n-Si (Mo: ZnO, In_2O_3, Al_2O_3) Schottky diodes grown by RF magnetron sputtering. *New Materials, Compounds and Applications*, *5*(2), 122-131.

Ji, C., Solomon, M. T., Grant, G. D., Tanaka, K., Hua, M., Wen, J., & Dibos, A. M. (2023). Nanocavity-mediated Purcell enhancement of Er in TiO thin films grown via atomic layer deposition. arXiv preprint arXiv:2309.13490. https://doi.org/10.48550/arXiv.2309.13490

Kong, M., Li, B., Guo, C., Zeng, P., Wei, M., & He, W. (2019). The optical absorption and photoluminescence characteristics of evaporated and IAD HfO_2 thin films. *Coatings*, *9*(5), 307, https://doi.org/10.3390/coatings9050307

Kosal, M., Marıl, E., & Altındal, Ş. (17 - 19 August 2019). *Temperature Dependent Current-Transport Mechanisms (CTMs) in the Al/Al₂O₃/p-Si (MIS) Diodes (SDs) Using Current-Voltage-Temperature (IVT) Characteristics in the Temperature Range of 200-320 K.* 1st International Conference on Optoelectronics, Applied Optics and Microelectronics, Erdebil, Iran.

Nicollian, E. H., & Brews, J. R. (1982). Experimental evidence for interface trap properties. *MOS (Metal Oxide Semiconductor) Physics and Technology, John Wiley and Sons, New York*, 291-314.

Rhoderick, E. H., & Williams, R. H. (1988). *Metal-semiconductor contacts* (Vol.129). Oxford: Clarendon Press.

Schilirò, E., Fiorenza, P., Lo Nigro, R., Galizia, B., Greco, G., Di Franco, S., Bongiorno, C., La Via, F., Giannazzo, F., & Roccaforte, F. (2023). Al₂O₃ Layers Grown by Atomic Layer Deposition as Gate Insulator in 3C-SiC MOS Devices. *Materials*, *16*(16), 5638. https://doi.org/10.3390/ma16165638

Seven, E., Orhan, E. Ö., Di Bartolomeo, A., Ertuğrul, M., & Taştekin, N. A. (2024). Graphene/Al₂O₃/Si Schottky diode with integrated waveguide on a silicon-on-insulator wafer. *Indian Journal of Physics*, 1-9. https://doi.org/10.1007/s12648-023-03062-7

Singh, A. (1985). Characterization of interface states at Ni/n CdF₂ Schottky barrier type diodes and the effect of CdF₂ surface preparation. *Solid-State Electronics*, *28*(3), 223-232. https://doi.org/10.1016/0038-1101(85)90002-4

Suntola, T. (1992). Atomic layer epitaxy. *Materials Science Reports*, *4*(5), 261-312. https://doi.org/10.1016/0040-6090(92)90874-B

Szatkowski, J., & Sierański, K. (1988). Interface effects on Mg Zn₃P₂ Schottky diodes. *Solid-state electronics*, *31*(2), 257-260. https://doi.org/10.1016/0038-1101(88)90138-4

Sze, S. M. (1981). *(Second edition) Physics of Semiconductor Devices.* New York: John Wiley & Sons, 362-390.

Tongpeng, S., Wannapaiboon, S., Amonpattaratkit, P., Silawong, P., Janphuang, P., Pattanakul, R., & Jiansirisomboon, S. (2023). Effects of La-Doped HfO₂ Films on Dielectric Properties by Sol-Gel Method. *Integrated Ferroelectrics*, *239*(1), 30-42. https://doi.org/10.1080/10584587.2023.2234607

Troncy, R. (2021). *Synthesis and high-temperature behavior of self-restoring coatings*. Doctoral dissertation, Université de La Rochelle.

Wang, Z. L. (2004). Zinc oxide nanostructures: growth, properties and applications. *Journal of physics: condensed matter*, *16*(25), R829. https://doi.org/10.1088/0953-8984/16/25/R01

Yildiz, D. E., & Cavuş, H. K., (2017). Electrical properties of Al/p-Si structure with Al₂O₃ thin film fabricated by atomic layer deposition system. *Surface Review and Letters*, *24*(06), 1750077. http://doi.org/10.1142/S0218625X17500779

Examining the Blood-Feeding Interactions During Intra- and Interspecific Adult Competition between *Aedes albopictus* and *Aedes aegypti* -a Laboratory Study

Fatma BURSALI[1*] (ID)

[1] *Adnan Menderes University Faculty of Science, Department of Biology, Aydin, Türkiye*

Keywords	Abstract
Aedes Interspecific Interactions Oviposition	*Aedes albopictus* and *Aedes aegypti* are striped mosquitoes with similar behavioral characteristics. They are known vectors of dangerous arboviruses and are expanding their reach globally. These species have established in specific areas of Türkiye, with *Ae. albopictus* expanding significantly than *Ae. aegypti*. While the larval competition of these two mosquito species has been studied, not much is known about their interactions during adulthood. We first investigated the effects of interspecific and intraspecific larval competition on the survival rate into adulthood and the wing length of females and males in containers of different sizes and food level conditions. This research also explored how females of these mosquitoes compete for blood meals in confined environments and its effects on blood feeding rates and female fecundity. Larval competition hinders *Ae. aegypti* emergence, *Ae. albopictus* remains resilient across varying resource levels. Notably, both species displayed increased blood feeding rates when housed together, suggesting potential facilitation or competitive avoidance strategies. Interspecific pressure caused a decrease in the number of eggs laid in mixed species cages for *Ae. aegypti* only. This study highlights the complex competitive dynamics between *Ae. albopictus* and *Ae. aegypti*. While larval competition appears to affect *Ae. aegypti* emergence. Further understanding of adult interactions is crucial for predicting their co-occurrence and effectively managing their populations, especially as *Ae. albopictus* shows greater adaptability and expansion within Türkiye.

1. INTRODUCTION

Aedes albopictus Skuse, 1894 and *Ae. aegypti* Linnaeus, 1762 (Diptera: Culicidae) are medically important vectors and closely related mosquitoes (Diptera: Culicidae) spreading across the world (WHO, 2022). They are vectors of important arboviruses. Infection from dengue, chikungunya, yellow fever and Zika viruses are threats to public health in endemic areas (Rossati et al., 2015). *Ae. aegypti* originated in tropical Africa and *Ae. albopictus* populations originated from Southeast Asia (Vezzani & Carbajo, 2008). The current global distributions of these *Aedes* species have increased significantly. They are highly adaptive, capable of withstanding ecological changes outside their native range (Lounibos, 2002; Rey & Lounibos, 2015). *Ae. albopictus* has been detected in several coastal provinces in Türkiye including Thrace, Black Sea, and Aegean regions (Akiner et al., 2016; Sakacı, 2021) whereas *Ae. aegypti* distribution is still restricted to northeastern part of Türkiye (Touray et al., 2023).

They share similar ecological niches. Both species breed and thrive in small artificial containers and in tires (Paton & Bonsall, 2019). Their ability to breed in small amounts of water and lay eggs that can survive dry periods for months makes them incredibly difficult to control. *Ae. aegypti* prefers to blood feed on humans, whereas *Ae. albopictus* is an opportunistic feeder, taking blood meals from both humans and animals (Bursali

& Simsek, 2023). Also, some researchers suggest that these species have distinct environmental preferences: *Ae. aegypti* generally thrive in urban landscapes whereas *Ae. albopictus* prefers suburban areas with higher flora (Heinisch et al., 2019).

Invasive mosquito species can invade new ecosystems and interactions including interspecific competition with native species can influence the ecosystem of invaded areas (ECDC, 2020). Such impacts can be seen in the early invasion of *Ae. aegypti* into Asia which triggered a significant displacement of endemic *Ae. albopictus* from large urban centers (Gilotra et al., 1967). Likewise, In the United States, studies established a competitive advantage of *Ae. albopictus* over *Ae. aegypti* (Braks et al., 2004). Interspecific larval competition among native and invasive mosquito species is one of the primary mechanisms that can cause competitive population reduction or displacement (Lounibos, 2007). When larvae of different species share the same ecological niche, the stronger larvae can negatively impact the growth and development of the weaker larvae through physical or chemical means. The stronger larvae may be better at finding and consuming food, leaving less for weaker larvae or occupy the best spaces in the environment, leaving weaker larvae with less suitable habitat and physically exclude weaker larvae from food sources (Giatropoulos et al., 2022). Hence, interspecific competition between *Ae. aegypti* and *Ae. albopictus* larvae have been widely investigated in the field and laboratory (Murrell & Juliano, 2008) and it has been shown that competitive elimination of *Ae. aegypti* by *Ae. albopictus* mostly relied on the seasonal changes in climate, type of food, and population source (Leisnham & Juliano, 2010; Juliano, 2010).

Both species are reared in various laboratories for scientific research (Juliano, 2010). Rearing in the laboratory holds significant importance for a variety of reasons. Mosquitoes encounter numerous biotic during their lifespan that affect their morphological and physiological characteristics (e.g. body size, blood feeding activity), fitness traits (survival, fecundity) and their population growth (Carrington et al., 2013). These biotic or abiotic factors impact adult mosquito phenotypes as well as their vector competence and transmission (Alto & Bettinardi, 2013). So, rearing mosquitoes enables studying their breeding patterns, feeding preferences, insecticide resistance mechanisms, and susceptibility to pathogens in a controlled environment. Thus, information is crucial and provides valuable insights that can inform disease control strategies. Sometimes, rearing both species in the same laboratory setting poses a significant risk of cross-contamination. Researchers can significantly reduce the risk of cross-contamination by physical separation and implementing strict hygiene protocols to prevent the transfer of immature stages and adult mosquitoes between rearing areas. As mentioned above, several studies have researched the interspecific larval competition between these mosquitoes; but few studies have taken a comprehensive approach of how these mosquitoes compete for blood meals and its effects on blood feeding rates and female fecundity. In this laboratory factorial experimental design study, we assessed the impact of container size, food ration, and their interactions on the mosquito emergence and adult body size of *Ae. aegypti* and *Ae. albopictus* mosquitoes. This study also explores how these mosquitoes compete for blood meals in confined environments and its effects on egg-laying.

2. MATERIAL AND METHOD

2.1. Maintenance of Mosquito Colonies

Aedes albopictus larvae were sampled from Güzelçamlı, Aydin, Türkiye, and *Ae. aegypti* eggs was obtained from the Biology Department of Hacettepe University, Türkiye. These insects are maintained in an insectarium at 70±10 relative humidity, 28±2°C, 12 h:12 h photoperiod, in the Vector Control Laboratory, Aydın Adnan Menderes University, Turkey. Adult mosquitoes were maintained in insect cages (40 × 40 × 40 cm) with ad libitum access to 10% sugary water. Every 2-3 days females were provided with a blood meal using defibrinated sheep blood through a membrane and eggs laid on filter papers in paper cups with water were hatched in tap water and emerged larvae were provided on fish food and maintained at 24 °C. For the experiments, sufficient eggs were hatched synchronously.

2.2. Experimental Design: Larval Competitive Treatments

Experiments were established to assess the impact of container size and food ration on mosquito interaction. The size of the containers was 11 cm length × 10 cm width × 5.5 cm depth filled with 250 ml water as small; 18 cm length × 11 cm width × 6 cm depth with 500 ml water for medium; or 22 cm height × 15.5 cm width ×

8 cm depth with 750 ml water for large. The ratio of the one-by-one interaction of the mosquitoes used (*Ae. aegypti* vs *Ae. albopictus*) was 50:0, 25:25, 0:50 and the interactions were. 0.1 g or 0.15 g of ground Tetramin fish food was added. This resulted in 18 treatment combinations with 2 replicates for a total of 36 containers. Food was added to containers after the first instar larvae were introduced and again 5 d later. All containers were maintained at 27±1°C, 70% RH, and a 12 h dark photoperiod in a cage until eclosion. The developmental rate (ratio of individuals developing into adults) and size of newly eclosed adults were recorded and used as measures of competitive outcome. Newly emerged adults were held for another 24 h at 28°C with access to sugary water until full expansion and sclerotization of the cuticle before measurement of wing span/length which is a proxy for body size of a mosquito (Nasci, 1990; Petersen et al., 2016; Yeap et al., 2013). The adults were freeze-killed, wings were detached, and wing lengths (axial incision to apical margin) of 20 (10 males: 10 females) randomly mosquitoes from each group were measured under a microscope with an ocular micrometer (precision ± 0.03 mm) (Nasci, 1990).

2.3. Blood Feeding and Female Fecundity Experiments

Eggs of both species taken from stock cultures hatched synchronously. Newly emerged female mosquitoes of each species were then housed in cages – either alone (with 25♀ and 15 ♂) or with equal numbers of the other species (*25♀ and 15 ♂* for each species). These cages were incubated in the insectary for a week before a restrained mouse (*Mus musculus*) was introduced to the cages. This blood feeding procedure was approved by Aydin Adnan Menderes University Ethics committee (Approval number: 64583101/2024/09). The mosquitoes fed for an hour and the number of engorged females was counted to determine the percentage number of blood-fed females. Then 10 females were randomly selected and transferred to a 400-ml screened paper cup with water. The females were left to lay eggs for 4 more days. The number of eggs laid in mixed cages was compared to single cages.

2.4. Statistics

Data on the emergence ratio and adult body size based on the wing length of adult mosquitoes were analyzed using the Shapiro–Wilk normality test and homogeneity of variance to address normal distribution. Differences in adult emergence and adult body size were determined using generalized linear models with competition, amount of food, container size, and their interactions as the main factors taken into consideration. Student t-test was used to compare the differences in the number of blood-fed females and the number of eggs laid per female in the adult experiments. P<0.05 was used as the significance level.

3. RESULTS

3.1. Larval Competitive Treatments

Analysis of variance in the adult emergence during competition between *Ae. albopictus* and *Ae. aegypti* are presented in Table 1 and Figure 1. Competition was the only main effect that had an impact on *Ae. aegypti* emergence. Fewer adults were collected from medium and large containers which both species as compared to with only *Ae. aegypti* at high food supply. Besides this, no statistical difference was determined on the effects of competition, food supply, and container size or their interactions on the emergence of both *Ae. aegypti* and *Ae. albopictus* species.

Looking at the size of the adults that emerged after larval competition, *Ae. aegypti* males collected from small containers with mixed species at both low and high food supply were slightly larger than those from containers with single species. Simple main effects of competition, food amount, container size, and their interaction had a statistical impact on *Ae. aegypti* male size (Table 2, Figure 2). No difference was observed in the other container sizes. For *Ae. albopictus* male sizes were similar in all treatments (P<0.05).

In the case of female size, *Ae. aegypti* adults from containers with interspecific competition at high food supply were larger than containers with intraspecific competition. At low food, interspecific competition caused a reduction in size as compared to intraspecific competition. For *Ae. albopictus*, female size was found to be larger in containers with interspecific competition regardless of food amount or container type (Table 2, Figure 3).

Table 1. *ANOVA output on Ae. aegypti and Ae. albopictus adult emergence during intra and interspecific competition*

Source	Ae. aegypti			Ae. albopictus		
	df	F	P.	df	F	P.
competition	1	6.248	0.02	1	1.09	0.307
ration	1	0.009	0.926	1	0.129	0.723
container	2	3.637	0.042	2	2.102	0.144
competition * ration	1	0.963	0.336	1	0.002	0.967
competition * container	2	3.369	0.051	2	0.309	0.737
ration * container	2	0.229	0.797	2	4.037	0.031
competition * ration * container	2	0.948	0.401	2	1.012	0.379
Footnote: df, degree of freedom; F, F-value; P, significance level (<0.05)						
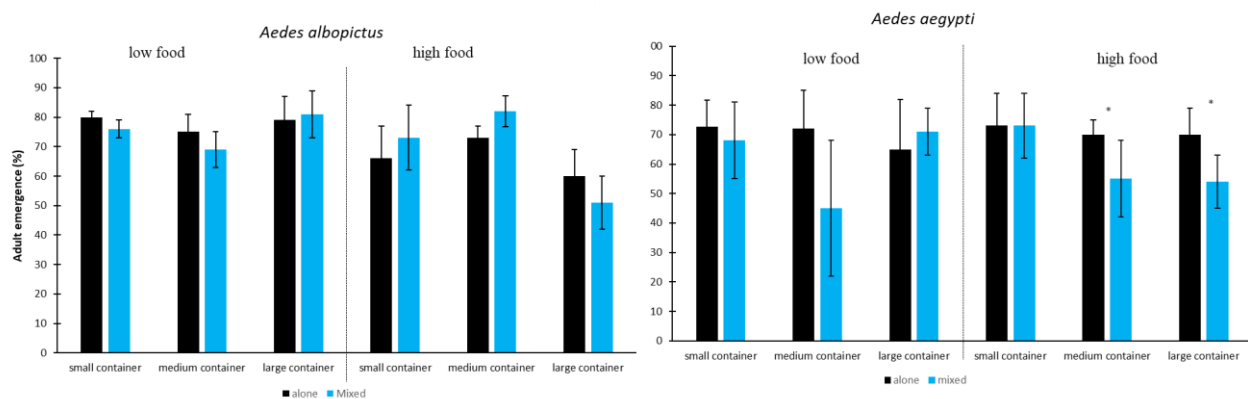
Figure 1. *Adult emergence of Ae. albopictus and Ae. aegypti during intra and interspecific larval competition in different containers and food level. (ANOVA, Tukey's test with significance level P<0.05)*

3.2. Blood Feeding and Female Fecundity Experiments

In these experiments, I investigated the effects of adult competition in confined spaces on blood feeding and female fecundity. Newly emerged female mosquitoes of each species were housed in cages either alone or with equal numbers of the other species. I observed that statistically fewer mosquitoes blood blood-fed in single cages as compared to mixed cases for both species (t=-20.86; df=4; p<0.001) (Figure 4). The number of *Ae. aegypti* that fed in mixed cultures was twice the amount in single cultures. For *Ae albopictus*, 60% of females fed in mixed cultures were as 43% fed in single cages (t=-5.838; df=4; p=0.004). There was a statistical difference in the number of eggs laid by females of *Ae. aegypti* (t=4.437; df=4; p=0.011), no difference was observed for *Ae. albopictus* (t=-1.106; df= 4; p=0.331) (Figure 5).

4. DISCUSSION

This study explored the differential competitive effects during larval competition. Results showed that interspecific competition hinders *Ae. aegypti* emergence, whereas *Ae. albopictus* remains resilient across varying resource levels. This disparity suggests *Ae. albopictus'* greater adaptability, a crucial factor in its observed wider reach in Türkiye.

There are numerous studies on the interspecific competition for space and food resources between *Ae. albopictus* and *Ae. aegypti* larvae, both in the field and laboratory. These studies have shown that competition during the larval stages can impact various growth and development parameters of weaker competitors (Juliano, 2010, Reiskind et al., 2012; Yan et al., 2021). Besides food, factors including seasonal changes in climate, and population origin can also influence this interaction (Leisnham & Juliano, 2010). Among these

studies, Noden et al. (2016) comprehensively explored the influence of intra- and inter-specific larval competition on *Ae. aegypti* and *A. albopictus* adult mosquito traits. They measured the impact over the entire life of these mosquitoes and reported that competitive pressures influenced adult emergence and development time for both species' females. Only the median wing length of *Ae. albopictus* females only were affected. They also demonstrated that adults collected from these competitive treatments had no effects on the blood feeding and reproductive success of the mosquitoes. Steinwascher (2020) found that *Ae. aeygpti* intraspecific competition was sex-based, females competed with females, and males with males, and an increase in density caused an increase in competition. The author also showed that the amount and timing of food inputs alter mosquito growth and competition, with effects varying among the sexes. In another study, Yan et al. (2021) provided high or low amounts of larval food to *Ae. aegypti* larval stages and found that low larval nutrition differentially influences female mosquito life history traits, i.e. adult survival, size, and fecundity, and that a positive connection existed between fecundity and size. Similarly, other studies on the interspecific interactions of *Aedes* spp. with other mosquito species have shown that interaction influences the development time, survival, adult body size, vectorial competence, and capacity of less competitive container-dwelling mosquitoes (Lizuain et al., 2022). Giatropoulos et al., (2022) reported that, *Ae. albopictus* larvae outcompeted and developed faster than larvae of *Ae. cretinus* especially when the food amount was low.

Also, I observed an unexpected adult interspecific dynamic. Both *Ae. albopictus* and *Ae. aegypti* show increased blood feeding rates when housed together, hinting at potential resource facilitation or competitive avoidance strategies. This contradicts the expected outcome of interspecific competition and warrants further investigation into the underlying behavioral or ecological factors driving this interaction. Species-specific impact on reproduction showed that while egg-laying of *Ae. aegypti* decreased under interspecific pressure, *Ae. albopictus* remains unaffected. This suggests differential vulnerability at the reproductive stage, which could influence population dynamics and disease transmission. This is the first study to assess the effects of adult competitive dynamics under confined spaces on blood feeding rates and reproduction (female fecundity). Other factors could influence *Aedes* population dynamics and virus transmission. Schmidt et al. (2018) examined the impact of desiccation stress on the survival of female *Ae. aegypti* and *Ae. albopictus* mosquitos and reported that humidity impacts the survival of female *Ae. aegypti* in controlled settings. Further research into the underlying mechanisms of these observed dynamics is crucial for effective control strategies.
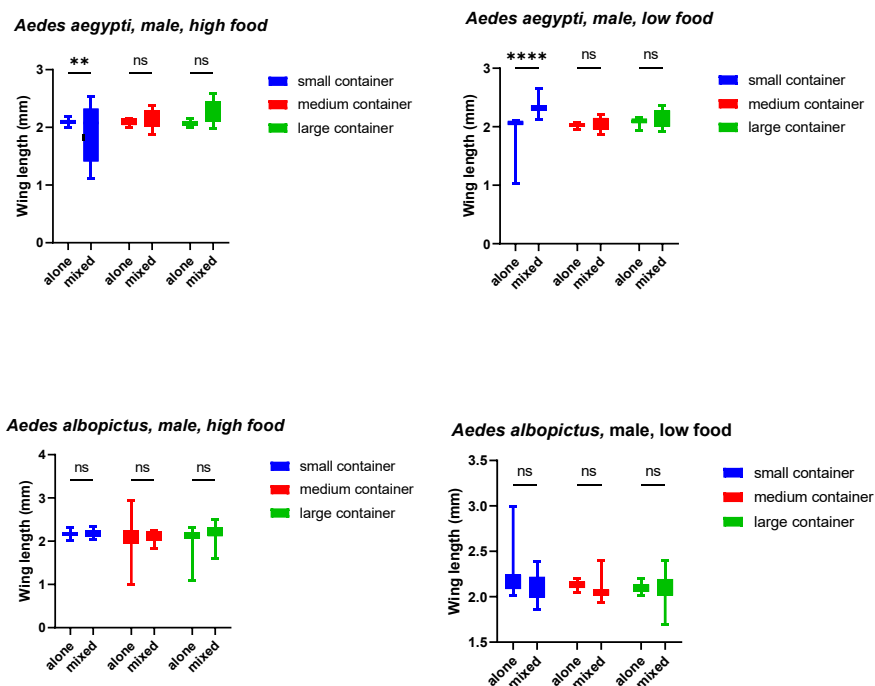
Figure 2**. Male wing length of Ae. aegypti and Ae. albopictus during intra and interspecific larval competition in different containers and food level. ns, non-significant; P ≤0.05*, P ≤0.01 **, P ≤0.001*
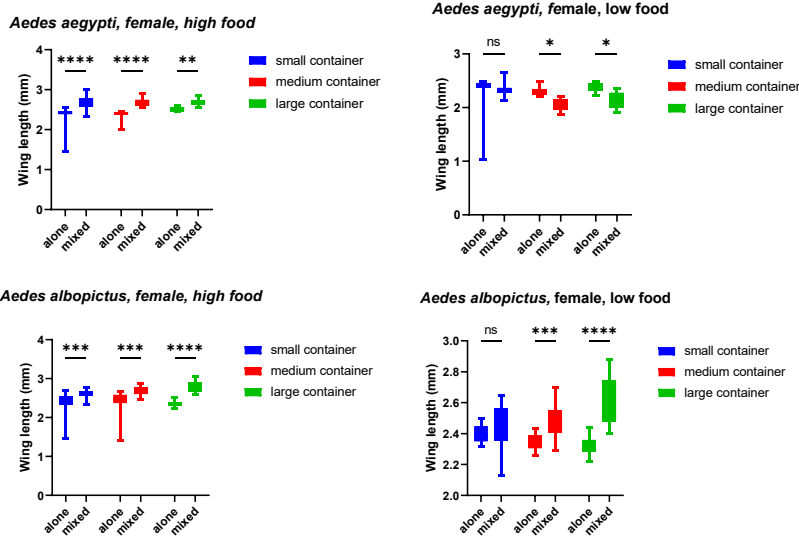
Figure 3. *Female wing length of Ae. aegypti and Ae. albopictus during intra and interspecific larval competition in different containers and food level. ns, non-significant; P ≤0.05*, P ≤0.01 **, P ≤0.001****

Table 2. *Analysis of variance output on Ae. aegypti and Ae. albopictus wing length during intra and interspecific competition*

Source	Ae. aegypti						Ae. albopictus					
	male			female			male			female		
	df	F	*p*	df	F	*p*	df	F	*p*	df	F	*p*
Competition	1	43.1	<0.001	1	41.826	<0.001	1	2.466	0.118	1	4.926	0.028
Food amount	1	6.544	0.011	1	0.321	0.572	1	2.623	0.107	1	4.38	0.038
Container	2	12.113	<0.001	2	24.496	<0.001	2	0.74	0.479	2	4.499	0.012
Competition * food amount	1	0.489	0.485	1	67.843	<0.001	1	0.049	0.825	1	4.51	0.035
Competition * container	2	5.007	0.008	2	26.859	<0.001	2	6.065	0.003	2	4.569	0.012
Food amount * container	2	2.573	0.079	2	21.164	<0.001	2	1.358	0.26	2	4.47	0.013
Competition * food amount * container	2	5.764	0.004	2	16.55	<0.001	2	3.37	0.037	2	4.41	0.014
Footnote: df, degree of freedom; F, F-value; P, significance level (<0.05)												
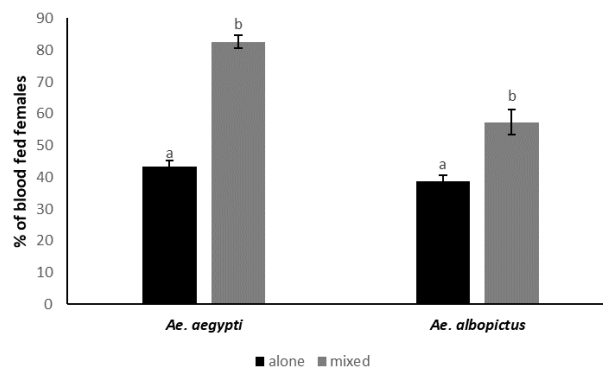
Figure 4. *The impact of adult competition on blood feeding rates of Ae. aegypti and Ae. albopictus. Different letters above bar indicate statistical significance*
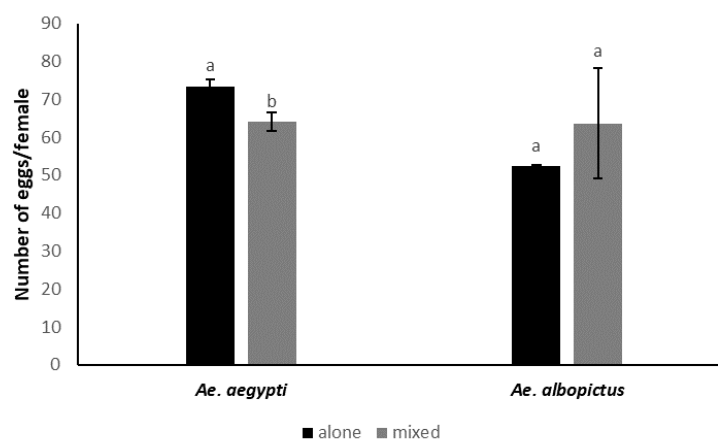
Figure 5. *The impact of adult competition on female fecundity of Ae. aegypti and Ae. albopictus. Different letters above bar indicate statistical significance*

5. CONCLUSION

Understanding the complex competitive dynamics between these mosquitoes allows for more accurate predictions of their co-occurrence and spread patterns. By highlighting *Ae. albopictus'* resilience and *Ae. aegypti's* susceptibility to competitive pressure, this study informs targeted control measures in regions facing both species, reducing the risk of arbovirus transmission in Turkey and globally.

CONFLICT OF INTEREST

The author declares no conflict of interest.

REFERENCES

Akiner, M. M., Demirci, B., Babuadze, G., Robert, V., & Schaffner, F. (2016). Spread of the invasive mosquitoes *Aedes aegypti* and *Aedes albopictus* in the Black sea region increases risk of chikungunya, dengue, and zika outbreaks in Europe. *Plos Neglected Tropical Disease, 10*(4), e0004664. https://doi.org/10.1371/journal.pntd.0004664

Alto, B. W., & Bettinardi, D. (2013). Temperature and dengue virus infection in mosquitoes: independent effects on the immature and adult stages. *The American Journal of Tropical Medicine and Hygiene*, *88*(3), 497-505. https://doi.org/10.4269/ajtmh.12-0421

Braks, M. A. H., Honório, N. A., Lounibos, L. P., Lourenço-de-Oliveira, R., & Lamp; Juliano, S. A. (2004). Interspecific competition between two invasive species of container mosquitoes, *Ae. aegypti* and *Ae. albopictus*

(Diptera: Culicidae), in Brazil. *Annals of Entomological Society of America, 97*(1), 130–139 . https://doi.org/10.1603/0013-8746(2004)097[0130:ICBTIS]2.0.CO;2

Bursali, F., & Simsek, F. M. (2023). Effects of different feeding methods and hosts on the fecundity and blood-feeding behavior of *Aedes aegypti* and *Aedes albopictus* (Diptera: Culicidae). *Biologia*, 1-9. https://doi.org/10.1007/s11756-023-01514-3

Carrington, L. B., Armijos, M. V., Lambrechts, L., Barker, C. M., & Scott, T. W. (2013). Effects of fluctuating daily temperatures at critical thermal extremes on *Aedes aegypti* life-history traits. *PloS one*, *8*(3), e58824. https://doi.org/10.1371/journal.pone.0058824

European Centre for Disease Prevention and Control (ECDC), 2020. Communicable Disease Threats report. 11-17 October 2020, Week 42. ECDC, Stockholm. https://www.ecdc.europa.eu/en/publications-data/communicable-disease-th

Gilotra, S. K., Rozeboom, L. E., & Bhattacharya, N. C. (1967). Observations on possible competitive displacement between populations of *Aedes aegypti* Linnaeus and *Aedes albopictus* Skuse in Calcutta. *Bulletin of the World Health Organization*, *37*(3), 437.

Giatropoulos, A., Papachristos, D., Michaelakis, A., Kapranas, A., & Emmanouel, N. (2022). Laboratory study on larval competition between two related mosquito species: *Aedes (Stegomyia) albopictus* and *Aedes (Stegomyia) cretinus*. *Acta Tropica*, 230, 106389.

Heinisch, M. R. S., Diaz-Quijano, F. A., Chiaravalloti-Neto, F., Menezes Pancetti, F. G., Rocha Coelho, R., dos Santos Andrade, P., Urbinatti, P. R., de Almeida, R. M. M. S., & Lima-Camara, T. N. (2019). Seasonal and spatial distribution of *Aedes aegypti* and *Aedes albopictus* in a municipal urban park in São Paulo, SP, Brazil. *Acta Tropica, 189*, 104–113. https://doi.org/10.1016/j.actatropica.2018.09.011

Juliano, S. A. (2010). Coexistence, exclusion, or neutrality? A meta-analysis of competitions between *Aedes albopictus* and resident mosquitoes. *Israel Journal of Ecology and Evolution, 56*(3-4), 325–351. https://doi.org/10.1560/IJEE.55.3-4.325

Leisnham, P. T., & Juliano, S. A. (2010). Inter-population differences in competitive effective and response of the mosquito *Ae. aegypti* and resistance to invasion by a superior competitor. *Oecologia, 164*(1), 221–230. https://doi.org/10.1007/s00442-010-1624-2

Lizuain, A. A., Maffey, L., Garzón, M., Leporace, M., Soto, D., Diaz, P., & Schweigmann, N. (2022). Larval Competition Between *Aedes albopictus* and *Aedes aegypti* (Diptera: Culicidae) in Argentina: Coexistence and Implications in the Distribution of the Asian Tiger Mosquito. *Journal of Medical Entomology*, *59*(5), 1636-1645. https://doi.org/10.1093/jme/tjac102

Lounibos, L. P. (2002). Invasions by insect vectors of human disease. *Annual Review of Entomology, 47*, 233-266. https://doi.org/10.1146/annurev.ento.47.091201.145206

Lounibos, L. P. (2007). Competitive displacement and reduction. *Journal of the American Mosquito Control Association, 23*(2), 276-282. https://doi.org/10.2987/8756-971x(2007)23[276:cdar]2.0.co;2

Murrell, E. G., & Juliano, S. A. (2008). Detritus type alters the outcome of interspecific competition between Aedes aegypti and *Aedes albopictus* (Diptera: Culicidae). *Journal of Medical Entomology, 45*(3), 375–383. https://doi.org/10.1603/0022-2585(2008)45[375:dtatoo]2.0.co;2

Nasci, R.S. (1990) Relationship of wing length to adult dry weight in several mosquito species (Diptera: Culicidae). *Journal of Medical Entomology*, *27*, 716–719. https://doi.org/10.1093/jmedent/27.4.716

Noden, B. H., O'Neal, P. A., Fader, J. E., & Juliano, S. A. (2016). Impact of inter- and intra-specific competition among larvae on larval, adult, and life-table traits of *Aedes aegypti* and *Aedes albopictus* females. *Ecological entomology*, *41*(2), 192–200. https://doi.org/10.1111/een.12290

Paton, R. S., & Bonsall, M. B. (2019). The ecological and epidemiologic consequences of reproductive interference between the vectors *Ae. aegypti* and *Ae. albopictus. Journal of the Royal Society Interface*, *16*(156), 20190270. https://doi.org/10.1098/rsif.2019.0270

Petersen, V., Marchi, M.J., Natal, D., Marrelli, M.T., Barbosa, A.C. & Suesdek, L. (2016) Assessment of the correlation between wing size and body weight in captive Culex quinquefasciatus. *Revista da Sociedade Brasileira de Medicina Tropical, 49*, 508–511. https://doi.org/10.1590/0037-8682-0039-2016

Reiskind, M. H, Zarrabi, A. A., & Lounibos, L. P. (2012). Effects of combination of leaf resources on competition in container mosquito larvae. *Bulletin of Entomological Research, 102*(4), 424–434. https://doi.org/10.1017/S0007485311000861

Rey, J. R., & Lounibos, P. (2015). Ecología de *Aedes aegypti* y *Aedes albopictus* en América y la transmisión de enfermedades. *Biomédica, 35*(2), 177–185. https://doi.org/10.7705/biomedica.v35i2.2514

Rossati, A., Bargiacchi, O., Kroumova, V., & Garavelli, P.L. (2015). The mosquito-borne viruses in Europe. *Recenti Progressi in Medicina, 106*(3), 125–130. https://doi.org/10.1701/1806.19702

Sakacı, Z. (2021). Contribution to mosquito (Diptera: culicidae) fauna of Sakarya province and the first record of the invasive vector *Aedes albopictus* (Skuse, 1894) for Kocaeli province. *Balıkesir Üniversitesi Fen Bilimleri Enstitüsü Dergisi, 23*(1), 10–21. https://doi.org/10.25092/baunfbed.826097

Schmidt, C. A., Comeau, G., Monaghan, A. J., Williamson, D. J., & Ernst, K. C. (2018). Effects of desiccation stress on adult female longevity in *Aedes aegypti* and *Ae. albopictus* (Diptera: Culicidae): results of a systematic review and pooled survival analysis. *Parasites & vectors*, *11*(1), 267. https://doi.org/10.1186/s13071-018-2808-6

Steinwascher, K. (2020). Competition and growth among *Aedes aegypti* larvae: Effects of distributing food inputs over time. *PloS one*, *15*(10), e0234676. https://doi.org/10.1371/journal.pone.0234676

Touray, M., Bakirci, S., Ulug, D., Gulsen, S. H., Cimen, H., Yavasoglu, S. I., & Hazir, S. (2023). Arthropod vectors of disease agents: their role in public and veterinary health in Turkiye and their control measures. *Acta Tropica,* 106893. https://doi.org/10.1016/j.actatropica.2023.106893

Vezzani, D., & Carbajo, A. E. (2008). *Aedes aegypti, Aedes albopictus,* and dengue in Argentina: current knowledge and future directions. *Memórias do Instituto Oswaldo Cruz, 103*, 66–74. https://doi.org/10.1590/S0074-02762008005000003

World Health Organisation, Dengue and Severe Dengue. (Accessed: 15/03/2022) https://www.who.int/news-room/fact-sheets/detail/dengue-and-severe-dengue

Yan, J., Kibech, R., & Stone, C. M. (2021). Differential effects of larval and adult nutrition on female survival, fecundity, and size of the yellow fever mosquito, *Aedes aegypti*. *Frontiers in zoology, 18*(1), 10. https://doi.org/10.1186/s12983-021-00395-z

Yeap, H.L., Endersby, N.M., Johnson, P.H., Ritchie, S.A. & Hoffmann, A.A. (2013) Body Size and Wing Shape Measurements as Quality Indicators of Aedes aegypti Mosquitoes Destined for Field Release. *The American Journal of Tropical Medicine and Hygiene*, *89*, 78–92. https://doi.org/10.4269/ajtmh.12-0719

Some Finite Summation Identities Comprising Binomial Coefficients for Integrals of the Bernstein Polynomials and Their Applications

Buket ŞİMŞEK[1*]

[1] *Faculty of Engineering, Department of Electrical and Electronics Engineering, Akdeniz University, Antalya, Türkiye*

Keywords	Abstract
Finite Sum Bernstein Polynomials Beta Function Euler Gamma Functions Binomial Coefficients Catalan Numbers	Certain finite sums, including the Catalan numbers, factorial functions, binomial coefficients, and their computational formulas are of indispensable importance both in probability and statistics applications and in other branches of science. The primary aim of this article is to give the integral representation of the finite sum containing the products of the Bernstein polynomials, given in our article, by applying the Beta function and the Euler gamma functions. Other aims of this paper are to bring to light novel finite sum formulae containing binomial coefficients by analyzing and unifying this integral representation. Finally, some relations among these sums, binomial coefficients, and the Catalan numbers are given. We also give the Wolfram language codes. By applying these codes to the finite sums, we give some numerical values.

1. INTRODUCTION

Finite sums appear in almost all scientific fields. In view of the literature that it has good harmony applications with probability theory, especially in areas such as probability, statistics, engineering and electronic engineering, especially the probability of signal detection. It is also well known that cumulative probability distribution can be represented by finite sum of elementary functions. Finite sums have many applications in the discrete probability distribution, and cumulative distribution function, real world problems involving expected value, moments, and variance (see also Chattamvelli & Shanmugam, 2020; Yalcin & Simsek, 2022; Kelly, 1981).

The motivation of this article is give finite sums involving the Catalan numbers C_a, which are related to the Ballot problem associated with probability theory. This problem shows that for the probability that candidate X is always ahead of candidate Y during a tallying process if they respectively end up with a and b votes where $a > b$. Without restrictions, the number of ways the votes are tallied is the binomial coefficient

$$\binom{a + b}{b} = \frac{(a + b)!}{a!\, b!}.$$

The numerator of the desired probability in which X remains ahead can counted recursively by the Catalan numbers, denoted by C_a. The numbers C_a are defined by

$$C_a = \frac{1}{a+1} \binom{2a}{a},$$ (1)

where $a \in \{0,1,2,\dots\}$ and

$$\binom{2a}{a} = \frac{(2a)!}{(a!)^2}$$

(Koshy, 2008; Stanley, 2015; 2021).

All of the results to be obtained in this article are based on integrals of the Bernstein polynomials, which we will only briefly define below. These polynomials take part momentous role in mathematics, approximation theory, theory of Computer Geometric Design, construction of the Bezier curves, spline and the B-spline theory, etc.

Let $v \in \{0,1,2,3\dots\}$ and $b \in \{0,1,2,\dots,v\}$. The Bernstein polynomials of degree d with real variable y are defined by

$$B_b^v(y) = \binom{v}{b} y^b (1-y)^{v-b},$$ (2)

where

$$\binom{v}{b} = \frac{v!}{b!\,(v-b)!},$$

(Bernstein, 1912, Gradshteyn & Ryzhik, 2007; Lorentz, 1986).

In this article, the following results will be taken into account when calculating the values of finite sums:

If $v < b$, then assuming that $\binom{v}{b} = 0$.

If $v < 0$, then assuming that $v! = 0$.

and $0^0 = 1$.

The above restrictions are used when writing the codes with the Wolfram language in Section 3.

Here we note that under the following restrictions, the Bernstein polynomials can be reduced to the Binomial distribution with parameters v independent the Bernoulli trials. Assuming that y is a random variable of this distribution with $0 \leq y \leq 1$. Thus, the probability of getting completely b successes in v independent the Bernoulli trials, given by the equation (2) (Chattamvelli & Shanmugam, 2020; Lorentz, 1986; Simsek, 2019; 2020; Simsek, 2014; Yalcin & Simsek, 2022).

The (Euler) gamma functions are defined by

$$\Gamma(\gamma) = \int_0^\infty w^{\gamma-1} e^{-w} dw,$$

where $\gamma > 0$, and provides

$$\Gamma(\gamma + 1) = \gamma \Gamma(\gamma)$$

and, for nonnegative integer a,

$$\Gamma(a+1) = a!$$

(Gradshteyn & Ryzhik, 2007; Moll, 2014; Srivastava & Choi, 2012).

Beta function, which is symmetric and member of special function, is defined by

$$B(\varepsilon, \gamma) = \int_0^1 w^{\varepsilon-1}(1-w)^{\gamma-1}dw,$$

where $\varepsilon > 0$ and $\gamma > 0$, and provides the following relation between $\Gamma(\gamma)$:

$$B(\varepsilon, \gamma) = \frac{\Gamma(\varepsilon)\Gamma(\gamma)}{\Gamma(\varepsilon+\gamma)}$$

(Gradshteyn & Ryzhik, 2007; Kaur & Shrivastav, 2020, Moll, 2014; Srivastava & Choi, 2012). This function is also so-called the first kind Euler integral.

For instance, when v and b are positive integers, then we have

$$B(v, b) = \frac{(v-1)!\,(b-1)!}{(v+b-1)!}.$$

If we integrate both sides of the equation (2) from $y = 0$ to $y = 1$, the following well-known integral formulas for the Bernstein polynomials can be obtained:

$$(v+1)\int_0^1 B_b^v(y)dy - 1 = 0$$

and

$$\frac{1}{\binom{v}{b}}\int_0^1 B_b^v(y)dy = \sum_{j=0}^{v-b}(-1)^{v-b-j}\frac{\binom{v-b}{j}}{v+1-j}$$

(Acikgoz & Araci, 2010; Lorentz, 1986; Simsek, 2019; 2020; Simsek, 2014;2015, Yalcin & Simsek, 2022).

Using the above integral formulas for the Bernstein polynomials, we also gave many formulas and finite sums (Simsek, 2019; 2020; Simsek, 2014; Yalcin & Simsek, 2022).

In order to reach the main formulas of this article, the finite sum expressed by the following our theorem involving the multiplication of Bernstein polynomials plays a vital role.

Theorem 1.1. Let $d \in \{0,1,2,3\ldots\}$ and $e \in \{0,1,2,\ldots,d\}$. Then

$$\sum_{j=0}^{d}\binom{d}{j}B_e^j(s)B_e^{d-j}(-s) = \frac{(-1)^e(2e)!\,2^{d-2e}\binom{d}{2e}}{(e!)^2}s^{2e}. \tag{3}$$

Proof of the above theorem was given by Simsek and Yardimci (2016).

By applying integral to (3), we gave the following combinatorial sums, see for detail (Simsek and Yardimci 2016):

$$\sum_{j=e}^{d}\sum_{b=0}^{j-e}\sum_{c=0}^{d-j-e}\binom{d}{j}\binom{j}{e}\binom{d}{j}\binom{j-e}{b}\binom{d-j-e}{c}\binom{d-j}{e}\frac{(-1)^{j-b}}{2j+c-2b+1}=\frac{(-1)^{e}(2e)!\,2^{d-2e}\binom{d}{2e}}{(2e+1)(e!)^2}.$$

If $2d$ is substituted for d and d is substituted for e, respectively, the following result is obtained:

$$\sum_{j=d}^{2d}\sum_{b=0}^{j-d}\sum_{c=0}^{d-j}\binom{2d}{j}\binom{j}{d}\binom{2d}{j}\binom{j-d}{b}\binom{d-j}{c}\binom{2d-j}{d}\frac{(-1)^{j-b}}{2j+c-2b+1}=\frac{(-1)^{d}(2d)!}{(2d+1)(d!)^2}.$$

Now it is time to briefly summarize the results obtained in this article:

In Section 2, with the help of the equation (1), equation (2) and equation (3), in the section 2, we derive many formulas for finite sums including binomial coefficients, the Catalan numbers, and the Euler gamma functions.

In Section 3, we give the Wolfram language codes. By using these codes, we give numerical values of finite and combinatorial sums.

This article ends with the conclusion section.

2. FINITE SUMS INVOLVING GAMMA FUNCTION AND THE CATALAN NUMBERS

In this section, new combinatorial finite sums and formulas that calculate their sums are given, using the finite sum containing the gamma function, beta function, and Bernstein polynomials. In addition, the relationships between these formulas and the Catalan numbers are also be proven.

Modification of the equation (3) is given as follows:

$$\sum_{j=e}^{d}\binom{d}{j}B_e^j(s)B_e^{d-j}(-s)=\frac{(-1)^{e}(2e)!\,2^{d-2e}}{(e!)^2}\binom{d}{2e}s^{2e}.$$

Combining equation (1) with the previous equation yields:

Corollary 2.1. Let $d \in \{0,1,2,3\dots\}$ and $e \in \{0,1,2,\dots,d\}$. Then

$$\sum_{j=e}^{d}\binom{d}{j}B_e^j(s)B_e^{d-j}(-s)=(-1)^{e}(e+1)2^{d-2e}\binom{d}{2e}s^{2e}C_e. \tag{4}$$

For $s \neq 0$, combining equation (2) with (4) yields:

Corollary 2.2. Let $d \in \{0,1,2,3\dots\}$ and $e \in \{0,1,2,\dots,d\}$. Then

$$\sum_{j=e}^{d}\binom{d}{j}\binom{j}{e}\binom{d-j}{e}(1-s)^{j-e}(1+s)^{d-j-e}=(e+1)2^{d-2e}\binom{d}{2e}C_e. \tag{5}$$

Theorem 2.3. Let $d \in \{0,1,2,3\dots\}$ and $e \in \{0,1,2,\dots,d\}$. Then

$$\sum_{j=e}^{d} \binom{d}{j}\binom{j}{e}\binom{d-j}{e}\frac{\Gamma(j-e+1)\Gamma(d-j-e+1)}{\Gamma(d-2e+2)} = (e+1)2^{d-2e}\binom{d}{2e}C_e. \tag{6}$$

Proof. If we integrate both sides of equation (5) from $s = -1$ to $s = 1$, the following equation can easily reach:

$$\sum_{j=e}^{d} \binom{d}{j}\binom{j}{e}\binom{d-j}{e}\int_{-1}^{1}(1-s)^{j-e}(1+s)^{d-j-e}ds = (2e+2)2^{d-2e}\binom{d}{2e}C_e.$$

Combining the above equation with following formula (Gradshteyn & Ryzhik, 2007; Moll, 2014; Simsek 2015, Srivastava & Choi, 2012):

$$\Gamma(\varepsilon+\delta+2)\int_{-1}^{1}(1-s)^{\varepsilon}(1+s)^{\delta}ds = 2^{\varepsilon+\delta+1}\Gamma(\varepsilon+1)\Gamma(\delta+1),$$

where $\varepsilon > 0$ and $\delta > 0$, gives us

$$\sum_{j=e}^{d} \binom{d}{j}\binom{j}{e}\binom{d-j}{e}\frac{2^{d-2e+1}\Gamma(j-e+1)\Gamma(d-j-e+1)}{\Gamma(d-2e+2)} = 2^{d-2e}\binom{d}{2e}(2e+2)C_e.$$

After some calculations proof of the theorem is ended.

Theorem 2.4. Let $d \in \{0,1,2,3\dots\}$ and $e \in \{0,1,2,\dots,d\}$. Then

$$\sum_{j=e}^{d} \binom{d}{j}\binom{j}{e}\binom{d-j}{e}(d-e-j)!\,(j-e)! = \binom{d}{2e}(d-2e+1)!\,(e+1)C_e. \tag{7}$$

Proof. Since $\Gamma(j+1) = j!$ for a nonnegative integer j, afterwards (6) reduces to

$$\sum_{j=e}^{d} \binom{d}{j}\binom{j}{e}\binom{d-j}{e}\frac{(d-e-j)!\,(j-e)!}{(d-2e+1)!} = \binom{d}{2e}(e+1)C_e.$$

After some calculations proof of the theorem is ended.

Theorem 2.5. Let $d \in \{0,1,2,3\dots\}$. Then

$$\sum_{j=d}^{4d} \binom{4d}{j}\binom{j}{d}\binom{4d-j}{d}(3d-j)!\,(j-d)! = (d+1)(2d+1)^2(2d)!\,C_dC_{2d}.$$

Proof. Replacing d by $4d$ and e by d in equation (7), we get

$$\sum_{j=d}^{4d} \binom{4d}{j}\binom{j}{d}\binom{4d-j}{d}(3d-j)!\,(j-d)! = (d+1)\binom{4d}{2d}(2d+1)!\,C_d.$$

Combining the previous equation with (1), then proof of theorem is completed.

3. NUMERICAL APPLICATIONS OF THEOREM 2.5 WITH WOLFRAM LANGUAGE CODES

By using the same method in (Kucukoglu, 2023) and coding the RHS (right-hand side) and the LHS (left-hand side) of the combinatorial sum, given in Theorem 2.5, in the Wolfram language, we get the following code snippets, which gives us the numerical values of the combinatorial sum mentioned above.

```
Unprotect[Power];
Power[0, 0] = 1;
Protect[Power];
Unprotect[Binomial];
Binomial[n_, k_] :=If[n<k, 0 ,n!/(k!  * (n-k)!)];
Protect[Binomial];
Unprotect[Factorial];
Factorial[n_] :=If[n<0, 0 ,Product[j,{j,1,n}]];
Protect[Factorial];
CombinatoralSumLHS[d_]:=Sum[Binomial[4*d,j]*Binomial[j,d]*Binomial[4*d-j,d]*((j-d)!)*((3*d-j)!),{j,d,4*d}]
```

```
TableForm[Table[CombinatoralSumLHS[d],{d,0,10}],TableHeadings -
>{Table["d="<>ToString[k],{k,0,10}]}]
```

By using the Wolfram language codes, which are given the above, Table of LHS of Theorem 2.5 is given as follows:

```
d=0    1
d=1    72
d=2    50400
d=3    93139200
d=4    326918592000
d=5    1858466811801600
d=6    15559084148402995200
d=7    180040830860091801600000
d=8    2751564018034783003852800000
d=9    53673842111798500461821952000000
d=10   1301182750011063967595672489164800000
```

```
CombinatoralSumRHS1[d_]:=(d+1)*Power[2*d+1,2]*Factorial[2*d]*CatalanNumber[d]*CatalanNumber[2*d]
```

```
TableForm[Table[CombinatoralSumRHS1[d],{d,0,10}],TableHeadings -
>{Table["d="<>ToString[k],{k,0,10}]}]
```

By using the Wolfram language codes, which are given the above, Table of RHS of Theorem 2.5 is given as follows:

```
d=0    1
d=1    72
d=2    50400
d=3    93139200
d=4    326918592000
```

d=5   1858466811801600
d=6   15559084148402995200
d=7   180040830860091801600000
d=8   2751564018034783003852800000
d=9   5367384211179850046182195200000
d=10   130118275001106396759567248916480000

CombinatoralSumRHS2[d_]:=(d+1)*Binomial[4*d,2*d]*Factorial[2*d+1]*CatalanNumber[d]

TableForm[Table[CombinatoralSumRHS2[d],{d,0,10}],TableHeadings   -
>{Table["d="<>ToString[k],{k,0,10}]}]

By using the above Wolfram language codes, we also give numerical values of the combinatorial sum by the following table:

d=0   1
d=1   72
d=2   50400
d=3   93139200
d=4   326918592000
d=5   1858466811801600
d=6   15559084148402995200
d=7   180040830860091801600000
d=8   2751564018034783003852800000
d=9   5367384211179850046182195200000
d=10   130118275001106396759567248916480000

By using computational algorithms with the Wolfram language codes, Kilar (Kilar 2023) gave numerical values for finite sums. With the aid of the Wolfram language codes, Kucukoglu (Kucukoglu, 2023) gave not only numerical values for finite sums, but also gave graphics of the special polynomials.

4. CONCLUSION

In this article, we investigated some properties of the certain family of the finite sums. By applying the Beta function and the Euler gamma functions to Theorem 2.1 in our article Simsek and Yardimci (2016), which involving products of the Bernstein polynomials with the finite sums, we derived some explicit formulas for these sums. These formulas were also covered the Catalan numbers, factorial functions and binomial coefficients. We think that our computational formulas are of indispensable importance both in probability and statistics applications and in other branches of science.

We gave the Wolfram language codes. By using these codes to the finite sums, we also gave some numerical values for the finite sums.

The formulas of this article may also potentially applied in the discrete probability distribution, and cumulative distribution function, involving moments, expected value, and variance.

CONFLICT OF INTEREST

The author declares no conflict of interest.

REFERENCES

Acikgoz, M., & Araci, S. (2010). On generating function of the Bernstein polynomials. *AIP Conference Proceedings*, 1281, 1141-1143. https://doi.org/10.1063/1.3497855

Bernstein, S.N. (1912). Démonstration du theoreme de Weierstrass fondee sur la calcul des probabilites. *Communications of the Kharkov Mathematical Society*, 13, 1-2.

Chattamvelli, R. & Shanmugam, R. (2020). Discrete distributions in engineering and the applied sciences. *Morgan & Claypool Publishers Series*. https://doi.org/10.1007/978-3-031-02425-2

Gradshteyn, I. S., & Ryzhik, I. M. (2007). Table of integrals Series and Products (Seventh Edition). *Academic Press is an imprint of Elsevier*. https://doi.org/10.1016/C2009-0-22516-5

Kaur, H., & Shrivastav, A. K. (2020). Summation formulae involving basic hypergeometric and truncated basic hypergeometric functions. *Journal of Information and Computational Science*, 1(4), 456-461. https://doi.org/10.15864/jmscm.1404

Kelly, E. J. (1981). Finite-sum expressions for signal detection probabilities. *Technical Report Massachusetts Institute of Technology Lincoln Laboratory*.

Kilar, N. (2023). A New Class of Generalized Fubini Polynomials and Their Computational Algorithms. *Applicable Analysis and Discrete Mathematics*, 17, 496–524. https://doi.org/10.2298/AADM210708023K

Koshy, T. (2008). Catalan numbers with applications. *Oxford University Press,* New York.

Kucukoglu, I. (2023). Identities for the multiparametric higher-order Hermite-based Peters-type Simsek polynomials of the first kind. *Montes Taurus Journal of Pure and Applied Mathematics,* 5(1), 102–123.

Lorentz, G. G. (1986). Bernstein polynomials. *Chelsea Publication Company,* New York.

Moll, V. H. (2014). Special integrals of Gradshteyn and Ryzhik the proofs (Volume 1). *CRC Press,* USA.

Stanley, R. P. (2015). Catalan numbers. *New York: Cambridge University Press*. https://doi.org/10.1017/CBO9781139871495

Stanley, R. P. (2021). Enumerative and algebraic combinatorics in the 1960's and 1970's. https://doi.org/10.48550/arXiv.2105.07884

Simsek, B., & Yardimci, A. (2016). Using Bezier curves in medical applications. *Filomat*, *30*(4), 937-943. https://doi.org/10.2298/FIL1604937S

Simsek, B. (2019). Formulas derived from moment generating functions and Bernstein polynomials. *Applicable Analysis and Discrete Mathematics*, *13*(3), 839-848. https://doi.org/10.2298/AADM191227036S

Simsek, B. (2020). A note on characteristic function for Bernstein polynomials involving special numbers and polynomials. *Filomat, 34*(2), 543-549. https://doi.org/10.2298/FIL2002543S

Simsek, Y. (2014). Generating functions for the Bernstein type polynomials: A new approach to deriving identities and applications for the polynomials. *Hacettepe Journal of Mathematics and Statistics*, *43*(1), 1-14.

Simsek, Y. (2015). Analysis of the Bernstein basis functions: an approach to combinatorial sums involving binomial coefficients and Catalan numbers*, Mathematical Methods in the Applied Sciences*, 38, 3007-3021. https://doi.org/10.1002/mma.3276

Srivastava, H. M., & Choi, J. (2012). Zeta and q-Zeta functions and associated series and integrals. *Amsterdam, London and New York: Elsevier*.

Yalcin, F., & Simsek, Y. (2022). Formulas for characteristic function and moment generating functions of beta type distribution. Revista de la Real Academia de Ciencias Exactas, Físicas y Naturales. *Serie A. Matemáticas, RACSAM*, 116(86). https://doi.org/10.1007/s13398-022-01229-1

One-pot Synthesis of Graphene Oxide-MnO₂-Polyaniline Nanocomposites and Their Photothermal Properties

Zafer ÇIPLAK[1*] 🆔 Furkan SOYSAL[2] 🆔

[1] Sivas Cumhuriyet University, Faculty of Engineering, Department of Chemical Engineering, Sivas, Türkiye
[2] Ankara Yıldırım Beyazıt University, Faculty of Engineering and Natural Sciences, Department of Chemical Engineering, Ankara, Türkiye

Keywords	Abstract
Graphene Oxide MnO₂ Polyaniline Photothermal	Graphene oxide-MnO₂-Polyaniline ternary nanocomposites were synthesized by a facile one-pot approach and characterized with UV-Visible spectroscopy, XRD and SEM. Photothermal properties of the nanocomposite dispersions were tested with an 808 nm wavelength near-infrared laser. Efficiency of the nanocomposites were calculated with time constant method and maximum efficiency was found to be 73.9 %. Additionally, cyclic heating cooling experiments proved the superb dispersion stability and photothermal performance of the nanocomposite.

1. INTRODUCTION

Cancer is one of the biggest medical issues, taking the lives of almost 10 million people a year (Wei et al., 2019). Surgery, chemotherapy, and radiotherapy are the main methods used in the traditional clinical treatment of cancer. Surgery is insufficient to completely remove tumor cells from the body. Chemotherapy and radiotherapy damage healthy tissues along with cancer cells and their side effects limit the patient's quality of life and treatment effectiveness. These disadvantages of traditional cancer treatment methods have led scientists to investigate alternative treatment methods that are more effective in clinical treatment and have more positive effects on the patient's quality of life (Wei et al., 2019). Photothermal therapy (PTT) is based on the idea of raising the temperature of the body region where the tumor tissue is located. Combining PTT with other forms of treatment has the potential to improve the efficacy of cancer treatment while lowering adverse effects on bodily systems (Lima-Sousa et al., 2024).

Nowadays, bacterial infections caused by drug-resistant microbes are another global health problem. 700,000 people in the world lose their lives annually, due to diseases caused by multi drug resistant bacteria (MDR) (Bai et al., 2023; Xing et al., 2024). With the rapid spread of antibiotic resistance, more bacterial species are becoming resistant to commercial antibiotics. More antibiotics lose their effectiveness every year (Guan et al., 2021). The discovery rate of new antibiotics is much slower than the increase of MDR bacteria (Bai et al., 2023). In 2050, human deaths caused by MDR bacteria are predicted to be 10 million per year (Bai et al., 2023). In recent years, unlike chemical treatments, physical approaches, such as, killing bacteria with heat and irradiation have emerged as more promising alternative methods against antibiotic resistance (Guan et al., 2021). Therefore, introducing new approaches that can replace traditional drug treatment is of great importance for public health. PTT and combined therapies containing PTT have great potential in the treatment of MDR, as in the treatment of cancer (Bai et al., 2023).

*Corresponding Author, e-mail: zaferciplak@cumhuriyet.edu.tr

Using PTT agents and near-infrared (NIR) laser to generate localized heat, as a non-invasive application, provides distinct advantages, such as, low systemic toxicity and good controllability. NIR light is in the wavelength range of 650 – 950 nm and can penetrate tissues. Additionally, NIR absorption of water and hemoglobin in the tissue is weak (Soysal et al., 2022). It is of great importance to produce photothermal agents with high photothermal conversion efficiency, high photothermal stability, low toxicity and stable aqueous dispersions that can be used in cancer treatment and antimicrobial applications.

Despite its limited photothermal properties, graphene oxide (GO) is an important composite component in the production of photoagent nanocomposites with its advantages such as excellent dispersion in aqueous environment, very large surface area, and low toxicity. GO, with its strong electrostatic and π-π interactions with metal oxide salts and monomers, prevents the agglomeration of photoagents during the nanostructure production and polymerization process, allowing them to be produced in small sizes and ultra-thin form. GO also contributes to the strong interaction of composite components with each other and with its hydrophilic feature provide effective dispersion of the composite in the aqueous media (İrez & Bayraktar, 2020).

Because of oxygen vacancies in their chemical structure MnO_2 nanomaterials can act as photoagents in NIR region for PTT applications. MnO_2 nanostructures are remarkable materials for biomedical applications due to their features such as easy synthesis, low cost and biodegradability (Liu et al., 2021). When MnO_2 reacts with hydrogen peroxide, oxygen production occurs. The Mn^{2+} ions formed by this reaction react with hydrogen peroxide again and hydroxyl radicals are directly formed (Xu et al., 2022). This feature also provides photodynamic properties to MnO_2 nanostructures and reveals significant potential for photothermal-photodynamic combined treatment applications for MnO_2-containing composites. Wang et al. (2019) fabricated Ag/chitosan/MnO_2 nanosheets and investigated photothermal properties of MnO_2 nanosheets (Wang et al., 2019). Under 808 nm NIR laser at 0.5 W/cm^2 laser power density for 10 min irradiation the temperature of 0.2 mg/mL MnO_2 suspension rised to 60 ºC and MnO_2 nanosheets exhibited photothermal conversion efficiency of 30.79%. Liu et al. (2021) enzymatically produced MnO_2 nanoparticles (Liu et al., 2021). At 1.5 W/cm^2 intensity, 0.15 mg/mL MnO_2 aqueous dispersion exhibited a photothermal conversion efficiency of 44%. Despite their good photothermal features, improvement of the PTT performance of MnO_2 nanostructures is still needed. Combining of MnO_2 with conducting polymers offers great potential for PTT applications. Conductive polymers have a much higher ability to absorb NIR light compared to graphene-based materials and metal oxides such as MnO_2. Thus, they demonstrate high temperature increase and photothermal conversion efficiency at low concentrations. Moreover, conductive polymers are promising photothermal therapy agents due to their advantages such as providing long-term photothermal stability and not causing toxicity problems (Yu et al., 2020; Pham et al., 2024). Among these conductive polymers, polyaniline (PANI) is a low-cost, biocompatible and easily produced conductive polymer, and has become the focus of attention in photothermal applications in recent years because it can demonstrate high photothermal performance.

In this study, GO-MnO_2-PANI (GMP) nanocomposite was fabricated with a facile, one-pot synthesis approach (Zeplin & Neiva, 2021). Simultaneous production of MnO_2 nanostructures and PANI conjugated polymer was realized by using $KMnO_4$ as oxidizing agent to initiate aniline monomer polymerization on the surfaces of GO nanosheets in dodecyl benzene sulfonic acid (DBSA) aqueous solution. DBSA organic acid aqueous solution, in addition to providing the doping of PANI, plays the role of stabilizing agent for the preparation of water-stable dispersions of the composite. Photothermal properties of ternary GMP nanocomposite were investigated for the first time in the literature. The nanocomposite photoagents exhibited high photothermal conversion efficiency and photothermal stability under 808 nm NIR laser.

2. MATERIAL AND METHOD

Synthesis of GMP Nanocomposites

50.0 mg graphite oxide was added to 25 mL deionized water (DI) with a concentration of 0.1 M DBSA. The mixture was ultrasonicated for 60 min to obtain GO dispersion. Monomer solution was prepared by adding 300 μL aniline to 20 mL DI with a concentration of 0.1 M DBSA. Then monomer solution was added to GO dispersion and resultant mixture was ultrasonicated and stirred for 30 min. Afterwards, three separate $KMnO_4$ solutions were prepared according to $KMnO_4$/aniline molar ratio; 0.5, 1.0, and 1.5. $KMnO_4$ solution was then added to GO-aniline mixture to initiate simultaneous polymerization and MnO_2 formation in an ice bath. After

polymerization was completed, the samples were centrifuged with absolute ethanol and DI numerous times and dried in a vacuum oven at 65°C. Samples were named according to their $KMnO_4$/aniline ratios, namely GMP 0.5, GMP 1.0 and GMP 1.5.

Characterization

Characterization of samples were carried out by UV-Visible spectrophotometer (Shimadzu, UV-1601), X-ray diffractometer (Rigaku, Miniflex-600, Cu-K$_\alpha$, $\lambda = 1.54056$ Å), and scanning electron microscope (SEM) (Quanta, 400F).

Photothermal Heating Experiments

Photothermal heating experiments were performed using an 808 nm wavelength laser (Power Technology Inc., Grande) equipped with a power-meter (Newport, 843-R). Nanocomposite dispersions were prepared at 0.06, 0.08, and 0.1 mg/mL concentrations and irradiated for 10 min at 0.8, 1.0, and 1.6 W/cm^2 power densities. Temperature values were recorded with a handheld thermal camera (FLIR, E50) and temperature versus time plots were obtained. In order to calculate the efficiency (η) time-constant method was applied (Soysal et al., 2022). Time versus $-\ln(\Delta T/\Delta T_{max})$ data were plotted during the cooling phase and the slope resulted in time-constant (τ) which is expressed by equation (1):

$$\tau = \frac{mC_p}{hA} \tag{1}$$

where, m is the mass of the dispersion, C_p is the heat capacity of the dispersion, h is the heat transfer coefficient, and A is the area perpendicular to the heat transfer. Since the dispersions were diluted, C_p value of water was used. Efficiency values were calculated using equation (2):

$$\eta = \frac{hA\Delta T_{max} - Q_{water}}{P(1 - 10^{-A})} \tag{2}$$

where, Q_{water} is the heat absorbed by water, P is the laser power, and A is the absorbance value obtained at 808 nm wavelength. Q_{water} was calculated using equation (3) by performing a heating experiment with deionized water:

$$Q_{water} = mC_{p,water}\Delta T_{max,water} \tag{3}$$

3. RESULTS AND DISCUSSION

UV-Visible spectrums of GMP 0.5, GMP 1.0, and GMP 1.5 were given in Figure 1a. GMP 0.5 shows the absorption band at 325 nm, which indicates $\pi - \pi^*$ transition of benzenoid segment of PANI (Ding, 2009). Absorption band at 400 – 450 nm corresponds to emeraldine salt phase of PANI, which can be observed in all samples (Ding, 2009). Absorption band between 700 – 1000 nm in GMP 0.5 and 500 – 750 nm in GMP 1.0 and GMP 1.5 corresponds to localized polaron bands of PANI (Ding, 2009). This blueshift and decreased absorbance in GMP 1.0 and GMP 1.5 are related to higher amount of MnO_2 in the samples. Increasing MnO_2 boosts the quantity of high oxidation state complexes in PANI and decreases degree of doping, which contributes to PANI deposition on MnO_2. This suggests how improved emeraldine structures have emerged in GMP 0.5 (Jianjun et al., 2011). It is clear that amount of $KMnO_4$ salt used both as a precursor for MnO_2 nanoparticles and as polymerization initiator, plays an important role for the fabrication of PANI structures. UV-Visible spectrums of GMP 0.5 with concentrations 0.06, 0.08, and 1.0 mg/mL and absorbance at 808 nm versus concentration plots are presented in Figure 1b and 1c. The linearity of absorbance with concentration shows the high stability of the dispersions, which is crucial for photothermal applications.
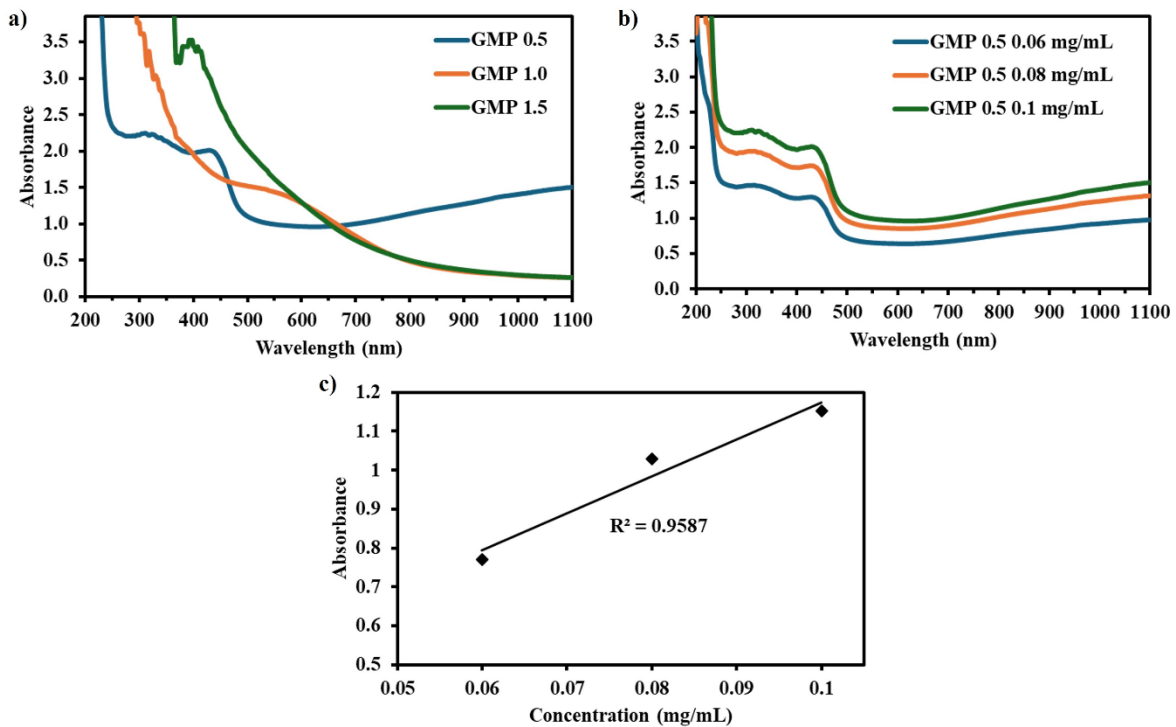
Figure 1. a) *UV-Visible spectrums of GMP 0.5, GMP 1.0, and GMP 1.5 at 0.1 mg/mL concentration,* ***b)*** *UV-visible spectrums of GMP 0.5 sample at 0.06, 0.08, and 0.1 mg/mL concentrations,* ***c)*** *Absorbance versus concentration plot of GMP 0.5*

X-ray diffraction patterns of GMP 0.5, GMP 1.0, and GMP 1.5 are given in Figure 2. All samples show the characteristic peaks of (020) and (200) planes of PANI at 19.52 and 26.02°, respectively (Çıplak & Yıldız, 2019). The prominence of PANI peaks in GMP 0.5 shows that the sample contains more polymeric structure than GMP 1.0 and GMP 1.5, in accordance with UV-visible results. At 26.20°, 37.32°, and 43.50° (310), (211), and (301) planes of α-MnO_2 (JCPDS No: 00-014-0644) can be observed (Izwan Misnon & Jose, 2021). In GMP 1.0 and GMP 1.5 samples (002) plane of GO is seen at 9.90° (Yürekli Bayar et al., 2023). The absence of this peak in GMP 0.5 might be due to complete coverage of GO with PANI structure.

Figure 3 displays SEM images of GO and GMP nanocomposites. GO nanosheets have a film structure with crooked and folded edges. It is noticed that, GMP nanocomposites exhibits different morphologic features according to their $KMnO_4$/aniline ratios. In GMP1 and GMP1.5 samples, where high amounts of $KMnO_4$ were used, MnO_2 nanostructures in the form of needles and nanoparticles can be seen on the surface of GO nanosheets within the polymer matrix. On the other hand, it was determined that in the GMP0.5 nanocomposite, where $KMnO_4$/aniline molar ratio was the highest, polymer production was higher, consistent with the UV-Visible spectrum of the samples, GO and MnO_2 nanostructures were embedded in the polymer matrix. It was also observed that the polymer matrix consisted of small-sized polymeric nanostructures. This situation is thought to be due to the strong interaction between the aniline monomer and the GO nanosheet, the fact that $KMnO_4$ is an effective oxidation agent for the monomer as well as being a source of MnO_2, and the role of DBSA as a stabilizing agent that prevents the composite from forming large agglomerations.

Firstly, to determine the nanocomposite with the highest efficiency, dispersions of GMP 0.5, GMP 1.0, and GMP 1.5 were prepared at 0.1 mg/mL concentration and irradiated at 1.0 W/cm^2 for 10 min and cooled for 20 min. Heating and cooling curves of the nanocomposites are given in Figure 4a. Highest temperature difference was obtained with GMP 0.5 as 34.7°C. Temperature difference values of GMP 1.0 and GMP 1.5 were 22.1 and 24.7°C, respectively. $-\ln(\Delta T/\Delta T_{max}) - t$ plots of nanocomposites were given in Figure 4b. Time constants of GMP 0.5, GMP 1.0, and GMP 1.5 were found as 312.47, 468.39, and 466.85, respectively. Applying equation (2) efficiency values were calculated as 73.9 % for GMP 0.5, 42.8 % for GMP 1.0, and 47.4 % for GMP 1.5. The highest temperature and efficiency values were achieved with GMP 0.5 nanocomposite, thus further experiments were performed using GMP 0.5.
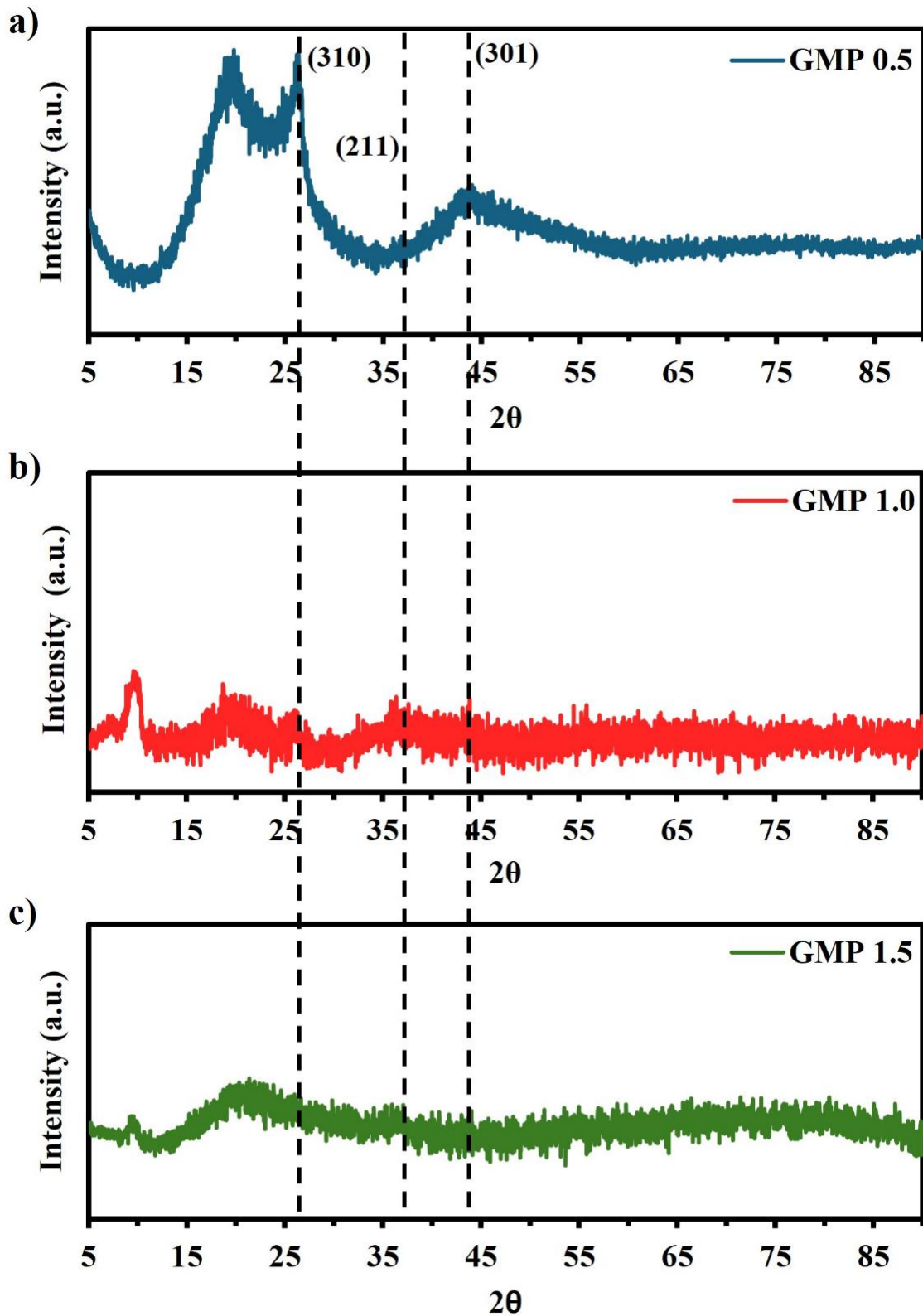
Figure 2. *X-ray diffraction patterns of **a)** GMP 0.5, **b)** GMP 1.0, **c)** GMP 1.5*
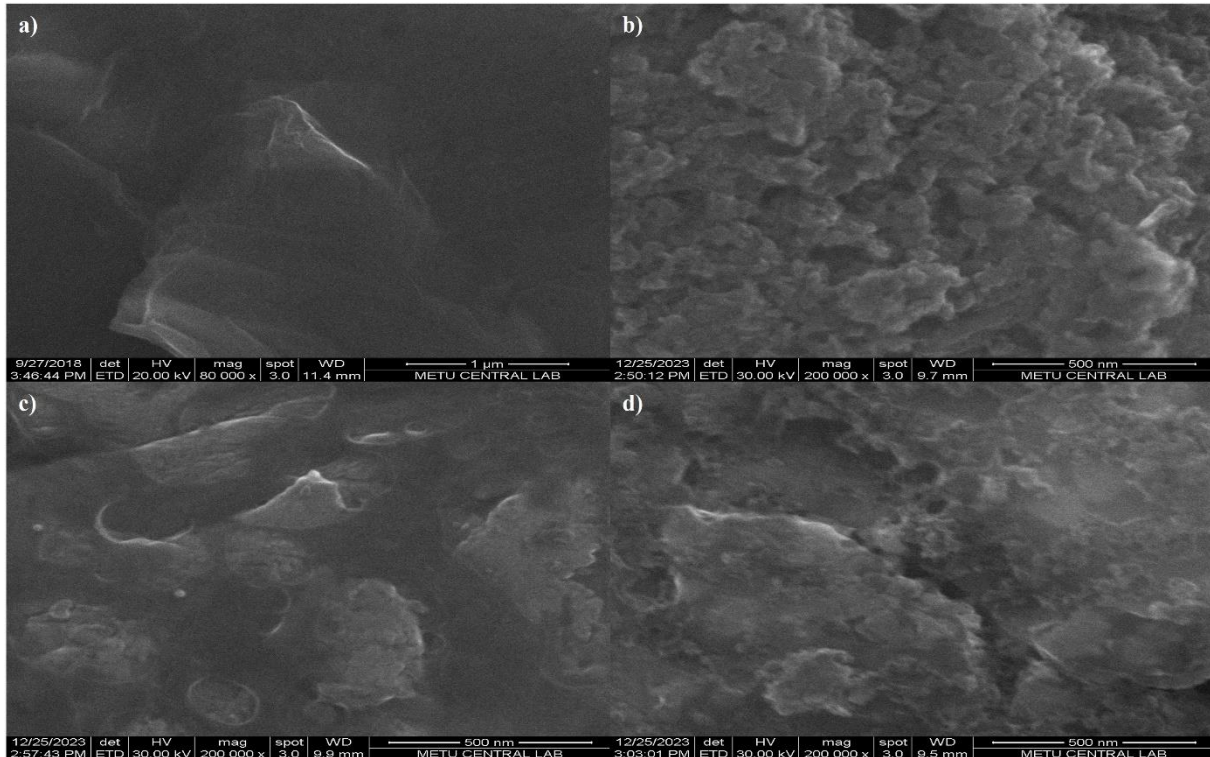
Figure 3. SEM images of a) GO b) GMP 0.5, c) GMP 1.0, d) GMP 1.5
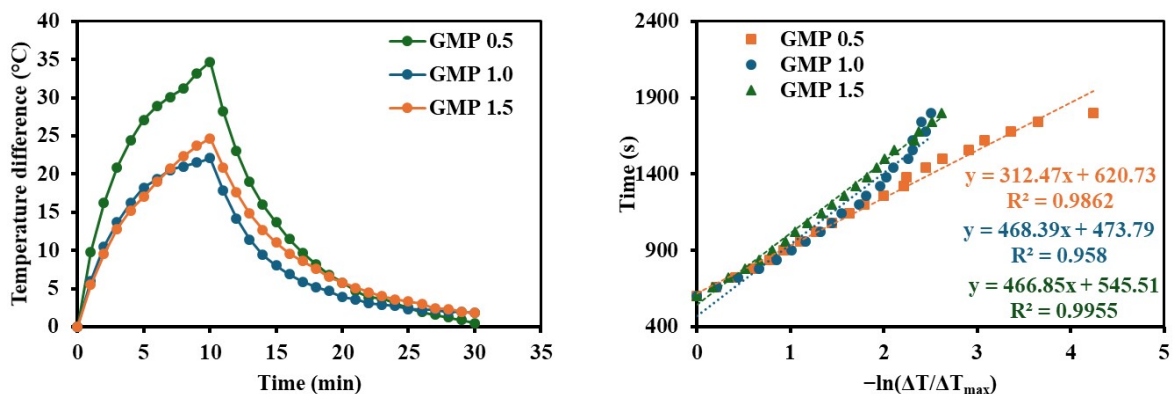
Figure 4. a) Heating and cooling curves of GMP 0.5, GMP 1.0, and GMP 1.5, b) – ln(ΔT/ΔTmax) – t plots of GMP 0.5, GMP 1.0, and GMP 1.5

In order to further evaluate the performance of GMP 0.5 sample, varied laser power densities were used to irradiate nanocomposite dispersions at varied concentrations. Heating curves of GMP 0.5 dispersions having concentrations of 0.06, 0.08, and 0.1 mg/mL and deionized water were given in Figure 5 a-c. At 0.8 W/cm^2 laser intensity, maximum temperatures of GMP 0.5 dispersions achieved were found to be 50.3, 55.6, and 54.7°C for 0.06, 0.08, and 1.0 mg/mL, respectively. Temperature difference of deionized water for this laser power density was only 1.3°C. Increasing power density to 1.0 W/cm^2 yielded in slightly increased maximum temperatures of 53.2, 57.8, and 57.9°C for 0.06, 0.08, and 1.0 mg/mL, respectively. Temperature difference of deionized water was found to be 1.6°C at 1.0 W/cm^2. Further increase in laser power density resulted in elevated maximum temperatures. At 1.6 W/cm^2, 0.06, 0.08, and 1.0 mg/mL dispersions were heated up to 70.8, 74.7, and 75.5°C. At this laser power density maximum temperature difference for deionized water was only 2.6°C. The maximum temperature differences obtained for nanocomposites were given in Figure 5d. Expectedly, the maximum temperatures of all samples increased with increasing laser intensity. At 1.6 W/cm^2 laser power density, increasing concentration resulted in increased maximum temperatures. However, at 0.8 W/cm^2, the maximum temperature of 0.08 mg/mL dispersion were higher than that of 0.1 mg/mL.

Additionally, at 1.0 W/cm^2, the maximum temperature differences of 0.08 and 0.1 mg/mL were identical. These may be due to the laser power densities being relatively low as well as concentrations being close.
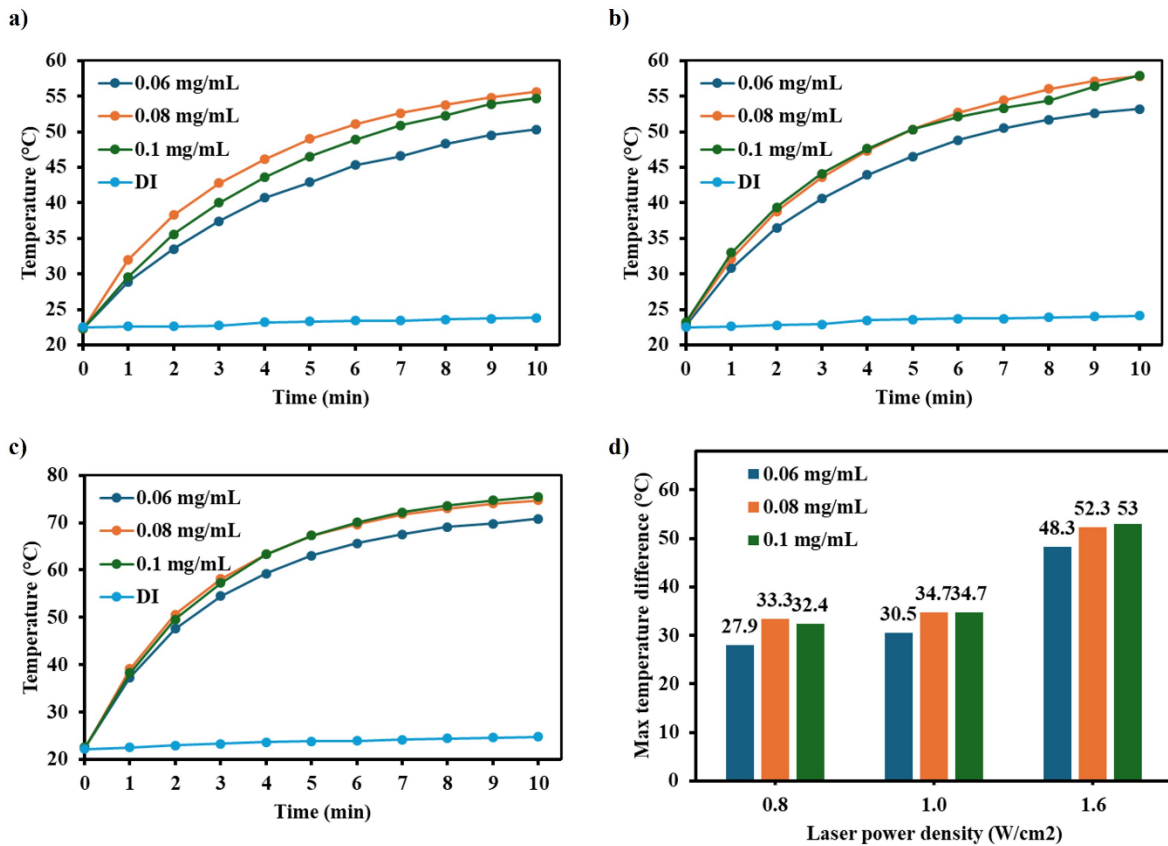
Figure 5. *Heating curves of GMP 0.5 and deionized water **a**) at 0.8 W/cm^2, **b**) at 1.0 W/cm^2, **c**) at 1.6 W/cm^2, **d**) achieved maximum temperature differences at different laser power densities*

Further evaluation of the photothermal performance of GMP 0.5 nanocomposite was performed by cyclic heating cooling experiments shown in Figure 6. A total of 6 cycles were exercised to GMP 0.5 dispersion with 0.1 mg/mL concentration at 1.0 W/cm^2 intensity. Maximum temperature values for the cycles were recorded as 57.9, 57.3, 58.7, 58.2, 57.8, and 58.7°C. There was no discernible shift in the highest temperature, which demonstrated the strong stability and high photothermal ability of the nanocomposite.
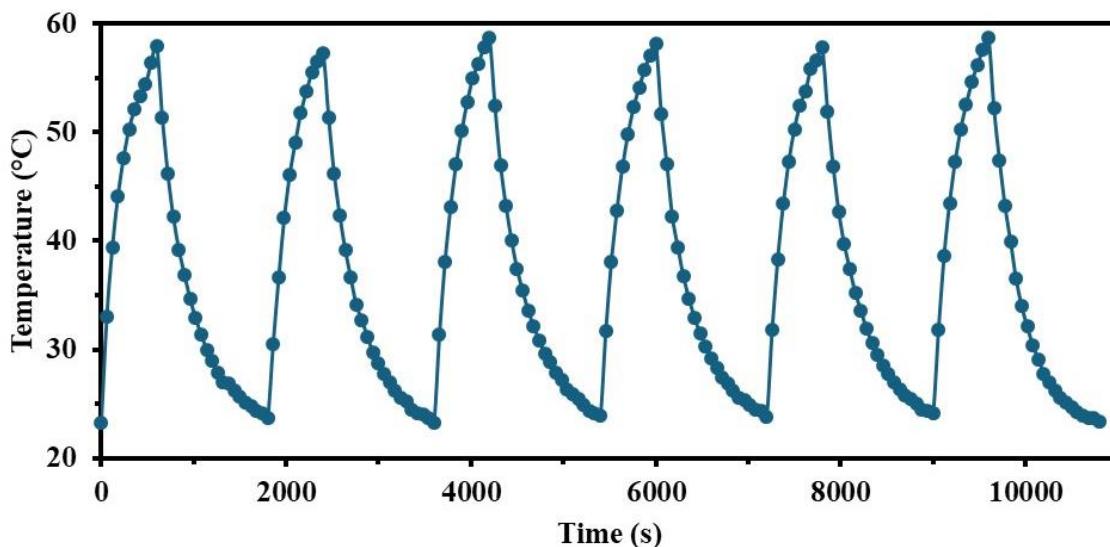
Figure 6. *Cyclic heating cooling experiments for GMP 0.5 0.1 mg/mL at 1.0 W/cm^2*

4. CONCLUSION

GO-MnO$_2$-PANI nanocomposites were fabricated by simultaneous aniline polymerization and MnO$_2$ formation over GO nanosheets. It has been seen that amount of KMnO$_4$ salt in the synthesis procedure plays an important role for PANI formation. The use of DBSA both as a stabilizing and doping agent, enabled water-stable dispersions, which is essential for photothermal exercises. The photothermal properties of the nanocomposites were tested for the first time in literature. The efficiency of GMP 0.5 nanocomposite was obtained as high as 73.9 %. Moreover, the cyclic heating cooling experiments demonstrated that the nanocomposite can be used in practical photothermal applications without a loss in its performance. These findings show that GO-MnO$_2$-PANI nanocomposites can be employed in both photothermal cancer treatment and antibacterial applications because of their strong NIR absorption, stable dispersion forming abilities, and high cyclic performances.

AUTHOR CONTRIBUTIONS

Conceptualization, Z.Ç. and F.S.; methodology, Z.Ç. and F.S.; title, F.S., validation, Z.Ç. and F.S.; laboratory work, Z.Ç. and F.S.; formal analysis, Z.Ç. and F.S.; research, Z.Ç. and F.S.; sources, Z.Ç. and F.S.; data curation, Z.Ç. and F.S.; manuscript-original draft, Z.Ç. and F.S.; manuscript-review and editing, Z.Ç. and F.S.; visualization, F.S.; supervision, Z.Ç.; project management, Z.Ç. and F.S.; funding, Z.Ç. and F.S.; All authors have read and legally accepted the final version of the article published in the journal.

CONFLICT OF INTEREST

The authors declare no conflict of interest.

REFERENCES

Bai, X., Yang, Y., Zheng, W., Huang, Y., Xu, F., & Bao, Z. (2023). Synergistic photothermal antibacterial therapy enabled by multifunctional nanomaterials: progress and perspectives. *Materials Chemistry Frontiers*, *7*(3), 355-380. https://doi.org/10.1039/D2QM01141G

Çıplak, Z., & Yıldız, N. (2019). Polyaniline-Au nanocomposite as electrode material for supercapacitor applications. *Synthetic Metals*, *256*, 116150. https://doi.org/10.1016/j.synthmet.2019.116150

Ding, K.-Q. (2009). Cyclic Voltammetrically Prepared MnO2 -Polyaniline Composite and Its Electrocatalysis for Oxygen Reduction Reaction (ORR). *Journal of the Chinese Chemical Society*, *56*(5), 891-897. https://doi.org/10.1002/jccs.200900132

Guan, G., Win, K. Y., Yao, X., Yang, W., & Han, M. (2021). Plasmonically Modulated Gold Nanostructures for Photothermal Ablation of Bacteria. *Advanced Healthcare Materials*, *10*(3). https://doi.org/10.1002/adhm.202001158

İrez, A. B., & Bayraktar, E. (2020). Design of Epoxy Modified Recycled Rubber-Based Composites: Effects of Different Contents of Nano-Silica, Alumina and Graphene Nanoplatelets Modification on the Toughening Behavior. *Gazi University Journal of Science*, *33*(1), 188-199. https://doi.org/10.35378/gujs.585446

Izwan Misnon, I., & Jose, R. (2021). Charge storage in the PANI–α-MnO$_2$ polymer–nanocomposite system. *Materials Today: Proceedings*, *41*(3), 513-519. https://doi.org/10.1016/j.matpr.2020.05.235

Jianjun, H., Yuping, D., Jia, Z., Hui, J., Shunhua, L., & Weiping, L. (2011). γ-MnO$_2$/polyaniline composites: Preparation, characterization, and applications in microwave absorption. *Physica B: Condensed Matter*, *406*(10), 1950-1955. https://doi.org/10.1016/j.physb.2011.02.063

Lima-Sousa, R., Melo, B. L., Mendonça, A. G., Correia, I. J., & de Melo-Diogo, D. (2024). Hyaluronic acid-functionalized graphene-based nanohybrids for targeted breast cancer chemo-photothermal therapy. *International Journal of Pharmaceutics*, *651*, 123763. https://doi.org/10.1016/j.ijpharm.2023.123763

Liu, J., Feng, L., & Wu, Y. (2021). Enzymatically synthesised MnO$_2$ nanoparticles for efficient near-infrared photothermal therapy and dual-responsive magnetic resonance imaging. *Nanoscale*, *13*(25), 11093-11103. https://doi.org/10.1039/D1NR02400K

Pham, T.-T. D., Phan, L. M. T., Nam, S.-N., Hoang, T. X., Nam, J., Cho, S., & Park, J. (2024). Selective photothermal and photodynamic capabilities of conjugated polymer nanoparticles. *Polymer*, *294*, 126689. https://doi.org/10.1016/j.polymer.2024.126689

Soysal, F., Çıplak, Z., Getiren, B., Gökalp, C., & Yıldız, N. (2022). Fabrication of polypyrrole enveloped reduced graphene oxide/iron oxide and determination of its photothermal properties. *Materials Research Bulletin*, *150*, 111792. https://doi.org/10.1016/j.materresbull.2022.111792

Wang, X., Su, K., Tan, L., Liu, X., Cui, Z., Jing, D., Yang, X., Liang, Y., Li, Z., Zhu, S., Yeung, K. W. K., Zheng, D., & Wu, S. (2019). Rapid and Highly Effective Noninvasive Disinfection by Hybrid Ag/CS@MnO 2 Nanosheets Using Near-Infrared Light. *ACS Applied Materials & Interfaces*, *11*(16), 15014-15027. https://doi.org/10.1021/acsami.8b22136

Wei, W., Zhang, X., Zhang, S., Wei, G., & Su, Z. (2019). Biomedical and bioactive engineered nanomaterials for targeted tumor photothermal therapy: A review. *Materials Science and Engineering: C*, *104*, 109891. https://doi.org/10.1016/j.msec.2019.109891

Xing, Z., Dong, B., Zhang, X., Qiu, L., Jiang, P., Xuan, Y., Ni, X., Xu, H., & Wang, J. (2024). Cypate-loaded hollow mesoporous Prussian blue nanoparticle/hydrogel system for efficient photodynamic therapy/photothermal therapy dual-modal antibacterial therapy. *Journal of Biomedical Materials Research Part A*, *112*(1), 53-64. https://doi.org/10.1002/jbm.a.37613

Xu, W., Qing, X., Liu, S., Chen, Z., & Zhang, Y. (2022). Manganese oxide nanomaterials for bacterial infection detection and therapy. *Journal of Materials Chemistry B*, *10*(9), 1343-1358. https://doi.org/10.1039/D1TB02646A

Yu, C., Xu, L., Zhang, Y., Timashev, P. S., Huang, Y., & Liang, X.-J. (2020). Polymer-Based Nanomaterials for Noninvasive Cancer Photothermal Therapy. *ACS Applied Polymer Materials*, *2*(10), 4289-4305. https://doi.org/10.1021/acsapm.0c00704

Yürekli Bayar, E., Getiren, B., Soysal, F., Çıplak, Z., Yıldız, N., & Bayraktar, E. (2023). Graphene oxide/polyaniline/silver nanocomposite synthesis and photothermal performance. *Materials Research Bulletin*, *166*, 112352. https://doi.org/10.1016/j.materresbull.2023.112352

Zeplin, G., & Neiva, E. G. C. (2021). One-pot green synthesis of graphene oxide/MnO2/polyaniline nanocomposites applied in aqueous and neutral supercapacitors and sensors. *Journal of Electroanalytical Chemistry*, *902*, 115776. https://doi.org/10.1016/j.jelechem.2021.115776

A Novel Method for Assessing the Weight Coefficients of Criteria within the Framework of Multi-Criteria Decision-Making: Measurement Relying on the Impacts of an Exponential Curve Function (MIEXCF)

Furkan Fahri ALTINTAŞ[1*] 🆔

[1] *Aydın Provincial Gendarmerie Command, Aydın, Türkiye*

Keywords	Abstract
MCDM Exponential Function Exponential Curve Function MIEXCF	In the realm of multi-criteria decision making (MCDM), this study introduces the Measurement Relying on the Impacts of an Exponential Curve Function (MIEXCF) as a novel approach for objectively determining criteria weight coefficients. Utilizing exponential curve interactions among criteria, MIEXCF is designed to enrich the MCDM literature. The dataset comprises criterion values extracted from Global Innovation Index (GII) evaluations for 19 G20 members. Results demonstrate the efficacy of MIEXCF in objectively deriving criteria weights for diverse nations. Comparative analyses with other methods (ENTROPY, CRITIC, SD, SVP, LOPCOW, MEREC) further validate MIEXCF's credibility, reliability, and stability. Notably, the simulation analysis indicates MIEXCF's effectiveness in discerning criteria weights and stability across scenarios. In conclusion, MIEXCF stands out as a robust objective criterion weighting technique, offering substantial contributions to exponential functions and the broader MCDM literature.

1. INTRODUCTION

Multi-criteria decision making (MCDM) is a field utilized in intricate decision-making processes and mathematical modelling, where a multitude of factors are considered. This method aims to assess and rank alternatives based on the preferences and priorities of decision-makers. To achieve this, it is imperative to ascertain the weights of the criteria that reflect the preferences of the decision-makers (Bircan, 2020).

In the extensive landscape of (MCDM) literature, one encounters a plethora of techniques (such as ENTROPY, CRITIC, SD, SVP, MEREC, LOPCOW) designed to ascertain weight coefficients (Keleş, 2023). Within this body of literature, the objective weights assigned to criteria exhibit two fundamental characteristics. The first pertains to the degree of contrast in the performance of decision alternatives concerning each criterion, encapsulating the disparity between maximum and minimum values across the criteria. The second characteristic relates to the distinctiveness or conflict among these criteria. By elucidating and leveraging these inherent characteristics embedded in the data defining the multi-criteria problem, decision-makers can derive valuable insights to inform their decision-making process (Ecer, 2020). Within this framework, criteria that exhibit a heightened degree of interdependence can manifest a more pronounced distinctiveness when compared to other criteria in terms of their discriminative capacity. Beyond these established methods, such as MIEXCF (Measurement Relying on the Impacts of an Exponential Curve Function), this study introduces a novel approach for calculating objective weight coefficients for variables based on exponential curve

*Corresponding Author, e-mail: furkanfahrialtintas@yahoo.com

functions. This method facilitates the analysis and modelling of variables in light of their exponential curve relationships. Consequently, the research centers its attention on exploring the analytical and modeling potential inherent in exponential curve, as these functions have a well-documented history of utility in diverse domains and have proven effective in addressing various problem-solving challenges (Chakrabarty & Rahman, 2007).

The primary objective of composing this article is to introduce an alternative and objective approach for determining weighting coefficients of criteria within the domain of MCDM methods, with a foundation in exponential curve measurement. It has come to our attention that the existing literature contains methods that rely solely on exponential curve calculations and are marked by limitations. Therefore, this study puts forth a novel method. The core aim of this research is to establish a framework that effectively captures the impact values among criteria through exponential curve functions, transforms these impact values into criteria weighting coefficients, and thereby produces dependable outcomes. The method outlined in this article is expected to more precisely reflect the intensity of the interplay among criteria, facilitating the calculation of criteria weighting coefficients. Consequently, this study is perceived as a valuable addition to the existing body of literature concerning methods for computing criteria weighting coefficients, offering a fresh perspective to the field.

Within this context, the research is two goals. First, it aims to introduce a novel method for computing the weight coefficients of criteria concerning decision alternatives within the realm of MCDM. The second objective is to promote the utilization of exponential curve functions and enhance awareness of their inherent potential, given their significant role in addressing and dissecting complex problems. To achieve these goals, the research literature elucidates both objective weighting methods and the attributes of exponential curve functions. In this context, the method section of the study elucidates objective criteria weight coefficients, the exponential curve function, relationship between calculating Criterion Weights and exponential curve function, data set and description of the proposed method (MIEXCF). According to the proposed method, the weights of criteria for the 19 countries in G20 group, demonstrating validity and reliability, are measured and ranked using the Logistic Performance Index data for these countries. Secondly, sensitivity analyses are conducted to assess the method's sensibility. Subsequently, thirdly, comparative analyses are performed to gauge the method's credibility and reliability levels. Finally, simulation analyses are provided to deconstruct the criteria weights and establish the stability level of the method.

2. MATERIAL AND METHOD

2.1. Methods for Calculating Criterion Weights in the Scope of MCDM

The process of choosing among different alternatives is a crucial aspect of many decision-making procedures. However, in such situations, it often happens that each alternative exhibits varying performances on different criteria. Therefore, accurately determining the relative importance of these criteria is essential for effectively comparing the performance of decision alternatives and ultimately selecting the most suitable one (Saaty, 2008). This is because, traditionally, the significance of criteria is established by assigning weight coefficients in MCDM problems (Ecer, 2020).

Subjective weight coefficients are primarily derived from the personal experiences and evaluations of decision-makers, making them inherently dependent on individual opinions. Consequently, these values tend to vary among different individuals (Baş, 2021). These weight coefficients are typically determined based on expert judgments. However, relying solely on subjective assessments by experts can introduce errors and biases into the decision-making process. In contrast, objective methodologies do not account for decision-makers' inconsistencies and uncertainties. Instead, they leverage mathematical models and the information within the decision matrix to compute the criteria weights. In essence, objective weighting techniques consider the underlying data structure in the evaluation process (Paksoy, 2017; Arslan, 2020; Demir et al., 2021).

Within the realm of MCDM literature, one encounters a variety of objective weighting methods, including CRITIC (Criteria Importance Through Inter Criteria Correlation), ENTROPY, CILOS (Criterion Impact Loss), IDOCRIW (Integrated Determination of Objective Criteria Weights), SVP (Statistical Variance Procedure), SD (Standard Deviation), MEREC (Method Based On Removal Effects of Criteria), LOPCOW

(Logarithmic Percentage Change-driven Objective Weighting) and, SECA (Simultaneous Evaluation of Criteria and Alternatives) (Ecer, 2020). The CRITIC method, in particular, operates on the principle of utilizing information inherent in a system. Accordingly, the more disorder or distinctiveness a criterion exhibits compared to others, the greater its importance becomes. Thus, the CRITIC method relies on the interrelationships among criteria. This technique involves scrutinizing the correlations between criteria to pinpoint any inconsistencies among them. Subsequently, these contradictions related to the criteria are weighted using the standard deviation, thus facilitating the determination of criterion weight coefficient values. The CRITIC method commences with the creation of a decision matrix. Next, the normalized values of this matrix are computed. By examining the correlations among the criteria based on these normalized values, the criteria weights can be quantified (Diakoulaki et al., 1995).

The ENTROPY method proves to be a valuable tool in the decision-making process. In this approach, after constructing the decision matrix, the standard values of the decision matrix and the ENTROPY measure of the criteria are employed to ascertain the ENTROPY-based criterion weights (Ayçin, 2019).

Within the CILOS method, the relative importance of criteria hinges on the degree of impact deviation of other criteria from their respective ideal maximum and minimum values. In essence, if a criterion exhibits a lower impact deviation, its weight coefficient is correspondingly increased. The methodology involves a step-by-step process, including the calculation of the decision matrix, normalization, square matrix, and the weight system matrix values. Subsequently, a system of linear equations is solved to determine the weight coefficients for the criteria (Zavadskas & Podvezko, 2016; Sel, 2020).

The IDOCRIW method is a fusion of both the ENTROPY and CILOS methods. This approach centers around the determination of the relative impact of a missing index. Initially, the weight coefficients for the criteria are ascertained through the ENTROPY and CILOS methods, utilizing the decision matrix values. Subsequently, the ENTROPY and CILOS weights are integrated to yield the IDOCRIW weights (Zavadskas & Podvezko, 2016).

SVP, as a target weighting method, is designed to provide objective weights for the computation of criterion weights or their relative importance levels (Nasser et al., 2019). This method quantifies the weight values assigned to criteria objectively, ensuring that they are not influenced by expert opinions or subjective evaluations. The SVP method's approach to calculating criterion weights is rooted in the variance metrics associated with these criteria (Gülençer & Türkoğlu, 2020) After determining the variance values for each criterion, the weights for individual criteria are computed by dividing the variance value of each criterion by the total variance value encompassing all criteria. In essence, the SVP method serves as an objective approach for determining weights, enabling the computation of criterion weights or their significance levels based on variance values linked to the criteria (Odu, 2019).

The SD method relies on assessing the distance of criteria values from the arithmetic mean of these criteria. To apply this method, the initial step involves normalizing the decision matrix using the values contained within it. Subsequently, the standard deviation values for each criterion are computed, serving as a basis for determining the criteria weights (Uludağ & Doğan, 2021). In the case of the SVP method, criterion weights are determined by calculating the variances of the criteria using the values from the decision matrix (Demir et al., 2021).

Within the MEREC method, much like other weighting methodologies, the process commences with obtaining the decision matrix and its normalized counterpart. Following this, the total performance values of the decision alternatives are computed using a structure based on natural logarithms. Subsequently, by considering the value of each decision alternative, adjustments in the performance values of the other decision alternatives are recalculated based on the natural logarithm. Towards the conclusion of this method, the weight values for the criteria are determined through the calculation of the removal effect on each criterion, specifically the sum of absolute deviations. Furthermore, in this method, as the impact of criteria on decision alternatives grows, the weight coefficients of the criteria also increase (Keshavarz-Ghorabaee et al., 2021).

The LOPCOW method involves the integration of data from various dimensions to derive appropriate or ideal weights. Additionally, this approach aims to narrow the gaps between the most significant and least significant criteria. Moreover, LOPCOW takes into consideration the relationships between criteria. In this method, the initial step involves preparing the decision matrix, followed by normalizing the values within that matrix. Subsequently, the average square value, expressed as a percentage of the criterion's standard deviation, is calculated to mitigate the variations caused by the data's magnitude, ultimately determining the weight coefficients for the criteria (Ecer & Pamucar, 2022).

The SECA method offers a means to assess both the performance of decision alternatives and the weight coefficients of criteria concerning these alternatives. In this approach, the values within the decision matrix are standardized. Subsequently, disagreement degrees and standardization values are computed using the standard deviation. This data serves as the basis for calculating the weights of the criteria, achieved by solving a multi-objective linear model through model optimization (Keshavarz-Ghorabaee et al., 2018).

The DEMATEL method can be used to reveal the interaction between criteria, as well as to subjectively determine the weights of criteria based on their relationships. To do this, the effects of criteria on each other are determined using subjective evaluations, where 0 represents no effect and 4 represents a very high effect. This information is used to create a direct relationship matrix, which is then used to calculate the standard relationship matrix, total relationship matrix, relationship diagram, threshold value, and finally, the weight coefficients of the criteria (Fontela & Gobus, 1976). Altıntaş (2021), emphasized that the effects of criteria on each other can also be determined using the Somers' d correlation coefficient, which allows for the objective calculation of the weight coefficients of the criteria. This eliminates the need for subjective evaluations in the direct relationship matrix. Upon a review of the literature, it becomes evident that numerous studies have utilized objective weighting and relationship-oriented DEMATEL methods. The ongoing research pertaining to the discussed weighting is outlined in Table 1.

Table 1. *Present Studies Concerning Criteria Weighting*

Author(s)	Methods	Research Theme
Alrababah & Gan, 2023	CRITIC based VIKOR	The Impact of the Hybrid CRITIC–VIKOR Method on Product Aspect Ranking in Customer Reviews
Wang et al., 2023	ENTROPY based MARCOS	Sustainable Evaluation of Major Third-Party Logistics providers
Ali et al., 2022	SAW-AHP, SAW-CILOS, SAW-AHP-CILOS, TOPSIS-AHP, TOPSIS-CILOS, TOPSIS-AHP-CILOS, CoCoSo-AHP, CoCoSo-CILOS, CoCoSo-AHP-CILOS, MARCOS-AHP, MARCOS-CILOS, and MARCOS-AHP-CILOS	Lessons learned from the COVID-19 pandemic in planning the future energy systems of developing countries
Ayan et al., 2023	CILOS, IDOCRIW, FUCOM, LBWA, SAPEVO-M, and MEREC	A Comprehensive Review of the Novel Weighting Methods
Vavrek, 2019	CRITIC, SD,SVP, MR based TOPSIS	Evaluation of the Impact of Selected Weighting Methods on the Results of the TOPSIS Technique
Mukhametzyanov, 2021	Entropy, CRITIC, SD	specific character of objective methods for determining weights of criteria
Sümerli Sarigül et al., 2023	MEREC based MARCOS and COCOSO	evaluating airport service quality
Ersoy, 2023	LOPCOW based RSMVC	Performance Measurement in the BIST Retail and Trade Sector
Rasmussen et al., 2023	F-AHP based F-TOPSIS and SECA	Supplier selection for aerospace & defense industry
Göncü & Çetin, 2022	Dematel and ANP Method	Supplier Selection Criteria in Healthcare Enterprises

2.2. Exponential Curve Function

The Exponential Curve function is based on the exponential function. A function written in the form of $f(x) = b^x$, where $b \in R^+ - \{1\}$ and $x \in R^+$, is referred to as an exponential function. Here, $''b''$ is called the base, and $''x''$ is referred to as the exponent. The domain of exponential functions is the set of real numbers, while the range consists of positive numbers (Önalan, 2010; Balaban, 2015; Ertik et al., 2015; Eroğlu, 2017). If $0 < b < 1$, the function $y = b^x$ exhibits a decreasing characteristic, approaching the $''y''$ axis for increasing values of the base "b". If $b > 1$, the function $y = b^x$ is an increasing function, and again, it approaches the $''y''$ axis for growing values of the base $''b''$ (Kartal et al., 2014; Bernett et al., 2015; Kuruüzüm & İpekçi, 2015; Pekkaya, 2016). In a function written as $y = b^x$, if the irrational number $''e \approx 2{,}718281829\ldots..''$ is used instead of the base $''b''$, the function becomes $y = e^x$ (Kuruüzüm & İpekçi, 2015).

The Exponential Curve function fundamentally arises from the composition of the $''e^x''$ ' function with any constant value, forming the function $y = a.e^{bx}$. The logarithmic transformation of this function can be expressed as $In(y) = In(a) + bx$ (Chakrabarty & Rahman, 2007; IBM, 2013).
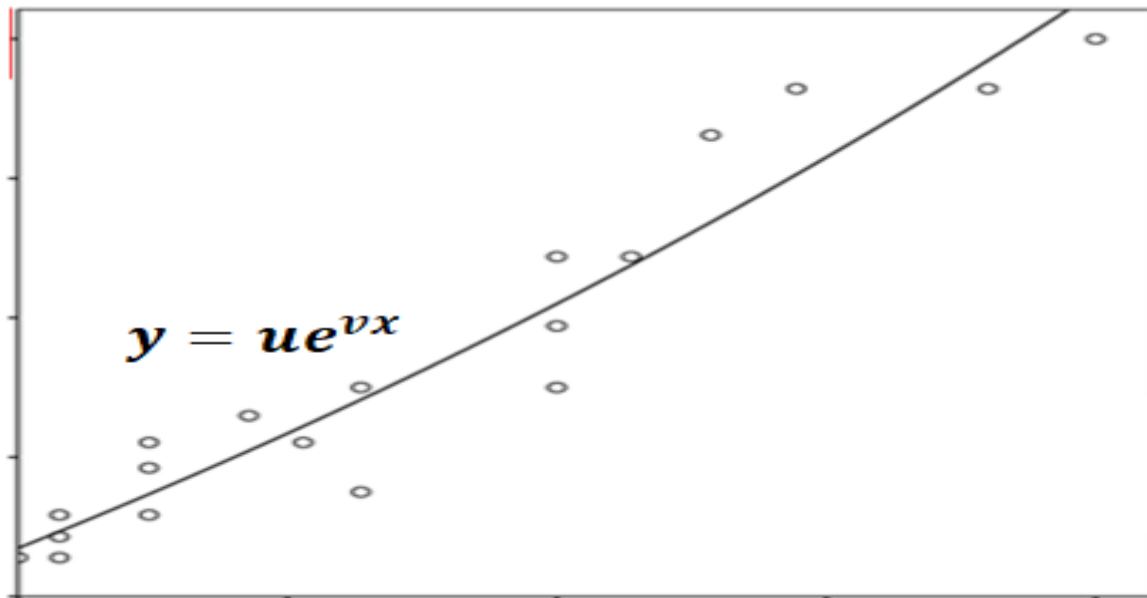
$$y = ue^{vx}$$

Figure 1. *Exponential Curve Function (Note: Figure 1 was obtained using the SPSS 23 program)*

The given expression $y = u.e^{vx}$ models the relationship between the constants "u" and "v" and the variable "x" in an exponential function. "u" represents the initial value of the function (the y-intercept) and "v" controls the rate of growth. As the value of "x" increases, the value of "y" changes exponentially, increasing if "v" is positive and decreasing if "v" is negative. Positive "v" indicates growth with increasing "x", while negative "v" indicates a decrease in "y" with increasing "x" (Thomas, 1991; Chakrabarty & Rahman, 2007).

The exponential curve function provides significant advantages in mathematical modeling. Firstly, due to the function's continuity and differentiability, it possesses a suitable structure for modeling physical systems. Secondly, the function's monotonic property facilitates the derivation, integration, and other operations, simplifying predictions of the function's behavior. This enhances the predictability of the function's behavior. Thirdly, the function's limits allow for easy estimation of how the function behaves at extreme points. Fourthly, the logarithmic transformation of the function results in a symmetric curve, making it easier to understand relationships between variables visually. Lastly, the logarithmic transformation can lead to a linear form, simplifying the function's structure and overcoming complexity (Shparlinski & Konyagin, 1999; Lin, 2014; Kahn, 2015; Joujan, 2018).

Upon reviewing the literature, it has been observed that many studies have been conducted utilizing the exponential curve function (Natalija, 2021). In their work, Landsberg (1977) explained that the exponential curve function is widely applicable in biological research and is an appropriate function for such studies.

Chakrabarty and Rahman (2007) utilized the exponential curve function to estimate and project the overall population in India. Weon & Je (2014) developed a versatile survival distribution based on the stretched exponential curve function, incorporating an age-dependent shaping exponent. Alfaro et al. (2020) employed the exponential curve function to forecast real-time returns of U.S.A stocks by considering unforeseen alterations in the progression of COVID-19 infections. Fosu and Edunyah (2020) employed the exponential curve function to estimate the effectiveness of measures developed against the COVID-19 pandemic in developing and impoverished countries. Hamill et al. (2005) utilized the exponential curve function in the development of a methodology that facilitates the creation of information security strategies and applies measures to assess them. Jones (2023) elucidated that the utilization of the exponential curve function is instrumental in describing the exponential growth resulting from combinatorially chosen samples extracted from standard thin-tailed distributions defined mathematically. Murillo-Escobar et al. (2023) introduced a methodology developed within the realm of encryption algorithms for clinical signals. This methodology enhances the randomness of five specifically chosen chaotic maps by incorporating trigonometric functions (sine, cosine, and tangent) and exponential curve functions. Wood (2023) has developed a new model using structural equation modeling software that allows for the combination of logistic and exponential curve functions.

2.3. Calculating Weight Coefficients for Criteria in the Context of MCDM with the Exponential Function (Theoretical Background)

In determining the weights of criteria, the distinctiveness and conflict among criteria bring out the nature of the criteria (Ecer, 2020). Accordingly, in the DEMATEL literature, criteria with higher impact values in interactional models lead to greater prioritization and significance compared to other criteria (Fontela & Gobus, 1976; Akın, 2017). Similarly, in structural equation modeling, especially in non-recursive models, when one criterion influences another criterion to a greater extent in absolute terms, the criterion causing a greater impact in the relationship between these two criteria is explained to contribute more to the relational structure and is considered more important in that relationship. On the other hand, in recursive models, if one criterion has a greater impact value in absolute terms on other criteria, it is stated to be the most important criterion (Bayram, 2010; Çelik & Yılmaz, 2013; Meydan & Şeşen, 2015; Özdamar, 2016; Civelek, 2018; Gürbüz, 2019; Kline, 2019).

Another attribute to consider in assessing the criteria is their potential for mutual influence, as quantified by quantitative outcomes. If one criterion has a modest positive impact on another, it opens up opportunities to develop strategies to enhance the influenced criterion by leveraging the influencing one. Conversely, when a positive influence of one criterion hinders the progress of another, strategies can be devised to reduce or mitigate the influence of the influencing criterion on the influenced one. Consequently, it becomes possible to formulate strategies, policies, and recommendations for advancing the criteria based on the interdependencies among them within a given context. In this context, exponential curve functions can be utilized to calculate the weight coefficients of criteria. This is due to the fact that, with exponential curve functions, the values of criteria influencing one another can be determined as dependent and independent variables (Karagöz, 2017).

Another crucial advantage of the exponential curve function is its capability to perform regression analysis between two variables. Accordingly, exponential curve equations describing the relationship between two variables based on the data of these variables can be established through regression analysis (curve estimation) using SPSS. This enables the calculation of the quantitative impact between two variables (IBM, 2013; Karagöz, 2017). In comparison to many functions in the literature, the exponential curve function allows for a more precise and controlled determination of how much the dependent variable changes with the smallest change in the independent variable (Lin, 2014). Therefore, this situation provides an opportunity for accurate and reliable modeling in the relationship or interaction structure between two variables (Chakrabarty & Rahman, 2007).

The derivative $f'(x)$ is referred to as the antiderivative or indefinite integral of the function $f(x)$. $f'(x)$ equals can be expressed as $f'(x)dx = df(x)$. This expression is commonly represented using the infinite and continuous summation symbol $\int$. From this equation, we can derive the equation $\int f'(x)dx = f(x)$. Hence, the function to be integrated is $f'(x)$. Moreover, $\int f(x)dx = F(x) + C$, where $\int_r^p f(x)dx = F(p) - F(r)$

represents the definite integral. In this context, $''r''$ denotes the lower limit of the integral, while $''p''$ signifies the upper limit (Kartal et al., 2014). Therefore, after establishing the exponential curve relationships between the criteria using the exponential curve, one can measure the extent to which the variation of the independent variable $''x''$ between the limits $''p''$ and $''r''$ impacts or alters the dependent variable $''y''$ through definite integration (Kuruüzüm & İpekçi Çetin, 2015). The visual representation of this situation is illustrated in Figure 2 (IBM, 2013).

$$\int_{b_{min.}}^{b_{max.}=1} f'(x)\,dx$$

$$y = ue^{vx}$$
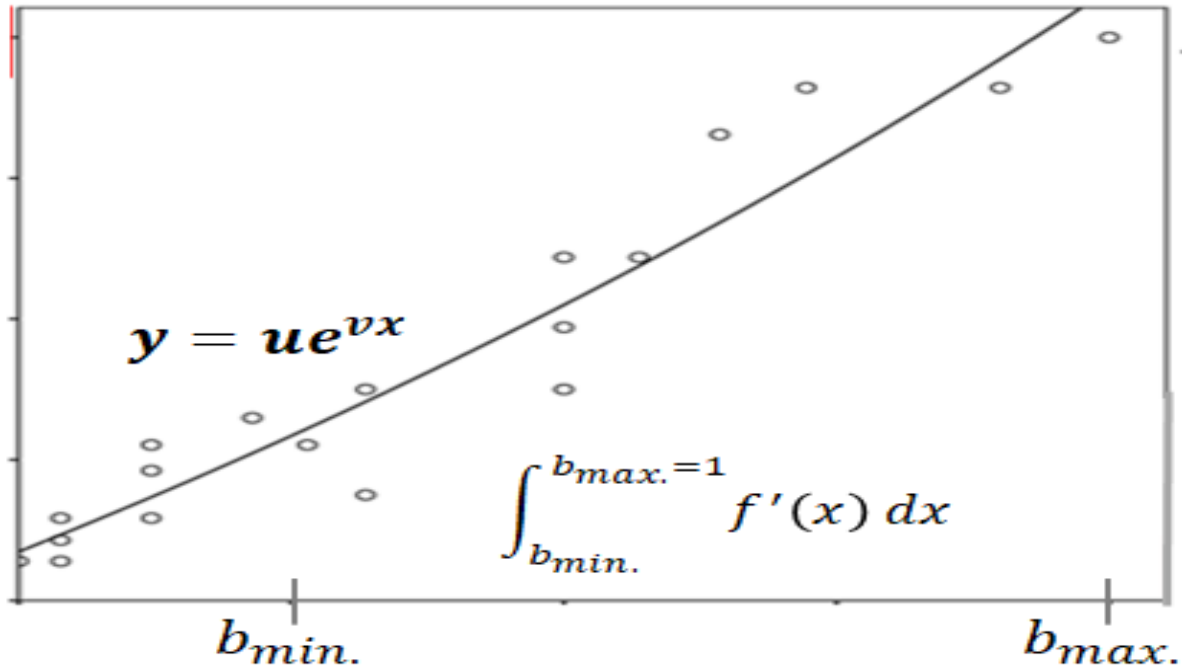
Figure 2. Exponential Curve Function and Its Impact on Criterion (p) with Criterion (r) Model (Note: Figure 2 was obtained using the SPSS 23 program)

After creating a exponential curve function between the values of two criteria (p, r) in the decision matrix based on decision alternatives, the impact of one criterion (p) on the other critera (r), or how changes in the independent variable (r) criterion affect the dependent variable criterion, can be calculated by determining the maximum and minimum values of the criterion taken as the independent variable in the decision matrix. In any decision matrix containing cost or benefit-oriented criteria with no zeros or negative values, the maximum value of the independent criterion is 1 when the criteria are normalized between 0 and 1. If any value in any decision matrix is negative or zero, the exponential curve interaction between the criteria does not occur (Kartal et al., 2014). Because the exponential curve function is logarithmically transformed, the relationship between the criteria remains undefined (Shparlinski & Konyagin, 1999; Lin, 2014). Accordingly, $f(x) = ue^{v.x}$ where $f(x)$'s derivative is determined as $f(x)' = uve^{ux}$. Subsequently, the impact of the p criterion on the r criterion can be calculated with Equation 1.

$$\int_{r_{min.}}^{p_{max.}=1} f(x)'\,dx = F(x)]_{r_{min.}}^{p_{max.}} = F(Pmax) - f(rmin) \tag{1}$$

2.4. Data Set and Analysis of the Study

The dataset for the research consists of the Logistic Performance Index (LPI) criteria for the year 2022 for 19 countries in the G20 group. The reason for selecting this dataset in the study is to determine the discriminative power of the proposed model criteria among countries, considering the significant differences in values within this dataset. In this regard, abbreviations for this dataset are explained in Table 2 for convenience in the research.

Table 2. LPI Criteria Abbreviations (Arvis et al., 2023)

LPI Criteria	Criteria Abbreviations
Customs	LPI1
Infrastructure	LPI2
International Shipments	LPI3
Logistics Competence and Quality	LPI4
Timeliness Score	LPI5
Tracking and Tracing	LPI6

2.4. Proposed Method: Measurement Relying on the Impacts of an Exponential Curve Function (MIEXCF)

The fundamental logic of the proposed method is based on the exponential curve effect of criteria on each other. Regarding this, the method for calculating the weight coefficients of criteria according to the MIEXCF method is explained below.

Altıntaş (2023) established the mathematical model based on cubic effects among the criteria to determine the weights of criteria. Within this scope, in this study, Altıntaş's (2023) modeling approach was utilized in the following steps: in the third step, functions were formulated; in the fourth step, impact values among the criteria were calculated based on these functions; in the fifth step, total impact values of each criterion according to the function structures were computed; and finally, in the sixth step, Altıntaş's (2023) logic was employed in determining the criterion weights.

Step 1: Obtaining the Decision Matrix

$i: 1, 2, 3 \ldots n$: where n represents the number of decision alternatives

$j: 1, 2, 3 \ldots m$: where m represents the number of criteria

D: Decision matrix

ECF: Criterion

d_{ij}: The decision matrix is constructed according to Equation 2, where "ij" represents the $i - th$ decision alternative on the $j - th$ criterion.

$$D = [d_{ij}]_{nxm} = \begin{bmatrix} ECF_1 & ECF_2 & \cdots & ECF_m \\ x_{11} & x_{12} & & x_{1m} \\ x_{21} & x_{22} & \cdots & x_{2m} \\ \vdots & \vdots & \vdots & \vdots \\ x_{n1} & x_{n2} & \cdots & x_{nm} \end{bmatrix} \tag{2}$$

Step 2: Normalization of Decision Matrix (d_{ij}^*)

The normalization of the decision matrix is conducted through the utilization of the subsequent equation. Benefit criteria undergo normalization using Equation 3, whereas cost criteria are subjected to normalization employing Equation 4.

$$d_{ij}^* = \frac{min. d_{ij}}{d_{ij}} \tag{3}$$

$$d_{ij}^* = \frac{d_{ij}}{max. d_{ij}} \tag{4}$$

Step 3: Generation of Exponential Curve Functions

Based on the number of criteria, m, exponential curve function $(f(x) = y = ae^{bx})$ are generated for the variables up to a quantity of using SPSS assistance (Regression-CURVE ESTIMATION), considering the exponential curve relationship between them.

$$(1)\ f(ECF_1) = ECF_2, f(ECF_1) = ECF_3, \dots\dots f(ECF_1) = ECF_m \tag{5}$$

$$(2)\ f(ECF_2) = ECF_1, f(ECF_2) = ECF_3, \dots\dots f(ECF_2) = ECF_m \tag{6}$$

$$(3)\ f(ECF_3) = ECF_1, f(ECF_3) = ECF_2, \dots\dots f(ECF_3) = ECF_m \tag{7}$$

$$\vdots\quad\vdots\quad\vdots \qquad \vdots\quad\vdots\quad\vdots \qquad \vdots\quad\vdots\quad\vdots$$

$$(m)\ f(ECF_m) = ECF_1, f(ECF_m) = ECF_2, \dots\dots f(ECF_m) = ECF_{m-1} \tag{8}$$

Step 4: Calculation of Exponential Curve Impact Value between Criteria

In this stage, we assess the influence or alteration of a dependent variable (one criterion) by an independent variable (another criterion) within the scope of its minimum and maximum values, achieved through the application of definite integral calculations. In this context, 't' represents the exponential curve impact value of one criterion on the other. It is important to ensure the absolute value of the impact values after the integral calculation.

$$(1)\ f(ECF_1) = ECF_2\ , \int_{ECF_{1min.}}^{ECF_{1max.}} (f'(ECF_1))\ dx = \left| t_{ECF_1 \to ECF_2} \right| \tag{9}$$

$$(2)\ f(ECF_1) = ECF_3\ , \int_{ECF_{1min.}}^{ECF_{1max.}} (f'(ECF_2))\ dx = \left| t_{ECF_1 \to ECF_3} \right| \tag{10}$$

$$(3)\ f(ECF_1) = ECF_4\ , \int_{ECF_{1min.}}^{ECF_{1max.}} (f'(C_1))\ dx = \left| t_{ECF_1 \to ECF_4} \right| \tag{11}$$

$$\vdots\quad\vdots\quad\vdots \qquad \vdots\quad\vdots\quad\vdots \qquad \vdots\quad\vdots\quad\vdots$$

$$\left(\frac{m!}{(m-2)!}\right) f(ECF_m) = ECF_{m-1}\ , \int_{ECF_{mmin.}}^{ECF_{mmax.}} (f'(ECF_m))\ dx = \left| t_{ECF_m \to ECF_{m-1}} \right| \tag{12}$$

Step 5: Calculation of the Total Exponential Curve Impact Values of Each Criterion (S_{ECF})

During this stage, we aggregate the exponential curve impact values of one criterion on the remaining criteria to quantify the comprehensive exponential curve impact value of that criterion on the others.

$$(1) \ for \ ECF_1 \ \left|t_{ECF_1 \to ECF_2}\right| + \left|t_{ECF_1 \to ECF_3}\right| \ldots\ldots + \left|t_{ECF_1 \to ECF_m}\right| = \left(\sum_{j=1}^{m-1} \left|t_{ECF_1 \to ECF_{j+1}}\right|\right) = S_{ECF_1} \qquad (13)$$

$$(2) \ for \ ECF_2 \ \left|t_{ECF_2 \to ECF_1}\right| + \left|t_{ECF_2 \to ECF_3}\right| \ldots\ldots + \left|t_{ECF_2 \to ECF_m}\right| = \left(\sum_{j=0, j\neq 1}^{m-1} \left|t_{ECF_2 \to ECF_{j+1}}\right|\right) = S_{ECF_2} \qquad (14)$$

$$(3) \ for \ ECF_3 \ \left|t_{ECF_3 \to ECF_1}\right| + \left|t_{ECF_3 \to ECF_2}\right| \ldots\ldots + \left|t_{ECF_3 \to ECF_m}\right| = \left(\sum_{j=0, j\neq 2}^{m-1} \left|t_{ECF_3 \to ECF_{j+1}}\right|\right) = S_{ECF_3} \qquad (15)$$

$$
\begin{matrix}
\vdots & \vdots & \vdots & & \vdots & \vdots & \vdots & & \vdots & \vdots & \vdots \\
\vdots & \vdots & \vdots & & \vdots & \vdots & \vdots & & \vdots & \vdots & \vdots \\
\vdots & \vdots & \vdots & & \vdots & \vdots & \vdots & & \vdots & \vdots & \vdots \\
\end{matrix}
$$

$$(m) \ for \ ECF_m \ \left|t_{ECF_m \to ECF_1}\right| + \left|t_{ECF_m \to ECF_2}\right| \ldots\ldots + \left|t_{ECF_m \to ECF_{m-1}}\right| = \left(\sum_{j=1}^{m-1} \left|t_{ECF_m \to ECF_{j+1}}\right|\right) = S_{ECF_m} \qquad (16)$$

Step 6: Determination of Criterion Weight Values (w_j)

In this stage, the collective exponential curve impact value of each criterion on the remaining criteria is divided by the sum of the collective exponential curve impact values of all criteria. This division enables the computation of the weight coefficient for each criterion.

$$w_j = \frac{S_{ECF_j}}{\sum_{j=1}^{m} S_{ECF_j}} \qquad (17)$$

The proposed method has numerous advantages. The first of these is the non-linear nature of the method. This is because the exponential curve function, being non-linear, is more successful in accurately predicting relationships between variables than linear methods. This situation ensures a more accurate resolution of relationships between variables compared to linear models (Chakrabarty & Rahman, 2007). Therefore, since the MIEXCF method is based on the exponential curve function, accurate results can be obtained in determining the relationships between criteria and, consequently, the weights of criteria. However, in other objective criterion weighting methods (ENTROPY, CRITIC, SD, SVP, and MEREC), the determination of criterion weights is not based on a non-linear linear structure. Therefore, these methods cannot benefit from the advantages provided by a non-linear structure.

Secondly, in the MIEXCF method, the calculation of the mutual influence value of variables is conducted through the integral method. The integral precisely and accurately demonstrates the total change or impact of the dependent variable in the variation of the independent variable within the boundary values of the independent variable. Therefore, this circumstance elucidates the original effect of the independent variable on the dependent variable without requiring a process (Bernett et al., 2015). In this context, within the scope of the MIEXCF method, the weights of criteria can be calculated more sensitively and realistically. In contrast, in other objective criterion weighting methods, the computation of criterion weights occurs as a result of highly transformative processes involving the values of the decision matrix.

Finally, the third aspect is the opportunity provided by the MIEXCF method for enhancing criteria. In the interactive analysis of variables, the variable or variables with the highest impact value can promote the development of other variables by influencing them (Karagöz, 2017). Because of the metric structure of the

relationship between criteria, within the scope of the MIEXCF method, the criterion with the highest weight coefficient can be evaluated to determine its impact on the criteria that need improvement (those with the least impact) or to assess whether the criteria with lower impact or requiring improvement need to enhance their influence on other criteria. In contrast, in other objective weighting methods, since the weight values of criteria are not determined based on their influence on each other, opportunities to enhance criteria remain limited.

The MIEXCF method possesses both advantages and also drawbacks. One of its disadvantage is the complexity of calculations required for determining criteria weight coefficients, particularly compared to many objective weighting methods in the literature. As the number of criteria increases, the calculations become more intricate due to the numerous interaction values between criteria. However, these calculations can be easily performed using the MATLAB program or the Python programming language. Another drawback is the reliance on SPSS or other statistical software programs to identify exponential relationships between criteria. Without SPSS, the calculation of weight coefficients becomes more complex and time-consuming. However, the exponential relationship between the criteria can be obtained by transferring the formulas to the EXCEL program within the scope of regression analysis. As a result, the calculation operations can be simplified. A third disadvantage arises when there is no theoretical cause-and-effect relationship between criteria, limiting opportunities for criteria improvement. The aforementioned disadvantage is also present in the CRITIC, MEREC and DEMATEL methods. This is because the CRITIC method determines the weight coefficients of the criteria based on the level of Pearson correlation between the criteria. On the other hand, the logic of calculating the weight values of the criteria in the MEREC method is based on the effect of the criteria on the decision alternatives. In addition to these, the weights of the criteria in the DEMATEL method depend on the extent to which they impact each other and are affected by each other. Therefore, in the determination of the weight coefficients of the criteria, the cause-and-effect relationship between the criteria in the CRITIC and DEMATEL methods and the cause-and-effect relationship between the criteria and the decision alternatives in the MEREC method are not taken into account in a theoretical sense. In other words, in the CRITIC and DEMATEL methods, there is no a theoretical necessity for a cause-and-effect relationship between the criteria and MEREC, there is a no theoretical necessity for a cause-and-effect relationship between the criteria and the decision alternatives. Finally, the fourth drawback involves the need for transformation using Z-scores when values in the decision matrix are negative or 0 to ensure positive and non-zero values. This challenge is also present in the ENTROPY and MEREC methods, both relying on logarithmic measurements.

3. RESULTS AND DISCUSSION (THE CASE STUDY)

3.1. Computational Analyses

Considering the data set of the research, the weight coefficients of criteria for the 19 countries in the G20 group in 2022 were calculated using the LPI criterion data with the MIEXCF method. In this regard, in the first step of the method, a decision matrix was created with the help of Equation 2 and is presented in Table 3.

In the second step of the method, as all LPI criteria are beneficial, the normalized decision matrix was calculated using Equation 3 based on the decision matrix values described in Table 3 and is presented in Table 4.

In the third step of the model, with the presence of six components, we employ the functional equation expressed as to demonstrate the exponential relationships among these components.

To capture the interactions among the components effectively, we established 30 exponential curve function equations, denoted as Equations 5, 6, 7, and 8, using CURVE analysis (regression models) through SPSS. These respective functions are detailed in Table 5.

In the fourth phase of the approach, we calculated exponential curve influence factors among the criteria using equations 9, 10, 11, and 12. The process for determining the impact values between criteria are explained in the following sections.

$$f(LPI1)$$

f(LPI1)=LPI2

$$\text{deriv}(0.305e^{1.22x}, x) = \frac{3721e^{\frac{61x}{50}}}{10000}$$

$$\int_{0.6}^{1} \frac{3721e^{\frac{61x}{50}}}{10000} dx = \frac{61e^{\frac{61}{50}} - 61e^{\frac{183}{250}}}{200} = 0,399$$

f(LPI1)=LPI3

$$\text{deriv}(0.381e^{0.827x}, x) = \frac{315087e^{\frac{827x}{1000}}}{1000000}$$

$$\int_{0.6}^{1} \frac{315087e^{\frac{827x}{1000}}}{1000000} dx = \frac{381e^{\frac{827}{1000}} - 381e^{\frac{2481}{5000}}}{1000} = 0,245$$

f(LPI1)=LPI4

$$\text{deriv}(0.32e^{1.112x}, x) = \frac{1112e^{\frac{139x}{125}}}{3125}$$

$$\int_{0.6}^{1} \frac{1112e^{\frac{139x}{125}}}{3125} dx = \frac{8e^{\frac{139}{125}} - 8e^{\frac{417}{625}}}{25} = 0,349$$

f(LPI1)=LPI5

$$\text{deriv}(0.477e^{0.688x}, x) = \frac{20511e^{\frac{86x}{125}}}{62500}$$

$$\int_{0.6}^{1} \frac{20511e^{\frac{86x}{125}}}{62500} dx = \frac{477e^{\frac{86}{125}} - 477e^{\frac{258}{625}}}{1000} = 0,228$$

f(LPI1)=LPI6

$$\text{deriv}(0.303e^{1.106x}, x) = \frac{167559e^{\frac{553x}{500}}}{500000}$$

$$\int_{0.6}^{1} \frac{167559e^{\frac{553x}{500}}}{500000} dx = \frac{303e^{\frac{553}{500}} - 303e^{\frac{1659}{2500}}}{1000} = 0,327$$

$$f(LPI2)$$

f(LPI2)=LPI1

$$\text{deriv}(0.287e^{1.229x}, x) = \frac{352723e^{\frac{1229x}{1000}}}{1000000}$$

$$\int_{0.628}^{1} \frac{352723e^{\frac{1229x}{1000}}}{1000000} dx = \frac{287e^{\frac{1229}{1000}} - 287e^{\frac{192953}{250000}}}{1000} = 0,360$$

f(LPI2)=LPI3

$$\text{deriv}(0.377e^{0.821x}, x) = \frac{309517e^{\frac{821x}{1000}}}{1000000}$$

$$\int_{0.628}^{1} \frac{309517e^{\frac{821x}{1000}}}{1000000} dx = \frac{377e^{\frac{821}{1000}} - 377e^{\frac{128897}{250000}}}{1000} = 0,226$$

f(LPI2)=LPI4

$$\text{deriv}(0.311e^{1.122x}, x) = \frac{174471e^{\frac{561x}{500}}}{500000}$$

$$\int_{0.628}^{1} \frac{174471e^{\frac{561x}{500}}}{500000} dx = \frac{311e^{\frac{561}{500}} - 311e^{\frac{88077}{125000}}}{1000} = 0,326$$

f(LPI2)=LPI5

$$\text{deriv}(0.474e^{0.678x}, x) = \frac{80343e^{\frac{339x}{500}}}{250000}$$

$$\int_{0.628}^{1} \frac{80343e^{\frac{339x}{500}}}{250000} dx = \frac{237e^{\frac{339}{500}} - 237e^{\frac{53223}{125000}}}{500} = 0,208$$

f(LPI2)=LPI6

$$\text{deriv}(0.298e^{1.698x}, x) = \frac{126501e^{\frac{849x}{500}}}{250000}$$

$$\int_{0.628}^{1} \frac{126501e^{\frac{849x}{500}}}{250000} dx = \frac{149e^{\frac{849}{500}} - 149e^{\frac{133293}{125000}}}{500} = 0{,}762$$

$$\boldsymbol{f}(\boldsymbol{LPI3})$$

f(LPI3)=LPI1

$$\text{deriv}(0.301e^{1.257x}, x) = \frac{378357e^{\frac{1257x}{1000}}}{1000000}$$

$$\int_{0.622}^{1} \frac{378357e^{\frac{1257x}{1000}}}{1000000} dx = \frac{301e^{\frac{1257}{1000}} - 301e^{\frac{390927}{500000}}}{1000} = 0{,}400$$

f(LPI3)=LPI2

$$\text{deriv}(0.313e^{1.239x}, x) = \frac{387807e^{\frac{1239x}{1000}}}{1000000}$$

$$\int_{0.622}^{1} \frac{387807e^{\frac{1239x}{1000}}}{1000000} dx = \frac{313e^{\frac{1239}{1000}} - 313e^{\frac{385329}{500000}}}{1000} = 0{,}404$$

f(LPI3)=LPI4

$$\text{deriv}(0.297e^{1.269x}, x) = \frac{376893e^{\frac{1269x}{1000}}}{1000000}$$

$$\int_{0.622}^{1} \frac{376893e^{\frac{1269x}{1000}}}{1000000} dx = \frac{297e^{\frac{1269}{1000}} - 297e^{\frac{394659}{500000}}}{1000} = 0{,}403$$

f(LPI3)=LPI5

$$\text{deriv}(0.424e^{0.886x}, x) = \frac{23479e^{\frac{443x}{500}}}{62500}$$

$$\int_{0.622}^{1} \frac{23479e^{\frac{443x}{500}}}{62500} dx = \frac{53e^{\frac{443}{500}} - 53e^{\frac{137773}{250000}}}{125} = 0{,}293$$

f(LPI3)=LPI6

$$\text{deriv}(0.28e^{1.268x},x) = \frac{2219e^{\frac{317x}{250}}}{6250}$$

$$\int_{0.622}^{1} \frac{2219e^{\frac{317x}{250}}}{6250}dx = \frac{7e^{\frac{317}{250}} - 7e^{\frac{98587}{125000}}}{25} = 0{,}379$$

$$\boldsymbol{f(LPI4)}$$

f(LPI4)=LPI1

$$\text{deriv}(0.283e^{1.286x},x) = \frac{181969e^{\frac{643x}{500}}}{500000}$$

$$\int_{0.619}^{1} \frac{181969e^{\frac{643x}{500}}}{500000}dx = \frac{283e^{\frac{643}{500}} - 283e^{\frac{398017}{500000}}}{1000} = 0{,}397$$

f(LPI4)=LPI2

$$\text{deriv}(0.277e^{1.229x},x) = \frac{340433e^{\frac{1229x}{1000}}}{1000000}$$

$$\int_{0.619}^{1} \frac{340433e^{\frac{1229x}{1000}}}{1000000}dx = \frac{277e^{\frac{1229}{1000}} - 277e^{\frac{760751}{1000000}}}{1000} = 0{,}354$$

f(LPI4)=LPI3

$$\text{deriv}(0.345e^{0.968x},x) = \frac{8349e^{\frac{121x}{125}}}{25000}$$

$$\int_{0.968}^{1} \frac{8349e^{\frac{121x}{125}}}{25000}dx = \frac{69e^{\frac{121}{125}} - 69e^{\frac{14641}{15625}}}{200} = 0{,}028$$

f(LPI4)=LPI5

$$\text{deriv}(0.447e^{0.78x},x) = \frac{17433e^{\frac{39x}{50}}}{50000}$$

$$\int_{0.619}^{1} \frac{17433e^{\frac{39x}{50}}}{50000}dx = \frac{447e^{\frac{39}{50}} - 447e^{\frac{24141}{50000}}}{1000} = 0{,}251$$

f(LPI4)=LPI6

$$\text{deriv}(0.277e^{1.229x},x) = \frac{340433e^{\frac{1229x}{1000}}}{1000000}$$

$$\int_{0.619}^{1} \frac{340433e^{\frac{1229x}{1000}}}{1000000}dx = \frac{277e^{\frac{1229}{1000}} - 277e^{\frac{760751}{1000000}}}{1000} = 0{,}354$$

$$\boldsymbol{f(LPI5)}$$

f(LPI5)=LPI1

$$\text{deriv}(0.191e^{1.687x},x) = \frac{322217e^{\frac{1687x}{1000}}}{1000000}$$

$$\int_{0.707}^{1} \frac{322217e^{\frac{1687x}{1000}}}{1000000}dx = \frac{191e^{\frac{1687}{1000}} - 191e^{\frac{1192709}{1000000}}}{1000} = 0{,}402$$

f(LPI5)=LPI2

$$\text{deriv}(0.203e^{1.646x},x) = \frac{167069e^{\frac{823x}{500}}}{500000}$$

$$\int_{0.707}^{1} \frac{167069e^{\frac{823x}{500}}}{500000}dx = \frac{203e^{\frac{823}{500}} - 203e^{\frac{581861}{500000}}}{1000} = 0{,}403$$

f(LPI5)=LPI3

$$\text{deriv}(0.228e^{1.411x},x) = \frac{80427e^{\frac{1411x}{1000}}}{250000}$$

$$\int_{0.707}^{1} \frac{80427e^{\frac{1411x}{1000}}}{250000}dx = \frac{57e^{\frac{1411}{1000}} - 57e^{\frac{997577}{1000000}}}{250} = 0{,}317$$

f(LPI5)=LPI4

$$\text{deriv}(0.198e^{1.64x},x)$$

$$\int_{0.707}^{1} \frac{4059e^{\frac{41x}{25}}}{12500} dx = \frac{99e^{\frac{41}{25}} - 99e^{\frac{28987}{25000}}}{500} = 0,389$$

$f(LPI5)=LPI6$

$$\text{deriv}(0.193e^{1.592x}, x) = \frac{38407e^{\frac{199x}{125}}}{125000}$$

$$\int_{0.707}^{1} \frac{38407e^{\frac{199x}{125}}}{125000} dx = \frac{193e^{\frac{199}{125}} - 193e^{\frac{140693}{125000}}}{1000} = 0,354$$

$$\boldsymbol{f(LPI6)}$$

$f(LPI6)=LPI1$

$$\text{deriv}(0.292e^{1.323x}, x) = \frac{96579e^{\frac{1323x}{1000}}}{250000}$$

$$\int_{0.595}^{1} \frac{96579e^{\frac{1323x}{1000}}}{250000} dx = \frac{73e^{\frac{1323}{1000}} - 73e^{\frac{157437}{200000}}}{250} = 0,455$$

$f(LPI6)=LPI2$

$$\text{deriv}(0.305e^{1.302x}, x) = \frac{39711e^{\frac{651x}{500}}}{100000}$$

$$\int_{0.595}^{1} \frac{39711e^{\frac{651x}{500}}}{100000} dx = \frac{61e^{\frac{651}{500}} - 61e^{\frac{77469}{100000}}}{200} = 0,460$$

$f(LPI6)=LPI3$

$$\text{deriv}(0.351e^{1.001x}, x) = \frac{351351e^{\frac{1001x}{1000}}}{1000000}$$

$$\int_{0.595}^{1} \frac{351351e^{\frac{1001x}{1000}}}{1000000} dx = \frac{351e^{\frac{1001}{1000}} - 351e^{\frac{119119}{200000}}}{1000} = 0,318$$

$f(LPI6)=LPI4$

$$\text{deriv}(0.303e^{1.271x}, x) = \frac{385113e^{\frac{1271x}{1000}}}{1000000}$$

$$\int_{0.595}^{1} \frac{385113e^{\frac{1271x}{1000}}}{1000000} dx = \frac{303e^{\frac{1271}{1000}} - 303e^{\frac{151249}{200000}}}{1000} = 0,435$$

f(LPI6)=LPI5

$$\text{deriv}(0.46e^{0.788x}, x) = \frac{4531e^{\frac{197x}{250}}}{12500}$$

$$\int_{0.595}^{1} \frac{4531e^{\frac{197x}{250}}}{12500} dx = \frac{23e^{\frac{197}{250}} - 23e^{\frac{23443}{50000}}}{50} = 0,276$$

In the fifth stage of the process, we computed the cumulative exponential curve impact values for each criterion using formulas 13, 14, 15, and 16. These calculated values are presented in Table 6.

Table 3. *Decision Matrix*

Economies	LPI1	LPI2	LPI3	LPI4	LPI5	LPI6
Argentina	2.7	2.8	2.7	2.7	3.1	2.9
Australia	3.7	4.1	3.1	3.9	3.6	4.1
Brazil	2.9	3.2	2.9	3.3	3.2	3.5
Canada	4	4.3	3.6	4.2	4.1	4.1
China	3.3	4	3.6	3.8	3.7	3.8
France	3.7	3.8	3.7	3.8	4.1	4
Germany	3.9	4.3	3.7	4.2	4.1	4.2
India	3	3.2	3.5	3.5	3.6	3.4
Indonesia	2.8	2.9	3	2.9	3.3	3
Italy	3.4	3.8	3.4	3.8	3.9	3.9
Japan	3.9	4.2	3.3	4.1	4	4
Korea, Rep.	3.9	4.1	3.4	3.8	3.8	3.8
Mexico	2.5	2.8	2.8	3	3.5	3.1
Russia Fed.	2.4	2.7	2.3	2.6	2.9	2.5
Saudi Arabia	3	3.6	3.3	3.3	3.6	3.5
South Africa	3.3	3.6	3.6	3.8	3.8	3.8
Türkiye	3	3.4	3.4	3.5	3.6	3.5
United King.	3.5	3.7	3.5	3.7	3.7	4
USA	3.7	3.9	3.4	3.9	3.8	4.2

Table 4. *Normalized Matrix*

Countries	LPI1	LPI2	LPI3	LPI4	LPI5	LPI6
Argentina	0.889	0.964	0.852	0.963	0.936	0.862
Australia	0.649	0.659	0.742	0.667	0.806	0.610
Brazil	0.828	0.844	0.793	0.788	0.906	0.714
Canada	0.600	0.628	0.639	0.619	0.707	0.610
China	0.727	0.675	0.639	0.684	0.784	0.658
France	0.649	0.711	0.622	0.684	0.707	0.625
Germany	0.615	0.628	0.622	0.619	0.707	0.595
India	0.800	0.844	0.657	0.743	0.806	0.735
Indonesia	0.857	0.931	0.767	0.897	0.879	0.833
Italy	0.706	0.711	0.677	0.684	0.744	0.641
Japan	0.615	0.643	0.697	0.634	0.725	0.625
Korea, Rep.	0.615	0.659	0.677	0.684	0.763	0.658
Mexico	0.960	0.964	0.821	0.867	0.829	0.807
Russia Fed.	1.000	1.000	1.000	1.000	1.000	1.000
Saudi Arab.	0.800	0.750	0.697	0.788	0.806	0.714
South Afr.	0.727	0.750	0.639	0.684	0.763	0.658
Türkiye	0.800	0.794	0.677	0.743	0.806	0.714
United Kin.	0.686	0.730	0.657	0.703	0.784	0.625
USA	0.649	0.692	0.677	0.667	0.763	0.595

Furthermore, in Equation 17, we calculate weight coefficients that represent the significance levels of each criterion. These coefficients measure the relative importance of the criteria within the scope of the analysis. The resulting values are presented in Table 7.

After a comprehensive analysis of Table 4, we have organized the significance attributed to the various components of the LPI (Exponential Impact) as follows: LPI6 carries the highest weight coefficient, followed by LPI2, LPI3, LPI5, LPI1 and, finally, LPI4. This sequence clarifies the differing levels of importance assigned to each constituent within the LPI framework.

3.2. Sensibility Analysis

In the context of this research, we conducted an evaluation of the MIEXCF method to assess its methodological sensitivity. Sensitivity analysis, within the framework of MCDM, involves applying various criteria weighting methods to the same dataset, enabling a comparison of the resulting values and rankings. To ensure the sensitivity of the weight coefficient calculation method, the weight rankings of the criteria identified using the method chosen for sensitivity analysis are expected to differ from the weight coefficient rankings obtained with other methods (Gigovic et al., 2016).

Following this approach, for the purpose of sensitivity analysis, we calculated and organized the weighting coefficients associated with the components of the LPI using well-established objective weighting techniques that are commonly found in scholarly literature. Some notable examples of these techniques include ENTROPY, CRITIC, SD (Standard Deviation), SVP (Statistical Variance Procedure), MEREC, and LOPCOW. The corresponding numerical results have been thoroughly documented in Table 8.

Table 5. *Exponential Curve functions Derived from the Correlation Among the Criteria*

IDC	DC	Function
LPI1→	LPI2	$y=0.305e^{1.220x}$
	LPI3	$y=0.381e^{0.827x}$
	LPI4	$y=0.320e^{1.112x}$
	LPI5	$y=0.477e^{0.688x}$
	LPI6	$y=0.303e^{1.106x}$
LPI2→	LPI1	$y=0.287e^{1.129x}$
	LPI3	$y=0.377e^{0.821x}$
	LPI4	$y=0.311e^{1.122x}$
	LPI5	$y=0.474e^{0.678x}$
	LPI6	$y=0.298e^{1.098x}$
LPI3→	LPI1	$y=0.297e^{1.269x}$
	LPI2	$y=0.301e^{1.257x}$
	LPI4	$y=0.313e^{1.239x}$
	LPI5	$y=0.424e^{0.886x}$
	LPI6	$y=0.280e^{1.268x}$
LPI4→	LPI1	$y=0.283e^{1.286x}$
	LPI2	$y=0.291e^{1.288x}$
	LPI3	$y=0.345e^{0.968x}$
	LPI5	$y=0.447e^{0.780x}$
	LPI6	$y=0.277e^{1.229x}$
LPI5→	LPI1	$y=0.191e^{1.687x}$
	LPI2	$y=0.203e^{1.646x}$
	LPI3	$y=0.228e^{1.411x}$
	LPI4	$y=0.198e^{1.640x}$
	LPI6	$y=0.193e^{1.592x}$
LPI6→	LPI1	$y=0.292e^{1.323x}$
	LPI2	$y=0.305e^{1.302x}$
	LPI3	$y=0.351e^{1.001x}$
	LPI4	$y=0.303e^{1.271x}$
	LPI5	$y=0.450e^{0.788x}$
IDC: Independent Criteria, DC: Dependent Criteria		

Table 6. *The Total Exponential Curve Impact Values of LPI Components on Each Other*

Independent Component	Dependent Criteria	Effect
LPI1→	LPI2	0.399
	LPI3	0.245
	LPI4	0.349
	LPI5	0.228
	LPI6	0.327
	Total	1.548
LPI2→	LPI1	0.36
	LPI3	0.226
	LPI4	0.326
	LPI5	0.208
	LPI6	0.762
	Total	1.882
LPI3→	LPI1	0.4
	LPI2	0.404
	LPI4	0.403
	LPI5	0.293
	LPI6	0.379
	Total	1.879
LPI4→	LPI1	0.397
	LPI2	0.354
	LPI3	0.028
	LPI5	0.251
	LPI6	0.354
	Total	1.384
LPI5→	LPI1	0.402
	LPI2	0.403
	LPI3	0.317
	LPI4	0.389
	LPI6	0.354
	Total	1.865
LPI6→	LPI1	0.455
	LPI2	0.46
	LPI3	0.318
	LPI4	0,435
	LPI5	0,276
	Total	1,944

194   Furkan Fahri ALTINTAŞ

GU J Sci, Part A   11(1) 173-202 (2024)   10.54287/gujsa.1419551

When Tables 6 and 7 are compared side by side, it becomes clear that the prioritization of criteria weighting coefficients for the Global Logistic Performance Index (LPI) differs when calculated using the MIEXCF method compared to other approaches. This demonstrates the sensitivity of the MIEXCF method.

3.3. Comparative Analysis

The comparative analysis assesses the relationships and positions of the proposed method against other objective weight coefficient calculation methods. The proposed method should be credible, reliable, and consistent with other methods, while also demonstrating a positive and significant correlation with different weight coefficient methods (Keshavarz-Ghorabaee et al., 2021). Based on the data presented in Table 7, the positions of the methods are illustrated in Figures 3, 4 and 5.

Table 7. *Weighting Coefficients* (w) *of the LPI Criteria*

LPI Criteria	Total Effects	(w)	Ranking
LPI1	1.548	0.1474	5
LPI2	1.882	0.1792	2
LPI3	1.879	0.1789	3
LPI4	1.384	0.1318	6
LPI5	1.865	0.1776	4
LPI6	1.944	0.1851	1
Total	10,502	------	-----

Table 8. *Results from Alternative Methods of Calculating Objective Weighting Coefficients*

| LPI Criteria	ENTROPY		CRITIC		SD	
	Score	Rank	Score	Rank	Score	Rank
LPI1	0.223513	1	0.157853	3	0.196183	1
LPI2	0.210311	2	0.130547	4	0.189777	2
LPI3	0.131934	5	0.295611	1	0.149215	5
LPI4	0.177685	3	0.088489	6	0.173718	3
LPI5	0.083043	6	0.204207	2	0.120169	6
LPI6	0.173513	4	0.123294	5	0.170939	4
LPI Criteria	SVP		LOPCOW		MEREC	
	Score	Rank	Score	Rank	Score	Rank
LPI1	0.200922	2	0.15136	5	0.147113	5
LPI2	0.224147	1	0.146976	6	0.131193	6
LPI3	0.113687	5	0.187393	1	0.180158	3
LPI4	0.183917	4	0.162869	4	0.151631	4
LPI5	0.091382	6	0.172376	3	0.190409	2
LPI6	0.185945	3	0.179025	2	0.199497	1
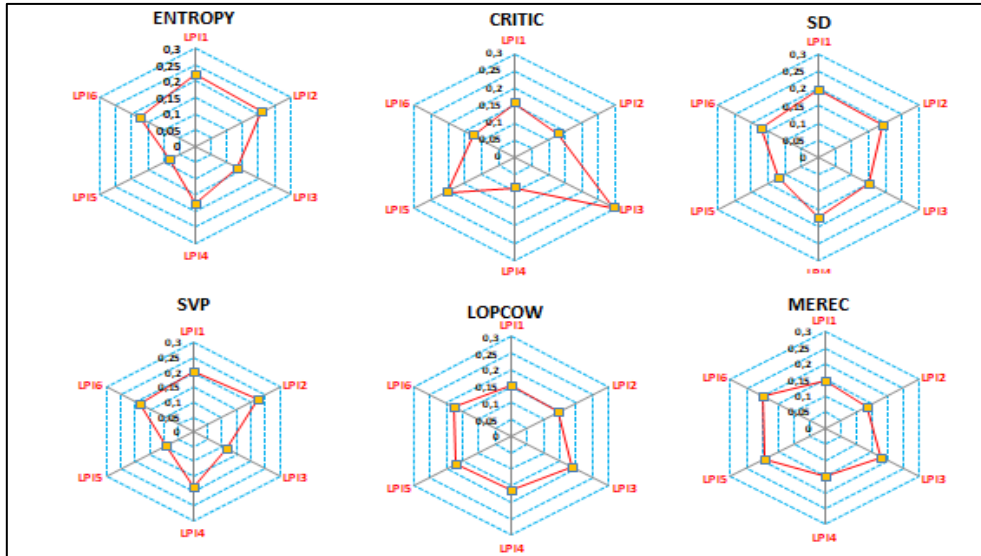
Figure 3. *Positions of the ENTROPY, CRITIC, SD, SVP, LOPCOW, and MEREC Methods (Note: The axises is graduated in increments of 0.30, 0.25, 0.20, 0.15, 0.10, 0.05, and 0)*
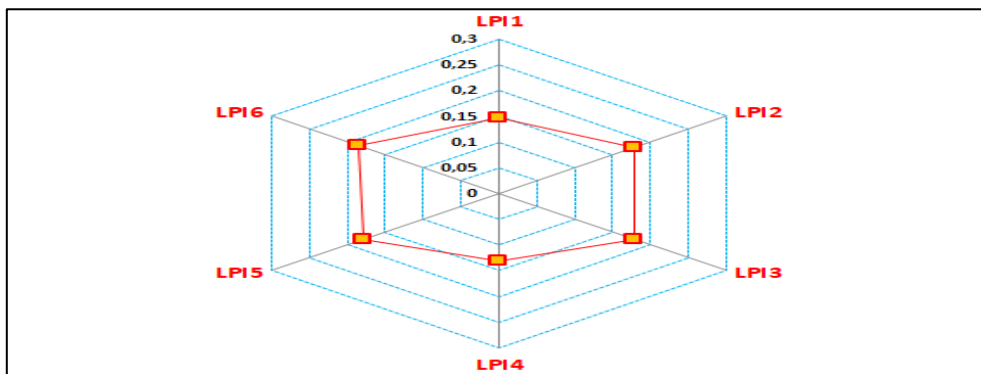
Figure 4. *Positions of the MIEXCF Methods (Note: The axis is graduated in increments of 0.30, 0.25, 0.20, 0.15, 0.10, 0.05, and 0)*
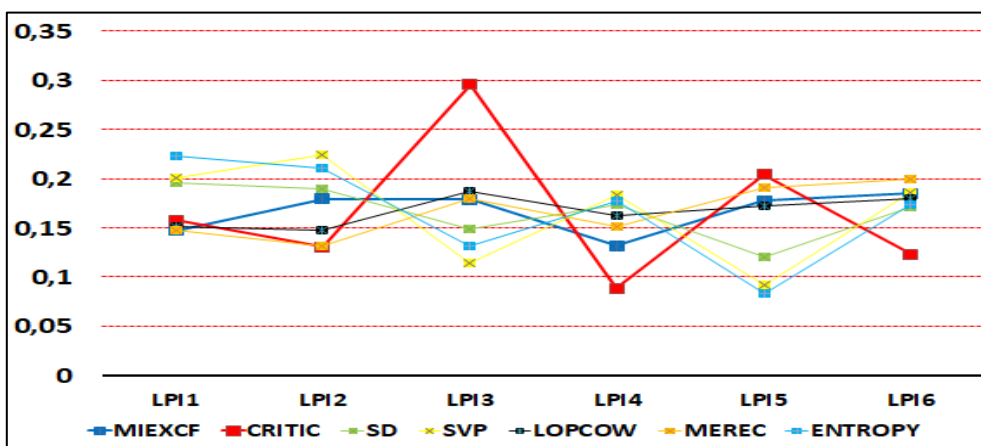
Figure 5. *Positions of the ENTROPY, CRITIC, SD, SVP, LOPCOW, MEREC, and MIEXCF Methods*

According to Figure 3, 4 and 5 the point locations of the MIEXCF method exhibit a higher degree of proportional similarity to the MEREC method compared to other methods. Moreover, in Figure 3, the differences between the MIEXCF method and the MEREC points are less pronounced than the differences between the MIEXCF method and the points associated with other methods. Based on this data, it can be

concluded that the relationship between the MIEXCF method and the MEREC method is positive, and significant, The correlation values of the MIEXCF method with other methods are presented in Table 8.

Table 8. *Pearson Correlation Values of the MIEXCF Method with Other Methods*

r	CRITIC	SD	SVP
MIEXCF	0.452*	-0.384	-0.293
r	**LOPCOW**	**MEREC**	**ENTROPY**
MIEXCF	0.422*	0.504*	-0.381
p*<.05			

Keshavarz-Ghorabaee et al. (2021), referring to Walters' (2009) study during the measurement of the Pearson correlation between the MEREC method and other methods (SD, ENTROPY, and CRITIC), stated that a positive significant relationship in the range of 0.400-0.600 indicates a moderate level of relationship between variables, and if it exceeds 0.600, the relationship is considered significant. In this context, according to Table 8, it is observed that the MIEXCF method has a significant, positive, and moderate-level relationship with the CRITIC, MEREC, and LOPCOW methods. Although the correlation values of the MIEXCF method with the CRITIC and LOPCOW methods are moderate, significant, and positive, these correlation values are not too far from the 0.600 correlation value. Therefore, based on these results, it can be inferred that the MIEXCF method is close to the credibility and reliability status.

3.4. Simulation Analysis

To conduct the simulation analysis, various scenarios are generated by assigning different values to decision matrices. To ensure the stability of results obtained using the proposed method, it is expected that the proposed method will exhibit differences from other methods as the number of scenarios increases. In the second step, the average of the variance values determined by the proposed method across the scenarios should be greater than one or more of the other objective weighting methods. This indicates that the proposed method is relatively effective in distinguishing the criteria weights. Lastly, the uniformity of variances in criterion weights across the methods within the scenarios must be established (Keshavarz-Ghorabaee et al., 2021). In the simulation analysis, the correlation values of the MIEXCF method with other methods were calculated based on the initial 10 scenarios and are presented in Table 9.

Table 9. *Pearson Correlation Values of the MIEXCF Method among Other Methods Within the Scope of Scenarios*

Group	Scenarios	ENTROPY	CRITIC	SD	SVP	LOPCOW	MEREC
First group	1. Scenario	-0.39	0.472*	-0.365	-0.305	0.445*	0.535*
	2. Scenario	-0.41	0.460*	-0.37	-0.315	0.436*	0.510*
	3. Scenario	-0.4	0.440*	-0.365	-0.285	0.438*	0.520*
Group	**Scenarios**	**ENTROPY**	**CRITIC**	**SD**	**SVP**	**LOPCOW**	**MEREC**
Second group	4. Scenario	-0.39	0.430*	-0.365	-0.315	0.448*	0,522*
	5. Scenario	-0.395	0.440*	-0.38	-0.335	0.420*	0,480*
	6. Scenario	-0.344	0.433*	-0.34	-0.285	0.435*	0,465*
	7. Scenario	-0.335	0.425*	-0.35	-0.29	0.405*	0,490*
	8. Scenario	-0.32	0.440*	-0.345	-0.27	0.410*	0,480*
	9. Scenario	-0.315	0.435*	-0.333	-0.225	0.390*	0.505*
	10. Scenario	-0.3	0.403*	-0.34	-0.24	0.382*	0.497*
Mean		-0,36	0.438	-0.355	-0.287	0.421	0.500
p*<.05							

As the number of scenarios increases, the criterion weights differ from each other based on the methods, as shown in Table 9. Notably, the MIEXCF method with CRITIC, LOPCOW and MEREC exhibit positive and significant relationships across all scenarios. This indicates a consistent pattern of correlation between the

MIEXCF and MEREC, CRITIC methods. The data presented in Table 9 were divided into two groups based on the values of the criterion weights. The correlation values between the two groups are shown in Figure 6.
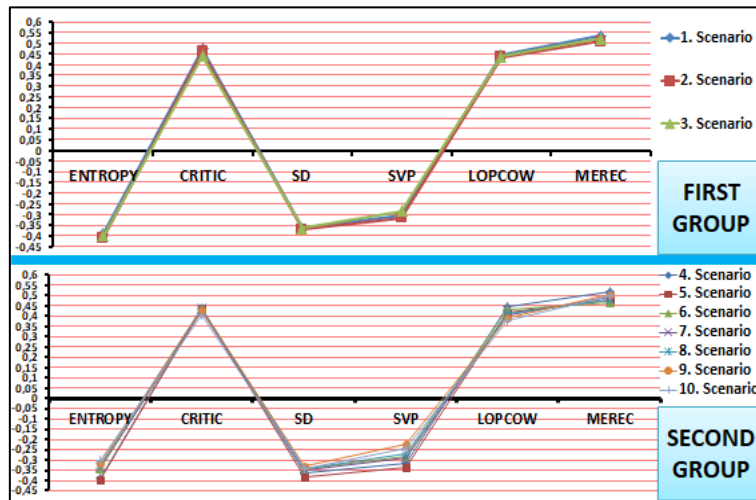

Figure 6. *The Correlation Status of MIEXCF Method with Other Approaches within Various Scenarios*
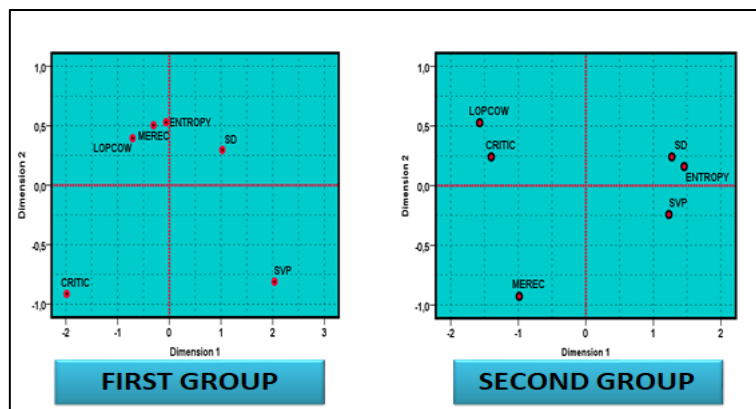

Figure 7. *The Discriminant Analysis of Correlation Status between MIEXCF Method and Other Methodologies across Different Scenarios*

Upon examination of Figure 7, it is observed that within the second group, the MIEXCF method exhibits variations in correlation values with other weight coefficient calculation methods compared to the first group, demonstrating a more pronounced dispersion in the space. Consequently, it has been observed that the distinctive features of the methods become increasingly prominent with the expansion of scenarios, resulting in a greater discernible differences between the methods. During the simulation analysis, the variance values of the methods were computed across different scenarios, and the resultant values are detailed in Table 10.

According to Table 10, it is observed that the average variance values of the MIEXCF method across scenarios are higher compared to the variance values of the ENTROPY, CRITIC, SD, and SVP methods. Conversely, these values are lower than those of the LOPCOW and MEREC methods. Hence, it can be assessed that the MIEXCF method exhibits a relatively enhanced capability in discerning criteria weights, as indicated by its higher average variance value compared to the ENTROPY, CRITIC, SD, and SVP methods. In the continuation of the simulation analysis, the homogeneity of variances in the criterion weights of the EXEBM method was examined through ADM (ANOM for variances with Levene) analysis across different scenarios. This analytical approach provides a graphical representation to assess the uniformity of variances. The graphical depiction comprises three variables: the general average ADM serves as the center line, along with the upper decision limits (UDL) and lower decision limits (LDL). If the standard deviation of a group (cluster) exceeds the decision limits, it indicates a significant difference from the general average ADM, signifying heterogeneity in variances. Conversely, if the standard deviations of all clusters fall within the LDL and UDL,

it confirms the homogeneity of variances (Keshavarz-Ghorabaee et al., 2021). The visual representation of the ADM analysis is presented in Figure 8.

Table 10. *Variability in Methodologies across Scenarios*

| Scenario	MIEXCF	ENTROPY	CRITIC	SD	SVP	LOPCOW	MEREC
1. Scenario	0.000279	0.000297	0.000280	0.000259	0.000252	0.000313	0.000328
2. Scenario	0.000297	0.000279	0.000291	0.000268	0.000259	0.000315	0.000290
3. Scenario	0.000302	0.000288	0.000282	0.000261	0.000254	0.000278	0.000327
4. Scenario	0.000285	0.000295	0.000288	0.000268	0.000256	0.000314	0.000304
5. Scenario	0.000290	0.000280	0.000297	0.000261	0.000257	0.000285	0.000326
6. Scenario	0.000287	0.000289	0.000283	0.000260	0.000258	0.000312	0.000315
7. Scenario	0.000301	0.000297	0.000286	0.000265	0.000255	0.000313	0.000285
8. Scenario	0.000295	0.000283	0.000294	0.000270	0.000260	0.000280	0.000310
9. Scenario	0.000289	0.000291	0.000290	0.000262	0.000257	0.000279	0.000321
10. Scenario	0.000297	0.000292	0.000289	0.000269	0.000259	0.000287	0.000297
Mean	0.000292	0.000282	0.000283	0.000264	0.000257	0.000315	0.000324
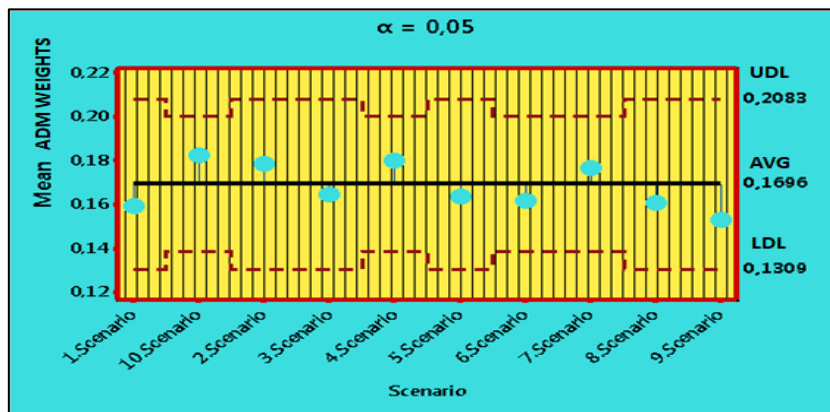
Figure 8. *ADM Visual*

As depicted in Figure 8, the ADM values calculated for each scenario are situated below the UDL values and above the LDL values. Consequently, the variances in the identified weights for each scenario exhibit homogeneity. This determination was further confirmed through the Levene Test. The fundamental statistics for the Levene Test are outlined in Table 11.

Table 11. *Levene Test*

Levene Statistic	df1	df2	Sig.
0.426	2	10	0.212
p**<.05			

Based on the findings from Table 11, the p-value (p=0.212) surpasses the significance threshold of 0.05, affirming the homogeneity of variances in criterion weights across scenarios. Overall, the outcomes of the simulation analysis suggest the robustness and stability of the MIEXCF method.

4. CONCLUSION

Multi-criteria decision-making is a widely used approach for complex problems, involving the consideration of various criteria. Assigning weights to these criteria is crucial as their importance may vary, ensuring an

unbiased decision-making process. Researchers have developed diverse methods for computing weight coefficients, contributing to the field of MCDM. In this study, we propose a Measurement Relying on the Impacts of an Exponential Curve Function (MIEXCF) as a novel approach for determining criterion weights.

The fundamental principle of the MIEXCF method lies in establishing exponential curve effects among criteria. Leveraging the benefits of exponential curve functions and the proposed method, effects among criteria can be computed. The criterion with the highest cumulative effect is then deemed the most significant. This criterion holds the potential to influence others, contributing to their development through associated activities or measures. Furthermore, a system can be devised to determine decision alternative strategies based on the most crucial criterion(s).

The study utilized 2023 Logistics Performance Index (LPI) data for 19 G20 countries. Initially, the MIEXCF method calculated weight coefficients for LPI components. A sensitivity analysis compared these with other methods (ENTROPY, CRITIC, SD, SVP, MEREC, and LOPCOW). Results revealed differing weight coefficient rankings for LPI criteria between the MIEXCF method and others. This underscores the proposed method's sensitivity.

The study's second approach involved a comparative analysis of the MIEXCF method, examining its similarity to other objective weight methods. Results showed a positive, significant, and moderate correlation with the MEREC method, and a positive, significant, and low correlation with the LOPCOW and CRITIC methods. Generally, the MIEXCF method was observed to have limited similarity with other criterion weighting methods. These findings led to the conclusion that the MIEXCF method is both credible and reliable.

In a simulation analysis, ten distinct Logistics Performance Index decision matrices were generated using the MIEXCF method and other weighting techniques. These matrices were divided into two groups: one with three scenarios and another with seven scenarios. Correlation values between the MIEXCF method and other weighting methods decreased as the number of scenarios increased, highlighting the unique features of the MIEXCF method. Variance analysis revealed that the MIEXCF method effectively distinguishes criteria weights, with higher average variance compared to alternative methods such as ENTROPY, CRITIC, SD and SVP. Homogeneity tests confirmed consistent variances within MIEXCF scenarios, indicating reliability. The Levene test showed no significant variance differences between the MIEXCF method and others.

According to the findings, it has been concluded that the MIEXCF method is a sensitive, stable and close to, credible, and reliable state. The study aims to demonstrate the feasibility of using the MIEXCF method to quantify criterion weights in MCDM literature, providing an objective tool for assessing decision option effectiveness. The outcomes have significant implications for scholars and decision-makers, anticipating increased attention to exponential curve functions in mathematical modeling. The MIEXCF method proves effective for decision-makers dealing with complex tasks, especially in performance evaluation. Simulation analysis data confirms the method's stability and robustness.

In future studies, the calculation of criterion weighting coefficients and the assessment of relationships among criteria can be expanded beyond exponential functions to include other functions like sigmoid, quadratic, cubic, linear, inverse, and so forth. Additionally, research endeavors can explore computing criterion weighting coefficients by considering not only the influence of criteria but also the values of criterion interdependence. The goal is to identify the criteria contributing to the intensity of relationships between two criteria.

CONFLICT OF INTEREST

The author declares no conflict of interest.

REFERENCES

Akın, N. G. (2017). İşletme bölümü öğrencilerinin meslek seçimini etkileyen faktörlerin bulanık dematel yöntemi ile değerlendirilmesi. *Uluslararası Yönetim İktisat ve İşletme Dergisi*, 13(4), 873-890. http://www.doi.org/10.17130/ijmeb.2017433413.

Alfaro, L., Chari, A., Greenland, A. N., & Schott, P. K. (2020). Aggregate and firm-level stock returns during pandemics, in real time. *NBER Working Paper* (26950), 1-31.

Ali, T., Aghaloo, K., Chiu, Y.-R., & Ahmad, M. (2022). Lessons learned from the COVID-19 pandemic in planning the future energy systems of developing countries using an integrated MCDM approach in the off-grid areas of Bangladesh. *Renewable Energy*, 189, 26-38. https://www.doi.org/10.1016/j.renene.2022.02.099.

Alrababah, S., & Gan, K. H. (2023). Effects of the hybrid CRITIC–VIKOR method on product aspect ranking in customer reviews. *Appl. Sci.*, 13, 1-14. https://www.doi.org/10.3390/app13169176.

Altıntaş, F. F. (2021). Sağlık güvenliği bileşenleri bileşenleri arasındaki ilişkilerin analizi: Somer's d temelli DEMATEL yöntemi ile bir uygulama. *Eurasian Academy of Sciences Social Sciences Journal*, 36, 48-63. https://www.doi.org/10.17740/eas.soc.2021.V36-04.

Altıntaş, F. F. (2023). A novel approach to measuring criterion weights in multiple criteria decision making: cubic effect-based measurement (CEBM). *Nicel Bilimler Dergisi*, 5(2), 151-195. https://www.doi.org/10.51541/nicel.1349382.

Arslan, R. (2020). Critic yöntemi. In: H. Bircan (Eds.), *Çok Kriterli Karar Verme Problemlerinde Kriter Ağırlıklandırma Yöntemleri* (pp. 120-122). Nobel Yayıncılık.

Arvis, J.-F., Ojala, L., Shepherd, B., Ulybina, D., & Wiederer, C. (2023). *Connecting to compete trade logistics in the global economy*. International Bank for Reconstruction and Development/The World Bank.

Ayan, B., Abacıoğlu, S., & Basilio, M. P. (2023). A comprehensive review of the novel weighting methods for multi-criteria decision-making. *Information*, 14(5), 1-28. https://www.doi.org/10.3390/info14050285.

Ayçin, E. (2019). *Çok Kriterli Karar Verme*. Ankara: Nobel Yayın.

Balaban, E. (2015). *Temel Matematik ve İşletme Uygulamaları*. İstanbul: Türkmen Kitapevi.

Baş, F. (2021). *Çok Kriterli Karar Verme Yöntemlerinde Kriter Ağırlıklarının Belirlenmesi*. Ankara: Nobel Bilimsel.

Bayram, N. (2010). *Yapısal Eşitlik Modellemesine Giriş: Amos Uygulamaları*. Bursa: Ezgi Kitapevi.

Bernett, M. A., Ziegler, M., & Byleen, K. E. (2015). *Calculus for business, economics, life sciences and social sciences*. Pearson.

Bircan, H. (2020). *Çok Kriterli Karar Verme Problemlerinde Kriter Ağırlıklandırma Yöntemleri*. Ankara: Nobel Yayıncılık.

Çelik, E. H., & Yılmaz, V. (2013). *Lisrel 9.1 ile Yapısal Eşitlik Modellemesi*. Ankara: Anı Yayıncılık.

Chakrabarty, D., & Rahman, A. (2007). Exponential curve: Estimation-using the just preceding observation in fitted curve. *Int.J.Agricult.Stat.Sci*, 3(2), 381-186.

Civelek, M. E. (2018). *Yapısal Eşitlik Modellemesi Metodolojisi*. İstanbul: Beta Yayımları.

Demir, G., Özyalçın, T., & Bircan, H. (2021). *Çok Kriterli Karar Verme Yöntemleri ve ÇKKV Yazılımı ile Problem Çözümü*. Ankara: Nobel.

Diakoulaki, D., Mavrotas, G., & Papayannakis , L. (1995). Determining objective weights in multiple criteria problems: The Critic method. *Computers & Operations Research*, 22(7), 763-770.

Ecer, F. (2020). *Çok Kriterli Karar Verme*. Ankara: Seçkin Yayıncılık.

Ecer, F., & Pamucar, D. (2022). A novel LOPCOW-DOBI multi-criteria sustainability performance assessment methodology: An application in developing country banking sector. *Omega*, 1-35. https://www.www.doi.org/10.1016/j.omega.2022.102690.

Eroğlu, E. (2017). *İşletme, İktisat Ve Sosyal Bilimler İçin Matematik*. Bursa: Dora Yayın.

Ersoy, N. (2023). BIST perakende ticaret sektöründe LOPCOW-RSMVC modeli ile performans ölçümü. *Sosyoekonomi*, 31(57), 419-436.

Ertik, H., Şendur, A., & Tulga, İ. (2015). *Matematik İşletme İktisat ve Ekonomi Uygulamaları*. Çanakkale: Paradigma Akademi Yayınları.

Fontela, E., & Gobus, A. (1976). *The DEMATEL observer*. Battelle Geneva Research Center.

Fosu, G. O., & Edunyah, G. (2020). Flattening the exponential growth curve of covid-19 in Ghana and other developing countries; Divine ıntervention is a necessity. *SSRN*, 1-13. http://www.www.doi.org/10.2139/ssrn.3565147.

Gigovic, L., Pamucar, D., Bajic, Z., & Milicevic, M. (2016). The combination of expert judgment and GIS-MAIRCA analysis for the selection of sites for ammunition depots. *Sustainability*, 8, 1-30. https://www.doi.org/10.3390/su8040372.

Göncü, K. K., & Çetin, O. (2022). A Decision model for supplier selection criteria in healthcare enterprises with dematel ANP method. *Sustainability*, 14, 1-16. https://www.doi.org/10.3390/su142113912.

Gülençer, İ., & Türkoğlu, S. P. (2020). Gelişmekte olan Asya ve Avrupa ülkelerinin finansal gelişmişlik performansının İstatistiksel Varyans Prosedürü temelli OCRA yöntemiyle analizi. *Üçüncü Sektör Sosyal Ekonomi Dergisi*, 55(2), 1330-1344. https://www.doi.org/10.15659/3.sektor-sosyal-ekonomi.

Gürbüz, S. (2019). *AMOS ile Yapısal Eşitlik Modellemesi*. Ankara: Seçkin Yayınevi.

Hamill, J. T., Deckro, R. F., & Kloeber, J. M. (2005). Evaluating Information Assurance Strategies. *Decision Support Systems*, 39(3), 463-484.

IBM. (2013). *SPSS tutorial*. IBM.

Jones, C. I. (2023). Recipes and Economic Growth: A combinatorial march down an exponential tail. *Journal of Applied Econometrics*, 38(55), 767–785. https://www.doi.org/10.1086/723631.

Joujan, A. (2018). *Summit Math Series: Algebra 2: Book 7: Exponential functions*. XanEdu Publishing Inc.

Kahn, D. S. (2015). *Attacking problems in logarithms and exponential functions*. Dover Publications.

Karagöz, Y. (2017). *SPSS ve AMOS 23 Uygulamalı İstatistiksel Analizler*. Ankara: Nobel Akademik Yayıncılık.

Kartal, M., Karagöz, Y., & Kartal, Z. (2014). *Temel Matematik*. Ankara: Nobel Yayın.

Keleş, N. (2023). *Uygulamalarla Klasik ve Güncel Karar Verme Yöntemleri*. Ankara: Nobel.

Keshavarz-Ghorabaee, M., Amiri, M., Zavadskas, E. K., Turskis, Z., & Antucheviciene, J. (2021). Determination of objectiveweights using a new method based on the removal effects of criteria (MEREC). *Symmetry*, 13, 1-20. https://www.doi.org/10.3390/sym13040525.

Keshavarz-Ghorabaee, M., Amiri, M., Zavadskas, E. K., Turskis, Z., & Antucheviciene, J. (2018). Simultaneous evaluation of criteria and alternatives (SECA) for multi-criteria decision-making. *Informatica*, 29(2), 265–280. https://www.doi.org/10.15388/Informatica.2018.167.

Kline, R. B. (2019). *Yapısal Eşitlik Modellemesinin İlkeleri ve Uygulaması*, Translate: Şen, S. İstanbul: Nobel Yayınları.

Kuruüzüm, A., & İpekçi Çetin, E. (2015). *İşletme ve Ekonomi Öğrencileri Için Uygulamalı Matematik*. Ankara: Gazi Kitapevi.

Landsberg, J. J. (1977). Some useful equations for biological studies. *Expl Agric.*, 13, 273-286.

Lin, C.-Y. (2014). *An Exponential function approach to parabolic equations*. World Scientific Publishing Company.

Meydan, C. H., & Şeşen, H. (2015). *Yapısal Eşitlik Modellemesi AMOS Uygulamaları*. Ankara: Detay Yayıncılık.

Mukhametzyanov, I. Z. (2021). Specific character of objective methods for determining weights of criteria in MCDM problems: Entropy, CRITIC, SD. *Decision Making: Applications in Management and Engineering* 4(2), 76-105. https://www.doi.org/10.31181/dmame210402076i.

Murillo-Escobar, M. A., Quintana-Ibarra, J. A., & Cruz-Hernández, C. (2023). Biosignal encryption algorithm based on Ushio chaotic map for e-health. *Multimed Tools Appl*(82), 23373–23399. https://www.doi.org/10.1007/s11042-022-14092-4.

Nasser, A. A., Alkhulaidi, A. A., Ali, M. N., Hankal, M., & Al-olofe, M. (2019). A weighted euclidean distance - statistical variance procedure based approach for ımproving the healthcare decision making system in Yemen. *Indian Journal of Science and Technology*, 12(3), https://www.doi.org/1-15. 10.17485/ijst/2019/v12i3/140661.

Natalija, B. (2021). Exponential functions through a real-world context. *Open Schools Journal for Open Science*, 3, 1-10. https://www.doi.org/10.12681/osj.24891.

Odu, G. 0. (2019). Weighting methods for multi-criteria decision making technique. *J. Appl. Sci. Environ. Manage*, 23(8), 1449-1457. https://dx.www.doi.org/10.4314/jasem.v23i8.7.

Önalan, Ö. (2010). *İşletme Matematiği*. İstanbul: Avcıol Basım Yayım.

Özdamar, K. (2016). *Eğitim, Sağlık ve Davranış Bilimlerinde Ölçek Geliştirme ve Yapısal Eşitlik Modellemesi*. Eskişehir: Nisan Kitapevi.

Paksoy, S. (2017). *Çok Kriterli Karar Vermede Güncel Yaklaşımlar*. Adana: Karahan Kitapevi.

Pekkaya, M. (2016). *İşletme ve Iktisat Için Genel Matematik ve Matematiksel Yöntemler*. Bursa: Ekin Yayınevi.

Rasmussen, A., Sabic, H., Saha, S., & Nielsen, I. E. (2023). Supplier selection for aerospace & defense industry through MCDM methods. *Cleaner Engineering and Technology*, 12, 1-12. https://www.doi.org/10.1016/j.clet.2022.100590.Saaty, T. L. (2008). Decision making with the analytic hierarchy process. *International Journal of Services Sciences*, 1(1), 83-98.

Sel, A. (2020). IDOCRIW Yöntemi, In: H. Bircan (Eds.), *Çok Kriterli Karar Verme Problemlerinde Kriter Ağirliklandirma Yöntemleri* (pp. 37-50). Nobel Akdemik Yayıncılık.

Shparlinski, I., & Konyagin, S. (1999). *Character sums with exponential functions and their applications*. Cambridge University Press.

Sümerli Sarigül, S., Ünlü, M., & Yaşar, E. (2023). A new MCDM approach in evaluating airport service quality: MEREC-Based MARCOS and CoCoSo Methods. *Uluslararası Yönetim Akademisi Dergisi*, 6(1), 90-108. https://www.doi.org/10.33712/mana.1250335.

Thomas, C. (1991). *Introduction to exponents and logarithms*. University of Sydney.

Uludağ, A. S., & Doğan, H. (2021). *Üretim Yönetiminde Çok Kriterli Karar Verme*. Ankara: Nobel.

Vavrek, R. (2019). Evaluation of the ımpact of selected weighting methods on the results of the TOPSIS technique. *International Journal of Information Technology & Decision Making*, 18(6), 1821–1843. https://www.doi.org/10.1142/S021962201950041X.

Walters, S. J. (2009). *Quality of life outcomes in clinical trials and health-care evaluation: A practical guide to analysis and interpretation*. Wiley.

Wang, C.-N., Nguyen, N.-A.-T., & Dang, T.-T. (2023). Sustainable evaluation of major third-party logistics providers: A framework of an MCDM-Based Entropy objective weighting method. *Mathematics*, 11, 1-27. https://www.doi.org/10.1142/S021962201950041X.

Weon, B. M., & Je, J. H. (2014). Plasticity and rectangularity in survival curves. *Scientific Reports*, 1(104), 1-5.

Wood, P. K. (2023). Combined logistic and confined exponential growth models. *A Multidisciplinary Journal*, 1-10. http://www.www.doi.org/10.1080/10705511.2023.2220918.

Zavadskas, E. K., & Podvezko, V. (2016). Integrated determination of objective criteria wights in MCMD. *International Journal of Information Technology & Decision Making*, 15(2), 267-283. https://www.doi.org/10.1142/S0219622016500036.

Strontium Accumulations by *Teucrium polium* which Grows Naturally in Serpentine Soils

Nevin KONAKCI[1*] iD

[1] *Firat University, Department of Geology Enginnering, Elazığ, Türkiye*

Keywords	Abstract
Strontium Teucrium Polium Guleman Serpentine Soils Accumulation	The study area is located in the Guleman region which hosts Turkey's most important chromite deposits and extensive serpentine soils. In this study, strontium uptake accumulations in the shoots and roots of the *Teucrium polium* plant growing on serpentine soils in the Guleman region were examined. In this context, 17 *Teucrium polium* plants growing in different locations of serpentine soils were collected together with their shoots, roots and soil, and then chemically analyzed for strontium. Chemical analyses were carried out in ICP-MS. On average, strontium values of 15.2 ppm in the soil, 26.4 in the root and 76.3 ppm in the shoots were detected. Strontium enrichment values in the soil, roots and shoots of this plant were determined as 1.8 for ECR (The enrichment coefficient for root), 5.3 for ECS (The enrichment coefficient for shoot) and 2.9 for TLF (Translocation factor). Results of this study show that the *Teucrium polium* plant accumulates significant amounts of strontium from the soil, both in the root and in the shoots. As a result, this plant can be used as a bioaccumulator plant, especially in the reclamation of strontium-polluted soils and the improvement of such areas.

1. INTRODUCTION

Weathering of ultramafic rocks results in formation of serpentine soils, which have low amounts of plant nutrients like P, K, and Ca but high quantities of metals such as Ni, Cr, and Co. Less than 45% of the silica in these rocks is composed of ferromagnesian silicate minerals (Nascimento et al., 2022). The serpentinite, dunite, and peridotite are the most common ultramafic rocks. Heavy metal levels in serpentine soils are high, including Mn, Ni, Co, Cr, and Zn. Although certain metal concentrations are necessary for plant growth at trace levels, excessive concentrations might be harmful since they can disrupt cellular processes (Konakci et al., 2023).

Strontium is one of the prevalent trace elements found in the lithosphere at amounts between 260 and 370 ppm. It is commonly contained in felsic magmatic and carbonate rocks. In carbonate rocks, sulfur is mobilized as readily soluble strontianite ($SrCO_3$), which subsequently precipitates as celestite ($SrSO_4$). These minerals breakdown and cause environmental issues for people, animals and plants, particularly in terrestrial settings (Kabata-Pendias, 2011; Sasmaz et al., 2021). The main factors controlling the Sr content in superficial soils are the type of host rocks and weathering. Strontium in mining soils and igneous rocks can be hazardous to the environment. Strontium is found in veins connected to gypsum and halite lenses or layers, within the sedimentary rocks, and is also observed as an accessory element in other minerals (Burger & Lichtscheidl, 2019; Kilic &Ates, 2015; Kilic & Inceoz, 2015). Sr levels vary 300 to 450 ppm in clay soils, 140 to 20 ppm in sandstones, 3100 to 20 ppm in cambisol soil, 500 to 70 ppm in histosols, and 1000 to 20 ppm in podzols, with the highest amounts seen in heavy loamy soils (Kabata-Pendias, 2011). Because of its non-biodegradability,

endurance in nature, and accumulation in living animals and plants, the toxicity of heavy metals is a large issue for the natural environments (Sasmaz & Sasmaz, 2017). In urban and mining areas, heavy metals of Sr, Th, U, Zn, Pb, Ni, Cr, Co, Hg, Tl, Sb, As and Se contaminate surface soils and streams/rivers (Rađenović et al., 2016). Element accumulation is possible for the plants through their stems, leaves, and roots. Different species have varying capacity for absorbing metals, and using these species for bioremediation offers a number of advantages for the environment and economy, including cheap cost, high efficiency, energy savings, and the avoidance of secondary pollution. Aquatic plants can uptake large amounts of metals from water and sediment through active and passive absorption. Sr is taken by plants for their metabolic needs and employed in exchange diffusion and mass transport mechanisms since it is not a micronutrient for plants like Ca. Few research have been conducted on the accumulation and toxicity of Sr in plants; Shacklette et al. (1978) determined the hazardous value of Sr in plants to be 30 ppm. Inhaled as dust or mist, strontium sticks to the lung surface, dissolves there, and mixes with blood rapidly. Sr may be hold in the lungs for an extended period of time if it does not sufficiently mix with the blood (ATSDR, 2004). As a result, it can affect the lungs in many ways resulting in undesired physiological and biochemical issues in both people and animals.

Heavy metals are extracted from soil using a variety of methods (Yalcin et al., 2008; Qi & Zhao, 2020; Pehoiu et al., 2020; Sharma, 2020; Yalcin et al., 2020; Mikavica et al., 2023; Uras & Yalcin, 2022; Mileti´c et al., 2024; Timofeeva et al., 2024). Phytoremediation illustrates each plant's capacity to remove metals based on its physiological, genetic, anatomical and morphological characteristics. Few researches have been done on stable Sr accumulation in terrestrial and aquatic plants, despite the fact that several have been carried out on radioactive Sr removing in terrestrial plants. Thus, the primary goals of this research are to examine the Sr accumulation in the root and shoots of 17 terrestrial *Teucrium polium* plants naturally growing in serpentine soils that are contaminated by strontium. The movement and absorption of Sr from the soil into plants and the usability of plants in studies pertaining to the restoration and rehabilitation of Sr-polluted soils are the other aspects of study.

2. MATERIAL AND METHOD

2.1. The Study Area

The serpentine soils in the Guleman chromite deposits are the material of this study (Figure 1). The Guleman region, one of the most significant areas for the chromite ore production in Turkey, is divided into several mining sectors based on the lithological features, type of deposits, structural and geographic locations. The dunite, peridotite and pyroxenites exposing near the Guleman district are rich in Cr, Ni and Co and linked to the chromium deposits (Engin et al., 1983). Open pits or galleries in the study area are used to recover the chromite ore. Following the application of open pit method, underground mining was introduced in the region in 1950 due to the diminishing number of ore. Today both open pit and underground mining techniques are in use (Engin et al., 1983).

2.2. Soil and Plant Samples

Seventeen plant samples grown in different areas on the serpentine soils of the Bahro and Dereboyu mining areas were collected together with their soil (Figure 1). *Teucrium polium* plant, locally called peryavşan was described by Semsettin Civelek (Firat University, Biology Department) and is one of the 300 species of the *Lamiaceace* family (Kırkık et al., 2020). *Teucrium polium* is a shrub that grows 20–50 cm high and has stemless, oblong or linear leaves. It is usually found in Iran and in rocky areas of practically in all the Mediterranean countries, Southwest Asia, Europe and the northern hills and deserts (Tapeh et al., 2018; Kırkık et al., 2020). *Teucrium polium* is a perennial herbaceous plant that resembles a semi-shrub and can grow up to 40 cm tall with pale blooms. This plant was sampled separately from the roots, shoots and soil on which it grows in ore/non-ore locations. It is a prominent species in the soils of the research area and grows widely throughout the region. At depths of 0.10 to 0.40 meters, soil samples were extracted from *Teucrium polium* root feeding zones. After being removed from the serpentine soil, the *Teucrium polium* plant was cleaned with pure water and then tap water. The root and shoot samples were burned for 24 hours at 300 °C in a flameless oven after dried for 24 hours at 60 °C. The result was ash.

In the laboratory, 0.10 g of ash and soil samples were mixed separately with 2 ml of pure HNO_3 (Merck, Darmstadt, Germany), then the mixture was heated at 95 °C for one hour to dry. The dried materials were mixed with 2 ml of HNO_3 and HCl-HNO_3-H_2O (6 ml of each mixture made by taking 1:1:1 from acid and 0.10 g of ash and soil sample) (Sasmaz & Sasmaz, 2017). Sr element analyses were performed with ICP-MS instrument once all soil samples were dissolved in the mixture. ICP-MS was used to assess Sr in plant ash samples in a manner similar to those of soils. Analysis was carried out at the ACME laboratory (Canada).

The calculation of the enrichment coefficients (ECR) for roots involved dividing the soil concentration of the plant roots for every individual plant. Dividing the soil metal contents of each plant by shoot values, the enrichment coefficients (ECS) for shoot were determined. The metal ratio that was transferred from the plant roots to the shoot was known as the translocation factor (TLF). TLF is greater than 1 in hyperaccumulator plants. Thisfactor shows the ability of the plant to move metal from its roots to its shoots (Sasmaz et al., 2021).
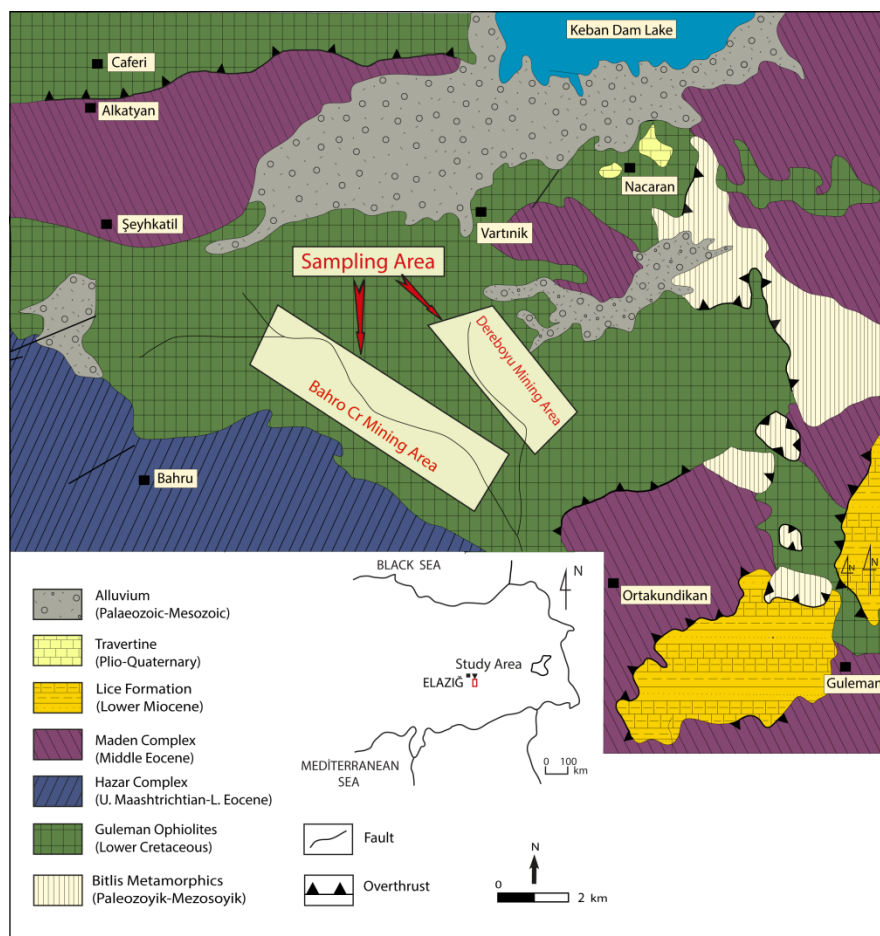

Figure 1. Geological map of the study area (Özkan, 1983)

3. RESULTS AND DISCUSSION

3.1. Strontium in Soil

Loamy and peaty clay with a pH of 7.6-7.8, an organic matter level of 8–12% and an average composition of 35% sand, 27% clay, and 23% silt make up the serpentine soils. Typically, their colour ranges from dark brown to light grey. It has been shown that the amount of organic matter is lower in serpentine soils than in other mineral soils. The studied soils had an average strontium content of 15.2 ppm, a maximum of 24.2 ppm and a minimum of 10.2 ppm (Figure 2). The low strontium content in Guleman serpentine soils is attributed to the chemistry of rocks. The Keban (Elazığ) Pb-Zn ore field had Sr values between 112 and 717 ppm (Sasmaz & Sasmaz, 2009), whereas the Gumuşkoy (Kütahya) mine field had Sr concentrations in the range of 22.6 to
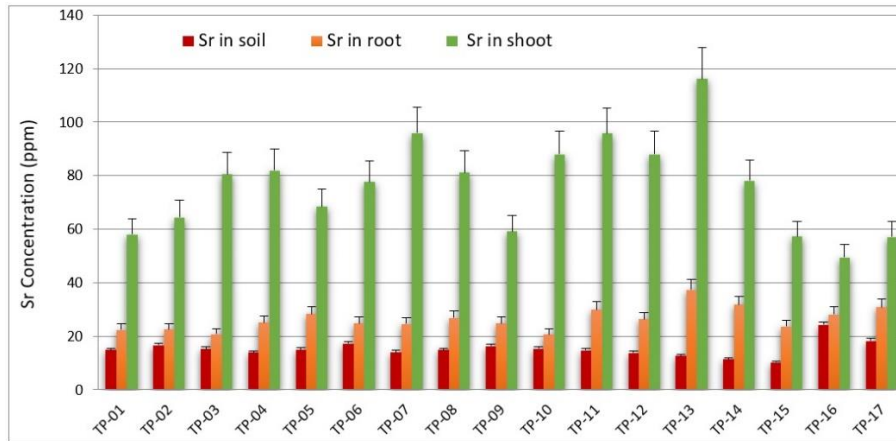
Figure 2. *Strontium accumulations in the soil, roots and shoots of the Teucrium polium plant grown in serpentine soils*

691.8 ppm (Sasmaz & Sasmaz, 2017). High amounts of Sr, ranging from 320 to 1300 ppm, have been recognized in the mineral soils of pyroxenite and carbonatitic rocks in the alkaline magmatic rocks in Norway (Myrvang et al., 2016). According to Kabata-Pendias (2011), the host rock composition is the primary indication of Sr abundance in soils and Sr concentration rises linearly from basic rocks to syenitic rocks (diorite), 13–39 ppm in Venezuela, 210 ppm in Canada, 715–1000 ppm Russia, 26–150 ppm China, 261 ppm in Great Britain, 32–130 ppm in Japan, 112–258 ppm in Sweden, and 305 ppm in USA are only a few of the nations with significantly varying Sr concentrations in their soils.

3.2. Strontium in *Teucrium polium*

In the region's serpentine soils, *Teucrium polium* plants were gathered from 17 distinct sites and chemical analyses were performed to check for strontium content in the roots and shoots. Strontium concentrations on the root fall in the range of 20.6 to 37.4 ppm. It was found that the root's average strontium content was 26.4 ppm (Figure 2). *Teucrium polium* branches have average Sr levels of 76.3 ppm with the maximum value of 116.1 ppm and the lowest value of 49.5 ppm (Figure 2). The following were calculated: ECS to show the relationship between the branch and soil; TLF values to show the strontium build up from root to shoot; and ECR, which is found by dividing the Sr levels in the root by the Sr levels in the soil of *T. polium.* The results of these computations showed that *Teucrium polium*'s average ECR values for Sr were 1.80, ECS was 5.27, and TLF was 2.93 (Figure 3). These findings display that the investigated plant's roots and shoots have a high capacity to absorb Sr from the soil. Regarding the Sr accumulation rates of the plant organs, the shoot exhibits significantly more accumulation ability than the root. This is clearly supported by the TLF results of this study (Figure 3).
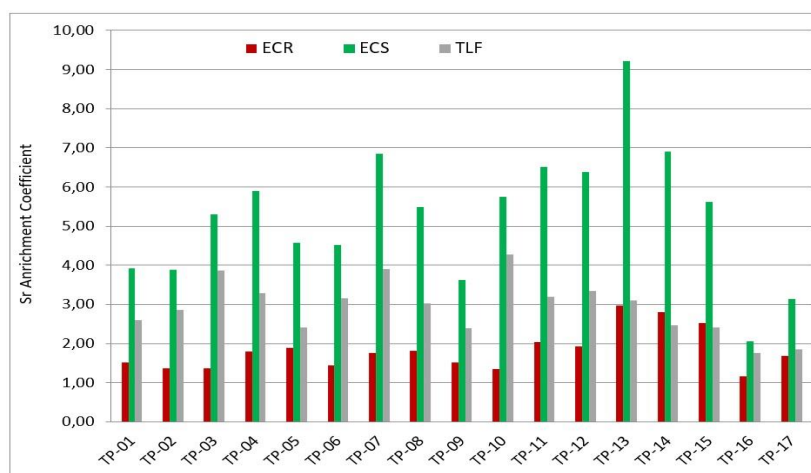

Figure 3. *ECR, ECS and TLF values for strontium in the Teucrium polium plant grown in serpentine soils*

The distribution and accumulation of Sr in barley, wheat, naked oats and groats were investigated by Qi, L., & Zhao (2020), in relation to their capacity for phytoremediation. They stated that there were high Sr concentrations on average in the shoots of the barley, oat kinds and naked oat. Grain samples had the lowest Sr concentrations whereas leaf samples had the highest values. The range of average ECS values observed was 0.52 to 1.34. It was discovered in the days that followed that the rate of Sr build up from soil to shoots was more than 1.4% for a maximum of 120 days. These findings demonstrated the efficacy of using these plants to restore Sr content in soils. Shahraki et al. (2008) had contaminated the Sr concentrations in terrestrial plants that are cultivated in the soils of Sarcheshmeh copper mines. They discovered that the Sr values in shoot and root samples for *Phragmites australis* and *Tamarix ramossima* were 47.4 and 132 ppm and 98.8 and 188 ppm, respectively. Sasmaz & Sasmaz (2017) investigated the Sr accumulation and translocation in 11 native plants grown in the soils of the Gümüşköy mine. Based on ECR and ECS, plants are categorized as candidate, good, and best plants. *Verbascum thapsus, Cynoglossum officinale*, and *Glaucium flavum*. considered to be effective plants for accumulating Sr from soil contaminated by Sr include *Isatis* and *Phlomis sp*. The greatest Sr values in conifers were discovered by Petrescu & Bilal (2006) in *Picea excelsa* and *Abies alba* plants that were grown in mining sites. It has been noted that the aboveground sections of *Picea excelsa* and *Abies alba* plants acquire more Sr than the root sections. According to Zu et al. (2005), a hyperaccumulator plant is one that absorbs metal several times more than uncontaminated soil. These plants also include *Euphorbia macroclada*.

Keban mine soils showed Sr accumulation several times greater than the soil samples (Sasmaz & Sasmaz, 2009). Region to both aquatic and terrestrial plants were studied by Sasmaz et al. (2021). On a dry weight basis, it was discovered that the average Sr concentrations in shoots, roots and soils of terrestrial and aquatic plants were 48.2, 80.5 and 101 ppm, respectively. The studied plants were classified as candidate, bioaccumulator, and hyperaccumulator plants based on the enrichment coefficients and translocation factors of their roots (ECR) and shoots (ECS), respectively. *Xanthium* and *Pragmites sp.* bioaccumulator plants, *Typha latifolia, Lythnium salicaria* and *Bolboscholnus ascbersus* were assessed as hyperaccumulator plants for Sr. *Salix sp*. and *Tamarix tetrandra* were chosen as candidate plants. The ability of both bioaccumulative and hyperaccumulator plant groups to accumulate from their soil to plant parts is demonstrated by these data. As a result, it has been proposed that these plants could be helpful for research on the rehabilitation of different mine soils and municipal wastewater that have been contaminated by Sr.

4. CONCLUSION

In this study, we examine the accumulations of strontium absorption in the roots and shoots of *Teucrium polium* plants that grow on serpentine soils in the Guleman region. The average soil concentration of boron was found to be low at 7.94 ppm while *Teucrium polium* strontium readings were 15.2 ppm in the soil, 26.4 ppm in the root and 76.3 ppm in the branch. The plant's soil, roots, and shoots had strontium enrichment levels of 1.8 for ECR, 5.3 for ECS, and 2.9 for TLF. These results show that the *Teucrium polium* plant accumulates significant amounts of strontium from the soil to both roots and shoots. Therefore, the *Teucrium polium* plant can be used as a bioaccumulator plant, especially in the reclamation of strontium-polluted soils and in the remediation of such areas.

ACKNOWLEDGEMENT

CONFLICT OF INTEREST

The author declares no conflict of interest.

REFERENCES

ATSDR, (2004). Agency for Toxic Substances and Disease Registry: Toxicological profile for Sr.

Burger, A., & Lichtscheidl, I. (2019). Strontium in the environment: Review about reactions of plants towards stable and radioactive strontium isotopes. *Sci. Total Environ., 653,* 1458-1512. https://doi.org/10.1016/j.scitotenv.2018.10.312.

Engin, T., Balcı M., Simer Y., & Ozkan, Y. Z. (1983). General geological setting and the structural features of the Guleman peridotite unit and the chromite deposits. *Bull. Min. Res. Exp. Ins. Turkey, 95,* 34-56.

Kabata-Pendias, A. (2011). Trace elements in soils and plants. CRC Press*, Boca Raton.* https://doi.org/10.1201/9781420039900.

Kilic, A. D., Ates, C. (2015). Geochronology of the Late Cretaceous magmatism and metamorphism, Puturge massif, Turkey, *Acta Petrol. Sin. 31*, (5), 1485-1493.

Kilic, A. D., İnceöz, M. (2015). Mineralogical, Geochemical and Isotopic Effect of Silica in ultramaphic systems. Eastern Anatolian Turkey. *Geochem. Int., 53*, (4), 369-382. https://doi.org/10.1134/S0016702915040035.

Kırkık, D., Sancak, N. P., Alragabi, J. M. (2020). Türkiye'de yetişen *Teucrium polium L.* bitkisinin HepG2 hücre hattı üzerindeki etkisi. *J. Med Palliat Care, 1*(3), 49-52. https://doi.org/10.47582/jompac.737218.

Konakci, N., Sasmaz Kislioglu, M., Sasmaz, A. (2023). Ni, Cr and Co Phytoremediations by *Alyssum murale* Grown in the Serpentine Soils Around Guleman Cr Deposits, Elazig Turkey. *Bull. Environ. Cont. Tox, 110,* 97. https://doi.org/10.1007/s00128-023-03736-2.

Mikavica, I., Ranđelovi´c, D., Djordjevi´c, V., Raki´c, T., Gaji´c, G., & Muti´c, J., (2023). Concentration and mobility of trace elements (Li, Ba, Sr, Ag, Hg, B) and macronutrients (Ca, Mg, K) in soil-orchid system on different bedrock types. *Environ. Sci. Pollut. Res. 30,* 979–995. https://doi.org/10.1016/j.ecoenv.2023.115875.

Mileti´c, Z., Markovi´c, M., Jari´c, S., Radulovi´c, N., Sekuli´c, D., Mitrovi´c, M., & Pavlovi´c, P. (2024). Lithium and strontium accumulation in native and invasive plants of the Sava River: Implications for bioindication and phytoremediation. *Ecotoxicology and Environmental Safety, 270,* 1-12. https://doi.org/10.1016/j.ecoenv.2023.115875.

Myrvang, M., Hillersøy, M., Heim, M., Bleken, M., & Gjengedal, E. (2016). Uptake of macro nutrients, barium, and strontium by vegetation from mineral soils on carbonatite and pyroxenite bedrock at the Lillebukt Alkaline Complex on Stjernøy, Northern Norway. *J. Plant Nutr. Soil Sci., 179,* 705–716. https://doi.org/10.1002/jpln.201600328.

Nascimento, C. W. A., Lima, L. H. V., Silva, J. A. B., Biondi, C. M. (2022). Ultramafic soils and nickel phytomining opportunities: a review. *Revista Brasileira de Ciência do Solo, 46,* 1–17. https://doi.org/10.36783/18069657rbcs20210099.

Özkan, Y. Z. (1983). Guleman (Elazığ) ofiolitinin yapısal incelenmesi. *MTA Dergisi, 37,*78-85.

Qi, L., & Zhao, W. (2020). Strontium uptake and antioxidant capacity comparisons of low accumulator and high accumulator oat (*Avena sativa* L.) genotypes. *Int. J. Phytoremediat., 22,* 227–235. https://doi.org/10.1080/15226514.2019.1658704.

Pehoiu, G., Murarescu, O., Radulescu, C., Dulama, I. D., Teodorescu, S., Stirbescu, R. M., Bucurica, I. A., & Stanescu, S. G. (2020). Heavy metals accumulation and translocation in native plants grown on tailing dumps and human health risk. *Plant Soil, 456*, 405-424. https://doi.org/10.1007/s11104-02004725-8.

Petrescu, L., & Bilal, E. (2006). Natural actinides studies in conifers grown on uranium mining dumps (the East Carpathians, Romania). *Carpathian Journal of Earth and Environmental Sciences, 1,* 63-80.

Rađenović, A., Medunić, G., & Sofilić, T. (2016). The use of ladle furnace slag for the removal of hexavalent chromium from an aqueous solution. *Metal Res & Techn., 113,* 6. https://doi.org/10.1051/metal/2016040.

Sasmaz, M., Senel, G. U., & Obek, E. (2021). Strontium accumulation by the terrestrial and aquatic plants affected by mining and municipal wastewaters (Elazig, Turkey). *Environ. Geochem. Health, 43*, 1-14. https://doi.org/10.1007/s10653-020-00629-9.

Sasmaz, M., & Sasmaz, A. (2017). The accumulation of strontium by native plants grown on Gumuskoy mining soils. *Journal of Geochemical Exploration, 181,* 236-242. https://doi.org/10.1016/j.gexplo.2017.08.001.

Sasmaz, A., & Sasmaz, M. (2009). The phytoremediation potential for strontium of indigenous plants growing in a mining area. *Environ & Exp. Bot, 67* (1), 139–144. https://doi.org/10.1016/j.envexpbot.2009.06.014.

Shacklette, H. T., Erdman, J. A., & Harms, T. F. (1978). Trace elements in plant foodstuffs in toxicity of heavy metals in the environments. *Part I. New York*, 25.

Shahraki, S. A., Ahmadimoghadam, A., Naseri, F., & Esmailzade, E. (2008). Study the Accumulation of Strontium in Plant Growing around Sarcheshmeh Copper Mine, Iran. *VSB Technical University of Ostrava, Ostrava,* 239–242.

Sharma, S., (2020). Uptake, transport, and remediation of strontium. Strontium Contamination in the Environment. Springer, *Cham,* 99–119. https://doi.org/10.1007/978-3-030-15314-4_6.

Tapeh, N. G., Bernousi, I., Moghadam, A. F., & Mandoulakani, B. A. (2018). Genetic diversity and structure of Iranian *Teucrium (Teucrium polium L.)* populations assessed by ISSR markers. *J. Agr Sci Tech., 20*, 333-345. https://jast-old.modares.ac.ir/article_18556_9be231cf11d0ae26926c1edc3390add5.pdf.

Timofeeva, Y., Karabtsov, A., Burdukovskii, M., & Vzorova, D. (2024). Strontium and vanadium sorption by iron-manganese nodules from natural and remediated Dystric Cambisols. *Journal of Soils and Sediments.* https://doi.org/10.1007/s11368-024-03714-z.

Uras, Y., & Yalçın, C. (2022). Malatya Floritlerinin NTE İçeriklerinin Regresyon Analizi ve Korelasyonu. *Geosound, 55* (1), 61-70.

Yalcin, F., Jonathan, M. P., Yalçın, M. G., Ilhan, S., & Leventelı, Y. (2020). Investıgatıon of heavy metal content ın beach sedıments on the of tasucu bay (Mersın) wıth geochemıcal and multıvarıate statistical approaches. *Journal of Engineering Sciences and Design, 8* (4), 1113-1125. https://doi.org/10.21923/jesd.802065.

Yalcin, M. G., Narin, I., & Soylak, M. (2008). Multivariate analysis of heavy metal contents of sediments from Gumusler creek, Nigde, Turkey. *Environmental Geology, 54* (6), 1155-1163. https://doi.org/10.1007/s00254-007-0884-6.

Zu, Y. Q., Li, Y., Chen, J. J., Chen, H. Y., Qin, L., & Schvartz, C. (2005). Hyperaccumulation of Pb, Zn and Cd in herbaceous grown on lead-zinc mining area in Yunnan, China. *Environ Int., 31,* 755-762. https://doi.org/10.1016/j.envint.2005.02.004.

Falling Body Motion in Time Scale Calculus

Neslihan Nesliye PELEN[1*] (iD) Zeynep KAYAR[2] (iD)

[1] *Ondokuz Mayıs University, Faculty of Science, Department of Mathematics, Samsun, Türkiye*
[2] *Van Yüzüncü Yıl University, Faculty of Science, Department of Mathematics, Van, Türkiye*

Keywords	Abstract
Time Scale Calculus	The falling body problem for different time scales, such as $\mathbb{R}$, $\mathbb{Z}$, $h\mathbb{Z}$, $q\mathbb{N}0$, $\mathbb{P}c,d$ is the subject of this study. To deal with this problem, we use time-scale calculus. Time scale dynamic equations are used to define the falling body problem. The exponential time scale function is used for the solutions of these problems. The solutions of the falling body problem in each of these time scales are found. Moreover, we also test our mathematical results with numerical simulations.
Falling Body Motion	
Delta Derivative	
H-Calculus	
Q-Calculus	

1. INTRODUCTION

Limits in calculating derivatives of real functions are the essential tools of regular calculus. However, many real-life problems are discussed in both continuous and discrete domains. To unify discrete and continuous domains Time Scale Calculus was established in the thesis of Stephan Hilger (Hilger, 1988). After that many studies were done about this issue. Bohner and Peterson (2001) is one of the most important books that explains the significant part of this calculus. The following articles show the results on the dynamic equations in time scale calculus; Akın and Bohner (2003), Akın et al. (2020), Anderson (2005), Kayar et al. (2022), Kayar and Kaymakçalan (2022a) and Kayar and Kaymakçalan (2022b). In the literature, many different kinds of calculus were defined. For instance, one can find the classical calculus, discrete calculus, h-calculus and q-calculus in the literature. Time scale calculus contains all of these in itself. Therefore, the results that we have found in time-scale calculus are general ones and one can reduce these results to these specific calculus types. In Alanazi et al. (2020), the falling body problem was studied by using q-calculus whose domain is $q^{\mathbb{N}}{}_0$. The basic formula for q-calculus is formerly obtained by Euler, nevertheless, its calculus was introduced by Jackson (1910). In this study, we generalize these results by using time scale calculus and we also show that our results coincide with the results in Alanazi et al. (2020). Moreover, we support our results with the numerical simulations.

2. METHODS AND PRELIMINERIES

The information in that section is taken from Bohner and Peterson (2001). The nonempty closed subset of real numbers is defined as a time scale and denoted by $\boldsymbol{T}$. The *forward jump* operator $\sigma: \boldsymbol{T} \to \boldsymbol{T}$ is defined as

$$\sigma(t) \coloneqq inf\{s \in \boldsymbol{T}: s > t\},$$

for $t \in \boldsymbol{T}$ while the *backward jump* operator $\rho: \boldsymbol{T} \to \boldsymbol{T}$ is defined by

*Corresponding Author, e-mail: neslihan.pelen@omu.edu.tr

$$\rho(t) := sup\{s \in \boldsymbol{T} : s < t\}.$$

If $t < sup\{\boldsymbol{T}\}$ and $\sigma(t) = t$, then t is called *right-dense*, and if $t > inf\{\boldsymbol{T}\}$ and $\rho(t) = t$, then t is called *left-dense*. Besides, if $\rho(t) < t$, we say that t is *left-scattered*. The graininess function $\mu : \boldsymbol{T} \to [0, \infty)$ is defined by

$$\mu(t) := \sigma(t) - t.$$

Definition 1: We say that a function $p : \boldsymbol{T} \to \mathbb{R}$ is regressive provided $1 + \mu(t)p(t) \neq 0$ for all $t \in \boldsymbol{T}^k = \boldsymbol{T}/(\rho(sup\{T\}), sup\{T\}]$ holds. The set of all regressive and rd-continuous functions $p : \boldsymbol{T} \to \mathbb{R}$ is denoted by

$$\boldsymbol{\mathcal{R}} = \boldsymbol{\mathcal{R}}(\boldsymbol{T}) = \boldsymbol{\mathcal{R}}(\boldsymbol{T}, \mathbb{R}).$$

Definition 2: If $p \in \boldsymbol{\mathcal{R}}$, then we define the exponential function by

$$e_p(t, s) = exp\left(\int_s^t \xi_{\mu(\tau)}(p(\tau))\Delta\tau\right) \quad \text{for} \quad s, t \in \boldsymbol{T}$$

where the cylinder transformation is defined by

$$\xi_h(z) := \begin{cases} \dfrac{Log(1 + zh)}{h}, h \neq 0 \\ z, h = 0 \end{cases}$$

Theorem 1: Time scale exponential function has following properties.

i. $e_p(t, s) = \dfrac{1}{e_p(s,t)}$

ii. $\left(\dfrac{1}{e_p(.,s)}\right)^\Delta = -\dfrac{p(t)}{e_p^\sigma(.,s)}$

iii. $e_{\ominus p}(t, \tau) = \dfrac{1}{e_p(t,\tau)}$

Definition 3: If $p \in \boldsymbol{\mathcal{R}}$ then the first order linear dynamic equation

$$y^\Delta = p(t)y(t) \tag{1}$$

is called regressive.

Theorem 2: *(Variations of Constants Formula)*

Suppose (1) is regressive. Let $t_0 \in \boldsymbol{T}$ and $y_0 \in \mathbb{R}$. The unique solution of the initial value problem

$$y^\Delta = p(t)y + f(t), y(t_0) = y_0 \tag{2}$$

is given by

$$y(t) = e_p(t, t_0)y_0 + \int_{t_0}^t e_p(t, \sigma(\tau))f(\tau)\Delta\tau \tag{3}$$

Theorem 3: *(Variations of Constants Formula)*

Suppose (1) is regressive. Let $t_0 \in \boldsymbol{T}$ and $y_0 \in \mathbb{R}$. The unique solution of the initial value problem

$$y^\Delta = -p(t)y^\sigma + f(t), y(t_0) = y_0 \tag{4}$$

is given by

$$y(t) = e_{\ominus p}(t, t_0)y_0 + \int_{t_0}^{t} e_{\ominus p}(t, \tau)f(\tau)\Delta\tau, \tag{5}$$

where $p(t) = \frac{p(t)}{1+\mu(t)p(t)}$.

2.1. Preliminaries for Falling Body Problem

Let us assume that in a constant gravitational field, a particle of mass m falls through the air from a height h with an initial speed v_0. It then encounters a resistance force that opposes the relative motion by which the particle moves relative to the air. It is known that this resistance force is related to relative speed. For slow speeds, the magnitude of the resistance force is proportional to the speed. But in other cases it may be proportional to the square of the velocity (or some other force). By applying Newton's second law we get

$$m\frac{dv}{dt} = -mg - mkv, \tag{6}$$

where k represents a positive constant indicating the strength of the retarding force, the inverse of seconds is its dimensionality and, $-mkv$, is a positive upward force because we take z and $v = z'$ to be positive upward, and the motion is downward, that is, $v < 0$, so that, $-kmv > 0$. The solution of the equation (6) with the initial condition $v(0) = v_0$ is given by

$$v(t) = -\frac{g}{k} + \left(v_0 + \frac{g}{k}\right)e^{-kt}. \tag{7}$$

By using the initial condition $z(0) = h$ and integrating (7), we get

$$z(t) = h - \frac{gt}{k} + \frac{1}{k}\left(v_0 + \frac{g}{k}\right)\left(1 - e^{-kt}\right), \tag{8}$$

see (Thornton, 2004).

3. MAIN RESULTS

3.1 Main Results for Falling Body Problem in Time Scale Calculus

The equation of motion (6) in view of the time scale calculus becomes

$$mv^\Delta = -mg - mkv \tag{9}$$

Or

$$v^\Delta = -g - kv. \tag{10}$$

Let

$$v^\Delta = -kv \tag{11}$$

be regressive. Then the solution of initial value problem

$$v^{\Delta} = -g - kv, \qquad v(0) = v_0 \tag{12}$$

can be obtained by Variation of Constants Formula (3) as

$$v(t) = e_{-k}(t,0)v_0 - g \int_0^t e_{-k}\left(t, \sigma(\tau)\right)\Delta\tau.$$

By using the properties given in Theorem 1 we have

$$e_{-k}(t, \sigma(\tau)) = \frac{1}{e_{-k}(\sigma(\tau), t)} = \frac{1}{k}\frac{k}{e_{-k}(\sigma(\tau), t)} = \frac{1}{k}\left(\frac{1}{e_{-k}(\tau, t)}\right)^{\Delta}.$$

Therefore,

$$\int_0^t e_{-k}\left(t, \sigma(\tau)\right)\Delta\tau = \int_0^t \frac{1}{k}\left(\frac{1}{e_{-k}(\tau, t)}\right)^{\Delta}\Delta\tau = \frac{1}{k}\left[1 - \frac{1}{e_{-k}(0, t)}\right] = \frac{1}{k}[1 - e_{-k}(t, 0)]$$

implies that

$$v(t) = e_{-k}(t, 0)\left[v_0 + \frac{g}{k}\right] - \frac{g}{k}. \tag{13}$$

The vertical distance $z(t)$ in time-scale calculus is governed by

$$z^{\Delta} = e_{-k}(t, 0)\left[v_0 + \frac{g}{k}\right] - \frac{g}{k} \tag{14}$$

where $v(t) = z^{\Delta}(t)$. Integrating (14) implies that

$$z(t) = h - \frac{gt}{k} + \left[v_0 + \frac{g}{k}\right]\int_0^t e_{-k}(s, 0)\Delta s = h - \frac{gt}{k} - \frac{1}{k}\left[v_0 + \frac{g}{k}\right][1 - e_{-k}(t, 0)] = h - \frac{gt}{k} + \frac{1}{k}\left[v_0 + \frac{g}{k}\right][1 - e_{-k}(t, 0)].$$

Remark 1: Let us choose the equation of motion (6) in view of the time scale calculus as

$$mv^{\Delta} = -mg - mkv^{\sigma}$$

or

$$v^{\Delta} = -g - kv^{\sigma}.$$

Let us assume that these equations are regressive. Then the solution of the initial value problem

$$v^{\Delta} = -g - kv^{\sigma}, \qquad v(0) = v_0$$

can be obtained by Variation of Constants Formula (5) as

$$v(t) = e_{\ominus(-k)}(t, 0)v_0 - g \int_0^t e_{\ominus(-k)}(t, \tau)\,\Delta\tau.$$

By using the properties given in Theorem 1 we have

$$e_{\ominus(-k)}(t, \tau) = \frac{1}{e_{-k}(t, \tau)} = e_{-k}(\tau, t).$$

Therefore,

$$\int_0^t e_{\ominus(-k)}(t,\tau)\Delta\tau = \int_0^t e_{-k}(\tau,t)\Delta\tau = -\frac{1}{k}\int_0^t -ke_{-k}(\tau,t)\Delta\tau = -\frac{1}{k}[1 - e_{-k}(0,t)] = \frac{1}{k}[e_{\ominus(-k)}(t,0) - 1]$$

implies that

$$v(t) = e_{\ominus(-k)}(t,0)v_0 - \frac{g}{k}[e_{\ominus(-k)}(t,0) - 1] = e_{\ominus(-k)}(t,0)\left[v_0 - \frac{g}{k}\right] + \frac{g}{k}.$$

The vertical distance $z(t)$ in time-scale calculus is governed by

$$z^\Delta = e_{\ominus(-k)}(t,0)\left[v_0 - \frac{g}{k}\right] + \frac{g}{k},$$

where $v(t) = z^\Delta(t)$. After integration, we get

$$z(t) = h + \frac{gt}{k} + \left[v_0 - \frac{g}{k}\right]\int_0^t e_{\ominus(-k)}(s,0)\,\Delta s = h + \frac{gt}{k} + \frac{1}{k}\left[v_0 - \frac{g}{k}\right][1 - e_{\ominus(-k)}(t,0)].$$

3.2 Special Cases

Below the falling body problems for the important special time scales is considered.

3.2.1. T=$\mathbb{R}$

We consider the special case where $\mu(t) = 0$ for all $t \in T$. In this case equation (9) becomes as equation (6) and solution (13) reduces to solution (7), see (Thornton, 2004).

3.2.2. T=$\mathbb{Z}$

We consider the special case where $\mu(t) = 1$ for all $t = n \in T$. In this case equation (10) becomes as

$$v(n + 1) - v(n) = \Delta v = -mg - mkv$$

and solution (13) reduces to

$$v(n) = (1-k)^n v_0 - g\sum_{i=0}^{n-1}(1-k)^{n-i-1} = (1-k)^n v_0 - g\sum_{i=0}^{n-1}(1-k)^i$$

$$= (1-k)^n v_0 - g\frac{1-(1-k)^n}{k} = (1-k)^n\left[v_0 + \frac{g}{k}\right] - \frac{g}{k},$$

see (Elaydi (2005), page 4).

The vertical distance $z(t)$ in time scale calculus is governed by

$$\Delta z = (1-k)^n\left[v_0 + \frac{g}{k}\right] - \frac{g}{k}, \tag{15}$$

where $v(n) = \Delta z(n)$. Summation (15) implies that

$$z(n) = h - \frac{gn}{k} + \frac{1}{k}\left[v_0 + \frac{g}{k}\right][1 - (1-k)^n]$$

3.2.3. T=$h\mathbb{Z}$, where $0 < h \in \mathbb{R}$

We consider the special case where $\mu(t) = h$ for all $t = n \in T$. In this case equation (10) becomes as

$$\frac{v(n+h) - v(n)}{h} = v^{\Delta} = -g - kv$$

and solution (13) reduces to

$$v(t) = (1 - kh)^{\frac{t}{h}} \left[v_0 + \frac{g}{k} \right] - \frac{g}{k}.$$

The vertical distance $z(t)$ becomes

$$z(t) = h - \frac{gt}{k} + \frac{1}{k} \left[v_0 + \frac{g}{k} \right] [1 - (1 - kh)^{t/h}]$$

Moreover, one can see falling body motion and its velocity behavior when T is taken as $\mathbb{Z}, h\mathbb{Z}$ and $\mathbb{R}$ in Figure 1, Figure 2, Figure 3 and Figure 4 for different initial velocities and initial heights.
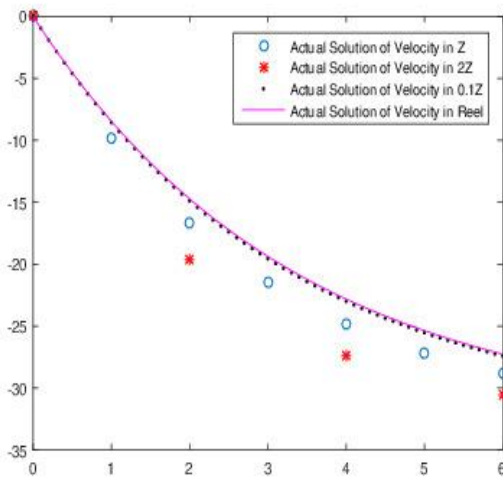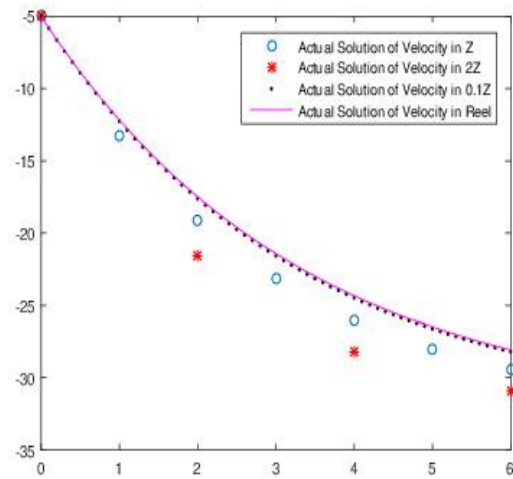

Figure 1. Graphs when $v_0 = 0$
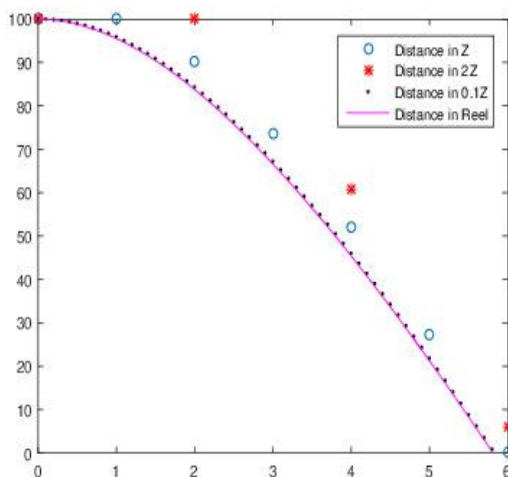

Figure 2. Graphs when $v_0 = -5$

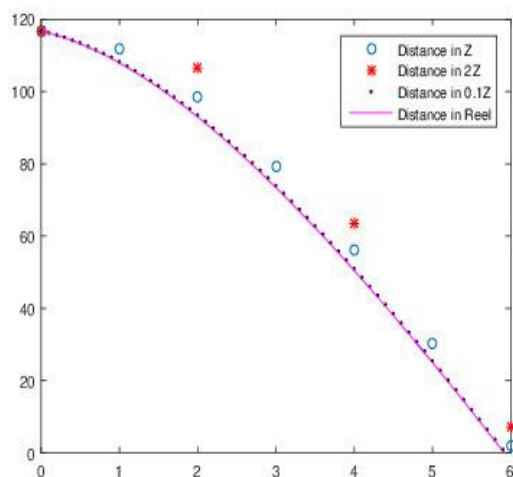Figure 3. Graphs when $v_0 = 0$ and $h_0 = 116,7$

Figure 4. Graphs when $v_0 = -5$ and $h_0 = 120$

3.2.4. T=$q^{\mathbb{N}_0} = \{1, q, q^2, q^3, ...\}$, where $1 < q \in \mathbb{R}$

We consider the special case where $\sigma(t) = qt$ and $\mu(t)$ depends on t for all $t \in \boldsymbol{T}$. In this case equation (9) becomes as equation (14) in Alanazi et al. (2020). and solution (13) reduces to equation (26) in Alanazi et al. (2020). In Figure 5 and Figure 6 one can see the velocity and distance behavior when T=$1.5^{\mathbb{N}_0}$.
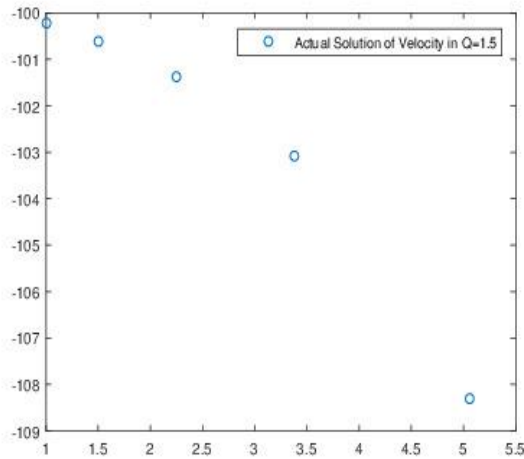

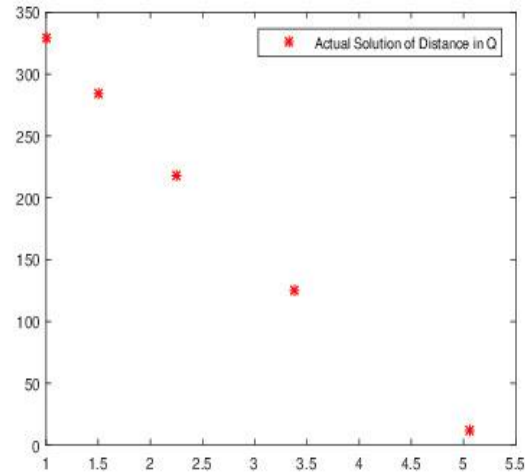*Figure 5. Velocity graphs for* $1.5^{\mathbb{N}_0}$

Figure 6. Distance graphs for $1.5^{\mathbb{N}_0}$

3.2.5. T=$\mathbb{P}_{c,d} = \cup_{i=0}^{\infty}[i(c+d), i(c+d)+c]$, where $0 < c, d \in \mathbb{R}, i \in \mathbb{N}_0$

We consider the special case where

$$\sigma(t) = \begin{cases} t, if\, t \in \cup_{i=0}^{\infty}[i(c+d), i(c+d)+c], \\ d, if\, t \in \cup_{i=0}^{\infty}\{i(c+d)+c\}, \end{cases}$$

$$\mu(t) = \begin{cases} 0, if\, t \in \cup_{i=0}^{\infty}[i(c+d), i(c+d)+c], \\ b, if\, t \in \cup_{i=0}^{\infty}\{i(c+d)+c\}, \end{cases}$$

In this case equation (10) becomes as

$$\frac{dv}{dt} = -g - kv, t \in [i(c+d), i(c+d)+c].$$

We will find the solution interval by interval.

First Case: Let us assume that the particle stops at the end of each interval $[i(c+d), i(c+d)+c]$ for all $i = 0,1,2,..$ automatically, i.e without a force.

In this case the initial velocity at the beginning of each interval should be

$$v_i = \frac{g}{k}[e^{kc} - 1]$$

for all $i = 0,1,2, \cdots$. Indeed, for the interval $t \in [0, c]$, we have

$$\frac{dv}{dt} = -g - kv,$$

$$v(0) = v_0$$

and the solution becomes

$$v(t) = e^P_{-k}(t, 0) \left[v_0 + \frac{g}{k} \right] - \frac{g}{k} = e^{-kt} \left[v_0 + \frac{g}{k} \right] - \frac{g}{k},$$

where $e^P_\alpha(t, t_0)$ is exponential function for $\mathbb{P}_{c,d}$ defined by $e^P_\alpha(t, t_0) = e^{\alpha(t-t_0)}$.

If the particle stops at the point when $t = c$, then its velocity should be zero at the point when $t = c$ and so, $v(c) = 0$. This implies that $v_0 = \frac{g}{k}[e^{kc} - 1]$.

For each interval $t \in [i(c + d), i(c + d) + c]$, we can find the solution as

$$v(t) = e^P_{-k}(t, i(c + d)) \left[v_i + \frac{g}{k} \right] - \frac{g}{k} = e^{-k(t-i(c+d))} \left[v_i + \frac{g}{k} \right] - \frac{g}{k}$$

and the initial velocity of each interval as $v_i = \frac{g}{k}[e^{kc} - 1]$ at the point $t = i(c + d)$ for all $i = 0,1,2,\cdots$.

In this case at the points when $t = i(c + d) + c$, we have

$$\Delta v(i(c + d) + c) = v((i + 1)(c + d)) - v(i(c + d) + c) = v((i + 1)(c + d)) = v_{i+1} = \frac{g}{k}[e^{kc} - 1]$$

Let us consider the displacement of the particle. Different than the other time scales, in this case z does not denote the vertical distance but it denotes the displacement of the particle.

For the interval $t \in [0, c]$, we have

$$\frac{dz}{dt} = v = e^{-kt} \left[v_0 + \frac{g}{k} \right] - \frac{g}{k}$$

$$z(0) = h$$

where $v_0 = v_i = \frac{g}{k}[e^{kc} - 1]$ for all $i = 0,1,2,...$ and the solution becomes

$$z(t) = h - \frac{gt}{k} + \frac{1}{k} \left(v_0 + \frac{g}{k} \right) (1 - e^{-kt})$$

which shows the displacement of the particle over the first c seconds.

For the displacement of the particle at the point when $t = c$, we need to compute

$$z(c) = h - \frac{gc}{k} + \frac{1}{k} \left(v_0 + \frac{g}{k} \right) (1 - e^{-kc}) = h_0.$$

Therefore, the particle is falling from the point $z = h$ and stops at the point $z = h - h_0$ at $t = c$.

For the interval $t \in [c + d, 2c + d]$, we have

$$\frac{dz}{dt} = v = e^{-kt} \left(v_0 + \frac{g}{k} \right) - \frac{g}{k},$$

$$z(c + d) = h - h_0$$

and the solution becomes

$$z(t) = h - h_0 - \frac{g}{k}(t - c - d) + \frac{1}{k}\left(v_0 + \frac{g}{k}\right)(e^{-k(c+d)} - e^{-kt})$$

which shows the displacement of the particle over the interval $[c + d, 2c + d]$.

For the displacement of the particle at the point when $t = 2c + d$, we need to compute

$$z(2c + d) = h - h_0 - \frac{gc}{k} + \frac{1}{k}\left(v_0 + \frac{g}{k}\right)(1 - e^{-kc})e^{-k(c+d)} = \frac{1}{k}\left(v_0 + \frac{g}{k}\right)(1 - e^{-kc})(e^{-k(c+d)} - 1) = h_1.$$

Therefore, the particle is falling from the point $z = h - h_1$ and stops at the point $z = h - h_0 - h_1$ at $t = 2c + d$.

For the interval $t \in [2c + 2d, 3c + 2d]$, we have

$$\frac{dz}{dt} = v = e^{-kt}\left(v_0 + \frac{g}{k}\right) - \frac{g}{k}$$

$$z(2c + 2d) = h - h_0 - h_1$$

and the solution becomes

$$z(t) = h - h_0 - h_1 - \frac{g}{k}(t - 2c - 2d) + \frac{1}{k}\left(v_0 + \frac{g}{k}\right)(e^{-k(2c+2d)} - e^{-kt})$$

which shows the displacement of the particle over the interval $[2c + 2d, 3c + 2d]$.

For the displacement of the particle at the point when $t = 3c + 2d$, we need to compute

$$z(3c + 2d) = h - h_0 - h_1 - \frac{gc}{k} + \frac{1}{k}\left(v_0 + \frac{g}{k}\right)(1 - e^{-kc})e^{-k(2c+2d)}$$

$$= \frac{1}{k}\left(v_0 + \frac{g}{k}\right)(1 - e^{-kc})(e^{-k(c+d)\}} - 1)e^{-k(c+d)} = h_2.$$

Therefore, the particle is falling from the point $z = h - h_1$ and stops at the point $z = h - h_0 - h_1 - h_2$ at $t = 3c + 2d$.

For the interval $t \in [3c + 3d, 4c + 3d]$, we have

$$\frac{dz}{dt} = v = e^{-kt}\left[v_0 + \frac{g}{k}\right] - \frac{g}{k}$$

$$z(3c + 3d) = h - h_0 - h_1 - h_2$$

and the solution becomes

$$z(t) = h - h_0 - h_1 - h_2 - \frac{g}{k}(t - 3c - 3d) + \frac{1}{k}\left(v_0 + \frac{g}{k}\right)(e^{-k(3c+3d)} - e^{-kt})$$

which shows the displacement of the particle over the interval $[3c + 3d, 4c + 3d]$.

For the displacement of the particle at the point when $t = 4c + 3d$, we need to compute

$$z(4c + 3d) = h - h_0 - h_1 - h_2 - \frac{gc}{k} + \frac{1}{k}\left(v_0 + \frac{g}{k}\right)(1 - e^{-kc})e^{-k(3c+3d)}$$

$$= \frac{1}{k}\left(v_0 + \frac{g}{k}\right)\left(1 - e^{-kc}\right)\left(e^{-k(c+d)} - 1\right)e^{-2k(c+d)} = h_3$$

Therefore, the particle is falling from the point $z = h - h_1 - h_2$ and stops at the point $z = h - h_0 - h_1 - h_2 - h_3$ at $t = 4c + 3d$.

Thus, the displacement $z(t)$ for the interval $t \in [i(c + d), i(c + d) + c]$ is

$$z(t) = h - \sum_{j=0}^{i-1} h_j - \frac{g}{k}(t - i(c + d)) + \frac{1}{k}\left[v_0 + \frac{g}{k}\right]\left[e^{-k(i(c+d))} - e^{-kt}\right]$$

$$= \frac{g}{k}[i(c + d) - t] + \frac{1}{k}\left[v_0 + \frac{g}{k}\right]\left[e^{-k(i-1)(c+d)} + e^{-k[(i-1)(c+d)+c]} + e^{-ki(c+d)} - e^{-kt}\right],$$

where

$$h_i = h - \sum_{j=0}^{i-1} h_j - \frac{gc}{k} + \frac{1}{k}\left(v_0 + \frac{g}{k}\right)\left(1 - e^{-kc}\right)e^{-ki(c+d)} = \frac{1}{k}\left(v_0 + \frac{g}{k}\right)\left(1 - e^{-kc}\right)e^{-k(i-1)(c+d)}[e^{-k(c+d)} - 1]$$

for all $i = 0,1,2,\cdots$ with $h_0 = h - \frac{gc}{k} + \frac{1}{k}\left(v_0 + \frac{g}{k}\right)\left(1 - e^{-kc}\right)$ and the displacement $z(t)$ for the interval $t \in [0, c]$ is

$$z(t) = h - \frac{gt}{k} + \frac{1}{k}\left(v_0 + \frac{g}{k}\right)\left(1 - e^{-kt}\right).$$

In this case, $\Delta z(i(c + d) + c) = 0$ for $i = 0,1,2,\cdots$.

Second Case: Let us assume that the particle stops at the end of each interval $[i(c + d), i(c + d) + c]$ for all $i = 0,1,2,\cdots$ by a force.

In this case the initial velocity at the beginning of each interval changes but the final velocities will be zero. Let the initial velocities at the beginning of each interval $t \in [i(c + d), i(c + d) + c]$ be $v(i(c + d)) = v_i$. Let us find the solution interval by interval.

For the interval $t \in [0, c]$, we have

$$\frac{dv}{dt} = -g - kv,$$

$$v(0) = v_0$$

and the solution becomes

$$v(t) = e^P_{-k}(t, 0)\left[v_0 + \frac{g}{k}\right] - \frac{g}{k} = e^{-kt}\left[v_0 + \frac{g}{k}\right] - \frac{g}{k}$$

where $e^P_\alpha(t, t_0)$ is exponential function for $\mathbb{P}_{c,d}$ defined by $e^P_\alpha(t, t_0) = e^{\alpha(t - t_0)}$.

For the interval $t \in [c + d, 2c + d]$, we have

$$\frac{dv}{dt} = -g - kv,$$

$$v(c + d) = v_1$$

and the solution becomes

$$v(t) = e^{-k(t-c-d)} \left[v_1 + \frac{g}{k}\right] - \frac{g}{k}.$$

For each interval $t \in [i(c + d), i(c + d) + c]$, we have

$$\frac{dv}{dt} = -g - kv,$$

$$v(i(c + d)) = v_i$$

and we can find the solution as

$$v(t) = e^P_{-k}(t, i(c + d)) \left[v_i + \frac{g}{k}\right] - \frac{g}{k} = e^{-k[t-i(c+d)]} \left[v_i + \frac{g}{k}\right] - \frac{g}{k}$$

for the initial velocity of each interval v_i at the point $t = i(c + d)$ for all $i = 0,1,2,\dots$.

In this case at the points when $t = i(c + d) + c$, we have

$$\Delta v(i(c + d) + c) = v((i + 1)(c + d)) - v(i(c + d) + c) = v((i + 1)(c + d)) = v_{i+1}$$

Let us consider the displacement of the particle. Different than the other time scales, in this case, z does not denote the vertical distance but it denotes the displacement of the particle. For the interval $t \in [0, c]$, we have

$$\frac{dz}{dt} = v = e^{-kt} \left[v_0 + \frac{g}{k}\right] - \frac{g}{k},$$

$$z(0) = h$$

and the solution becomes

$$z(t) = h - \frac{gt}{k} + \frac{1}{k}\left(v_0 + \frac{g}{k}\right)(1 - e^{-kt})$$

which shows the displacement of the particle over the first c seconds. For the displacement of the particle at the point when $t = c$, we need to compute

$$z(c) = h - \frac{gc}{k} + \frac{1}{k}\left(v_0 + \frac{g}{k}\right)(1 - e^{-kc}) = h_0.$$

Hence, the particle is falling from the point $z = h$ and stops at the point $z = h - h_0$ at $t = c$.

For the interval $t \in [c + d, 2c + d]$, we have

$$\frac{dz}{dt} = v = e^{-kt} \left[v_1 + \frac{g}{k}\right] - \frac{g}{k}$$

$$z(c + d) = h - h_0,$$

and the solution becomes

$$z(t) = h - h_0 - \frac{g}{k}(t - c - d) + \frac{1}{k}\left(v_1 + \frac{g}{k}\right)(e^{-k(c+d)} - e^{-kt})$$

which shows the displacement of the particle over the interval $[c + d, 2c + d]$. For the displacement of the particle at the point when $t = 2c + d$, we need to compute

$$z(2c + d) = h - h_0 - \frac{gc}{k} + \frac{1}{k}\left(v_1 + \frac{g}{k}\right)(1 - e^{-kc})e^{-k(c+d)} = \frac{1}{k}(1 - e^{-kc})\left[-\left(v_0 + \frac{g}{k}\right) + \left(v_1 + \frac{g}{k}\right)e^{-k(c+d)}\right] = h_1.$$

Hence, the particle is falling from the point $z = h - h_1$ and stops at the point $z = h - h_0 - h_1$ at $t = 2c + d$. For the interval $t \in [2c + 2d, 3c + 2d]$, we have

$$\frac{dz}{dt} = v = e^{-kt}\left[v_2 + \frac{g}{k}\right] - \frac{g}{k}$$

which shows the displacement of the particle over the interval $[2c + 2d, 3c + 2d]$. For the displacement of the particle at the point when $t = 3c + 2d$, we need to compute

$$z(3c + 2d) = h - h_0 - h_1 - \frac{gc}{k} + \frac{1}{k}\left[v_2 + \frac{g}{k}\right](1 - e^{-kc})e^{-k(2c+2d)}$$

$$= \frac{1}{k}(1 - e^{-kc})\left[-\left(v_1 + \frac{g}{k}\right)e^{-k(c+d)} + \left(v_2 + \frac{g}{k}\right)e^{-2k(c+d)}\right] = h_2$$

Thus, the particle falls from the point $z = h - h_1$ and stops at the point $z = h - h_0 - h_1 - h_2$ at $t = 3c + 2d$. For the interval $t \in [3c + 3d, 4c + 3d]$, we have

$$\frac{dz}{dt} = v = e^{-kt}\left[v_3 + \frac{g}{k}\right] - \frac{g}{k}$$

$$z(3c + 3d) = h - h_0 - h_1 - h_2$$

and the solution becomes

$$z(t) = h - h_0 - h_1 - h_2 - \frac{g}{k}(t - 3c - 3d) + \frac{1}{k}\left(v_3 + \frac{g}{k}\right)(e^{-k(3c+3d)} - e^{-kt})$$

which shows the displacement of the particle over the interval $[3c + 3d, 4c + 3d]$. For the displacement of the particle at the point when $t = 4c + 3d$, we need to compute

$$z(4c + 3d) = h - h_0 - h_1 - h_2 - \frac{gc}{k} + \frac{1}{k}\left(v_3 + \frac{g}{k}\right)(1 - e^{-kc})e^{-k(3c+3d)}$$

$$= \frac{1}{k}(1 - e^{-kc})\left[-\left(v_2 + \frac{g}{k}\right)e^{-2k(c+d)} + \left(v_3 + \frac{g}{k}\right)e^{-3k(c+d)}\right] = h_3.$$

Therefore, the particle is falling from the point $z = h - h_1 - h_2$ and stops at the point $z = h - h_0 - h_1 - h_2 - h_3$ at $t = 4c + 3d$. Thus, the displacement $z(t)$ for the interval $t \in [i(c + d), i(c + d) + c]$ is

$$z(t) = h - \sum_{j=0}^{i-1} h_j - \frac{g}{k}(t - i(c + d)) + \frac{1}{k}\left[v_i + \frac{g}{k}\right]\left[e^{-k(i(c+d))} - e^{-kt}\right]$$

$$= \frac{g}{k}[i(c + d) + c - t] - \frac{1}{k}(1 - e^{-kc})\left[v_{i-1} + \frac{g}{k}\right]e^{-(i-1)k(c+d)} + \frac{1}{k}\left[v_i + \frac{g}{k}\right]\left[e^{-ki(c+d)} - e^{-kt}\right],$$

where

$$h_i = h - \sum_{j=0}^{i-1} h_j - \frac{gc}{k} + \frac{1}{k}\left(v_i + \frac{g}{k}\right)\left(1 - e^{-kc}\right)e^{-ki(c+d)} = \frac{1}{k}\left(1 - e^{-kc}\right)\left[-\left(v_{i-1} + \frac{g}{k}\right)e^{-(i-1)k(c+d)} + \left(v_i + \frac{g}{k}\right)e^{-ik(c+d)}\right]$$

for all $i = 0,1,2,\cdots$ with $h_0 = h - \frac{gc}{k} + \frac{1}{k}\left(v_0 + \frac{g}{k}\right)(v\_0 + (1 - e^{-kc}))$ and the displacement $z(t)$ for the interval $t \in [0, c]$ is

$$z(t) = h - \frac{gt}{k} + \frac{1}{k}\left(v_0 + \frac{g}{k}\right)\left(1 - e^{-kt}\right).$$

In this case, $\Delta z(i(c + d) + c) = 0$ for $i = 0,1,2,\cdots$. In Figure 7 and Figure 9, the velocity and distance graph for the first case of $\mathbb{P}_{5,2}$ is drawn and in Figure 8 and Figure 10, their behaviors are given in the graph for the second case of $\mathbb{P}_{5,2}$.
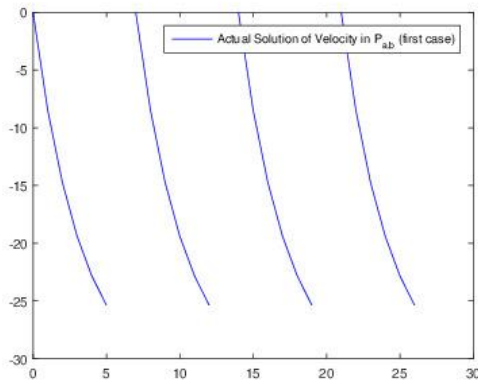

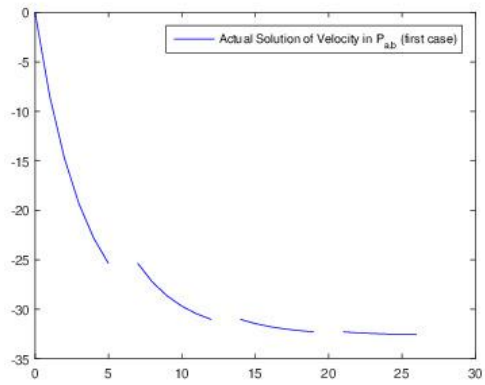Figure 7. Velocity graphs for first case of $\mathbb{P}_{5,2}$

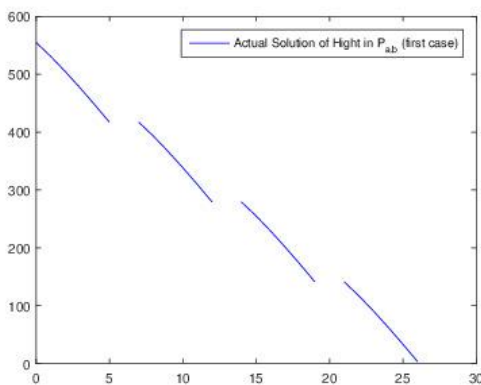Figure 8. Velocity graphs for second case of $\mathbb{P}_{5,2}$

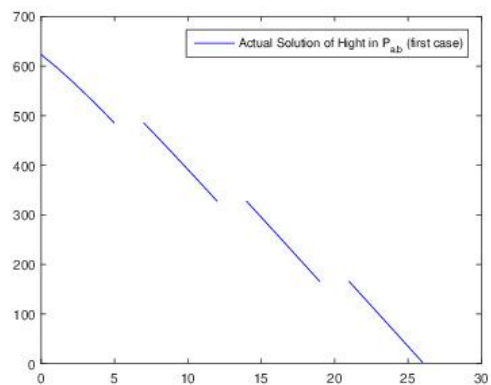Figure 9. Distance graphs for first case of $\mathbb{P}_{5,2}$

Figure 10. Distance graphs for first case of $\mathbb{P}_{5,2}$

4. DISCUSSIONS AND CONCLUSIONS

In Newtonian physics, free fall is any motion of an object in which the only force acting on it is gravity. Gravity reduces to the curvature of space-time in general relativity context, there is no force acting on a freely falling object and gravity acts almost equally in a roughly uniform gravitational field on every part of an object. When the object starts to move, it encounters a resistance force that opposes the relative motion by which the particle moves relative to the air.

In this study, we have mainly concentrated on the falling body motion in different kind of time scales. We obtained the above results for each of them. Additionally, numerical simulation of these results was obtained by using determined coefficients.

We have compared velocity and distance in $\mathbb{R}$ with the results obtained in $2\mathbb{Z}$, $0.1\mathbb{Z}$ and $\mathbb{Z}$. Based on the findings, the results of the discrete model on $0.1\mathbb{Z}$ yield the best fit to that of $\mathbb{R}$. We can conclude that the time scale $h\mathbb{Z}$ with $0 < h < 1$ provides the best approximation to $\mathbb{R}$, as expected. Moreover, in the time scale $\mathbb{P}_{c,d}$ if the particle stops at the end of each interval $[i(c+d), i(c+d)+c]$ for all $i = 0,1,2,\cdots$ automatically, i.e without a force, the initial velocity at the beginning of each interval is the same and the velocity function is periodic. In the second case where the particle stops at the end of each interval $[i(c+d), i(c+d)+c]$ for all $i = 0,1,2,\cdots$ by a force, the initial velocity at the beginning of each interval changes and the velocity function is decreasing and not periodic. The distance functions for both cases show similar behaviors.

Considering falling body motion under different kind of time scales, helps us to evaluate this physical event under different kind of media. In other words, different kind of time scales can explain the different media in real-world applications. As a result, these kinds of results can be useful for the media with different kind of physical properties, which shows the importance of this study.

AUTHOR CONTRIBUTIONS

Conceptualization, Z.K. and N.N.P.; methodology, Z.K. and N.N.P; fieldwork, Z.K.; software, N.N.P.; title, Z.K.; validation, Z.K. and N.N.P; formal analysis, Z.K. and N.N.P; research, Z.K. and N.N.P; sources, Z.K. and N.N.P; manuscript-original draft, Z.K. and N.N.P; manuscript-review and editing, Z.K. and N.N.P; visualization, Z.K. and N.N.P; supervision, Z.K. and N.N.P. All authors have read and legally accepted the final version of the article published in the journal.

CONFLICT OF INTEREST

The authors declare no conflict of interest.

REFERENCES

Akın, E. & Bohner, M. (2003). Miscellaneous Dynamic Equations. *Methods and Applications of Analysis*, *10*(1), pp.11-30. https://dx.doi.org/10.4310/MAA.2003.v10.n1.a2

Akın, E., Pelen, N. N., Tiryaki I. U., & Yalcin, F. (2020). Parameter identification for gompertz and logistic dynamic equations. *Plos One, 15*(4): e0230582. https://doi.org/10.1371/journal.pone.0230582

Alanazi, A. M., Ebaid, A., Alhawiti W. M., & Muhiuddin, G. (2020). The Falling Body Problem in Quantum Calculus. *Front. Phys.*, *8*, 43. https://doi.org/10.3389/fphy.2020.00043

Anderson, D. R. (2005). Time-scale integral inequalities. *J. Inequal. Pure Appl. Math.*, *6*(3), 66.

Bohner, M., & Peterson, A. (2001). Dynamic Equations on Time Scale: An Introduction with Applications. Birkhauser, Boston, Inc., Boston, MA. https://doi.org/10.1007/978-1-4612-0201-1

Elaydi, S. (2005). *An Introduction to Difference Equations*. Springer SBM. https://doi.org/10.1007/0-387-27602-5

Hilger, S. (1988). *Ein Maßkettenkalkül mit Anwendung auf Zentrumsmannigfaltigkeiten*. PhD Thesis. Universitat Würzburg

Jackson, F. H. (1910). On a q-definite integrals. *The Quarterly Journal of Pure and Applied* Mathematics, *41*, 193-203.

Kayar, Z., Kaymakçalan, B., & Pelen, N. N. (2022). Diamond alpha Bennett-Leindler type dynamic inequalities and their applications. *Mathematical Methods in the Applied* Sciences, *45*(5), 2797-2819. https://doi.org/10.1002/mma.7955

Kayar, Z., & Kaymakçalan B. (2022a). Applications of the novel diamond alpha Hardy–Copson type dynamic inequalities to half linear difference equations. *Journal of Difference Equations and Applications*, *28*(4), 457-484. https://doi.org/10.1080/10236198.2022.2042522

Kayar Z., & Kaymakçalan, B. (2022b). Some new extended nabla and delta Hardy-Copson type inequalities and their applications in oscillation theory. *Bulletin of the Iranian Mathematical Society*, *48*, 2407-2439. https://doi.org/10.1007/s41980-021-00651-2

Thornton, S. T., & Marion, J. B. (2004). *Classical dynamics of particles and systems*, Thomson Brooks/Cole 24.

Study on the Optical and Gas-Sensing Performance of Zn-doped CuO Films

Sezen TEKIN[1*] iD

[1] Department of Medical Services and Techniques, Eldivan Medical Services Vocational School, Çankırı Karatekin University, Çankırı, Türkiye

Keywords	Abstract
CuO Thin Films Linear Optics Gas-Sensing Dopant Effect	The pure copper oxide thin film was deposited on glass substrates by SILAR method with 30 cycles. To examine the doping effect, Zn-doped films at different doping ratios were prepared under the same conditions as the undoped film. The XRD, SEM and Raman measurements were performed to investigate the morphological and structural properties of the samples. Analysis showed increasing aggregation and amorphous structure with doping. The optical parameters were characterized by spectrophotometer measurement and relevant formulas. The band gap energies were determined to increase from 2.50 to 2.79 eV with the increasing Zn rate. The Hervé and Vandamme, Moss and Ravindra relations were used to determine the refractive index. The room temperature gas-sensing performance for the undoped and doped samples were reported and the responses for 5 ppm gas were calculated as 249 %, 800 %, 189 % and 15 % for the CuO, 1Zn:CuO, 3Zn:CuO and 5Zn:CuO, respectively. The response of CuO thin films changed with doping, and 1% Zn doping rate was determined as the optimal rate in this study.

1. INTRODUCTION

CuO is a p-type semiconductor, and one of the transition metal oxides (TMOs) with a relatively small monoclinic crystal system. CuO films are used in numerous application areas such as photocatalysts, gas sensors, solar cells, field emission devices, high temperature superconductors and lithium batteries, due to the advantages of copper being abundant in nature, having a low production cost, being non-poisonous, and having high thermal stability, optical and electrical properties (Mnethu et al., 2020). Metal doping, the addition of the impurity ions to its lattice, is one of the known methods to control the properties of a semiconductor. The transition metals and rare-earth metals can be as doping materials. Various thin film preparation methods are available in the literature, but among them, the SILAR method is one of the simplest and most cost-effective techniques as it is flexible in the selection of substrates, at low processing temperatures, repeatable and provides large-area production (Mnethu et al., 2020).

There are some reports based on optical properties, gas selectivity and sensitivity for undoped and doped CuO produced by different methods. For example, Mnethu et al. (2020) deposited CuO and Zn doped CuO nanoplatelets by hydrothermal synthesis and investigate the sensing characteristics at various concentrations and for 9 different gases. In another study, the temperature dependent conductivity and energy band structure of p-type amorphous film produced by magnetron sputtering method were investigated with the theoretical calculation and experimental measurement (Huang et al., 2015). Maebana et al. (2023) reported extremely sensitive and selective xylene detector system produced from CuO-ZnO. Ezenwa (2012) studied optical and structural characterization of the films with 1.7 eV and high density of grains, deposited on glass with chemical

bath deposition at 300K. The variation of refractive index and other optical properties with PEG content were investigated by Çavuşoğlu (2018). The optical band gap energies increased, and film thickness reduced depending on the increasing amount of PEG (Çavuşoğlu, 2018).

The aim of this study is to control the optical and gas sensing properties of pure CuO films, deposited with SILAR method using Zn doping and doping ratio variation under constant production conditions.

2. MATERIAL AND METHOD

The undoped and Zn-doped CuO thin films were produced by SILAR with 30 cycles.The SILAR cycle was performed as follows: The glass substrate was kept in CuO solution for 20 sec. Then the substrate was removed from the solution and immediately immersed in hot water at 90°C for 7 sec. After hot water, the substrate was left in the air for 1 minute, and then the cycle was completed by dipping it into deionized water for 30 sec. In this way, the undoped CuO thin film were grown on the glass substrate in 30 cycles, and the same cycle was performed for Zn-doped CuO solution. To see the effect of the doping rate, the Zn ratio in the solution was changed as 0, 1, 3 and 5%. and the films were coded as CuO, 1Zn:CuO, 3Zn:CuO and 5Zn:CuO, respectively. The structural properties of the CuO and (M) Zn:CuO (M=1,3,5) films were researched using XRD, SEM and Raman spectroscopy. The linear absorbance of all produced films were measured with SHIMADZU double beam spectrophotometer (model UV-1800) in a wavelength range of 300–1000 nm. The produced sensors will be tested electrically, and 99.999% purity CO_2 gas will be used in these testing stages. Since the measurements had to be carried out in a CO_2 atmosphere for the sensor tests, a sealed chamber and probe tips positioned inside the chamber were used. Gas sensor measurement system consists of Keithley 2400, LakeShore 325 temperature controller, Keysight E4990A impedance meter, MKS flow controllers (MFC), modified sensor cell for gas measurements, dry air, CO_2 gas and vacuum pump. Gas sensor cell; It consists of a sample holder, gas valves that provide the inlet and outlet of the target gas, and BNC connectors for connecting the sensor to the Keithley 2400 device and the Keysight E4990A impedance device. Gas flow was provided by the mass flow controller (MFC) and the measuring chamber outlet was connected to the exhaust line. By measuring the base resistance of the sensors in the atmospheric environment, the resistance change that occurred after the start of CO_2 gas flow was examined. The obtained measurement data were instantly transferred to the computer and recorded.

3. RESULTS AND DISCUSSION

The SEM images of the produced (a) CuO, (b) 1Zn:CuO, (c) 3Zn:CuO and (d) 5Zn:CuO are represented in Figure 1. The produced CuO sample is distributed homogeneously on the surface and its size is clearly visible. With the doping, the samples started to clump and the size change of the CuO nanoparticles with the creation of aggregation and small nanostructures was observed.

The XRD patterns of the undoped and Zn-doped films are given in Figure 2. The peaks observed in the produced CuO and 1Zn:CuO films at ~ 35° and 38° specify (-111) and (111) reflections. However, when the XRD analysis of the structures is examined completely, they are seen to be amorphous. No peak was observed for the 3Zn:CuO and 5Zn:CuO samples, indicating that the deposited films had an amorphous structure. This may be related to the growth method. The observed results were associated with the literature results (Patil et al., 2017; Daoudi et al., 2019). Patil et al. (2017) reported that an amorphous structure was observed in the XRD analysis of CuO thin films produced by SILAR method. In the XRD analysis of CuO thin films obtained by Daoudi et al. (2019) it was reported that the intensities of the peaks were low and almost amorphous structures grew.

Raman spectroscopy, one of the important techniques used to examine the vibration properties and structure of the produced films, is given in Figure 3. The peaks seen between 557-554 and 784-786 cm^{-1} and shown in yellow are associated with ZnO and indicate the presence of dopant atoms in the structure. While A$_g$ mode was obtained as 278, 276, 275 and 273 cm^{-1}, B$_{g(1)}$ mode was found as 330, 328, 327 and 325 cm^{-1} for CuO, 1Zn:CuO, 3Zn:CuO and 5Zn:CuO, respectively. And also, 613, 609 and 607 cm^{-1} were observed for B$_{g(2)}$ mode. When the dopant atoms were included into the structure, a blue shift for the A$_g$, B$_{g(1)}$ and B$_{g(2)}$ modes was obtained.
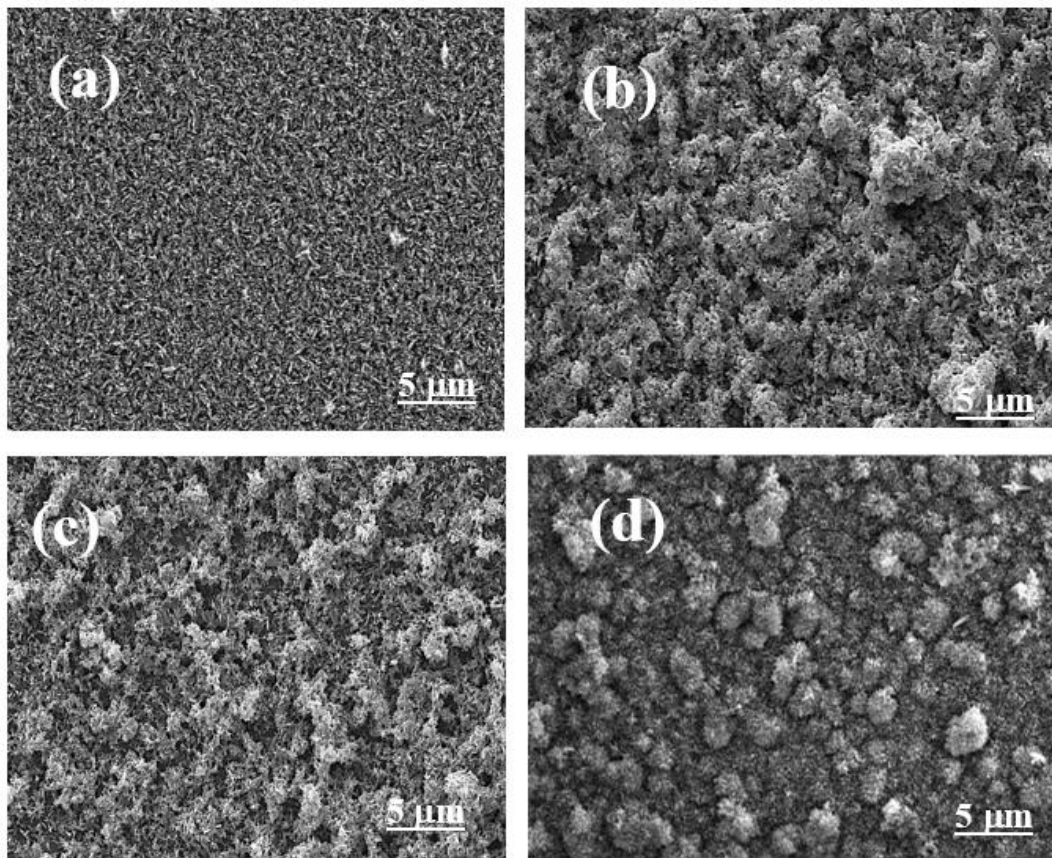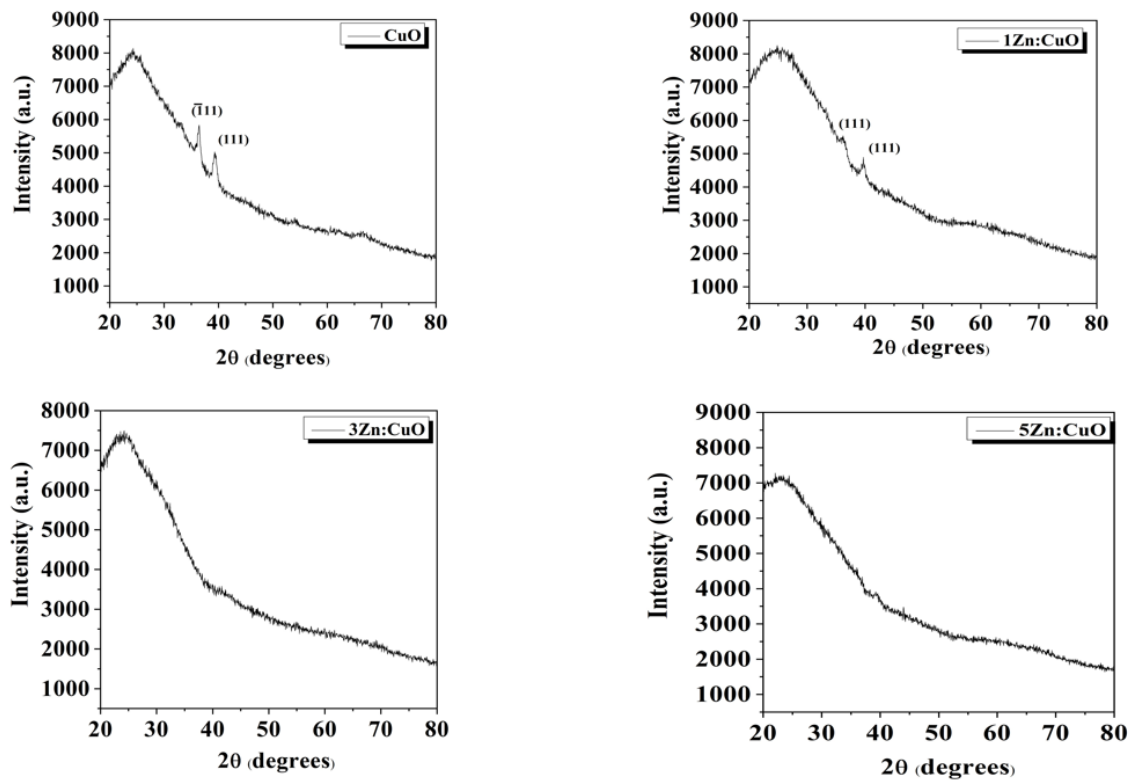
Figure 1. The SEM analysis of produced films

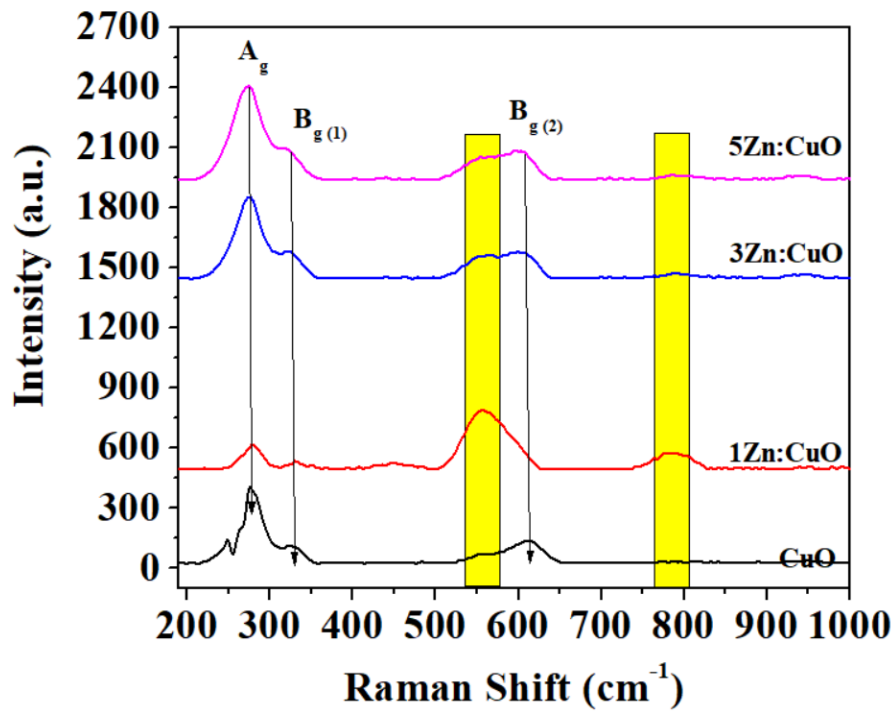*Figure 2.* The XRD for the produced samples

Figure 3. *The Raman spectra of produced films*

Figure 4 depicts the linear absorption of the CuO and (M) Zn:CuO (M=1,3,5) films. The absorption decreased towards longer wavelengths for all samples. As seen from the figure, as the Zn additives ratio increases, the absorbance feature decreases. The absorption (α) and extinction (k) coefficient are defined using absorption results and related by $\alpha=2.303A/d$ and $k=\alpha\lambda/4\pi$ (Dhineshbabu et al., 2016). The α (Figure 5) and k (Figure 6) coefficient results are compatible with the absorption graph (Figure 4) as expected. It is clear from Figure 5 that the high values of α ($> 10^4$ cm^{-1}) are obtained for all films, so, the direct transition can be mentioned. This result agrees with literature (Balamurugan & Mehta, 2001; Ezenwa, 2012).
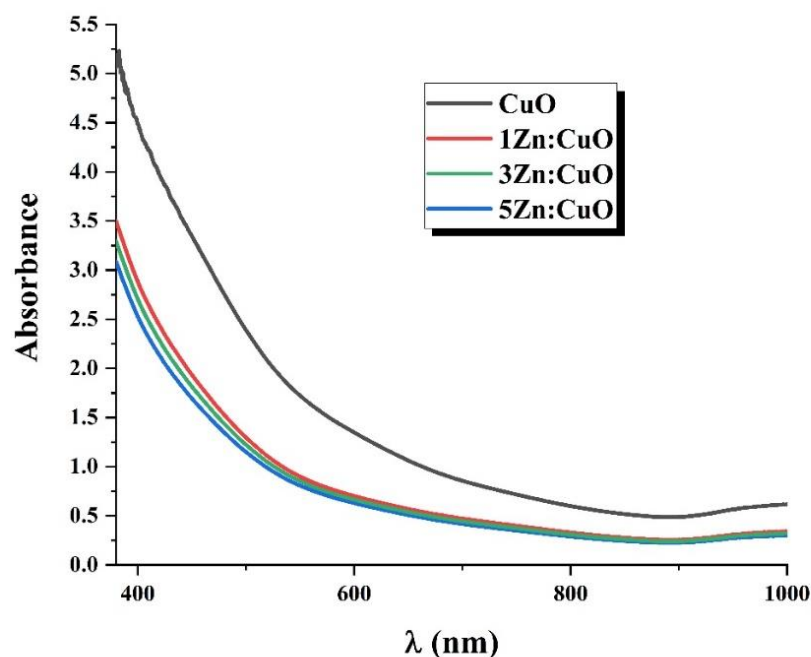

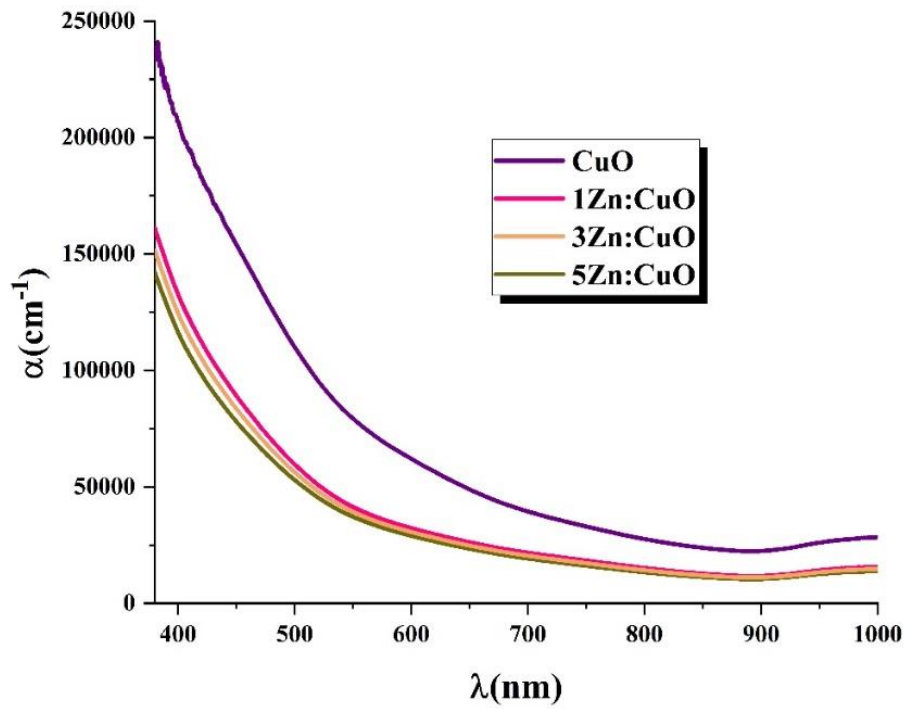**Figure 4.** *The absorbance vs. wavelength for undoped and doped samples*

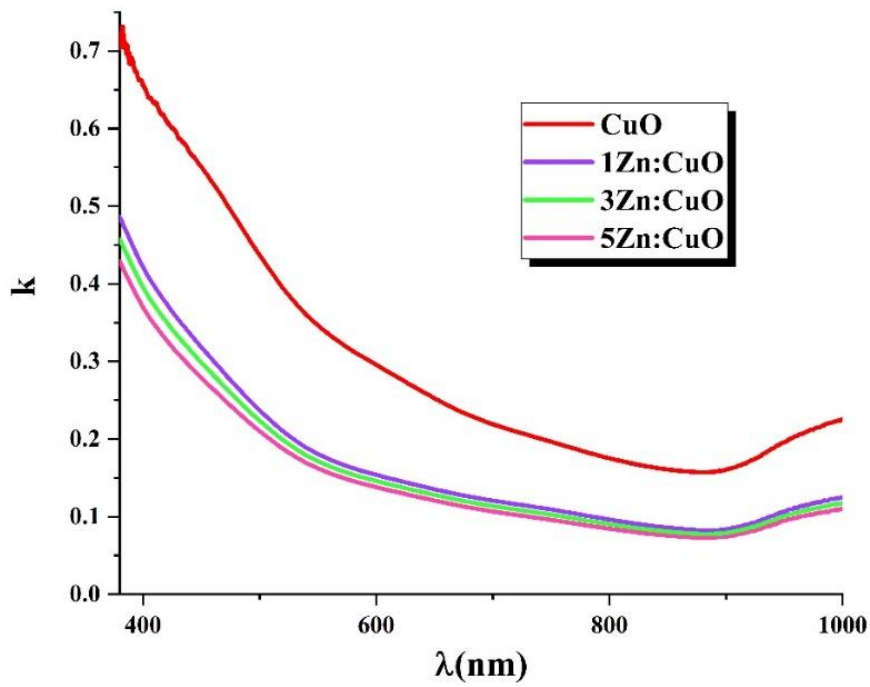***Figure 5.*** *The α vs. wavelength of the produced films*

Figure 6. *The extinction coefficient for all films*

Figure 7 depicts a plot of $(\alpha h\nu)^2$ vs. photon energy to find the band gap for CuO and (M) Zn:CuO (M=1,3,5) samples. Eg energy ranges were determined at the point where the linear part of these graphs intersects the energy axis at $(\alpha h\nu)^2=0$. As seen in Table 1, the band gaps are defined as 2.50, 2.69, 2.75 and 2.79 eV for CuO, 1Zn:CuO, 3Zn:CuO and 5Zn:CuO, respectively. CuO has a relatively low bandgap (1.2-1.9 eV) (Lu et al., 2009). The pure CuO film in our study has a higher band gap, and this can be explained by the amorphous structure (Figure 2) and aggregation (Figure 1). There are other studies in the literature that achieve high bandgap such as 2.24 (Güngör, 2019) and 3,19 eV (Das & Alford, 2013). The band gap values of the films increase depending on the increasing Zn concentration; as shown in Figure 7. This change in optical band gap energy values is a result of the change in the amorphous structure of Zn:CuO films (Figure 2) with increasing amounts of Zn doping. Huang et al. (2015) reported the similar behavior for crystalline and amorphous Cu_2O films. They obtained ~2.0 and ~2.7 eV for the crystalline and amorphous films, respectively. Additionally, Abdel Rafea and Roushdy (2009) reported a decreasing band gap from 2.3 to 1.7 eV due to annealing and crystallization.

The refractive index (n) of the films can be determined with different models. The Hervé and Vandamme (Hervé & Vandamme, 1994), Moss and Ravindra (Tripathy, 2015) relations were used, and the results are given in Table 1. The value of the refractive index is compatible with Ezenwa (2012) which found it as 2.7 for CuO thin films. Çavuşoğlu (2018) determined higher refractive index values (~3.02, ~3.06) using the Moss and Hervé and Vandamme model. This is due to the lower band gap of the films in the study.

Table 1. Optical calculations for all films

Samples	E_g (eV)	n (Moss)	n (Ravindra)	n (Hervé & Vandamme)
CuO	2.50	2.48	2.53	2.51
1Zn:CuO	2.69	2.44	2.42	2.45
3Zn:CuO	2.75	2.42	2.38	2.43
5Zn:CuO	2.79	2.41	2.35	2.41

Gas sensors often indicate the presence of a toxic gas in room conditions. Therefore, under normal room conditions, in the presence of only air, the parameter to be measured must be constant. For this purpose, the change over time of the current parameter used in the study was measured. Dynamic CO_2 gas sensor measurements were performed at room temperature in the air environment (Figure 8). First, dry air was sent at a constant flow rate to ensure that the surface was stable. Then, different concentrations of CO_2 gas were sent. The experimental results showed that the sensors of different designs covering the same area, under the same gas flow, operate with lower sensitivity as the additive ratio increases (except 1Zn:CuO). It was observed that the 5Zn:CuO sensor reached its saturation point and was not sensitive to different gas concentrations.

Since CuO is a p-type and ZnO is an n-type semiconductor, a p-n heterojunction structure is formed by doping Zn into the CuO structure. As a result of this joint structure, an increase in current conduction is observed (Poloju et al., 2018). The hole density in the p-type semiconductor and the electron density in the n-type semiconductor are high, and the Fermi energy levels also differ from each other. Therefore, when these two structures are brought atomically close to each other, a flow of electrons occurs between them. It causes a bending of the energy band structures associated with p- and n-type semiconductors when they are combined. For this reason, an increase is observed in doped thin films compared to the response of undoped CuO thin films. However, there was a decrease after a certain doping rate and 1% doping rate was determined as the optimal doping rate in this study. Maebana et al. (2023) have reported the gas sensing properties of the Zn-doped CuO structure and observed that there was a decrease in sensitivity with increasing Zn doping. The highest response was obtained for 1 % Zn-doped CuO. They attributed this to aggregation between ZnO and CuO , thus reporting a lower detection performance (Maebana et al., 2023). Mnethu et al. (2020) have determined the selective behavior with responses of 42 and 53 for pure CuO and 0.1% doped Zn:CuO, respectively. They commented that the hypothesized mechanism of electronic chemo-resistant gas sensing goes beyond the attributes of intrinsic defects such as oxygen vacancies and their interstitials.
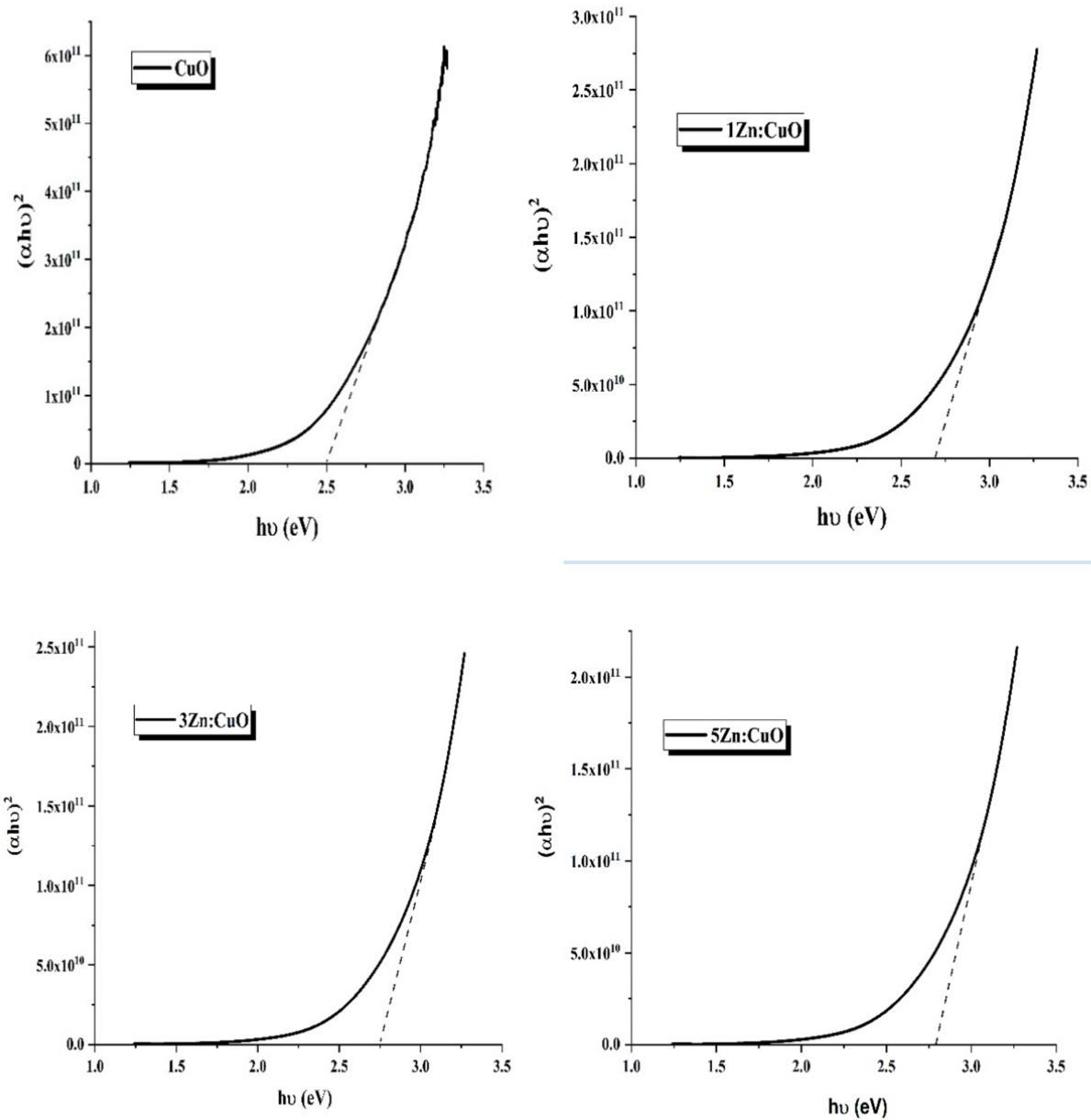
Figure 7. Tauc plots for undoped and doped samples

Figure 9 depicts the responses vs. gas concentrations for the produced samples. The responses of the 5 ppm CO_2 gas were calculated 249 %, 800 %, 189 % and 15 % for the CuO, 1Zn:CuO, 3Zn:CuO and 5Zn:CuO, respectively. No selectivity was observed for the 5Zn:CuO sample towards different gas concentrations, although a small amount of sensitivity was obtained when the gas was sent to the surface. The maximum sensitivity was obtained for the 1Zn:CuO sample. When the 3Zn:CuO sample was examined, a decrease in sensitivities began to be seen. The results obtained are compatible with the literature (Mnethu et al., 2020; Maebana et al., 2023). Differences in responses were observed depending on the doping rate, and the responses started to decrease after 1% Zn. Therefore, to achieve an increase in sensitivity, lower additive rates should be preferred. At higher Zn concentrations, neutral defects gradually form, which causes the charge carriers to be neutralized between the p-n heterojunction (Yathisha & Arthoba, 2018). As seen in Figure 9, the lowest sensitivity was obtained at 1 ppm for all samples. The responses of the 1 ppm CO_2 gas were calculated 136%, 201 %, 50 % and 15 % for the CuO, 1Zn: CuO, 3Zn:CuO and 5Zn:CuO, respectively. Response and recovery times of the produced samples are represented in Figure 10. Since no selectivity towards gases was observed

for the 5Zn:CuO sample, response and return calculations were not made and the graph included only 3 samples. The response and recovery times at room temperature (1 ppm) were calculated 1.7, 1.5, 1.5 minutes and 0.7, 0.6 and 0.6 minutes for the CuO, 1Zn: CuO and 3Zn:CuO, respectively; as shown in Figure 10. It is important that the produced sensor materials have low response and return times to be used commercially. Sensor devices produced from materials with fast response and return times for application areas such as mining are of great importance in protecting human health.
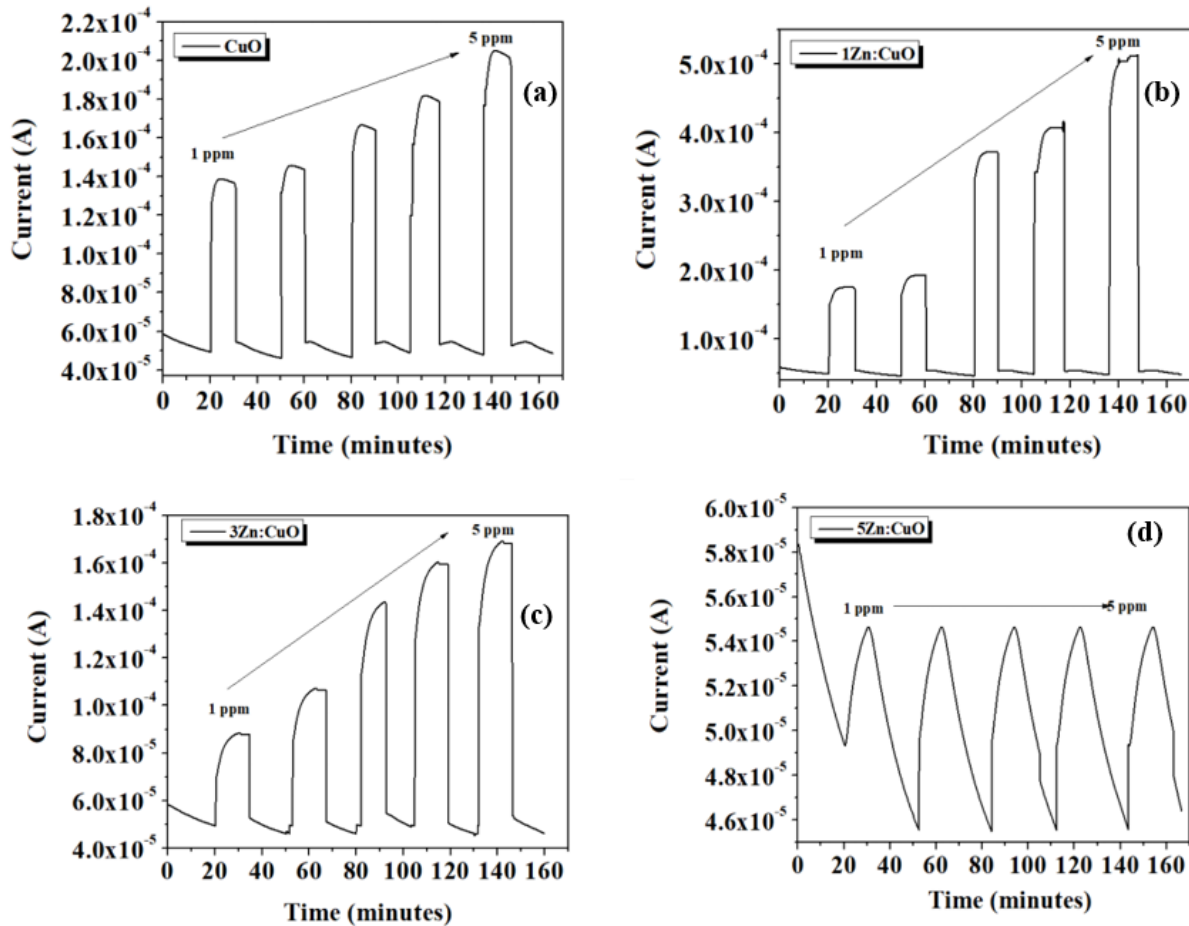

Figure 8. *The dynamic gas sensing measurements of the produced films*

4. CONCLUSION

The preparation of undoped and Zn-doped CuO films with different doping ratios have been successfully carried out using SILAR method. When the SEM and XRD analysis of the produced films were examined, increasing aggregation and amorphous structure were observed as the doping rate increased. The doping led to increase the band gap; however, the absorbance was reduced with increasing Zn content. The obtained absorption coefficient values confirmed that there was a direct transition for CuO. Theoretical calculations of the refractive index were made using different models and were compatible with each other and with the literature. Gas sensor measurements were performed at room temperature to investigate the doping effect. It was observed that an increase is occurred for doped thin films compared to the response of undoped CuO thin films. However, there was a decrease after a certain doping rate and 1%Zn doping rate was determined as the optimal rate in this study. The results showed that Zn doping strongly affected the structural, optical, and gas-sensing properties of CuO films. The thin films examined in this study may have potential applications in the optics and sensor industries.
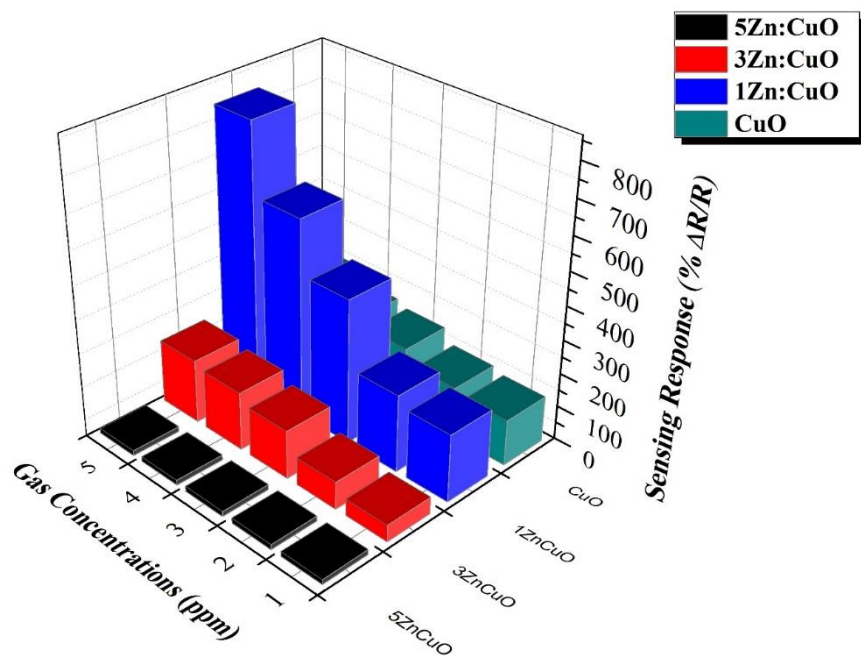
Figure 9. Response of the produced samples versus gas concentrations
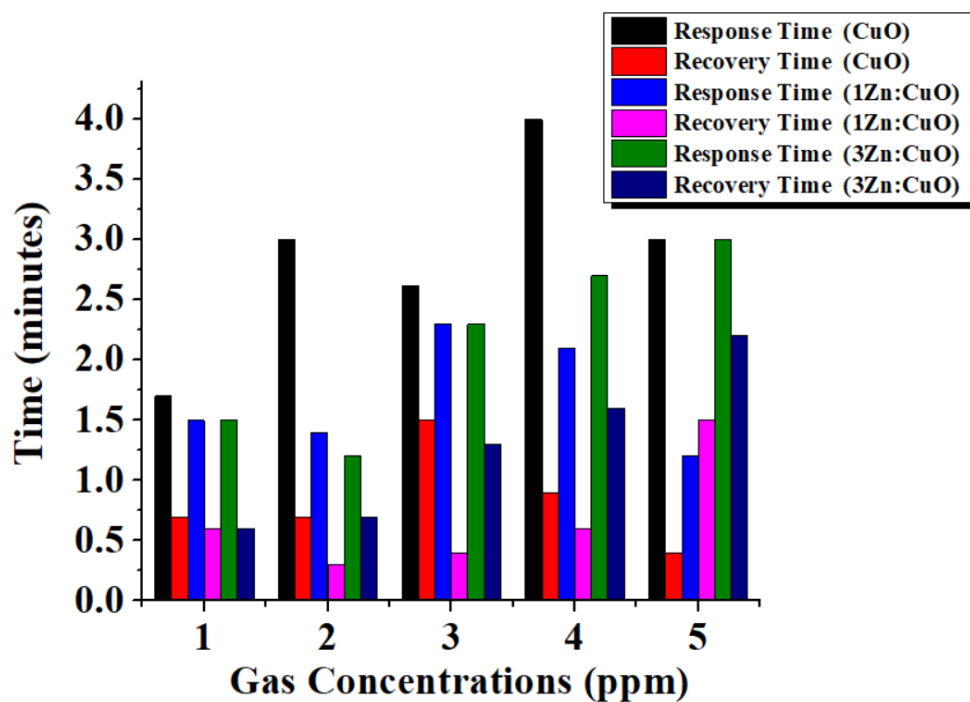
Figure 10. Response and recovery times of the produced samples

CONFLICT OF INTEREST

The author declares no conflict of interest.

REFERENCES

Abdel Rafea, M., & Roushdy, N. (2009). Determination of the optical band gap for amorphous and nanocrystalline copper oxide thin films prepared by SILAR technique. *Journal of Physics D: Applied Physics*, *42*, 015413. https://doi.org/10.1088/0022-3727/42/1/015413

Balamurugan, B., & Mehta, B. (2001). Optical and structural properties of nanocrystalline copper oxide thin films prepared by activated reactive evaporation. *Thin Solid Films*, *396*(1-2), 90-96. https://doi.org/10.1016/S0040-6090(01)01216-0

Çavuşoğlu, H. (2018). Band-gap Control of Nanostructured CuO Thin Films using PEG as a Surfactant. *European Journal of Science and Technology*, *13*, 124-128. https://doi.org/10.31590/ejosat.417941

Daoudi, O., Qachaou, Y., Raidou, A., Nouneh, K., Lharch, M., & Fahoume, M. (2019). Study of the physical properties of CuO thin films grown by modified SILAR method for solar cells applications. *Superlattices and Microstructures*, *127*, 93-99. https://doi.org/10.1016/j.spmi.2018.03.006.

Das, S., & Alford, T. L. (2013), Structural and optical properties of Ag-doped copper oxide thin films on polyethylene napthalate substrate prepared by low temperature microwave annealing. *Journal of Applied Physics*, *113*, 244905. https://doi.org/10.1063/1.4812584

Dhineshbabu, N. R., Rajendran, V., Nithyavathy, N., & Vetumperumal, R. (2016) Study of structural and optical properties of cupric oxide nanoparticles. *Applied Nanoscience*, *6*, 933-939. https://doi.org/10.1007/s13204-015-0499-2

Ezenwa, I. (2012). Optical Analysis of Chemical bath Fabricated Cuo Thin Films. *Research Journal of Recent Sciences*, *1*(1), 46-50.

Güngör, E. (2019). Zn:CuO Heteroyapıların Yapısal, Optik, Fotolüminesans ve İletim Özellikleri. *Nevsehir Journal of Science and Technology*, *8*(1), 1-13 https://doi.org/10.17100/nevbiltek.509354

Hervé, P., & Vandamme, L. K. J. (1994). General relation between refractive index and energy gap in semiconductors. *Infrared Physics & Technology*, *35*(4), 609-615. https://doi.org/10.1016/1350-4495(94)90026-4

Huang, Q., Li, J., & Bi, X. (2015). The improvement of hole transport property and optical band gap for amorphous Cu_2O films. *Journal of Alloys and Compounds*, *647*, 585-589. https://doi.org/10.1016/j.jallcom.2015.06.147

Lu, H.-C., Chu, C.-L., Lai, C.-Y., & Wang, Y.-H. (2009). Property Variations of Direct-Current Reactive Magnetron Sputtered Copper Oxide Thin Films Deposited at Different Oxygen Partial Pressures. *Thin Solid Films*, *517*(15), 4408-4412. https://doi.org/10.1016/j.tsf.2009.02.079

Maebana, L. M.., Motsoeneng, R. G., Tshabalala, Z. P., Swart, H. C., Cummings, F. R., Jozela, M., Nkosi, S. S., & Motaung, D. E. (2023). Low-operational temperature for selective detection of xylene gas using a p-n CuO-ZnO heterostructure-based sensor. *Journal of Alloys and Compounds*, *960*, 170683. https://doi.org/10.1016/j.jallcom.2023.170683

Mnethu, O., Nkosi, S. S., Kortidis, I., Motaung, D. E., Kroon, R. E., Swart, H. C., Ntsasa, N. G., Tshilongo, J., & Moyo, T. (2020). Ultra-sensitive and selective p-xylene gas sensor at low operating temperature utilizing Zn doped CuO nanoplatelets: Insignificant vestiges of oxygen vacancies. *Journal of Colloid and Interface Science*, *576*, 364-375, https://doi.org/10.1016/j.jcis.2020.05.030

Patil, A. S., Patil, M. D., Lohar, G. M., Jadhav, S. T., & Fulari, V. J. (2017). Supercapacitive properties of CuO thin films using modified SILAR method. *Ionics*, *23*, 1259-1266 https://doi.org/10.1007/s11581-016-1921-9

Poloju, M., Jayababu, N., & Ramana Reddy, M. V. (2018). Improved gas sensing performance of Al doped ZnO/CuO nanocomposite based ammonia gas sensor. *Materials Science and Engineering: B*, *227*, 61-67. https://doi.org/10.1016/j.mseb.2017.10.012.

Tripathy, S. K. (2015). Refractive indices of semiconductors from energy gaps. *Optical Materials*, *46*, 240-246 https://doi.org/10.1016/j.optmat.2015.04.026

Yathisha, R. O., & Arthoba, N. Y. (2018). Structural, optical and electrical properties of zinc incorporated copper oxide nanoparticles: doping effect of Zn. *Journal of Materials Science*, *53*, 678-691. https://doi.org/10.1007/s10853-017-1496-5

On the Voltage Dependent Series Resistance, Interface Traps, and Conduction Mechanisms in the Al/(Ti-doped DLC)/p-Si/Au Schottky Barrier Diodes (SBDs)

Sabreen A. HAMEED[1*] Öznur BERKÜN[2] Seçkin ALTINDAL YERIŞKIN[3]

[1] Department of Physics, College of Science, University of Diyala, Diyala, Iraq
[2] Department of Nanotechnology Engineering, Faculty of Sciences, Zonguldak Bulent Ecevit University, Zonguldak, Türkiye
[3] Vocational Highschool of Technical Sciences, Department of Chemistry and Chemical Processing Technologies, Gazi University, Türkiye

Keywords	Abstract
(Ti:DLC) Interlayer Al/(Ti:DLC)/p-Si Schottky Diodes Origin of Series Resistance and Interface States Conduction Mechanisms I-V, and C-V and G-V Measurements	In this study, Al-(Ti:DLC)-pSi/Au Schottky barrier diode (SBD) was manufactured instead of conventional metal / semiconductor (MS) with and without an interlayer and then several fundamental electrical-characteristics such as ideality factor (n), barrier height Φ_B series and shunt resistances (R_s, R_{sh}), concentration of acceptor atoms (NA), and width of depletion-layer (Wd) were derived from the forward-reverse bias current/voltage (I-V), capacitance and conductance as a function of voltage (C/G-V) data using various calculation-methods. Semi logarithmic IF-VF plot shows a linear behavior at lower-voltages and then departed from linearity as a result of the influence of series resistance/Rs and organic-interlayer. Three linear regions can be seen on the double-logarithmic IF-VF plot. with different slopes (1.28, 3.14, and 1.79) in regions with low, middle, and high forward bias, which are indicated that Ohmic-mechanism, trap-charge-limited-current (TCLC) mechanism, and space-charge-limited-current (SCLC) mechanism, respectively. Energy dependent surface states (Nss) vs (Ess-Ev) profile was also obtained from the Card-Rhoderick method by considering voltage-dependence of n and Φ_B and they were grown from the mid-gap energy up to the semiconductor's valance band (Ev). To see the impact of Rs for 1 MHz, the measured C/G-V graphs were amendment. All results are indicated that almost all electrical parameters and conduction mechanism are quite depending on R_s, N_{ss}, and calculation method due the voltage dependent of them.

1. INTRODUCTION

The metal/semiconductor (MS) Schottky barrier diodes (SBDs) with and without an insulator-layer are main electronic devices due to their quick switching times, low-forward bias voltage operation, long lifetime and low capacitance (Card & Rhoderick, 1971; Sze & Ng, 2006; Cheung & Cheung, 1986; Nicollian & Brews, 1982; Reddy et al., 2022). In application, many sources may be affected on their performance like the formed a native or deposited interlayer on a semiconductor wafer's surface, its thickness and homogeneity, the availability of many interface traps or states at interlayer (semiconductor) interface and (Rs), barrier in-homogeneities at junction, fabrication processes, and electric field (Cheung & Cheung, 1986; Nicollian & Brews, 1982; Reddy et al., 2022; Ulusoy et al., 2023). The perfect case in structures of MS and MIS is diverged from by all of these sources. Among them, the most effective ones are the fabrication processes of them, the existence of high value of Rs, interface traps (Nss), and the thickness and homogeneity of deposited interlayer at M/S interface, applied electric field (E=V/d), and the concentration of atoms injected into the semiconductor (Sharma & Tripathi, 2013).

It is thought that by using a high-dielectric interlayer, the efficiency of MS type SDs can be improved. For instance, the use such interlayer can be decreased leakage current, ideality factor, R_s, N_{ss} and maximize the rectification ratio ($RR=I_f/I_r$), barrier height (BH), shunt resistance (R_{sh}), respectively (Yerişkin et al., 2017; Berkün et al., 2023). As a result, over the past twenty years, several physicists, chemists and materials researchers have begun to use new interfacial layers like pure or polymers doped with metal or metal-oxide, DLC with or without metals, and some composites among semiconductor and metal to enhance the effectuation of MS type SDs (Berkün et al., 2023; Lin et al., 2013).

Diamond like carbon (DLC) thin film is a Amorphous carbon that is moderately stable (a:C) with sp^2 and sp^3 bonds, or amorphous-carbon (a-C:H) which is including H atom in its structure and also it has high solidity, infrared energy transmittance, chemical stability, low thermal, large thermal conductivity and stellar characteristics like large electrical resistance. The Ti doped DLC has a great interlayer (35-100 nm) and excellent transparency (Berkün et al., 2023; Lin et al., 2013; Güçlü, 2023; Demirezen et al., 2022). Doping of DLC can be formed by metallic or non-metallic elements. Ti has a particular appeal among non-metals since it makes DLC more conductive and reduces the band gap. Therefore, in this study, Al-(Ti:DLC)pSi-Au (MIS) type SBDs were created instead of conventional MS SD with/without an insulator layer. Following that some of their important electrical variables were computed using various calculating methods by I-V and (C/G)-V graphs to determine how voltage-dependent they were.

2. MATERIAL AND METHOD

In this research, To create Al-(Ti: DLC)-pSi-Au SDs, the (Ti: DLC) inter-layer was formed onto Boron-doped (p-Si) single wafer by electrochemical deposition technique. Before the fabrication, wafer doped with B with <100> orientaion, ~300 µm thickness, 5.08 cm diameter, and 1–10 Ω.cm resistivity had been washed in an ultrasonic-bath using the RCA cleaning method in a solution of (18 M) deionized-water, HF, and (H_2O: HCl) solution. The wafer was then dried by N_2-gas before being processed into a 150 nm thick, at 10^{-7} Torr. The back-side of wafer was coated with Au by using thermal evaporation technique and then annealed at 500 °C to ensuring ohmic contact. After that (Ti:DLC) interlayer was grown onto wafer utilizing electrochemical-deposition method. Finally, 150nm thick and 1mm diameter high-pure (99.999%) Al Schottky contacts were coated on the (Ti:DLC) interlayer at 10^{-7} Torr. The IV and (C/G) – V of the sample have been measured utilizing Keithley – 2400 I-V source meter and HP 4192 A impedance analyzer, respectively. For more information on the fabricated processes, prepared (Ti:DLC), and structural analysis can find in our previous study (Berkün et al., 2023).

3. RESULTS AND DISCUSSION

3.1. Forward/reverse bias iv characteristics

Al/(Ti:DLC)/p-Si/Au SD produced at room temperature (RT) forward bias $\ln(I_f)$-V_f plot is shown in Figure 1. It is clear that this curve has good rectifier-behavior and linear-part between 0.04 V and 0.25 V and then deviated from linearity due to (Ti:DLC) interlayer and R_s effects (Card & Rhoderick, 1971; Sze & Ng, 2006). The conventional thermionic emission (TE) theory is usually used in MS/MIS type SDs to study the CM and calculation electrical-parameters. Based on TE theory, the current-voltage relation in the SDs with R_s and higher value of n could be described as follows (Card & Rhoderick, 1971; Sze & Ng, 2006; Cheung & Cheung, 1986).

$$I = (AA^*T^2).\exp\left(-\frac{q\Phi_{B0}}{kT}\right)[\exp(q(V-IR_s)/nkT)-1)] = I_o\left[\exp\left(\frac{q}{nkT}(V-IR_s)-1\right)\right] \tag{1}$$

Here; k, T, IRs, and I_o or Is are the Boltzmann-constant, temperature (K), voltage drops SD, and saturation-current. Based on TE theory, the values of I_o, n, Φ_{B0} have been calculated from the intercept and slope of $\ln(I_f)$-V_f plot as 1.71×10^{-7} A, 1.98, 0.64 eV, respectively.

$$n = \frac{q}{kT}\left(\frac{d(V)}{d(\ln(I))}\right) \tag{2a}$$

$$\Phi_{Bo} = \frac{kT}{q} \, Ln \left(\frac{AA^* \, T^2}{I_0} \right) \tag{2b}$$

The biggest value of n is the result of presence of N_{ss}, Interlayer, its thickness, and barrier inhomogeneity's (Card & Rhoderick, 1971; Sze & Ng, 2006; Cheung & Cheung, 1986), but the non-saturated reverse current was attributed to image-force reducing BH, and generation-recombination (Card & Rhoderick, 1971; Sze & Ng, 2006).
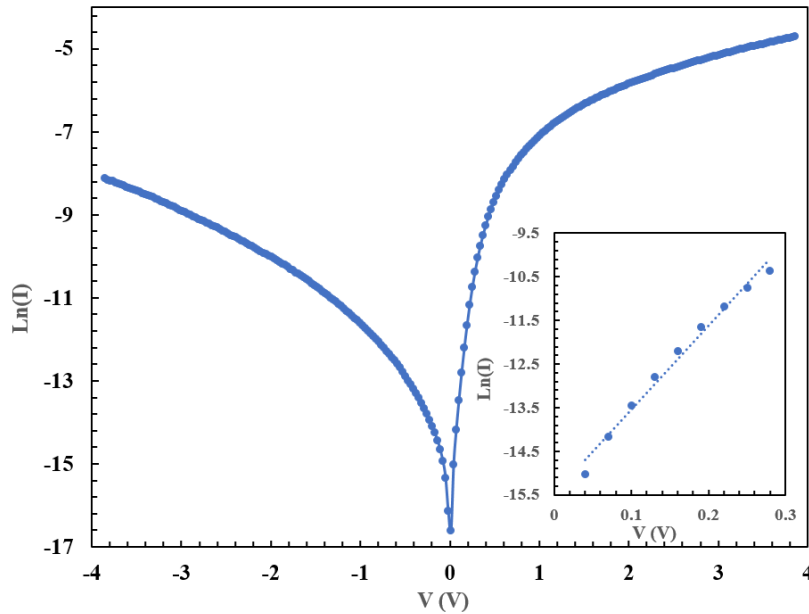
***Figure 1**. The Ln(I)−V curve of the Al-(Ti:DLC)-pSi-Au SBD*

The voltage-dependent resistance (R_i) of the Al-(Ti:DLC)-pSi-Au SBD was calculated with Ohm−Law and depicted in Figure 2.
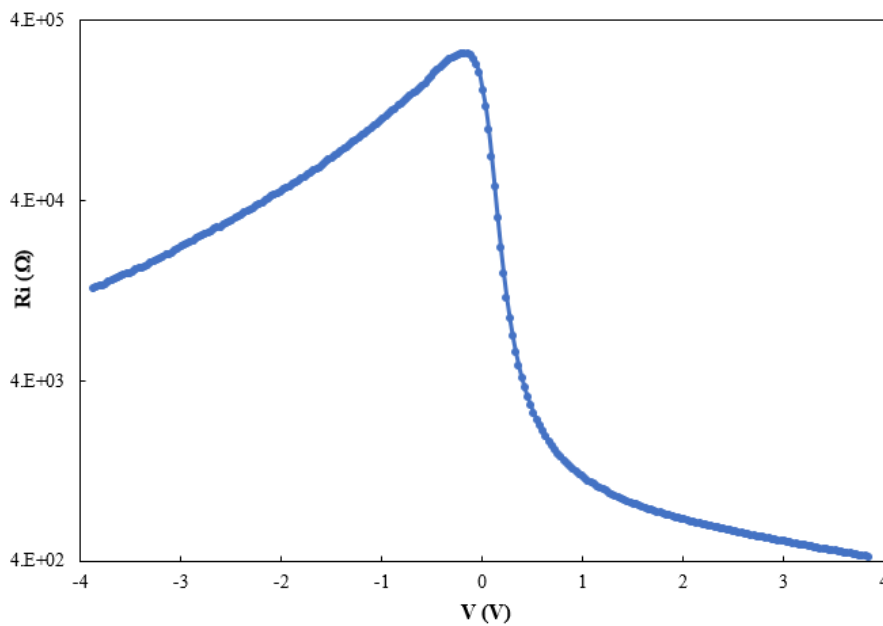
***Figure 2**. The (Ri)- V curve of the Al/(Ti:DLC)/P-Si/Au SBD*

Figure 2 illustrates, the R_i beginning as almost constant both the higher forward and reverse voltages, and so corresponds actual values of R_s (=407Ω) and R_{sh} (=11800Ω). To see the voltage/method dependent of them (n, Φ_{Bo}, and R_s), they were also calculated from Cheung's functions and it allow us to calculate in the

descending curve of the $\ln(I_f)$-V_f plot at moderate- forward-voltages given in Eq. 2(a) and (b). As shown in Figure 3, both $dV/d\ln(I)$ and $H(I)$ versus V curves have excellent linear in large range of current/voltage (Cheung & Cheung, 1986).

$$\frac{dV}{d\ln(I)} = \frac{nkT}{q} + R_S I \tag{3a}$$

$$H(I) = V - \frac{nkT}{q} . \text{Ln} \left[\frac{I}{T^2 A^* A} \right] = R_S I + \Phi_{B0} n \tag{3b}$$

From Eq. 3(a), the intercept voltage and slope (Figure 3) is given the nkT/q and Rs. The intercept and slope of the Eq. 3(b) by using the n value (=intercept/(kT/q)) is also given the $n\Phi_B$ and R_s as directly. Thus, R_s and n were determined as 324 Ω and 12.65 from Eq-3(a) and Rs and Φ_B are 293Ω and 0.486eV, respectively. The voltage dependence and calculation method lead to some discrepancies between TE and Cheng Functions. Because, whereas the TE theory is valid at moderate forward-voltages. Cheung functions are valid at high forward voltages.
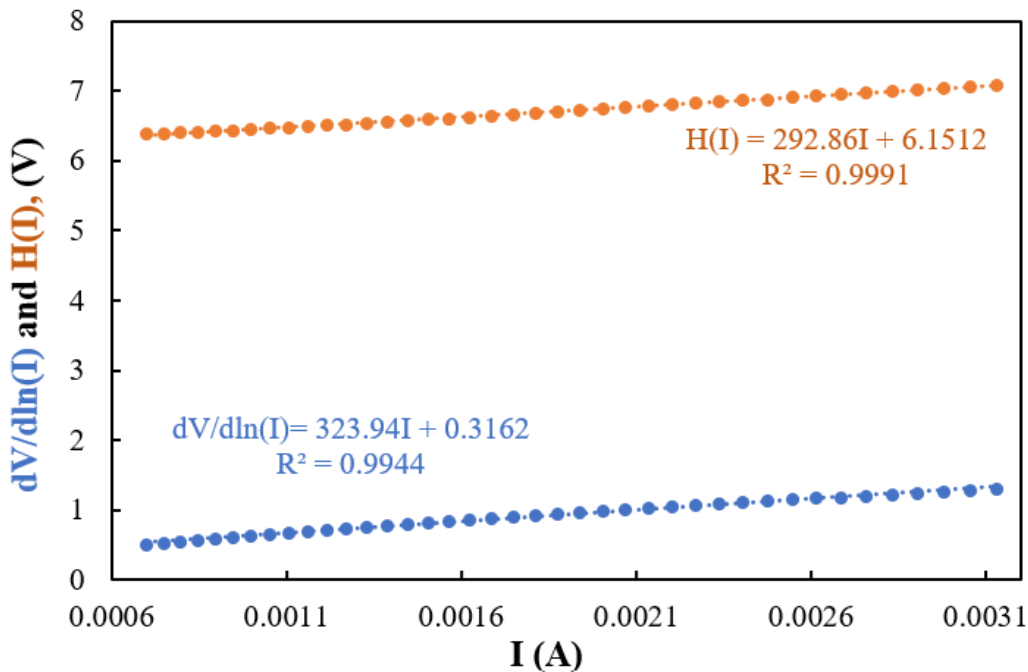
Figure 3. The $dV/d\ln(I) - I$ and $H(I) - I$ curves of the Al-(Ti:DLC)-pSi-Au SBD

To calculate the possible conduction mechanisms (CMs) in region of I_f-V_f graphic with a double-logarithmic scale were drawn in the forward bias regime (Figure 4). In this Figure $Ln(I_F)$–$Ln(V_F)$ curev of the SBD has three linear-regions with unlike slopes because of the present changes in the form $I \propto V^m$ (Sze & Ng, 2006; Sharma & Tripathi, 2013; Demirezen et al., 2022). which are associate to low, inter-mediate in addition to at enough high voltages. The slope of them were found as 1.279, 3.141, and 1.796, respectively and so we can say that in lower-voltages Ohmic-behavior, in moderate-voltages, trap-charge limited current (TCLC), at high forward voltages, space-charge limited current (SCLC) are dominate CMs, respectively. Because, Ohm's law appears to be effective in first-region, with slope closes ~1. The TCLC is effective when slope higher than 2, and SCLC is effective when the slope is closer ~2.

Each of the existence of N_{ss} between interlayer and semiconductor interface is too more influential on the moderate voltages I-V properties and they often formed when the surface periodic lattice was interrupted, preparation for cleaning and manufacturing, doping donor/acceptor atoms, impurities and other organic contaminations in laboratory environment. Based on Card-Rhoderick (Card & Rhoderick, 1971; Sze & Ng, 2006), n value becomes more than unity for SDs with N_{ss} that is equivalent to semiconductor (if inter-layer is more than a few nm), and is given as follow:

$$n(V) = \frac{q}{kT}\frac{dV}{dln(I)} = 1 + \frac{d_i}{\varepsilon_i}\left[\frac{\varepsilon_s}{W_D} + qN_{ss}(V)\right] \qquad (4a)$$
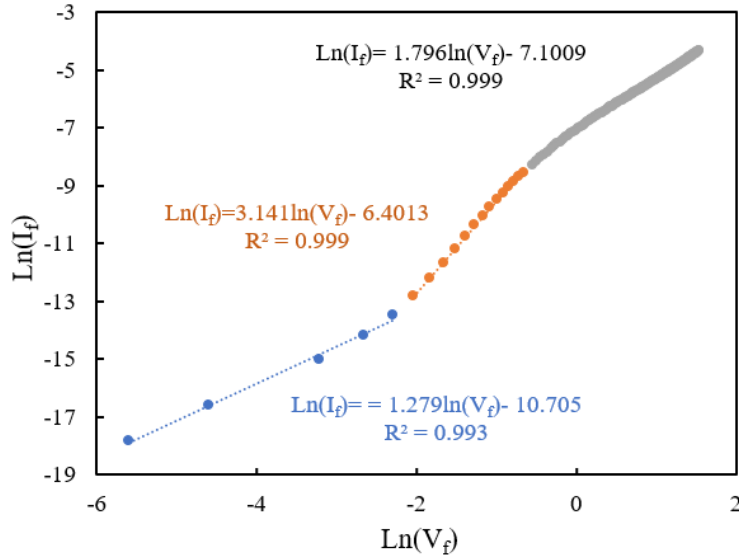
Figure 4. *The Ln(I_F) and Ln(V_F) curves of the Al-(Ti:DLC)-pSi-Au SBD*

Here, the values of $\varepsilon_i / \varepsilon_s$, W_D, and d_i are the dielectric permittivity of the inter-layer and semiconductor, width of the depletion layer, the inter-layer thickness, respectively. The magnitude of εi and ε_s was taken as $113\varepsilon_o$ and $11.8\varepsilon_o$. Here, (ε_o = permittivity of vacuum). As a result, the energy-dependent N_{ss} profile in relation towards the highest region of the valance-band (E_v) is as below. (Card and Rhoderick, 1971; Sze & Ng, 2006).

$$E_{ss} - E_v = q(\Phi_e - V) \qquad (4b)$$

In Eq.4, $\Phi_e(V)$; V-dependence BH. The N_{ss}- (E_{ss}-E_v) plot was obtained by using following relation suggested by Card-Rhoderick (Card & Rhoderick, 1971) is shown in Figure 5.

$$N_{ss}(V) = \frac{1}{q}\left[\frac{\varepsilon_i}{\delta}(n(V) - 1) - \frac{\varepsilon_s}{W_D}\right] \qquad (4c)$$

From Figure 5, the N_{ss} increases at about from mid bandgap of semiconductor (~Eg/2) towards top of E_v as exponentially which means they range from 6.42×10^{12}/(eVcm²) at (0.6263-E_{ss}) eV to 5.92×10^{13}/(eVcm²) at (0.385-E_{ss}) eV which are suitable for MIS type SBD.
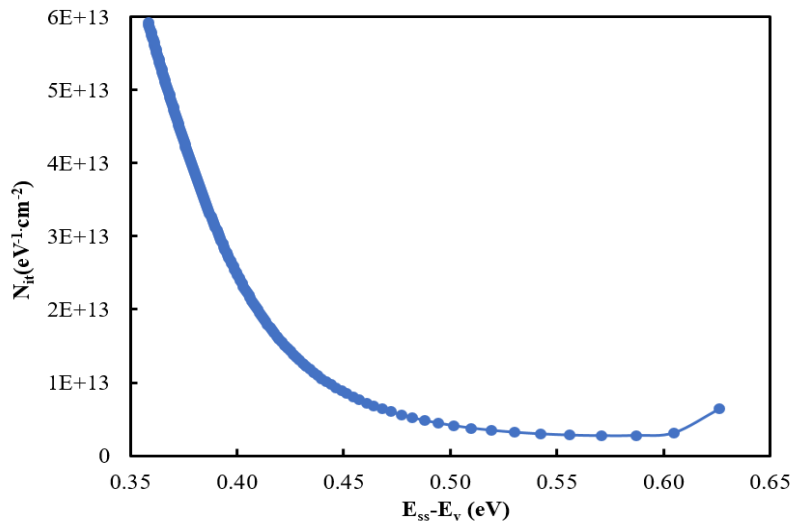
Figure 5. *The Nss- (Ess-Ev) curve of the Al-(Ti:DLC)-pSi-Au SBD*

3.2. Forward & reverse bias c/g-v characteristics

Figure 6 shows the C-V and G/ω-V graphs of the Al-(Ti:DLC)-pSi-Au SBD. As depicted in Figure 6, these two-plots have accumulation, depletion, and inversion regimes such as metal/oxide/semiconductor (MOS) structure. But, the (G/ω-V) plot, exhibits a distinctive peak at ~0.8 V as a result of a special arrangement of N_{ss} between (Ti:DLC)/P-Si interface (Sze & Ng, 2006; Cheung & Cheung, 1986). The R_s has also increased effectiveness on each of the C-V and G/ω-V curves like I-V at enough high positive voltages. R_s value are usually derived from the back and Schottky contacts, the cables used for the probe from rectifier contact, the semiconductor bulk-resistivity, and in-homogeneities of the doping concentration atoms (Sze & Ng, 2006; Cheung & Cheung, 1986; Nicollian & Brews, 1982; Reddy et al., 2022). But, N_{ss} are usually originated from are interruption in the periodic lattice of the semiconductor-surface, cleaning, fabrication-processes, and some contaminates in the bulk semiconductor, within the confines of a laboratory (Sze & Ng, 2006; Cheung & Cheung, 1986; Reddy et al., 2022; Ulusoy et al., 2023; Sharma & Tripathi, 2013).
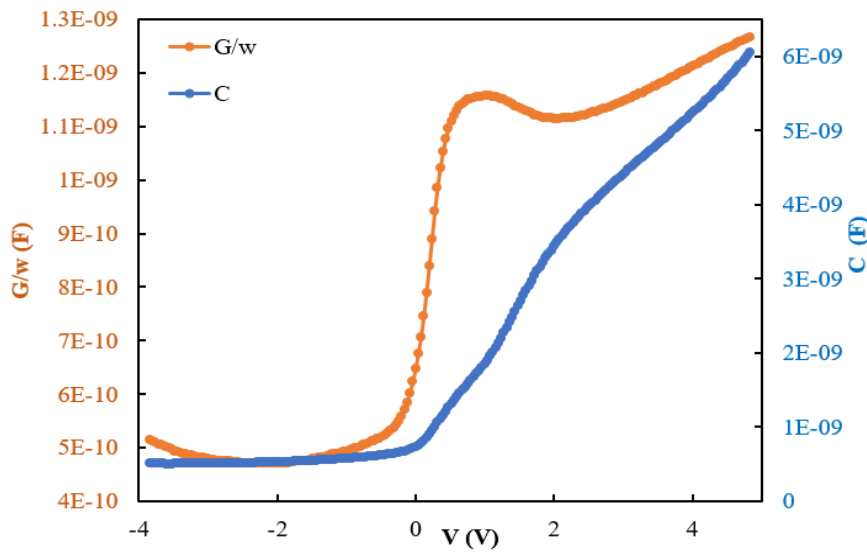
Figure 6. The C-V and G/ω-V curves of the Al-(Ti:DLC)-pSi-Au SBD

In order to investigate the voltage dependent resistance (R_i) on the $C-V$ and $G/\omega-V$ graphs of Al-(Ti:DLC)-Psi-Au SBD, it was derived from these values by using Nicollian-Brews technique by applying the following relation which is presented in Figure 7. (Nicollian & Brews, 1982).

$$R_i (V) = G_{mi} /[(G_{mi}^2+(\omega C_{mi})^2)] \tag{5}$$
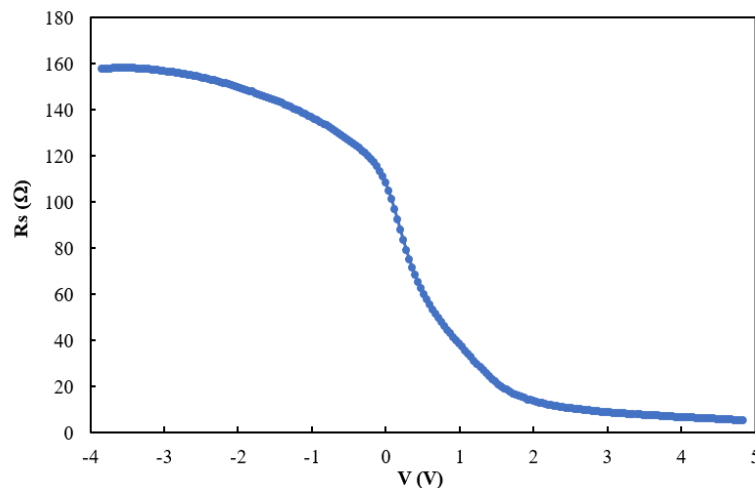
Figure 7. The $R_s - V$ plot of the Al-(Ti:DLC)-pSi-Au SBD

In Eq.5, C_{mi} is the capacitance, G_{mi} is the conductance which calculated for a bias voltage, ω refers to angular frequency and it's equal to $(2\pi f)$. As depicted in Figure 7, the Ri quantity reduces with increasing voltage before reaching a nearly constant value (5.29) at accumulation regime which is identical to the actual value of Rs. This is considerably suitable for MIS type SBD. The effect of Rs can be minimized when The impedance-measurements carried out at low frequency or adjustable of them at sufficient frequencies ($f \geq 500$ kHz) to eliminate Rs influence on them. To view the Rs influence on this high frequency C−V and G−V graphs of the Al-(Ti: DLC)-Psi-Au SBD, they fixed by utilizing the value of Rs as given next relations and then both the measured and corrected Cc/V and Gc/V plots are presents in the Figure 8 a) and b), respectively (Sze & Ng, 2006; Cheung & Cheung, 1986).

$$C_c = \frac{[G_{ma}^2 + (\omega C_{ma})^2]C_{ma}}{a^2 + (\omega C_{ma})^2} \tag{6a}$$

$$G_c = \frac{[G_{ma}^2 + (\omega C_{ma})^2]a}{a^2 + (\omega C_{ma})^2} \tag{6b}$$

In Eqs-6(a, b); ($a = G_{ma} - [G_{ma}^2 + (\omega C_{ma})^2]R_s$) is a correction-coefficient. When the corrected plots were represented in Figure 8 and Figure 9. When these fixed Cc-V and Gc/-V plots compared the calculated C_m−V and G_m/ω−V plots (Figure 8); there is an important discrepancy between of them in reverse-bias region, but the Cc starts to increase both in depletion and accumulation region. While G_c/ω−V plot has a recognizable peak at 0.8V. Therefore, we show that Rs especially is more efficient at accumulation-region, while N_{ss} are efficient in depletion-region. Recently, similar findings for MIS type structures have been also documented in the literature (Sze & Ng, 2006; Nicollian & Brews, 1982; Demirezen et al., 2022).
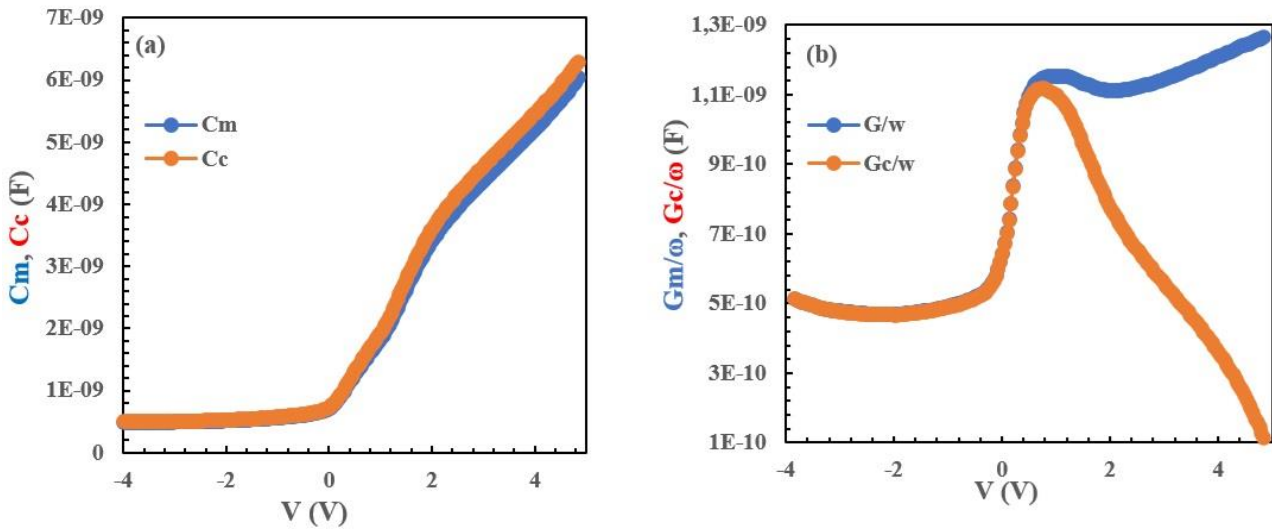

Figure 8. a) The C_m-V and Cc-V, b) G_m/ω-V and Gc/ω-V curves of the Al-(Ti:DLC)-pSi-Au SBD at 1MHz

The depletion-layer capacitance (C) for MIS type SBDs is given as follows (Sze & Ng, 2006).

$$C = \frac{|\partial Q_{SC}|}{\partial V} = \sqrt{\frac{q\varepsilon_s\varepsilon_0 N_A}{2\left(V_o - V - \frac{kT}{q}\right)}} \tag{7a}$$

Eq. 7(a) can be arranged as follows for the extraction of fundamental electrical characteristics of the MIS-structures in the region of reverse bias as given follow.

$$C^{-2} = \frac{2\left(V_o - Vr - \frac{kT}{q}\right)}{q\varepsilon_s\varepsilon_0 N_A} \tag{7b}$$

Here, V_o is intercept-voltage of (C^{-2}-V) graph, the V_D value (diffusion potential) is obtained from ($V_D = V_o + kT/q$). The total number of N_A was extracted from the slope of C^{-2}-V curve (Figure 9):

$$N_A = \frac{2}{q\varepsilon_s\varepsilon_o A^2\left(\frac{dC^{-2}}{dV}\right)} \tag{7c}$$

$$y = -2.81E{+}18x + 1.83E{+}18$$
$$R^2 = 0.99$$
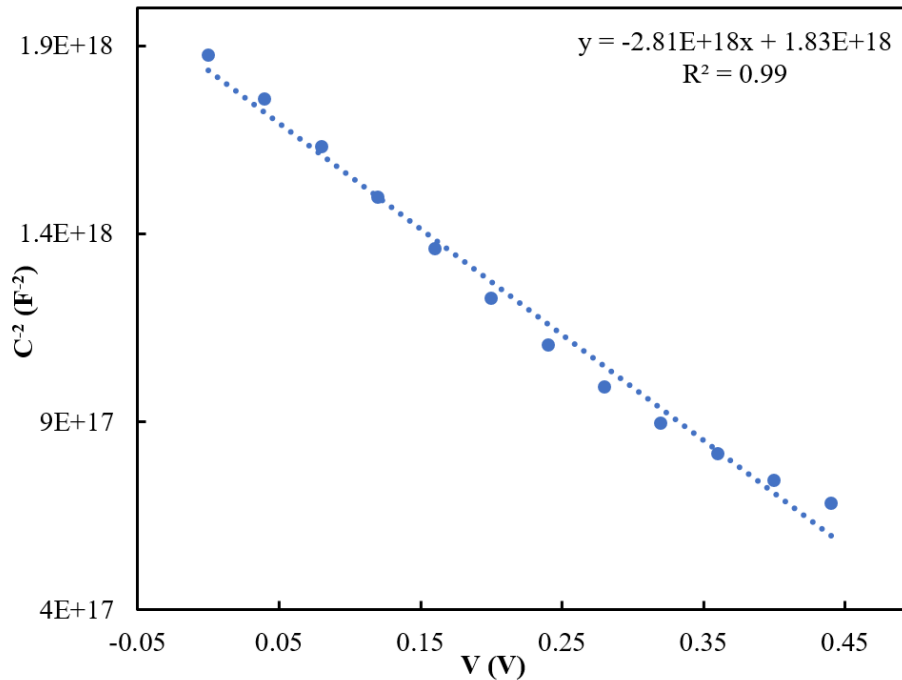
Figure 9. *The C^{-2} - V curves of the of the Al-(Ti:DLC)-pSi-Au structure SBD*

Following relations used to calculate some basic electrical parameters such W_D, E_F, and Φ_B (CV), this values obtained through the use of intercept-voltage (Vo) and $(1/C^2$-V) slope, respectively (Sze & Ng, 2006; Reddy et al., 2022).

$$W_D = \sqrt{\frac{2\varepsilon_s\varepsilon_0 V_o}{qN_D}}, \qquad E_F = \left(\frac{kT}{q}\right)Ln\left(\frac{N_c}{N_D}\right) \qquad \text{and} \quad \Phi_{B(CV)} = V_0 + \frac{kT}{q} + E_F \tag{8}$$

Thus, the V_o, N_A, W_D, E_F and Φ_B(CV) values were calculated as 0.651 V, 6.90×10^{16} cm^{-3}, 11.10×10^{-6}cm, 0.133 eV, and 0.89 eV, respectively. Estimated amount of BH from the intercept of C^{-2}-V plot (Φ_B(CV)=0.89 eV is lower than that observed from forward bias plot ln(I)-V plot (Φ_{Bo}(IV)=0.64 eV) at about the value of E_F. The Φ_B(CV) and (Φ_{Bo}(IV)) differences related to the nature of measuring systems which are associated to forward & reverse voltages. That is the apparent BH from the semiconductor to the metal is always at about E_F smaller than the BH they from the metal to the semiconductor. Recently, some basic electrical parameters of the MIS type SBD$_S$ were obtained from TE theory and Cheung functions by various researchers as given in the Table 1. The observed some discrepancies between these parameters are the result of different calculated method and voltage dependent of them. On the other hand, the observed higher value of n can be explained by the existence of interlayer and surface states, doping concentration of acceptor atoms, and barrier inhomogeneity.

4. CONCLUSION

Within this study, Al-(Ti: DLC)-pSi-Au (SD) was fabricated instead of normal MS and MIS type SDs and then it's some main electrical-parameters n, Φ_B, R_s, R_{sh}, N_a, and W_d which has been derived from the I-V and C/G-V measurements by various calculation- techniques. The I_F-V plot shows good linear behavior at lower voltages and then deviated linear case due to effect of Rs and polymer/organic interlayer. On the other hand, ln(I_F)-ln(V_F) plot shows three different linear regions with different-slopes (1.28, 3.14, and 1.79) at low, intermediate and high bias voltages. These regions are corresponding to the Ohmic, TCLC, and SCLC, respectively. Energy dependent profile of N_{ss} located between (Ti: DLC) and p-Si was extracted by using the Card-Roderick method by taken into account voltage dependence of n and Φ_B and they were grown from the midgap towards the top of Ev of semiconductor. Voltage-dependent profile of Ri is also determined by Ohm-Law and Nicollian-Brews method to observe the impact of Rs on the I−V and C/G−V characteristics at 1 MHz. Several important electrical-characteristics like n, Φ_B, and Rs values were derived from forward bias I-V

measurements with using theory of TE and Cheung-functions show some inconsistency as a result of the calculating procedure and voltage-dependent of them. The Φ_B value resultant from the C^{-2}-V graphs is larger than the forward I-V measurements as nearly Fermi level (E_F) is also a result measured method. All findings indicate that the created Al-(Ti:DLC)-pSi-Au (SD) may successfully replace traditional MS or MIS type SDs in terms of economical in cost, flexibility, and easy grown method without more energy consumption.

Table 1. Some basic electrical parameters of the Al-(Ti:DLC)-pSi/Au SBD obtained from various methods.

Symbol	This work	Zeyrek,S. (2015)	Güçlü, Ç.Ş. (2023)	Doğan,H. (2022)	Yerişkin, S.A., et al. (2017)
n	1.89 (TE) 12.6 (Cheung)	6.17 (TE) 6.91 (Cheung)	2.348	1.27	1.464
Φ_{Bo} (eV)	0.64 (TE) 0.486 (Cheung)	0.714 (TE) 0.66 (Cheung)	0.576	0.82	0.790
R_s ($\square$)	407 (TE) 308.5 (Cheung)	448.5 (Cheung)	-	9.3 (Cheung)	530
R_{sh} (M$\square$)	0.0118	-	-	-	512
w_d (cm)	11.1x10^{-6}	-	-	-	-

ACKNOWLEDGEMENT

AUTHOR CONTRIBUTIONS

In this article, the contributions of the authors are equal.

CONFLICT OF INTEREST

The authors declare no conflict of interest.

REFERENCES

Berkün, Ö., Ulusoy, M., Altındal, Ş., & Avar, B. (2023). On frequency and voltage dependent physical characteristics and interface states characterization of the metal semiconductor (MS) structures with (Ti:DLC) interlayer. *Physica B: Condensed Matter*, 666, 415099. https://doi.org/10.1016/j.physb.2023.415099

Card, H. C., & Rhoderick, E. H. (1971). Studies of tunnel MOS diodes I. Interface effects in silicon Schottky diodes. Journal of Physics D: *Applied Physics*, 4(10), 1589-1601. https://doi.org/10.1088/0022-3727/4/10/319/meta

Cheung, S. K., & Cheung, N.W. (1986). Extraction of Schottky diode parameters from forward current-voltage characteristics. *Applied physics letters*, 49(2), 85–87. http://dx.doi.org/10.1063/1.97359

Demirezen, S., Altındal, Ş., Kalandaragh Y. A, & Akbaş, A. M. (2022). A comparison of Au/n-Si Schottky diodes (SDs) with/without a nanographite (NG) interfacial layer by considering interlayer, surface states (Nss) and series resistance (Rs) effects. *Physica Scripta*, 97(5), 055811. https://doi.org/10.1088/1402-4896/ac645f

Dogan, H. (2022). Parameter estimation of aı/p-si schottky barrier diode using different meta-heuristic optimization techniques. *Symmetry*, 14(11), 2389. https://doi.org/10.3390/sym14112389

Güçlü, Ç. Ş. (2023). A Comparison Electronic Specifications of the MS & MPS type Schottky Diodes (SDs) via Utilizing Voltage-Current (V-I) Characteristics. *Gazi University Journal of Science Part A: Engineering and Innovation*, 10, 62-69. https://doi.org/10.54287/gujsa.1212696

Lin, Y., Weng, C., Lin, Y., Shiesh, C., & Chen, F. (2013). Effect of C content and calcination temperature on the photocatalytic activity of C doped TiO$_2$ catalyst. *Separation and Purification Technology*, 116, 114 –123. https://doi.org/10.1016/j.seppur.2013.05.018

Nicolian, E. H., & Brews, J. R. (1982). Metal oxide semiconductor MOS physics and technology. *A Wiley Interscience Publication*, 495-502.

Reddy, N. N. K., Vattikuti, S. V. P., Verma, V. K., Singh, V. R., Alhammadi, S., Kummara,V.K., Manjunath, V., Dhanalakshmi, M., & Reddy,V. R. M. (2022). Highly sensitive and cost-effective metal-semiconductor-metal asymmetric type Schottky metallization based ultraviolet photodetecting sensors fabricated on n-type GaN. *Materials Science in Semiconductor Processing*, 138, 106297. https://doi.org/10.1016/j.mssp.2021.106297

Sharma. M., & Tripathi, S. K. (2013). Analysis of interface states and series resistance for Al/PVA:n-CdS nanocomposite metal–semiconductor and metal–insulator–semiconductor diode structures. *Applied Physics A*, 113, 491-499. https://doi.org/10.1007/s00339-013-7552-3

Sze, S. M., & Ng, K. K. (2006). Physics of Semiconductor Devices. New York, John Wiley & Sons, Inc.

Ulusoy, M., Badali,Y., Pirgholi Givi, G., Azizian Kalandaragh,Y., & Altındal, Ş. (2023). The capacitance/conductance and surface state intensity characteristics of the Schottky structures with ruthenium dioxide-doped organic polymer interface. *Synthetic Metals*, 292, 11343. https://doi.org/10.1016/j.synthmet.2022.117243

Yerişkin, S. A., Balbaşı, M., & Orak, İ. (2017). The effects of (graphene doped-PVA) interlayer on the determinative electrical parameters of the Au/n-Si (MS) structures at room temperature. *Journal of Materials Science: Materials in Electronics*, 28, 14040–14048. https://doi.org/10.1007/s10854-017-7255-1

Zeyrek, S. (2015).The effect of interface states and series resistance on current-voltage characteristics in (MIS) Schottky Diodes. *Afyon Kocatepe University Journal of Science & Engineering*, 15(2), 021101, 1-9. https://doi.org/10.5578/fmbd.9657

A Conceptual Model to Measure Digital Maturity Level in Electricity Distribution Companies

Ezgi AVCI[1*] (iD)

[1] Applied Data Science Department, TED University, Ankara, Türkiye

Keywords	Abstract
Digital Maturity Assessment Conceptual Model Technology Adoption Digital Transformation	Digitalization, while being one of the primary objectives in today's business world, increases its significance with technological advancements. Recently, there has been a need for tools to determine the levels of digitalization within certain standards and metrics for companies seeking to understand and accelerate their digitalization process, and to determine how these companies should proceed to address their shortcomings. When specifically looking at electricity distribution companies, the technological advancements such as distributed production, storage, and electricity vehicles make the digitalization process not just a choice but a necessity to operate distribution systems reliably and effectively. This study proposes a conceptual model specifically for electricity distribution companies for the first time, by researching digital maturity models developed for other sectors in the literature.

1. INTRODUCTION

The development of computer and software technologies and their increased mobile usage have transformed data storage and processing from a significant problem into a structure that can be used as meaningful wholes, influencing processes and creating autonomous decision support mechanisms. Tasks previously recorded in human brains and on paper are now being performed based on computers and networks, making them fast and easily accessible by many users at the same time (Bharadwaj et al., 2013). The widespread use of sensor and data storage technologies, as costs have decreased, has accelerated the processes of data acquisition, monitoring, analysis, and storage. Consequently, data is utilized more effectively, the efficiency of processes and decision support systems is increased, and the transition to autonomous processes is becoming more widespread (Westerman et al., 2011; Majchrzak et al., 2016; Kraus et al., 2021; Vial, 2021).

Digitalization can be defined as organizations integrating the technological advancements in information and data management into their structures, both infrastructurally and culturally. As such, digitalization remains a paramount objective in today's business world, increasingly gaining importance with each passing day and technological development (Dahlström et al., 2017; Zaoui & Souissi, 2021). It has been clearly observed that companies investing in digitalization in the industrial and service sectors have a competitive advantage in the market over those who do not prioritize digitalization (Matt et al., 2015; World Economic Forum, 2018).

Recently, there has arisen a need for tools that can determine at what levels companies stand in terms of digitalization, within certain standards and metrics, and how these companies should proceed to address their deficiencies (Karimi & Walter, 2015; Svahn et al., 2017; Feliciano-Cestero et al., 2023). Hence, concepts like digital maturity level or digital maturity index have emerged. The digital maturity level describes a company's

or institution's competencies and deficiencies in the area of digitalization, based on specific metrics, and various methods are employed to determine this level (Perera et al., 2023).

As the fundamental building blocks of digitalization, developments in information, communication, and sensor technologies have greatly facilitated the processes of data collection, transmission, and processing across nearly all sectors, especially distribution systems, making it much easier than in the past. Primarily, technology adaptation has accelerated the digitalization of existing analog/manual processes and the widespread implementation of IT-OT interactive systems such as telemetry (Agarwal et al., 2010).

When looking specifically at electricity distribution companies; unlike other sectors, technological advancements such as distributed production, storage, and electricity vehicles have made the digitalization process not just an option but a necessity for operating distribution systems in a reliable and effective manner (Leroi & Martynov, 2020). Furthermore, determining the level of digitalization in the electricity distribution sector in Türkiye will also be quite beneficial in terms of creating regulations that will affect financials.

The main question addressed by this research focuses on assessing the level of digitalization within companies, particularly in the context of electricity distribution companies. We investigate how digital maturity can be measured, the impact of digitalization on operational efficiency, and the competitive advantage it may provide. The hypothesis involves a positive correlation between a company's level of digitalization (digital maturity) and its operational effectiveness, efficiency, and competitive stance in the market.

The primary aim is to develop a specialized digital maturity model that is specifically tailored to the electricity distribution sector, enabling a thorough assessment of digital maturity levels within this field. This model seeks to bridge the identified gap in both academic and industry literature, where there is a noticeable lack of comprehensive frameworks for accurately gauging the digital advancement of electricity distribution companies. Furthermore, the research endeavors to facilitate benchmarking by providing a standardized framework that will allow these companies to measure their digital maturity against recognized industry best practices and standards. Collectively, the manuscript underscores the necessity of a robust, actionable, and sector-specific framework that is essential for electricity distribution companies to effectively evaluate and enhance their digital maturity, which is increasingly vital for their adaptation to the rapidly evolving digital landscape.

The structure of the paper is organized as follows: In Section 2 we conducted a thorough literature review of existing studies on digital maturity models, highlighting the gap in research regarding electricity distribution companies. In Section 3 we present the conceptual framework in which we discuss the theoretical underpinnings of digital maturity and its relevance to the electricity distribution sector. In Section 4 methodology is provided with a detailed explanation of how the digital maturity model was developed, including research design, data collection, and analysis methods. In Section 5 we present the proposed conceptual model, including its components, metrics, and the rationale behind its structure, Description of the methodology used to assess digital maturity within electricity distribution companies, including both self-assessment and expert evaluation processes. In Section 6 we discuss potential limitations and challenges of the proposed model and then provide suggestions for future research to refine and validate the model, as well as its application to other sectors or in different regulatory environments. In Section 7 we give a summary of the study's contributions to the field, the significance of the findings, and the potential impact on the electricity distribution sector.

2. DIGITAL MATURITY IN THE ELECTRICITY DISTRIBUTION SECTOR

The digital world has three main components: (1) Data: Digital information (2) Analytics: The use of data to produce useful information and insights (3) Connectivity: The transfer of data between people and devices via digital communication networks (IEA, 2017). Higher-level digital transformation is achieved through developments in these three areas; namely, the increase in data volume thanks to the decrease in sensor and data storage costs, rapid development in advanced analytics and scientific computing, and greater connectivity with faster and cheaper data transmission.

Digital maturity is a concept that demonstrates an institution or company's capability to effectively compete in an increasingly digital environment. Although the foundation of digital maturity is the integration of new technologies, this definition alone is insufficient. Digital maturity goes beyond simply applying new technology; it changes the company's strategy, workforce, culture, technology, and organizational structure to meet the digital expectations of customers, employees, and business partners. Therefore, digital maturity is a continuous adaptation process to a changing digital landscape. (Haryanti et al., 2023)

Digital Maturity Level (DML) measures an organization's flexibility in adapting to this process. DML is a concept that describes the competencies and deficiencies of a firm or institution in terms of digitalization based on certain metrics, and various methods are used to determine it. It turns out that digitalization is not only about technology but is a more comprehensive concept that includes factors such as data analysis, customer satisfaction, corporate culture, and employees' competencies (Schumacher et al., 2016). The perspective of company managers on the digitalization process, the company's future strategies, employees' competencies regarding digital integration, technological investments, and company culture are also factors that determine the company's level of digital maturity.

Digital technologies have been contributing to the development of energy systems for a long time. In fact, the energy sector is among the first sectors to adopt large-scale information technologies compared to other sectors. In the 1970s, electricity companies became digital pioneers by using information and communication technologies to facilitate the operation and management of electricity grids. Since the production and consumption of electricity must be balanced instantaneously, real-time monitoring and optimization at each production, consumption, and transportation (transmission, distribution) point have an efficiency-increasing effect. Today, electricity markets serve many customers spread over extensive geographic areas and are monitored and controlled instantaneously.

Investments in digital technologies by energy companies have increased rapidly in the last five years. The transformation processes experienced in this rapid development sometimes lead to the misconception that digitalization is merely the application of technology and the forgetfulness that digitalization actually means the integration of technology into innovative strategies, products, processes, and customer experiences to achieve growth and efficiency. Therefore, a significant part of the digitalization practices of distribution companies have remained only as the replacement of existing technologies, the transfer of analog/manual processes to digital platforms without changing the current ways of doing business, or the faster proliferation of operational technologies such as SCADA. However, the goal of becoming a digital company requires a major transformation both internally and externally. The future of the electricity distribution sector lies in adapting to digital technologies. Thus, an efficient, low-cost, sustainable, and flexible structure will be obtained. The digital transformation process in the electricity distribution sector requires new infrastructure and technology investments. Rapidly increasing electricity demand, transmission, and distribution losses, and unexpected grid outages appear as prominent challenges. In this process, in addition to technological infrastructure, training employees on the subject and investments in cybersecurity are of critical importance.

There are some steps that the electricity distribution sector must follow on the path to digital maturity. Analytical models are needed to determine the balance of the production portfolio. These models should aim for maximum economic benefit with minimum cost and CO_2 emissions. Production and demand forecasts based on the power source should be made depending on the weather. Considering the technological trends in the sector, the necessity of automating devices with analytical models emerges. Information technology and operational processes are now intertwined. In parallel, smart meters and distributed production should be designed with smart grids. Equipment should be able to supply electricity quickly and flexibly. Problems and interruptions experienced by consumers should be quickly identified. Thefts can be detected with analytical models, and losses can be reduced with real-time line voltage optimization (Annunziata & Bell, 2015).

Efficient control of distributed production areas, such as rooftop solar power plants and electricity vehicles, which can be used on both the demand and production sides, is crucial. Thus, peak demand can be reduced. Energy consumption should become more transparent, and everyone should be able to compare their consumption accordingly. This can lead to progress in consumption habits in terms of energy efficiency. Electricity prices and tariffs can change according to consumption. Demand-side participation should be

initiated. Smart homes should be activated with remote control. Electricity sector companies may partner with technology companies. Equipment maintenance should be determined based on optimization results. Companies will now be those that communicate with customers and guide them regarding energy consumption. There should be a digital platform where people can share innovative ideas (Annunziata & Bell, 2015).

3. CONCEPTUAL FRAMEWORK

3.1. International Studies

Numerous studies have been conducted internationally to determine levels of digital maturity, and it is often seen that global consulting firms are leading these projects. The digital maturity model created by the collaboration of Google and Boston Consulting Group (BCG) classifies companies into four categories according to their maturity levels (Corr, 2022). The identified four classes, in ascending order of digitalization level, are: beginners, developing, effectively using digitalization, and companies that elevate digitalization to the highest level in a multi-resource manner. Companies at the highest level effectively use all data and can offer personalized solutions to customers and employees.

Deloitte has developed a digital maturity methodology applicable to all sectors (Deloitte, 2018). Deloitte's general digital maturity model is categorized under five main headings: customer, strategy, technology, operations, organization, and culture. Under these main headings, sub-headings have been identified for more detailed analysis. For example, under the customer category, there are sub-headings like customer experience, and under the technology category, there are data and analytics, with a total of 28 sub-headings identified. The digital maturity for each title has been measured separately. Finally, a guide is provided for actions to be taken for the measured digital maturity level.

The Forrester Digital Maturity Model 4.0 stands out with the company's continuous comparison with other firms (Gill & Van Boskirk, 2016). They define the digital maturity level on four different axes and run a scoring system out of 84 through surveys. These axes are culture, technology, organization, and insights. According to the results of the scores, they classify companies into four different groups. These are defined as skeptics, adopters, collaborators, and differentiators. The behaviors, strategies, and score ranges of companies with different maturity levels are given in Table 1.

Table 1. Forrester digital maturity classification

Maturity Segment	Characteristic Behavior	Strategy	Score Range
Differentiator	Consistently exhibiting excellence	Systematization of best practices	75 – 84
Collaborator	Cooperative but not using insights	Adopting advanced analytics applications	57 – 74
Adopter	Stuck in traditional practices	Focusing on current digitalization efforts	34 – 56
Skeptic	Rejecting digitalization	Reflect	0 – 33

McKinsey offers its measurements as a service without making them public. It presents the measurement results as Digital Quotient to companies. It offers 6 building blocks to being a digital company: strategy and operation, understanding customer decisions, process automation, organization, technology, data, and analytics (Catlin et al., 2015; Dahlström et al., 2017).

The Open Digital Maturity Model prepared under the leadership of Huawei aims to provide community users with the opportunity to measure the digital maturity levels of their companies themselves and aims to gain an advantage in terms of popularity because it does not charge for this (Open Roads Community, 2020). The greater the number of companies reached, the more valuable the results will be as it means a healthier comparison. The Open Digital Maturity Model calculates a digital maturity index by evaluating approximately 140 metrics in six different titles out of 10. Each metric's own weight is also calculated by the model owners. The titles of the metrics are as follows: strategic dynamism, customer focus, digital culture, innovation and lean delivery, big data and artificial intelligence, and finally technology leadership.

Price Waterhouse Coopers (PwC) addressed digitalization in distribution companies in its 2015 report (PwC, 2015). The report presents the results of surveys about digitalization conducted with managers in distribution companies. As the building blocks of digitalization; data and IT infrastructure, organization and governance, digital culture, and change management have come to the forefront. Especially abroad in the energy sector, since data-orientedness already exists, data analytics opportunities have been seen as opportunities that can be implemented more quickly, but new business models (smart homes, etc.) have been seen as concepts that can be implemented later. An increase in complexities in business models and data structures is definitely expected. Distribution companies still do not use an open data approach and do not plan to use it in the near future.

Under the leadership of the German National Academy of Science and Engineering (Acatech) and with contributions from many stakeholders, the Industry 4.0 Maturity Index study was conducted in the 2016-2017 period to help companies manage their digital transformations (Schuh et al., 2018). The methodology identifies four main categories (resources, information systems, organizational structure, and company culture) and five functional areas (development, production, logistics, services and marketing&sales) to help show at what levels digital maturity is in different areas. Each category receives a score between 1 and 6 according to the criteria determined.

The Growth Hub, supported by the European Regional Development Fund (ERDF), has developed the Digital Maturity Index methodology to help create a digitalization roadmap for small and medium-sized enterprises, especially to keep up with the rapidly growing digital economy (Growth Hub, 2019). Digital maturity is evaluated in six main categories; strategy and company culture, technology and cybersecurity, marketing, finance and operations, R&D and innovation, and sales.

CISCO and the International Data Corporation (IDC) have collaborated on a project to calculate the Digital Maturity Index for SMEs in 14 countries in Asia (CISCO, 2019). For this, a survey was prepared and a total of 1,340 SMEs from different sectors participated in the survey. The digital maturity index was developed based on the responses of these firms and benchmark analysis. The methodology identified four main categories; strategy and organization, process management, technology, human resources, and skills.

Deloitte Europe; Middle East and Africa (EMEA) has conducted a study to measure the Digital Maturity levels of companies in the finance sector. With a survey conducted on a total of 8274 banks, benchmark analysis was performed (Deloitte Digital, 2018). The study, which evaluates the finance sectors of countries according to digital maturity in four categories, placed Türkiye in the highest category.

A market research company, Forrester, has developed a digital maturity survey, which has been completed by over 350 finance sector companies through Akamai. Thus, Akamai offers services to companies to determine the level of digital maturity and identify the steps in this path (Akamai, 2018). When determining the digital maturity level, priority was given to the use of online channels, user experience, and cybersecurity issues specific to the finance sector. The assessment of the digital maturity index is made under 5 main headings; cybersecurity, strategy, digital experience, cloud solutions, and technology.

The UK government is measuring how digitized the health system is and how easily processes can be performed. This aims to eliminate long paperwork and procedures (NHS, 2019). The digital maturity level is determined using a self-assessment survey methodology, and three main headings have been identified for assessment. These are; the ease and prediction ability of planning digital services, the competencies needed for digital services to support the health service, and the infrastructure that enables the use of these competencies.

PwC has developed a digital maturity model for the energy sector (PwC, 2019). As a result of a survey conducted with a total of 509 companies, benchmark analysis and digital maturity level determination have been made. The assessment was carried out over three main topics: the ability to adapt new technologies such as artificial intelligence, digital twins, cloud, blockchain; the digital ecosystem, including digital platforms, partnerships, and revenue models; and digital culture, which includes customer experience, education, and innovation. In the methodology to determine the digital maturity level, companies are evaluated out of a total

of 100 points, with 40 points from new technology adaptation, 40 points from the digital ecosystem, and 20 points from digital culture.

When looking at private sector studies, it is observed that the models developed gain meaning and find a place in the industry when used by as many companies as possible. Therefore, these models are usually developed by consulting firms that can hold the results of competitor companies and are present in the market. Most of the studies have been conducted by global consulting firms such as BCG, McKinsey, Deloitte and PwC. The digital maturity level measurement methods developed by consulting firms have usually been applied to many companies and their results have been reported, thus more visible results have been obtained. However, consulting firms also tend to develop these models independently of the industry. For this reason, models developed specifically for the electricity sector are quite limited.

3.2. Studies from Türkiye

The Informatics Industry Association of Türkiye (TÜBİSAD) measures the digital transformation in Türkiye with a methodology involving other countries (TÜBİSAD, 2023). The results are examined in four components: ecosystem, proficiency, usage, and transformation. The digital index is divided into sub-units of component, dimension, and indicator; respectively. The arithmetic average of the indicators determines the dimension score, the arithmetic average of the dimensions determines the component score, and finally, the arithmetic average of the components determines the digital index score. For example, under the usage component, there is a dimension for business world usage, and under this dimension, there is an indicator for personnel training investment. In the digital index, which is evaluated over a total of 64 indicators and on a scale of 1-5, Türkiye scored 2.94, 3.06, 3.21, 3.12 in 2019-2022. This methodology is also applied by companies abroad and the results are regularly published.

Accenture, in collaboration with Vodafone, Boğaziçi University, the Turkish Informatics Foundation, and Middle East Technical University, measured the digitalization level of various sectors in Türkiye in 2016 according to its own methodology and published the results in a report (Accenture, 2017). Accenture assessed digitalization in three main categories and ten subcategories linked to these categories. These are; digital services (industry trends and company objectives), digitized company (products and solutions, services, interaction, sales functions, and service functions), and digital operational competence (operations and processes, resources and organization, and workflow). For the digitalization index study, Accenture conducted interviews with executives from 106 companies in Türkiye. According to the results of the digitalization index, the most digitally mature sector was finance with 81%, while the least advanced sector was construction with 40%. The energy sector also received a relatively low score of 48%.

Turkish Industry and Business Association (TUSİAD) has conducted a comprehensive research study with 108 technology user companies and 110 technology supplier companies (TÜSİAD, 2017). The competence levels of technology user companies have been evaluated in 23 application areas with 118 survey questions under the titles of operational improvement, performance management, employee participation, and fundamental components. According to the research results, while the majority of companies indicate that their knowledge and interest in digital transformation in the industry are high, the proportion of companies that think they are ready for transformation is relatively lower. It is seen that industrial companies in Türkiye are still at the stage of carrying out pilot projects in digital transformation application areas. It is observed that companies, especially their digitalization strategy and roadmap competencies, are low. It appears that the competence levels of companies do not vary according to sectors. However, large-scale companies (companies with annual revenues of more than 250 million TL) have higher digital transformation competence levels in the industry compared to small-scale companies (33/100). Companies state that the biggest obstacles in front of digital transformation are the high cost of investment and the uncertainty of the return on investment.

The studies on digital maturity within Turkish firms present a comparative analysis of the progression, impact, and measurement of digital transformation across different frameworks and empirical findings. Gürder (2022) delves into the levels of digital maturity among Turkish firms, highlighting the critical nature of risk management and adaptation in the digital age. The categorization of businesses into various levels of digital maturity, such as digital champions and digital novices, underscores the varying degrees of digital integration

and data utilization across industries. In contrast, Asiltürk (2021) approaches digital maturity from a theoretical standpoint, emphasizing the need for firms to tailor their digital transformation roadmaps to their specific contexts, acknowledging that digital transformation is a relatively new and complex concept for many.

Düzcan and Fidan (2023) further this comparative analysis by examining the relationship between digital maturity and innovation performance, particularly through the lenses of big data analytical capabilities and data-driven culture. Their findings reveal the direct impact of digital maturity on innovation but also show that the expected moderating effect of a data-driven culture may not be as significant as hypothesized. This suggests that while digital maturity is crucial, the pathway to innovation may not be linear or solely dependent on cultural factors.

Nuroğlu and Nuroğlu (2018) provide a comparative study that extends beyond the Turkish context by juxtaposing the digital transformation roadmaps of Turkey and Germany. This comparative lens reveals gaps in Turkey's approach, particularly in standardization and legal infrastructure, indicating that while Turkish companies are aware of the importance of digital transformation, they may be overemphasizing investment costs at the expense of addressing broader structural issues such as data security and technical infrastructure.

Collectively, these studies provide a multifaceted comparison of digital maturity in businesses. They suggest that while there is a general movement towards digitalization, the depth of integration and strategic approach vary significantly. This variance is influenced by a range of factors including but not limited to the level of understanding of digital transformation concepts, the ability to manage and foresee digital risks, the analytical capabilities to utilize big data effectively, and the broader infrastructural and cultural readiness to implement digital changes. The comparative nature of these studies offers a comprehensive understanding of where businesses stand in terms of digital maturity and what factors contribute to their success or failure in this digital evolution.

The categories determined in digital maturity index methodologies used in international and Turkish private sector applications are summarized in Table 2.

4. METHODOLOGY

The developed models for determining the Digital Maturity Level (DML) initially aimed only to measure the economic impact of technology usage on companies. However, as digitalization has been enriched with various other topics such as customer satisfaction, information security, and the ability to make instant decisions, there has been a need for more comprehensive and detailed models. In addition to measuring the current level of digital maturity, the models are also designed to help determine a roadmap for digitalization.

This section explains the basic digital maturity models developed for DML determination in literature. The two primary types of assessment methods used in evaluating digital maturity, organizational capabilities, or performance are self-assessment and expert assessment. These methods provide insight into where an organization currently stands in a particular area and identify opportunities for improvement.

Self-assessment is a reflective process where an organization evaluates its own performance, capabilities, or maturity level based on predefined criteria. This method is introspective and relies on internal stakeholders to provide their perceptions of how well the organization is doing. Organizations typically use surveys, checklists, or assessment tools that are filled out by employees, managers, or executives. These instruments are designed to capture information about various aspects of the organization's operations and strategies. Self-assessments are usually cost-effective since they don't require external consultants. They can be done relatively quickly and can engage a broad range of employees, fostering a sense of ownership over the results and subsequent action plans. The main challenge is the potential for bias. Respondents may overestimate capabilities due to a lack of objectivity or underreport issues due to fear of negative repercussions. The quality of the results depends heavily on the honesty and self-awareness of the participants. For example, a company might use a digital maturity model self-assessment tool to determine where it stands regarding digital transformation. Employees rate their company's performance across several areas, such as digital customer experience, analytics capability, and IT infrastructure. The aggregated results give an overview of perceived digital maturity.

Expert assessment involves external professionals or consultants evaluating an organization. These experts use their specialized knowledge and experience to provide an unbiased view of the organization's performance or maturity. Experts conduct audits, interviews, and observations to collect data. They might also review documentation and processes to evaluate how the organization compares to best practices or industry standards. An expert assessment is typically more objective and can provide a fresh perspective. Experts can benchmark the organization against others in the industry and offer insights that internal staff might miss. This method can be more expensive and time-consuming than self-assessment. There's also a risk that employees may not be as forthcoming with external assessors, which can affect the quality of the data collected. For example, a financial institution wanting to improve its cybersecurity posture may hire a team of IT security consultants to conduct an expert assessment. The consultants would evaluate the bank's cybersecurity measures against regulatory requirements and industry benchmarks to identify vulnerabilities and recommend improvements.

Both assessment methods can be used together to provide a comprehensive view of an organization's status. Self-assessment can help prepare for an expert assessment, and findings from an expert assessment can be used to refine self-assessment tools for ongoing monitoring. When used effectively, these assessment methods can significantly contribute to an organization's continuous improvement and readiness to adapt to new challenges.

For the purpose of determining DML, 10 academic studies have been selected based on prevalence and appropriateness criteria and are shown in Table 3.

From the 10 selected articles above, 3 studies (Schumacher et al., 2016; Canetta et al., 2018; Durek et al., 2018) are explained below as they form the basis for the conceptual model.

Academics at the Vienna University of Technology have argued that existing methodologies for determining the level of digital maturity are solely technology-focused and have aimed to develop these methodologies by also including company culture and organizational structure (Schumacher et al., 2016). The methodology, which also encompasses technological components like cloud technology, cybersecurity, and the Internet of Things (IoT), has identified a total of 9 main categories for evaluation. Under these 9 main categories, a total of 62 sub-dimensions have been determined. The 9 main categories and sample sub-dimensions are as follows:

- Product: Product system integration, customization of products for customers

- Customers: Use of customer data, digitalization of sales and services

- Operations: Distribution of responsibilities in processes, modeling, and simulation

- Technology: Modern information and communication technologies, machine-to-machine communication

- Strategy: Industry 4.0 roadmap, adaptation to new business models

- Leadership: Leaders' desire for digitalization, central coordination

- Corporate Management: Implementation of technological standards, determination of employee rights compatible with Industry 4.0

- Culture: Knowledge sharing, openness to collaboration with other companies

- Employees: Employees' aptitude for information and communication technologies, speed of adaptation to new technologies

For each of the 62 sub-dimensions, a question has been formulated, and the answers to each question are designed to be scored between 1 and 5. A score of 1 indicates no digital maturity, while a score of 5 indicates that digitalization is at the best possible level (Table 4). Thus, the methodology indicates one of the five levels of digital maturity for each category based on the responses to the self-assessment.

Table 2. *Categories Identified in Studies of Digital Maturity Level Measurements*

Institution	Categories
Deloitte	- Customer - Strategy - Technology - Operations - Organization - Culture
Forrester	- Culture - Technology - Organization - Insight
McKinsey	- Strategy and Innovation - Understanding Customer Decisions - Process Automation - Organization - Technology - Data and Analytics
Huawei	- Strategic Dynamism - Customer Focus - Digital Culture - Innovation and Lean Delivery - Big Data and Artificial Intelligence - Technology Leadership
Acatech	- Resources - Information Systems - Organizational Structure - Culture
European Regional Development Fund (ERDF)	- Strategy and Company Culture - Technology & Cybersecurity - Marketing - Finance & Operations - R&D & Innovation - Sales
CISCO	- Strategy and Organization - Process Management - Technology - Human Resources and Talent
Akamai	- Cybersecurity - Strategy - Digital experience - Cloud solutions - Technology
NHS (Health sector)	- Data literacy - Competencies - Technological Infrastructure
PWC (Energy sector)	- Ability to adapt New Technologies - Digital Ecosystem - Digital Culture
TÜBİSAD	- Ecosystem - Competence - Usage - Transformation
Accenture	- Strategy - Digital Services - Digital Operational Capabilities
BCG - TÜSİAD	- Strategy and Roadmap - Governance - Infrastructure - Data Security

***Table 3.*** *Selected Academic Studies on Digital Maturity Index*

Study Name	Country	Publication Year	Sector	Methodology Type	Citation Count
Industry 4.0 Maturity Readiness and Maturity (Schumacher et al., 2016)	Austria	2016	Manufacturing / Industry	Self-Assessment	528
Digitalization Maturity Model for Manufacturing (Canetta et al., 2018)	Switzerland	2018	Manufacturing / Industry	Self-Assessment	28
Digital Maturity Level of Higher Education Institutions (Durek et al., 2018)	Croatia	2018	Education	Expert Assessment	10
Digital Readiness Assessment Maturity Model (DREAMY) (De Carolis et al., 2017)	Italy	2017	Manufacturing / Industry	Self-Assessment	80
The Maturity Model Industry SIMMI 4.0 (Leyh et al., 2016)	Germany	2017	Manufacturing / Industry	Expert Assessment	71
VTT Model of Digimaturity (Leino et al., 2017)	Finland	2017	All Sectors	Self-Assessment	4
Empirical Maturity Study (Berghaus & Back, 2016)	Switzerland	2016	All Sectors	Self-Assessment	64
Digital Maturity in Traditional Industries (Remane et al., 2017)	Germany	2017	Manufacturing / Industry	Self-Assessment	26
SME's Maturity Model Assessment (Hamidi et al., 2018)	Malaysia	2018	Small – Medium Enterprises	Self-Assessment	13
Digital Hospital Transformation– Maturity Assessment (Williams et al., 2019)	Australia	2019	Health		Expert Assessment	4

Table 4. *Sample Question for Determining the Level of Digital Maturity*

Question	1	2	3	4	5
Do you use a roadmap for the planning required under digitalization and Industry 4.0?	X				

1: We do not use it at all 5: The plan has been completed and we fully act according to it

Not all questions contribute equally to digital maturity, therefore each question has been given a weight. A total of 23 researchers and experts have scored the importance of the questions between 1 and 4, and weights have been determined by averaging these scores. For example, while modern information and communication technologies have received a score of 3.5, the use of mobile devices has received a score of 3.2. Then, weighted averages have been calculated using the weights of the questions, the scores obtained from the answers, and the category to which the questions belong, and the level of digital maturity for each category has been determined. As a result, the digital maturity level that emerges is shown as a score between 1 and 5 across 9 categories (Figure 1), allowing a company to easily see which areas they excel in and which areas are lacking.
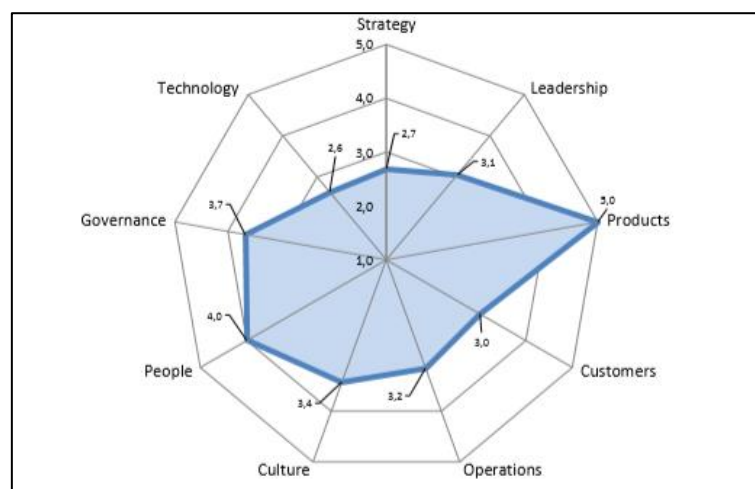
Figure 1. *Sample Digital Maturity Index Assessment Result for a Company*

In the second examined study, a digital maturity model has been developed for the manufacturing/industry sector (Canetta et al., 2018). The methodology in this study consists of three main steps: (i) conducting a survey

to determine the company's current state in the digitalization process and digitalization targets, (ii) conducting interviews with employees for process and operation analysis, and (iii) determining the steps to be taken in the digitalization process through discussions with employees. In the first step, the current level of digital maturity is generally measured, while the remaining steps involve determining more detailed steps for improvement and creating a roadmap. The evaluations measure how much technology has made processes efficient, how much digitalization will reduce the need for human labor, the level of information security, and how integrated technological systems are with devices. For the purpose of evaluations, a total of 36 questions have been determined under 5 main categories. The questions are designed to be inclusive and applicable for the entire industry sector. The 5 main categories and some of the key questions under these categories are as follows:

- Strategy: The company's production and sales strategy (R&D, order methods, stocking, etc.)

- Processes & Operations: Data collection, information security, device system integration, and collaborations

- Products & Services: Product tracking, product and service data management

- Technology: Implementation of new technologies, robust technological infrastructure

- Employees: Technological proficiency of employees and their adaptations to digitalization

It is emphasized that companies should have different digitalization roadmaps due to their distinct production and sales strategies. Accordingly, companies are classified based on the answers given in the strategy category. Different weights are assigned to each question according to this classification. Each question is scored as 0, 1, 2, 3 (none, low, medium, very good) based on the given answers. A digital maturity score between 0 and 3 is calculated for each category using a weighted average based on scores and weights. As a result, an example outcome as shown in Figure 2 is obtained.
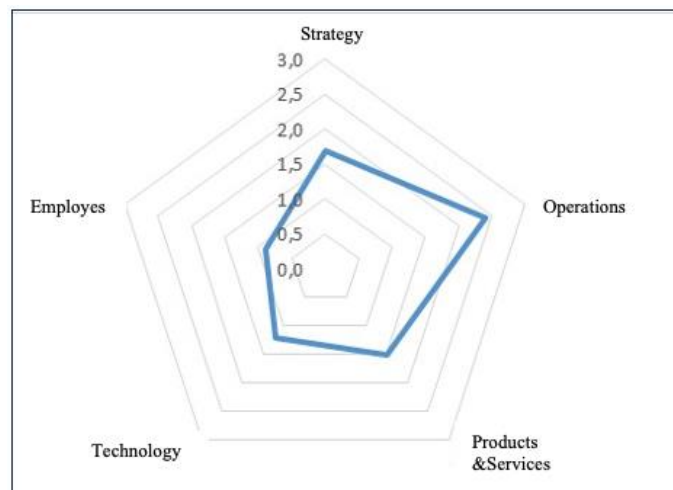

Figure 2. An Example Digital Maturity Index Evaluation Result for a Company

In the third and final study reviewed, academics at the University of Zagreb have conducted a methodology development study to measure the digital maturity level of schools in Croatia (Durek et al., 2018). The study evaluated 15 digital maturity index methods based on surveys and developed their methodology based on these evaluations. Initially, 7 main categories and 53 subheadings were identified by examining the 15 methods. Experts were asked to place these 53 headings into 7 main categories and also to rank them in order of importance. Consequently, the less important headings were eliminated, reducing the number from 53 to 43, which were then matched with the 7 main categories.

The determined 7 main categories and some associated headings are as follows:

- Leadership, Planning, and Management: Financial investments in technology use in teaching, public cooperation in technology integration

- Quality Control: Evaluation of teachers in lecture delivery, research, and other areas

- Scientific Research: Publications and research related to information and technology systems

- Technology Transfer and Community Services: Collaboration with stakeholders, increasing researchers' networks with technology assistance

- Teaching and Learning Processes: Digital competencies of teachers and students

- Information and Communication Technologies Culture: Training and incentivizing employees on digitalization

- Information and Communication Technologies Infrastructure: Network, technical support, and maintenance

Since the importance of the determined 43 elements is not the same, weights have been assigned using the analytical hierarchy method. This method compares all elements in pairs and defines categories such as equally important, slightly more important, and much more important. As a result, each element is assigned a weight between 0 and 1. Similarly, a weight assignment has been made for the determined 7 main categories. The evaluation elements were assessed by experts through discussions with relevant individuals in schools, and a score between 1 and 5 was given for each of the 43 elements, which was then multiplied by the weights to calculate the total score. In total, 5 different maturity levels have been determined for 151 schools.

5. CONCEPTUAL MODEL

After examining digital maturity index models used in academic literature, international and private sector studies in Türkiye, a conceptual model proposal has been developed for the Turkish electricity distribution sector. It has been observed that the studies show very similar characteristics but there was no study specifically for the electricity distribution sector. A model proposal to determine the digital maturity level specifically for the electricity distribution sector has been suggested.

In order to develop a robust set of survey questions for assessing digital maturity within the electricity distribution sector, a multi-faceted approach is employed. Initially, a literature review is conducted to thoroughly examine existing academic research, industry reports, and case studies. This review is crucial for identifying key factors and metrics previously used to measure digital maturity, ensuring that the survey is comprehensive and rooted in established theories and practices. Following this, consultations with industry experts, such as IT professionals, digital transformation consultants, and senior executives from electricity distribution companies, are undertaken to obtain practical insights into the sector's digitalization. These professionals can assess the survey's relevance and provide practical input that might not be immediately apparent from the literature.

Next, benchmarking is carried out to analyze digital maturity models from various industries and sectors, identifying those that could be adapted or serve as reference points for the electricity distribution sector. This involves customizing questions to address the specific challenges and opportunities present in the energy sector. Additionally, focus groups and interviews are organized with employees at different levels within electricity distribution companies. These discussions aim to capture their perceptions and experiences of digital transformation, with in-depth interviews offering nuanced insights that further refine the survey questions.

Finally, pilot testing is implemented. This stage involves creating an initial set of survey questions derived from the aforementioned methods and conducting a pilot survey to test them. Feedback gathered from this pilot phase is instrumental in fine-tuning the questions, ensuring clarity, lack of ambiguity, and effective measurement of the intended constructs. This comprehensive process is essential for crafting a survey that accurately gauges digital maturity in the electricity distribution sector.

To determine the digital maturity level in detail, different categories and subtopics have been identified. The aim here is to reduce complexity by dividing the assessment into as many independent small business units as possible. Also, this method will help to indicate which areas the companies are successful in and which areas they are lacking when the digital maturity level is determined. The identified categories and subtopics are shown in Figure 3.
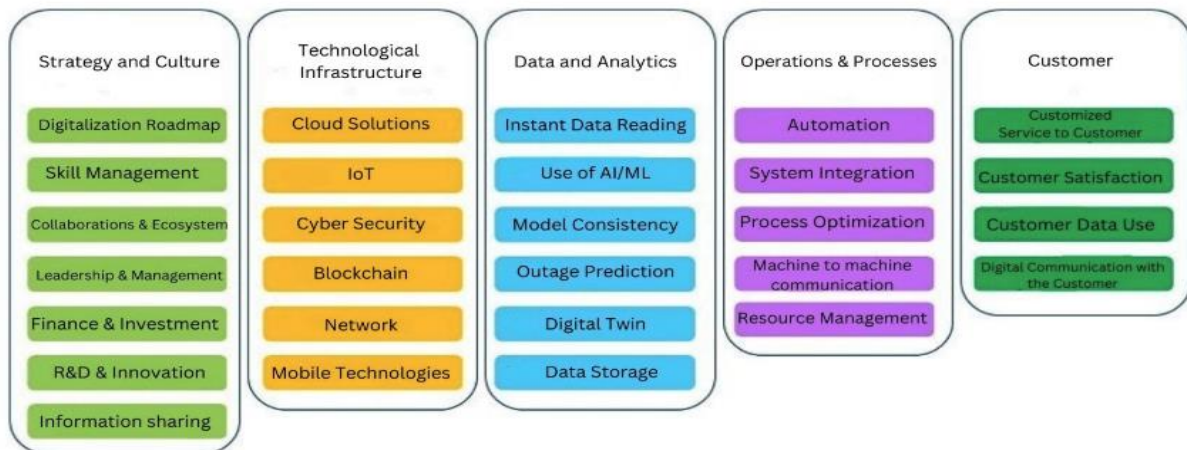

Figure 3. Categories and Subtopics of the Digital Maturity Model

For each subcategory, typically 3-4 survey questions are determined. These survey questions are designed to have multiple-choice answers only. Each option corresponds to a score between 0 and 100, predetermined. The questions have different weights due to their different contributions to digital maturity. These weights are determined by the average score given by subject matter experts rating the questions from 1 to 5. The final weight coefficient will be determined by rounding the result of the average score to the nearest decimal.

The proposed conceptual model for measuring the digital maturity level in electricity distribution companies is underpinned by a set of equations that systematically derive a Final Digital Maturity Index (FDMI).

Equation 1 is the FDMI which is a weighted average that gives you the overall digital maturity score for the company:

1. Each category of digital maturity within the company is given a score, which we call Digital Maturity Index (DMI_i) where i represents the category number (for example, 1 for 'Infrastructure', 2 for 'Skills', etc.).

2. Each of these category scores is multiplied by its importance to the company, represented by a weight coefficient W_i. If you think the 'Infrastructure' category is twice as important as 'Skills', you might give 'Infrastructure' a weight of 4 and 'Skills' a weight of 2.

3. You then add up all these weighted scores.

4. To get the average, you divide the total by the sum of all the weight coefficients. This ensures that the FDMI score is normalized and not skewed by the number of categories or the scale of their weights.

Equation 2 calculates the (DMI_i,) for each category. It is similar to Equation 1 but at a category level:

1. Within each category, every question about digital maturity is scored, Maturity Score (MS_s), with s representing the specific survey question.

2. Each question score is multiplied by its own weight (W_s), because some questions are more important than others.

3. These weighted question scores are added together.

4. The sum is then divided by the total weight of all questions in that category to get the average score for the category (DMI$_i$,).

Equation 3 defines how to calculate the weight coefficient (W_i) for each category:

1. It sums the weights of all the questions within a category (W_s).

2. Then it divides this sum by the number of questions (n_i) in that category to get an average weight for the category.

In summary:

- Equation 1 gives the big picture: the final digital maturity score for the whole company.

- Equation 2 zooms into each category, giving a score for that category based on the survey questions it contains.

- Equation 3 helps to understand the average importance given to each category based on the weights of the questions it includes.

Together, these equations provide a comprehensive mathematical model to assess and quantify the digital maturity of electricity distribution companies, allowing for comparisons across different categories and the company as a whole.

$$FDMI = \sum_{i=1}^{5} \frac{DMI_i * W_i}{\sum_i W_i} \tag{1}$$

$$DMI_i = \frac{\sum_{s \in i} MS_s * W_s}{\sum_{s \in i} W_s} \tag{2}$$

$$W_i = \frac{\sum_{s \in i} W_s}{n_i} \tag{3}$$

FDMI: *Final Digital Maturity Index*

DMI$_i$: *Digital Maturity Index for category i.*

MS$_s$: *Maturity score for question s (between 0 and 100)*

W$_s$: *Weight coefficient for question s (between 1 and 5)*

W$_i$: *Weight coefficient for category i (between 1 and 5)*

n$_i$: *Number of questions in category i*

Using these formulas, a digital maturity index score for each category is obtained between 0 and 100, and the average of these scores constitute the FDMI. Based on this index score, companies are labeled with one of five digital maturity level categories. Example question scoring is shown in Tables 5 and 6.

Table 5. Example Question for Determining Digital Maturity Level

Score	Digital Level
0-20 points	Unaware
21-40 points	Mediocre
41-60 points	Follower
61-80 points	Effective User
81-100 points	Leader

Table 6. Example Question for Determining Digital Maturity Level

Question Category	Strategy and Culture
Subcategory	Finance & Investment
Question	How much have you invested in the digitalization process in the last 5 years?
Question Weight (1-5)	3.8
Options and Scoring	• 0 - 250,000 TL (0 points) • 250,000 TL – 1 million TL (20 points) • 1 – 5 million TL (40 points) • 5-10 million TL (60 points) • 10-25 million TL (80 points) • Above 25 million TL (100 points)

6. LIMITATIONS AND FUTURE WORK

Potential limitations and challenges are: The electricity distribution sector is inherently complex, with a wide array of regulatory, technical, and operational factors. A model that aims to measure digital maturity must be sensitive to these complexities, which can vary widely between regions and companies. The model may struggle to account for all these nuances, leading to oversimplifications. Reliable data is the backbone of any maturity assessment. However, the availability and quality of data within electricity distribution companies can be a limiting factor. Some companies may not have the required data collection infrastructure in place or may have data that is incomplete or not up to date, which can skew the assessment results. Organizational culture and resistance to change can be significant barriers. The model's effectiveness is contingent on the company's willingness to accurately self-assess and implement recommended changes. A company that is resistant to acknowledging its digital shortcomings may not fully benefit from the model. The model suggests a hybrid approach of self-assessment and expert evaluation. However, finding experts with the requisite knowledge of both the digital and electricity distribution domains to perform these evaluations can be difficult. The electricity distribution sector is heavily regulated. Any model that seeks to measure and improve digital maturity must be aligned with regulatory requirements, which can be a moving target as regulations evolve. To address these limitations and challenges, the proposed model need to include mechanisms for regular updates to keep pace with technological changes, flexible metrics that can be customized for different company profiles, and a clear, actionable roadmap for companies to follow in addressing their digital maturity gaps.

Further research could focus on refining the digital maturity model based on feedback from initial implementations. Validation of the model through longitudinal studies across various companies could strengthen its reliability and predictive power. Customization for different market regulations through developing tailored versions of the model to account for different regulatory environments across countries or regions could improve the robustness of the model. This would involve studying the impact of regulations on digital maturity and incorporating these insights into the model. Future research could also focus on exploration of how the model interacts with and supports the adoption of smart grid technologies. Future studies moreover could measure the economic impact of increased digital maturity on electricity distribution companies, including cost savings, return on investment, and impact on revenue. Since digitalization increases cybersecurity risks, future work could develop methodologies for incorporating cybersecurity assessments into

the digital maturity model. Using machine learning and data mining techniques to predict the outcomes of digital maturity efforts could be another future work which help companies anticipate the benefits and challenges of their digitalization strategies.

7. CONCLUSION

In conclusion, this study has proposed a conceptual model for measuring the digital maturity level in electricity distribution companies, filling a critical gap in the existing literature. With the increasing importance of digitalization and technological advancements, the need for tools to assess and accelerate the digital transformation process in various sectors, including electricity distribution, has become imperative. The unique challenges and opportunities within the electricity distribution sector necessitate a tailored approach to digital maturity assessment.

The conceptual model presented here is grounded in an extensive review of digital maturity models across diverse sectors, with a specific focus on electricity distribution. Recognizing the multifaceted nature of digital maturity, the proposed model encompasses categories and subtopics crucial for a comprehensive evaluation. By adopting a hybrid approach that combines self-assessment surveys and expert evaluations, the model aims to provide a nuanced understanding of the digitalization landscape within electricity distribution companies.

The significance of digital maturity in the electricity distribution sector cannot be overstated, given the transformative impact of technology on grid management, energy efficiency, and customer engagement. The proposed model addresses key areas such as finance and investment, strategy and culture, and technological trends, aligning them with the specific needs of electricity distribution companies. Furthermore, the model incorporates a quantitative measure in the form of a Digital Maturity Index, allowing for a standardized and comparative assessment across companies. The index, derived through a systematic formula involving survey responses and expert weights, provides a numerical representation of digital maturity levels. This numerical scoring system enables companies to benchmark their progress and categorize themselves into distinct digital maturity levels, ranging from Unaware to Leader.

It is crucial to note that the success of the proposed model lies not only in its ability to evaluate the current digital maturity of electricity distribution companies but also in guiding them toward a strategic roadmap for future digitalization efforts. As the electricity distribution sector continues to evolve with advancements such as smart grids, distributed production, and electric vehicles, the proposed model can serve as a valuable tool for companies to stay competitive and resilient in an increasingly digital environment.

In summary, this study contributes to the literature by introducing a tailored conceptual model for assessing digital maturity in electricity distribution companies. The model provides a structured framework for companies to evaluate, strategize, and enhance their digitalization efforts, ultimately paving the way for a more efficient, sustainable, and technologically advanced electricity distribution sector.

CONFLICT OF INTEREST

The author declares no conflict of interest.

REFERENCES

Accenture. (2017). Accenture Türkiye dijitalleşme endeksi. (Technical Report).

Agarwal, R., Gao, G. (Gordon), DesRoches, C., & Jha, A. K. (2010). The digital transformation of healthcare: Current status and the road ahead. *Information Systems Research*, *21*(4), 796-809. https://doi.org/10.1287/isre.1100.0327

Akamai. (2018). Advancing digital maturity in financial services.

Annunziata, M., & Bell, G. (2015). Powering the future: Leading the digital transformation of the power industry. General Electric.

Asiltürk, A. (2021). İşletmelerde dijital dönüşüm yönetiminde nihai hedef: Dijital olgunluk. *Alanya Akademik Bakış*, *5*(2), 647-669. https://doi.org/10.29023/alanyaakademik.859300

Berghaus, S., Back, A. (2016). *Stages in digital business transformation: Results of an empirical maturity study*. In: Proceedings of the Mediterranean Conference on Information Systems (MCIS).

Bharadwaj, A., El Sawy, O. A., Pavlou, P. A., & Venkatraman, N. (2013). Digital business strategy: Toward a next generation of insights. *MIS Quarterly*, *37*, 471-482. https://doi.org/10.25300/MISQ/2013/37:2.3

Canetta, L., Barni, A., & Montini, E. (2018, June 17-20). *Development of a digitalization maturity model for the manufacturing sector*. In: Proceedings of the IEEE International Conference on Engineering, Technology and Innovation, Stuttgart, Germany. https://doi.org/10.1109/ICE.2018.8436292

Catlin, T., Scanlan, J., & Willmott, P. (2015). Raising your digital quotient. *McKinsey Quarterly*, *3*, 30-43.

Cisco. (2019). Cisco APAC SMB Digital maturity index. Cisco Systems.

Corr, J. (2022, April 6). *Unleashing the power of digital marketing: The digital maturity model explained*. Seer Interactive. URL: https://www.seerinteractive.com/insights/introduction-to-digital-maturity

Dahlström, P., Desmet, D., & Singer, M. (2017). The seven decisions that matter in a digital transformation: A CEO's guide to reinvention. *Digital/McKinsey: Insights*, *3*, 18-23.

De Carolis, A., Macchi, M., Negri, E., & Terzi, S. (2017, September 3-7). *A maturity model for assessing the digital readiness of manufacturing companies*. In: H. Lödding, R. Riedel, K-D. Thoben, G. von Cieminski, & D. Kiritsis (Eds.), Proceedings of the Advances in Production Management Systems. The Path to Intelligent, Collaborative and Sustainable Manufacturing (APMS 2017), (pp 13-20), Hamburg, Germany. https://doi.org/10.1007/978-3-319-66923-6_2

Deloitte. (2018). Digital maturity model achieving digital maturity to drive growth.

Deloitte Digital (2018). *EMEA digital banking maturity 2018: How to become a digital champion and why only few succeed?*.

Durek, V., Kadoic, N., & Redjep, N. B. (2018, May 21-25). *Assessing the digital maturity level of higher education institutions*. In: Proceedings of the 41st International Convention on Information and Communication Technology, Electronics and Microelectronics (MIPRO), Opatija, Croatia. http://doi.org/10.23919/MIPRO.2018.8400126

Düzcan, A., & Fidan, Y. (2023). İşletmelerde dijital olgunluk düzeyinin yenilik performansı üzerindeki etkisinde büyük veri analitik yeteneğinin aracı ve veri odaklı kültürün düzenleyici rolü. *İstanbul Ticaret Üniversitesi Sosyal Bilimler Dergisi*, *22*(46), 356-389. https://doi.org/10.46928/iticusbe.1294014

Feliciano-Cestero, M. M., Ameen, N., Kotabe, M., Paul, J., & Signoret, M. (2023). Is digital transformation threatened? A systematic literature review of the factors influencing firms' digital transformation and internationalization. *Journal of Business Research*, *157*, 113546. https://doi.org/10.1016/j.jbusres.2022.113546

Gill, M., & VanBoskirk, S. (2016). The digital maturity model 4.0. Benchmarks: digital transformation playbook.

Growth Hub. (2019). Digital maturity index. Growth Hub. URL: https://www.thegrowthhub.biz/digital-maturity-index

Gürder, F. (2022, August 17-18). *Türkiye'deki işletmelerin dijital olgunluğu*. In: Proceedings of the İzmir International Conference on Technology and Social Sciences (IICTSS 2022), New Studies and Trends in Social Sciences, (pp. 40-41), İzmir, Türkiye.

Hamidi, S. R., Aziz, A.A., Shuhidan, S.M., Aziz, A.A., & Mokhsin, M. (2018, March 19-22). *SMEs maturity model assessment of IR4.0 digital transformation*. In: A. M. Lokman, T. Yamanaka, P. Lévy, K. Chen, & S. Koyama (Eds.), Proceedings of the International Conference on Kansei Engineering & Emotion Research, (KEER 2018), (pp 721-732), Kuching, Sarawak, Malaysia. http://dx.doi.org/10.1007/978-981-10-8612-0_75

Haryanti, T., Rakhmawati, N. A., & Subriadi, A. P. (2023). The extended digital maturity model. *Big Data and Cognitive Computing*, *7*(1), 17. https://doi.org/10.3390/bdcc7010017

IEA. (2017). Energy Access Outlook 2017. URL: https://www.iea.org/reports/energy-access-outlook-2017

Karimi, J., & Walter, Z. (2015). The role of dynamic capabilities in responding to digital disruption: A factor-based study of the newspaper industry. *Journal of Management Information Systems*, *32*, 39-81. https://doi.org/10.1080/07421222.2015.1029380

Kraus, S., Jones, P., Kailer, N., Weinmann, A., Chaparro-Banegas, N., & Roig-Tierno, N. (2021). Digital transformation: An overview of the current state of the art of research. *Sage Open*, *11*(3). https://doi.org/10.1177/21582440211047576

Leino, S.-P., Kuusisto, O., Paasi, J., & Tihinen, M. (2017). VTT model of digimaturity. In: J. Paasi (Eds.), *Towards a new era in manufacturing: Final report of VTT's for industry spearhead programme*, (pp. 41-46). VTT Technical Research Centre of Finland.

Leroi, A., Martynov, A., (2020). How utilities can regain control of their technology roadmap. Bain & Company. URL: https://www.bain.com/insights/how-utilities-can-regain-control-of-their-technology-roadmap/

Leyh, C., Bley, K., Schäffer, T., & Forstenhäusler, S. (2016, September 11-14). *SIMMI 4.0-a maturity model for classifying the enterprise-wide IT and software landscape focusing on Industry 4.0*. In: Proceedings of the Federated Conference on Computer Science and Information Systems (FedCSIS), Gdansk, Poland.

Majchrzak, A., Markus, M. L., & Wareham, J. (2016). Designing for digital transformation: Lessons for information systems research from the study of ICT and societal challenges. *MIS Quarterly*, *40*(2), 267-277. https://doi.org/10.25300/misq/2016/40:2.03

Matt, C., Hess, T., & Benlian, A. (2015). Digital transformation strategies. *Business & Information Systems Engineering*, *57*(5), 339-343. http://dx.doi.org/10.1007/s12599-015-0401-5

NHS. (2019). Connected digital systems-Maturity Index. National Health Service UK.

Nuroğlu, E., & Nuroğlu, H. H. (2018). Türkiye ve Almanya'nın sanayide dijital dönüşümü: Yol haritaları ve şirketlerin karşılaştırması. *Süleyman Demirel Üniversitesi İktisadi ve İdari Bilimler Fakültesi Dergisi*, *23*(Endüstri 4.0 ve Örgütsel Değişim Özel Sayısı), 1537-1560.

Open Roads Community. (2020). Open Digital Maturity Model. Open Roads Community.

Perera, S., Jin, X., Das, P., Gunasekara, K., & Samaratunga, M. (2023). A strategic framework for digital maturity of design and construction through a systematic review and application. *Journal of Industrial Information Integration*, *31*, 100413. https://doi.org/10.1016/j.jii.2022.100413

PwC. (2015). The digitalization of utilities. PwC.

PwC. (2019). Digital operations study for energy - Power and utilities. PwC.

Remane, G., Hanelt, A., Wiesboeck, F., & Kolbe, L (2017). *Digital maturity in traditional industries–an exploratory analysis*. In: Proceedings of the 25th European Conference on Information Systems (ECIS 2017).

Schuh, G., Anderl, R., Gausemeier, J., ten Hompel, M., & Wahlster, W. (Eds.) (2018). Industrie 4.0 Maturity Index: Managing the Digital Transformation of Companies. Acatech.

Schumacher, A. S., Erol, S., & Sihn, W. (2016). A maturity model for assessing Industry 4.0 readiness and maturity of manufacturing enterprises. *Procedia CIRP*, *52*(1), 161-166. https://doi.org/10.1016/j.procir.2016.07.040

Svahn, F., Mathiassen, L., & Lindgren, R. (2017). Embracing digital innovation in incumbent firms: How Volvo Cars managed competing concerns. *MIS Quarterly*, *41*(1), 239-253. http://dx.doi.org/10.25300/MISQ/2017/41.1.12

TÜBİSAD. (2023). Türkiye'nin dijital dönüşüm endeksi 2022. TÜBİSAD.

TÜSİAD. (2017). Türkiye'nin sanayide dijital dönüşüm yetkinliği. TÜSİAD.

Vial, G. (2021). Understanding digital transformation: A review and a research agenda. *The Journal of Strategic Information Systems*, *28*(2) 118-144. https://doi.org/10.1016/j.jsis.2019.01.003

Westerman, G., Calméjane, C., Bonnet, D., Ferraris, P., & McAffee, A. (2011). Digital transformation: A roadmap for billion-dollar organizations. MIT Sloan Management.

Williams, P. A. H., Lovelock, B., Cabarrus, T., & Harvey, M. (2019). Improving digital hospital transformation: Development of an outcomes-based infrastructure maturity assessment framework. *JMIR Medical Informatics*, *7*(1). https://doi.org/10.2196/12465

World Economic Forum. (2018). The digital enterprise: Moving from experimentation to transformation. URL: https://www.weforum.org/publications/the-digital-enterpise-moving-from-experimentation-to-transformation/

Zaoui, F., & Souissi, N. (2020). Roadmap for digital transformation: A literature review. *Procedia Computer Science*, *175*, 621-628. https://doi.org/10.1016/j.procs.2020.07.090

JOURNAL OF SCIENCE

PART A: ENGINEERING AND INNOVATION